Preface

The 2019 Geophysical Fluid Dynamics Summer Study Program theme was *Stratified Turbulence and Ocean Mixing Processes.*Two principal lecturers, Stephanie Waterman (University of Victoria) and Colm-cille Caulfield (University of Cambridge) were our expert guides for the first two weeks. Colm covered the theoretical aspects of stratified turbulence, from simple scaling laws to sophisticated, modern numerical results. Stephanie kept the enthusiastic audience grounded with her lectures on ocean mixing processes, observations, and their many technical challenges.

The first ten chapters of this volume document these lectures, each prepared by pairs of the summer's GFD fellows. Following the principal lecture notes are the written reports of the fellows' own research projects. This summer's fellows were:

- Houssam Yassin, Princeton University
- Channing Prend, Scripps Institution of Oceanography
- Andre Paloczy Filho, University of California San Diego
- Jeremy Parker, University of Cambridge
- Wanying Kang, Harvard University
- Lois Baker, Imperial College London
- Kelsey Everard, The University of British Columbia
- Anuj Kumar, University of California Santa Cruz
- Alessia Ferraro, Ecole Polytechnique Federale de Lausanne
- Samuel Boury, ENS de Lyon
- Jelle Will, University of Twente
- Wenjing Dong, New York University

The 2019 Sears Public Lecture was delivered by Professor Lydia Bourouiba (Massachusetts Institute of Technology) on *Fluids and Health.* Lydia's entertaining and interesting talk introduced the audience to, among several topics, the fluid mechanical details of a sneeze. Everyone was motivated to get their flu shot.

Claudia Cenedese, Bruce Sutherland and Karl Helfrich were co-directors. The summer was marked by a large number of long-term staff members, as well as one of our largest-ever audiences for the principal lectures (necessitating an overflow room). The staff members and many long-term visitors ensured that the fellows never lacked for guidance, and the seminar series was filled by a steady stream of more than 30 talks on topics as diverse as microgravity snow and hydrothermal megaplumes.

As usual, laboratory experiments were facilitated by able support from Anders Jensen. Janet Fields and Julie Hildebrandt made sure that the administrative side of the summer ran smoothly. We continue to be indebted to WHOI Academic Programs Office, who once more provided a perfect atmosphere.

Table of Contents

Principal Lectures

Fellows' Reports

2019 Geophysical Fluid Dynamics Participants

FELLOWS

Lois Baker	Imperial College London
Samuel Boury	École Normale Supérieure de Lyon
Wenjing Dong	New York University
Kelsey Everard	University of British Columbia
Alessia Ferraro	École Polytechnique Fédérale de Lausanne
Wanying Kang	Harvard University
Anuj Kumar	University of California Santa Cruz
André Palóczy Filho	University of California San Diego
Jeremy Parker	University of Cambridge
Channing Prend	Scripps Institution of Oceanography
Jelle Will	University of Twente
Houssam Yassin	Princeton University

STAFF AND VISITORS

Matthew Alford	University of California San Diego
Dwight Barkley	University of Warwick
Neeraja Bhamidipati	University of Cambridge
Kenneth Brink	Woods Hole Oceanographic Institution
Oliver Bühler	New York University
Jorn Callies	California Institute of Technology
Claudia Cenedese	Woods Hole Oceanographic Institution
Eonho Chang	University of California Santa Cruz
Gregory Chini	University of New Hampshire
Navid Constantinou	Australian National University
Baptiste Coquinot	University of Texas at Austin
Predrag Cvitanovic	Georgia Institute of Technology
Megan Davies Wykes	University of Cambridge
David Deepwell	University of Alberta
Charles Doering	University of Michigan
Thomas Eaves	University of Dundee
Raffaele Ferrari	Massachusetts Institute of Technology
Glenn Flierl	Massachusetts Institute of Technology
Federico Fuentes	Cornell University
Basile Gallet de St-Aurin	CEA, Saclay
Pascale Garaud	University of California Santa Cruz
Renske Gelderloos	Johns Hopkins University
David Goluskin	University of Victoria
Karl Helfrich	Woods Hole Oceanographic Institution
Jeffrey Heninger	University of Texas at Austin
Christopher Howland	University of Cambridge
Bryan Kaiser	Woods Hole Oceanographic Institution

Alexis Kaminski	University of Washington
Jacob Langham	University of Bristol
Michael Le Bars	Institut de Recherche sur les Phénoménes Hors Equilibre
Norman Lebovitz	University of Chicago
Daniel Lecoanet	Princeton University
Sonya Legg	Princeton University
Tyler Lutz	Yale University
Alireza Mashayekhi	Imperial College London
Jim McElwaine	Durham University
Eckart Meiburg	University of California Santa Barbara
Colin Meyer	Dartmouth College
Philip Morrison	University of Texas at Austin
Isabelle Sindizwa Nunes da Costa	University of Cape Town
James Parkinson	University of Oxford
Joseph Pedlosky	Woods Hole Oceanographic Institution
Samuel Pegler	University of Leeds
Larry Pratt	Woods Hole Oceanographic Institution
James Riley	University of Washington
Hesam Salehipour	University of Toronto
Matthew Scase	University of Nottingham
Sutirtha Sengupta	University of California Santa Cruz
Katherine Smith	University of Cambridge
William Smyth	Oregon State University
Alexander Soloviev	NOVA Southeastern University
Andre Souza	Massachusetts Institute of Technology
Geoff Stanley	University of New South Wales
Bruce Sutherland	University of Alberta
Jim Thomas	University of North Carolina
Laurette Tuckerman	Sorbonne University
Barbara Turnbull	University of Nottingham
Geoffrey Vallis	University of Exeter
Ton van den Bremer	University of Oxford
Geoffrey Vasil	University of Sydney
Subhas Karan Venayagamoorthy	Colorado State University
Stephanie Waterman Block	University of British Columbia
Andrew Wells	University of Oxford
Jack Whitehead	Woods Hole Oceanographic Institution

2019 Principal Lecturers

Colmcille-Caulfield & Stephanie Waterman

2019 Geophysical Fluid Dynamics Summer School Participants

First Row (L-R): (All seated) Wanying Kang, Jelle Will, Samuel Boury, Alessia Ferraro, Jeremy Parker, Wenjing Dong, Anuj Kumar, Houssam Yassin, Lois Baker, Channing Prend, Kelsey Everard, André Palóczy Filho

Second Row (L-R): Charlie Doering, Greg Chini, David Goluskin, Ali Mashayek, Karl Helfrich, Phil Morrison, Renske Gelderloos, Megan Davies Wykes, Alexis Kaminski, Katherine Smith, Neeraja Bhamidipati, Stephanie Waterman Block, Laura Cimoli, Oliver Bühler, Pascale Garaud, Chun Zhou

Third Row (L-R): (All standing) Jeffrey Heninger, Andrew Wells, Shuwen Tan, William Smyth, Colm Caulfield, Andre Souza, Baptiste Conquinot, Guilherme Salvador Viera, Larry Pratt, Jacob Langham, Brian von Herzen, Glenn Flierl, Bruce Sutherland, Tyler Lutz, Alexander Soloviev, Joe Pedlosky, Jim Riley, Isabelle Giddy, Geoff Vasil, Geoff Stanley, Claudia Cenedese, Jim McElwaine, Bofu Zheng, Dezhou Yang

Missing from photo: Matthew Alford, Dwight Barkley, Jorn Callies, Eonho Chang, Navid Constantinou, Predrag Cvitanovic, Tom Eaves, Federico Fuentes, Basile Galletm Isabelle Giddy, Chris Howland, Michael Le Bars, Daniel Lecoanet, Sonya Legg, Eckart Meiburg, Colin Meyer, James Parkinson, Sam Pegler, Hesam Salehipour, Matthew Scase, Sutirtha Sengupta, Jim Thomas, Laurette Tuckerman, Barbara Turnbull, Ton van den Bremer, Karan Venayagamoorthy, George Veronis

Lecture Schedule

PRINCIPAL LECTURES

Monday, June 17
Ocean Mixing Processes 1: Why Ocean Turbulence Matters
Stephanie Waterman

Tuesday, June 18
Ocean Mixing Processes 2: Measuring and Quantifying Ocean Mixing
Stephanie Waterman

Wednesday, June 19
Ocean Mixing Processes 3: Rates and Mechanisms —What We Observe and Interpret from Observations of Mixing and Turbulence in the Ocean Interior
Stephanie Waterman

Thursday, June 20
Stratified Turbulence 1: Introduction to Turbulence Theory for Stratified Flows
Colm-cille Caulfield

Friday, June 21
Stratified Turbulence 2: Effects of Stratification and/or Shear on Turbulence and Their Description by Nondimensional Parameters
Colm-cille Caulfield

Monday, June 24
Stratified Turbulence 3: Shear Instabilities in Stratified Fluids
Colm-cille Caulfield

Tuesday, June 25
Stratified Turbulence 4: Stratified Shear Instabilities
Colm-cille Caulfield

Wednesday, June 26
Stratified Turbulence 5: Open Questions and Controversies in Stratified Turbulence Mixing Research
Colm-cille Caulfield

Thursday, June 27
Stratified Turbulence and Oceanic Mixing Processes 1: Challenges in and Promising Approaches for Connecting Theory to Observation
Stephanie Waterman and Colm-cille Caulfield

Friday, June 28
Part I: Stratified Turbulence and Ocean Mixing Processes 2: Future Directions for Research into Stratified Turbulence and Ocean Mixing Processes
Stephanie Waterman

SEMINARS

Monday, July 15
Self-organized Criticality and Mixing in Geophysical Flows
William Smyth, Oregon State University

Tuesday, July 16

1) Thermosolutal Convection as a 2 x 2 Matrix Problem
2) Taylor-Couette Flow: Self-sustaining Process and Heteroclinic Cycles
Laurette Tuckerman, Physique et Mécanique des Millieux Hétérogènes

Wednesday, July 17
Making Snow in Microgravity
Barbara Turnbull, University of Nottingham

Thursday, July 18
Effects of Upper Ocean Turbulence on Biogeochemical Tracers
Katherine Smith, University of Cambridge

Friday, July 19
Diapycnal Mixing in Stably Stratified Turbulence: An Overview and Some Insights for Improved Prediction
Karan Venayagamoorthy, Colorado State University

Monday, July 22
A Mushy Dragon: Convective Localization in Sea Ice
Andrew Wells, Oxford University

Tuesday, July 23
Towards using Machine Learning for the Discovery of Sub-grid Scale Dynamics
Hesam Salehipour, University of Toronto

Wednesday, July 24
Instability of Sheared Density Interfaces
Tom Eaves, University of British Columbia

Thursday, July 25
Ocean Turbulence: Importance, Techniques and Case Studies
Matthew Alford, University of California San Diego

Friday, July 26
What on Earth is Going on on Mars?
Jim McElwaine, Durham University

Monday, July 29
Thermals in the Atmosphere and in Stars
Daniel Lecoanet, Princeton University

Tuesday, July 30
Unsteady Turbulent Plumes
Matthew Scase, University of Nottingham

Wednesday, July 31
The Mechanics of a Large Pendulum Chain
Geoffrey Vasil, University of Sydney

Thursday, August 1
Transition to Turbulence
Dwight Barkley, University of Warwick

Friday, August 2
The Topology of Neutral Surfaces and Their Exact Geostrophic Streamfunction
Geoff Stanley, University of New South Wales

Monday, August 5
Tides and Libration as Sources of Turbulence and Dynamo in Planetary Cores
Michael Le Bars, Institut de Recherche sur les Phénomènes Hors Equilibre

Tuesday, August 6
Some Converging Thoughts on the Role of Shear-induced Turbulent Mixing in Deep Ocean Circulation
Ali Mashayek, Imperial College London

SEARS PUBLIC LECTURE – Redfield Auditorium
Fluids and Health
Lydia Bourouiba, Massachusetts Institute of Technology

Wednesday, August 7
Water-to-Air Transfer: Bubbles at the Interface
Lydia Bourouiba, Massachusetts Institute of Technology

Thursday, August 8
Dispersal of Volcanic Material during Deep-sea Eruptions and the Generation of Hydrothermal Megaplumes
Sam Pegler, University of Leeds

Friday, August 9
Internal-tide Driven Mixing: Processes, Parameterizations and Impacts
Sonya Legg, Princeton University

FELLOWS' PRESENTATIONS

Monday, August 19

Sensitivity of the Ocean's Deep Circulation to Westerly Winds
Houssam Yassin, Princeton University

Eddy Mixing of Biogeochemical Tracers
Channing Prend, Scripps Institution of Oceanography

Reduced Models for Wave-balanced Flow Interactions
André Palóczy Filho, University of California San Diego

Exploiting Sum-of-squares Optimisation for Chaotic Hamiltonian Systems
Jeremy Parker, University of Cambridge

Tuesday, August 20

Symmetry Breaking on the Enceladus Ice Shell
Wanying Kang, Harvard University

Interaction Between Internal Modes and Their Superharmonics
Lois Baker, Imperial College London

Wednesday, August 21

Free Convection with Large Viscosity Variations
Kelsey Everard, The University of British Columbia

Maximal Heat Transport in Rayleigh-Bénard Convection: Reduced Models, Bifurcations, and Polynomial Optimization
Anuj Kumar, University of California Santa Cruz

Exploiting Marginal Stability in Slow-fast Quasilinear Dynamical Systems
Alessia Ferraro, Ecole Polytechnique Federale de Lausanne

A Mushy Source for the Geysers of Enceladus
Samuel Boury, ENS de Lyon

Thursday, August 22

Optimal Mixing of a Passive Scalar Field in Kolmogorov Flow
Jelle Will, University of Twente

Structure and Stability of Flow Around Noncircular Islands
Wenjing Dong, New York University

GFD 2019 Lecture 1: Why Ocean Turbulence Matters

Stephanie Waterman; notes by Lois Baker and Houssam Yassin

June 17, 2019

This lecture series, given over 2 weeks in summer 2019 at the Woods Hole Oceanographic Institution (WHOI) Geophysical Fluid Dynamics (GFD) summer school aims to address:

1. Recent theoretical developments in the fluid dynamical description of turbulent stratified mixing
2. The relevance of such mixing to the world's oceans from the perspective of an observational oceanographer

We begin with the latter, with lectures given by Physical Oceanographer Dr Stephanie Waterman. The following 3 lectures aim to:

1. Keep it real
2. Ask the tough questions:
    - Why does this matter?
    - What can we actually measure?
    - What does turbulence & mixing in the ocean actually look like?
    - How does the theory relate to what we see?

This lecture aims to answer the question: **why does ocean turbulence matter?**

1 The Downscale Cascade of Energy

To motivate the importance of turbulence in ocean flows, first consider the spatial scales relevant to ocean circulation, some of which are illustrated in figure 1.

Solar insolation incident on the Earth is unevenly distributed. Averaged over a year, the equator receives more energy from the sun than the poles. This implies that in steady state, there must be a net transfer of heat from the equator to the pole. On Earth, this poleward heat transport is accomplished predominantly through the turbulent large-scale circulation of the atmosphere. It is this circulation of the atmosphere that is responsible for ocean circulation.

At the largest scales, the alternating pattern of easterlies and westerlies produces the gyre circulation in the world's ocean basins. Typical length-scales of an ocean gyre are on the order of thousands of kilometers. The ocean's gyre circulation is not laminar; rather it is turbulent and is susceptible to a host of hydrodynamic instabilities that produce smaller scale features (on the order of 100km) called mesoscale eddies. Further instabilities and interaction of these eddies with topography can then produce smaller scale (submesoscale) fronts and eddies with length scales of less than 10km. At even smaller scales, shear instabilities of either submesoscale features or internal

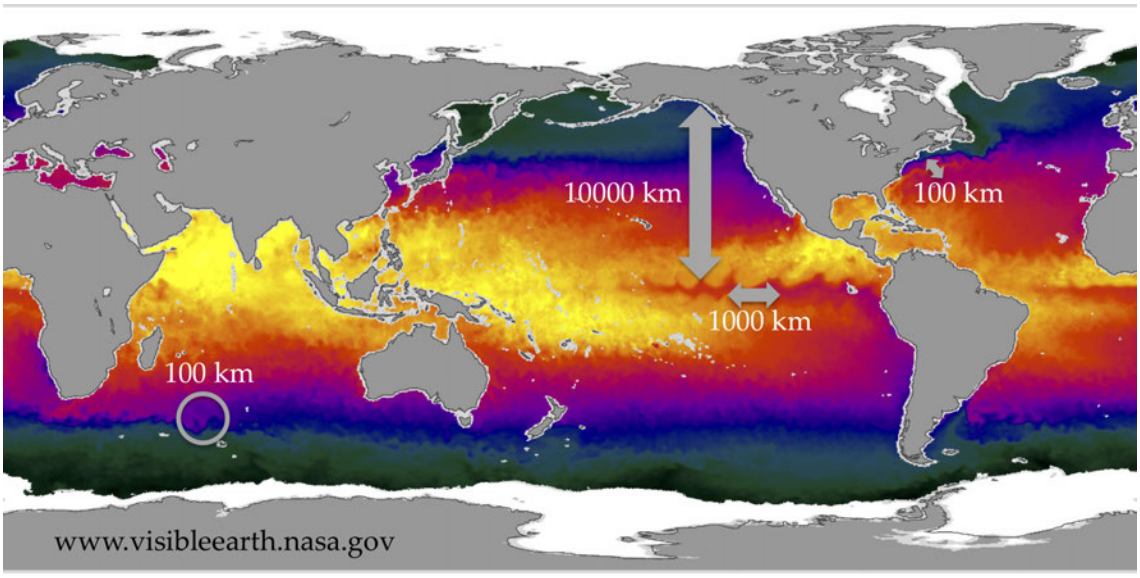

Figure 1: Sea Surface Temperature from AMSR-E satellite data, courtesy of Emily Shoyer

waves lead to turbulence on the scale of centimeters. Ocean circulation thus spans a wide range of scales, from thousands of kilometers to a few centimeters. In addition, the phenomena at different scales do not exist in isolation. Nonlinearities of the thermohydrodynamic equations governing ocean circulation leads to interactions between a wide range of scales.

In the ocean, energy is injected at large planetary scales but is dissipated at the molecular scale through viscous stresses. This implies that there must be a net transfer of energy from the large-scale gyre circulations of the ocean to the centimeter scale where molecular viscosity acts efficiently. In addition to this downscale transfer of energy, there is also downscale transfer of scalar gradients. For example, on a planetary scale, there is a latitudinal equator-to-pole gradient in sea surface temperature. Ocean circulation stirs this large-scale gradient until sea surface temperature gradients are found at the centimeter scale where they are then destroyed by molecular diffusion.

2 The Definition of Turbulence

To an oceanographer, turbulence refers to the chaotic motion of the ocean at all length-scales. It is characterized by the presence of unsteady features such as transient fronts and jets and unsteady vortices. The Jet Stream is turbulent, the Antarctic Circumpolar Current is turbulent, and a breaking internal wave is turbulent. This is the sense the word 'turbulence' has been used above. However, in the rest of this document, the word turbulence will be restricted to refer to motions that result in the irreversible mixing of water properties at the molecular scale. In the ocean, this typically occurs for flows with characteristic length-scales of a few centimeters. Irreversible mixing results in the removal of both energy (through viscous dissipation) and gradients (through molecular diffusion).

Motions at small scales matter because it is only at these scales that we can dissipate kinetic energy of the ocean circulation and mix away the variance of water properties.

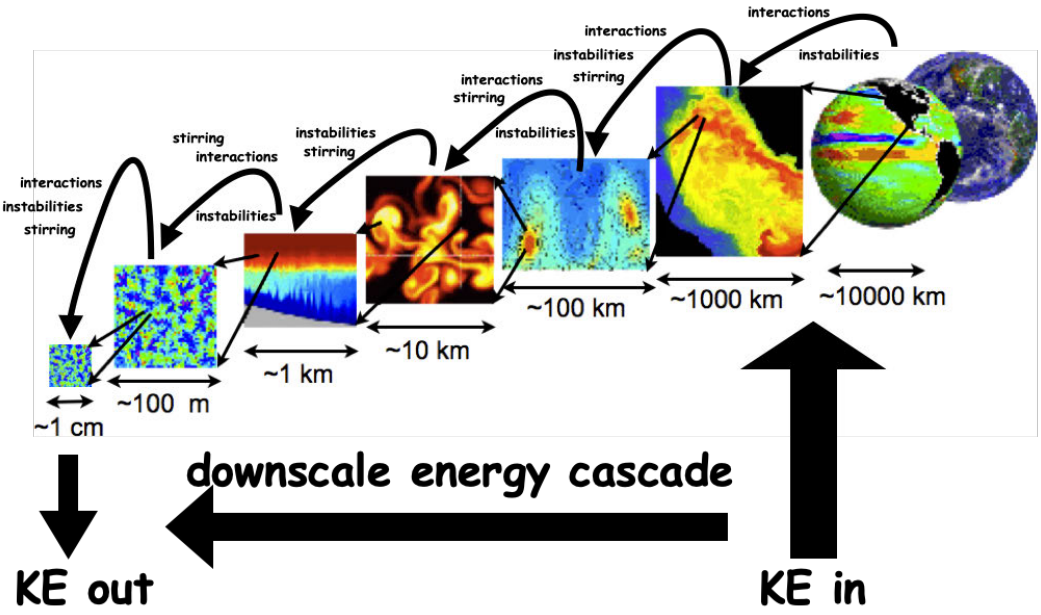

Figure 2: Turbulent length scales and interactions, illustrating the necessary downscale cascade of energy from global scale input of energy to centimetre scale dissipation of energy. Figure adapted from the MITgcm group

3 Why Does Small-scale Turbulence Matter for Large-scale Circulation?

3.1 The meridional overturning circulation (MOC)

To answer this question, one needs a rudimentary understanding of the ocean's meridional overturning circulation (MOC). The MOC can be thought of as a global scale 'conveyor belt' transporting water between the surface and abyssal ocean with characteristic time-scale of hundreds of years. The overturning circulation is one mechanism by which heat is transported from the equator to the pole. The sluggishness of the circulation means that once a parcel of fluid sinks from the surface, it may take hundreds of years before it re-emerges. This makes the overturning circulation important in sequestering heat and carbon and has important implications for thermosteric sea level rise and the global radiative budget of the planet.

The overturning circulation in the Atlantic is formed of two stacked cells. The upper cell consists of North Atlantic Deep Water (NADW) sinking to mid-depths and then being transported along isopycnals (surfaces of constant density) to the Southern Ocean where Ekman suction (due to intense mid-latitude westerlies) causes the water to upwell. This cell is essentially adiabatic and water sinking at high-latitudes is brought to the surface mechanically by the wind. The lower cell consists of Antarctic Bottom Water (AABW) sinking to the abyssal ocean. Unlike NADW, the isopycnals that make up AABW do not upwell to the surface anywhere in the ocean. In the absence of any other processes, the continuous sinking of AABW would fill the deep ocean with water of that density resulting in a homogeneous layer of dense water. However, this is not the case in the real ocean. The abyssal ocean then somehow remains stratified despite the continuous sinking of cold dense water at high latitudes. To avoid becoming a homogeneous layer of cold salty water, there must be some process that makes abyssal waters less dense. What is this process that sustains

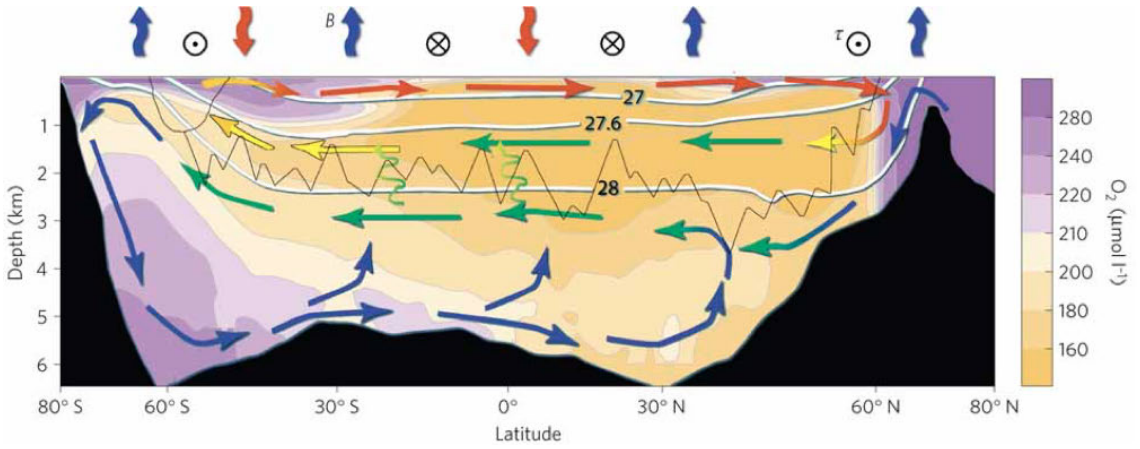

Figure 3: A schematic diagram of the Upper Cell and Lower Cell of the global MOC emanating from, respectively, northern and southern polar seas. The zonally averaged oxygen distribution is superimposed, yellows indicating low values and hence older water, and purples indicating high values and hence recently ventilated water. The density surface 27.6 kg m^{-3} is the rough divide between the two cells (neutral density is plotted) [1].

the abyssal ocean stratification? That is, how does the dense water sinking at high latitude return to the surface?

3.2 Munk's model of uniform upwelling

Despite water sinking at high latitudes, the ocean abyss remains stratified. The thermocline remains, on average, at the same depth. Thus abyssal water must be returning to the surface. In 1966, Walter Munk proposed a simple model of how the dense abyssal water returns to the surface [2]. Since water is warmed at the surface and cold water sinks, the surface of the ocean is much warmer than at depth. This vertical temperature gradient results in a downward diffusion of heat. The deep ocean is warmed as heat slowly diffuses from the surface to the abyss. As it warms, the water becomes more buoyant and rises. Thus water sinks at high latitudes and upwells uniformly throughout the ocean due to diffusive heating.

3.3 How much mixing is required?

Munk used this model along with radiocarbon measurements in the Pacific to independently determine the upwelling velocity and the thermal diffusivity [2]. The measured vertical velocity was about three meters per year and this is approximately what is required to balance the water sinking at high latitudes. The more intriguing finding was that the measured diffusivity ($K = 10^{-4}\mathrm{m}^2\mathrm{s}^{-1}$) was three orders of magnitude (that is, a thousand times) larger the molecular thermal diffusivity of water ($K = 10^{-7}\mathrm{m}^2\mathrm{s}^{-1}$). If one uses the molecular thermal diffusivity of seawater, Munk's model predicts an effectively homogeneous abyssal ocean. Thus a large diffusivity term is necessary to maintain the abyssal stratification. This diffusivity is clearly not of molecular origin; it is much more efficient at diffusing heat vertically throughout the ocean. Instead, this is an eddy diffusivity – a diffusivity due to turbulent fluid motions. Munk's calculation reveals that the abyssal ocean is not a quiescent motionless pool as many imagine, rather, it is a turbulent fluid and it is precisely this turbulence that allows it to maintain its stratification.

Exercise for the reader: Can you reproduce Munk's estimate of the global deep ocean K_ρ?

Munk estimated the intensity of small scale turbulent mixing in the deep ocean by considering the density (ρ) conservation equation

$$\frac{D\rho}{Dt} = K_\rho \frac{\partial^2 \rho}{\partial z^2}, \tag{1}$$

where K_ρ is the diapycnal (cross density surface) diffusivity, measuring the rate at which small-scale turbulence mixes waters of different density. K_ρ is assumed to be constant.

Assuming the ocean to be in steady state ($\frac{\partial \rho}{\partial t} = 0$) and averaging horizontally across the ocean such that the horizontal advective terms drop out, (1) simplifies to

$$w \frac{\partial \rho}{\partial z} = K_\rho \frac{\partial^2 \rho}{\partial z^2} \tag{2}$$

where w is the vertical velocity. Solving (2) for K_ρ, we obtain

$$K_\rho = w \frac{\partial \rho}{\partial z} \Big/ \frac{\partial^2 \rho}{\partial z^2} \tag{3}$$

This is the basis for Munk's calculation of the rate of turbulent mixing in the deep ocean. You have the information in figure 4. Can you reproduce his result $K_\rho \sim 10^{-4}$kg?

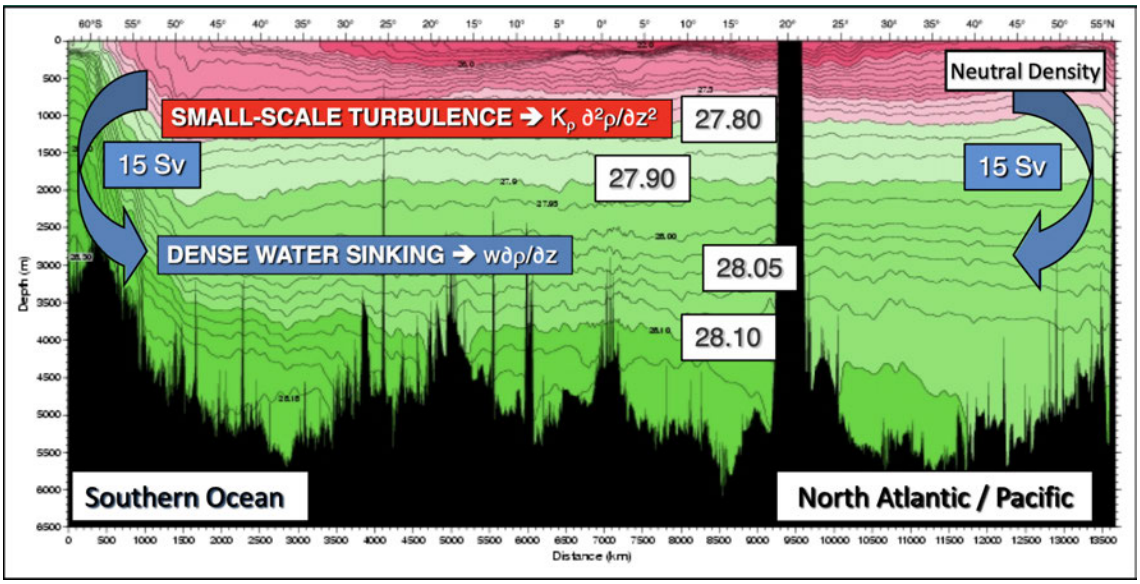

Figure 4: Schematic of estimated downwelling and isopycnal surfaces averaged zonally over the global oceans. Courtesy of Alberto Naveira Garabato.

Hint: $1\text{Sv} = 10^6\text{m}^3\text{s}^{-1}$, the global ocean area $A \sim 3 \times 10^{14}\text{m}^2$, and $\frac{\partial^2 \rho}{\partial z^2} = \frac{\partial}{\partial z}\left(\frac{\partial \rho}{\partial z}\right)$

Solution

First calculate the vertical velocity w from the downwelling shown in figure():

$$w \sim \frac{(15\text{Sv} + 15\text{Sv})}{A\text{m}^2} \simeq \frac{30 \times 10^6 \text{m}^3\text{s}^{-1}}{3 \times 10^{14}\text{m}^2} = 10^{-7}\text{ms}^{-1} = 3\text{m per year} \tag{4}$$

Now find an estimate for $\frac{\partial \rho}{\partial z}$, using a first order approximation to the derivative. At 1000m, $\rho = 1027.8\text{kgm}^{-1}$ and at 4000m, $\rho = 1028.1\text{kgm}^{-1}$, so:

$$\frac{\partial \rho}{\partial z} \simeq \frac{1027.8\text{kgm}^{-1} - 1028.1\text{kgm}^{-1}}{3000\text{m}} = -1 \times 10^{-4}\text{kgm}^{-4} \tag{5}$$

Now find an estimate for $\frac{\partial^2 \rho}{\partial z^2}$ using the intermediate values of ρ. First find two more estimates for $\frac{\partial \rho}{\partial z}$ at 1500m and 3500m:

At 1500m, $\frac{\partial \rho}{\partial z} \simeq \frac{1027.8\text{kgm}^{-1} - 1027.9\text{kgm}^{-1}}{1000\text{m}} = -1 \times 10^{-4}\text{kgm}^{-4}$
At 3500m, $\frac{\partial \rho}{\partial z} \simeq \frac{1028.05\text{kgm}^{-1} - 1028.1\text{kgm}^{-1}}{1000\text{m}} = -5 \times 10^{-5}\text{kgm}^{-4}$

So, since $\frac{\partial^2 \rho}{\partial z^2} = \frac{\partial}{\partial z}\left(\frac{\partial \rho}{\partial z}\right)$:

$$\frac{\partial^2 \rho}{\partial z^2} \simeq \frac{(-1 + 0.5) \times 10^{-4}\text{kgm}^{-4}}{2000\text{m}} = -2.5 \times 10^{-8}\text{kgm}^{-5} \tag{6}$$

Using (3), we then have

$$K_\rho \simeq \frac{(10^{-7}\text{ms}^{-1}) \times (-1 \times 10^{-4}\text{kgm}^{-4})}{-2.5 \times 10^{-8}\text{kgm}^{-5}} = 4 \times 10^{-4}\text{m}^2\text{s}^{-1} \sim 10^{-4}\text{kgm}^{-5} \tag{7}$$

We have thus recovered Munk's estimate of the global deep ocean K_ρ.

3.4 How turbulence mixes fluids

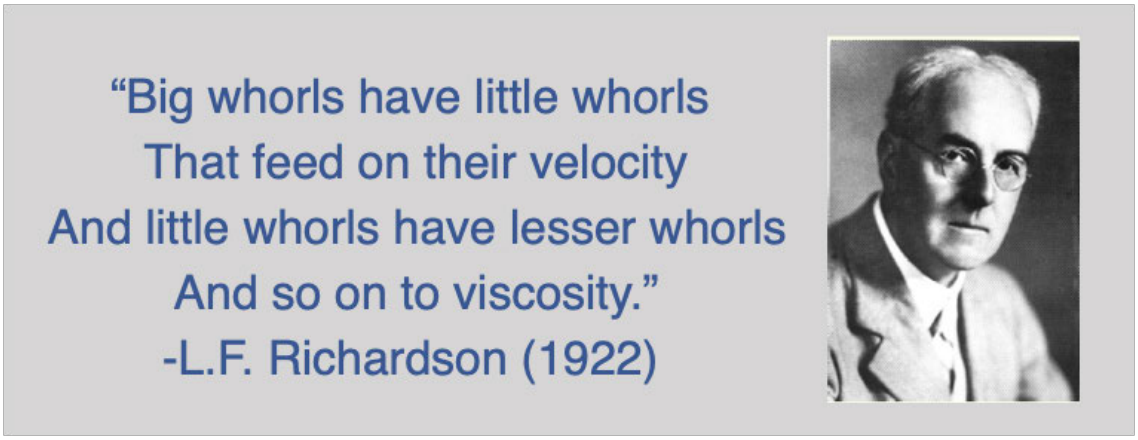

Suppose a small amount of dye is released into a localized region in a fluid. After a sufficiently long time, the random motion of fluid molecules results in the irreversible dilution of the dye throughout the entire container. This is an example of molecular diffusion. This process acts to transport flow tracers, such as temperature or dye, down-gradient from regions of high to low tracer concentration. As a consequence, diffusion tends to ultimately homogenize fluids. The rate at which diffusion occurs depends on the initial tracer distribution: a blob of dye will take much longer to diffuse than, say, an equivalent amount distributed as a narrow streak. This is because diffusion is most effective in regions of large tracer gradients (in this case, the boundaries between the dye and the fluid). Increasing the volume-averaged gradient results in more effective diffusion.

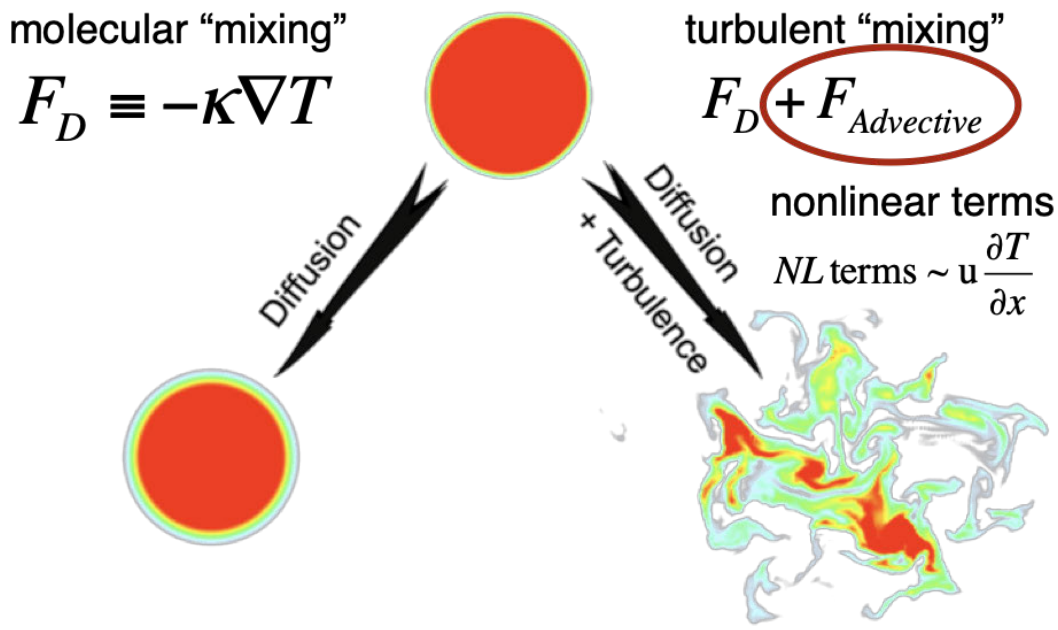

Figure 5: Diagram of the effect of molecular diffusion alone versus turbulent mixing on diffusing the temperature of some fluid parcel. The turbulent diffusivity is due to the nonlinearities in the fluid flow, making it a property of the flow, not the fluid. Adapted from [4], courtesy of Emily Shroyer.

One way to increase the volume averaged tracer gradients is by stirring. This is why we stir milk in tea rather than wait for the milk to diffuse on its own.

The diffusivity Munk found in his calculation is an eddy diffusivity. This diffusion-like parameter is a way to parametrize the highly nonlinear effects of turbulent fluid motions in simple models. Rather than viewing the fluid as a collection of fluid particles, we instead view the fluid as consisting of eddies. Eddies are an idealization of coherent fluid regions: they are regions moving in the same direction and having the same fluid properties. With eddies as our basic building blocks, we extend the concept of molecular diffusion to eddies. The random motion of eddies results in the down-gradient transport of tracer properties. As in the previous case, this acts to homogenize the fluid.

Molecular diffusivity is an irreversible process. One cannot unmix the dye after it has been diluted throughout the fluid container. Stirring however is reversible. This is because stirring fundamentally is simply the movement of fluid parcels – it only results in their rearrangement. We then see that, unlike molecular diffusivity, eddy diffusivity does not actually irreversibly mix the fluid. Rather, turbulent fluid motions stir the fluid, stretching and filamenting fluid parcels into highly convoluted shapes and patterns.

Mathematically, it is the non-linear terms in the equations of motion (such as $u\frac{\partial T}{\partial x}$, where T is temperature and u is the x component of the fluid velocity) that are responsible for stirring of the fluid and the interaction across disparate scales. Non-linear advective motions stir the fluid, drastically increasing the volume-averaged tracer gradients, and allow molecular diffusivity to act with increased efficiency. Turbulence stirs the fluid and allows molecular diffusion to proceed much faster than it would have alone. To capture this enhanced mixing in simple models, an enhanced diffusivity parameter is used. This is the eddy diffusivity Munk found in his calculation.

3.5 Turbulent length scales

Having described how stirring introduces a cascade of scales to those on which molecular diffusion can act, we now formalise some of the length scales relevant to stratified turbulence.

When stratification is important, the initial (largest) size of isotropic turbulent whirls is defined by the **Ozmidov scale**

$$L_O = \left(\frac{\epsilon}{N^3}\right)^{\frac{1}{2}} \tag{8}$$

where ϵ is the rate of dissipation of turbulent kinetic energy, and will be discussed further in the following lectures. L_O is the scale of the smallest turbulent motions that can 'feel' the stratification - that is turbulent length-scales $\ll L_O$ are not deformed by buoyancy.

The final (smallest) scale of turbulent whirls is defined by the **Kolmogorov scale**

$$L_K = \left(\frac{\nu^3}{\epsilon}\right)^{\frac{1}{4}} \tag{9}$$

where ν is the molecular viscosity. This is the scale on which the smallest whirls are homogenized by viscosity. Consider figure 6, which shows the spectral energy and dissipation as a function of

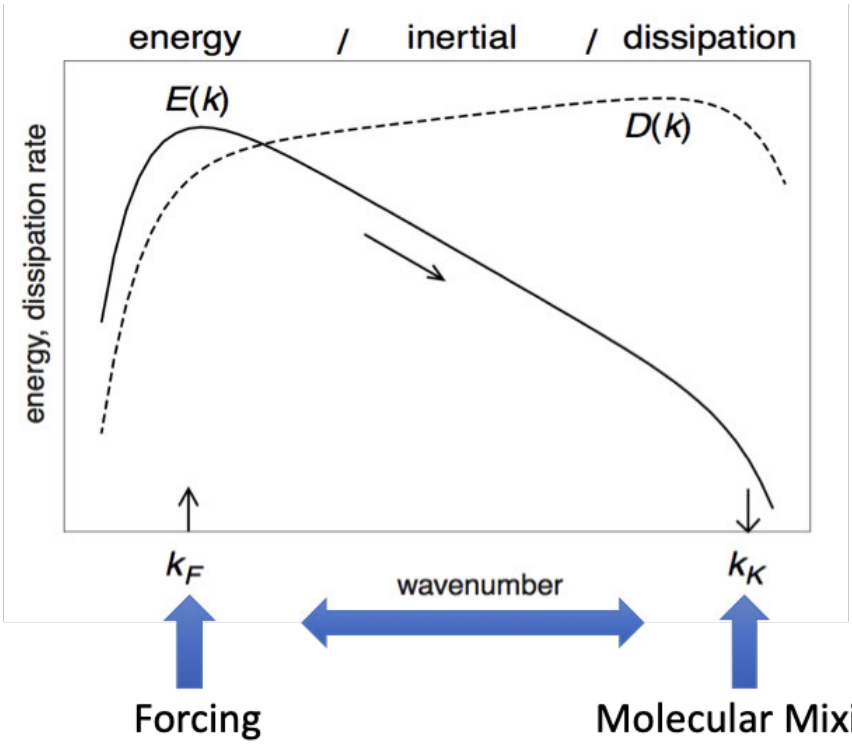

Figure 6: Diagram showing the cascade of scales of turbulence. The forcing is input at the Ozmidov Scale (the scale of the largest 3D isotropic eddy), and dissipated at the Kolmogorov Scale (the scale of the smallest 3D isotropic eddy). The range between these scales is known as the inertial subrange. [4], Courtesy of Emily Shoyer.

wavenumber. The energy subrange is characterised by length scales L_O, at which the small-scale turbulence is forced by the largest 3D isotropic eddy. The energy then cascades to smaller scales

through the inertial subrange, moving the gradients to the dissipation subrange where molecular viscosity dissipates the motion. The stronger the stratification, the smaller the Ozmidov scale and thus the smaller the distance between the energy and dissipation subranges. Conversely, the larger the Reynolds number, the smaller the Kolmogorov scale, and the larger the distance between the energy subrange and the dissipation subrange.

The molecular mixing at the smallest scales homogenises both momentum and density. The energy residing in the field of turbulent whirls can thus have two fates: it can go into **mixing the fluid** or it can be **dissipated as friction**. This can be expressed as

$$P = B + \epsilon \tag{10}$$

where P is the rate of production or turbulent energy (that is, the rate at which energy enters the turbulent energy cascade at scale L_O), B is the rate at which turbulent energy is expended in mixing the fluid, and ϵ is the rate at which energy is dissipated.

For shear induced turbulence in the ocean, typically only approximately 17% of the turbulent energy production ends up as mixing, and the remaining 83% is dissipated, giving $B \sim 0.17P$. It is a topic of active research whether this so called 'mixing efficiency' can be taken to be a constant, expect to hear more about this in future lectures!

3.6 Energetics

Let us now consider the energetics of mixing. Suppose we have a container with two layers of fluid. A thin dense layer near the bottom and much thicker, more buoyant, fluid on top. The center of mass of this system will be offset below the center of the container towards the dense fluid because the container is bottom heavy. After a very long time, diffusion will mix the two into a single homogeneous fluid. By symmetry, the center of mass will now be at the center of the container. It follows that the mixing process did work against gravity on the fluid to bring the center of mass upwards. The kinetic energy of fluid molecules was converted into gravitational potential energy in the mixing process.

In the case of the ocean it is eddy diffusion rather than molecular diffusion that is acting to raise the center of mass of a fluid column. Here, the kinetic energy of eddies is partially converted into potential energy (as above) and partially dissipated. The fraction of eddy kinetic energy converted into potential energy through mixing (rather than being dissipated) is called the mixing efficiency Γ and typically has a value of $\Gamma \approx 0.2$. That is, one-fifths of the eddy kinetic energy is used to mix the fluid and raise the center of mass while the remainder is dissipated by viscous stresses.

Mixing is thus driven mechanically in the ocean by whatever is providing eddies (or seawater in general) with kinetic energy. Since the overturning circulation depends crucially on mixing to return the water to the surface, it is therefore dependent on this source of mechanical energy.

3.7 What causes deep ocean turbulence

To maintain the abyssal stratification against the rate of deep water formation, approximately two terawatts are needed (2 TW $= 2 \times 10^{12}$ W, for reference, a typical human requires 100W). There are two dominant energy sources to the deep ocean: winds and tides.

The forcing of the ocean by the wind contributes enormous amounts of energy into the ocean. Most of this energy is dissipated in mixing the surface (mixed) layer and into the production of surface gravity waves. A small portion goes into the development of the large scale wind-driven ocean circulation. Wind can add mechanical energy into the ocean in two ways. The first is by direct forcing at the surface resulting in, for example, isopycnal outcrops in the southern ocean. The

other, less direct method, involves instabilities of the large-scale ocean circulation. Such instabilities result in the pinching off of large ocean eddies which then radiate internal waves into the ocean interior. These wave eventually break, depositing energy into the interior.

Unlike wind-stresses which can only act at the boundary, gravity is a body force meaning that it can directly act on the ocean interior. The lunisolar tides, caused by the gravitational attraction of the sun and moon and their relative position to the earth, result in the horizontal movement of entire water columns. If these columns move over bottom topography, they will radiate internal waves into the ocean interior. This converts gravitational lunisolar potential energy into mechanical wave energy.

Thus, both winds and tidal forcing result in the production of internal waves and their emission to the deep ocean. These mechanisms produce internal waves with scales of hundreds of meters. Nonlinear interactions amongst propagating internal waves consequently produce a cascade towards smaller vertical scales. Once internal waves have vertical scales on the order of meters, they become prone to shear instabilities. Such instabilities cause internal waves to break, vigorously mixing the surrounding fluid in the process. The breaking of internal waves is believed to be the main mechanism behind the mixing of the ocean interior.

3.8 Mixing matters - impacts beyond physics

Besides the implications of mixing for the large scale ocean circulation, there are also important impacts of mixing on the ecosystem. For example, primary production by phytoplankton in the euphotic zone (the upper 100m or so of the ocean that receives enough light for photosynthesis to occur) is highly sensitive to the concentration of nutrients. Nutrient concentrations are higher below the euphotic zone, where they are not consumed, so upwelling and vertical mixing is a necessary mechanism for primary production in the ocean. Figure 7 demonstrates some of the many mechanisms by which microscale turbulence can impact the ocean's ecosystem.

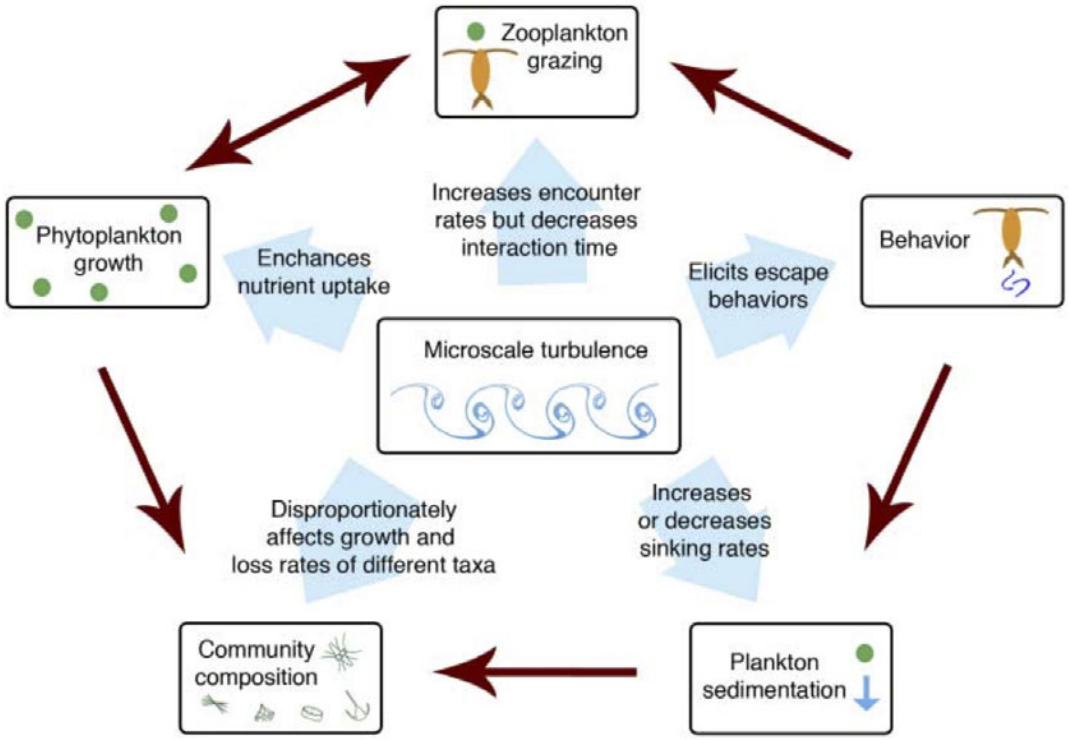

Figure 7: A diagram showing the impact of microscale turbulence on the phytoplankton and zooplankton ecosystem [3].

3.9 Why mixing matters

So why does mixing matter? The slow overturning timescale of the ocean means that the ocean is a reservoir for both heat and carbon. This allows it to control the rate at which we expect sea level to rise due to the thermal expansion of sea water. The overturning circulation is also responsible for sequestering carbon in the deep ocean and so is important for feature projections of Earth's climate. However, for the overturning circulation to operate, two components are needed. The first is convection – regions of dense water formation where new bottom water is created and sinks to the abyss. The second is a mechanism to bring the abyssal water back to the surface. In the deep ocean, this mechanism is mixing. Thus the properties of ocean mixing exert a strong control on the overturning circulation and hence on Earth's climate. Figure 8 demonstrates the importance of understanding mixing and other poorly understood processes for creating accurate climate projections.

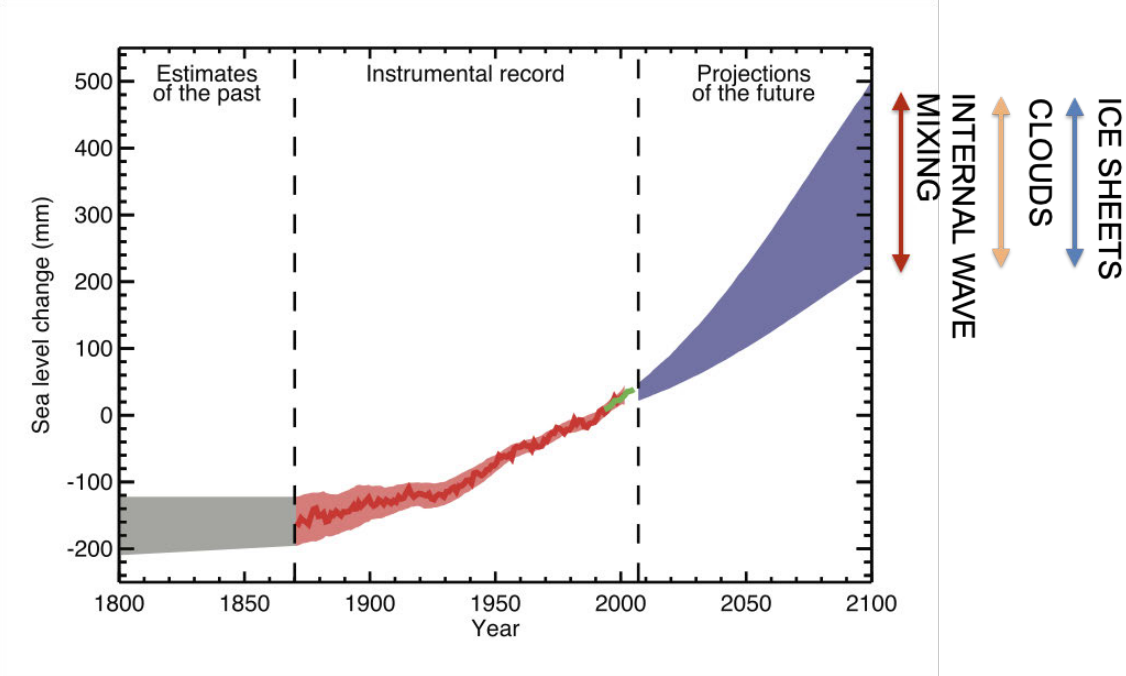

Figure 8: Diagram illustrating the necessity of good parametrizations for mixing and other processes in predicting sea level rise. Courtesy of Matthew Alford.

Key Points

- Ocean circulation is turbulent, with Reynolds number $\gg 1$.
- Small spatial scales and large spatial scales are inseparably linked through nonlinearities in fluid motion.
- Turbulence is a property of the flow.
- Small scale turbulence mixes water masses vertically, and is essential for preventing the abyssal ocean from becoming stagnant and unstratified.
- A turbulent energy cascade ensues between the Ozmidov and Kolmogorov scales. The majority (approximately 83%) of the turbulent energy ends up being dissipated as friction, and a smaller fraction (approximately 17%) goes into diapycnal mixing.
- Turbulence influences gradients and has implications for the local environment and large scale circulation.
- The accuracy of numerical models relies heavily on a good representation of turbulence.

References

[1] J. Marshall and K. Speer, *Closure of the meridional overturning circulation through Southern Ocean upwelling*, Nature Geoscience, 5 (2012), pp. 171–180.

[2] W. H. Munk, *Abyssal recipes*, Deep-Sea Research and Oceanographic Abstracts, 13 (1966), pp. 707–730.

[3] J. C. Prairie, K. R. Sutherland, K. J. Nickols, and A. M. Kaltenberg, *Biophysical interactions in the plankton: A cross-scale review*, Limnology and Oceanography: Fluids and Environments, 2 (2012), pp. 121–145.

[4] W. D. Smyth and J. N. Moum, *Three-Dimensional (3D) Turbulence*, in Encyclopedia of Ocean Sciences: Second Edition, 2001.

GFD 2019 Lecture 2: Measuring and Quantifying Ocean Mixing

Stephanie Waterman; notes by Wenjing Dong and Samuel Boury

June 18, 2019

1 Challenges of Measuring Ocean Mixing

1.1 Why is it so difficult to measure ocean mixing?

There are some challenges in quantifying ocean mixing. This is a non-exhaustive list:

- The oceanic processes involve a **large range of scales** in both space and time: energy is mostly injected at large scales (of order $\mathcal{O}(10^5$ m)) but dissipated at small scales (of order $\mathcal{O}(10^{-3}$ m)).
- The process is **non-deterministic** and needs to be adressed using a stochastic/statistical method.
- The rate of turbulent kinetic energy dissipation (noted ε) is **highly variable** in the ocean, spreading over more than six orders of magnitude.
- Direct sampling of oceanic mixing also complicated due to the **high intermittency in space and time**, so we need a high density of observations in both space and time.
- Because of intermittency, turbulent statistics are approximately log-normally distributed in space and time. Since the **distribution is non-normal**, one must sample the relative rare but extreme events to be able to quantify the mean.
- Ocean mixing involves a **rich range of different processes and instabilities**.
- Point measurements are typically **contaminated** by transient reversible processes (like internal waves) which makes it difficult to find out what really plays a role in mixing.
- Turbulent transports are best quantified at the molecular level, which means at very **small scales**. In order to sample at that small scale, sensing elements have to be small and able to sample with a high sensitivity at high frequency.
- The **difference between turbulence and mixing** is not obvious: what amount of turbulence is part of mixing? Given sparse measurements of turbulence at a point in space and time, how can we infer representative estimates of mixing?
- There is also a **theoretical issue**: how do observed signals relate to theory? And how can we use the relevant theory given sparse and missing information?

Spectra from measurement campaigns often show very clearly these different issues. For example, Moum *et al*'s measurements from the Oregon Shelf [6] demonstrate the richness of oceanic turbulent motions and some of the sampling challenges. From the observed data (figure 1, top panel), the Turbulent Kinetic Energy (TKE) dissipation ε that can be derived (figure 1, bottom panel) shows variability and intermittency, and provides evidence that the turbulent dissipation varies by multiple orders of magnitude even in a short period of time (within only two days).

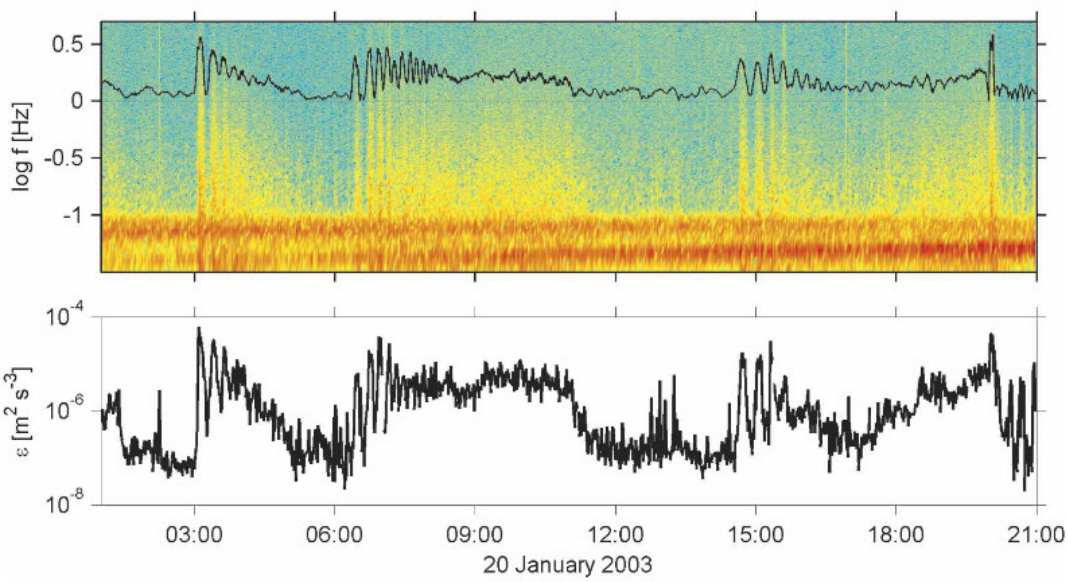

Figure 1: Above: spectrogram of velocity measured by Acoustic Doppler Velocimeter (ADV) on bottom lander. Bottom: Time series of Turbulent Kinetic Energy dissipation (ε) estimated from the above spectrogram. Oregon Shelf measurement campaign, from [6].

1.2 A closer look at a single isolated event

From an oceanographic perspective, we are concerned with the large-scale thermodynamic transformation of water masses caused by mixing or, alternatively, the irreversible change in potential energy created when down-gradient, Fickian-like diffusion moves the fluid's center of mass upward.

From the complete knowledge of the flow field produced by a properly constrained DNS, we can assess the net result of the mixing as a time-space integral. The net change in potential energy can be used to estimate an average turbulent diffusivity needed to represent the complexities of the modelled turbulent flow. As shown in figure 2, the dynamics of such events and their impact on mixing efficiency can be isolated and study numerically [8].

It is, however, utterly impossible to reproduce such a calculation in natural geophysical flows, simply because the density of time-space observations in the model cannot be replicated in the field and because other events happen at the same time.

1.3 Different approaches to quantifying ocean mixing

In order to overcome these challenges, we can use different approaches, such as:

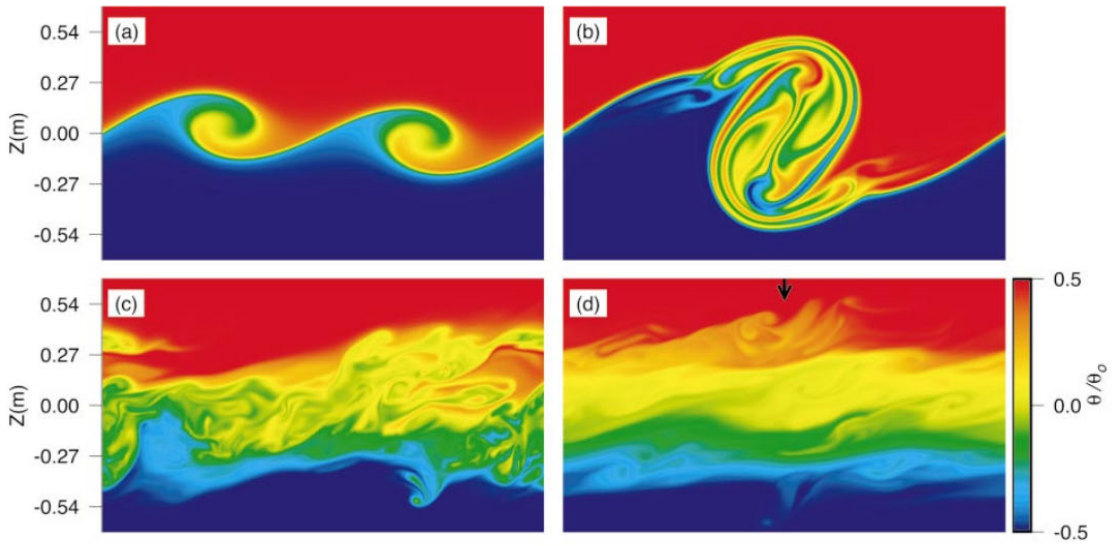

Figure 2: DNS of a single isolated wave breaking event in a stratified medium, showing the temporal evolution of the temperature anomaly evolution. At: (a) $t = 565$ s, (b) $t = 1414$ s, (c) $t = 4242$ s, and (d) $t = 6222$ s. Extracted from [8].

1. Employ an **integral approach**: we compute integral estimates based on large-scale observations;
2. Use **highly specialised instrumentation**: we look for "direct" estimates, based on microstructures observations;
3. Try to **parametrize**: understanding how larger scale processes create and modulate turbulence to appropriately parametrize the phenomenon, for example through turbulent parameterizations.

2 Approach 1: Integral Estimates

2.1 Purposeful tracer releases

Idea

To quantify the mixing efficiency, we release a manmade passive tracer and measure its spread over time. It is arguably the simplest method to measure mixing. Measurement campaigns can go over several years to quantify how much does the tracer release spread.

This method is based on several assumptions: we assume a constant vertical (or *isopycnal*) turbulent diffusivity K; we assume that the stratification of the ocean suppresses mean vertical flow motion so turbulence is the only effective mechanism that causes vertical spreading of the patch; and, following a parcel of water, the spread of the tracer C is governed by the diffusion equation:

$$\frac{\partial \bar{C}}{\partial t} = K \frac{\partial^2 \bar{C}}{\partial z^2}, \tag{1}$$

where $\bar{C}$ is the concentration of the tracer. The solution of this equation is a widening Gaussian profile, that helps to estimate the turbulent diffusivity K [9].

In practice

The tracer is released on a surface of constant density. Then, another measurement campaign returns to the site (or around) to measure and compare the actual spreading of the tracer to the original distribution. As shown in figure 3, profiles of succesive measurements can be fitted by Gaussian distributions [5]. Such measurements have been proved useful to provide estimates of turbulent diffusivity in different regions of the world (see for example [10]; and figure 4 from [11]).

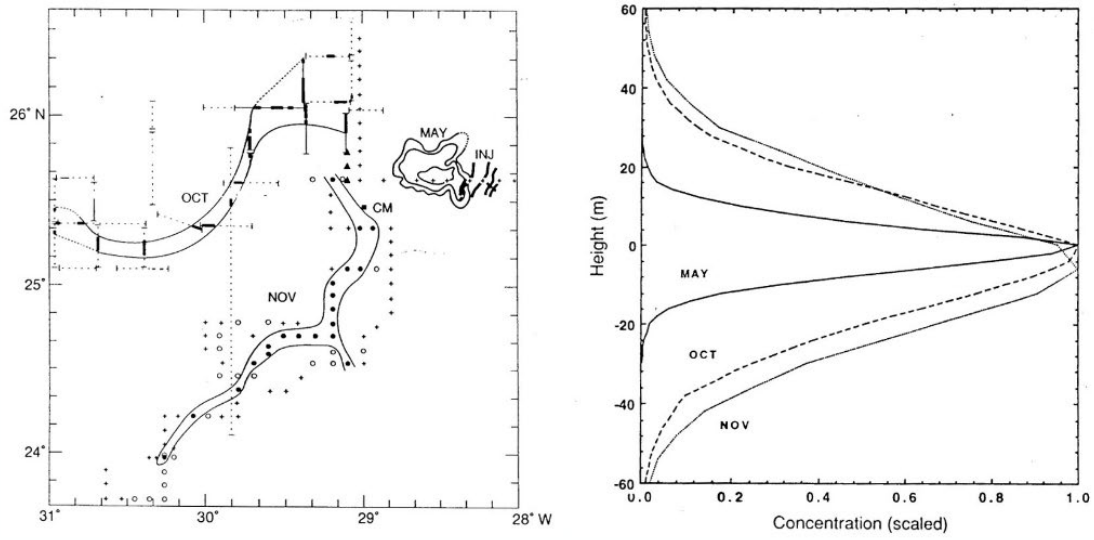

Figure 3: Tracer release experiment in the North Atlantic. From [5].

Advantages

This technique is elegant and definitive in its results: no confounding sources or sinks of the dye in the ocean, so tracking the vertical spread is an unambiguous way to estimate mixing.

Limitations

Nonetheless, there are several limitations. The technique is difficult to perform and requires specialized equipment and analysis methods to release the dye and then analyze the water samples to find minute quantities of tracer in the water (the spreading of the tracer is eventually large so the measured concentrations $\bar{C}$ are likely to be very low). Also, horizontal stirring and advection of a dye patch can spread it horizontally to such an extent that it is very difficult to find all the dye using finite ship resources (how many 2D transects needed to cover the whole extension of the 3D spreading?).

2.2 Tracer budgets (inverse methods)

Idea

Mixing is estimated through an integrated version of the mean tracer equation

$$\frac{\partial \bar{C}}{\partial t} + \mathbf{u} \cdot \nabla \bar{C} = \nabla \cdot (K \nabla \bar{C}) \tag{2}$$

in a constrained volume of water, in which we *assume* that its contents are in steady state.

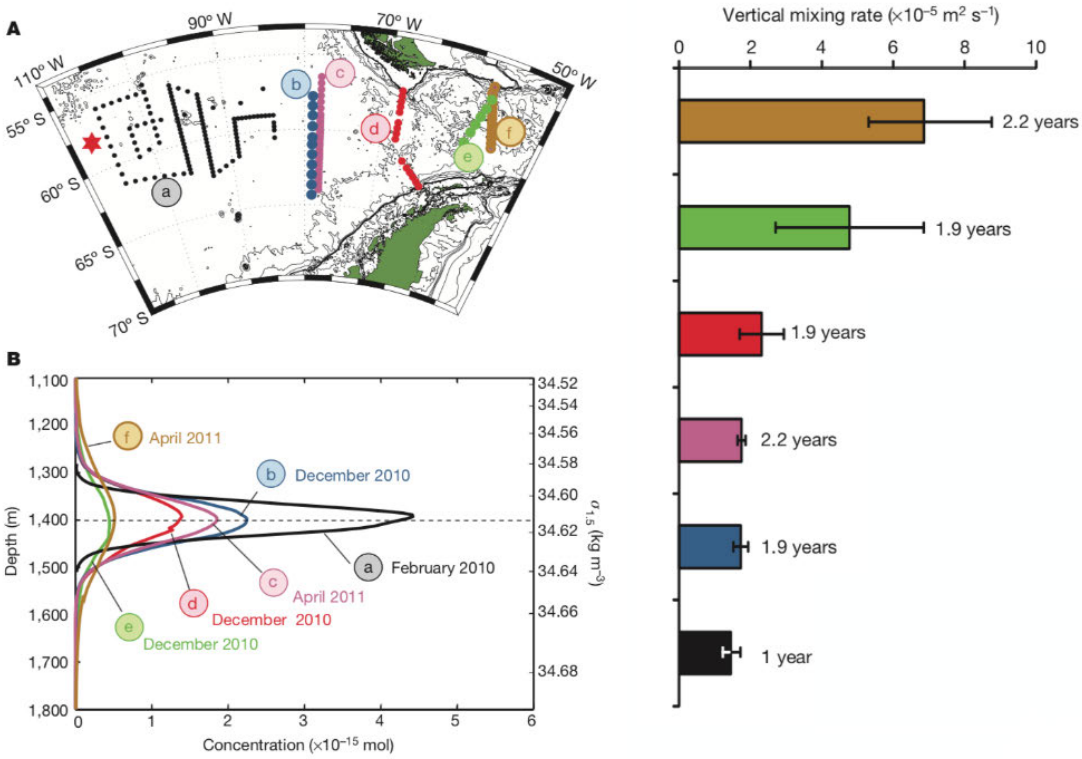

Figure 4: Tracer release experiment in the Drake Passage. From [11].

In practice

A budget method is applied to the environment we are looking at. For example, if we look at the schematic of the Brazilian Basin depicted in figure 5 [4], cold water enters the basin (arrow on the right side in picture 5) but no water that cold is found in the basin: the only way for this to happen is that the water mixes and goes up. Water exiting the basin must be warm and leave either by vertical advection or by vertical mixing. Further reading in [2] and [1].

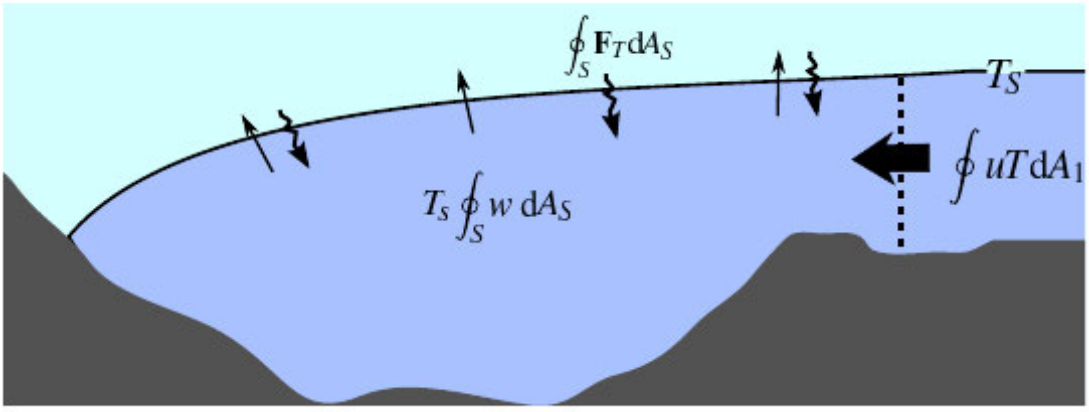

Figure 5: Schematic of the Brazilian Basin, from [4]. The $1°C$ water isotherm is the line between light blue and cyan. Arrows show possible exchanges.

Advantages

This method can be made from routinely made hydrographic sections in the ocean (usual ship transects) and would be unambiguous if perfectly constrained in providing basin-averages.

Limitations

This method, however, requires the assumption that the system is in steady state, which is not true in general. The velocities and tracer concentrations measured at the boundaries of the volume must be well constrained and shown to be in steady state: this is very difficult as these measurements are typically estimated from scarce individual ship tracks. Budget balance also requires well-constrained topographies and geometries like the Brazil Basin, where inflowing velocities and tracers and bounding isotherm can be mapped with high degree of confidence: these geometries are very rare in the ocean!

3 Approach 2: "Direct" Microscale Estimates

The goal of this method is to estimate turbulent stirring and/or mixing by directly observing the turbulence (can we actually have a "direct" measurement of turbulence?). Examples of this method include:

1. directly measuring the turbulent stirring of a fluid using the eddy correlation technique;
2. directly measuring the molecular destruction of temperature gradients (Osborn-Cox method); and
3. estimating mixing by relating the buoyancy-flux to the energetics of the turbulence (Osborn method).

3.1 Direct eddy correlation

Idea

Using Direct Eddy Correlation, we try to estimate the mixing by quantifying the stirring of the fluid via measuring turbulent fluxes (e.g., in the overturning example in figure 2 [8] that mixes warm and cold water, this means measuring vertical velocity fluctuations, w', and temperature fluctuations, T', to quantify $< w'T' >$).

In practice

We need high frequency records of temperature and velocity acquired along a horizontal path using a towed instrument outfitted with thermistors and shear probes. There are lots of them (MMP, and so on). One example, *marlin*, is presented in figure 6 (figure from [3]).

Though the measurement instruments are more accurate now, there are still many challenges. In particular, raw signals are large and very active, and the product $w'T'$ is not one-sided: it has instantaneous values that are large and can be of either sign, so that the fluctuations are far greater than the mean correlation $< w'T' >$. This is a general problem since turbulence is sporadic and stirring in both down-gradient (i.e. transports heat from regions of warm fluid) and up-gradient (i.e., transports heat to regions of warm fluid). Since much of $w'T'$ is reversible (i.e., just stirring fluid that is not immediately mixed), the eddy-correlation technique must be made over long times to produce stable estimates of the irreversible flux, but such measurements are hard to sample.

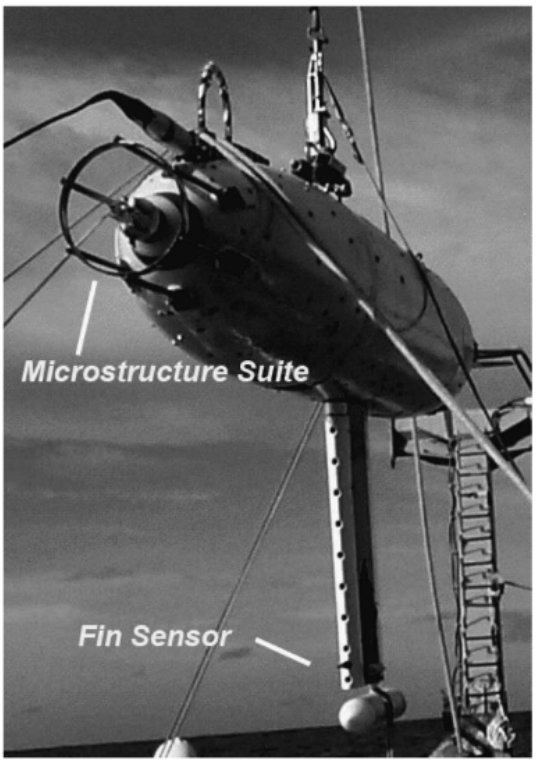

Figure 6: *Marlin* on the deck. Figure from [3].

Advantages

This method provides a direct measure of the turbulent transport that is of interest.

Limitations

It is hard to determine what is "mean" and what is "turbulent" from the limited measurements possible with a vertical or horizontal profiler; choosing what is "large scale" requires some art! Also, estimating the vertical velocities in the ocean is hard. In this instance, the vertical velocities were anomalously large. Finally, it is challenging to gathering enough statistics of the turbulence to make robust estimates of mean fluxes.

As a consequence, this method does not enjoy wide use!

3.2 Microscalars (Osborn-Cox) [1972]

Idea

The Osborn-Cox method deals with quantifying the rate of molecular diffusion of scalar variance at the microscale level. It is owed to Osborn and Cox who showed, by considering the evolution equation for microscale scalar variance, that diffusivity κ_T is related to the rate of destruction of scalar variance χ_T via

$$\chi_T = 2\kappa_T < |\nabla T'|^2 > . \tag{3}$$

The scalar-gradient variance is a non-intuitive quantity to consider, but it is the best measure of "stirring", and is intimately related with the thermodynamic quantity of entropy. In order to get the turbulent diffusivity K, we also need larger scale scalar gradients, and apply

$$K = 3\kappa_T \frac{< (\partial T'/\partial z)^2 >}{(\partial \bar{T}/\partial z)^2} = \frac{\chi_T}{2(\partial \bar{T}/\partial z)^2}. \tag{4}$$

Here, we are assuming steady state, homogeneous turbulence so that the net production of gradient variance by turbulent velocities is locally balanced by its destruction by molecular diffusion, i.e., we are assuming that the transport terms are negligible.

In practice

To measure such small scales, a sensor must be small and respond very rapidly. The most commonly measured scalar is temperature, as it is relatively easy to measure and as it diffuses at larger scales (i.e., 1 mm to 1 cm) than chemical constituents like salt. The other problem with considering salt is you have to measure micro-conductivity, which depends mostly on temperature. Measurements of microstructure temperature are typically made with Microbead thermistors – coated with a thin film of glass to electrically insulate them from seawater. Typically only one dimension of the gradient is measured so we assume the turbulence is isotropic and estimate χ as

$$\chi = 6\kappa_T \left\langle \left(\frac{\partial T'}{\partial z} \right)^2 \right\rangle, \tag{5}$$

rather than the exact χ.

Advantages

Because this method measures the rate of irreversible molecular mixing, it is one of the most direct measures of quantifying the turbulent diffusivity K.

Limitations

Like other methods, we need to make assumptions: steady-state, homogeneous isotropic turbulence; no transport terms (i.e., production = dissipation locally). We also need to collect enough measurements for long enough time that the irreversible part of the "turbulent" flux is measured and a robust mean can be calculated; unlike the estimate of $< w'T' >$, χ_T is a direct measure of irreversible mixing, so it does not need many realizations of the same turbulent event. From a technical point of view, we need to move probes slowly enough for the probes to respond (takes time for heat to diffuse through probes' insulation) but fast enough to capture a synoptic snapshot of a turbulent event: there is a trade off between resolution and statistics.

In practice, most sensors are deployed too rapidly and not all the variance is measured; it is then common to apply corrections by fitting data to a universal spectrum to extrapolate resolved measurements to higher wavenumber. Doing so accurately requires an independent measure of ε.

The discussion of measurement techniques will be continued in tomorrow's lecture. First we will discuss the Osborn method, which uses velocity microstructure data and is based on energy considerations. Then we will also discuss parameterization estimates.

References

[1] Ganachaud, A. and Wunsch, C. 2000. Improved estimates of global ocean circulation, heat transport and mixing from hydrographic data. *Nature*, 408, 453–457.

[2] Hogg, N., Biscaye, P., Gardner, D. and Schmitz, W.J.Jr. 1982. On the transport and modification of Antarctic bottom water in the Vema Channel. *J. of Mar. Res.*, 40, supplement.

[3] Klymak, J.M. and Moum, J.N. 2007. Oceanic Isopycnal Slope Spectra. Part I: Internal Waves. *J. Phys. Oceanogr.*, 37, 1215–1231.

[4] Klymak, J.M. and Nash, J.D., S. 2008. Estimates of Mixing *in* Encylopedia of Ocean Sciences. *Elsevier*, 288–298.

[5] Ledwell, J.R., Watson, A.J. and Law, C.S. 1993. Evidence for slow mixing across the pycnocline from an open-ocean tracer-release experiment. *Nature*, 364, 701–703.

[6] Moum, J.N., Klymak, J.M., Nash, J.D., Perlin, A. and Smyth, W.D. Energy Transport by Nonlinear Internal Waves. *J. Phys. Oceanogr.*, 37, 1968–1988.

[7] Shroyer, E.L., Nash, J.D., Waterhouse, A.F. and Moum, J.N. 2017. Measuring Ocean Turbulence *in* Observing the Oceans in Real Time. *Springer*, 99–122.

[8] Smyth, W.D., Moum, J.N. and Cadwell, D.R. 2001. The efficiency of mixing in turbulent patches: inferences from direct simulations and microstructure observations. *J. Phys. Oceanogr.*, 31, 1969–1992.

[9] Watson, A.J. and Ledwell, J.R. 1988. Purposefully released tracers. *Phil. Trans. R. Soc. Lond.*, A 325, 189–200.

[10] Watson, A.J. and Ledwell, J.R. 2000. Oceanographic tracer release experiments using sulphur hexafluoride. *J. Phys Oceanogr.*, 105, 325–337.

[11] Watson, A.J., Ledwell, J.R., Messias, M.-J., King, B.A., Mackay, N., Meredith, M.P., Mills, B. and Naveira Garabato, A.C. 2013. Rapid cross-density ocean mixing at mid-depths in the drake passage measured by tracer release. *Nature*, 501, 408–411.

GFD 2019 Lecture 3: Rates and Mechanisms—What We Observe and Interpret from Observations of Mixing and Turbulence in the Ocean Interior

Stephanie Waterman; notes by Kelsey Everard and Alessia Ferraro

June 19, 2019

1 Introduction

One of the most challenging tasks in physical oceanography is the achievement of a comprehensive physical model able to accurately describe the global oceanic circulation in its entirety. The challenge is due to the large range of spatio-temporal scales and the numerous processes in ocean mixing that interact in a messy non-linear way, making comprehensive numerical simulation difficult and the development of simplified models for the various processes a necessity. Of the numerous complications in modelling global oceanic circulation, small-scale turbulence poses perhaps the most challenging problem. Thus, in an effort to accurately close the equations governing global oceanic circulation, much attention has been given to the role of micro-scale processes as it is believed that these processes control the turbulent mixing in the ocean in need of parameterisation.

At the micro-scale, rotation can be neglected and stratification dominates, thus creating the physical conditions for the excitation of internal waves. These waves, generated by the interaction of tides with the bottom topography (in the deep ocean) or by atmospheric winds (at the surface), can propagate horizontally and vertically, transporting heat, momentum, and nutrients. Complicating matters further is the non-linear interaction of internal waves with each other and with the surrounding topography which can lead to wave breaking. The evolution and the fate of internal waves is the result of a complex scenario that involves a plethora of different phenomena (as shown in figure 1) and is still matter of active research. However, despite the rich dynamics that controls their evolution, the internal wave breaking has been recognized as one the main cause of enhanced turbulent dissipation in the deep ocean and thus a key ingredient to parametrise ocean mixing.

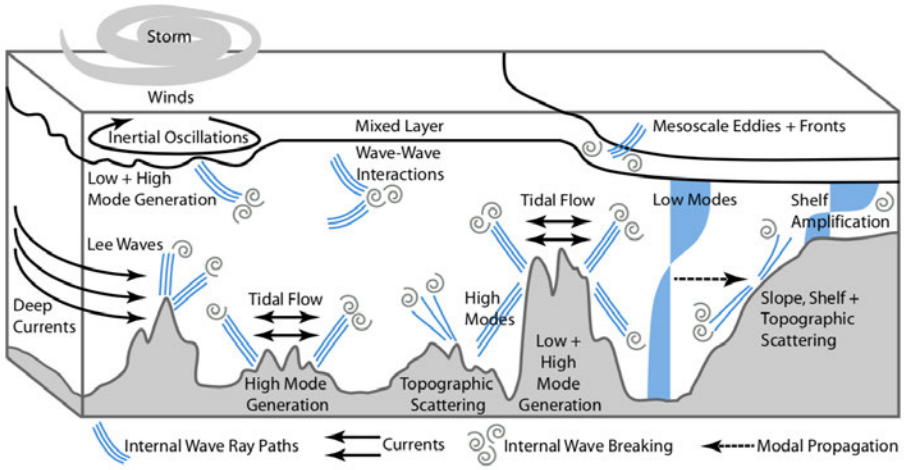

Figure 1: Schematic of internal wave mixing processes in the open ocean taken from [6]. Tides interact with topographic features to generate high-mode internal waves (e.g., at midocean ridges) and low-mode internal waves (e.g., at tall steep ridges such as the Hawaiian Ridge). Deep currents flowing over topography can generate lee waves (e.g., in the Southern Ocean). Storms cause inertial oscillations in the mixed layer, which can generate both low- and high-mode internal waves (e.g., beneath storm tracks). In the open ocean, these internal waves can scatter off of rough topography and potentially interact with mesoscale fronts and eddies until they ultimately dissipate through wave–wave interactions. Internal waves that reach the shelf and slope can scatter or amplify as they propagate toward shallower water.

2 Parameterisation Estimates and Finescale Parametrisations

Among the numerous approaches to quantify ocean mixing, estimations can also be made using large-scale observations and 'models' designed to make explicit predictions on the amount of expected turbulence.
With this approach, parameterisations for turbulent processes are included in large-scale models such that estimations of mixing from large-scale measurements can be made more readily. A major disadvantage, however, is that parameterisations necessitate a number of assumptions which can lead to many limitations of the model from which these estimates eventually arise. Some examples include the estimation of mixing from a statically unstable fluid (Thorpe-scales method [1]) and from fine-scale models. While in the first case the estimate is based on vertical density profiles, in the second, mixing is quantified by means of the observed temperature, salinity and velocity profiles. Due to the fundamental role of internal wave dynamics in the closure of the global oceanic circulation [11], the key idea behind fine-scale parametrizations is the link between turbulent energy dissipation and energy transfer due to the non-linear interactions of these waves. Figure 2 shows a schematic of the energy spectrum associated with the evolution of internal waves at different scales.

The Gregg-Henyey-Polzin (GHP) method, one of the most used fine-scale parameterisation methods, computes the turbulent dissipation rate based on the downscale transfer of energy through the internal wave spectrum via weakly nonlinear wave-wave interactions ([3], [4], [8]). Taking in to account the latitudinal variation of the internal wave interactions and the background wave spectrum field given by the Garret-Munk (GM) model, the dissipation rate can be expressed in terms of the variance of shear $\langle V_z^2 \rangle$ and strain $\langle \xi_z^2 \rangle^2$ as

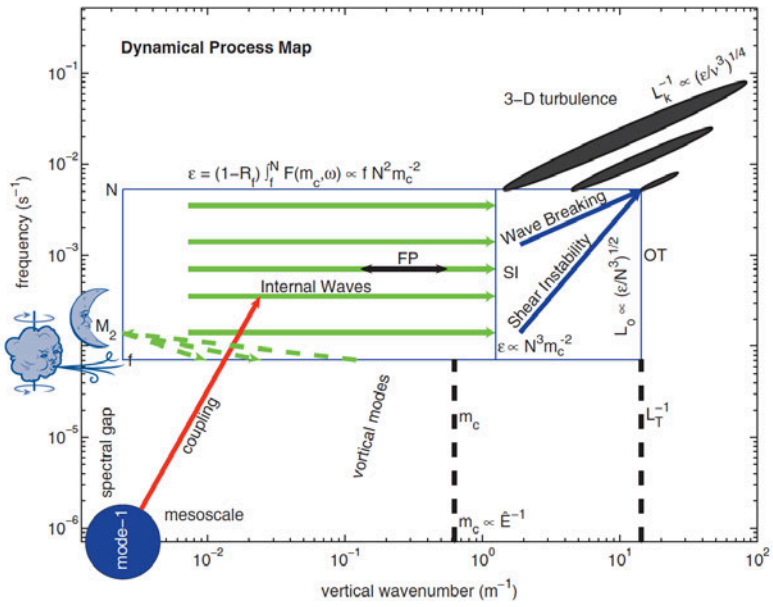

Figure 2: From [7]. A map of dynamical processes in the vertical wave number-frequency domain. Red colors represent sources associated with wave mean effects, green nonlinear transfers, and blue sinks associated with shear instability and wave breaking. Arrows denote the dominant direction of energy transfer. Nonlinear transfers in the frequency domain are uncertain. Wind forcing and barotropic tidal conversion are regarded here as boundary conditions on the radiation balance equation.

$$\varepsilon_{IW[strain]} = \varepsilon_0 \frac{\overline{N^2}}{N_0^2} \frac{\langle \xi_z^2 \rangle^2}{\langle \xi_{zGM}^2 \rangle^2} h(R_\omega)\, L(f,N) \tag{1}$$

$$\varepsilon_{IW[shear]} = \varepsilon_0 \frac{\langle V_z^2/\overline{N^2} \rangle^2}{\langle V_{zGM}^2/N_0^2 \rangle^2} h(R_\omega)\, L(f,N) \tag{2}$$

where both the strain and the shear variance are integrated over internal wave scales (up to a finite maximum wave number k_{max} in order to filter high frequency instrumental noise). Here ε_0 is the reference dissipation rate, N_0 represents the stratification, $\overline{N}$ is the average stratification, and $h(R_\omega)$ and $L(f,N)$ are empirical correction factors that account for latitude effects and wave frequency, respectively.

Allowing for the calculation of the average dissipation over many wave periods, this approach has been proven to be incredibly useful in capturing the spatio-temporal variability of the energy dissipation rate. The relatively easy access to measurements of the wave-field energy, together with the abundance of vertical profiles of shear and strain from numerous platforms and locations around the ocean, makes fine-scale parametrisation methods practically more advantageous over microscale estimates.

However, the strong assumptions at the basis of this approach limits the applicability of the GHP method. Although agreement with microscale estimates exists over smooth topography, discrepancies are observed whenever the wave-wave interaction cannot be considered at most weakly

non-linear or the wave field deviates from the GM model. The failure of the GHP parametrization, often observed near coastal environments or over rough topography, usually relates to the presence of physical processes that modify the evolution of internal waves not accounted for in the model. For example, a systematic over-prediction of the energy dissipation rate from fine-scale estimates has been observed by Waterman *et al.* [10] in the bottom ocean where intense flow speed and lower shear-to-strain ratios R_ω were observed (fig.3). In spite the numerous plausible explanations for this phenomenon, from the role of a non isotropic background state to a possible mean flow-wave interaction, among others, the mechanistic underpinning behind the phenomenon still remains unclear.

An additional drawback of the GHP parametrization method is its extremely high sensitivity to implementation choices and accuracy in the value of input parameters, like the reference buoyancy frequency, the presence of spatial non-homogeneity and the lack of instrumental resolution or bandwidth [7].

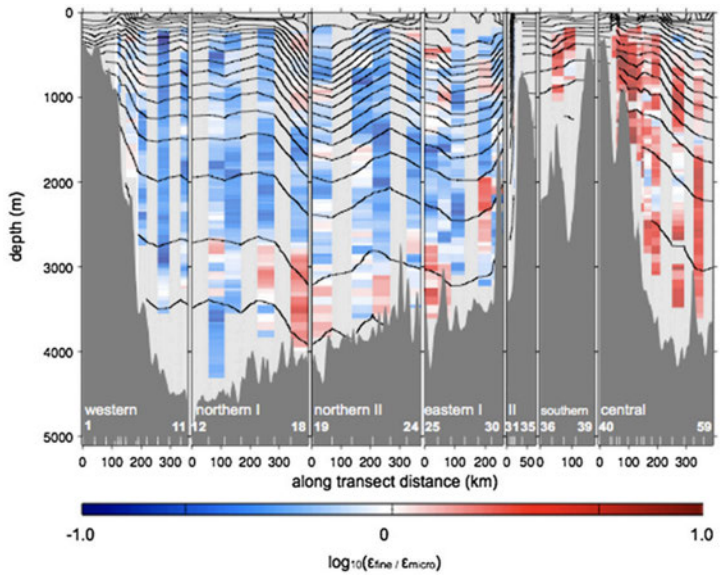

Figure 3: From [10]. An along-transect distance–depth section of the ε ratio $\varepsilon_{fine}/\varepsilon_{micro}$ both displayed on a logarithmic scale. The section, as displayed, starts in the southwestern corner of the survey domain, then runs clockwise along the rim of the region, and finally runs northeastward along the central transect, with each subsection corresponding to an individual transect as indicated. White ticks at the bottom of delineate individual stations with key station numbers labeled to help orient the reader. Neutral density contours in the range of 26˘28.4kgm^{-3} in 0.1kgm^{-3} intervals are shown by the black contours.

Due to the restricted validity of fine-scale parametrization in specific conditions, different techniques to estimate mixing from observational data have been developed:

- measurements of wavenumber spectra from acoustic Doppler currents [9]
- measurements of temperature microstructure from high-frequency acoustics [5]
- in situ particle imaging and tracking [2]

3 Closing Thoughts

Substantial effort has gone into estimating the rates of turbulence mixing in the ocean. Due to the highly non-linear and opaque nature of turbulence in general, a high degree of ingenuity has lead to the creation indirect methods for solving the problem with observations. The use of observational-based parameterisations and estimates has seen both successes and failures.

In the Brazil Basin, where the source of deep water is well-constrained, estimates of turbulent eddy viscosity, K, from the basin-scale estimates agree quite well with micro-structure estimates (see for a nice summary St. Laurent et al. 2001). In the open ocean, however, use of a large-scale diffusivity to estimate a fine- or micro-scale diffusivity poses an issue. For example, inverse methods indicate turbulent diffusivities on the order of K = 10-4 m2 s-1, however, micro-structure measurements indicate that turbulent diffusivities in the open ocean are rarely ever this large (see Wunsch and Ferrari 2004, for a review).

Because of the strengths and weaknesses associated with the variety of different methods, we continue to rely on multiple approaches, and our understanding of turbulence in the ocean continues to develop through intuition gained from a combination of laboratory studies, fieldwork, theory, and numerical simulations.

References

[1] T. S. A., *Turbulence and mixing in a scottish loch*, Royal Society of London Philosophical Transactions Series A, 286 (1977), pp. 125–181.

[2] B. M. M. A. . H. O. Doron, M., *Estimation of light penetration, and horizontal and vertical visibility in oceanic and coastal waters from surface reflectance.*, Journal of Geophysical Research: Oceans, 112 (2007).

[3] M. Gregg, *Scaling turbulent dissipation in the thermocline*, Journal of Geophysical Research: Oceans, 94 (1989), pp. 9686–9698.

[4] W. J. . F. S. M. Henyey, F. S., *Energy and action flow through the internal wave field-an eikonal approach*, J Geophys Res-Oceans., 91 (1986), pp. 8487–8495.

[5] W. R. G. Lavery, Andone C. and M. E. Scully, *Broadband acoustic quantification of stratified turbulence.*, The Journal of the Acoustical Society of America, 134.1 (2009), pp. 40–54.

[6] J. A. MacKinnon, Z. Zhao, C. B. Whalen, A. F. Waterhouse, D. S. Trossman, O. M. Sun, L. C. St. Laurent, H. L. Simmons, K. Polzin, R. Pinkel, et al., *Climate process team on internal wave–driven ocean mixing*, Bulletin of the American Meteorological Society, 98 (2017), pp. 2429–2454.

[7] K. L. Polzin, A. C. N. Garabato, T. N. Huussen, B. M. Sloyan, and S. Waterman, *Finescale parameterizations of turbulent dissipation*, Journal of Geophysical Research: Oceans, 119 (2014), pp. 1383–1419.

[8] T. J. M. . S. R. W. Polzin, K. L., *Finescale parameterizations of turbulent dissipation*, J Phys Oceanogr., 25 (1995), pp. 306–328.

[9] F. Veron and W. K. Melville, *Pulse-to-pulse coherent doppler measurements of waves and turbulence*, Journal of Atmospheric and Oceanic Technology, 16 (1999), pp. 1580–1597.

[10] S. Waterman, K. L. Polzin, A. C. Naveira Garabato, K. L. Sheen, and A. Forryan, *Suppression of internal wave breaking in the antarctic circumpolar current near topography*, Journal of Physical Oceanography, 44 (2014), pp. 1466–1492.

[11] F. R. Wunsch, C., *Vertical mixing, energy, and the general circulation of the oceans.*, Annu. Rev. Fluid Mech., 36 (2004), pp. 281–314.

GFD 2019 Lecture 4: Introduction to Turbulence Theory for Stratified Flows

Colm-cille Caulfield; notes by Anuj Kumar and Wanying Kang

June 20, 2019

1 Introduction

Some of the characteristics that capture the behavior of turbulence are the unsteady, random, chaotic and irregular motion of the fluid. However, it is difficult to give a precise definition of turbulent flow. Turbulent flows typically consist of several vortices/eddies whose interaction gives rise to a wide range of scales in the system. This phenomenon is inherently nonlinear and complex, such that creating a complete theory of turbulent flows is very hard. However, certain characteristics of turbulent flows can be understood. One of the most important ways of approaching the problem is to study the energetics of the flow. In these notes, we define what we mean by mean flow and fluctuations and analyze their energetics. We then briefly discuss some differences between turbulence in two and three dimensions.

2 Description of Turbulence

The motion of a Newtonian fluid is described by the Navier-Stokes equations:

$$\frac{\partial \mathbf{u}}{\partial t} + \mathbf{u} \cdot \nabla \mathbf{u} = -\frac{1}{\rho}\nabla p + 2\mathbf{u} \times \mathbf{\Omega} + \nu \nabla^2 \mathbf{u} + \frac{1}{\rho}\mathbf{F}, \tag{1}$$

where $\mathbf{F}$ is a generic forcing and other variables follow standard notation. For simplicity, we ignore the Coriolis term, $2\mathbf{u}\times\mathbf{\Omega}$, and assume the fluid is incompressible, $\nabla\cdot\mathbf{u} = 0$. Applying the divergence operator to the unforced version of equation 1 yields[1]

$$\nabla \cdot (\mathbf{u} \cdot \nabla \mathbf{u}) = \nabla \cdot (-\frac{1}{\rho}\nabla p). \tag{2}$$

This partial differential equation is know as a Poisson equation, and it describes the evolution of the pressure field. It is immediately clear that pressure here is a non-local quantity, whose sole purpose is to enforce the incompressibility condition. The motion is governed by two competing factors: the advection term (second term on the left-hand side of equation 1) and the diffusion term (last term on the right-hand side of equation 1). Based on the characteristic velocity scale U and length scale L involved in the problem, the relative strength of these two factors is given by the Reynolds number, defined as

$$\mathrm{Re} = \frac{U^2/L}{\nu U/L^2} = \frac{UL}{\nu}. \tag{3}$$

[1] Alternatively, this equation can be derived by studying the variation of the Lagrangian functional of this system. From there, one can see p is the Lagrangian multiplier that constrains the mass conservation.

Figure 1: 1513 sketch by Leonardo da Vinci, illustrating the coexistence of multiple scales and the complexity of turbulent flow.

At sufficiently small Reynolds number, when diffusion of momentum (friction) is dominant, the fluid motion is smooth and we term it *laminar*. However, at large Reynolds number, when the fluid's inertia overpowers diffusion, fluid motion becomes turbulent, with a range of time-dependent and disordered "eddies". Analysis to understand turbulent flow typically proceeds by decomposing the total velocity field into its mean component and fluctuations, under the assumption that there is a sufficiently large spectral gap between the scales of the background mean flow and those of the turbulent eddies. Here, the mean flow's velocity field should be understood as the ensemble average of the total velocity field, i.e.,

$$\mathbf{u}(\mathbf{x},t) = \mathbf{U}(\mathbf{x},t) + \mathbf{u}'(\mathbf{x},t),\ \mathbf{U}(\mathbf{x},t) = \langle \mathbf{u}(\mathbf{x},t) \rangle, \tag{4}$$

$$\mathbf{p}(\mathbf{x},t) = \mathbf{P}(\mathbf{x},t) + \mathbf{p}'(\mathbf{x},t),\ \mathbf{P}(\mathbf{x},t) = \langle \mathbf{p}(\mathbf{x},t) \rangle. \tag{5}$$

Here, angle brackets are used to denote ensemble average, whereas the prime quantities denote fluctuations. Substituting the above decomposition into the momentum equation gives

$$\frac{\partial(\mathbf{U}+\mathbf{u}')}{\partial t} + (\mathbf{U}+\mathbf{u}')\cdot\nabla(\mathbf{U}+\mathbf{u}') = -\frac{1}{\rho}\nabla(P+p') + \nu\nabla^2(\mathbf{U}+\mathbf{u}') + \frac{1}{\rho}\mathbf{F}. \tag{6}$$

Taking the ensemble average of equation 6, all terms that are linear in fluctuation variables vanish.

$$\frac{\partial \mathbf{U}}{\partial t} + \mathbf{U}\cdot\nabla\mathbf{U} = -\nabla\cdot\langle \mathbf{u}'\mathbf{u}' \rangle - \frac{1}{\rho}\nabla P + \nu\nabla^2\mathbf{U} + \frac{1}{\rho}\mathbf{F}. \tag{7}$$

In the above equation, $\mathbf{F}$ is an external forcing with dimensions $[\mathbf{F}] = [\rho]L/T^2$. The first term on the right hand side is the acceleration induced by the "Reynolds stress," $-\rho\nabla\cdot\langle \mathbf{u}'\mathbf{u}' \rangle$, whose divergence works as an additional force. This term scales as $[\rho](U^2/L)$.

Remembering that "energetics is the key," we next derive the energy equation for the mean flow by taking the inner product of $\mathbf{U}$ and equation 7. Using index notation with the Einstein

summation convention, we get

$$\frac{\partial}{\partial t}\left(\frac{1}{2}U_i^2\right)+\frac{\partial}{\partial x_j}\left(\frac{1}{2}U_i^2U_j\right)=-\frac{1}{\rho}U_i\frac{\partial}{\partial x_i}P-U_i\frac{\partial}{\partial x_j}\langle u_i'u_j'\rangle+\nu\frac{\partial}{\partial x_j}\left(U_i\frac{\partial U_i}{\partial x_j}\right)$$
$$-\nu\frac{\partial U_i}{\partial x_j}\frac{\partial U_i}{\partial x_j}+F_iU_i/\rho. \tag{8}$$

Switching the index wherever required and collecting the transport terms on the right hand side, we obtain,

$$\frac{\partial}{\partial t}\left(\frac{1}{2}U_i^2\right)+\frac{\partial}{\partial x_j}\left[\frac{1}{2}U_i^2U_j+U_j\langle u_i'u_j'\rangle-\nu U_i\frac{\partial U_i}{\partial x_j}\right]=-\frac{1}{\rho}U_i\frac{\partial}{\partial x_i}P-\langle u_i'u_j'\rangle\frac{\partial U_i}{\partial x_j}$$
$$-\nu\frac{\partial U_i}{\partial x_j}\frac{\partial U_i}{\partial x_j}+F_iU_i/\rho. \tag{9}$$

Since dissipation happens when there is fluid strain, one can define the dissipation rate,

$$\bar{\epsilon}=2\nu S_{ij}S_{ij}, \tag{10}$$

where S_{ij} is the symmetric component of the strain tensor $S_{ij}=\frac{1}{2}\left(\frac{\partial U_i}{\partial x_j}+\frac{\partial U_j}{\partial x_i}\right)$. Reorganizing this terms yields

$$\bar{\epsilon} \;=\; \nu\frac{\partial U_i}{\partial x_j}\frac{\partial U_i}{\partial x_j}+\nu\frac{\partial}{\partial x_i}\left(U_j\frac{\partial U_i}{\partial x_j}\right). \tag{11}$$

Substituting the above expression back into equation 9 yields,

$$\frac{\partial}{\partial t}\left(\frac{1}{2}U_i^2\right)+\frac{\partial}{\partial x_j}\left[\frac{1}{\rho}U_jP\frac{1}{2}U_i^2U_j+U_j\langle u_i'u_j'\rangle-\frac{\nu}{2}\frac{\partial U_i^2}{\partial x_j}-\nu U_j\frac{\partial U_i}{\partial x_j}\right]= \;-\langle u_i'u_j'\rangle\frac{\partial U_i}{\partial x_j}$$
$$-\bar{\epsilon}+\frac{F_iU_i}{\rho}. \tag{12}$$

Making the isotropic assumption, or assuming that there is no flux crossing the boundary, the divergence term on the left hand side vanishes after integrating over the domain. We then see that the mean flow is maintained by the external forcing F_i, and is damped by kinetic energy dissipation $\bar{\epsilon}$. Mean flow energy can also be converted to (or from) the eddy kinetic energy when the eddies are coherent with the mean flow shear, i.e., when $\langle u_i'u_j'\rangle\frac{\partial U_i}{\partial x_j}\neq 0$. (We have also implicitly made the so-called "Boussinesq" approximation to ignore the spatial variability of the density in absorbing the pressure work term into the square bracket on the right hand side, and to be honest there are further subtleties with the meaning of the pressure which we don't want to get involved with at this stage: variable density makes things complicated!)

3 Energy in the Perturbed Flow

To obtain the energy equation for the fluctuation flow field, we first subtract the governing equation for the mean flow from the governing equation for the total flow. We then take the dot product of the resulted equation with fluctuation flow field and take an ensemble average. The governing equation for the energy in the fluctuation flow field is then found to be

$$\frac{\partial}{\partial t}\frac{\langle u_i'u_i'\rangle}{2}=\frac{\partial}{\partial x_i}\left[-\frac{1}{\rho}\langle p'u_i'\rangle-U_i\frac{\langle u_j'u_j'\rangle}{2}-\frac{\langle u_j'u_j'u_i'\rangle}{2}+\nu\frac{\partial}{\partial x_i}\frac{\langle u_j'u_j'\rangle}{2}\right.$$
$$\left.+\nu\frac{\partial}{\partial x_j}\langle u_i'u_j'\rangle\right]-\langle u_i'u_j'\rangle\frac{\partial U_i}{\partial x_j}-\varepsilon'+\frac{1}{\rho}\langle F_iu_i'\rangle \tag{13}$$

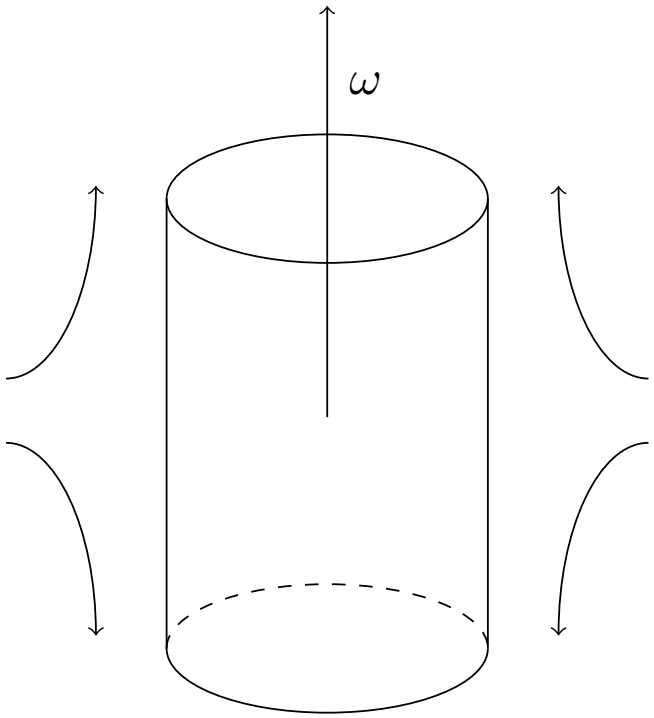

Figure 2: A schematic of vortex stretching mechanism

where

$$\varepsilon' = 2\nu S' : S'$$
$$S'_{ij} = \frac{1}{2}\left(\frac{\partial u'_i}{\partial x_j} + \frac{\partial u'_j}{\partial x_i}\right). \tag{14}$$

The last term in the equation (13) is nonzero only if the forcing $\mathbf{F}$ has a nonzero fluctuation part.

4 Inertial Scaling of Dissipation

Therefore, if we consider a situation where the term in the square bracket on the left hand side can be ignored (as it can be thought of as a divergence of a flux, it often integrates to zero over closed or periodic domains for example) the energy in the fluctuation field decreases monotonically due to the **turbulent dissipation rate** ϵ', and can increase (or decrease) due to exchanges with the mean flow via the **turbulence production** $-\langle u'_i u'_j\rangle \partial U_i/\partial x_j$. Let us first consider a simple case, where $U(z,t)\hat{\mathbf{x}}$, in the "geophysical" coordinate system where z points upwards. Then the turbulence production term reduces to

$$P = -\langle u'w'\rangle \frac{\partial U}{\partial z}. \tag{15}$$

Now, to fix ideas, let's assume that the mean velocity increases with height and there are characteristic scales $\mathcal{U}$ and $\mathcal{L}$ for the mean velocity and its scale of variation. Two scaling observations follow.

1. A fluctuation with $w' > 0$ would be expected to have $u' < 0$ as it would involve "lifting up" a slower moving parcel of fluid. Therefore, it seems natural that in such shear flows u' and w' are negatively correlated thus leading to $P > 0$.

2. For vigorously turbulent flows, it seems at least plausible that the fluctuations u' and w' would also scale with the characteristic velocity scale $\mathcal{U}$, and so $P \sim \mathcal{U}^3/\mathcal{L}$.

Therefore (and appreciating that this is piling assumption upon assumption), if the turbulence is sustained, so that the fluctuation kinetic energy is approximately in steady state, the dissipation rate and the production should roughly balance, and so

$$\epsilon' \sim P \sim \frac{\mathcal{U}^3}{\mathcal{L}}. \tag{16}$$

This "inertial scaling" has been proposed for decades (dating at least as far back as the great G. I. Taylor) and is an example of the so-called "zeroth law of turbulence", as it suggests that as $\nu \to 0$, ϵ' remains finite. Although this has very interesting connections with regularity of solutions of the Navier-Stokes equations, we are not going to get involved with such issues here, as we are actually more interested in how the presence of stratification might affect this (empirically suggested) scaling "law".

5 The Difference Between Two-dimensional and Three-dimensional Turbulence

The vorticity equation can be obtained by applying the curl operator on the momentum equation:

$$\frac{\partial \boldsymbol{\omega}}{\partial t} + \mathbf{u} \cdot \nabla \boldsymbol{\omega} = \boldsymbol{\omega} \cdot \nabla \mathbf{u} + \nu \nabla^2 \boldsymbol{\omega} \tag{17}$$

The first term on the right-hand side of equation 17 describes stretching and tilting of vortex tubes. In three-dimensional turbulence, vortex tubes can stretch and then conservation of angular momentum implies that vorticity can intensify ($\frac{\partial \omega}{\partial t} \neq 0$) if it is not dissipated locally (last term on the right-hand side) or advected away (second term on the left-hand side). This vortex stretching mechanism tends to increase the enstrophy $\langle \boldsymbol{\omega} \cdot \boldsymbol{\omega} \rangle$ of the system. If we neglect the effect of body forces and viscosity, the total energy of the system is conserved.

The only possible way in which enstrophy can increase while the total energy stays the same is when there is transfer of energy to smaller scales, which we call a forward cascade of energy. (As a further aside, this approaching smaller and smaller scales suggests a possible way by which the above-mentioned zeroth law might actually be possible, with extremely small-scale vortical structures developing in turbulent flows. Indeed, as an exercise for the reader, it is possible to show that ϵ' can be written as the viscosity times the fluctuation enstrophy plus a transport term.)

The first term on the right hand side of equation 17, however, is absent if the flow is two-dimensional, and therefore a forward cascade of energy is not possible. This makes three-dimensional turbulence fundamentally different from two-dimensional turbulence. Therefore, in any type of analysis of turbulence in real-world flows, it is important to consider whether the flow is in fact three-dimensional.

References

[1] Frank M. White and Isla Corfield *Viscous fluid flow* volume 3, McGraw-Hill New York, 2006.

[2] Stephen B. Pope *Turbulent flows* IOP Publishing, 2001.

[3] Charles R. Doering and John D. Gibbon *Applied analysis of the Navier-Stokes equations* volume 12, Cambridge University Press, 1995.

GFD 2019 Lecture 5: Effects of Stratification and/or Shear on Turbulence and Their Description by Nondimensional Parameters

Colm-cille Caulfield; notes by André Palóczy and Jeremy Parker

June 21, 2019

1 Key Scales of Turbulence

The most significant result from the last lecture was to present an argument that the turbulent dissipation rate

$$\epsilon' \propto \frac{\mathcal{U}^3}{\mathcal{L}}, \tag{1}$$

where $\mathcal{U}$ and $\mathcal{L}$ are characteristic velocity and length scales of the flow. As mentioned, in a unidirectional shear flow, the turbulence production is dominated by

$$P \sim -\left\langle u'w' \right\rangle \frac{\partial U}{\partial z}. \tag{2}$$

It is "obviously" very challenging to determine $\langle u'w' \rangle$, as it is (effectively) a second-order correlation of fluctuation quantities. Dimensionally, (when multiplied by density) this term is

$$[\rho \left\langle u'w' \right\rangle] = ML^{-1}T^2, \tag{3}$$

which we can recognise as a force per unit area, i.e., a stress, and so this term (even without the density) is commonly referred to as a "Reynolds stress".

By analogy with the viscous stress in a shear flow, a common simplifying assumption in an attempt to parameterise this term is to assume that $-\langle u'w' \rangle = \nu_T \frac{\partial U}{\partial z}$, where ν_T is the **eddy** or **turbulent viscosity**. This expression can be thought of as a closure that relates a second-order correlation of fluctuation quantities (hard to compute/measure) to a first order quantity (the shear in the ensemble mean velocity U), with a proportionality factor ν_T inevitably having the dimensions of a (kinematic) viscosity. Of course, this can't be right, not least because of the strange things that must happen when $\partial U/\partial z$ gets small, or even changes sign.

However, **if** the turbulent viscosity assumption is appropriate, combining it with the inertial scaling for the dissipation rate we obtain:

$$\frac{\mathcal{U}^3}{\mathcal{L}} \propto \nu_T \left(\frac{\partial U}{\partial z}\right)^2 \propto \nu_T \frac{\mathcal{U}^2}{\mathcal{L}^2}, \tag{4}$$

so $\nu_T \propto \mathcal{L}\mathcal{U}$. (Therefore, for consistency, the characteristic length scale L of the flow should be thought of as a "mixing length".)

This turbulent viscosity does not depend on the actual molecular viscosity, but there must come a scale on which this actual viscosity is important: viscosity must be comparable to the turbulent dissipation on some timescale T_K. Dimensionally, remember

$$[\nu] = L^2T^{-1}, \tag{5}$$

and

$$\left[\epsilon'\right] = L^2T^{-3}, \tag{6}$$

so we must have

$$T_K = \left(\frac{\nu}{\epsilon'}\right)^{1/2}. \tag{7}$$

This is equivalent to saying we are (here) concerned with a length scale L_K and velocity scales $U_K \sim L_K/T_K$ such that the local Reynolds number is about 1. Therefore, we wish to identify the length scale such that

$$\frac{L_K}{\nu}\frac{L_K}{T_K} \approx 1, \tag{8}$$

which implies that

$$L_K = \left(\frac{\nu^3}{\epsilon'}\right)^{1/4}. \tag{9}$$

This is the *Kolmogorov length scale*, which can be interpreted (loosely, but we're all relaxed in Walsh Cottage) as the length scale of eddies that are killed after one turnover time.

We then find, using (1) that the outer Reynolds number with velocity scale $\mathcal{U}$ and length scale $\mathcal{L}$ is given by

$$Re^3 = \frac{\mathcal{U}^3\mathcal{L}^3}{\nu^3} = \frac{\epsilon'\mathcal{L}^4}{\nu^3} = \frac{\mathcal{L}^4}{L_K^4}, \tag{10}$$

using the inertial scaling to eliminate $\mathcal{U}$. Here, and elsewhere, remember that $\mathcal{L}$ is some external characteristic length scale of the flow.

Therefore, to resolve a numerical simulation of these equations at high Re, we must resolve the very fine length scale

$$L_K = LRe^{-3/4}. \tag{11}$$

In practice, in truth this is very rarely done, not least because the averaging to arrive at an estimate of ϵ' may smooth out (and suppress) significant spatio-temporal variability.

For any hope of a universal description of turbulence, we must have a situation where

$$L \gg L_E \gg L_K,$$

where L_E is the length scale of an eddy. In fact, this must hold for a significant range of L_E. Experiments on a jet [1] suggest that we may need Re as high as 10^4 for this to hold (see figure 1).

Finally, let us consider briefly a classical simple model flow: stationary, homogeneous, isotropic turbulence.[1] For such a flow, a spectral description in terms of wave numbers is appropriate, as it is only the magnitude of the wave vector that can be important. Therefore, we can define the energy spectrum $\mathcal{E}(k)$ such that the turbulent kinetic energy (density) is given by

$$E_K = \frac{1}{2}\left\langle u_i'u_i'\right\rangle = \int_0^\infty \mathcal{E}(k)\mathrm{d}k. \tag{12}$$

Note that

$$\left[\mathcal{E}\right] = L\left[E\right] = L^3T^{-2}. \tag{13}$$

Therefore, if we make the reasonable assumption that $\mathcal{E}(k)$ can depend only on the length scale of the eddy and the turbulent dissipation rate, dimensional analysis immediately yields

$$\mathcal{E}(k) \propto k^{-5/3}\epsilon'^{2/3}. \tag{14}$$

[1] Devising a suitable mnemonic for these requirements is left as an exercise to the reader.

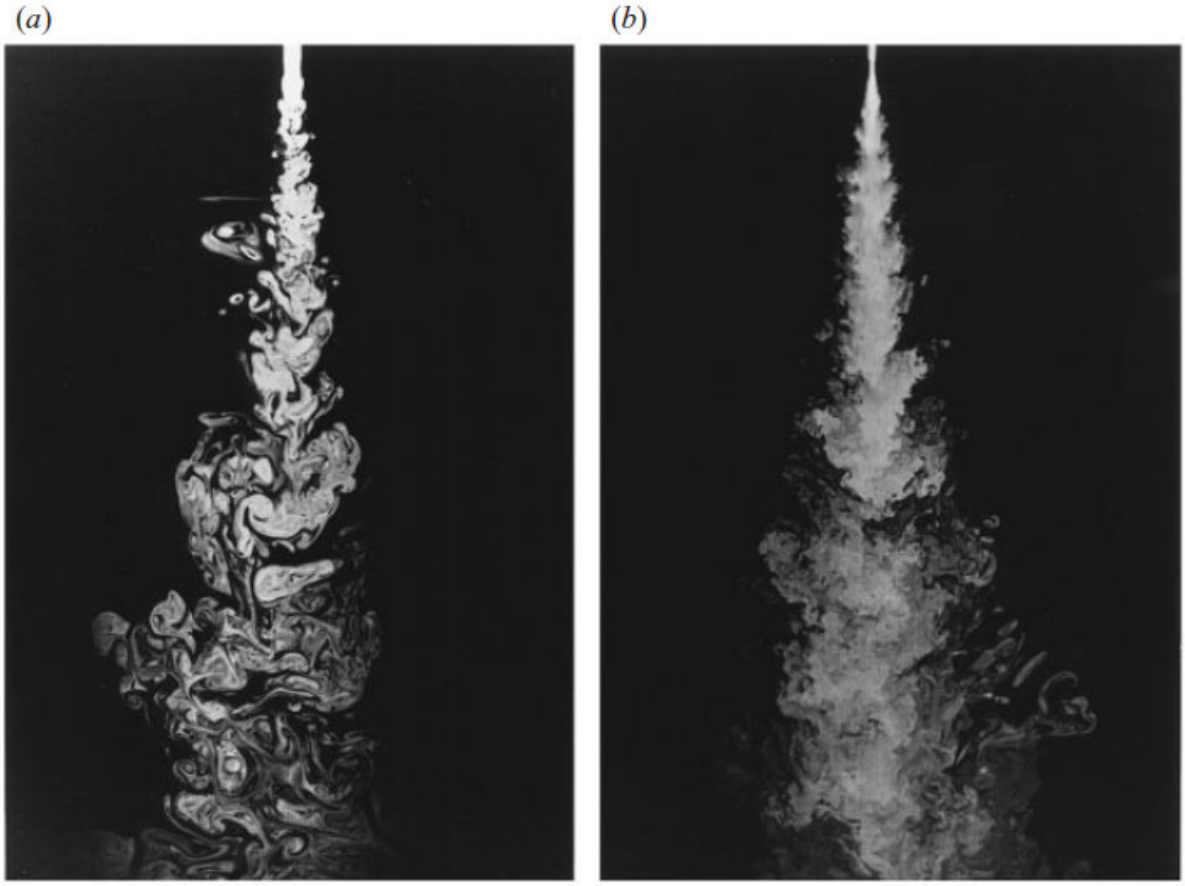

Figure 1: Jet-fluid concentration in the plane of symmetry of a round turbulent jet [2]. (a) $Re \approx 2.5 \times 10^3$ (b) $Re \approx 2.5 \times 10^4$. Notice the clear difference as Re is increased.

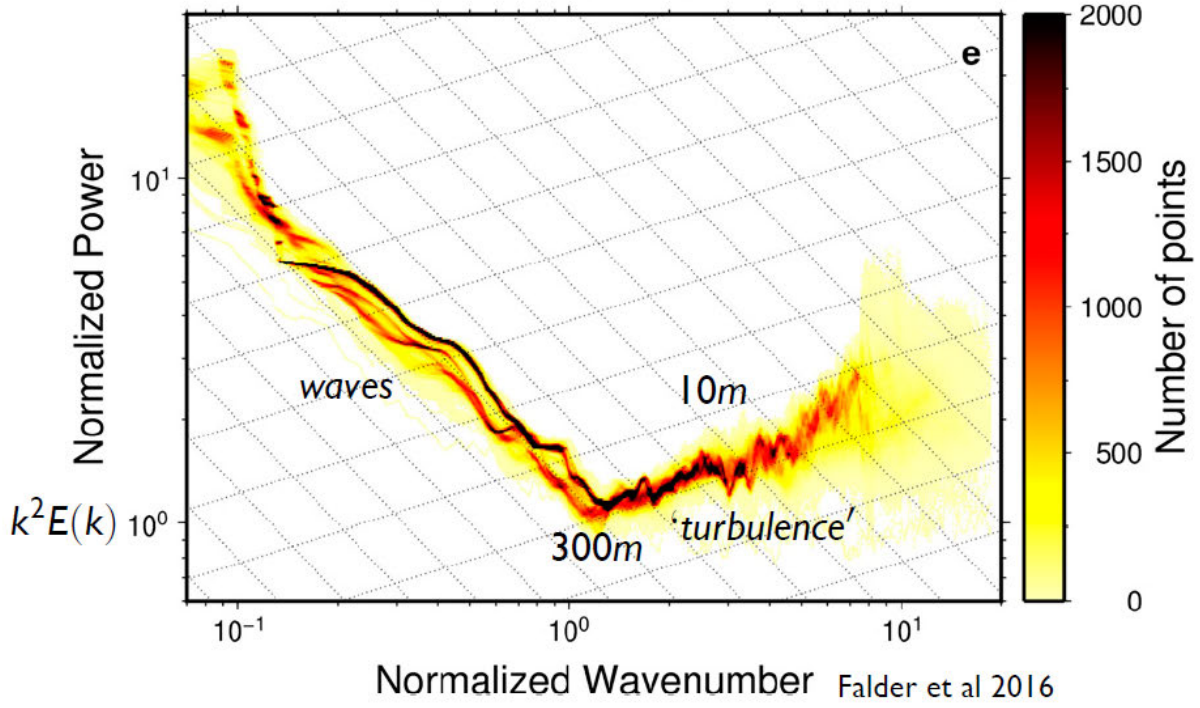

Figure 2: Observations with a $k^{-5/3}$ spectrum, which definitely cannot be isotropic turbulence [3].

This is the classic Kolmogorov spectrum of turbulence. It is important to note here that merely observing a $k^{-5/3}$ spectrum is not sufficient to say that the Kolmogorov argument (for example of isotropy so that only the wavenumber (i.e., the **magnitude** of the wave vector) k matters) such as that presented above is correct, because of the assumptions (see figure 2).

2 Stratification Effects on Turbulence

As already noted, turbulence is hard to define, but has (at least) three key attributes: a wide range of scales; vorticity (through eddying motion, vortex stretching etc) plays a central role; and kinetic energy dissipation is significantly enhanced, through the turbulent dissipation rate ϵ'. The presence of a density stratification affects all three of these attributes, in complicated (and deeply interesting) ways.

For a density-stratified fluid where $\rho = \rho(\boldsymbol{x}, t)$, the Navier-Stokes equation may be written in the form

$$\rho\left(\frac{\partial \boldsymbol{u}}{\partial t} + \boldsymbol{u}\cdot\boldsymbol{\nabla}\boldsymbol{u}\right) = -\boldsymbol{\nabla}p - \rho g\hat{\boldsymbol{z}} + \rho\nu\boldsymbol{\nabla}^{\mathbf{2}}\boldsymbol{u}. \tag{15}$$

Separating the density and pressure fields into perturbations (primed variables) and background, hydrostatic fields (with subscript h, that depend only the vertical coordinate direction in which the gravitational field acts), we have

$$p(\boldsymbol{x},t) = p_h(z) + p'(\boldsymbol{x},t) \quad \text{and} \qquad (16)$$
$$\rho(\boldsymbol{x},t) = \rho_h(z) + \rho'(\boldsymbol{x},t),$$

where the hydrostatic fields p_h and ρ_h (generically nontrivial functions of z) are defined by the hydrostatic relation

$$\frac{\partial p_h}{\partial z} \equiv -g\rho_h. \qquad (17)$$

Using Equation 16 in Equation 15 and making the Boussinesq approximation ($\rho'/\rho_0 \ll 1$ where ρ_0 is a reference value of $\rho_h(z)$ so density differences can be ignored in all terms except $-\rho g\hat{\boldsymbol{z}}$)[2], we have

$$\rho_h\left(1+\frac{\rho'}{\rho_h}\right)\left(\frac{\partial \boldsymbol{u}}{\partial t} + \boldsymbol{u}\cdot\boldsymbol{\nabla}\boldsymbol{u}\right) = -\boldsymbol{\nabla}(p_h+p') - \rho_h\left(1+\frac{\rho'}{\rho_h}\right)\nu\boldsymbol{\nabla^2}\boldsymbol{u} - (\rho_h+\rho')g\hat{\boldsymbol{z}}, \qquad (18)$$

and dividing through by ρ_h, Equation 18 becomes

$$\frac{\partial \boldsymbol{u}}{\partial t} + \boldsymbol{u}\cdot\boldsymbol{\nabla}\boldsymbol{u} = -\frac{1}{\rho_h}\boldsymbol{\nabla}p' - \frac{g\rho'}{\rho_h}\hat{\boldsymbol{z}} + \nu\boldsymbol{\nabla^2}\boldsymbol{u}. \qquad (19)$$

The mass conservation equation is

$$\frac{\partial \rho}{\partial t} + \boldsymbol{\nabla}\cdot(\rho\boldsymbol{u}) = 0, \qquad (20)$$

and a linearized form of the equation of state ignoring salinity and pressure effects is

$$\rho(T) = \rho_0\big[1-\alpha(T-T_0)\big], \qquad (21)$$

where ρ_0 and T_0 are, respectively, a reference density and salinity and α is the thermal expansion coefficient. Within the Boussinesq approximation, $\rho_h(z)$ in the denominators of the first two terms on the right hand side can be replaced consistently with ρ_0.

The temperature satisfies an advection-diffusion equation:

$$\frac{\partial T}{\partial t} + \boldsymbol{u}\cdot\boldsymbol{\nabla}T = \kappa\nabla^2 T. \qquad (22)$$

Differentiating Equation 21 with respect to time and using Equation 22, we obtain a conservation equation for density:

$$\frac{\partial \rho}{\partial t} + \boldsymbol{u}\cdot\boldsymbol{\nabla}\rho = \kappa\nabla^2\rho, \qquad (23)$$

[2]Formally, the Boussinesq approximation means that we are in the distinguished limit where $g\to\infty$ and $\rho'\to 0$, while the product $g\rho'$ remains finite.

or

$$\frac{\partial \rho'}{\partial t} + w\frac{d\rho_h}{dz} + \boldsymbol{u}\cdot\boldsymbol{\nabla}\rho' = \kappa\nabla^2\rho_h + \kappa\nabla^2\rho'. \tag{24}$$

The presence of a gravitational field and a statically stable tratification (or buoyancy gradient) gives the fluid the natural frequency of vertical oscillation or the **buoyancy frequency** N, which in the Boussinesq approximation is defined as

$$N^2 \equiv -\frac{g}{\rho_0}\frac{\partial \rho}{\partial z}. \tag{25}$$

Note that $g\rho'/\rho_0 = g'$ is called the **reduced gravity**, and many authors prefer using the **buoyancy** $b = -g'$ (the negative convention capturing the concept that negative density perturbations do indeed correspond to buoyant parcels, in the non-technical meaning of the word). Stratified fluids with nonzero buoyancy frequency are prone to internal waves, with frequencies of oscillation bounded above by N. The existence of internal waves makes turbulence more non-local than in the unstratified case, since internal waves can propagate energy injected in one location across the system, making it available for turbulence and mixing elsewhere.
A particularly elegant form of Equation 24 arises if ρ_h is a linear function of z, of the form:

$$\rho_h = \rho_0\left(1 - \frac{N_h^2}{g}z\right). \tag{26}$$

With this form of ρ_h the first (diffusive) term on the right hand side disappears, and upon multiplying across by $-g/rho_0$, the equation becomes

$$\frac{\partial b}{\partial t} + N_h^2 w + \boldsymbol{u}\cdot\boldsymbol{\nabla}b = \kappa\nabla^2 b. \tag{27}$$

Remember that N_h^2 here is the buoyancy frequency associated with the (assumed by construction) linearly varying hydrostatic density field, and the density perturbations ρ' (and hence the buoyancy b) are defined as the perturbations away from this time-invariant density field, which is not necessarily the same as the horizontal mean/time average/ensemble average of the density field. Stratified fluids are complicated!

To add to the complications, stratification also modifies the vorticity balance. Taking the curl of the Boussinesq equation 19, we obtain

$$\frac{\partial \boldsymbol{\omega}}{\partial t} + \boldsymbol{u}\cdot\boldsymbol{\nabla}\boldsymbol{\omega} = \boldsymbol{\omega}\cdot\boldsymbol{\nabla}\boldsymbol{u} + \nu\boldsymbol{\nabla}^{\mathbf{2}}\boldsymbol{\omega} + \frac{1}{\rho^2}\boldsymbol{\nabla}\rho\times\boldsymbol{\nabla}p, \tag{28}$$

where $\boldsymbol{\omega}$ is the vorticity vector. We note that the last term is a baroclinic torque term by which the stratification can be a source or sink of vorticity. As the dominant component of the (total) pressure is the hydrostatic part p_h associated with the hydrostatic density distribution ρ_h, to leading order the (total) pressure gradient points in the (negative) $z-$direction. Therefore, if the density isosurfaces are tilted away from the horizontal, and so $\boldsymbol{\nabla}\rho$ is not purely vertical, there can be (baroclinic) creation or destruction of vorticity, explicitly due to the presence of density variations.

The last of the three key attributes of the flow affected by stratification is the energy budget. The Navier-Stokes equations for an incompressible fluid can be written as (once again applying the Boussinesq approximation to replace ρ_h with ρ_0 when allowed):

$$\frac{\partial u_i}{\partial t} + \frac{\partial}{\partial x_j}(u_i u_j) = -\frac{1}{\rho_0}\frac{\partial p'}{\partial x_i} - \frac{g\rho'}{\rho_0}\delta_{i3} + \nu\nabla^2 u_i, \tag{29}$$

for the total velocity field u_i. Taking the dot product of this equation with velocity naturally leads to a kinetic energy equation. If there were no density variations, we would obtain the classical equations with transport terms, dissipation through viscosity, and exchanges between mean and fluctuation (with the mean defined as an ensemble or a time or space averaging) via turbulent production terms and Reynolds stress. However, the ρ' term in the vertical direction will inevitably lead to a new term:

$$B \equiv \frac{g}{\rho_0}\langle \rho' w \rangle, \tag{30}$$

such that $-B$ appears on the right hand side of an evolution equation for kinetic energy. This term, often called the **buoyancy flux** (though more appropriately should be called the density flux) quantifies exchanges between the kinetic energy and the potential energy reservoirs. For example, if on average dense parcels are lifted up, (and so $\langle \rho' w \rangle > 0$), kinetic energy is converted to potential energy. Two fascinating (and still highly controversial) questions then arise? First, how does this exchange affect turbulence? Second, is this exchange irreversible (like the conversion of kinetic energy into internal energy via viscous dissipation) or reversible (like the bobbing up and down of a wave)?

Much of the rest of the lectures will be focussed on trying to answer (at least partially) these questions. As a first step, we can think about defining a turbulent or eddy diffusivity for heat κ_T (or equivalently density within the Boussinesq approximation) analogously to the turbulent viscosity ν_T defined above. Once again we want to relate hard-to-measure second-order correlations to easier-to -measure first order mean quantities, and so

$$\kappa_T \equiv \frac{-\frac{g}{\rho_0}\langle \rho' w' \rangle}{-\frac{g}{\rho_0}\frac{\partial \langle \rho \rangle}{\partial z}} = \frac{B}{\langle N^2 \rangle}, \tag{31}$$

where we now have defined an ensemble-averaged (squared) buoyancy frequency $\langle N^2 \rangle$. There are further subtleties that we don't want to consider here concerning when this ensemble average could or should be made equal to the buoyancy frequency N_h associated with the hydrostatic constant gradient background density field ρ_h. Using this definition, the turbulent Prandtl number is defined as

$$\mathrm{Pr}_T \equiv \frac{\nu_T}{\kappa_T} = \frac{P}{B}\frac{\langle N^2 \rangle}{\langle S^2 \rangle}, \tag{32}$$

and can be thought of as the ratio of the time scales associated with changes in shear and stratification.

References

[1] Dimotakis, P. E. (2000) The mixing transition in turbulent flows. *J. Fluid Mech.* **409** 69–98.

[2] Dimotakis, P. E., Miake-Lye, R. C. & Papantoniou, D. A. (1983) Structure and Dynamics of Round Turbulent Jets. *Phys. Fluids* **26** 3185–3192.

[3] Falder, M., White, N. J. and Caulfield, C. P. (2016) Seismic Imaging of Rapid Onset of Stratified Turbulence in the South Atlantic Ocean. *J. Phys. Oceanogr.* **46** 1023–1044.

[4] Kundu, P. K., Cohen, I. M. & Dowling, D. (2016). Fluid Mechanics, sixth edition, Elsevier.

GFD 2019 Lecture 6: Mixing Mechanisms in Forced and Freely Evolving Flows

Colm-cille Caulfield; notes by Channing Prend and Jelle Will

June 24, 2019

1 Introduction

What is the effect of stratification on turbulence? This is the fundamental question that these lectures are trying to address though (spoiler alert) the question is fundamentally ill-posed as there is no unique (or even generic) answer. We have seen that stratification perturbs many of the fundamental aspects of turbulence, including crucially its vorticity and energetics. The original intention of this lecture was to discuss mixing mechanisms, but unfortunately there are certain preliminaries that need to be covered, and due to the classic (and in fact really welcome) chit-chat and questioning in the Cottage, the discussion of those mixing mechanisms will have to be covered later. The preliminaries covered here are two-fold: first a brief introduction to two classical approaches towards modelling mixing in stratified flows; and second a gentle introduction to the crucial importance of velocity shear for turbulence transition via instability of laminar flows. The two modelling approaches we will introduce are typically called (after their initial proposers) the "Osborn" method [1] and the "Osborn-Cox" method [2], and are commonly used to obtain microscale estimates of mixing in the ocean. One is based on arguments concerning the energetics (Osborn), while the other depends on arguments concerning scalar variance (Osborn-Cox). The key assumptions on which these methods depend are discussed (briefly) below.

2 The Osborn Method

The Osborn method at its heart assumes that the turbulent energy production is balanced by the turbulent buoyancy flux and viscous dissipation, and that those two terms can be related, which is quite a strong pair of assumptions to say the least. These assumptions come from consideration of the evolution of the turbulent kinetic energy (TKE) of a fluid, defined as $E_K = \frac{1}{2}\langle u_i' u_i' \rangle$ (and already discussed in lecture 5, strictly speaking this is an energy per unit mass). The TKE evolution equation (in a Boussinesq stratified fluid, i.e., the stratified generalisation of Equation 13 of lecture 4) is then:

$$\frac{\partial E_K}{\partial t} = -\nabla \cdot (\text{transport terms}) + P + \epsilon' - B + \frac{\langle F_i u_i' \rangle}{\rho_0}. \tag{1}$$

Therefore, the time rate of change in TKE is given by:

- the (negative) of the divergence of transport terms (often called "flux", but one must be careful about what we call flux in the earshot of a chemical engineer, for example, as the dimensions must be correct; whatever these terms do not affect the global balance in a closed or periodic system);

- turbulent production $P = \langle u'w' \rangle \frac{\partial U}{\partial z}$ (if for simplicity the mean flow U is assumed to be in the $x-$direction, and to vary only in the $z-$direction and possibly with time);
- the TKE dissipation rate ϵ';
- and the exchange with the potential energy reservoir via the "buoyancy flux" $B = \frac{g}{\rho_0} \langle w'\rho' \rangle$.

The Osborn method assumes that the flow is in equilibrium, such that the production term is balanced by the buoyancy flux and dissipation and so

$$P = B + \epsilon'. \tag{2}$$

As previously noted, the buoyancy flux, B, should really be split into a reversible part (think sloshing of waves) and an irreversible part associated with irreversible (duh!) mixing of fluid parcels. The situation is further complicated for applications to the real ocean, as diapycnal transport (i.e., transport in the direction normal to surfaces of constant density) is not necessarily equivalent to vertical transport, but that is one of the very many real-world issues that we are at least going to pretend we don't need to worry about.

This equilibrium assumption of the Osborn method naturally begs the question: "how much of the energy is dissipated and how much goes into (irreversibly) rearranging the density gradient?". It seems natural (and, indeed, is correct) to assume that there is some correlation between viscous dissipation and irreversible mixing. Appealing perhaps to Occam's razor, it is then tempting to make Osborn's second fundamental assumption, that this correlation is a linear relationship, and so

$$B = \Gamma \epsilon', \tag{3}$$

for some coefficient Γ, known as the turbulent flux coefficient.[1] Γ is the ratio between the portion of the kinetic energy that goes into the potential energy reservoir (via the buoyancy flux) and the portion that is viscously dissipated, i.e., the "taxation" rate of stratification on turbulence. The first equilibrium assumption implicitly requires the conversion of TKE to PE to be irreversible, and so this conversion can be considered to quantify the rate of irreversible mixing. Although the definition of Γ is appealing, unfortunately, there is not typically a linear relationship between B and ϵ', and, indeed, B and ϵ' can have markedly different distributions. However, all is not lost, as there are sometimes convincing arguments to assume that Γ, indeed, globally has a constant value for some specific flow conditions, as we discuss in more detail below.

We also now define a (related) dimensionless parameter that will be used quite extensively over the remainder of these lectures. The flux Richardson number is defined as

$$Ri_f = \frac{B}{P}. \tag{4}$$

Note, **if** the equilibrium assumption of Osborn applies,

$$Ri_f = \frac{\Gamma}{1+\Gamma}. \tag{5}$$

Notice that Ri_f is, indeed, (by construction) restricted to be in the range $0 \leq Ri_f \leq 1$, and so can be (reasonably) considered to be an "efficiency" of mixing, though it most definitely is not the

[1] Or rather should be known as the turbulent flux coefficient. There is an unfortunate convention to refer to this quantity as a "mixing efficiency", which really should wind up any right-minded person who thinks that efficiencies should be strictly in the closed interval $[0, 1]$ by construction.

unique definition of such an efficiency, since it is based around the idea of shear-driven turbulence production. Using this definition, the turbulent Prandtl number can now be interpreted as a ratio:

$$Pr_T = \frac{P\langle N^2\rangle}{B\langle S\rangle^2} = \frac{\langle Ri\rangle}{Ri_f}, \tag{6}$$

where $\langle Ri\rangle$ is a (gradient) Richardson number, defined in terms of the ratio of ensemble-averaged time scales, the ensemble-averaged (square) buoyancy frequency and shear.

With these definitions, we have a particularly useful way to think about the ultimate objective of our modelling, the determination of κ_t. Remember, we want to understand how fluid motions enhance mixing. To produce a model or parameterisation for that enhancement, it would be really nice if we could model the enhancement as a diffusive process, i.e., via κ_t. In other words, we would like to be able to determine the relative enhancement of density diffusivity by fluid motions, i.e.,

$$\frac{\kappa_T}{\kappa} = \frac{B}{\nu\langle N^2\rangle} = \Gamma Pr_m \frac{\epsilon'}{\nu\langle N^2\rangle}, \tag{7}$$

where Pr_m is the molecular Prandtl number and ν the kinematic viscosity or momentum diffusivity of the fluid. However, even within the framework of the Osborn method, for this expression to be useful we still require intimate knowledge of the energy dissipation rate as a function of space and time. Unfortunately, a fundamental issue is that $\epsilon' = 2\nu\langle S'_{ij}S'_{ij}\rangle$ is prone to strong spatiotemporal intermittency, which is further enhanced when the flow is stratified. Thus, understanding where in the flow energy is dissipated and how this is correlated to other quantities is key to understanding turbulent mixing, even when making the sweeping assumption that B and ϵ' are linearly related. Furthermore, it is actually reasonable to argue that the Osborn method complicates the modelling unnecessarily, as both Γ and ϵ' need to be modelled, and so any error or uncertainty in the estimation of κ_t/κ may be due to either uncertainties in Γ or ϵ', or, indeed, both. Not entirely a satisfactory state of affairs.

3 The Osborn-Cox Method

In contrast to the energetic argument of the Osborn method, which inevitably introduces a need to model both Γ and ϵ', the Osborn-Cox method is based on quantifying the destruction of scalar variance. This is perhaps more appealing (at least from the point of view of simplicity), since this approach is direct in that it requires the modelling of only one quantity, this destruction rate. There is no such thing as a free lunch however, as it is important to note that there are different scales associated with dissipation of scalar as opposed to dissipation of energy. We have already met the Kolmogorov length scale in lecture 5:

$$L_K = \left(\frac{\nu^3}{\epsilon'}\right)^{1/4}, \tag{8}$$

loosely the length scale at which eddies are smoothed out by viscous diffusion in one turn over time. The equivalent scale at which variability in scalar (as opposed to variability in velocity/momentum) is smoothed out in one turn over time is known as the *Batchelor length scale*:

$$L_B = \left(\frac{\nu\kappa^2}{\epsilon'}\right)^{1/4} = \frac{L_K}{Pr_m^{1/2}}, \tag{9}$$

which, for oceanographically relevant scalars, is smaller than L_K since $Pr_m \sim O(10)$ for heat in water, and (mangling notation somewhat as it should really be called a Schmidt number)

$Pr_m \sim O(1000)$ for salinity in water, thus leading to challenges in computation and experimental/observational measurement.

For the Osborn-Cox method, in contrast to Equation 1, we will instead construct an equation for the *buoyancy variance*. This can be directly related to an appropriately defined *available potential energy* of the system, i.e., the potential energy to drive the flow, as originally introduced by [3], but there are many subtleties to be considered that we don't want to go into here: a good starting place to find out about those subtleties is the review of Tailleux [4], both for cited references, and subsequent references to that review. We again make the Boussinesq approximation, with the further assumption that the density varies linearly with the scalar "temperature" field (often called the *Oberbeck-Boussinesq* approximation). We again decompose the density field into the aforementioned hydrostatic linearly varying with depth part $\rho_h(z)$ and a fluctuating part $\rho'(\mathbf{x}, t)$:

$$\rho(\mathbf{x}, t) = \rho_0 \left(1 - \frac{N_h^2}{g} z\right) + \rho' = \rho_h(z) + \rho', \tag{10}$$

(re-)defining the hydrostatic buoyancy frequency N_h, where we are considering sufficiently small differences of z so that the Boussinesq approximation is still valid, and $|\rho'| \ll \rho_0$.

With this decomposition, the advection-diffusion equation for (total) density ρ becomes

$$\frac{\partial \rho'}{\partial t} + w' \frac{d\rho_h}{dz} + \boldsymbol{u} \cdot \nabla \rho' = \kappa \nabla^2 \rho', \tag{11}$$

where we make the (reasonable) extra assumption that there is no background mean flow in the vertical direction so $w = w'$. Multiplying this equation by ρ' and rearranging with a bit of integration-by-parts action yields:

$$\frac{\partial}{\partial t}\left(\frac{\rho'^2}{2}\right) = -\nabla \cdot \left(\frac{\rho'^2}{2}\boldsymbol{u} - \kappa \rho' \nabla \rho'\right) - \kappa \nabla \rho' \nabla \rho' + w \rho' N_h^2 \frac{\rho_0}{g}. \tag{12}$$

Looking at this equation, the last term in the right hand side is very reminiscent of the buoyancy flux B arising in Equation 1, particularly if we multiply across by $\dfrac{g^2}{\rho_0^2 N_h^2}$:

$$\frac{\partial}{\partial t}\left(\frac{g^2 \rho'^2}{2\rho_0^2 N_h^2}\right) = -\nabla \cdot (\text{transport}) - \kappa \nabla \left(\frac{g\rho'}{\rho_0 N_h}\right) \nabla \left(\frac{g\rho'}{\rho_0 N_h}\right) + \frac{g}{\rho_0} w' \rho'. \tag{13}$$

Furthermore, $g\rho'/\rho_0 = g' = -b$ is the (Boussinesq) *reduced gravity* or the (negative) of the *buoyancy*. The term on the left hand side is "clearly" the time derivative of a *scaled buoyancy variance*. A particular attraction of the buoyancy variance being scaled in this way is that this quantity has dimensions $[L^2 T^{-2}]$, i.e., the dimensions of the TKE E_K defined above, thus showing the intimate connection to the potential energy.

Averaging in the same fashion as Equation 1, we obtain

$$\frac{\partial}{\partial t}\left(\frac{g^2 \rho'^2}{2\rho_0^2 N_h^2}\right) = -\nabla \cdot (\text{transport}) - \chi + B, \tag{14}$$

where

$$\chi = \kappa \left\langle \left| \frac{\nabla g'}{N_h} \right|^2 \right\rangle, \tag{15}$$

is the destruction rate of (scaled) buoyancy variance, and has dimensions $[\chi] = L^2 T^{-3}$. There are multiple attractions of this formulation. χ is clearly sign-definite, and is also clearly an inherently

diffusive term quantifying the rate at which $|\rho'|$ decreases, and hence a rate at which the fluid is irreversibly mixed. Analogously to the argument of the Osborn-Cox method, in equilibrium in an appropriately closed or periodic domain, χ destroys buoyancy vaariance at precisely the rate that the buoyancy flux B increases it, further reinforcing the connection between the buoyancy variance equation and an equation for an appropriately defined available potential energy. Due in no small part to all these attractive properties, the Osborn-Cox method then defines the eddy diffusivity of density in terms of this destruction rate of buoyancy variance, (usually determined in the ocean from temperature microstructure measurements):

$$\kappa_T = \frac{\chi}{\langle N^2 \rangle}. \tag{16}$$

Of course, this definition can still be posed in terms of a flux coefficient, as implicitly, this expression defines a (subtly different) flux coefficient

$$\Gamma_\chi = \frac{\chi}{\epsilon'}, \tag{17}$$

though it is reasonable to argue that reintroducing the TKE dissipation rate is not immediately obviously a good idea. Often in practice the averaged buoyancy frequency is determined from a resorting of the observations, or is assumed to be equal to N_h. Again there are several subtleties that we are not getting into here, but is reasonable to think of χ when defined in this way as a destruction rate of an appropriately defined available potential energy.

4 Part II: Effects of Stratification and Shear

4.1 Introduction

We now turn our attention to thinking about when and how flows can actually become turbulent and lead to enhanced mixing. An appealing way by which energy might be injected is through velocity shear, as (empirically) uniform distributions of background vorticity associated with such shear are often "unstable", and break up into vortices. However, as you will be completely unsurprised to read, for flows that are both stratified and sheared, things can become very complicated. We will frame our consideration in terms of thinking about several questions. For example, we need to think about: which parameters are important in classification of flows; whether flow mechanisms actually matter for understanding mixing; and especially does the particular form of the forcing of the fluid make a difference? Indeed, the key issue that we would like to understand is whether or not sufficiently "strong" statically stable density stratification can either prevent the onset of turbulence or inevitably make the turbulence die out. A related issue is understanding the role of spatio-temporal intermittency in stratified turbulence, as it is not a priori clear that very strong stable stratification can completely damp out turbulent motion, as there is at least the possibiliity that small regions of turbulence could still persist locally. Of course, even if they do, it's not clear how material their existence is for a model of the overall mixing within a flow.

The scale of the challenge can at least be started to be appreciated by thinking about the dimensional qualities that could go into constructing (nondimensional) parameters, which fall into three (at least) natural categories:

1. intrinsic properties of the fluid, such as ν and κ;

2. characteristic properties of the ensemble/mean/background, such as the shear or the buoyancy frequency;

3. characteristic properties of the fluctuations/perturbations, such as the turbulent kinetic energy E_K, the (available) potential E_P and/or the scaled buoyancy variance, as well as their associated destruction rates ϵ' and χ.

Furthermore, the second and third categories require an implicit averaging to determine the "characteristic" value, further complicating the picture.

4.2 Role of Shear

As a first step, we will consider some aspects of the importance of the background properties of the flow. To keep things simple, we will first consider inviscid parallel flow, and we will assume that there is a known (time-constant, and so "steady") background density distribution $\rho_b(z)$ and velocity distribution $U_b(z)\hat{\mathbf{x}}$ with associated buoyancy frequency $N_b(z)$ and (vertical) shear $S_b(z)$ defined as

$$N_b(z) = -\frac{g}{\rho_0}\frac{d\rho_b}{dz};\ S_b(z) = \frac{dU_b}{dz}. \tag{18}$$

We assume that this background flow is perturbed by a sufficiently small and smooth perturbation that the underlying equations can be linearised, and that the perturbation can be represented as a sum of Fourier modes. We further assume (for good reasons, but there's not time to go into it here) that we can focus on two-dimensional perturbations, and so we assume we have a plane wave solution the perturbation $\boldsymbol{u} = (u, 0, w)$:

$$\boldsymbol{u} = [\hat{u}(z), 0, \hat{w}(z)]\mathrm{e}^{ik(x-ct)}, \tag{19}$$

where the (streamwise) wavenumber k is real, while the phase speed $c = c_r + ic_i$ may be complex. We are therefore focussing on the possibility of temporal instability, which will occur if $c_i > 0$ (with exponential growth rate kc_i). It is also important to remember that the real part of this expression is understood, and that the wavenumber and/or (real) frequency $\omega_r = kc_r$ may be negative, i.e., there are complex conjugates flying around all over the place. Assuming wave-like forms for the perturbation pressure p' and density ρ', manipulation of the linearised equations of motion for incompressible inviscid flow perturbations to the background flow yields the Taylor-Goldstein equation:

$$\frac{d^2\hat{w}}{dz^2} - \frac{\hat{w}\frac{d^2U_b}{dz^2}}{U_b - c} - k^2\hat{w} + \frac{N_b^2}{(U_b-c)^2}\hat{w} = 0 \tag{20}$$

Note that there is a (regular) singularity at $U_b - c$, which is associated with a critical layer where the (real) phase speed of the mode is the same as the background flow speed, but once again this is not the place to get into the fascinating issues associated with that, but [5] is a good reference for critical layers and also for much of the classical material described here. Indeed, the Taylor-Goldstein equation in the unstratified limit (i.e., $N = 0$) reduces to the more well-known "Rayleigh equation". Several general criteria for instability can be derived from the Rayleigh equation. For example, multiplying by the complex conjugate $\hat{w}^*$ and integrating leads to the Rayleigh inflection point theorem, which states that a necessary condition for instability is that the background velocity profile must have an inflection point (i.e., d^2U_b/dz^2 must change sign).

If we instead multiply by $\hat{W}^*$, where $\hat{W} = \hat{w}/(U_b - c)$, we recover Howard's semicircle theorem (one of the gems in the amazing four page paper by Lou Howard of this parish[6]). This states that a necessary condition for instability is that the real and imaginary components of the phase speed must satisfy:

$$\left(c_r - \frac{U_{\max} + U_{\min}}{2}\right)^2 + c_i^2 \leq \left(\frac{U_{\max} - U_{\min}}{2}\right)^2, \tag{21}$$

where $U_{\min} \leq U_b(z) \leq U_{\max}$. Geometrically, this means that (as Lou put it so beautifully) "the complex wave velocity c for any unstable mode must lie inside the semi-circle in the upper half-plane which has the range of U for diameter."

Howard also proved that a different change of variables, $H = \frac{\hat{w}}{(u-c)^{1/2}}$ in the Taylor-Goldstein equation, leads to the Miles-Howard theorem[7, 6]:

$$c_i \left(\int \left[\left| \frac{dH}{dz} \right|^2 + k^2 |H|^2 + \frac{|H|^2}{|U_b - c|^2} \left(N_b^2 - \frac{1}{4} \left(\frac{dU_b}{dz} \right)^2 \right) \right] dz \right) = 0. \tag{22}$$

Since the first two terms in the integrand are clearly positive definite, if $4N_b^2 > (dU_b/dz)^2$ everywhere, then the integral is positive definite and we must have $c_i = 0$. Therefore, a necessary condition for instability is that somewhere in the domain

$$N_b^2 < \frac{1}{4} \left| \frac{dU_b}{dz} \right|^2 = \frac{1}{4} S_b^2. \tag{23}$$

In other words, a necessary condition for such a steady inviscid parallel stratified shear flow to be linearly unstable is that the *gradient Richardson number* $Ri_g < 1/4$ somewhere in the flow, where Ri_g is defined here as

$$Ri_g(z) = \frac{N_b^2}{S_b^2}. \tag{24}$$

As an aside, remembering our definitions of the flux Richardson number Ri_f and the turbulent Prandtl number Pr_t from Equation (6), **if** we can identify the averaged quantities $\langle N^2 \rangle$ and $\langle S^2 \rangle$ with the background quantities, $Pr_t = Ri_g/Ri_f$, a very interesting relationship...

4.3 The hyperbolic tangent shear layer

To consider a specific example, it is very convenient (and traditional) to consider the *hyperbolic tangent* background velocity and density profiles:

$$U_b(z) = \frac{\Delta U}{2} \tanh\left(\frac{z}{h}\right); \ \rho = \rho_0 - \frac{\Delta \rho}{2} \tanh\left(\frac{z}{h}\right). \tag{25}$$

These profiles have several attractions which have meant that they are very commonly used. These functions are quite similar to the error function profiles that would be expected to form if two streams of fluid with different velocities and different densities (and $Pr_m = 1$, so density and momentum would diffuse at the same rate) came into contact. They also have the attraction that the *bulk Richardson number* Ri_b (aka J) corresponds to the minimum value of the gradient Richardson number at $z = 0$:

$$Ri_b = \frac{g \Delta \rho [2h]}{\Delta U^2} = Ri_g(0) = \min_z Ri_g(z), \tag{26}$$

remembering that h is **half** the characteristic depth of the shear layer (and here the density interface), with total velocity jump ΔU and density jump $\Delta \rho$. It is natural to scale lengths with this half-depth, and so to define a nondimensional wavenumber $\alpha = kh$. Perhaps the most elegant attraction of this background flow is that the *stability boundary*, i.e., the locus in $\alpha - Ri_b$ space where $c_i = 0$ and so the flow is marginally stable can be determined analytically to be the very simple curve:

$$Ri_b = \alpha(1 - \alpha), \tag{27}$$

This simple curve has the maximum possible $Ri_b = 1/4$, nicely making the Miles-Howard theorem "sharp", and thus being a great "smoking gun" motivating proving the general result. The stability boundary for the tanh profiles is a "known" result that I have set as an examination question, and its first mention appears to be in lecture notes of J. Holmboe, a professor at UCLA, whose name will feature significantly in later lectures. The stability boundary and curve of maximum growth for smaller Ri_b is shown in figure 1 [8], remembering that $Ri_b \equiv J$.

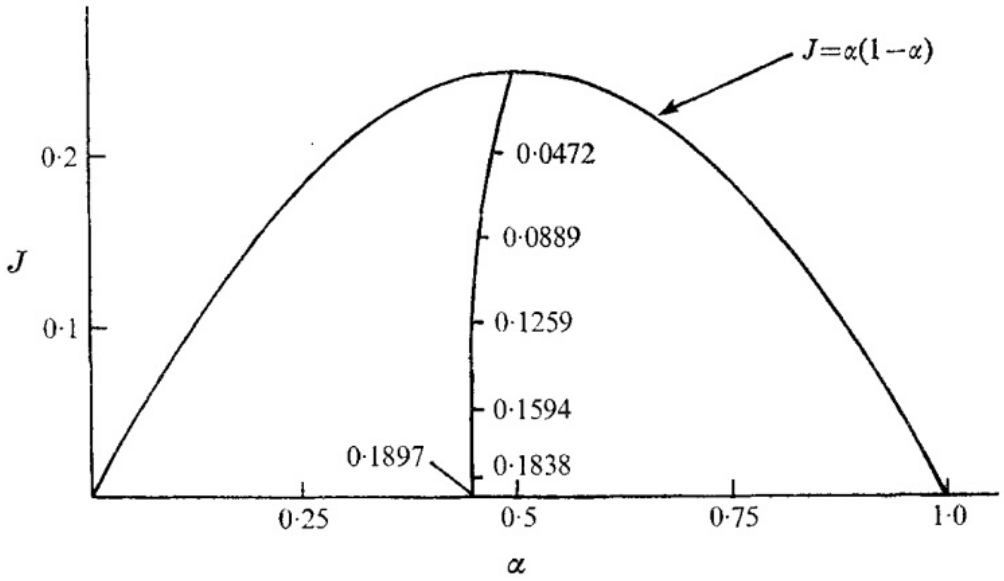

FIGURE 1. Stability boundary and curve of maximum growth rate for 'tanh' profiles, with growth rates marked.

For sufficiently small Ri_b, this instability is clearly the stratification-modified version of the classical "Kelvin-Helmholtz" instability, though it is perhaps more appropriately called the Rayleigh instability since it is the instability of a finite depth shear layer and exists even in the absence of density variations. It is clear from the figure that stable stratification acts in the intuitive fashion expected, reducing the growth rate and range of wavenumbers that are unstable. However, the view of stratification as an always stabilizing mechanism can be misleading. For example, it is conceivable that Ri_b could be very large (defined in terms of shear layer depths and total velocity and density jumps) while locally $Ri_g < 1/4$, thus meaning "all bets are off" in terms of the Miles-Howard theorem. Perhaps counterintuitively, there are also instabilities that inherently require the presence of a stable stratification, which we will discuss in the next lecture as part of our larger aim to understand the effects of stratification on turbulence.

References

[1] Osborn, T. R. (1980). Estimates of the local-rate of vertical diffusion from dissipation measurements. *J. Phys. Oceanogr.* **10** 83–89.

[2] Osborn, T. R. & Cox, C. S. Oceanic fine structure. *Geophys. Fluid Dyn.* **3** 321–345.

[3] Lorenz, E. N. (1955). Available potential energy and the maintenance of the general circulation. *Tellus* **7** 157–167.

[4] Tailleux, R. (2013). Available potential energy and exergy in stratified fluids. *Annu. Rev. Fluid Mech.* **45** 35–58.

[5] Drazin, P. G. & Reid, W. H. (1981). Hydrodynamic Stability. Cambridge University Press.

[6] Howard, L. N. (1961). A note on a paper of J. W. Miles. *J. Fluid Mech.* **10** 509–512.

[7] Miles, J. W. (1961). On the stability of heterogeneous shear flows. *J. Fluid Mech.* **10** 496–508.

[8] Hazel, P. (1972). Numerical studies of the stability of inviscid stratified shear flows. *J. Fluid Mech.* **51** 39–61.

GFD 2019 Lecture 7: Mixing Modelling and Parameterization in Stratified Turbulence

Colm-cille Caulfield; notes by Lois Baker and Houssam Yassin

June, 25 2019

1 Introduction

In the previous lecture, we discussed how (for example, considering the Miles-Howard theorem) stratification can stabilize shear instabilities, presumably thus preventing the onset of turbulence or reducing turbulent motion. However, this can be deeply misleading. There is increasing evidence that the generic base state of a stratified fluid is not one with a constant density gradient, but rather with a layered "staircase"-like structure. That is, a typical vertical structure for the density field consists of relatively deep, relatively weakly stratified "layers" separated by relatively thin or "sharp" interfaces of enhanced density gradient. The Doppler-shifted interaction of the various waves present in such a layered fluid when affected by (vertical) velocity shear may actually lead to instability. Especially since "sharp" density interfaces can sustain localised (internal) gravity waves, it is actually entirely possible for stratification to trigger new classes of instabilities, as we discuss in more detail below.

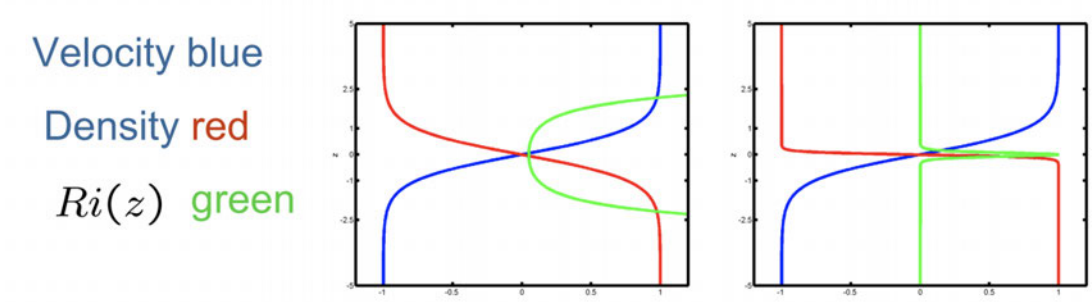

Figure 1: For the same shear profile, a relatively weak density interface (left) and a sharper density interface (left) lead to qualitatively different gradient Richardson number profiles, indicating that instability is possible even in a strongly stratified fluid if the interface is sufficiently sharp.

2 The importance of "sharp" density interfaces

To illustrate how stratification may not necessarily be stabilising, consider first a generalization of the hyperbolic tangent flow considered in the last lecture:

$$\rho = \rho_0 - \frac{\Delta\rho}{2}\tanh\left(\frac{z}{\delta}\right) \tag{1}$$

$$u = \frac{\Delta U}{2}\tanh\left(\frac{z}{h}\right). \tag{2}$$

This is a simple representation of an arbitrarily "sharp" density interface in the presence of shear, as the density varies from $\rho \approx \rho_0 + \Delta\rho/2$ below to $\rho \approx \rho_0 - \Delta\rho/2$ above the interface, which has characteristic half-depth δ, and which crucially can be different from the shear layer half-depth h. Indeed, as $\delta \to 0$, the interface between the two layers becomes infinitely thin and we obtain a two layer fluid. The gradient Richardson number of this background flow is

$$Ri_g(z) = \frac{N^2}{S^2} = R\ Ri_b \frac{\cosh^4(z/h)}{\cosh^2(z/\delta)}, \tag{3}$$

where $R = h/\delta$ is the ratio of the velocity length scale to the density length scale and the bulk Richardson number Ri_b is as in Lecture 6:

$$Ri_b = \frac{g\Delta\rho[2h]}{\rho_0\Delta U^2}, \tag{4}$$

which is now only equal to $Ri_g(0)$ when $R = 1$. As mentioned in the previous lecture, such hyperbolic tangent profiles can be thought of as convenient approximations to the error function profiles which would arise diffusively when two streams of fluid of different density and velocity come into contact. $R = 1$ only when $\nu = \kappa$, and in general it would be expected that $R = \sqrt{Pr_m}$[10]. Since $Pr_m \sim O(10)$ for heat in water, there is a clear motivation to consider flows when $R > 1$ nontrivially. Far from the shear layer and the density interface, Ri_g tends towards

$$Ri_g \approx \frac{1}{4}R\ Ri_b e^{(4-2R)\frac{|z|}{h}} \qquad \text{as} \qquad |z| \to \infty. \tag{5}$$

The stability properties (and in particular the relevance of the Miles-Howard theorem) of the fluid flow then depends on the relative depths of the shear layer and the density interface.[1] If $R < 2$, then Ri gets arbitrarily large away from the interface and so considering the value of Ri_g near $z = 0$ is useful to understand the stability properties. If $Ri_g > 1/4$ at the midplane, then the Miles-Howard theorem can be applied to yield that the flow is stable to normal mode instabilities, as in the classical Kelvin-Helmholtz instability (KHI) considered in the previous lecture. However, if $R > 2$ (that is, if the velocity "interface" is at least twice as thick as the density "interface"), then Ri $\to 0$ as $|z| \to \infty$, irrespective of the value of Ri_b, or indeed $Ri_g(0) = RRi_b$. In this case, once we are sufficiently far from $z = 0$, then Ri $< \frac{1}{4}$ and shear instabilities are at least in principle possible, as the Miles-Howard theorem does not apply. This is a simple demonstration that layered or staircase background states can remain susceptible to shear instabilities and that stratification

[1] It would be cognitively easier if they were both commonly referred to either as layers or interfaces, but unfortunately that is not the convention. The situation is somewhat analogous to the ill-informed and inherently ambiguous pedantry of insisting on referring to Association Football as "football" in English, whereas the abbreviation of "association" to "soccer" dates back to the earliest mid-nineteenth century genesis of the codified laws by **English** public school alumni at the University of Cambridge, who naturally had to distinguish between "soccer" (you can't carry the ball) and "rugger" (short for Rugby football, where you can carry the ball)...but I digress...

is not necessarily stabilizing. These two cases ($R = 1$ on the left, $R \gg 1$ on the right) are shown in figure 1.

Indeed, for "sharp" density interfaces, the resulting instability may take two different forms depending on the strength of the stratification. If the density difference between the two layers is not too large then the resulting instability "rolls up" the initially streamwise-invariant strip of spanwise vorticity in the shear layer into trains of elliptical vortices. This roll-up brings higher density fluid above lower density fluid—a convectively unstable situation that, at least at sufficiently high flow Reynolds number, leads to turbulent mixing between the two layers. This is the nonlinear finite amplitude manifestation of the well-known KHI. As noted last time, this should really be called the Rayleigh instability, since Kelvin and Helmholtz only considered a discontinuous background velocity distribution, and the ensuing delta-function vorticity sheet is indeed unstable, but in inviscid flow in the absence of surface tension there is no scale selection, and the growth rate (in an inviscid flow) increases monotonically with wavenumber. Conversely, Rayleigh demonstrated that there was a unique finite wavenumber with maximum linear growth rate in finite-depth shear layers, i.e., when there was a characteristic (vertical) scale in the system that the strip of spanwise vorticity in the shear layer "knows about". Whoever the instability should be named after, this particular strongly overturning instability is monotonically stabilised by stratification.

However, if the density difference between the two layers is sufficiently large and the density interface is sufficiently sharp, then the unstable strip of vorticity in the shear layer cannot completely roll up and overturn because of the relatively greater potential energy cost associated with the roll-up of the sharp interface. Instead, the density interface "splits" the strip of spanwise vorticity, and (smaller) vortices roll up on either side of the interface. As these trains of vortices are embedded within the shear layer, and hence have different characteristic streamwise velocities as they are centered at different vertical locations, these trains of vortices propagate relative to each other. The finite amplitude manifestation of the instability appears to lead to significantly less mixing between the layers, but induces counter-propagating cusped waves on the interface, associated with the fluid wrapping around the "scouring" counter-propagating trains of vortices. This instabilty is known as the Holmboe Wave Instability, (HWI) after J. Holmboe, though at least in this case a paper was published[4]. To summarize, at weak stratification, shear instability takes the form of an overturning KHI that mixes the two layers and hence spreads out the (already relatively broad) interface between the layers, thus actually having a hope to be represented as a turbulent diffusive process. Conversely, for a strongly stratified interface, overturning the layers is no longer possible and we obtain a scouring HWI, which (appears) to keep the interface relatively sharp, and so a description as a diffusive process is not really appropriate[9].

There appears to be a continuous transition between KHI and HWI as the interface strength is increased, as quantified by the value of the bulk Richardson number Ri_b. In the simplest symmetrical case we are considering here, the billows associated with KHI have zero phase speed, while the vortices associated with the HWI have equal and opposite phase speeds. At low Ri_b, the fastest growing mode has zero phase speed and is associated with the KHI. At some critical value of Ri_b there is a bifurcation—we obtain two modes with opposite phase speeds characteristic of the HWI. It is important to appreciate that HWI only exists because the flow is statically stable: the more one thinks about that, the stranger it should seem that stable stratification **destabilises** the flow. To understand why these different instabilities can arise in a sheared stratified flow, it is actually very instructive to consider the limit of discontinuous density distributions, as significant analytical progress can be made, particularly when the vorticity field is also allowed to become piecewise constant, modelling the shear layer as a uniform strip of vorticity rather than the smooth $\mathrm{sech}^2(z)$ distribution implicit in the assumption of a tanh-like background velocity distribution. In such a situation, it is possible to get a handle on how statically stable density distributions can destabilise

shear flows. The key ingredients are that stratification leads to internal waves, and shear leads to Doppler shifting, thus allowing the internal waves to interact in just the right way to lead to instability.

3 Discontinuous density distributions

Remember (from the last lecture) the Taylor-Goldstein equation for linear disturbances to a parallel background flow $\mathbf{U}_b = (U_b(z), 0, 0)$ in a Boussinesq stratified fluid with background buoyancy frequency distribution $N_b(z)$:

$$\frac{d^2\hat{w}}{dz^2} - \left[k^2 + \frac{d^2U_b/dz^2}{U_b - c} - \frac{N_b^2}{(U_b - c)^2}\right]\hat{w} = 0. \tag{6}$$

where w is the vertical (perturbation) velocity, and is assumed to be of the form

$$w(x, z, t) = \hat{w}(z)e^{ik(x-ct)}, \tag{7}$$

where k is the horizontal wavenumber, and c is the horizontal phase speed.

This equation actually also can be thought of as the governing equation for the dynamics of internal waves in the presence of arbitrary stratification and vertical shear. The Taylor-Goldstein equation is a second-order linear differential equation with regular singular points. Note that non-zero stratification introduces a second-order singularity while the singularity associated with vertical shear is first-order. This equation simplifies considerably in a layered fluid with arbitrarily sharp interfaces, i.e., where we assume that the density and spanwise vorticity are piecewise constant. We assume that the velocity remains continuous while becoming piecewise linear so that there remains a finite depth shear layer of depth $2h$ with a constant gradient, and so piecewise constant vorticity. Therefore, N_b^2 vanishes everywhere except at the interfaces between the density layers where $N_b^2 \to \infty$, and so N_b^2 is actually proportional to (in general) sums of Dirac δ-functions. In addition, if we take the shear to be piecewise constant, then d^2U_b/dz^2 vanishes within each layer, though again d^2U_b/dz^2 is actually proportional to sums of δ-functions.

For convenience, nondimensionalize lengths with h, velocities with $\Delta U/2$ and density differences from a reference density ρ_0 with $\Delta\rho/2$, where ΔU and $\Delta\rho$ are the total differences in background velocity and density across the flow

The equation within each layer (for nondimensional variables) becomes very nice:

$$\frac{d^2\hat{w}}{dz^2} - \alpha^2\hat{w} = 0;\ \alpha = kh, \tag{8}$$

and so the eigenfunction within each layer takes the form of a sum of exponentials $\hat{w} = C_i^+ \exp(\alpha z) + C_i^- \exp(-\alpha z)$. Stratification and shear then enter the problem only through the matching conditions between each layer (of constant density and/or constant shear) associated with integrating across the δ-functions while maintaining key physical properties of continuity. These matching conditions, along with the boundary conditions determine the various constants $C_i^\pm$ to construct a polynomial *dispersion relation* relating c to α. "Clearly" the vertical velocity across each interface must be continuous– this leads to the requirement that

$$\left[\frac{\hat{w}}{U_b - c}\right]_-^+ = 0 \tag{9}$$

across the interface (where again either background density and/or background vorticity jumps). Continuity of pressure across each interface is equivalent to

$$\left[(U_b - c)\frac{d\hat{w}}{dz} - \frac{dU_b}{dz}w - Ri_b\rho_b\frac{\hat{w}}{(U-c)}\right]_-^+ = 0, \tag{10}$$

where once again it is important to remember that U_b and ρ_b have been scaled with $\Delta U/2$ and $\Delta\rho/2$, respectively. Solving this system leads to a polynomial equation for the phase speed c. Instability occurs when c has an imaginary component.

4 Wave resonance interpretation

When considered in such a piecewise linear way, instabilities can then be interpreted in terms of resonance between waves localised at the different interfaces. At a velocity interface, *Rayleigh waves* can develop on the jump in the vorticity at the interface at the edge of a shear layer. Analogously, at a density interface, internal gravity waves can develop. If we make the assumption that the distance between the relevant interfaces is large compared to the wavelength of the wave, we may consider each interface in isolation to help build a picture of the resonances that can occur. However, it should be noted that (especially in the case of asymmetric interfaces), it is not clear (and is an area of active research) where the boundary between, for example HWI and KHI lies.

4.1 Kelvin Helmholtz Instability

Kelvin-Helmholtz instability is the result of the coupling of two Rayleigh waves, and may occur in a stratified or unstratified flow. Consider an unstratified fluid with piecewise constant shear as shown in figure 2.

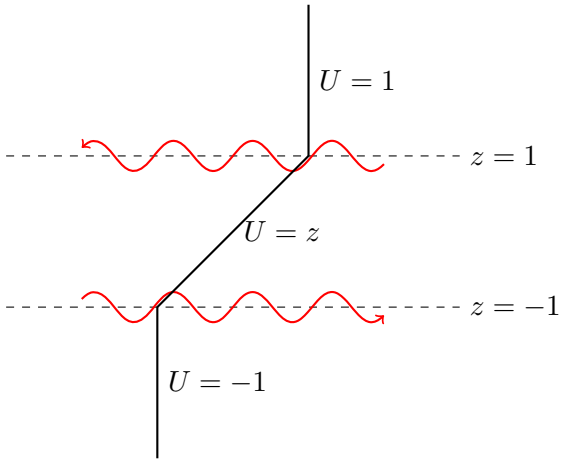

Figure 2: Wave resonance can take place between the two Rayleigh waves at each velocity interface, forming Kelvin Helmholtz instability. Figure adapted from [1].

There is a discontinuity in vorticity at the edges of the shear layer at $z = \pm 1$. Assuming these discontinuities are very far apart (relative to the wavelength of the wave, so when $\alpha \gg 1$), each discontinuity can support the existence of a trapped Rayleigh wave that decays exponentially away

from the interface. At $z = 1$ there is a (relatively) leftward propagating wave with $c_+ = 1 - \frac{1}{2\alpha}$, while at $z = -1$ there is a relatively rightward propagating wave with $c_- = -1 + \frac{1}{2\alpha}$. Instability occurs when the two waves have the same phase speed $c_+ = c_-$ at the same wavenumber. This occurs for waves with a wavenumber of $\alpha = 1/2$. Although the asymptotic assumption of $\alpha \gg 1$ is clearly violated, this estimate is actually pretty good, as the full problem (doing the proper matching of the jump conditions across the two interfaces at $z = \pm 1$) leads to the quadratic dispersion relation:

$$c^2 = \frac{(2\alpha - 1)^2 - e^{-4\alpha}}{4\alpha^2}, \tag{11}$$

which predicts instability for $0 < \alpha \lesssim 0.64$, with the largest growth rate at $\alpha \simeq 0.4$, very similar to the hyperbolic tangent case considered in the previous lecture. The key generic idea is that the instability arises through the interaction of two Doppler-shifted interfacial waves.

4.2 Holmboe Wave Instability

If, in addition to shear, the flow is also stratified, there is another class of interfacial waves, i.e., gravity waves which also exist in the fluid. The presence of such waves can lead to new instabilities. Consider the shear and density profile in figure 3. Holmboe Wave Instability (HWI) may be interpreted as an instability involving the coupling of a gravity wave with a Rayleigh wave. In a two-layer fluid, gravity waves have phase speeds of $c_{g,\pm} = \pm\sqrt{\frac{\mathrm{Ri}_b}{\alpha}}$. There is coupling (in $z > 0$) between the rightward propagating gravity wave $c_{g,+}$ and the leftward propagating Rayleigh wave when $\sqrt{\frac{\mathrm{Ri}_b}{\alpha}} = 1 - \frac{1}{2\alpha}$. This occurs when $\alpha \approx \mathrm{Ri}_b + 1$. Therefore, there can be instability for arbitrarily high stratification in some wave number range. (In this symmetric case, there is an analogous resonance in the lower half-plane between the left-going internal wave and the Rayleigh wave at $z = -1$.) In this case, the resonance continues to arbitrarily large Ri_b, (not violating the Miles-Howard theorem, since the **gradient** Richardson number is zero everywhere except at the density interface $z = 0$) when the asymptotic high wavenumber assumption definitely is satisfied. This prediction is consistent with the solution of the full problem, which leads (in the symmetric case) to a biquadratic dispersion relation for the phase speed:

$$c^4 + c^2\left(\frac{e^{-4\alpha} - (2\alpha - 1)^2}{4\alpha^2} - \frac{Ri_b}{\alpha}\right) + \frac{Ri_b}{\alpha}\left(\frac{e^{-2\alpha} + (2\alpha - 1)}{2\alpha}\right)^2 = 0. \tag{12}$$

This (as described above) predicts KHI (with zero phase speed) for sufficiently small Ri_b but then a band of unstable wavenumbers with non-zero (both negative and positive) phase speeds for all Ri_b, the band getting narrower as $Ri_b \to \infty$ and tending towards $\alpha = Ri_b + 1$.[4].

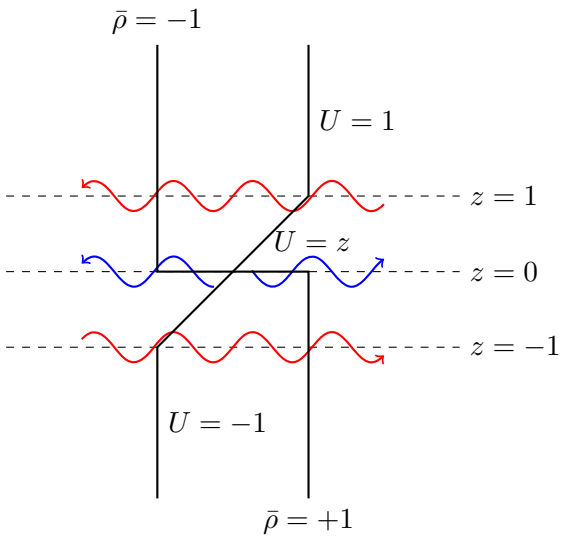

Figure 3: One density interface and two vorticity interfaces allow coupling between the top leftward propagating red Rayleigh wave and the blue rightward propagating internal gravity wave, and similarly for the other pairing in $z < 0$. Figure adapted from [1].

4.3 Taylor - Caulfield Instability

The actual first stratified shear problem considered by G. I. Taylor (originally in his Adams Prize Essay in 1915 on "Turbulent motions in fluids" but only published in 1931[12] since S. Goldstein had independently derived the key equation) considered a three-layer density distribution, crucially with two sharp density interfaces embedded within a shear layer. Such a flow is difficult to realise experimentally (and to interpret mathematically) as Taylor noted when he explained why he had not published before 1931:

"*The chief part of the work described in this paper was done in 1914 and formed part of the essay for which the Adams Prize was awarded in 1915. During the war years it was laid aside, and since then I have delayed publication, hoping to be able to undertake experiments designed to verify, or otherwise, the results... It is a simple matter to work out the equations which must be satisfied by waves in such a fluid, but the interpretation of the solutions of these equations is a matter of considerable difficulty...*

The simplest distillation of the case he considered is shown in figure 4, where there is a constant shear with two density interfaces. Interestingly, it is possible to achieve instability even though the shear profile would be stable with no stratification. The mechanism in this case is the resonant coupling of the two interfacial gravity waves at the two different and separated density interfaces. It is necessary to have shear in this situation, to modify the phase velocities of the gravity waves such that the phase speeds can be equal. However, a uniform shear is sufficient to allow this instability to develop - a situation which would not be unstable to Kelvin Helmholtz instability without stratification by the Rayleigh inflection point criterion. Doing the full calculation for the flow shown in the figure it is possible to show that there is a band of instability (i.e., $c_i > 0$) for

$$\frac{2\alpha}{1+e^{-2\alpha}} < Ri_b < \frac{2\alpha}{1-e^{-2\alpha}}, \tag{13}$$

which (amazingly) implies instability **only** for Ri_b strictly greater than zero, due to the essential requirement for the interaction of Doppler-shifted interfacially trapped internal gravity waves. Remembering that here each interface has half of the total density jump, the lower density interface (if isolated) supports a (relatively) rightward propagating wave with phase speed

$$c = -1 + \left(\frac{Ri_b}{2\alpha}\right)^{1/2}, \tag{14}$$

while the upper density interface (if isolated) supports a (relatively) leftward propagating wave with phase speed

$$c = 1 - \left(\frac{Ri_b}{2\alpha}\right)^{1/2}. \tag{15}$$

Resonance thus occurs at $c = 0$ and $Ri_b = 2\alpha$, which is clearly the asymptote of the band of instability as Ri_b and α get large.

This is another example of the introduction of a stratification destabilising an otherwise stable flow- contrary to the widely held view of stratification as a stabilising mechanism. To distinguish it from the many other instabilities identified by Taylor, this instability is now often referred to (at least by the lead author of the first experimenatl observation[2]) as the Taylor-Caulfield instability (TCI).

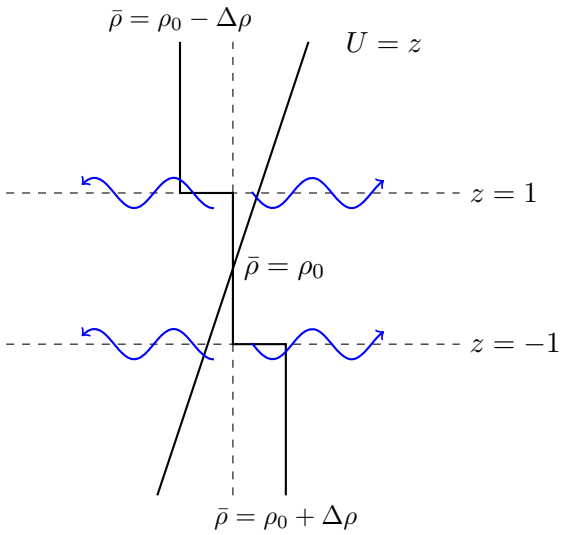

Figure 4: Wave resonance between the leftward propagating interfacial gravity wave at the top density interface and the rightward propagating interfacial gravity wave at the bottom density interface allows Taylor-Caulfield instability to develop. Figure adapted from [1].

4.4 Realisations of stratified shear instabilities

KHI has been widely observed in nature, experiments, and simulations. When the stratification is sufficiently weak, finite amplitude classical Kelvin Helmholtz billows form at the interface, overturning and acting to mix effectively the dense and lighter fluids, smoothing out the interface. If instead there is a sharp density interface, Kelvin Helmholtz billows have insufficient energy to overturn the interface, and the instability is instead susceptible to HWI. The finite amplitude realisation

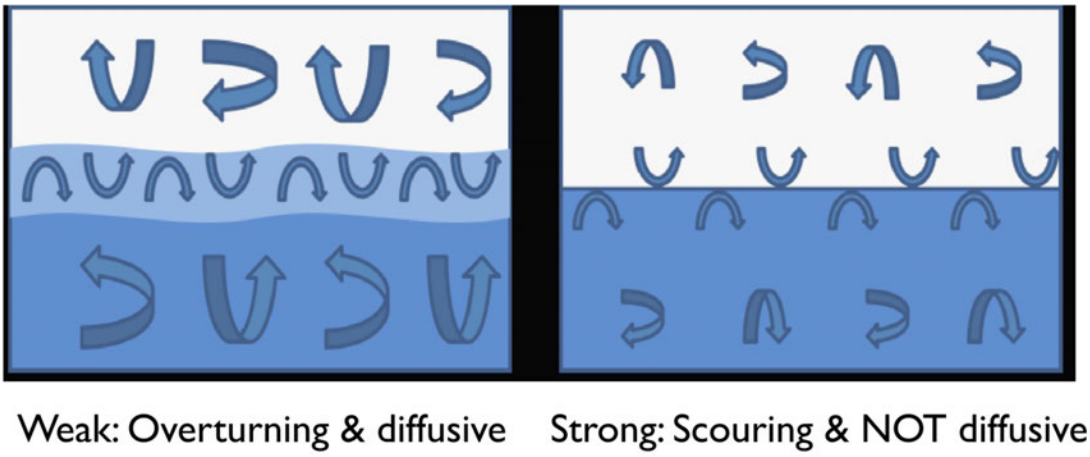

Figure 5: A weak diffusive interface versus a strong scouring interface. The left figure could result from Kelvin Helmholtz instability, whereas the right figure could result from Holmboe Wave instability [14].

of (symmetric) HWI is two trains of counter propagating elliptic vortices above and below the interface, which instead of mixing scour the interface, sharpening it further. Figure 5 demonstrates how a gradual interface may become more well mixed and a sharp interface may become sharper as a result of shear instabilities. Unfortunately for the ego of the lead author of the first experimental observation at least, while KHI and HWI can be readily observed in natural systems, experiments and simulations, TCI appears to be much more fragile, and to be very unstable to secondary instabilities, only (apparently) occuring for a very narrow band of flow parameters, consistently with Taylor's difficulties to observe it experimentally. (He had the good sense to move onto the much better behaved Taylor-Couette problem[11]). As a closing point, in all linear stability problems, it is important to note that the finite amplitude realisation of an instability does not necessarily represent the most unstable wave number of the linear problem, and the finite amplitude manifestation may be very different in structure from the linear eigenfunction.

5 Lateral Shear

Having investigated instabilities that can occur at sharp density interfaces, it is natural to ask the question: do sharp interfaces, or density layering, occur naturally? Typically, we have considered "vertical" shear, in the sense that the velocity and density gradients are (anti-) parallel. If we instead have lateral shear (associated with vertical vorticity) in a stratified system, i.e., the velocity and density gradients are orthogonal, the vertical vorticity will create rolls that can spontaneously form layers, typically with the vertical scale $\frac{U}{N}$. Figure 6 shows such layers forming in an experimental rotating stratified flow [5].

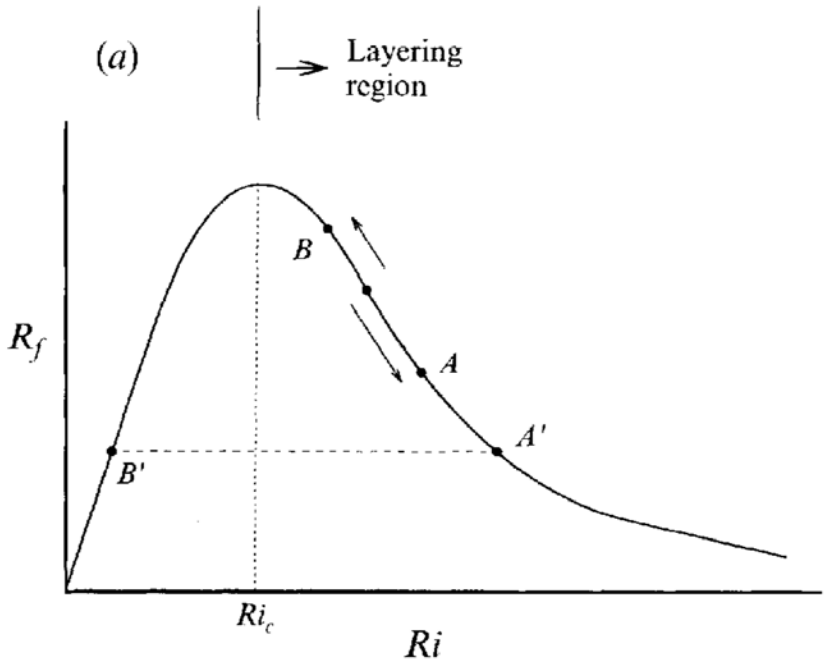

Figure 7: A conceptual non-monotonic relation of Ri_f to Ri_b. To the right of the critical Ri_c, it is expected that layering can take place [8].

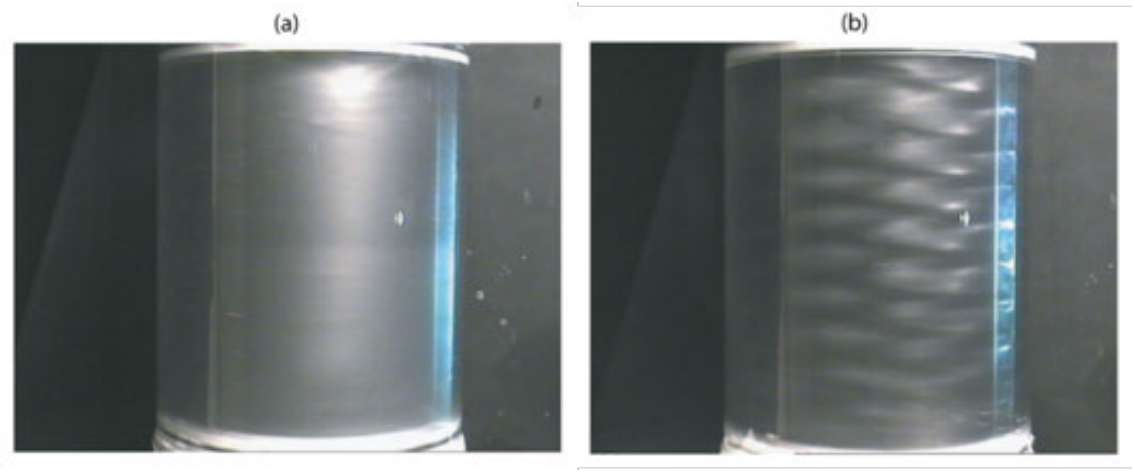

Figure 6: Couette flow in pure water (a) and the stratified rotational instability in vertically stratified salt water (b) at the same Reynolds number. See [5].

One suggested mechanism for layer formation relies on a non-monotonic flux Richardson number as a function of the stratification. Recall that the flux Richardson number is defined as $Ri_f = B/P$ where B is the rate at which turbulent energy is expended in mixing the fluid and P is the rate of production of turbulent energy. Suppose that the flux Richardson number (remember this can be thought of as an *efficiency* of mixing) reaches a maximum at some critical value of the (gradient) Richardson number and then decreases for larger Ri_g, as demonstrated in figure 7. Suppose that

we are in the *left flank* regime to the left of Ri_c, such that Ri_f increases with Ri_b. Then moving to an area of stronger stratification increases mixing, creating a divergent flux away from the strongly stratified region and eroding gradients and sharp interfaces, analogously to "diffusive" overturning. If instead we are in the *right flank* regime where Ri_f is decreasing with stratification, then moving towards an area of stronger stratification decreases mixing, causing a convergent flux towards the interface and sharpening gradients, analogously to "anti-diffusive" scouring. This is a proposed mechanism for the formation of layered flow. Molecular diffusion eventually becomes important to regularise the interface thickness.

Another remarkable manifestation of this layering was found in horizontally sheared vertically stratified plane Couette flow[7]. By direct numerical simulation, this flow was shown to exhibit layering and turbulence, consistent with the prediction that such a flow had linear instabilities at **strong stratification**[3] although it is well-known that the unstratified flow is linearly stable for all Reynolds numbers. The layering of such stratified flows is due to the tendency for strong stratification to become anisotropic or "patchy". Vertical velocities are suppressed by the strong stratification, and this anisotropy in the velocity field means horizontal velocities are much larger than vertical velocities, allowing pancake-like layering [6].

5.1 Mixing associated with layering

Buoyancy changes can be reversible and we want to be able to distinguish between reversible buoyancy changes due to stirring and irreversible changes associated with turbulent mixing events, that is between PE and APE (available potential energy). One way to do this is by sorting densities. Suppose you have a box with four regions of fluid with different densities as described in (I). These regions can be rearranged so that they are stacked in a stable sense in the vertical (II). Clearly, arrangement II has a lower (indeed minimum) potential energy compared to arrangement I. Arrangement II is the *background potential energy* (BPE or P_B) of arrangement II, and the difference between the potential energy of arrangement I and this BPE is the *available potential energy* which could drive fluid motions. Now suppose if, after the rearrangement, the middle two boxes mix irreversibly, leading to arrangement (III). The BPE has now increased as arrangement III has higher potential energy than arrangement I, and so the amount of APE has also dropped, showing again why mixing (reduction of variance in the density field) is associated with destruction of APE. In numerical experiments, using such a sorting algorithm for density is a way to distinguish between available potential energy and a minimum background potential energy, and hence to capture irreversible mixing. This approach can be used to look at different mixing regimes as turbulence develops, as the background potential energy will monotonically increase with (irreversible) mixing, as originally argued in the very influential paper of Winters et al., building on Lorenz's original APE ideas.[13]

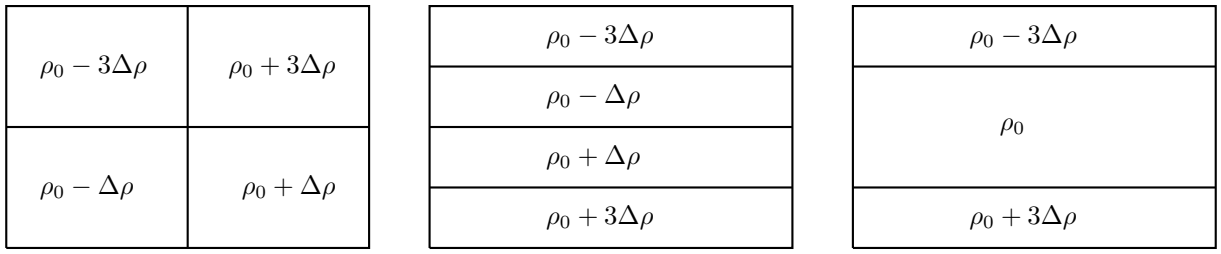

References

[1] C. P. Caulfield, *Hydrodynamic Stability Lecture Notes*, Lecture series given Autumn 2017 at the University of Cambridge, notes by Dexter Chua.

[2] C. P. Caulfield, W. R. Peltier, S. Yoshida, and M. Ohtani, *Layer formation in horizontally forced stratified turbulence: connecting exact coherent structures to linear instabilities*, Physics of Fluids, 7 (1995), pp. 3028–3041.

[3] G. Facchini, B. Favier, P. Le Gal, M. Wang, and M. Le Bars, *The linear instability of the stratified plane Couette flow*, Journal of Fluid Mechanics, 853 (2018), pp. 205–234.

[4] J. Holmboe, *On the behavior of symmetric waves in stratified shear layers*, Geofysiske Publikasjoner, 24 (1962), pp. 67–113.

[5] M. Le Bars and P. Le Gal, *Experimental analysis of the stratorotational instability in a cylindrical couette flow*, Physical Review Letters, 99 (2007), pp. 1–4.

[6] D. Lucas, C. P. Caulfield, and R. R. Kerswell, *Layer formation in horizontally forced stratified turbulence: connecting exact coherent structures to linear instabilities*, Journal of Fluid Mechanics, 832 (2017), pp. 409–437.

[7] ——, *Layer formation and relaminarisation in plane Couette flow with spanwise stratification*, Journal of Fluid Mechanics, 868 (2019), pp. 1–22.

[8] Y. G. Park, J. A. Whitehead, and A. Gnanadeskian, *Turbulent mixing in stratified fluids: layer formation and energetics*, Journal of Fluid Mechanics, 279 (1994), pp. 279–311.

[9] H. Salehipour, C. P. Caulfield, and W. R. Peltier, *Turbulent mixing due to the Holmboe wave instability at high Reynolds number*, Journal of Fluid Mechanics, 803 (2016), pp. 591–621.

[10] W. D. Smyth, G. P. Klaassen, and W. R. Peltier, *Finite amplitude Holmboe waves*, Geophysical and Astrophysical Fluid Dynamics, 43 (1988), pp. 181–222.

[11] G. I. Taylor, *Stability of a viscous liquid contained between two rotating cylinders*, Philosophical Transactions of the Royal Society of London A, 223 (1923), pp. 289–343.

[12] ——, *Effect of variation in density on the stability of superposed streams of fluid*, Proceedings of the Royal Society of London A, 132 (1931), pp. 499–523.

[13] K. B. Winters, P. N. Lombard, J. J. Riley, and E. A. D'Asaro, *Available potential-energy and mixing in density-stratified fluids*, Journal of Fluid Mechanics, 289 (1995), pp. 115–128.

[14] A. W. Woods, C. P. Caulfield, J. R. Landel, and A. Kuesters, *Non-invasive turbulent mixing across a density interface in a turbulent Taylor-Couette flow*, Journal of Fluid Mechanics, 663 (2010), pp. 347–357.

GFD 2019 Lecture 8: Open Questions and Controversies in Stratified Turbulent Mixing Research

Colm-cille Caulfield; notes by Wenjing Dong and Samuel Boury

June 26, 2019

Choosing the Parameters for Mixing Efficiency

Now that we have thought about ways by which stratified flows may become unstable, and thus presumably become turbulent, it is time to think about how we might describe and perhaps parameterize the ensuing turbulent mixing. Any parameterization requires parameters after all, and that leads to some complicated issues, not least in defining the parameters themselves. As perhaps already has been hinted in these lectures, there is a real issue with a proliferation of subtly different definitions for key quantities within stratified turbulent flows, which can lead to the potential for confusion and unnecessary disagreement. Indeed, Gregg *et al.* 2018 suggest a few standard definitions should be adopted for mixing efficiency and mixing coefficients [1]. They recommend focusing on two parameters we define below: the instantaneous efficiency, $\mathcal{E}_i$; and the cumulative efficiency, $\mathcal{E}_c$; and two parameters already encountered: the flux Richardson number, Ri_f; and the mixing coefficient for κ_T, using the "Osborn method" via the TKE equation, here referred to (I hope) as Γ.

When choosing parameters to parameterize mixing efficiency, it is clear that great care should be taken over the definitions of their parameters. For example, the gradient Richardson number $Ri_g = N_b^2/S_b^2$ can be a function of vertical coordinate z and time t, and there can clearly be a whole can of worms to be opened concerning how the background fields are actually defined. Similarly, in the apparently innocuous definition of a Froude number, $Fr = U/NL$, N can be spatially varying and it is not clear how to choose the right length scale L or velocity scale U. Indeed, the very same issues arise in the definition of the appropriate Reynolds number $Re = UL/\nu$.

It perhaps goes without saying that choosing which parameters to characterize the flow depends strongly on the flow itself. For example, Fr does not need shear, however Ri_g does require (strictly vertical) shear. Indeed, for horizontal shear, it is more natural to describe the flow in terms of Fr instead of Ri_g, because Ri_g should (I believe) always describe a competition between the restoring force of stratification and the destabilising effect of (vertical) shear, loosely in a balance between PE and KE. Nevertheless, there are certainly examples in the literature where "Richardson numbers" are defined for horizontal shear, and indeed often as the inverse square of a Froude number, as $Fr^{-2} = N^2(L^2/U^2)$, which is the same as Ri_g **if** $S_b^2 = U^2/L^2$ and the characteristic N in the Fr definition is the same as the background N_b in the definition of Ri_g.

Analogously, there is some (to put it politely) divergence of opinion concerning how precisely to define the *buoyancy Reynolds number*. One school of thought, emerging entirely reasonably from a careful consideration of the appropriate scaling of the underlying governing equations[2], is that the correct definition for this naturally-emerging parameter is:

$$Re_b = ReFr^2 = \frac{U^3}{N^2 L\nu}, \tag{1}$$

for appropriate choices of characteristic scales of U, N and L.

However, another school of thought is that the natural way to define this parameter is in terms of emergent properties of the turbulence, in particular the dissipation rate of turbulent kinetic energy ϵ'. This is particularly natural if we assume the zeroth law of turbulence holds, since then $\epsilon' \sim U^3/L$. Often it is assumed that this scaling is an equality (implicitly defining either U or L) and then

$$Re_b = \frac{\epsilon'}{\nu N^2}. \tag{2}$$

Some authors[2] argue that this latter definition based on emergent turbulence properties should more naturally be called the *Gibson number Gn* after Carl Gibson who first used it to describe the *intensity* of stratified turbulence, and indeed in older papers it is sometimes called the *turbulence intensity* or the *intensity parameter* of stratified turbulence. It is still more common to refer to both expressions given in Equations 1 and 2 as Re_b interchangeably, and so real caution needs to be exercised when comparing different studies.

A particular attraction of the "turbulent" form of Re_b is that it can be naturally interpreted in terms of a ratio of length scales, (the four-thirds power of) the ratio of the *Ozmidov scale* L_O to the Kolmogorov length scale L_K, i.e.,

$$Re_b = \left[\left(\frac{\epsilon'}{N^3} \right)^{1/2} \left(\frac{\nu^3}{\epsilon'} \right)^{-1/4} \right]^{4/3} = \left[\frac{L_O}{L_K} \right]^{4/3}. \tag{3}$$

Loosely, L_O is the largest scale of eddies that are largely unaffected by the stratification. (Another way to think about it is for an eddy of that scale, the kinetic energy in the eddy is just enough to turn over, and thus exchange energy with the potential energy reservoir, in the stratification defined by N.) Therefore, for there to be any chance for the ensuing turbulence to have an inertial range, $L_O/L_k \gg 1$, which implies $Re_b \gg 1$. Indeed, there is a lot of evidence that the world's oceans are in the regime (when Re_b is defined by Equation 1 using **horizontal** scales of velocity and length) where $Re \gg 1$, $Fr \ll 1$ yet $ReFr^2 \gg 1$, though as ever, it is very important to appreciate just exactly how the various characteristic scales are determined, especially over which volume they are averaged. Just how such "strongly stratified" turbulence can be born and maintained is still a topic of great controversy, which we will briefly discuss in the following lectures. In this lecture, we will focus our attention on attempting to parameterize mixing in shear-driven mixing events.

1 The Thorpe Scale and the Age of Mixing Events

Another (actually purely geometric) length scale that can be useful for the interpretation (and perhaps the parameterization) of mixing events is the Thorpe scale. Consider a density profile, $\rho(z)$ that has regions of static instability. Discretize the profile into a large number of parcels, perhaps in terms of the resolution of the observational measurement or numerical simulation. Rearrange those parcels vertically so that the density distribution is everywhere monotonic and statically stable, recording the displacement distance for every parcel that needs to be moved because of initial static instability. The root-mean-square of that displacement distance is the Thorpe scale, which is thus a measure of the characteristic scale of the overturnings. It then seems reasonable to suppose that larger values of Thorpe scale imply at least the potential for more mixing.

Furthermore, applying the definition of the Ozmidov scale, it is clear that

$$\kappa_T = \Gamma \frac{\epsilon'}{N^2} = \Gamma L_o^2 N = \Gamma \frac{L_o^2}{L_T^2} L_T^2 N = \Gamma R_{OT} L_T^2 N. \tag{4}$$

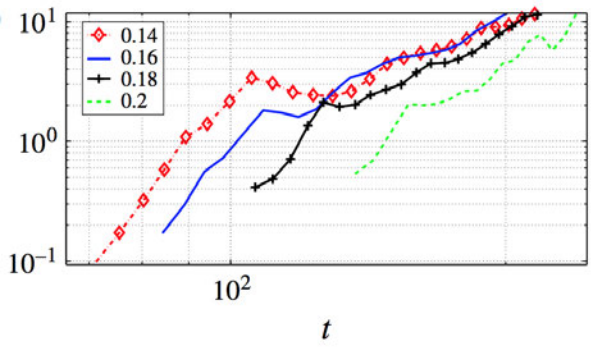

Figure 1: The evolution of R_{OT} for Kelvin-Helmholtz instability for $Re = 6000$ for flows with different initial minimum gradient Richardson number. From [5].

Although this seems an arbitrary manipulation, observationally it is much easier to estimate L_T and N, as both can be constructed directly from a density profile measurement, whereas estimating dissipation rate is very hard. Therefore, if useful estimates for Γ and the ratio R_{OT} can be made, then there is a chance to use observational profiles to construct estimates of κ_T. This may thought of as a third *Thorpe method* to estimate diffusivity, complementary to the aforementioned *Osborn method* and *Osborn-Cox method*. As a "rule of thumb" based on observation (rather like the $\Gamma = 0.2$ union agreement), it has been suggested that $R_{OT} \sim 0.8$[3]. However, using DNS prone to primary KHI as a model for an overturning mixing event, it seems that as KHI with various initial minimum Ri_g break down and transition to turbulence, R_{OT} monotonically increases, suggesting that R_{OT} should be used more as a measure of the age of turbulence rather than for parameterization[4, 5]. It is clear from figure 1 that $R_{OT} = 0.8$ is right only in the sense that a stopped clock is right.

2 Parameterization of Γ in Terms of Re_b and Ri

We continue to want to get our head around how we might understand and describe stratified turbulent mixing and now we have defined Re_b, the key relationship between κ_T and Γ using the Osborn method described in Lecture 6 can be understood in terms of Re_b, if we assume the ensemble average $\langle N^2 \rangle$ of Lecture 6 can be identified with the "characteristic" value of N being used here as:

$$\frac{\kappa_T}{\kappa} = \Gamma Pr_m \frac{\epsilon'}{\nu N^2} = \Gamma Pr_m Re_b. \tag{5}$$

If only Γ were constant (and especially not a function of Re_b), then the enhancement of the mixing would be entirely determined by the *intensity* of the turbulence as quantified by Re_b. Indeed Osborn argued, based on experimental evidence, that $\Gamma \lesssim 0.2$, and this bounding value has been widely used as a rule of thumb, even missing the careful and thoughtful inequality in the original paper.

However, one might reasonably expect Γ to decrease with Re_b when N is very small and Re_b is large because there is little density difference that can be mixed. It has also been found that Ri_f depends non-monotonically on some overall characteristic value Ri of Ri_g, consistently with the left-flank/right-flank dichotomy discussed in the previous lecture. Since $Ri_f = \Gamma/(1+\Gamma)$ by definition, it seems reasonable that Γ needs to be parameterized (at least) by both Re_b and Ri, or perhaps Fr if there is no vertical shear. A fundamental assumption embedded in this parameterization approach is that Re_b and Ri are uncorrelated, which unfortunately is (extremely) unlikely to be true. However, we have to start somewhere, and it is also apparent (I think) that

a single parameter parameterization of mixing is unlikely to be robust and generic enough to be useful. We now consider various (relatively recent) attempts to construct parameterizations of mixing.

2.1 Optimal Ri for mixing in shear instability

In the previous lecture we (very briefly) introduced the concept of the *background potential energy* P_B and the sorting algorithm introduced by Winters et al. [6]. The rate of increase of this energy naturally defines the rate of irreversible mixing $M(t)$:

$$\frac{dP_B}{dt} = M(t), \tag{6}$$

inevitably associated with fluid motions, and using this it is possible to define the instantaneous mixing efficiency $\mathcal{E}_i$ and cumulative mixing efficiency $\mathcal{E}_c$ as

$$\mathcal{E}_i = \frac{M(t)}{M(t) + \varepsilon'(t)}, \quad \mathcal{E}_c(t) = \frac{\int_0^t M(s)ds}{\int_0^t M(s)ds + \int_0^t \varepsilon'(s)ds}, \tag{7}$$

where the $t = 0$ time is chosen on some reasonable physical grounds (for example when the turbulent dissipation has reached a particular enhanced value). It is also important to remember that sum authors use the dissipation rate of **total** kinetic energy, not the dissipation rate of TKE as in this definition.

Through a series of direct numerical simulations (DNS) of KHI undergoing the transition to turbulence with different (minimum) initial gradient Richardson numbers Ri, it appears that the optimal mixing efficiency occurs at $Ri = 0.16$ for Kelvin-Helmholtz instability[7]. Figure 2 shows the evolution of density and dissipation rate for KHI for different Richardson number of hyperbolic tangent velocity and density profiles. When Ri is too low, there is little to be mixed. When Ri is too high, e.g., for the flow with $Ri = 0.20$, the turbulence is suppressed by stratification as the primary instability is very weak, and mixing is also low. Thus, mixing varies non-monotonically with Richardson number. Figure 3 shows the proportion of loss of kinetic energy is highest for $Ri = 0.16$. The loss of kinetic energy is either dissipated or converted to potential energy. Figure 4 shows the cumulative mixing efficiency η_c ($\mathcal{E}_c$, labelled as η_c in the figure) and η_c^{3D} (i.e., $\mathcal{E}_c$ integrated from the beginning of turbulence) both peak around $Ri = 0.16$, showing clearly that at least the cumulative mixing efficiency for flows prone to primary KHI exhibits non-monotonic variation with Ri, analogously to the left-flank/right-flank paradigm discussed earlier.

2.2 Dependence of Γ on Re_b

From analysis of both DNS (for flows prone to primary KHI) and observational data, it also appears that Γ varies non-monotonically with Re_b (however defined) as shown in Figure 5[8]. In this study, the "age" of the turbulence was also inferred from appropriate estimates of R_{OT}. There is clearly reasonable agreement between observation and simulation, suggesting that the KHI simulations may actually be useful models of oceanic mixing events. Furthermore Γ for relatively young turbulence associated with approximately two-dimensional Kelvin-Helmholtz billows is higher than when the turbulence is more mature.

The figure also shows (clearly) a non-monotonic dependence of Γ on Re_b. Figure 6 taken from the same paper shows: $\Gamma \propto Re_b^{1/2}$ for $Re_b \ll Re_b^*$ where Re_b^* represents the buoyancy Reynolds

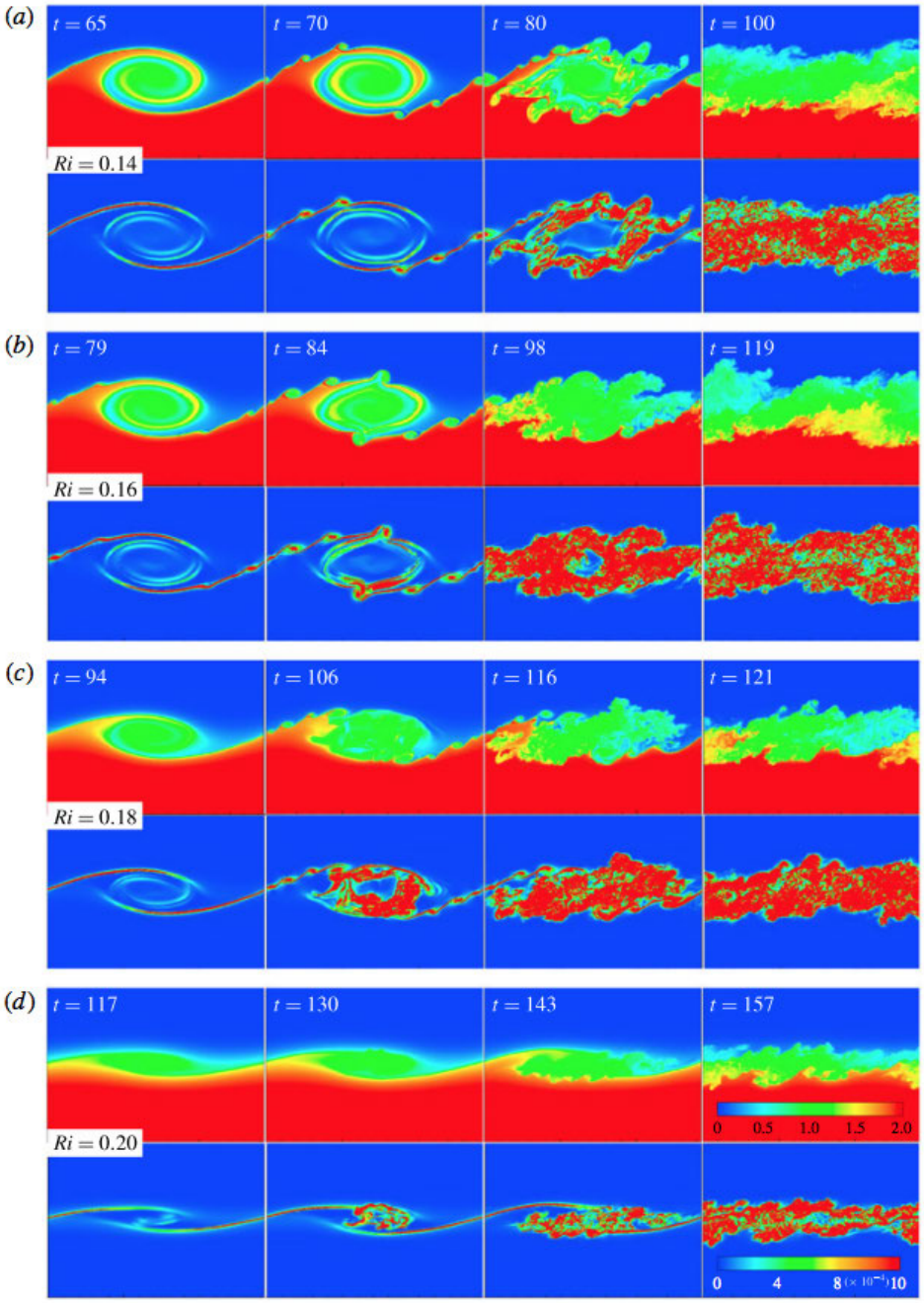

Figure 2: The evolution of flow during the transition phase. For each Ri value, the upper panels show contours of density and the lower panels show contours of the rate of dissipation of kinetic energy. The color maps for both contours are linear. (a) $Ri = 0.14$; (b) $Ri = 0.16$; (c) $Ri = 0.18$; (d) $Ri = 0.20$. From [7].

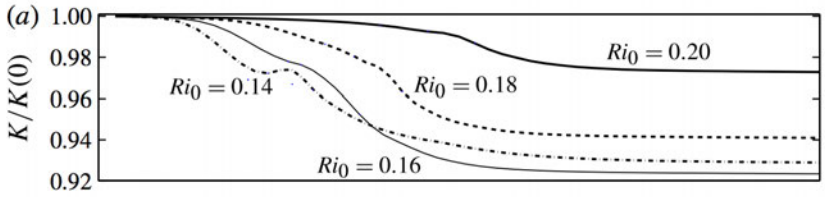

Figure 3: Time evolution of the total kinetic energy. From [7].

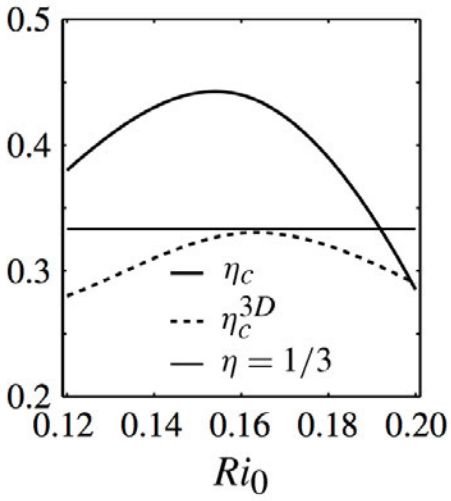

Figure 4: Cumulative mixing efficiency from the beginning of the simulation (here labelled asη_c) and cumulative mixing efficiency for the turbulent stage (here labelled as η_c^{3D}) for simulations prone to primary KHI with different initial minum gradient Richardson number. From [7].

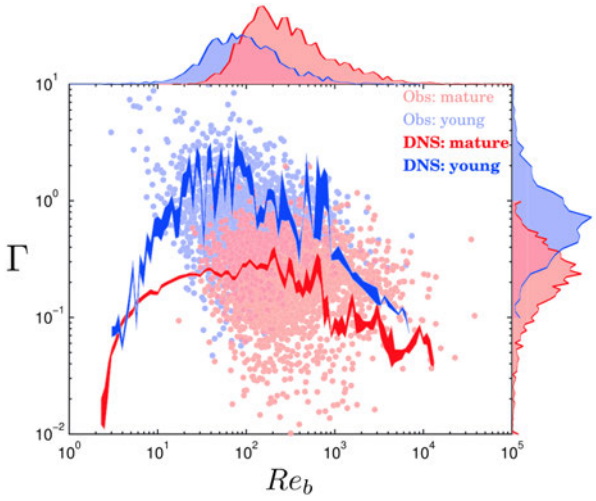

Figure 5: Re_b dependence of Γ, comparing the young and mature mixing events obtained from oceanic measurements and DNS analyses. From [8].

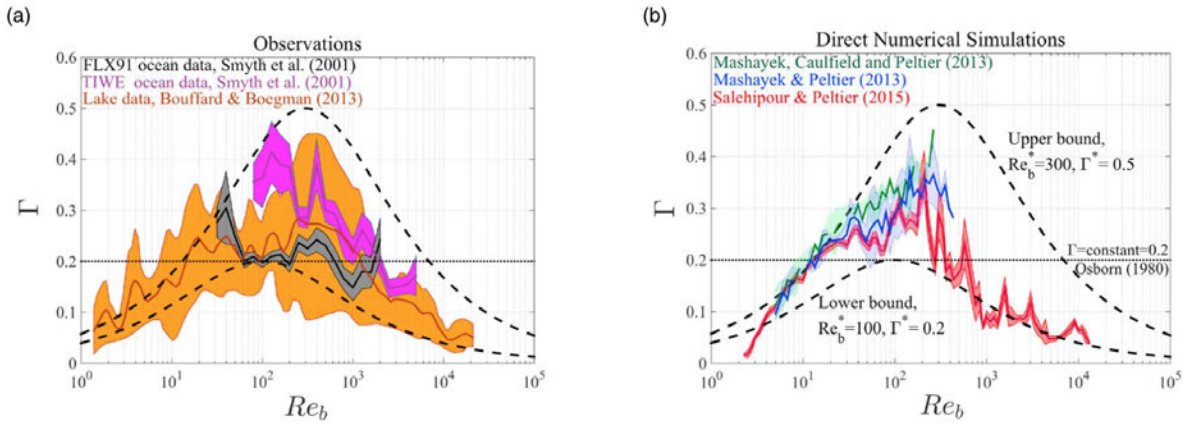

Figure 6: Re_b dependence of Γ as inferred from (a) observational data sets and (b) DNS data sets. From [8].

number associated with peak Γ, and $\Gamma \propto Re_b^{-1/2}$ for $Re_b \gg Re_b^*$. By joining these two scaling regimes, they approximate the dependence by

$$\Gamma(Re_b) = \frac{2\Gamma^*(Re_b/Re_b^*)^{1/2}}{1 + Re_b/Re_b^*}. \tag{8}$$

It is clear from this figure that the constant value of $\Gamma = 0.2$ is once again only true in the stopped-clock sense.

3 Mixing by Different Mechanisms: KHI vs. HWI

Flows prone to primary KHI have been much more widely studied than HWI, particularly at sufficiently high Re to exhibit a vigorous transition to turbulence, and (to my knowledge) there has only been one comparison of the mixing properties of flows prone to primary KHI and HWI at sufficiently high Re to be vigorously turbulent.[9] Figure 7 shows the spanwise vorticity component ω_y for flows prone to primary KHI and HWI, showing the expected characteristic overturning of the interface and scouring above and below the interface, respectively. Figure 8 (a) shows the (instantaneous) mixing efficiency as well as enhanced mixing κ_T/κ for both types of mixing events as a function of Re_b during the mixing events for both classes of mixing event. Interestingly, the HWI flow at later time proceeds along a trajectory in $Re_b - \mathcal{E}_i$ space similar to the trajectory of earlier time. However, the KHI flow follows a wide loop in $Re_b - \mathcal{E}_i$ space, (and reaches much larger values of efficiency) due to the existence of the organised, essentially two-dimensional Kelvin-Helmholtz billows. Moreover, the maximal mixing efficiency of Kelvin-Helmholtz instability is much larger than the canonical value 1/6, corresponding to $\Gamma = 0.2$, since $\mathcal{E}_i \simeq Ri_f = \Gamma/1+\Gamma$. However, focus on *efficiency* or equivalently *flux coefficient* Γ can be misleading, as figure 8 (b) shows during the turbulent stage, the trajectory in $Re_b - \kappa_T/\kappa$ space for these two flows is similar, suggesting that the enhanced mixing **might be** generic for shear-driven mixing events. Much more work on this issue needs to be done however, before anything can be said with any real confidence.

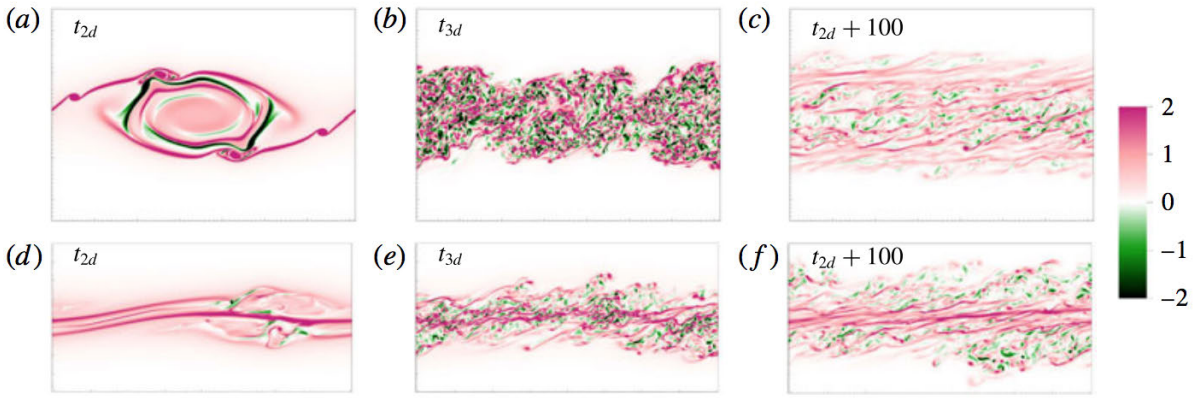

Figure 7: Contour plots of vorticity ω_y for a simulation prone to primary KHI $(a - c)$ and for a simulation prone to primary HWI $(d - f)$. From [9].

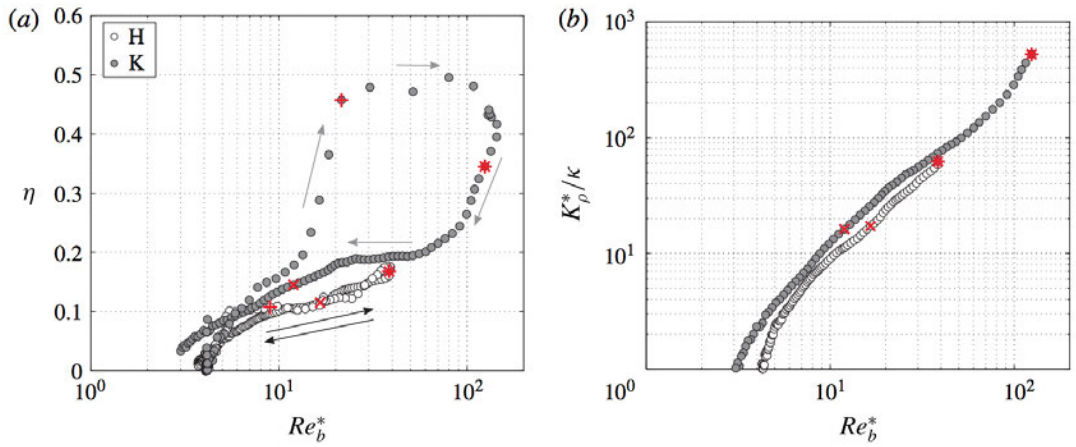

Figure 8: Variation with Re_b for a KHI flow (grey circles) and HWI flow (white circles) of: (a) the instantaneous irreversible mixing efficiency for the entire life cycle; and (b) the irreversible diapycnal diffusivity for the turbulent stage. From [9].

3.1 Self-organized criticality in sheared stratified turbulence

Mixing events associated with primary HWI are much longer-lived than those associated with primary KHI: a useful metaphor is that HWI "burn", while KHI "flare". Interestingly, there is a strong suggestion that the HWI-mediated turbulence induces horizontally-averaged velocity and density fields that have $Ri_g(z,t) \simeq 0.25$ for a significant period after the onset of turbulence, and throughout the "mixing layer" depth[10]. Figure 9 shows that the probability density function(p.d.f.) of $Ri_g(z,t)$ for HWI flows calculated from the horizontally-averaged fields peaks around 0.25 irrespective of initial density and shear layer depths. The authors of this study conjectured that $Ri \approx 1/4$ is a critical state that acts as an "attractor" toward which the flow tends to self-organize. However, this does not appear to be the case for flows prone to primary KHI. Figure 10 shows for KHI-induced turbulence, the peak of p.d.f. is either larger than 0.25 or less than 0.25, depending on whethere the initial minimum Ri_g is "large" (in this case 0.16) or "small" (here 0.04). Indeed, KHI flows requires specific initial conditions so that the p.d.f. peaks around 0.25.

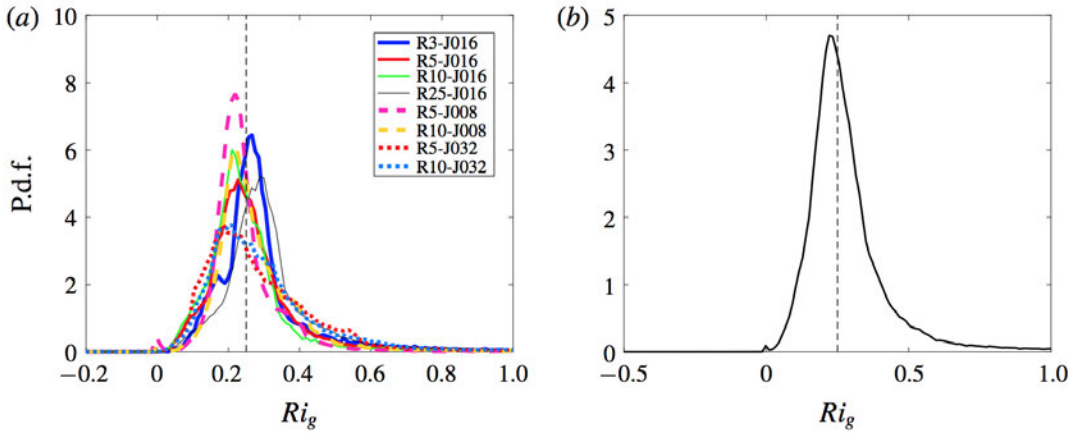

Figure 9: (a) The probability density function of $Ri_g(z,t)$ for turbulent stage for different simulations (with various initial R and midplane Ri_g) prone to primary HWI. (b) The probability density function of $Ri_g(z,t)$ during the turbulent stage aggregated from all HWI flows. From [10].

A further indicator (or to be more cautious "hint") of self-organised criticality is the emergence of an invariant turbulent length scale with a power-law dependence in its p.d.f. E_k and ϵ' define an *energy-containing length scale* L_{en}:

$$L_{en} = \frac{E_k^3}{\epsilon'}. \tag{9}$$

For the HWI flows figure 11 (left panel) shows the p. d. f. of this length scale is close to invariant with time during the turbulent phase of flow evolution and follows approximately a power law, at least superficially consistent with the key characteristics of self-organised criticality. Subsequently, Smyth et al 2019 also demonstrated that the vertical scale of turbulent overturns follows approximately a power law within a suitable range of observational data, as shown in figure 11 (right panel)[11].

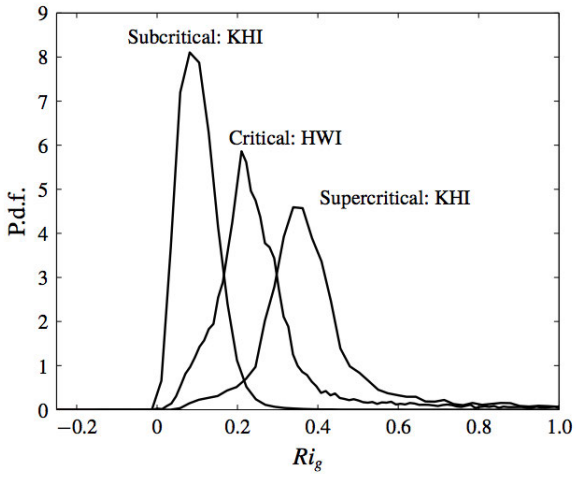

Figure 10: P.d.f.s for Ri_g for a flow prone to primary HWI and two flows prone to primary KHI. From [10].

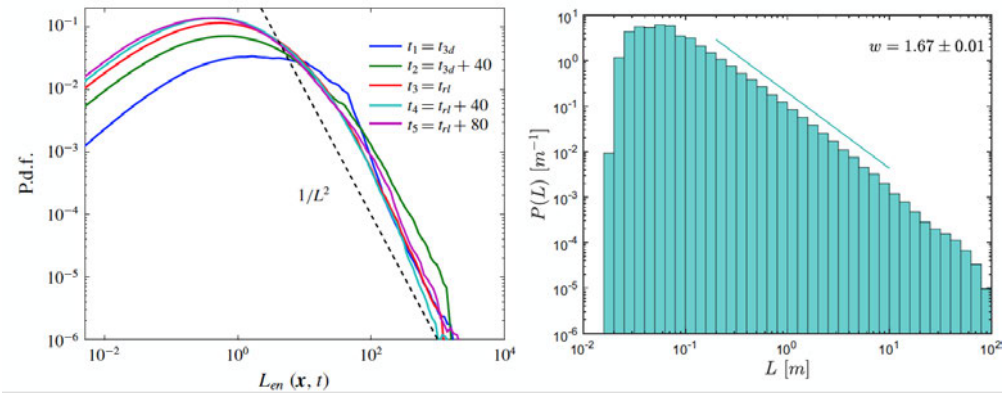

Figure 11: Left: the p.d.f. of energy containing length scale $L_{en} = (3/2)^3 k'^3/\varepsilon'$ at five characteristic times. From [10]. Right: probability density function P of the vertical scale L of turbulent overturns in the upper equatorial Pacific. Straight line with slope w shows the maximum likelihood estimate of the exponent. From [11]

3.2 Stratified shear instability in pre-existing turbulence, optimal perturbation, and marginal instability

Of course, geophysical flows are rarely laminar, yet the vast majority of numerical simulations of stratified shear instability have used a laminar flow as the base state, assuming that such a smooth and calm (yet fundamentally linearly unstable remember...) has somehow come into existence. In a beautiful and innovative recent study (wish I'd thought of it) Kaminski & Smyth 2019 examined the evolution of stratified shear instability in pre-existing turbulence. Their results show that adding turbulence can significantly reduce the growth of a primary KHI, and indeed completely disrupt the primary billow roll-up for sufficiently strong ambient noise, as shown in figure 12[12].

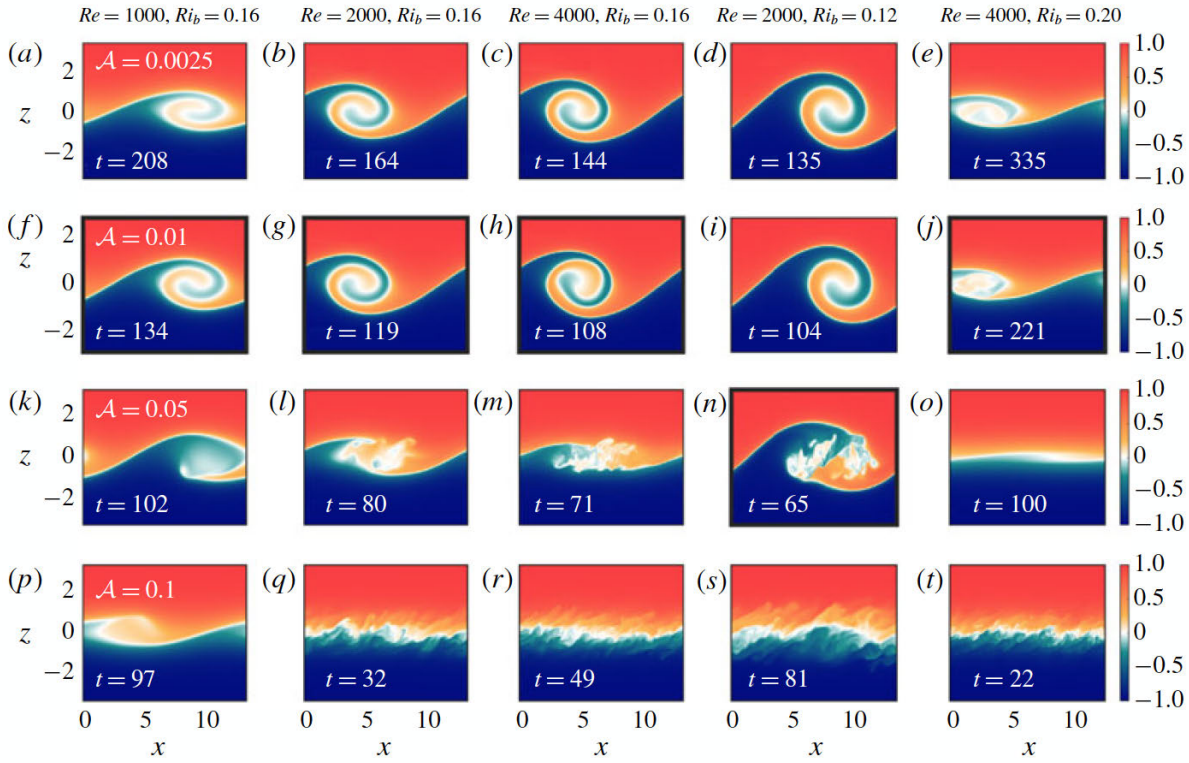

Figure 12: Vertical slices of buoyancy at various times. $\mathcal{A}$ is a measure of initial turbulence intensity. From [12]

Another dirty little secret of classical studies of mixing events induced by shear instabilities is the focus on classical normal modes. As the underlying linear operator is *non-normal* transient growth is actually possible however, and using *direct-adjoint looping* it is possible to identify "optimal" perturbations that grow non-trivially, but inherently transiently, for flows with minimum $Ri_g > 1/4$. It is important to remember that such perturbation growth does not violate the Miles-Howard theorem, which (as noted above) is inherently based on an inviscid analysis of the linear stability of steady parallel flows, perturbed by normal (exponentially growing) models. Figure 13 shows the evolution of the total buoyancy field of a DNS seeded with the linear optimal perturbation of a hyperbolic tangent flow with $R = 1$ and minimum $Ri_g = 0.4$[13] . For this flow, the optimal perturbation grows enough actually to modify the mean flow, distorting the buoyancy field until it becomes very reminiscent of a classical Kelvin-Helmholtz billow.

Indeed, at finite Re and for finite amplitude perturbations, the behaviour of stratified shear

flows with minimum $Ri_g \simeq 1/4$ prone to KHI is quite subtle, calling into question exactly how the *marginal stability* dynamics of such stratified shear flows should be interpreted. For example, if a viscous shear layer is forced to maintain steady hyperbolic tangent density and velocity profiles with minimum $Ri_g \lesssim 1/4$, it is possible to establish that the energy gain of perturbations becomes small, but is strictly bounded away from zero as (minimum) $Ri_g \to 1/4$ from below, as shown in figure 14[14]. However, as is also shown in the figure, the amount of time for the perturbation to reach finite amplitude increases dramatically as the minimum Ri_g approaches 1/4 from below, suggesting that in practice, KHI do not roll up vigorously for flows with minimum $Ri_g \simeq 1/4$. Furthermore, treating a high Reynolds number $Re = 4000$, $Pr = 1$ forced steady hyperbolic tangent base flow shear later as a dynamical system, it is possible to establish that a saddle-node bifurcation exists for $Ri_g(0) > 1/4$, with an associated finite amplitude structure, highly reminiscent of a Kelvin-Helmholtz billow, as shown in figure 15[15]. Nevertheless, these really weak billows when $Ri_g \lesssim 1/4$ suggest that the apparent self-organized criticality cannot be interpreted in a strictly Miles-Howard theorem sense, as the primary instabilities are apparently too weak to trigger the required strong turbulence as the background flows just dip under the stability criterion.

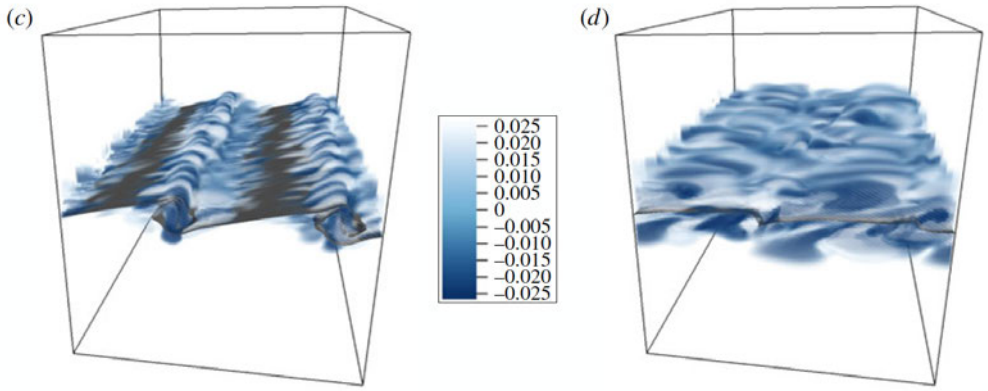

Figure 13: Evolution of total buoyancy through centre of shear layer (isosurface) and vorticity $\omega_z = \partial_x v_0 - \partial_y u_0$ (colour) for a simulation with $Re = 4000, Ri_g(0) = 0.40$. From [13]

.

4 Parameterizing Turbulent Diffusivity

Simulations of turbulent mixing induced by the break down of stratified shear flow instabilities (typically KHI) can also be used to test the various different methods of estimating and/or parameterizing turbulent diffusivity. As shown in figure 16, turbulent diffusivity computed using the Osborn-Cox method matches the actual turbulent diffusivity significantly better than turbulent diffusivity computed using the Osborn method[16]. As already discussed, this is perhaps unsurprising, as the Osborn-Cox method is more "direct". Figure 17 (also from [16]) shows that turbulent Prandtl number Pr_T becomes approximately 1 provided Re_b is sufficiently large. This shows that density is diffusing like a passive tracer and density and momentum essentially mixes at the same scale in such overturning stratified shear flows. Again this is not really surprising, as these flows are inevitably "weakly" stratified as the primary instability requires the minimum value of Ri_g to be (actually nontrivially) less than 1/4 to grow to significant amplitude, as noted above.

It is also (of course) possible to use increasingly fashionable data-driven methods to estimate

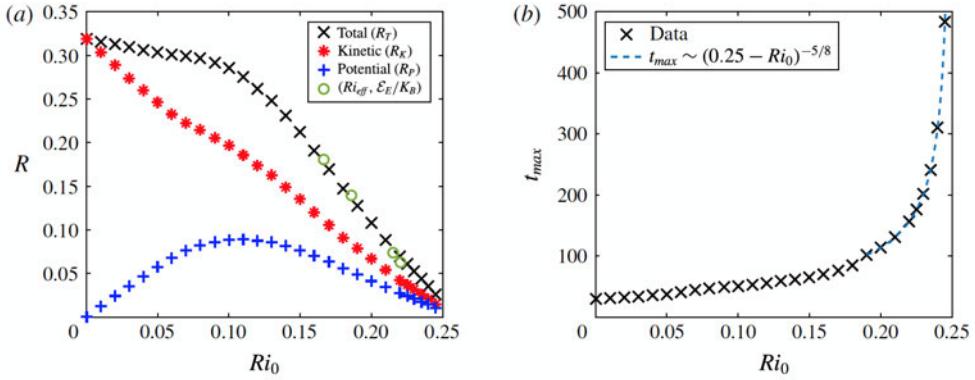

Figure 14: variation with Ri_0 of (a) scaled maxima of total perturbation energy R_T (crosses), perturbation kinetic energy R_K (asterisks) and perturbation potential energy R_P (pluses) ; (b) time to saturation t_{max}. From [14]

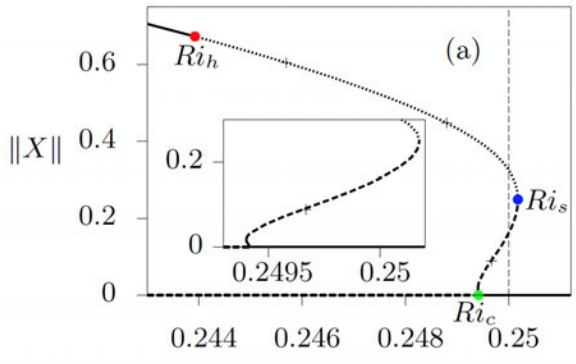

Figure 15: Bifurcation diagram for the flow with hyperbolic tangent background stratification, at $Re = 4000$, showing the variation of $||X||$ over a (very narrow) range of Ri_b, where $||X||$ is a measure of perturbation energy. At different points, the solution branch has one stationary unstable direction (dashed line), two stationary unstable directions (dotted line), or is stable to stationary disturbances (solid line). From [15]

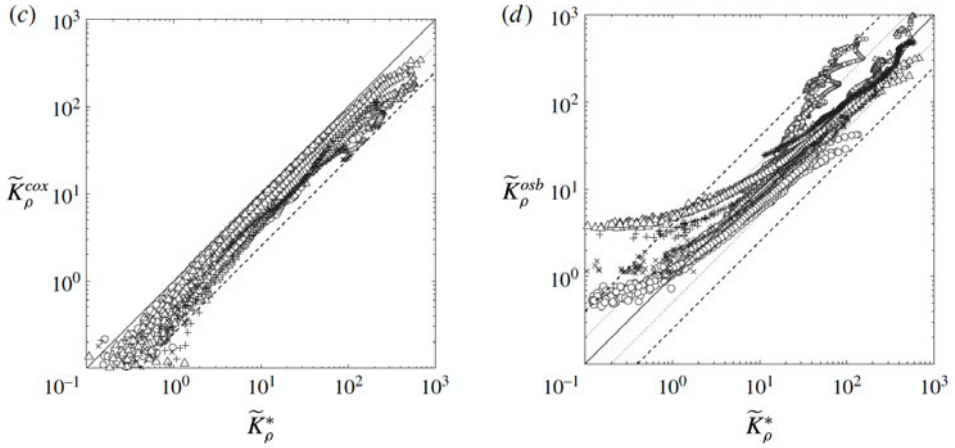

Figure 16: Left: turbulent diffusivity computed by the Osborn-Cox model. Right: turbulent diffusivity computed by the Osborn method. From [16].

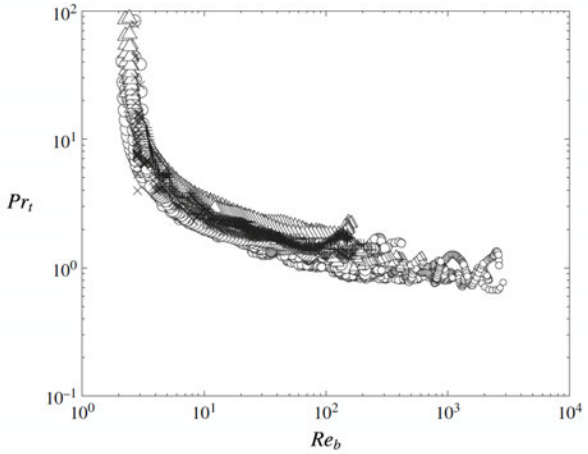

Figure 17: Variation of Pr_t with Re_b. From [16].

mixing properties, particularly as numerical simulations provide more and more data for "training". Figure 18 shows the comparison between the exact value of the instantaneous mixing efficiency $\mathcal{E}_i$ computed directly from DNS of flows prone to either primary KHI or primary HWI with the predictions of a convolutional neural network, the Osborn-Cox method, and an alternative empirical multiparameter parameterization[17]. Although not perfect, it is apparent that the CNN outperforms the more traditional parameterizations as an estimator of the real mixing efficiency[18].

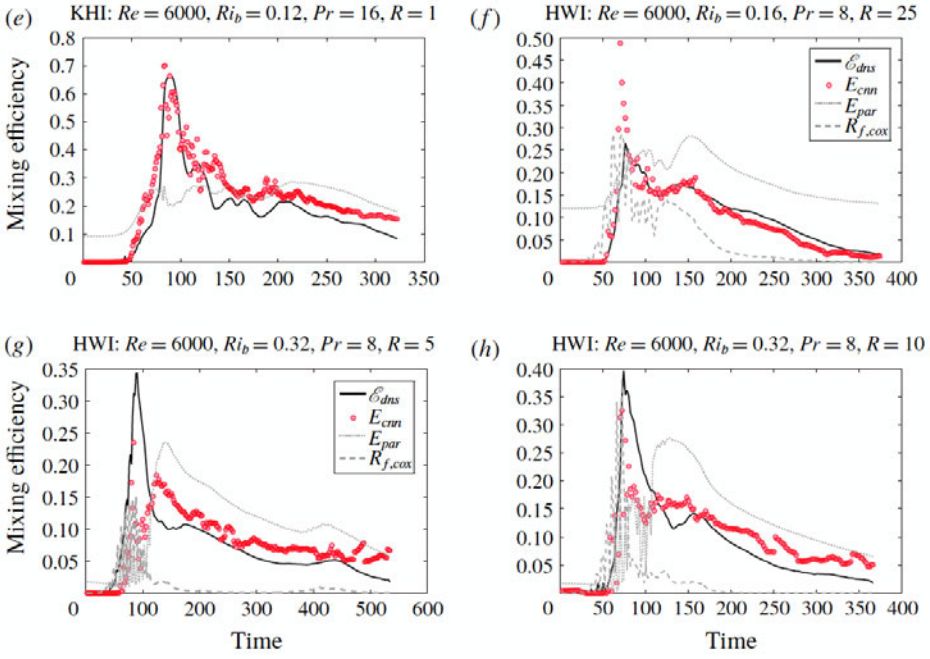

Figure 18: Comparing the precise calculation of (instantaneous) mixing efficiency, $\mathcal{E}_{dns}$ with those predicted by: a convolutional neural network E_{cnn}; an empirical multi-parameter parameterization E_{par}[17]; and the Osborn-Cox method, $R_{f,cox}$. From [18].

4.1 Parameterization in forced stratified turbulence

Heretofore, this lecture has only considered shear-driven instabilities as the "source" of a stratified turbulent mixing event. Of course, other mixing events are available, and (both unfortunately and unsurprisingly) the evidence is that nothing really generic can be said about stratified mixing events, as different forcing mechanisms appear to lead to different mixing properties. Figure 19 shows three regimes of the variation of $(\kappa_T+\kappa)/\kappa$ with Re_b from simulations of forced stratified shear turbulence with uniform shear and stratification[19]. When $Re_b \sim O(1)$, turbulence is weak and κ_T is negligible, and so the plotted quantity tends towards one. When Re_b is in the range $O(10) - O(10^2)$, κ_T appears to be largely linearly dependent on Re_b, and quantitatively the prediction of $(\kappa_T + \kappa)/\kappa$ using the constant upper bound of the Osborn method (i.e., $\Gamma = 0.2$, in Equation 5) actually agrees quite well with the exact value, as shown by the red line.[20] When $Re_b \gtrsim O(10^2)$, this linear dependence appears no longer to hold, and indeed $\kappa_T \propto Re_b^{1/2}$, or equivalently (when using the Osborn method) $\Gamma \propto Re_b^{-1/2}$, and so energetic turbulence (at least for this flow) appears to get **less** efficient at mixing, consistently with the model assumption of Equation 8, and the data shown

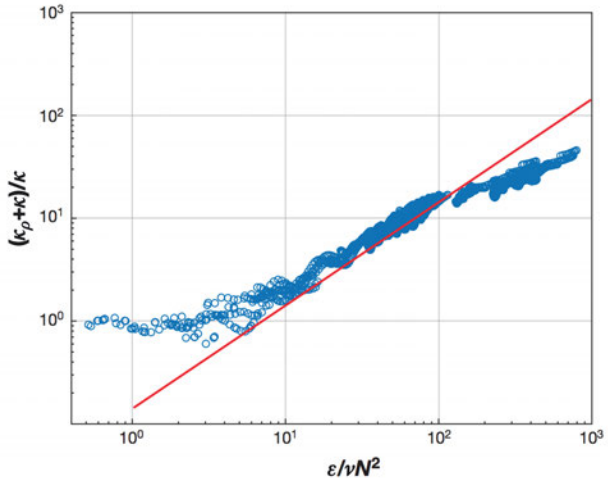

Figure 19: The variation of $(\kappa_T + \kappa)/\kappa$ with Re_b. The prediction using constant $\Gamma = 0.2$ is shown by the red line. Figure extracted from [20] based on data from [19].

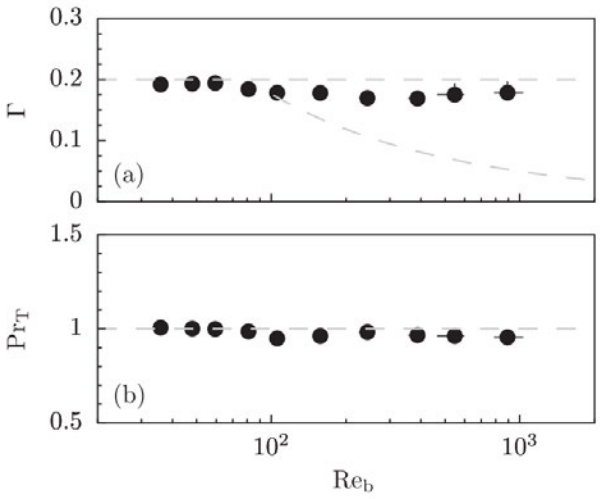

Figure 20: (a) Variation of turbulent flux coefficient Γ with Re_b.The upper bound proposed by Osborn is indicated by the gray dashed line where $\Gamma \approx 0.2$, and the $Re_b - 1/2$-based parameterization suggested by the data shown in figure 19 is plotted for their energetic regime of $Re_b > 100$. (b) Variation of turbulent Prandtl number Pr_T with Re_b. From [21].

in figure 6. As Ivey et al note in their review[20]: *"Both laboratory and DNS work indicate that at these extremes, when either* $\epsilon'/\nu N^2 \sim O(1)$ *or* $\epsilon'/\nu N^2 \sim O(10^5)$, $Ri_f \to 0$ *and the use of large* $Ri_f \sim 0.2$ *in field situations in these limits cannot be justified."*

However, this somewhat surprising evidence of decreasing mixing efficiency for high values of Re_b is not universally observed in turbulent stratified shear flows, especially when particular care is taken through the forcing mechanism to ensure statistically steady flow. For example it is possible numerically to impose linear vertical variation in both the horizontally-averaged streamwise velocity and horizontally-averaged density[21]. If the value of both the Reynolds number Re and the magnitude of the shear S is fixed, and a target value of TKE E_K is chosen, then g can be varied smoothly using a control mechanism to ensure that the simulation remains statistically steady. This method leads to emergent values for Ri_g (due to the variation of g, and because of the linear distributions in both velocity and density, Ri_g is constant across the computational domain) and the two dissipation rates ϵ' and χ to ensure the imposed forcing via the shear maintains the constant target value of E_K. Therefore, Re_b and Γ are also emergent quantities, though it is to be expected that as the target value of E_K increases, Re_b will also increase.

As shown in figure 19, this is indeed observed, with Re_b increasing as the target E_K increases, and indeed the simulations had Re_b ranging between $O(10)$ and $O(10^3)$. Interestingly, the emergent value of Γ was constant, and really quite close to the canonical value of 0.2, with no evidence of the $Re_b^{-1/2}$ dependence at high Re_b mentioned above, and shown with a dashed line in the upper panel of the figure. The close to constant value of Γ appears to be associated with the (at least superficially somewhat surprising) emergent close-to-constant value of $Ri_g \simeq 0.16$ for all the simulations. This can actually be (at least partially) understood by consideration of the turbulent Prandtl number, as shown in the lower panel of the figure. Since $Pr_T = Ri_g/Ri_f = Ri_g(1+\Gamma)/\Gamma$, this emergent value of Ri_g appears to be a "consequence" of $Pr_T \simeq 1$ for all the simulations, once again suggesting this statistically steady flow converges to a "weakly stratified" state, where the density field is effectively being mixed as a passive tracer. However, this argument is not complete, as it is not clear why $\Gamma \simeq 0.2$, consistently with Osborn's original (and still deeply influential) arguments, as the transient stratified shear instability flows discussed earlier in this lecture definitely do not exhibit constant $\Gamma \simeq 0.2$, although as shown in figure 4 there does seem to be something special about $Ri_g \simeq 1/6$. There is still very much to do...

References

[1] Gregg, M.C., D'Asaro, E.A., Riley, J.J. and Kunze, E., 2018. Mixing efficiency in the ocean. *Annual review of marine science*, 10, 443–473.

[2] Portwood, G.D., de Bruyn Kops, S.M., Taylor, J. R., Salehipour, H. and Caulfield, C.P., 2016. Robust identification of dynamically distinct regions in stratified turbulence. *Journal of Fluid Mechanics*, 807, R2.

[3] Dillon, T. M. 1982. Vertical overturns: A comparison of Thorpe and Ozmidov length scales. *Journal of Geophysical Research*, 87 (C12), 9601–9613.

[4] Smyth, W.D., Moum, J.N. and Caldwell, D. 2001. The efficiency of mixing in turbulent patches: inferences from direct simulations and microstructure observations. *Journal of Physical Oceanography*, 31, 1969-1992.

[5] Mashayek, A., Caulfield, C.C.P. and Peltier, W.R., 2017a. Role of overturns in optimal mixing in stratified mixing layers. *Journal of Fluid Mechanics*, 826, 522–552.

[6] Winters, K.B., Lombard, P.N., Riley, J.J. and D'Asaro, E.A., 1995. Available potential energy and mixing in density-stratified fluids. *Journal of Fluid Mechanics*, 289, 115–128.

[7] Mashayek, A., Caulfield, C.P. and Peltier, W.R., 2013. Time-dependent, non-monotonic mixing in stratified turbulent shear flows: implications for oceanographic estimates of buoyancy flux. *Journal of Fluid Mechanics*, 736, 570–593.

[8] Mashayek, A., Salehipour, H., Bouffard, D., Caulfield, C.P., Ferrari, R., Nikurashin, M., Peltier, W.R. and Smyth, W.D., 2017b. Efficiency of turbulent mixing in the abyssal ocean circulation. *Geophysical Research Letters*, 44(12), 6296–6306.

[9] Salehipour, H., Caulfield, C.C.P. and Peltier, W.R., 2016a. Turbulent mixing due to the Holmboe wave instability at high Reynolds number. *Journal of Fluid Mechanics*, 803, 591–621.

[10] Salehipour, H., Peltier, W.R. and Caulfield, C.C.P., 2018. Self-organized criticality of turbulence in strongly stratified mixing layers. *Journal of Fluid Mechanics*, 856, 228–256.

[11] Smyth, W.D., Nash, J.D. and Moum, J.N., 2019. Self-organized criticality in geophysical turbulence. *Scientific reports*, 9(1), 3747.

[12] Kaminski, A.K. and Smyth, W.D., 2019. Stratified shear instability in a field of pre-existing turbulence. *Journal of Fluid Mechanics*, 862, 639–658.

[13] Kaminski, A.K., Caulfield, C.P. and Taylor, J.R., 2017. Nonlinear evolution of linear optimal perturbations of strongly stratified shear layers. *Journal of Fluid Mechanics*, 825, 213–244.

[14] Howland, C.J., Taylor, J.R. and Caulfield, C.C.P., 2018. Testing linear marginal stability in stratified shear layers. *Journal of Fluid Mechanics*, 839, R4.

[15] Parker, J.P., Caulfield, C.P. and Kerswell, R.R., 2019. Kelvin-Helmholtz billows above Richardson number 1/4. *Journal of Fluid Mechanics*, 879, R1.

[16] Salehipour, H. and Peltier, W.R., 2015. Diapycnal diffusivity, turbulent Prandtl number and mixing efficiency in Boussinesq stratified turbulence. *Journal of Fluid Mechanics*, 775, 464–500.

[17] Salehipour, H., Peltier, W.R., Whalen, C.B. and MacKinnon, J.A., 2016b. A new characterization of the turbulent diapycnal diffusivities of mass and momentum in the ocean. *Geophysical Research Letters*, 43(7), 3370–3379.

[18] Salehipour, H. and Peltier, W.R., 2019. Deep learning of mixing by two 'atoms? of stratified turbulence. *Journal of Fluid Mechanics*, 861, R4.

[19] Shih, L.H., Koseff, J.R., Ivey, G.N. and Ferziger, J.H., 2005. Parameterization of turbulent fluxes and scales using homogeneous sheared stably stratified turbulence simulations. *Journal of Fluid Mechanics*, 525, 193–214.

[20] Ivey, G.N., Winters, K.B. and Koseff, J.R., 2008. Density stratification, turbulence, but how much mixing?. *Annu. Rev. Fluid Mech.*, 40, 169–184.

[21] Portwood, G.D., de Bruyn Kops, S.M. and Caulfield, C.P., 2019. Asymptotic dynamics of high dynamic range stratified turbulence. *Physical Review Letters*, 122(19), 194504.

GFD 2019 Lecture 9: Challenges in and Promising Approaches for Connecting Theory to Observation

Colm-cille Caulfield & Stephanie Waterman; notes by Alessia Ferraro and Kelsey Everard

June 27, 2019

Introduction to CPC's section

In the last lecture we largely considered stratified turbulence in (vertical) shear flows, which inevitably are "weakly" stratified so that the primary instabilities can grow, saturate and then break down to turbulence. However, as already mentioned, it is thought that much of the world's oceans are very, very strongly stratified, in the sense that an appropriate Froude number based on characteristic horizontal length and velocity scales L_H and U_H is very small, i.e., $Fr = U/(NL) \ll 1$ for an appropriate characteristic buoyancy frequency N. We then want to think about the properties, and indeed the very existence of turbulence in such a strongly stratified regime. There are (at least!) three important questions we wish to consider. First, is it even possible for turbulence to exist in such a strongly stratified regime? Second, if so, how can we model the required energy injection to maintain strongly stratified turbulence? Finally, and perhaps most importantly, how can fluid dynamicists and oceanographers harmonise their skill sets in the most optimal way so as to answer these questions in a relevant way?

1 Mixing Regimes

Before attempting to understand whether turbulence can exist in strongly stably stratified fluids, it is clearly necessary to define what is meant by *strongly*. Indeed, it is also worth discussing whether or not stably stratified turbulence can exist in only some flow regimes, but not others. To classify flow regimes (and indeed to define what is meant by *strongly*) it is natural to use an appropriate definition of a Froude number. As we are (above all) interested in turbulence, it is conventional[4, 18, 9] to use a turbulent Froude number Fr_T, defined as

$$Fr_T = \frac{\epsilon'}{NE_K}, \tag{1}$$

where as usual ϵ' is the dissipation rate of the turbulent kinetic energy (TKE) E_K and N is a characteristic value of the buoyancy frequency. In terms of this parameter, three regimes can immediately be identified: *weakly stratified flow* with $Fr_T \gg 1$; *moderately stratified flow* with $Fr_T \simeq 1$; and *strongly stratified flow* with $Fr_T \ll 1$. Each will be considered in turn.

1.1 Weakly stratified flow

Simple scaling arguments can be presented for this regime, which are in fact closely related to the previously discussed behaviour of stratified shear-driven turbulence. Remember in the previous

lecture we saw that the turbulent Prandtl number $Pr_T \simeq 1$, implying that density is mixed as a passive scalar, and also that the flux Richardson number (and hence the mixing efficiency, and even the flux coefficient since $\Gamma = Ri_f/(1+Ri_f))$ $Ri_f \simeq Ri$ for some characteristic value Ri of the gradient Richardson number.

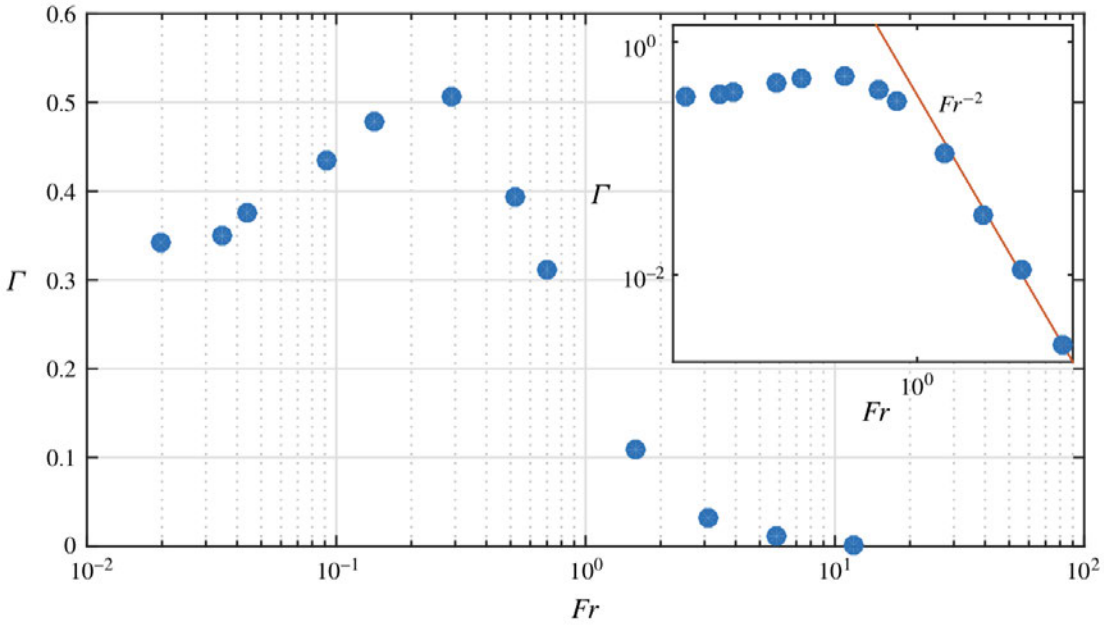

Figure 1: Mixing coefficient as a function of Froude number (log-log plot shown in inset). From [9].

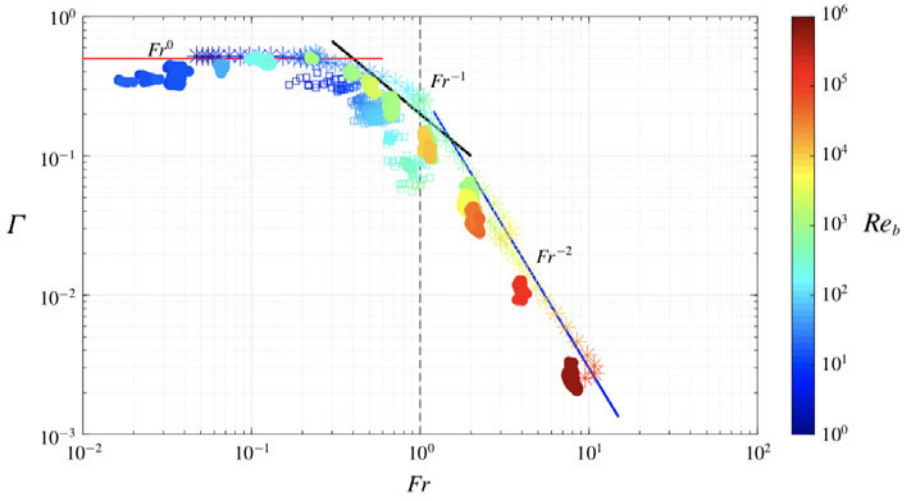

Figure 2: Mixing coefficient Γ as a function of turbulent Froude number Fr. The colour bar shows values of Re_b. Star: decaying DNS; circle: forced DNS of Maffioli et *al.* [9]; square: sheared DNS of Shih et *al.* (2005). Solid lines display the scaling relations derived in [2], from which this figure is taken.

We assume further that the flow is at sufficiently high Reynolds number Re and Péclet number

$Pe = RePr_m$ (where Pr_m is the molecular Prandtl number, $O(10)$ in the ocean) so that the effects of ν and κ can be ignored. Then, following the argument presented in [9], the dissipation rates of turbulent kinetic energy and available potential energy approach finite positive limits of the same order as the advection terms in their respective evolution equations [9], and so the zeroth law of turbulence applies to ϵ' with the classic inertial scaling:

$$\epsilon' =\sim \mathbf{u} \cdot \nabla \left(\frac{|\mathbf{u}|^2}{2} \right) \sim \frac{U^3}{L}, \tag{2}$$

for some characteristic velocity scale U and length scale L, while

$$\chi \sim \mathbf{u} \cdot \nabla \left(\frac{b^2}{2N^2} \right) \sim \frac{b^2 u}{N^2 l} \sim N^2 UL, \tag{3}$$

as the characteristic buoyancy frequency and buoyancy are expected to be related as $N^2 \sim b/L$. Therefore, supposing that the flow is in equilibrium so that the buoyancy flux $B \simeq \chi$, the mixing coefficient Γ is given by:

$$\Gamma \simeq \frac{\chi}{\epsilon'} \sim \frac{N^2 L^2}{U^2} \sim Fr_T^{-2}, \tag{4}$$

using the inertial scaling for ϵ' in the definition of Fr_T, and also assuming that $E_K \sim U^2$. If U/L can further be identified with the vertical shear S, then this scaling is clearly consistent with the $Ri \simeq Ri_f$ scaling implicit in the $Pr_T \simeq 1$ weakly stratified behaviour already encountered. This scaling is clearly observed in forced simulations, as shown in figures 1 and 2. Note that this, particularly for large values of Fr_T, implies a very small efficiency of mixing, effectively as there is not much density variation to mix.

Following an argument originally presented by [2], this scaling can actually be couched in terms of the length scale ratio $R_{OT} = L_O/L_T$ as introduced in Lecture 8 when discussing the *Thorpe method*, where L_T is the Thorpe scale (i.e., the rms of the displacements required to sort an overturning density profile into a statically stable monotonic profile) and L_O is the *Ozmidov scale*:

$$L_O = \left(\frac{\epsilon'}{N^3} \right)^{1/2}. \tag{5}$$

They argued that for weakly stratified flows, $L_T < L_O$ and also that the characteristic length scale L in the various expressions above is approximately L_T and so

$$\Gamma \sim \frac{N^2 L^2}{U^2} \sim \left(\frac{L_T}{L_O} \right)^{4/3} = R_{OT}^{-4/3}, \tag{6}$$

which again is expected to be very small since $L_T < L_O$. [1]

[1] They actually presented the argument in terms of assuming the Thorpe scale L_T could be approximated by the *Ellison scale* $L_E = \langle \rho'^2 \rangle^{1/2} / [\partial \langle \rho \rangle / \partial z]$. $\langle \rho'^2 \rangle^{\frac{1}{2}}$ is the standard deviation of density fluctuations from the ensemble mean, and $\partial \langle \rho \rangle / \partial z$ is the ensemble mean vertical density gradient. It is entirely reasonable that L_T and L_E are closely related, and there are operational reasons why one or the other might be easier to calculate in a particular circumstance. The key assumptions are that the characteristic scale of the density fluctuations is smaller than L_O in weakly stratified flow, and that the density fluctuation scale is the same as the characteristic scale of the dissipation rate(s).

1.2 Moderately stratified flow

Moderately stratified flow can be assumed to exhibit hybrid scaling[2]. The stratification is sufficiently strong to set the time scale for the mixing, and so

$$\chi \sim w'^2 N. \tag{7}$$

However, the velocity field remains (largely) unaffected, and it remains close to isotropic, and so $w'^2 \sim E_K$, and so

$$\Gamma \sim \frac{w'^2 N}{\epsilon'} \sim E_K N \epsilon' = Fr_T^{-1}. \tag{8}$$

This scaling is at least consistent with the data shown in figure 2, although there is quite a bit of scatter, and the behaviour may possibly be just associated with the transition between the two extreme weakly and strongly stratified regimes.

1.3 Strongly stratified flow

In the case of strongly stratified turbulence, i.e., in the limit $Fr_T \ll 1$, it is reasonable to assume that buoyancy is the dominating factor in the mixing dynamics, so that both dissipation rates "know" about the buoyancy frequency, and so

$$\Gamma \sim \frac{w'^2 N}{w'^2 N} = const. \sim Fr_T^0, \tag{9}$$

thus tending towards a constant in the limit of strong stratification. There are some case studies that would suggest that it can indeed be possible to maintain turbulence in highly stratified flows, and thus approach a constant value for Γ. Unfortunately, the question is now more complex in that it becomes necessary to address the possibility that factors like initial stratification [17] and form of forcing may lead to **different** constant values, a point we shall return to below. There is also a critical issue of how the various characteristic quantities used to construct the turbulent Froude number are calculated and, in particular, averaged. Cursory observation of any turbulent stratified flow shows that the turbulence is (typically) highly anisotropic and spatio-temporally intermittent.

Just to consider one example, we have already mentioned the prevalence of density "staircases", and for such flows, what are the characteristic value of N, U and L? Are they the values in the layers, in the interfaces, or in some average of the two? Along the same vein, it has been argued that the very concept of a "strongly stratified turbulence" regime may be misleading in the first place. Looking at a slice through a forced stratified turbulent simulation as shown in figure 3, it is apparent that there are three qualitatively different types of region, which actually can be identified robustly and algorithmically[15]. There are:

1. "quiescent regions" where $Re_b = \epsilon'/(\nu N^2) \sim O(1)$;
2. intermittent "layers" where $Re_b \sim O(10)$;
3. "turbulent patches" where $Re_b \sim O(100)$.

These three types of regions occur even in a flow where the overall value of $Re_b \simeq 13$, with $Fr_T \simeq 0.015$ when the dissipation rate was determined by averaging over the whole domain. For this flow, (shown in the figure) the turbulent patches only occupy 4% of the flow volume. Nevertheless, these patches are effectively just as turbulent as the entire domain of a flow with overall $Re_b \simeq 200$ and $Fr_T \simeq 0.075$, which is thus more weakly stratified and is over 96% by volume classified as a

"turbulent patch". The turbulent patch in the figure is strongly correlated with a region of static instability, thus suggesting that "strongly stratified" turbulent flows may just be flows with very rare regions of weak stratification in which turbulence can be vigorous, although that view is quite controversial.

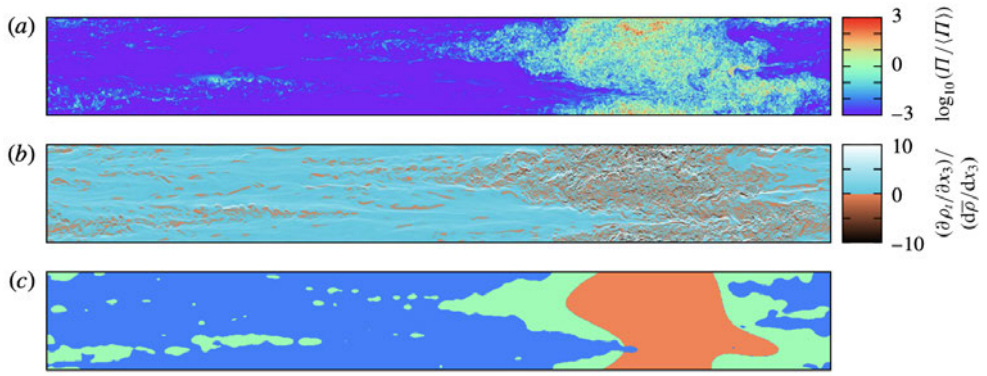

Figure 3: A vertical slice through a forced stratified flow illustrating: (a) the logarithm of the potential enstrophy normalised by its domain average, (b) $\partial\rho_t/\partial x_3/d\bar{\rho}/dx_3$ and (c) the result of flow classification as implemented in [15]. The colouring in (b) highlights the convectively unstable fluids elements in red. The colouring in (c) corresponds to the region classification, where red indicates a turbulent patch region, green an intermittent layer region and blue a quiescent flow region. From [15].

1.3.1 Mixing at sharp interfaces

Such spatio-temporal inhomogeneity appears to be generic in stratified turbulent flows. For example, axially stratified Taylor-Couette flow spontaneously forms a density staircase[13]. In the limit of strong stratification, the buoyancy flux across the layer interfaces asymptotically tends to a constant value as shown in figure 4. Assuming (as is reasonable) that the viscous dissipation rate remains roughly constant, this is strongly suggestive of a constant value of Γ at high stratification.

The possibility for strongly stratified turbulence to approach constant mixing efficiency (or equivalently constant flux coefficient Γ) as the stratification gets arbitrarily strong has also been demonstrated experimentally through considering the mixing induced by vortex rings impinging on a sharp interface as shown in figure 5 [14]. These experiments suggest that mixing can exist at arbitrarily strong stratifications so long as some sort of forcing is applied.

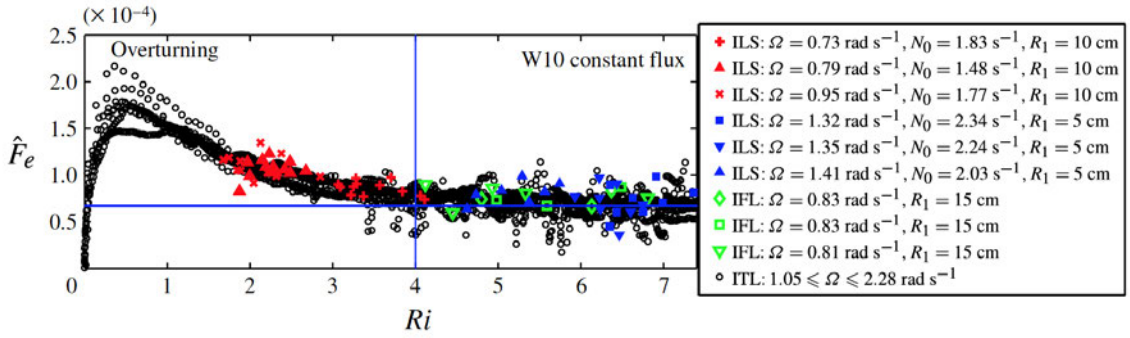

Figure 4: Non-dimensional [turbulent entrainment] flux $\widehat{F}_e$ through individual interfaces: six Initially-Linear-Stratification (ILS) experiments (filled coloured symbols); three Initially-Five-Layer (IFL) experiments (open green symbols); 12 Initially-Two-Layer (ITL) experiments with varying R_1, Ω and initial $\Delta\rho$ (open black circles). Each coloured symbol represents a different interface in one experiment. The solid blue lines show the constant $\widehat{F}_e$ in the [19] asymptotic regime and the empirical value of Ri_a. From [13].

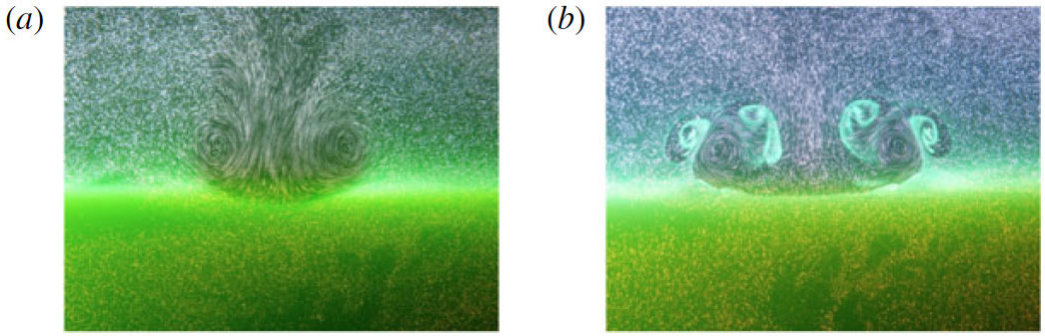

Figure 5: Long-exposure photographs of a vortex ring impinging on a sharp interface between an upper tracer-particle-laden fresh-water layer and a lower green-dyed salt-water layer. Photographs display a vortex ring (a) just prior to and (b) during the vortex-ring interaction. Here $Ri \gg 1$. From [14].

1.3.2 Optimal mixing

Returning to consideration of the data presented in figure 3 as Ri decreases, it is apparent that the density staircase breaks down due to vigorous overturning of the various interfaces. This overturning is clearly associated with an enhanced flux, again suggestive of a non-monotonic mixing efficiency with a clear *left flank-right flank* structure as discussed in Lecture 7. The flux curve is also consistent with there being an "optimal" stratification at which the mixing efficiency is maximal, analogously to the KHI-driven mixing discussed in Lecture 8. Using stably stratified plane Couette flow as a model flow, constructing a rigorous upper bound (across all possible Richardson numbers, and at asymptotically large Reynolds number) on the long-time-averaged buoyancy flux leads to a flow with bulk Richardson number (and also maximum gradient Richardson number) of 1/6. The associated

flux coefficient is $\Gamma = 1/4$[16], associated with a cumulative efficiency $\mathcal{E}_c = 1/3$, as shown in figure 6. This is consistent with classical observations[7], and it is at least curious that the particular value of $Ri = 1/6$ has popped up yet again. In some sense this seems to be the largest possible Richardson number that still behaves as a weakly stratified flow, and thus is able to mix vigorously due to turbulence.

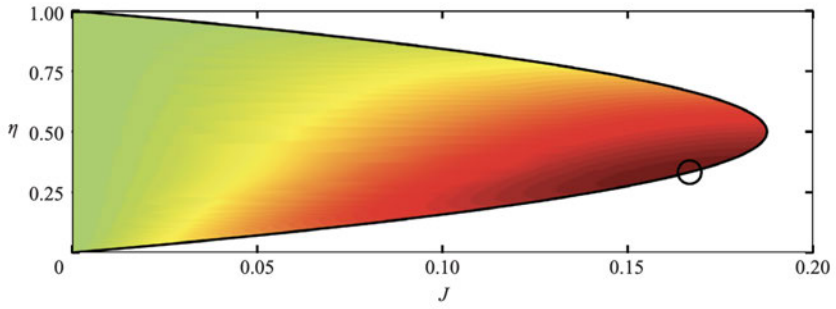

Figure 6: Contours of the upper bound on the mixing-efficiency specific buoyancy flux, $\mathcal{B}^{\eta}_{max}(J, Re; \eta)/\mathcal{B}_{\infty}$, as the bulk Richardson number, here labelled as J, and (cumulative) mixing efficiency, here labelled as η, are varied for an asymptotically large value $Re = 20000$. The thick solid line marks the envelope of $J^{\eta}_{max}(Re; \eta)$ while the circle marks $J_{max}(Re) \simeq J_{infty} = 1/6$, which corresponds to $\eta_{max}(Re) \simeq \eta_{infty} = 1/3$. From [16].

1.3.3 Impact of initial buoyancy profile

By means of a statistical mechanics approach, it is possible to infer the cumulative mixing efficiency for a given amount of energy injection in a Boussinesq flow[17]. As shown in figure 7, the mixing efficiency **and** the final state can very much depend on the chosen initial condition. If the initial condition is initially two layer (as shown in the left panel), a non-monotonic dependence on the appropriate definition of Ri is observed, with clear evidence of a "right flank" with a sharp interface surviving, and very small mixing efficiency for very strong stratification. Conversely, if the initial profile is linear (right panel), the mixing efficiency is a monotonic function of Ri, tends to a constant value $\simeq 0.25$ in the limit of large Ri. Clearly, it is very difficult to say something generic about mixing when such strong dependence on initial conditions can be observed.

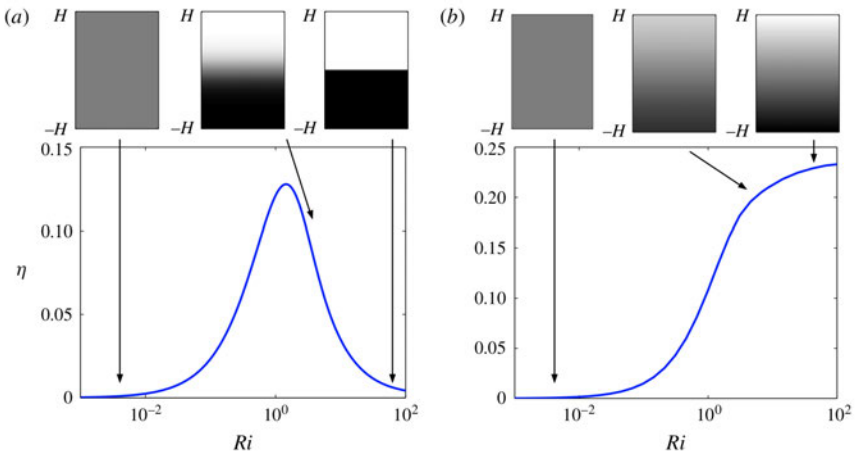

Figure 7: Variation of the cumulative mixing efficiency (here labelled as η) with an appropriately defined Richardson number $Ri = H\Delta b/e_c$ (a) for an initial background buoyancy profile with two homogeneous layers, (b) for an initial linear background buoyancy profile. The three insets show the equilibrium buoyancy field $\bar{b}$ for $Ri = 0.07, 7, 70$. From [17].

1.3.4 Dependence on forcing mechanism

The situation becomes even more disheartening when different forcing mechanisms are used to maintain turbulence in a strongly stratified flow[3]. In figure 8, horizontally averaged Γ is plotted against the horizontally averaged local value of Fr_T for three different stratified turbulence simulations. Each simulation is forced differently: simulation H is forced purely horizontally; simulation R is forced with internal waves with random phase; while simulation P is forced with a propagating wave field. There is clear evidence of the predicted strongly-stratified regime with Γ being independent of Fr_T. However, the particular asymptotic mean value is different for the three simulations: $\Gamma = 0.37$ for simulation H; $\Gamma = 0.518$ for simulation R; and $\Gamma = 0.496$ for simulation P, showing marked sensitivity of the mixing properties to the particular form of the forcing: again very difficult to say anything generic and quantitative about stratified mixing from a theoretical viewpoint.

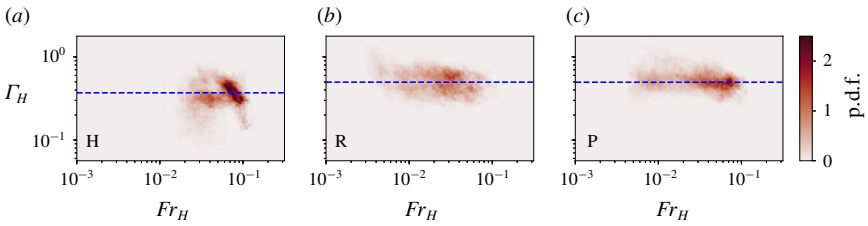

Figure 8: Two dimensional p.d.f. of horizontally averaged turbulent Froude number Fr_H and Γ_H for three simulations with different forcing strategies. From [3].

Introduction to SW's section

Numerical models of the oceans at both regional and global scales require the specification of a mixing rate to model unresolved sub-grid scale processes. However, obtaining realistic turbulence

mixing rates from observational data is non-trivial as this requires proper identification of uncontaminated turbulence from a signal. The difficulty lies in the fact that there is often no clear scale separation between turbulence and the processes generating the turbulence in the real ocean, making the identification of turbulence from observational data a difficult task. Exacerbating this difficulty is the relative sparsity of measurements taken in the ocean. Further, even if a proper mixing rate is found and included in the numerical model, numerical challenges exist, such as numerical diffusion. In view of making scientific progress, the approach must necessarily be "move on and do the best we can".

2 A History of Vertical Mixing in Models

Prior to the 1990s, approximations of turbulent mixing were dominated by a Fickian diffusion approach, whereby turbulence flux occurs across vertical or diapycnal gradients,

$$\overline{w'\psi'} = K\frac{\partial \psi}{\partial z} \tag{10}$$

where the eddy diffusivity, K, was taken as a constant, aside from in a few exceptions (e.g., [1]). It wasn't until the 1990s when oceanographers began to add turbulence parameterisations based upon individual physical processes such as shear-driven mixing and mixing due to double-diffusion.

In the early 2000s, oceanographers began to include parameterisations that considered the impact of internal wave breaking, starting with Jayne and St. Laurent (2001) [6]. Since this introduction, a lot of attention has been given to the role of internal wave action on turbulent mixing (see [8]). With the understanding that internal wave breaking is an important turbulent mixing process, the next step is in identifying the processes generating the internal waves in the first place. McKinnon *et al.* (2018) identify four main processes,

- near-field mixing due to breaking of tidally driven internal waves
- far-field mixing due to breaking of tidally driven internal waves
- mixing due to breaking of internal lee waves
- mixing due to breaking of wind driven internal waves.

In addition to McKinnon *et al.* (2018), Ed Wunsch added that the breaking of near-inertial internal waves, whatever their source, is also an important process.

2.1 Near-field breaking of tidally driven internal waves

The waves generated by tidal flow over topography that break near their place of origin tend to be higher mode waves. These near-field processes include, for example, hydraulic jumps, and experience enhanced interaction with other internal waves higher in the water column. The enhanced dissipation, ε, is given in [8] as,

$$\varepsilon = \frac{1}{\rho}\, E(x,y)\, q\, F(z) \tag{11}$$

where $E(x,y)$ is the spatially dependent energy input into the internal wave from the tides, q is the fraction of the generated internal waves that break locally, and $F(z)$ is the vertical structure function

that models the vertical distribution of turbulent mixing. Relating this enhanced dissipation back to the eddy diffusivity,

$$K = K_b + \frac{q\,\Gamma\,E(x,y)\,F(z)}{\rho\,N^2} \tag{12}$$

where K_b is the constant value that was assumed prior to the 1990s. [5] find that use of this eddy diffusion parameterisation has noticeable impact on oceanic circulation, but a modest effect on the poleward transport of heat. [11] find that ocean circulation is slightly sensitive to $F(z)$, but that this sensitivity is robust and statistically significant. [8] devote a lot of effort to improving the parameterisation of $F(z)$, particularly to account for wave-wave interactions.

2.2 Far-field breaking of tidally driven internal waves

The lower mode waves from tidal flow over topography in contrast can propagate thousands of kilometres before breaking, however the mechanism by which the breaking of non-local internal waves enhances dissipation is not well understood. A ray tracing method is used for the parameterisation of these far-propagating internal waves, which allows for 'tracking' of these waves to provide insight into where they travel. [12] include a parameterisation of the enhanced dissipation due to the far-field breaking of internal waves, and find that ocean dynamics are sensitive to the vertical distribution of mixing due to the far-field tidally driven internal wave breaking enhanced dissipation.

2.3 Breaking of internal lee waves

Internal lee waves are generated by mean flows over topography and have significant impacts on the ocean state [10]. Despite the known impacts of internal lee waves on ocean dynamics, the relative importance of both local and non-local breaking of internal lee waves on dissipation is not known.

References

[1] K. Bryan and L. Lewis, *A water mass model of the world ocean*, Journal of Geophysical Research: Oceans, 84 (1979), pp. 2503–2517.

[2] A. Garanaik and S. K. Venayagamoorthy, *On the inference of the state of turbulence and mixing efficiency in stably stratified flows*, Journal of Fluid Mechanics, 867 (2019), pp. 323–333.

[3] C. Howland, J. Taylor, and C. Caulfield, *Mixing in forced stratified turbulence and its dependence on large-scale forcing*, Journal of Fluid Mechanics, 898 A7 (2020).

[4] G. Ivey and J. Imberger, *On the nature of turbulence in a stratified fluid. part i: The energetics of mixing*, Journal of Physical Oceanography, 21 (1991), pp. 650–658.

[5] S. R. Jayne, *The impact of abyssal mixing parameterizations in an ocean general circulation model*, Journal of Physical Oceanography, 39 (2009), pp. 1756–1775.

[6] S. R. Jayne and L. C. St. Laurent, *Parameterizing tidal dissipation over rough topography*, Geophysical Research Letters, 28 (2001), pp. 811–814.

[7] P. F. Linden, *Mixing in stratified fluids*, Geophysical & Astrophysical Fluid Dynamics, 13 (1979), pp. 3–23.

[8] J. A. MacKinnon, Z. Zhao, C. B. Whalen, A. F. Waterhouse, D. S. Trossman, O. M. Sun, L. C. St. Laurent, H. L. Simmons, K. Polzin, R. Pinkel, et al., *Climate process team on internal wave–driven ocean mixing*, Bulletin of the American Meteorological Society, 98 (2017), pp. 2429–2454.

[9] A. Maffioli, G. Brethouwer, and E. Lindborg, *Mixing efficiency in stratified turbulence*, Journal of Fluid Mechanics, 794 R3 (2016).

[10] A. Melet, R. Hallberg, S. Legg, and M. Nikurashin, *Sensitivity of the ocean state to lee wave–driven mixing*, Journal of physical oceanography, 44 (2014), pp. 900–921.

[11] A. Melet, R. Hallberg, S. Legg, and K. Polzin, *Sensitivity of the ocean state to the vertical distribution of internal-tide-driven mixing*, Journal of Physical Oceanography, 43 (2013), pp. 602–615.

[12] A. Melet, S. Legg, and R. Hallberg, *Climatic impacts of parameterized local and remote tidal mixing*, Journal of Climate, 29 (2016), pp. 3473–3500.

[13] R. Oglethorpe, C. Caulfield, and A. W. Woods, *Spontaneous layering in stratified turbulent taylor–couette flow*, Journal of Fluid Mechanics, 721 R3 (2013).

[14] J. Olsthoorn and S. B. Dalziel, *Vortex-ring-induced stratified mixing*, Journal of Fluid Mechanics, 781 (2015), pp. 113–126.

[15] G. D. Portwood, S. M. de Bruyn Kops, J. R. Taylor, H. Salehipour, and C. Caulfield, *Robust identification of dynamically distinct regions in stratified turbulence*, Journal of Fluid Mechanics, 807 R2 (2016).

[16] W. Tang, C. Caulfield, and R. Kerswell, *A prediction for the optimal stratification for turbulent mixing*, Journal of Fluid Mechanics, 634 (2009), pp. 487–497.

[17] A. Venaille, L. Gostiaux, and J. Sommeria, *A statistical mechanics approach to mixing in stratified fluids*, Journal of Fluid Mechanics, 810 (2017), pp. 554–583.

[18] M. Wells, C. Cenedese, and C. P. Caulfield, *The relationship between flux coefficient and entrainment ratio in density currents.*, Journal of Physical Oceanography, 40 (2010), pp. 2713–2727.

[19] A. W. Woods, C. Caulfield, J. Landel, and A. Kuesters, *Non-invasive turbulent mixing across a density interface in a turbulent Taylor–Couette flow*, Journal of Fluid Mechanics, 663 (2010), pp. 347–357.

GFD 2019 Lecture 10 Part I: Stratified Turbulence and Ocean Mixing Processes 2: Future Directions for Research into Stratified Turbulence and Ocean Mixing Processes

Stephanie Waterman; notes by Wanying Kang and Anuj Kumar

June 28, 2019

1 Challenges in Quantifying Ocean Mixing

There are several reasons as to why measuring ocean mixing is difficult. One of the main reasons is that the process of ocean mixing involves a wide range of scales and to be able to perform a computer simulation that captures the large scales, as well as small scales, is currently out of reach. Therefore, any model for ocean mixing should proceed by making assumptions about either small scales or large scales. This makes the problem non-deterministic as these assumptions should be modeled as a stochastic process. High variation in turbulent kinetic energy dissipation which can vary up to six orders of magnitude; a wide range of processes and instabilities that can lead to turbulence; contamination of point measurements by transient reversible processes; and quantifying mixing based on sparse data are among the other reasons that make quantifying ocean mixing challenge. Besides the scientific reasons, going into the middle of the ocean to take measurements in itself is a challenging task. These expeditions require financial investments, manpower and highly depend on the weather.

Some of the above-mentioned problems, however, can be resolved if we have a better sampling. By better sampling, we mean

- more measurements
- higher density of measurements in space and time
- longer sampling durations
- increased number of locations/environments/regimes sampled
- coincident measurements of multiple variables
- coincident measurements of multiple scales

With a better sampling, the following problem may be improved:

1. contamination of point measurements typically by transient reversible processes.
2. problem of sparse measurements.
3. making better stochastic models.

2 Robots are Coming

Turbulence measurement was particularly challenging until recently. Sensors needed to be fast and passivated. To make sure measurement is taken in the right place, platform needs to be designed to have stable and minimal motion as well as to be easy for deploy and recovery. Calibration procedures need to be repetitively tested and the noice in a circuitry has to be lowered to an acceptable level (which is quite low).

Robots and the autonomous sampling platforms coming along significantly boost the measurement of microstructures in the ocean. They allow measurement to be taken at high temporal and spatial frequency, while requiring much less efforts.

- Sampling is typically near-continuous
- Sampling typically can be sustained for long observing periods
- Does not require ship time or resources → relatively cheap → We can have lots! They can be out most of the time!
- Typically sample with high resolution in space and/or time
- Allows for adaptive sampling strategies based on near-real time data
- Ideal for sampling places a ship can't go (e.g. in a hurricane, under ice)
- Typically can accommodate multiple sensors for concurrent measurements of multiple variables and/or at multiple scales
- Gliders love the age-old problems of doing free-ascent based measurements as allow for measurements into the near-surface layer (upper 1 m)
- Can have no moving parts → very low noise levels

Shown in Fig. 1 are the upcoming robots that will help us with the sampling issue. Instead of having ships/people go to a spot and take measurement, robots (e.g. glider and Turbulence AUV) can be programmed to collect high-frequency data through a path. Not only can they significantly increase the sampling frequency, but they can also go to places that are too dangerous for ships and people. Recently, these data start to be used to better understand the turbulence statistics, which can then push forward the mesoscale parameterization.

3 Future Directions

Future is bright. We would hope for

- extended moored time series of 'direct' turbulence measurements
- widespread turbulence measurements from gliders and floats
- deep ocean turbulence measurements from deep gliders
- autonomous under-ice turbulence measurements
- process studies with everything in the 'kitchen sink'

RSI "MicroRider" on a Slocum glider

epsi on a "Wire Walker" profiler

OSU chi-pod on a SOLO profiling float

RSI "MicroRider" on an ALAMO (air-launched profiling float)

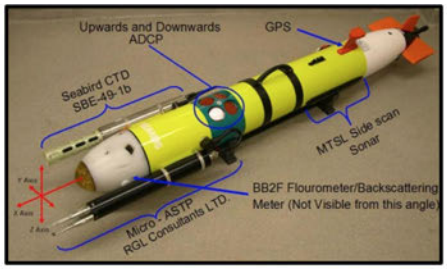

REMUS-100 Turbulence AUV

REMUS-600 Turbulence AUV

courtesy of Lou St. Laurent

Boaty McBoatface

courtesy of Eleanor Frajka-Williams

Figure 1: The upcoming robots that may help us resolve the bad sampling issue.

As a closing statement, by adapting sensing technology to new platforms (moorings, floats, gliders etc.), we are excited to have the opportunity to see a step change in the number and time/space resolution of ocean turbulence measurements. These achievements let us see the ocean in new ways, and will almost certainly produce transformative insights. That said, hypothesis-driven experiments are essential to move process understanding forward. Process experiments/adaptive sampling will always require ships. Nothing replaces dedicated research ships for adaptive sampling.

GFD 2019 Lecture 10 Part II: Future Directions for Research into Stratified Turbulence and Ocean Mixing

Colm-cille Caulfield; notes by Wanying Kang and Anuj Kumar

June 28, 2019

1 How Good Are Our Estimates for Turbulent Diffusivity?

Throughout these lectures we have tried to get to grips with stratified turbulent mixing in general, and in possible models for the associated enhanced turbulent diffusivity κ_T in particular. There are many different causes of uncertainty in the estimates of those models, and we will here focus on two main classes. First, there are different methods to estimate κ_T, based on different fundamental modelling assumptions, and the different methods are (most definitely) not necessarily consistent with each other. Second, a limited number of data points (typically oceanographic profile measurements) can be collected for one estimation. Therefore, even using one specific method, the results may not be convergent, due to the inherent variability present in a turbulent mixing event, as it is self-evident that stratified turbulence in the world's oceans is both spatially and temporally intermittent. As is clearly apparent in figure 1, even in one direct numerical simulation (DNS), turbulent regions with different intensity have completely different fingerprints in the buoyancy distribution, ϵ', and χ. Such intermittency of ocean turbulence in space and time makes the sampling problem even more severe[6].

There are then two natural issues which can be investigated in terms of the convergence and reliability of estimating turbulent diffusivity from profiles using different methods. Firstly, it is not at all clear whether estimates using a particular method will converge to the "ground truth" value of the diffusivity as more and more profiles (or equivalently a data volume) are used. Second, and perhaps more optimistically, it is of interest to see how uncertainty in the estimates decreases (hopefully!) as more and more estimates are constructed from distinct vertical profiles. As previously discussed in Lectures 6 and 8, there are three classical methods used to estimate turbulent diffusivity κ_T, i.e., the Osborn method, Osborn-Cox method and the Thorpe method. Briefly (and loosely) the Osborn method estimates κ_T by assuming the buoyancy flux is linearly related to the dissipation rate via a (often-assumed) constant flux coefficient $\Gamma \simeq 0.2$. The Osborn-Cox method is more "direct", assuming that the mixing is well-described by the destruction rate of buoyancy variance χ, and so

$$\kappa_O = \Gamma \frac{\epsilon'}{N^2} \tag{1}$$

$$\kappa_{O-C} = \frac{\chi}{\langle N^2 \rangle}, \tag{2}$$

where as usual, there are real issues to be addressed concerning the particular space-time volume which is used to estimate the various quantities on the right-hand side of these expressions. In the Thorpe method, the dissipation rate is estimated based on the vertical profiles of the (potential) density field. For a given density profile, the various parcels are displaced to create a sorted density

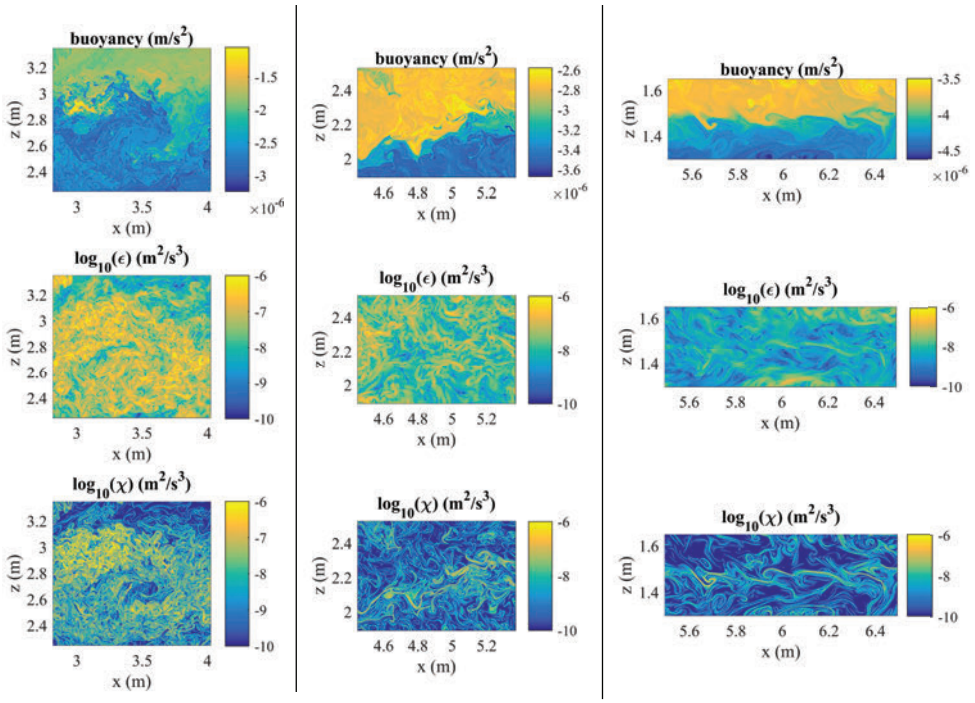

Figure 1: The buoyancy, turbulent kinetic energy dissipation rate and perturbation potential energy dissipation rate for three regions with strong, moderate and weak dissipation from a particular DNS. From [6].

field which is a monotonic function of height. The associated displacements L_d of the various parcels then can be used to estimate the Thorpe scale:

$$L_T^P = \langle L_d^2 \rangle_P^{1/2}. \tag{3}$$

Assuming that the Thorpe scale is linearly proportional to the profile's characteristic Ozmidov scale $L_O^P = \langle \epsilon' \rangle_P^{1/2} \langle N^2 \rangle_P^{-3/2}$, it is then possible to construct an estimate of the dissipation rate:

$$\langle \epsilon \rangle_P = R_{OT}^2 (L_T^P)^2 \langle N^2 \rangle_P^{3/2}. \tag{4}$$

The next heroic (and not really justified by more recent data, particularly from numerical simulations) assumption is that R_{OT} takes a fixed value $R_{OT} \simeq 0.8$. Substitituting this estimate for ϵ' into the expression at the heart of the Osborn method, the Thorpe method's estimate for the turbulent diffusivity is now

$$\kappa_T = 0.64 \Gamma (L_T^P)^2 \langle N^2 \rangle_P^{1/2}, \tag{5}$$

where somewhat confusingly, the subscript now refers to the *Thorpe method*.

Considering the first "issue" mentioned above, these three model estimations when averaged across an entire computational volume are compared against the turbulent vertical diffusivity diagnosed directly from the volume-averaged buoyancy flux $\kappa_d^V = \langle B \rangle / \langle N^2$ for three different simulations with different characteristic Re_b in figure 2 from [6]. Encouragingly, the Osborn method and the Osborn-Cox method both give a good estimate of κ_d^V in all cases. On the other hand, the Thorpe method underestimates κ_d^V by about 50% in the highly turbulent case, but significantly overestimates it in the less turbulent cases, demonstrating just how unreliable the assumption of constant length scale ratio R_{OT} is.

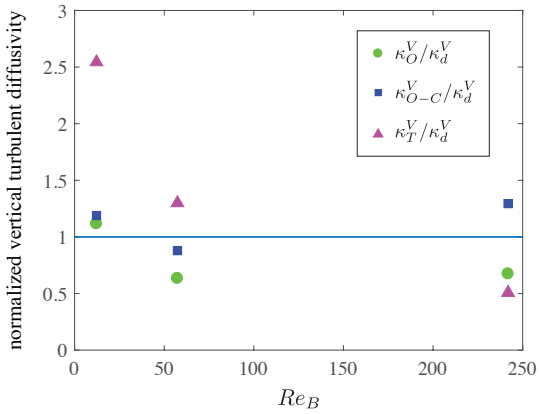

Figure 2: Vertical diffusivity estimated using the Osborn method κ_O^V, Osborn-Cox method κ_{O-C}^V and Thorpe method κ_T^V, each calculated using data extracted from the full computational volume and normalized by the turbulent vertical diffusivity diagnosed directly from the volume-averaged buoyancy flux κ_d^V. From [6].

However, such a volume-average will not in general be available. Actual estimates will be constructed from individual profiles, and the second-mentioned issue concerns the reduction in uncertainty as more and more profiles are used to construct estimates. Figure 3 shows the results of just such an analysis. For each simulation, the black dashed line shows the true value of the diffusivity. Unsurprisingly, due not least to the non-sign definiteness of the buoyancy flux B, profile-based estimates using the "direct method" are very uncertain. There is also clear evidence that, at least for these simulations, the Thorpe method is inherently biased. The other two methods are somewhat more reliable, with approximately 20 profiles typically yielding reasonable estimates for the "true" value with the Osborn-Cox method being perhaps the best of all. However, it is important to remember that it is not (yet) usual observational practice to take multiple profiles in the same place. Perhaps it should be...

2 The Effects of Boundaries

Throughout these lectures, we have only considered highly idealized flows, either with an initial shear or artificial imposed forcing to keep the turbulence energised. However, real flows inevitably have boundaries, and there is an overwhelmingly large amout of evidence that shows the importance of boundary-mediated mixing. For example, we know that diffusivity increases exponentially approaching the bottom of the ocean as shown in figure 4 [5], and it has become increasingly appreciated that boundary layers play a key (indeed governing) role in the abyssal ocean upwelling [4].

Consider the schematic situation shown in figure 5. In the interior of an ocean basin, stronger mixing near the basin floor (where the density is naturally highest), will tend to lead to a relative local increase in the density of a water parcel, thus leading to an interior sinking in a basin. Conversely, a water parcel right at the boundary cannot mix from below as the buoyancy flux has to vanish at the boundary, while it can mix from above. This will bring lighter water into this water parcel and cause rising. Crucially, this upwelling mechanism only works when the boundary is tilted, but fortunately that is a natural characteristic of shelf regions of ocean basins. Furthermore, a tilted side boundary also means a decreasing basin cross-section (and boundary perimeter) with depth. As

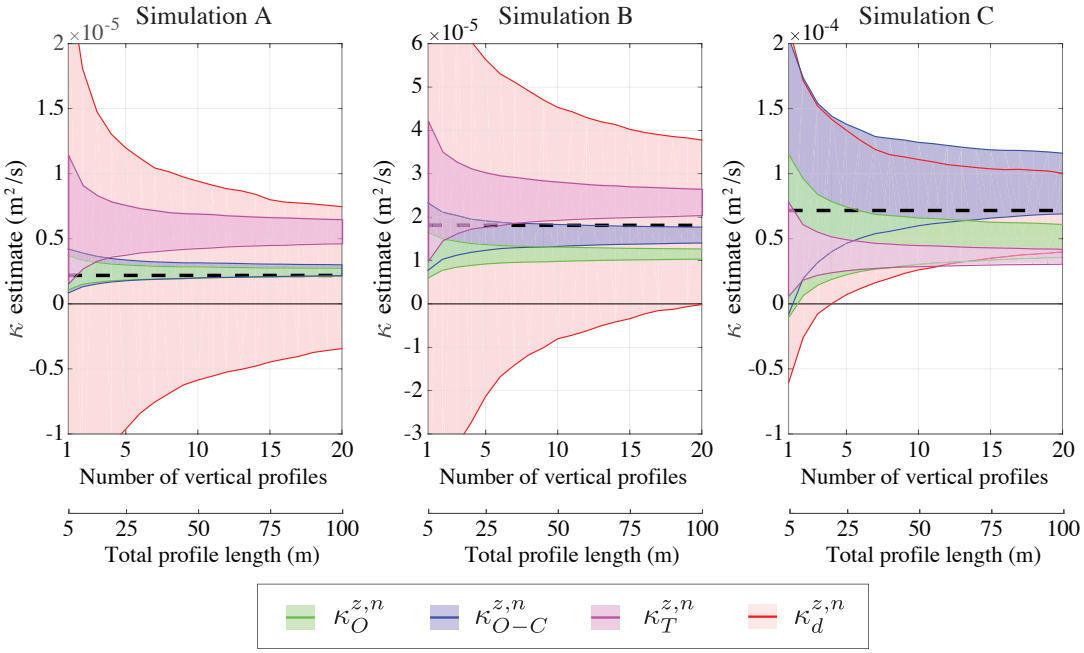

Figure 3: Estimates of the vertical diffusivity using the Osborn method (green), Osborn-Cox method (blue), Thorpe method (magenta), and the "direct" method (red), calculated using n vertical profiles. Lines denote one standard deviation about the mean and the area between these limits is shaded. The dashed line indicates the "true" vertical diffusivity calculated by directly averaging the flux over the full volume of the simulations. From [6].

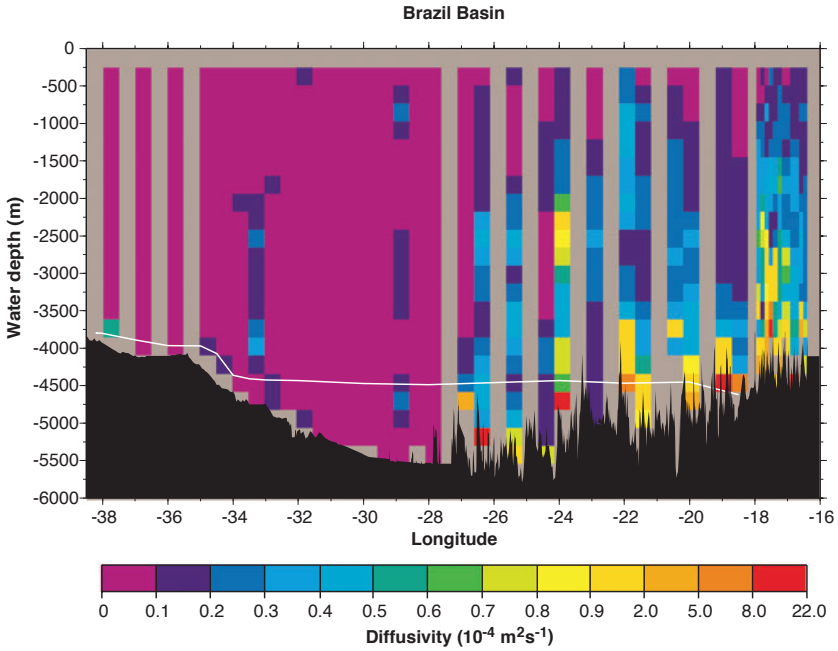

Figure 4: Depth-longitude section of cross-isopycnal diffusivity in the Brazil Basin inferred from velocity microstructure observations. Note the non-uniform contour scale. Microstructure data from the two quasi-zonal transects have been combined without regard to latitude. The underway bathymetric data to 32°W is from the eastward track, the balance comes from the westward track. The white line marks the observed depth of the 0.8°C surface. From [5].

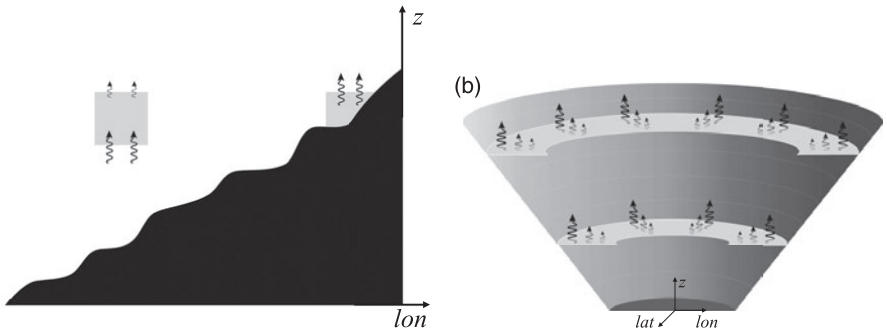

Figure 5: Schematics from [4] to demonstrate the role of side boundaries in the abyssal upwelling.

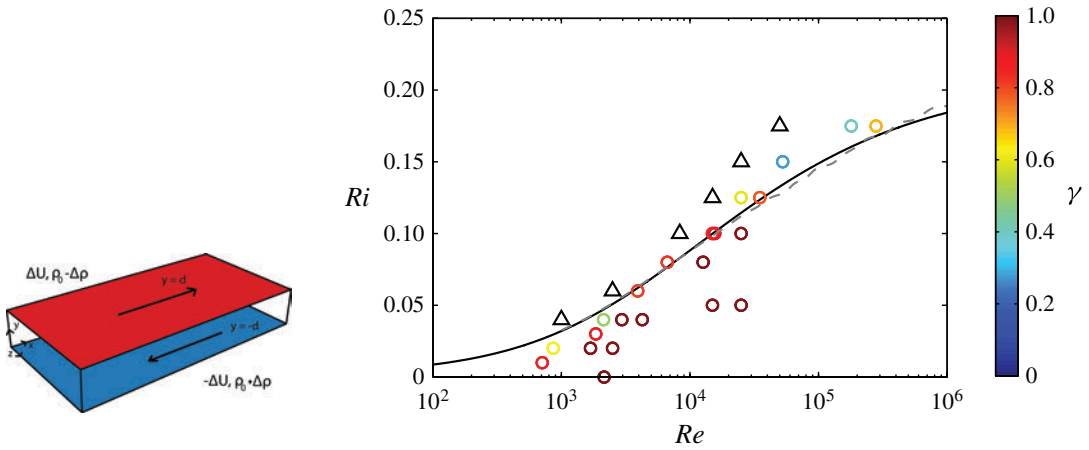

Figure 6: Left: schematics of stratified plane Couette flow. Right: Summary of the direct numerical simulations (circles) and predictions of the intermittency boundary given by the Monin–Obukhov theory (solid black line) and the explicit algebraic models (dashed grey line) for simulations with $Pr_m = 0.7$. The symbols are coloured by the turbulent fraction, ranging from blue (laminar) to red (fully turbulent). Triangles representing simulations that fully relaminarised are also shown for reference. From [2].

shown schematically in figure 5b, the total length of the ocean basin boundary perimeter increases with height. As a result, although the (local) strength of the mixing and upwelling increases with depth, the total upwelling transport may actually decrease with depth. Understanding the trade-offs and subtle balances of these various spatially-dependent transports is an active and exciting area of research, where there is a real need for observationalists and theoreticians to work together.

2.1 Monin-Obukhov theory and stratified plane Couette Flow

Considering wall-bounded idealized flow proves to be surprisingly challenging, as it does not appear possible to maintain purely wall-boundary forced flows in a turbulent state when the stratification is in any sense "strong". Nevertheless, we shall press on, not least because there is a ready-made theory available to "understand" the behaviour of wall-bounded stratified flows. As briefly discussed in Lecture 9 from a bounding viewpoint, we here consider *stratified plane Couette flow* (SPC) as shown schematically in the left panel of figure 1. The fluid in contact with the two horizontal boundaries are maintained at constant density: $\rho_0 - \Delta\rho$ at the upper boundary and $\rho_0 + \Delta\rho$ at the lower boundary (effectively by fixing the temperature T of the upper boundary to be a constant hot value, and the temperature of the lower boundary to be a constant cold value). The upper boundary (at $y = d$, sorry the diagram uses the engineering coordinate system) moves at constant streamwise velocity ΔU, while the lower boundary (at $y = -d$) moves at constant streamwise velocity $-\Delta U$. This flow thus has a natural static stability, and characteristic bulk Richardson number. *Monin–Obukhov Similarity Theory (MOST)* is found to be useful in understanding the behavior of such a flow in steady state [2, 7], in particular identifying the boundary between fully developed turbulence and intermittent flow for flows with various Reynolds numbers and (bulk) Richardson numbers, the gradient Richardson number profile $Ri_g(y)$ being an emergent property of the statistically steady flow.

According to MOST, the only nondimensional group in the boundary layer is $\xi = y/L$, where $L = \frac{u_\tau^3}{C_\kappa q_w}$ is the Monin–Obukhov length scale, $u_\tau = \sqrt{\tau_w/\rho_0}$ is friction velocity, and τ_w and q_w

are the shear stress and heat flux at the wall. Therefore, the vertical gradient of velocity and temperature should satisfy

$$\frac{\partial u}{\partial y} = \frac{u_\tau}{C_\kappa y}\phi_m(\xi) \quad \text{and} \quad \frac{\partial T}{\partial y} = \frac{T_\tau}{C_\kappa y}\phi_h(\xi). \tag{6}$$

As the first order approximation, it is natural to assume that the key functions are linear functions of ξ, and so

$$\phi_m(\xi) = 1 + \beta\xi \quad \text{and} \quad \phi_h(\xi) = \mathrm{Pr}_T + \beta\xi, \tag{7}$$

where Pr_T is our old friend the turbulent Prandtl number, and β is a nondimensional constant. Integrating Equation 6 vertically, yields an expression for the velocity and buoyancy jumps between the upper and lower walls,

$$U = 2\frac{u_\tau}{C_\kappa}\left(\log Re_\tau + \beta\frac{h}{L} + C_\kappa C_1\right) \tag{8}$$

$$T = 2\frac{T_\tau}{C_\kappa}\left(\mathrm{Pr}_T \log \mathrm{Re}_\tau + \beta\frac{h}{L} + C_\kappa C_2\right), \tag{9}$$

where C_1, C_2 are both constants, and Re_τ is the Reynolds number corresponding to the friction velocity

$$Re_\tau = \frac{u_\tau h}{v}.$$

Rearranging Equation 8 and Equation 9 yields

$$Re = \frac{Re_\tau}{C_\kappa}\left(\log Re_\tau + \beta\frac{Re_\tau}{L^+} + C_1\right) \tag{10}$$

$$Ri_b = \frac{h}{L}\frac{Pr_T \log Re_\tau + \beta\frac{Re_\tau}{L^+} + C_2}{\left(\log Re_\tau + \beta\frac{Re_\tau}{L^+} + C_1\right)^2}, \tag{11}$$

from which $L^+ = \frac{L}{l} = \frac{u_\tau L}{v}$ can be solved. L is the Monin-Obukhov scale, and $l = v/u_\tau$ is the wall viscous length scale. With reasonable choices of parameters, the critical L^+ separating the full turbulence and intermittency is estimated to be ~ 200[2], a result which appears to be largely independent of (molecular) Prandtl number Pr_m. This critical L^+ is denoted by the solid curve in the $Re - Ri_b$ (here labelled Ri) parameter space in the right panel of figure 6 for flows with $Pr_m = 0.7$. This prediction is verified by numerical simulations and by a more complicated explicit algebraic model. The key point to observe is that the maximum Ri that can sustain turbulence appears to be bounded so $Ri_b \lesssim 0.2$, (although for these flows this also corresponds to the maximum gradient Richardson number, occuring at midplane). As many times discussed before in these lectures, in these flows the turbulent Prandtl number $Pr_T \simeq 1$, thus suggesting that the flux Richardson number Ri_f (and hence the mixing efficiency) is also bounded above by 0.2. Crucially, irrespective of Re, the flow cannot be forced to maintain turbulence in anything other than a "weakly stratified" flow regime.

Changing Prandtl number can still strongly affect the the mean velocity and temperature (or equivalently density/buoyancy) profiles between the two walls, as shown in figure 7[7]. At fixed values of (Re,Ri)=(4250, 0.04), the mean temperature gradient (as shown in figure 7a) sharpens significantly in the near-wall region while it weakens in the interior, as Pr_m increases by two orders of magnitudes from 0.7 to 70. The changes of gradient Richardson number (for given Re) are plotted in figure 7c.

$$Ri_g(y) \equiv \frac{N^2}{S^2} = \frac{-\left(g/\rho_0\right)\left(\mathrm{d}\overline{\rho}/\mathrm{d}y\right)}{(\mathrm{d}U/\mathrm{d}y)^2} = \frac{g\alpha_V(\mathrm{d}\Theta/\mathrm{d}y)}{(\mathrm{d}U/\mathrm{d}y)^2} \tag{12}$$

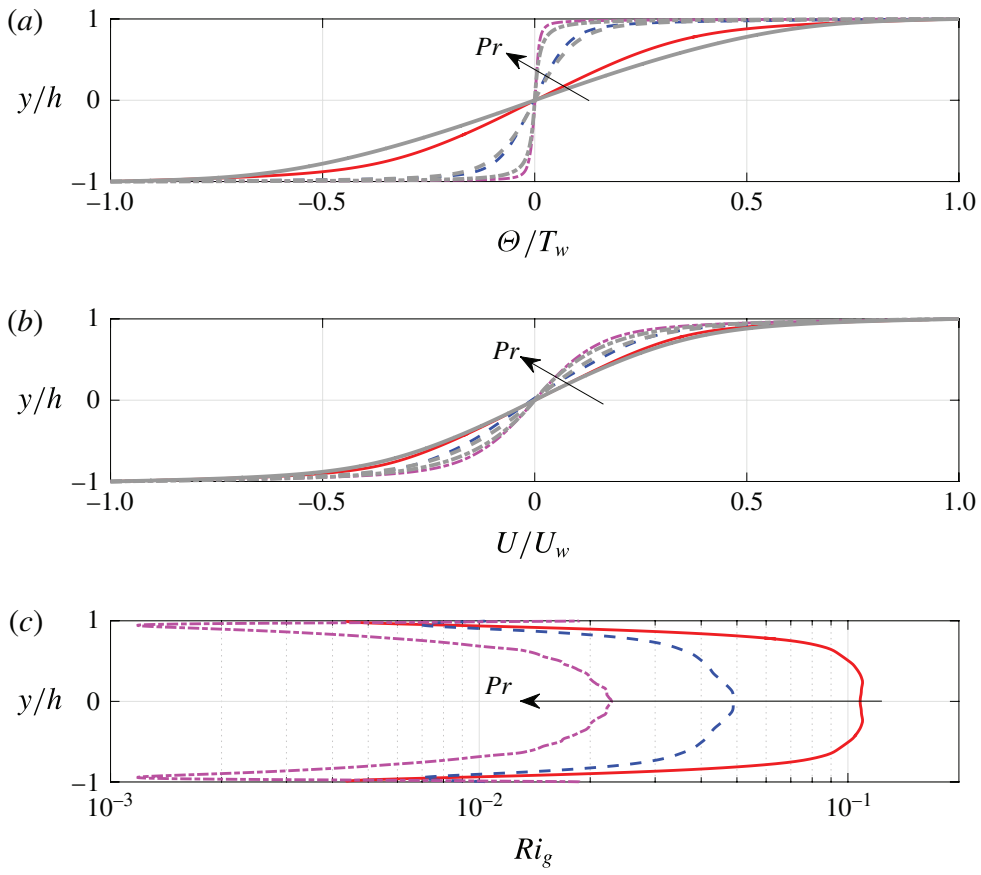

Figure 7: (Colour online) Vertical profiles of: (a) normalized mean temperature variation (T_w is the flow temperature at the wall); (b) normalized mean velocity variation (U_w is the flow velocity at the wall); and (c) gradient Richardson number Ri_g at (Re, Ri)=(4250, 0.04). Results with Pr=0.7, Pr = 7 and Pr = 70 are shown. From [7].

Ri_g varies sharply in the near-wall region and reaches a plateau in the channel gap interior. Given that the mean shear S (as shown in 7b) is less sensitive to Pr, the Ri_g values at midgap ($y = 0$) decrease with Pr_m for a given Re and Ri, which is mainly attributed to the sharpening of temperature variation in the near-wall region and weakening of those gradients (and thus the strength of stratification, as measured by N^2) in the channel gap interior. Nevertheless, the key result concerning intermittency remains, as even for large values of Pr_m, sustained turbulence cannot survive for flows with a maximum (midplane) $Ri_g \gtrsim 0.21$. Weird, not least because this is half-way between the often-mentioned "optimal" value of $Ri_g \simeq 1/6$, and the marginally stable canonical value of $Ri_g = 1/4$. Are these just fortuitous coincidences or is there something deeper going on?

3 The LAST Regime?

Although it appears essentially impossible to sustain strongly stratified turbulence through wall-forcing, as already noted (several times) there is observational evidence that the world's oceans are in a *strongly stratified turbulence* (SST) regime characterized by very large Reynolds number and very small (horizontal) Froude number in a particular distinguished limit:

$$Re = \frac{U_H L_H}{\nu} >> 1;\ F_h = \frac{U_H}{N L_H} \ll 1;\ ReF_H^2 = \frac{U_H^3}{L_h \nu N^2} \gg 1 \tag{13}$$

where U_H and L_H are characteristic *horizontal* scales. Motivated by some very elegant scaling arguments due to Paul Billant and Jean-Marc Chomaz, a self-consistent, SST regime has been proposed, with some suggestive (though still preliminary) numerical evidence[1]. The key idea is that characteristic **vertical** scales adjust self-similarly so that the *vertical Froude number* $F_V \simeq 1$:

$$F_V = \frac{U}{L_V N} \rightarrow L_V = \frac{U}{N}. \tag{14}$$

This vertical scale is larger than the Ozmidov scale L_O, which, since $Re_b = \epsilon' \nu N^2 \gg 1$ (under the reasonable assumption that $\epsilon' \sim U_H^3/L_H$, the classical large scale inertial scaling) is in turn very much larger that the Kolmogorov scale L_K. There is thus a strict hierarchy of scales:

$$L_K \ll L_O \ll L_V \ll L_H, \tag{15}$$

defining pancake-like layers of horizontal extent L_H and vertical extent L_V.

Interestingly, when such pancakes encounter each other and "rub" past each other, they inevitably induce significant values of vertical shear (due to generic differences in the U_H orientation between different layers) thus yielding a natural route for injection of relatively "weakly stratified" spatio-temporally intermittent bursts of shear-driven turbulence. Within the individual pancakes however, the turbulence must be extremely anisotropic, as for scales in the interval $[L_O, L_V]$ vertical velocities must be strongly suppressed. This interval is expected to be quite broad, as using the inertial scale $\epsilon' = U_H^3/L_H$, $F_H = \epsilon'/(NU_H^2)$ and so

$$\frac{L_V}{L_O} = \frac{U_H N^{1/2}}{\sqrt{\epsilon'}} = F_H^{-1/2} \gg 1. \tag{16}$$

Due to the particular layered and anisotropic characteristics of this regime, an alternative and perhaps more specific name for this regime that has been proposed is the *Layered Anisotropic Stratified Turbulence* (LAST) regime[3]. Whatever it's called, an especially interesting prediction

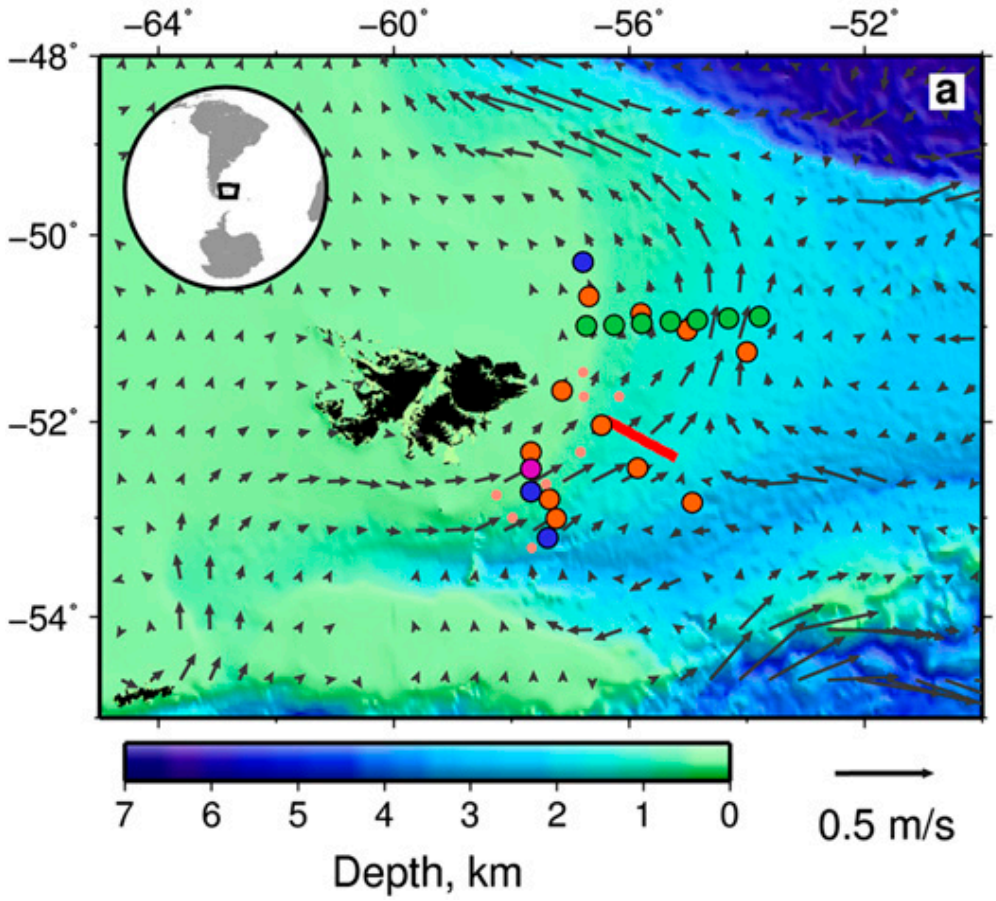

Figure 8: Red stripe shows location of seismic reflection profile acquired by WesternGeco Ltd. in February 1993. From [3].

for this regime is that the energy spectrum in the horizontal motions should still exhibit a $k_H^{-5/3}$ scaling for horizontal wavenumbers, even for scales bigger than L_O, and so the turbulence is expected to be highly anisotropic. It is critical to remember that in this range of scales the turbulence is definitely **not** stationary, homogeneous and isotropic turbulence, (don't you dare think about an acronym for this regime) and so this predicted $k_H^{-5/3}$ horizontal energy spectrum has nothing to do with the classic Kolmogorov K41 spectrum.

Fortunately, evidence for just such a horizontal spectrum can be found using the methods of *seismic oceanography*[3]. Figure 8 shows the location of a seismic profile taken 100km east of the Falkland Islands (aka Las Malvinas) in the South Atlantic Ocean. This seismic reflection experiment was performed by WesternGeco Ltd in Feburary 1993, principally to image the hydrocarbon reserves in the subsurface of these islands' territorial waters. (No inferences should be drawn concerning the economic value of those reserves to whoever asserts sovereignty of these particular islands.)

An array of 36 guns with a volume of 119L of compressed air was towed behind a vessel moving with a speed of 2ms^{-1}. This array of guns was at a depth of 7.5m. Acoustic energy generated by air guns was directed vertically which was then reflected by temperature contrasts. Behind the vessel, a 4.8km long streamer consisting of 240 hydrophones spaced every 20m was towed at a depth of 10m. Reflected energy was recorded by these hydrophones. The first active streamer was 97m behind

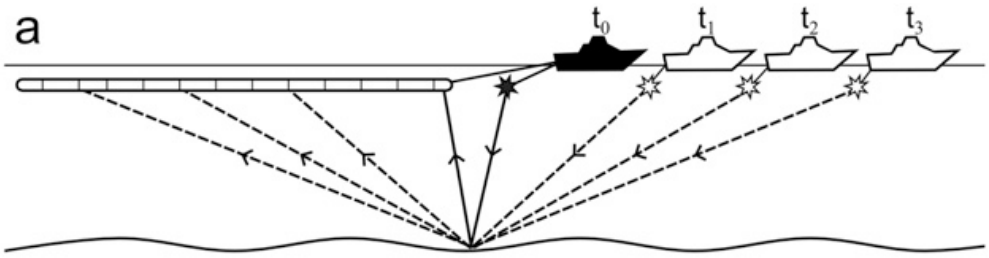

Figure 9: Figure shows the location of vessel at different times t_0, t_1, t_2, and t_3. Thin horizontal band with vertical lines shows $4.8km$ long streamer. Stars with solid/dashed lines and arrows show successive acoustic shots and associated ray paths. From [3].

the vessel. This procedure is shown schematically in figure 9. Although the primary objective of the survey was to image the subsurface, changes in sound speed associated with temperature contrasts, and associated reflections, allow the close-to-contemporaneous imaging of the entire water column, as shown in figure 10. Very close to horizontal reflections (note the scales of the figures) of temperature isosurfaces (here very similar to density surfaces) can be extracted from these images (laboriously!) with horizontal resolution of approximately 10m.

After careful averaging and normalization of the data, it is possible to consider the normalized and averaged power spectrum. For convenience the *slope spectrum* i.e., $k_H^2 E(k_H)$ is plotted in figure 11. For ease of interpretation lines with slope -1 (corresponding to $E(k_H) \propto k_H^{-3}$ characteristic of an internal wave field) and slope $+1/3$ (corresponding to $E(k_H) \propto k_H^{-5/3}$) are shown on the figure. There is clear evidence of a sharp transition (at horizontal scales $O(300m)$) to the predicted LAST regime, strongly suggesting that (at least in this part of the ocean) the LAST regime actually occurs, and indeed onsets quite suddenly due to an as yet not-understood wave-breaking process.

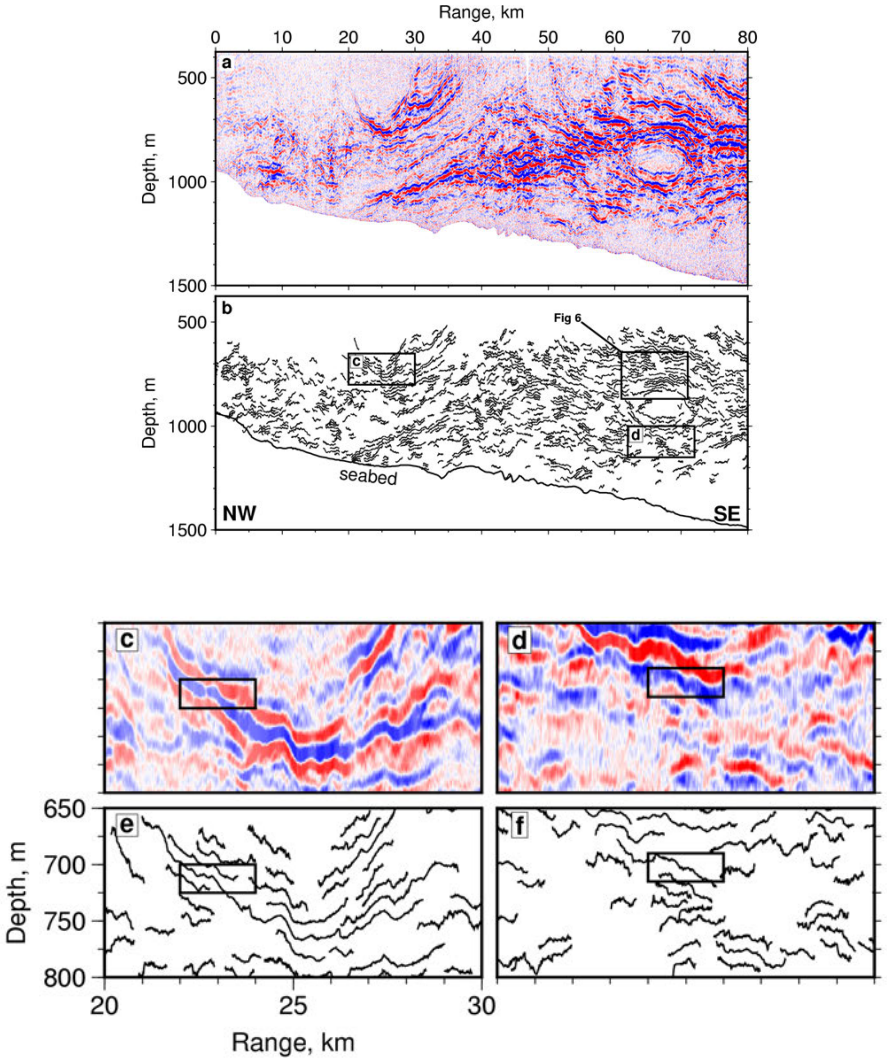

Figure 10: a) and b) show 856 tracked reflections. c) and e), and d) and f) are zoomed panels located in b). From [3].

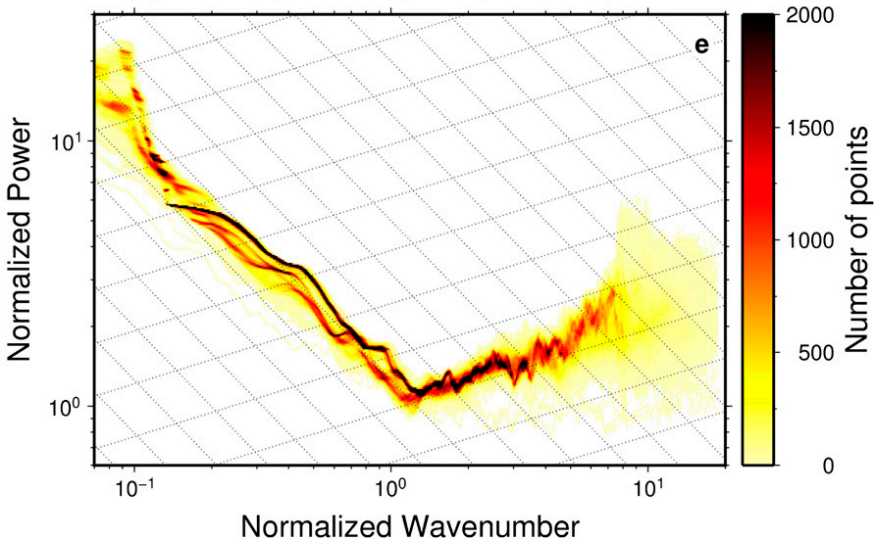

Figure 11: Density plot of linear averaged and normalized slope spectra $k_H^2 E(k_H)$ for horizontal numbers. Grey lines show slopes of -1 characteristic of internal waves and $-5/3$ characteristic of the LAST regime. Shading shows standard deviation, with noise onsetting on scales of $O(10m)$. From [3].

4 Open Questions

I trust it is clear that I still have essentially no idea what is going on, and there are a huge number of open questions which fluid dynamicists need to answer before academic fundamental studies of stratified turbulence can really be useful to oceanography. Nevertheless, it is both a really important and really beautiful topic of study, so I hope to spend the next years convincing as many people as possible to work on this fascinating subject. Thanks for listening and reading these exceptionally incoherent lectures. To end, here's just a very short list of some of the open questions which I think need answering.

- What do "characteristic" values of parameters even mean in a turbulent or spatio-temporally varying flow?
- Is emergent criticality related in any way to linear stability theory?
- Do forced flows have any connection with freely evolving flows?
- How can the history/memory/advection of a flow be captured in a parametric description?
- Are layered states generic or even accessed?
- Is stratified turbulence ever strongly stratified and does LAST ever actually occur?
- Can forcing and/or boundaries ever be ignored or modelled appropriately?
- Is there any hope to use deterministic "physics" models to describe mixing in stratified turbulence?

References

[1] G. Brethouwer, P. Billant, E. Lindborg, and J.-M. Chomaz, *Scaling analysis and simulation of strongly stratified turbulent flows*, Journal of Fluid Mechanics, 585 (2007), pp. 343–368.

[2] E. Deusebio, C. Caulfield, and J. Taylor, *The intermittency boundary in stratified plane couette flow*, Journal of Fluid Mechanics, 781 (2015), pp. 298–329.

[3] M. Falder, N. J. White, and C.-c. P. Caulfield, *Seismic imaging of rapid onset of stratified turbulence in the south atlantic ocean*, Journal of Physical Oceanography, 46 (2016), pp. 1023–1044.

[4] R. Ferrari, A. Mashayek, T. J. McDougall, M. Nikurashin, and J.-M. Campin, *Turning ocean mixing upside down*, Journal of Physical Oceanography, 46 (2016), pp. 2239–2261.

[5] K. L. Polzin, J. M. Toole, J. R. Ledwell, and R. W. Schmitt, *Spatial variability of turbulent mixing in the abyssal ocean*, Science, 276 (1997), pp. 93–96.

[6] J. R. Taylor, S. M. de Bruyn Kops, C. P. Caulfield, and L. P. F., *Testing the assumptions underlying ocean mixing methodologies using direct numerical simulations*, Journal of Physical Oceanography, 49 (2019), pp. 2761–2779.

[7] Q. Zhou, J. Taylor, and C. Caulfield, *Self-similar mixing in stratified plane Couette flow for varying Prandtl number*, Journal of Fluid Mechanics, 820 (2017), pp. 86–120.

Sensitivity of the Deep Overturning Circulation to Southern Ocean Westerly Winds

Houssam Yassin

August 19, 2019

1 Introduction

The ocean is a rotating stratified fluid forced at its upper boundary by the circulation of the atmosphere and is subject to gravitational and tidal body forces. The combined effect of these forces is to set up a mean ocean circulation and density structure that is unstable to a host of fluid dynamical instabilities. These instabilities grow and develop in such a way as to eliminate their energy source and revert the fluid to its original unforced state. In the ocean, this energy source is continuously replenished by the external forces acting on the ocean and a steady state is attained where energy extraction from the mean flow by eddies balances the energy injected at large scales. The ocean is thus a highly nonlinear fluid exhibiting turbulent, eddying structures with a wide range of temporal and spatial scales.

One consequence of the nonlinear eddying dynamics of the ocean is that a neutrally buoyant particle (or a tracer) is not advected by the mean circulation. Rather, one must also take into account the advective effects of ocean eddies. For overturning circulations, these eddies typically advect tracers in a direction opposing that of the mean flow. The net transport of the tracer is the sum of these two processes, and since they tend to be in opposing directions, the net transport tends to be a small 'residual' of two larger terms. This gives rise to the term 'residual velocity' for the velocity that advects tracers in the ocean. If one wants to study how tracers (such as heat and nutrients) are transported and distributed within the ocean, it is the residual velocity that is of interest.

Another aspect of ocean circulation that is of relevance to this report is the highly adiabatic nature of eddies in the ocean interior. At scales sufficiently large such that the rotation of the planet is relevant to the dynamics, the flow is quasi-two-dimensional with circulation primarily taking place on surfaces of constant density (or buoyancy). Indeed, analogous to two-dimensional turbulence, rotating stratified turbulence exhibits an inverse cascade of energy to larger spatial scales and a forward cascade of (potential) enstrophy to smaller scales where it can be efficiently dissipated by molecular diffusion. At large-scales, turbulent stirring along surfaces of constant density can be up to eight order of magnitude larger than turbulent stirring across density surfaces. Thus, we expect that tracers will also be advected primarily along density surfaces.

In this report, we derive the Nikurashin-Vallis model [12] of the residual overturning circulation beginning from the residual-mean theory presented in [14]. We then present

possible scaling laws that the residual overturning circulation may follow and then proceed to present numerical solutions.

2 Residual-mean Theory

If we take a simple zonal average of the equations governing rotating stratified flows (in a zonally re-entrant domain), we obtain (*e.g.* [14])

$$\overline{u_t} + \overline{\boldsymbol{v}} \cdot \nabla \overline{u} - f v = -\nabla \cdot \overline{\boldsymbol{v}' u'} + \overline{\mathcal{X}} \tag{1}$$

$$f \overline{u}_z = -\overline{b}_y \tag{2}$$

$$\overline{v}_y + \overline{w}_z = 0 \tag{3}$$

$$\overline{b}_t + \overline{\boldsymbol{v}} \cdot \nabla \overline{b} = -\nabla \cdot \overline{\boldsymbol{v}' b'} + \overline{\mathcal{Q}} \tag{4}$$

where $\boldsymbol{v} = (0, v, w)$ is the velocity in the meridional plane, $\mathcal{X}$ and $\mathcal{Q}$ denote mechanical and diabatic forcing, respectively. Note that, in the above set of equations, we have assumed that meridional flows are weak. We see that this simple averaging approach produces equations for mean fields $\overline{u}, \overline{b}$ that are forced by the divergence of an eddy fluxes $\overline{\boldsymbol{v}' u'}$ and $\overline{\boldsymbol{v}' b'}$. These equations have two undesirable properties:

1. Advection is by the zonal mean velocity rather than the residual velocity.
2. The buoyancy equation is forced by the divergence of an eddy flux. For adiabatic eddies, eddy-forcing belongs in the zonal mean momentum equation.

There are several approaches to ameliorating these issues (see, for example, [5], [9], [10], [14], [17]). Below, we follow the approach outlined in [14].

When both diabatic and mechanical forcing vanish ($\mathcal{X} = \mathcal{Q} = 0$), the zonal mean buoyancy and zonal velocity terms are forced by the divergence of an eddy flux. These eddy fluxes have components that are both along the mean gradient (of a given tracer) and a component that is 'skew', that is, along iso-surfaces of the tracer. Residual mean theory involves redefining the velocity to repartition the fluxes so that the 'eddy flux' that forces the mean terms contains no skew component.

As an example, consider a tracer that satisfies the following zonal mean equation

$$\overline{c}_t + \overline{\boldsymbol{v}} \cdot \nabla \overline{c} = -\nabla \cdot \overline{\boldsymbol{v}' c'} + \overline{S} \tag{5}$$

where S is a source term. We define a 'residual velocity' $\boldsymbol{v}^\dagger$ by

$$\boldsymbol{v}^\dagger = \overline{\boldsymbol{v}} + \nabla \wedge \hat{\boldsymbol{x}} \psi^\star \tag{6}$$

where $\psi^\star$ is a 'psuedo-Stokes' streamfunction that needs to be specified (the 'psuedo' refers to the non-divergent nature of the resulting velocity whereas the 'usual' Stokes velocity tends to be divergent [9]). Eliminating $\overline{\boldsymbol{v}}$ from the zonal mean tracer equation gives

$$\overline{c_t} + \boldsymbol{v}^\dagger \cdot \nabla \overline{c} = -\nabla \cdot \left[\overline{\boldsymbol{v}' c'} - \psi^\star \hat{\boldsymbol{x}} \wedge \nabla c \right] + \overline{S}. \tag{7}$$

We now choose $\psi^\star$ so that the eddy flux only has a component along $\nabla \overline{c}$. The direction in the meridional plane orthogonal to $\nabla \overline{c}$ is $\hat{\boldsymbol{x}} \wedge \nabla \overline{c}$. It follows that the skew component of the

flux is $(\hat{\boldsymbol{x}} \wedge \nabla \overline{c}) \cdot \overline{\boldsymbol{v}' c'}$. Consequently, to ensure that the eddy flux has no skew component, we choose

$$\psi^\star = \frac{1}{|\nabla c|^2} \left[\hat{\boldsymbol{x}} \wedge \nabla \overline{c}\right] \cdot \overline{\boldsymbol{v}' c'}. \tag{8}$$

The eddy forcing term on the right hand side becomes

$$\left[\overline{\boldsymbol{v}' c'} - \psi^\star \hat{\boldsymbol{x}} \wedge \nabla \overline{c}\right] = \overline{\boldsymbol{v}' c'} - \left[\left(\hat{\boldsymbol{x}} \wedge \frac{\boldsymbol{\nabla} \overline{c}}{|\boldsymbol{\nabla} \overline{c}|}\right) \cdot \overline{\boldsymbol{v}' c'}\right] \left(\hat{\boldsymbol{x}} \wedge \frac{\boldsymbol{\nabla} \overline{c}}{|\boldsymbol{\nabla} c|}\right) \tag{9}$$

The skew component of the eddy flux is subtracted from the total flux so that the eddy flux forcing the tracer equation only has a component along $\boldsymbol{\nabla} c$.

The velocity obtained from the streamfunction is the quasi-Stokes velocity $\boldsymbol{v}^\star = \nabla \wedge \hat{\boldsymbol{x}} \psi^\star$. The residual velocity is then

$$\boldsymbol{v}^\dagger = \overline{\boldsymbol{v}} + \boldsymbol{v}^\star. \tag{10}$$

The above equation shows the analogy between the residual velocity and the Lagrangian velocity in, say, wave dynamics. Both the residual and Lagrangian velocities are equal to a mean (Eulerian) velocity plus a velocity arising from the non-linearities of the governing equations (a Stokes velocity).

2.1 Residual mean buoyancy equation

Define $\hat{\boldsymbol{n}} = \nabla \overline{b} / |\nabla \overline{b}|$ to be the unit vector normal to buoyancy surface and $\hat{\boldsymbol{s}} = \hat{\boldsymbol{n}} \wedge \hat{\boldsymbol{x}}$ to be the unit vector along buoyancy surfaces. The buoyancy flux can then be written as the sum of a skew flux (along b-surfaces) and a diapycnal flux (across b-surfaces),

$$\overline{\boldsymbol{v}' b'} = \left(\overline{\boldsymbol{v}' b'} \cdot \hat{\boldsymbol{s}}\right) \hat{\boldsymbol{s}} + \left(\overline{\boldsymbol{v}' b'} \cdot \hat{\boldsymbol{n}}\right) \cdot \hat{\boldsymbol{n}}. \tag{11}$$

To eliminate the skew component of the eddy buoyancy flux, we can choose a streamfunction to be of the form

$$\psi^\star = -\frac{1}{|\nabla \overline{b}|^2} \hat{\boldsymbol{s}} \cdot \overline{\boldsymbol{v}' b'}. \tag{12}$$

It turns out the buoyancy equation retains the same form under the more general transformation

$$\psi^\star = -\frac{1}{|\nabla \overline{b}|^2} \left[\hat{\boldsymbol{s}} \cdot \overline{\boldsymbol{v}' b'} - \alpha \, \hat{\boldsymbol{n}} \left(\overline{\boldsymbol{v}' b'}\right)\right] \tag{13}$$

where α is some arbitrary function. Under this transformation, the buoyancy equation takes the form

$$\overline{b}_t + \boldsymbol{v}^\dagger \cdot \nabla \overline{b} = -\nabla \cdot \left[\left(\overline{\boldsymbol{v}' b'} \cdot \hat{\boldsymbol{n}}\right) (\hat{\boldsymbol{n}} + \alpha \hat{\boldsymbol{s}})\right] + \overline{\mathcal{Q}}. \tag{14}$$

The residual flux only depends on the diapycnal component of the raw eddy buoyancy flux $\overline{\boldsymbol{v}' b'}$. This immediately displays one of the advantages of the mean residual formulation– in the adiabatic ocean interior, the diapycnal eddy flux vanishes. In steady state, the buoyancy equation is only forced by sources and sinks of buoyancy.

There are three canonical choices for the function α.

1. **Non-quasigeostrophic case:** Here we choose $\alpha = 0$. The quasi-Stokes streamfunction then is the projection of the eddy flux along buoyancy surfaces $\psi^\star = |\nabla \overline{b}|^{-1} \left(\hat{\boldsymbol{s}} \cdot \overline{\boldsymbol{v}' b'} \right)$ and the residual eddy flux is then simply the diapycnal component of the raw eddy flux directed along the mean buoyancy gradient.

2. **Quasigeostrophic case:** We set $\alpha = -\overline{b}_y / \overline{b}_z$ (*i.e.* α is now the slope of the buoyancy surfaces in the meridional plane). The quasi-Stokes streamfunction then takes the particularly simple form $\psi^\star = -\overline{v'b'}/\overline{b}_z$. In the quasigeostrophic limit when buoyancy slopes are shallow, the non-quasigeostrophic case is equivalent to the quasigestrophic case. In this case, the residual eddy flux is directed along the vertical.

3. **The Held-Schneider:** The third case corresponds to $\alpha = \overline{b}_z / \overline{b}_y$. This leads to a residual eddy flux directed along the meridional direction. This formulation is useful for dealing with surface boundary conditions in residual-mean problems. This choice for the streamfunction was first introduced in [6].

2.2 Residual mean momentum equation

We now express the zonal mean momentum equation in terms of the residual velocity to obtain the residual momentum equation. We adopt the non-quasigeostrophic quasi-Stokes streamfunction where $\alpha = 0$. The zonal mean momentum equation then takes the form

$$\overline{u}_t + \boldsymbol{v}^\dagger \cdot \nabla \overline{u} = -\nabla \cdot \left[\overline{\boldsymbol{v}' u'} - \psi^\star \overline{\boldsymbol{\zeta}}_a \right] + \overline{\mathcal{X}} \tag{15}$$

where $\overline{\boldsymbol{\zeta}}_a = \overline{u}_z \hat{\boldsymbol{y}} - (f + \overline{u}_y)\, \hat{\boldsymbol{z}}$ is the absolute momentum of the zonal flow. Alternatively, we can rewrite the equation so that the residual Coriolis acceleration appears explicitly

$$\overline{u}_t + \boldsymbol{v}^\dagger \cdot \nabla \overline{u} - f v^\dagger = -\nabla \cdot \left[\overline{\boldsymbol{v}' u'} - \psi^\star \boldsymbol{\zeta} \right] + \overline{\mathcal{X}} \tag{16}$$

where $\boldsymbol{\zeta}_a = \boldsymbol{\zeta} + f \hat{\boldsymbol{z}}$.

3 The Marshall-Radko Model

In this section we derive the Marshall-Radko model [7] of Southern Ocean overturning in the limit of no residual circulation. Making use of Held-Schneider quasi-Stokes streamfunction, the steady residual buoyancy equation takes the form

$$\boldsymbol{v}^\dagger \cdot \nabla \overline{b} = -\nabla \cdot \left[\frac{|\nabla \overline{b}|}{\overline{b}_y} \left(\hat{\boldsymbol{n}} \cdot \overline{\boldsymbol{v}' b'} \right) \hat{\boldsymbol{y}} \right] + \overline{\mathcal{Q}} = -\partial_y \left[\overline{v'b'} - \frac{1}{s} \overline{w'b'} \right] + \overline{\mathcal{Q}} \tag{17}$$

where $s = -\overline{b}_y / \overline{b}_z$ is the slope of buoyancy surfaces.

The steady residual zonal momentum equation is

$$\boldsymbol{v}^\dagger \cdot \nabla \overline{u} - f v^\dagger = -\nabla \cdot \left[\overline{\boldsymbol{v}' u'} + \psi^\star \overline{\boldsymbol{\zeta}} \right] - f \psi^\star_z + \overline{\mathcal{X}}. \tag{18}$$

To simplify the above two equations, a few assumptions are made:

1. In the interior of the ocean, there is no buoyancy forcing $\overline{Q} = 0$ and the buoyancy eddy fluxes are directed entirely along isopycnals. The residual buoyancy equation simplifies to

$$\boldsymbol{v}^\dagger \cdot \nabla \overline{b} = 0. \tag{19}$$

   Thus, in the ocean interior, the residual circulation is along buoyancy surfaces.

2. Note that we can write the momentum equation as

$$-f v^\dagger = -\nabla \cdot \left[\overline{\boldsymbol{v}}\ \overline{u} + \overline{\boldsymbol{v}' u'} \right] - f \psi^\star_z + \overline{\mathcal{X}}. \tag{20}$$

   We now assume that the eddy momentum terms can be ignored and that we can write the momentum source term as a vertical divergence $\overline{\mathcal{X}} = \overline{\tau}_z$. The residual momentum equation then reduces to

$$f v^\dagger = f \psi^\star_z - \overline{\tau}_z.$$

   Another way to think about this approximation is as follows. We suppose that the residual circulation is weak enough such that the advection of zonal momentum by the residual flow may be neglected. This allows us to ignore the $\boldsymbol{v}^\dagger \cdot \nabla \overline{u}$ term. We also assume the meridional component of the eddy flux may be neglected. Then, assuming $\overline{X} = \mathcal{T}_z$ where $\mathcal{T}$ is the wind stress, we have

$$-f \psi^\dagger_z = \tau_z - f \psi^\star_z \tag{21}$$

   where $\tau = \mathcal{T} - \overline{w' u'} + \psi^\star \overline{u}_y$.

We introduce a residual streamfunction by $\boldsymbol{v}^\dagger = \nabla \wedge \hat{\boldsymbol{x}} \psi^\dagger$, then the governing equations in the interior of the ocean are

$$J\left(\ {}^\dagger, \overline{b} \right) = 0 \tag{22}$$

$$\psi^\dagger_z = -\frac{1}{f} \overline{\tau}_z + \psi^\star_z \tag{23}$$

where $J(A, B) = A_y B_z - A_z B_y$ is the Jacobian. The vanishing of the Jacobian implies that there must be a functional relationship $\psi^\dagger = \psi^\dagger(\overline{b})$.

Since the the vertical velocity vanishes at the surface $z = h_m$, both streamfunctions must vanish there. Integrating the momentum equation from the surface to some depth z in the interior, we obtain

$${}^\dagger = \frac{\overline{\tau}}{f} + \psi^\star \tag{24}$$

where $\overline{\tau_0}$ is the zonal mean stress at the surface.

To close the circulation, there must be a mixed layer where the residual streamfunction crosses buoyancy surfaces. We suppose that there is a vertically homogeneous mixed layer of constant depth h_m (whose bottom boundary is $z = 0$). In the mixed layer, the buoyancy eddy flux will have a diapycnal component. Rewrite the buoyancy equation as

$$\boldsymbol{v}^\dagger \cdot \nabla \overline{b} = -\partial_y \left[(1 - \mu) \overline{v' b'} \right] + \overline{B}_z \tag{25}$$

where $\mu = \frac{1}{s}\frac{\overline{w'b'}}{\overline{v'b'}}$ is a measure of diapycnal eddy buoyancy flux.We also assumed that the buoyancy forcing at the surface takes the form $\overline{\mathcal{Q}} = \overline{B}_z$ In the mixed layer, we suppose that μ varies linearly from $\mu = 0$ at the base of the mixed layer $z = 0$ to $\mu = 1$ at the surface $z = h_m$. Noting that $\boldsymbol{v}^\dagger \cdot \nabla \overline{b} = -J(\psi^\dagger, \overline{b}) = \psi^\dagger_z \overline{b}_y$, then the buoyancy equation in the mixed layer is

$$\overset{\dagger}{}_z \partial_y b_s = -(1-\mu)\,\partial_y \overline{v'b'} + \overline{B}_z \tag{26}$$

where $b_s = b_s(y)$ is the buoyancy in the mixed layer. Integrating from the surface to the base of the mixed layer yields

$$\overset{\dagger}{}|_{z=0} = -\frac{\mathcal{B}_0}{\partial_y b_s}$$

where $\mathcal{B}_0 = B|_{z=0} - \int dy\ (1-\mu)\overline{v'b'}$. Here we have assumed that entertainment fluxes at the base of the mixed layer vanish $B|_{z=0} = 0$. The above expression sets the functional relationship between the residual streamfunction and the buoyancy. If $\mathcal{B}_0 > 0$ so that the mixed layer is locally gaining buoyancy, then since $\partial_y b_s > 0$, $\psi^\dagger > 0$ (and $\psi^\dagger$ vanishes at the surface) then the flow is equatorward in the mixed layer. If the buoyancy gradient in the mixed layer is constant, then the circulation is proportional to the surface buoyancy forcing.

To summarize, the equations governing the Marshall-Radko model [7] are

$$\overset{\dagger}{} = \frac{\tau_0}{f} + \psi^\star \tag{27}$$

$$J\left(\overset{\dagger}{}, \overline{b}\right) = 0 \tag{28}$$

$$\overset{\dagger}{}|_{z=0} = -\frac{\mathcal{B}_0}{\partial_y b_s} \tag{29}$$

The wind stress at the surface $\tau_0(y)$, the buoyancy in the mixed layer $b_s(y)$, and the net buoyancy supplied to the mixed layer $\mathcal{B}(y)$ are given, and we solve for the residual circulation $\psi^\dagger$ (and hence the buoyancy).

Although we use the Held-Schneider eddy streamfunction $\psi^\star = \frac{\overline{v'b'}}{\overline{b}_y}$, the fact that the interior is adiabatic implies that all three choices of eddy streamfunctions are equivalent, so

$$\psi^\star = \frac{\overline{w'b'}}{\overline{b}_y} = -\frac{\overline{v'b'}}{\overline{b}_z}.$$

Finally, to close the system, we need to specify the functional dependence of $\psi^\star$. We do this by using a simple down-gradient buoyancy closure $\overline{v'b'} = -K\overline{b}_y$ where K is a positive eddy transfer coefficient (equivalent to the Gent-McWilliams parameterization [5]). The eddy streamfunction then is $\psi^\star = -Ks$ where $s = -b_y/b_z$ is the slope of buoyancy surfaces.

4 Nikurashin-Vallis Model

The Nikurahsin-Vallis model [12] consists of a diabatic circumpolar channel governed by the Marshall-Radko [7] model coupled to an ocean basin where Munk's advective-diffusive balance [11] holds. The stratification and circulation of the circumpolar channel are required

to match those of the ocean basin. There is an extension of the model to include an Atlantic deep water source [13], but for the remainder of the report, we restrict our attention to a Pacific-like basin with deep water formation near the southern boundary.

The governing equations in the circumpolar channel are

$$-fv^\dagger = \partial_z \tau - fv^\star \tag{30}$$

$$f\overline{u}_z = -\overline{b}_y \tag{31}$$

$$v^\dagger_y + w^\dagger_z = 0 \tag{32}$$

$$\boldsymbol{v}^\dagger \cdot \nabla \overline{b} = \partial_z \left(\kappa \overline{b}_z \right). \tag{33}$$

As before, we have $\psi^\dagger = \overline{\psi} + \psi^\star$ where $\overline{\psi} = -\tau_0/f$ and $\psi^\star = Ks$ where the eddy transfer coefficient K is taken to be constant. Note that, for consistency with [12], we have redefined all streamfunctions to include a negative sign (*i.e.* $\psi \to -\psi$).

At the base of the mixed layer (at $z = 0$), the buoyancy distribution is given by

$$\overline{b}|_{z=0} = b_0(y). \tag{34}$$

At the northern edge of the channel (at $y = 0$), the buoyancy and overturning circulation in the channel are required to match those of the basin.

In the basin north of the channel, we assume that the buoyancy surfaces are horizontal and that Munk's advective diffusive balance holds,

$$^\dagger_y \overline{b}_z = \partial_z (\kappa \overline{b}_z). \tag{35}$$

Note that, in the ocean basin, $\psi^\dagger = \overline{\psi}$ since $\psi^\star = 0$ for flat isopycnals. We can integrate this equation from the northern edge of the channel (at $y = 0$) to the northern edge of the basin (at $y = L$) to obtain the northern boundary condition for the channel

$$^\dagger = \int_0^L dy \; \frac{\partial_z \left(\kappa \overline{b}_z \right)}{\overline{b}_z} = - \, L \frac{\partial_z \left(\kappa \overline{b}_z \right)}{\overline{b}_z} \tag{36}$$

where the last equality follows from the fact that isopycnals are flat within the ocean basin. Note that if $\kappa = 0$ the residual circulation vanishes everywhere.

In this model, we prescribe the wind forcing $\tau(y)$ and the buoyancy in the mixed layer $b_s(y)$. We then obtain the stratification and the residual circulation in the channel and the ocean basin. The air-sea buoyancy flux is part of the solution and need not be prescribed. The governing equations for the model (in the channel) are then

$$^\dagger_y + s_b \psi^\dagger_z = \frac{1}{\overline{b}_z} \partial_z \left(\kappa \overline{b}_z \right) \tag{37}$$

$$^\dagger = -\frac{\tau}{f} + \psi^\star \tag{38}$$

$$^\dagger|_{y=0} = -L \frac{\partial_z \left(\kappa \overline{b}_z \right)}{\overline{b}_z} \tag{39}$$

$$\overline{b}|_{z=0} = b_s(y). \tag{40}$$

We now non-dimensionalize the governing equations using the following scales

$$z = D\hat{z} \qquad y = l\hat{y} \qquad \tau = \tau_0\hat{\tau} \tag{41}$$

$$f = |f_0|\hat{f} \quad \psi^\dagger = \tfrac{\tau_0}{|f_0|}\hat{\psi}^\dagger \quad s = \frac{D}{l}\hat{s} \tag{42}$$

where D the depth of the channel and l is the width of the channel. In [12] the vertical diffusivity κ is taken to be constant. We instead suppose that κ has an exponential vertical structure in depth with a characteristic e-folding scale of H. Mathematically, κ takes the form

$$\kappa = \kappa_0 e^{-(z+D)/H} = \kappa_0 e^{-(\hat{z}+1)/\eta} \tag{43}$$

where $\eta = H/D$ is the ratio of the vertical scale of the stratification to the depth of the basin. The non-dimensional governing equations in the channel are

$$^\dagger_y + s\psi^\dagger_z = \lambda\varepsilon\kappa\left(\frac{b_{zz}}{b_z} - \frac{1}{\eta}\right) \tag{44}$$

$$\psi^\dagger = T\tau + s \tag{45}$$

$$^\dagger|_{y=0} = -\varepsilon\kappa\left(\frac{b_{zz}}{b_z} - \frac{1}{\eta}\right) \tag{46}$$

$$\overline{b}|_{z=0} = b_s(y). \tag{47}$$

where the non-dimensional numbers λ, ϵ, T are defined by

$$\lambda = \frac{l}{L} \qquad \epsilon = \frac{\kappa_0 L/D}{KD/l} \qquad T = \frac{\tau/(\rho|f_0|)}{KD/l}. \tag{48}$$

The first parameter λ is the ratio is of the meridional extent of the channel to the basin with a value of $\lambda \sim \mathcal{O}(0.1) \ll 1$. The second parameter ϵ is a non-dimensional measure of the mixing. Using $D \sim 10^3 m, K \sim 10^3 m^2 s^{-1}, L \sim 10^7 m$, we find that $\epsilon \sim \kappa_0 \cdot 10^4 m^{-2} s$ so that $\kappa_0 \sim 10^{-4} m^2 s^{-1}$ would make ϵ of first order importance. T is a non-dimensional measure of the wind forcing. For $\tau \sim 0.1 N m^{-2}$ typical of the Southern Ocean, we obtain $T \sim 1$. Finally, η is the ratio of the decay-scale of the vertical diffusivity to the ocean depth and is typically order one.

The governing equations (for constant wind stress) can be rewritten as

$$\left[b_{yy} + \lambda\epsilon\left(\kappa b_z\right)\right] b_z^2 - 2b_{yz}b_y b_z + b_{zz}b_y^2 = 0 \tag{49}$$

$$b_y - Tb_z = \epsilon(\kappa b_z)_z \text{ at } y = 0. \tag{50}$$

Note that, in the case of constant wind stress, the wind forcing only appears in the boundary condition.

The quantity we are interested in is the minimum of ψ at the northern edge of the channel (at $y = 0$). Requiring that $\psi = T - b_y/bz$ be a minimum in the vertical yields the relation

$$b_{yz}b_z = b_{zz}b_y \tag{51}$$

which provides the relation

$$\left[b_{yy} + \lambda\epsilon\left(\kappa b_z\right)\right] b_z^2 - b_{zz}b_y^2 = 0 \text{ at } z = z_{\text{peak}} \tag{52}$$

Substituting in the boundary condition at $y = 0$ then gives a relationship between the gradients of the buoyancy at the position of the maximum.

5 Scaling Arguments

5.1 Uniform κ

First, we consider the case when κ is independent of depth as in [12]. This implies that the (non-dimensional) vertical diffusivity is $\kappa = 1$. In addition, if we also assume constant wind forcing, then $\tau = 1$ and wind forcing only appears in the northern boundary condition. At the northern edge of the channel, the following balance holds,

$$= T + s = -\epsilon \frac{b_{zz}}{b_z}. \tag{53}$$

We have dropped the dagger superscript on the residual circulation $\psi^\dagger$. From here on in the report, $\psi = \psi^\dagger$.

5.1.1 Adiabatic limit

We now consider the adiabatic limit when ϵ is small (or more precisely, $\epsilon \ll T$). Then there are two possible scalings that emerge from the governing equations.

One possibility, if we assume b_{zz}/b_z is $\mathcal{O}(1)$, is that the slopes are set by the wind to leading order

$$T + s \approx 0. \tag{54}$$

Here, stratification in the channel is set by wind. But how does this physically occur? And why is it that the wind forcing appears only at the northern boundary condition? To understand this, we must be more careful in how we represent the wind. In deriving the model, we assumed that there is some wind forcing that leads to an Eulerian circulation $\overline{\psi} = T\tau(y)$ in the channel. For constant wind forcing, $\tau = 1$ *in the channel*, that is, $\tau(y) = 1$ for $y \in [-l, 0)$. In the basin, at $y > 0$, the wind forcing is assumed to vanish. Therefore, $\tau(y) = 1 - \theta(y)$ where θ is the step function. It then follows that $\overline{w} = \partial_y \overline{\psi} = -T\delta(y)$ where $\delta(y)$ is the delta function. Consequently, although a constant wind forcing results in no Ekman upwelling or downwelling in the interior of the channel (since $\overline{\psi}_y = 0$), we do obtain a downward velocity exactly at the northern edge of the channel. This negative velocity pushes buoyancy surfaces deep into the ocean and, in the adiabatic limit, sets the large-scale stratification of the circumpolar channel. This is the balance implied in the equation above.

The above balance implies that stronger winds lead to buoyancy surfaces with steeper slopes. Let us write the slope as a ratio of the vertical and horizontal length scales of the stratification $s \propto -h/\ell$. Now, we suppose that $\ell = 1$ so that changes in the slope are due to changes in the vertical scale of the stratification h, then $-s \propto h \propto T$. Substituting this expression into the northern boundary condition

$$= -\epsilon \frac{b_{zz}}{b_z} \propto -\frac{\epsilon}{h} \propto -\frac{\epsilon}{T}. \tag{55}$$

where $b_{zz}/b_z \propto h$. We see that, in the adiabatic limit, ψ is expected to be linearly proportional to the diffusivity and inversely proportional to wind stress.

Alternatively, for small ϵ, the ratio b_{zz}/b_z can become large enough so that $\epsilon b_{zz}/b_z$ does not become negligible in comparison to the other terms. In terms of the length scale h, this

involves $h \propto \epsilon^{-1}$, then

$$T - \frac{h}{\ell} = -\frac{\epsilon}{h}. \tag{56}$$

Both T and ϵ/h are now $\mathcal{O}(1)$. The term representing the slope can only be order one if $\ell \propto \epsilon$ which represents a case where the buoyancy field in the circumpolar channel has small horizontal and vertical characteristic scales. If we assume $\ell = 1$ as before, then we obtain

$$T = -\frac{\epsilon}{h}. \tag{57}$$

Since $T > 0$, this balance is only possible if $h < 0$, which is equivalent to $b_{zz} < 0$ for stable stratification. This implies a balance between the δ-downwelling at the northern edge of the channel and diffusion. The meridional overturning circulation implied by this balance is

$$\propto -\frac{\epsilon}{h} \propto 1 \tag{58}$$

we obtain a circulation that is independent of wind and diffusion and is in a direction opposite to the circulation observed in the southern ocean. This alternative scaling is never observed in the model runs described later in the report.

5.1.2 Diabatic limit

Now consider the limit that ϵ is large ($\epsilon \gg T$). Again, as before, then the system can respond in two ways. The first corresponds to the case when b_{zz}/b_z is $\mathcal{O}(1)$. This then implies that we may ignore T and that

$$s \approx -\epsilon \frac{b_{zz}}{b_z} \tag{59}$$

so that buoyancy slopes become large $|s| \propto \epsilon \gg T$. As before, we write the slope as a ratio between the characteristic vertical and vertical scale of the buoyancy $s \propto -h/\ell$.

In [12], they assume that $\ell = 1$ so that changes in the slopes are due to changes in the stratification. Then, as in the adiabatic case, $b_{zz}/b_z \propto h$. This then implies

$$-h \propto -\frac{\epsilon}{h} \tag{60}$$

which leads a $h \propto \sqrt{\epsilon}$ and

$$\propto -\sqrt{\epsilon}. \tag{61}$$

In this scaling, increasing diffusivity increases the vertical scale of the stratification so that b_z and b_{zz} both become smaller. The slopes become steeper not because of any modifications to b_y, but rather due a decreasing stratification b_z.

Although the $\psi \propto \sqrt{\epsilon}$ is observed in the model, it is not for the reason [12] suggest. To obtain the correct scaling, we must use the buoyancy equation in the channel. At the depth of an extrema of ψ, the buoyancy equation may be written as

$$s^2 = \frac{b_{yy}}{b_{zz}} + \lambda\epsilon \tag{62}$$

subject to the boundary condition $Tb_z + b_y = \epsilon b_{zz}$. Recall that $T \ll \epsilon$ in the diabatic limit. Consequently, we can neglect the term Tb_z if we assume $b_z \sim \mathcal{O}(1)$. Let $C = b_{zz}$ denote the vertical curvature of the buoyancy profile. The lateral gradient of buoyancy has the form $b_y = \Delta b/\ell$ where Δb is the buoyancy difference between the circumpolar channel and the basin. This also implies that $b_{yy} \propto \Delta b/\ell^2$. If we assume $\ell = 1$ then we obtain

$$(\Delta b)^2 = \frac{\Delta b}{C} + \lambda\epsilon \tag{63}$$

while the boundary condition gives

$$\Delta b = \epsilon C. \tag{64}$$

Solving this system of equations gives

$$C \propto \sqrt{\frac{1+\lambda}{\epsilon}} \tag{65}$$

$$\Delta b \propto \sqrt{(1+\lambda)\,\epsilon} \tag{66}$$

which implies a circulation that scales as

$$\propto -\epsilon C \propto -\sqrt{(1+\lambda)\,\epsilon}. \tag{67}$$

Again, the circulation is proportional to the square root of the diffusivity. However, unlike in [12], here b_z at the minimum of ψ is independent of ϵ. In the diabatic limit, the $\psi \propto \sqrt{\epsilon}$ scaling emerges due to the curvature decreasing with increasing diffusivity. This scaling also predicts that the fields b and b_y should display a $\sqrt{\epsilon}$ dependence. This is verified later in the report.

Now we address the physical meaning of this scaling. The northern boundary condition is essentially a statement that the circulation and stratification of the channel must be consistent with the advective-diffusive balance in the basin. We can rewrite this as

$$w^\star b_z = \epsilon b_{zz} \tag{68}$$

where we have neglected the contribution from the wind-driven δ-downwelling velocity $\overline{w}$ because we are in the diffusive limit. Note that $w^\star = -\partial_y(b_y/b_z)$. Therefore, this statement is that the stratification in the channel must be configured so that the eddy induced upwelling can balance the downward diffusion of buoyancy. This is why, unlike the scaling of [12], the above scaling required the use of the buoyancy equation in the channel.

5.2 Bottom enhanced diffusivity

In the adiabatic limit, it is irrelevant whether the diffusivity is uniform or bottom enhanced. The adiabatic limit is therefore identical to that discussed above. In this section, we instead look at the diabatic limit when ϵ is large and $\kappa = e^{-(z+1)/\eta}$.

We begin with a perturbation expansion of the buoyancy field. In the diffusive limit, ϵ is large, this motivates the use of ϵ^{-1} as our small parameter,

$$b = b^{(0)} + \epsilon^{-1} b^{(1)} + \cdots. \tag{69}$$

Substituting into the governing equations yields

$$0 = -\kappa \left(\frac{b^{(0)}_{zz}}{b^{(0)}_z} - \frac{1}{\eta} \right) \tag{70}$$

$$b^{(0)}_{yy}[b^{(0)}_z]^2 - 2b^{(0)}_{yz} b^{(0)}_y b^{(0)}_z + b^{(0)}_{zz}[b^{(0)}_y]^2 = 0 \tag{71}$$

at zeroth order in ϵ. We see that, to leading order, the buoyancy of the deep ocean is set by the diffusivity. The constant wind stress, which appears in the boundary condition, does not appear at leading order.

At the next order, the northern boundary condition becomes

$$T b^{(0)}_z - b^{(0)}_y = -\kappa \left(b^{(1)}_{zz} - \frac{b^{(1)}_z}{\eta} \right) \tag{72}$$

We see that although the $\mathcal{O}(\epsilon^0)$ buoyancy fields $b^{(0)}$ are independent of wind, the $\mathcal{O}(\epsilon^{-1})$ buoyancy fields depend on wind in the diffusive limit.

Now, the overturning streamfunction in the basin has the form

$$= -\epsilon \frac{(\kappa b_z)_z}{b_z} = -\kappa \left(b^{(1)}_{zz} - \frac{b^{(1)}_z}{\eta} \right) + \mathcal{O}(\epsilon^{-1}) \tag{73}$$

That is, the $\mathcal{O}(\epsilon^0)$ buoyancy field $b^{(0)}$ that is independent of wind does not contribute to the residual circulation. To leading order in ϵ^{-1}, it is the perturbation buoyancy field $b^{(1)}$ that determines the magnitude of the residual circulation. In order to obtain the perturbation buoyancy field, the wind stress must be taken into account, even in the diffusive limit. This is the fundamental difference in the sensitivity to wind stress between the case with uniform diffusivity and bottom-intensified diffusivity. In the case with uniform diffusivity, it is the zeroth order buoyancy field $b^{(0)}$ that sets the overturning circulation, and in the diffusive limit, $b^{(0)}$ is independent of wind. This leads to an overturning circulation that is independent of wind stress. In the case with a bottom-enhanced κ, the leading order buoyancy field $b^{(0)}$ that is determined by the diffusivity does not contribute to any overturning. It is the higher order buoyancy fields that are sensitive to wind that are important to overturning. This leads to a circulation that retains its sensitivity to wind stress, even in the diffusive limit.

6 Numerical Solutions

6.1 Numerical solver

The equations are solved on a staggered Cartesian grid in a domain $y \in [-l, 0]$ and $z \in [-D, 0]$ where $l = 1000km$ and $D = 4km$. A grid spacing of $\Delta y = 50km$ and $\Delta z = 50m$ is used. The buoyancy flux is required to vanish at the bottom and the streamfunction is set to zero on all boundaries aside from the northern boundary (which connects the channel to the basin). To step the equations forward in time, the time tendency in the buoyancy equation is retained, and the model is run until a steady state is reached.

In all the solutions below, a constant wind stress, in both space and time, is used. The surface buoyancy distribution is prescribed to be

$$b_s(y) = b_0 \left(1 + \frac{y}{l}\right) \tag{74}$$

with $b_0 = 2 \times 10^{-2} ms^{-2}$.

After obtaining the numerical solutions in the channel, the solutions are analytically continued into the basin through the (dimensional) relation

$$^\dagger = -L \frac{(\kappa b_z)_z}{b_z} \left(1 - \frac{y}{L}\right) \text{ for } 0 < y < L. \tag{75}$$

This relation is obtained by integrating the vertical advective-diffusive balance in the basin from latitude $y = 0$ to some arbitrary latitude y.

There is one subtlety that differentiates the numerical solver from the mathematical model presented above. In the mathematical model, the eddy streamfunction is exactly $\psi^\star = Ks$ and is required to vanish at the top and bottom. However, this is numerically challenging as can be seen from the following example. Near the upper and lower boundaries of the ocean the stratification becomes weak making the eddy streamfunction $\psi^\star$ large in the boundary layers. But then $\psi^\star$ is also required to vanish at the upper and lower boundaries. One way to avoid this difficulty is to make $\psi^\star$ a nonlocal function of the stratification. In [4], the following boundary value problem for $\psi^\star$ is presented

$$\left(c^2 \frac{d^2}{dz^2} - b_z\right) \psi^\star = K b_y \tag{76}$$

with $\psi^\star$ vanishing at the upper and lower boundaries. The parameter c that appears above is a depth-independent speed that needs to be specified. If $c = 0$, we obtain $\psi^\star = Ks$, equivalent to the mathematical model presented in the previous sections. In general, c is typically set to a baroclinic wave speed c_m approximated by

$$c_m \approx \frac{1}{m\pi} \int_{-D}^{0} b_z dz. \tag{77}$$

Choosing a low baroclinic wave speed (*i.e.* a small m) emphasizes lower vertical modes. All the solutions presented below have $m = 2$.

We now look at the regions where $\psi^\star$ in the numerical model (as obtained from the boundary value problem) approximates the $\psi^\star = Ks$ in the mathematical model. A non-dimensional form of the boundary value problem is

$$\left(\varepsilon^2 \frac{d^2}{dz^2} - b_z\right) \psi^\star = \Gamma b_y \tag{78}$$

where $\varepsilon^2 = c^2/(N_0^2 D^2)$ and $\Gamma = K N_0^2 D/L$. In the limit $\epsilon \to 0$, we expect $\psi^\star$, as computed from the boundary value problem, to equal Ks in the interior of the ocean, and approach zero quadratically in thin boundary layers near the upper and lower boundaries. We now compute the thickness of these boundary layers. Any analysis done on the mathematical model is expected to hold only outside these boundary layers.

In the case of uniform stratification $b_z = 1$, we obtain $\varepsilon = (m\pi)^{-1}$. The boundary layer thickness is then given by $\delta_z = \varepsilon = (m\pi)^{-1}$, or including dimensions,

$$\delta_z = \frac{D}{m\pi}. \tag{79}$$

For $m = 2$, $\delta_z = D/(2\pi) \approx D/6 \approx 630m$. In the upper and lower $630m$ of the ocean, $\psi^\star \neq Ks$ and $\psi^\star$ is determined by a combination of quadratic interpolation in addition to the stratification in the water column.

It is also worth noting that, in regions of weak stratification, ε becomes large and Γ becomes small reducing the boundary value problem to

$$\varepsilon^2 \frac{d^2\psi^\star}{dz^2} = 0. \tag{80}$$

In weakly stratified regions, the $\psi^\star$ in the model has essentially no resemblance to the form $\psi^\star = Ks$ and is simply a quadratic in the vertical.

6.2 Uniform diffusivity

We now verify the scaling relations derived earlier by conducting a sweep of parameter space for a range wind stress and vertical diffusivity values given by

$$0.05Nm^{-2} < \tau < 0.25Nm^{-2} \qquad\qquad 10^{-5}m^2s^{-1} < \overline{\kappa} < 10^{-3}m^2s^{-1} \tag{81}$$

Where $\overline{\kappa}$ is the vertical average of κ. The values of τ are linearly space while a logarithmic spacing is chosen for the values of $\overline{\kappa}$. For the case with uniform κ we choose ten points for each of τ and κ. For all other simulations, twenty points are chosen (*i.e.* 20×20 simulations are done, one for each pair of $(\tau, \overline{\kappa})$)

First we show some cross sections in (τ, κ) space displaying the dependence of ψ on wind stress and vertical diffusivity. The value of ψ is diagnosed at $y = 0$ and the vertical position of the minimum of ψ (see figure 1). The minimum of ψ at the northern edge of the channel is a measure of the overturning circulation in the basin. By continuity, the minimum of psi at the northern edge of the channel must equal the amount of water upwelling in the basin.

Figure 2 shows the dependence of the overturning to diffusivity. We see that, even for the weakest wind stress, the overturning streamfunction scales with the square root of the vertical diffusivity. Thus, we conclude that our simulations are in the diffusive regime of [12].

In Figure 3, we see the dependence of the overturning streamfunction to wind stress. For the largest values of diffusivity, there is a weak dependence of wind stress as expected from the diffusive limit of [12]. Even for the smallest diffusivity displayed in figure 3, the dependence on wind is weaker than the expected τ^{-1} scaling. This is consistent with the fact that our simulations are in the diffusive limit.

We show the dependence of the circulation to both τ and κ in figure 4. Observe that the slope of the contours of ψ in (τ, κ) space indicate that the strength of the overturning circulation will always decrease with increasing wind and increase with increasing diffusivity. The contours also become more vertical for stronger diffusivity, which is a manifestation of the insensitivity of the circulation to wind in the diffusive limit.

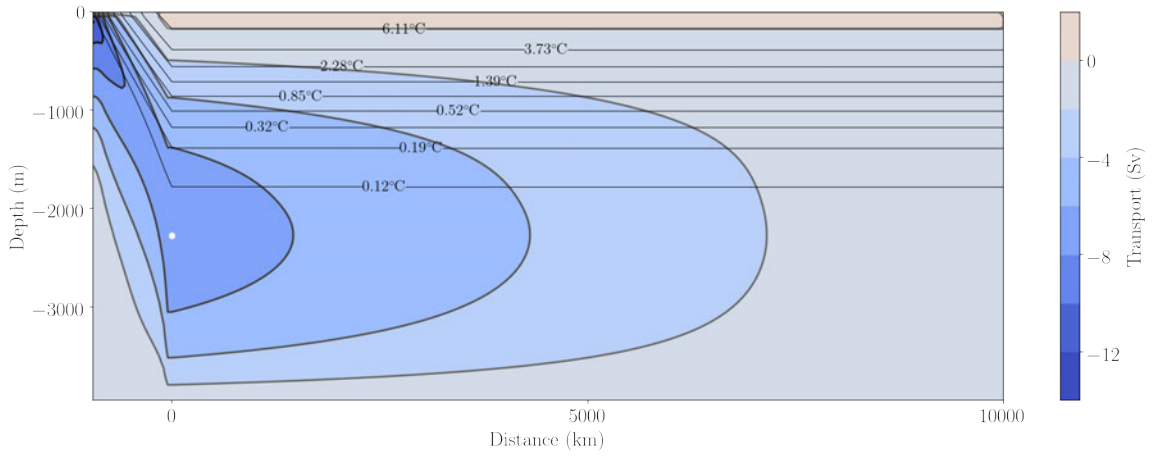

Figure 1: The overturning circulation for an exponentially enhanced diffusivity profile (as described in the text). The thin black lines are lines of constant temperature (or, equivalently, buoyancy). The thick black lines are lines of constant transport and the color represents the value of ψ. The white dot represents the maximum value of the overturning streamfunction at the northern edge of the channel and is a measure of the overturning circulation in the basin. For this plot $\tau = 0.13 N m^{-2}$ and $\kappa_b = 1.4 \times 10^{-3} m^2 s^{-1}$.

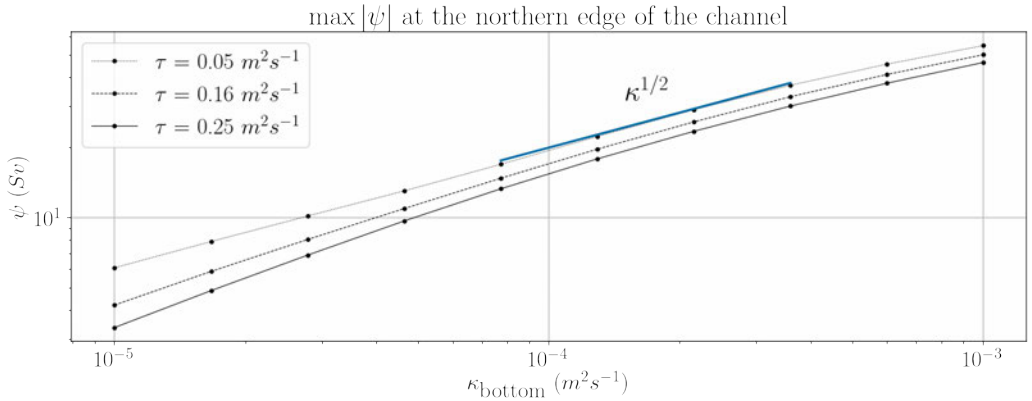

Figure 2: The minimum of ψ at the northern edge of the channel as a function of κ for the case of uniform diffusivity. Different lines represent different values of the applied constant wind stress.

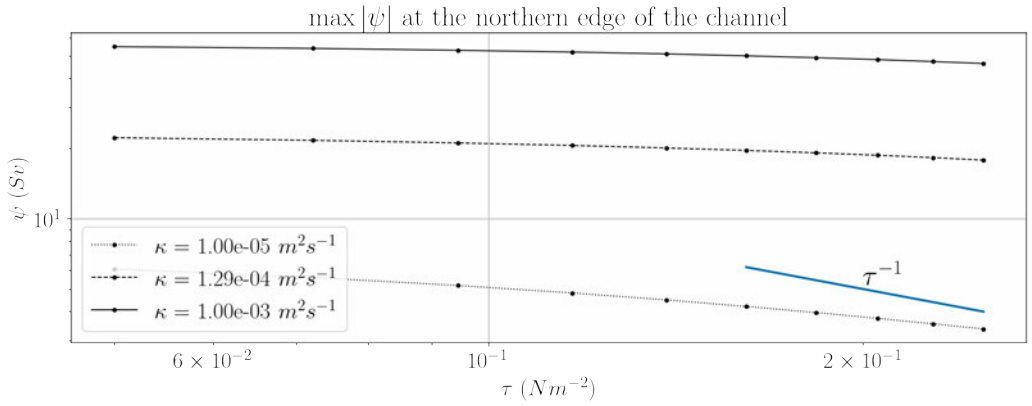

Figure 3: The minimum of ψ at the northern edge of the channel as a function of τ for the case of uniform diffusivity. Different lines represent different values of the vertical diffusivity.

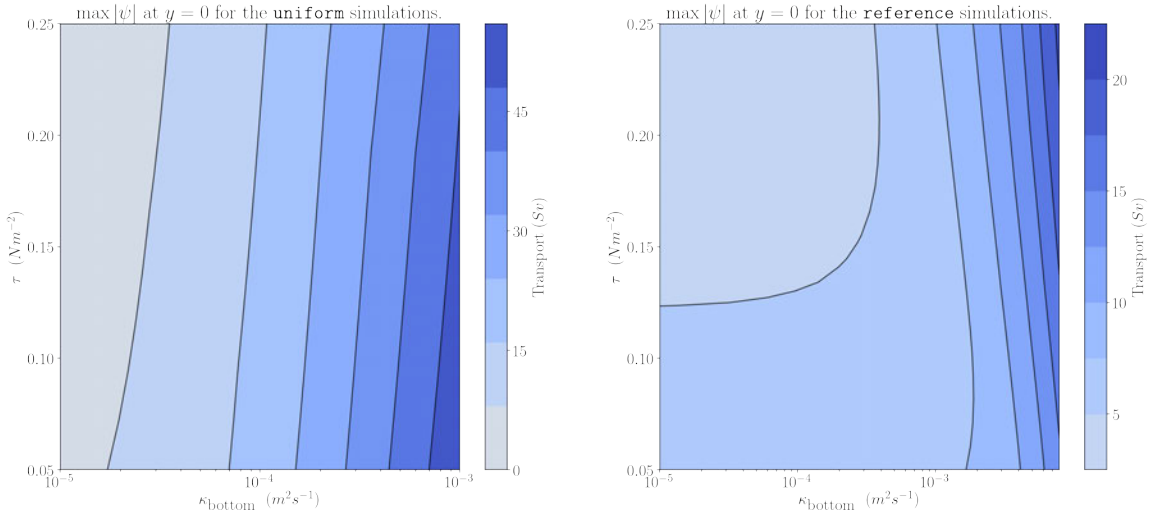

Figure 4: The maximum of $|\psi|$ as a function of τ and κ for a uniform diffusivity (left) and an exponential, bottom enhanced diffusivity (right).

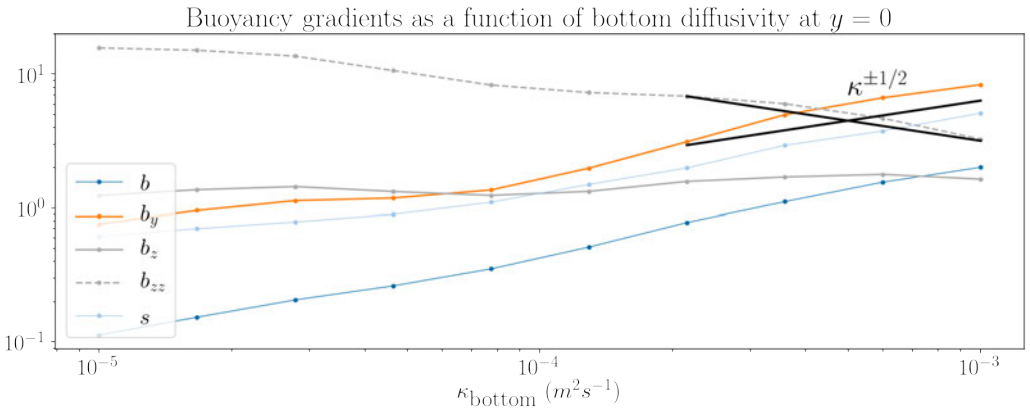

Figure 5: Buoyancy and its gradients as a function of vertical diffusivity for $\tau = 0.25 N m^{-2}$. The slope s is defined by $s = -b_y/b_z$.

We can also look at how buoyancy and its gradients are modified as either vertical diffusion or wind stress are modified. In figure 5, we see the stratification is essentially independent of diffusivity. Rather, the slope increases because $b_y \propto \sqrt{\kappa}$. Furthermore, we see that the buoyancy b also increases with the $\sqrt{\kappa}$ and that the vertical curvature of the buoyancy b_{zz} decreases with $\sqrt{\kappa}$. This implies that, unlike what is suggested in [12], it is not the vertical scale of the stratification that is decreasing with diffusivity but only the vertical curvature of the buoyancy. In addition, the steepening of the slopes is entirely due to the larger buoyancy gradient between the channel and the basin,

$$\frac{db}{dy} \approx \frac{b_{\text{basin}} - b_{\text{channel}}}{\Delta y} \approx \frac{b_{\text{basin}}}{\Delta y} + \mathcal{O}(\lambda) \tag{82}$$

where, from figure 5, we have $b_{\text{basin}} \propto \sqrt{\kappa}$. Thus, the slopes of buoyancy surfaces (and hence the overturning circulation) are increasing with diffusivity not because of any changes in the characteristic vertical or horizontal scales of the stratification, but because of the larger buoyancy gradient between the channel and the basin.

Finally, in figure 6, we show the dependence of the buoyancy gradients on wind stress. All fields are largely insensitive to wind stress, although both b_y and b_z show greater sensitivity than the other fields. However, both increase with wind in such a way so that the slope $s = -b_y/b_z$ (and hence the overturning) is insensitive to wind. What this tells us is that, in the diffusive limit, stronger winds will enhance stratification at the peak of the overturning circulation, but this enhancement is largely confined near the northern edge of the channel (more so with stronger winds, hence the increasing b_y),

6.3 Bottom intensified diffusion

We now impose a diffusivity that is exponentially enhanced near the ocean bottom. Vertical diffusion now has the form

$$\kappa(z) = \kappa_t + (\kappa_{\text{b}} - \kappa_t) e^{-(z+D)/H}. \tag{83}$$

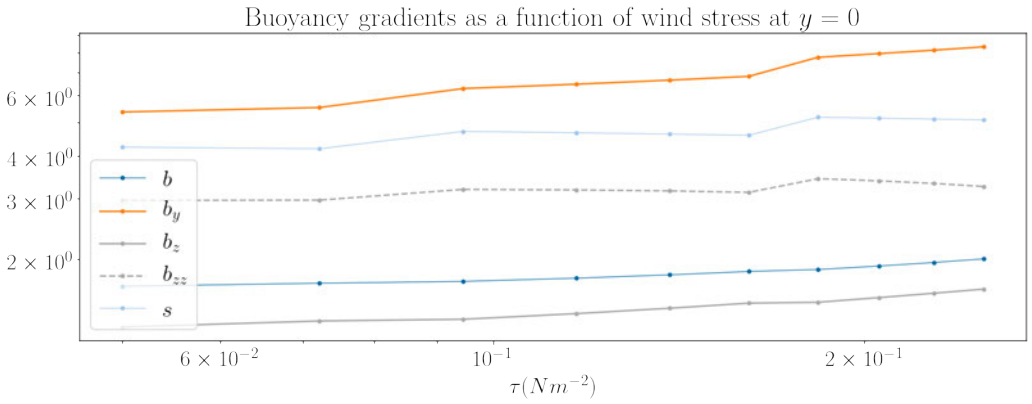

Figure 6: Buoyancy and its gradients as a function of wind stress τ for $\overline{\kappa} = 10^{-3}m^2s^{-1}$. The slope s is defined by $s = -b_y/b_z$.

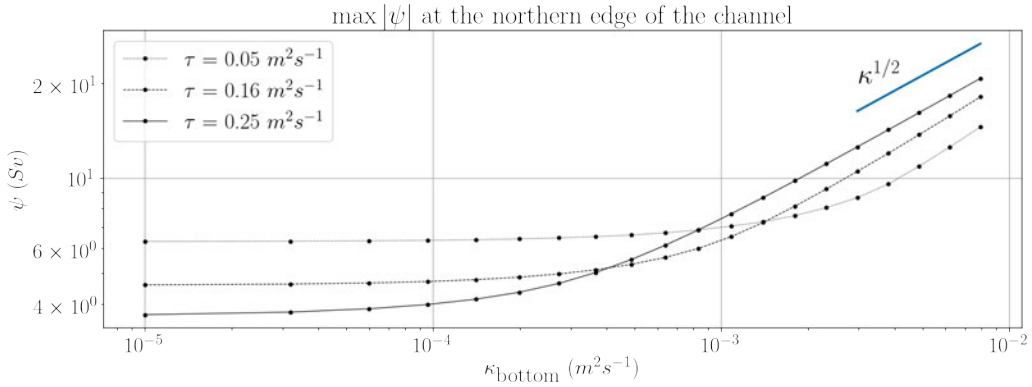

Figure 7: ψ_p as a function of κ for the case of bottom intensified diffusivity. Different lines represent different values of the applied constant wind stress.

Here, κ_t is some background value of vertical diffusivity away from the bottom boundary. In all simulations it, is chosen to have a value of $\kappa_t = 10^{-5}m^2s^{-1}$. The value of the diffusivity at the bottom is κ_b. The vertically averaged value of $\kappa(z)$ is denoted by $\overline{\kappa}$. The simulations below are done for values of $\overline{\kappa}$ between $10^{-5}m^2s^{-1}$ and $10^{-3}m^2s^{-1}$. One can then compute the appropriate value of κ_b in the above expression. There are two vertical length scales in the expression for $\kappa(z)$. The first is the ocean depth which is given by D. The vertical length scale H is the $e-$folding scale of the bottom diffusivity. In the limit that $H \to \infty$ we recover the vertically uniform bottom diffusivity. For the following simulations we choose a value $H = 500m$.

As before, we proceed by showing cross sections of ψ in (τ, κ) space. Figure 7 shows the dependence of the strength of the overturning circulation to the value of diffusivity at the ocean bottom. We see that, as in the case with uniform diffusivity, the overturning displays a $\sqrt{\kappa}$ dependence on the diffusion. However, the mechanism giving rise to this dependence differs from a uniform diffusivity ocean.

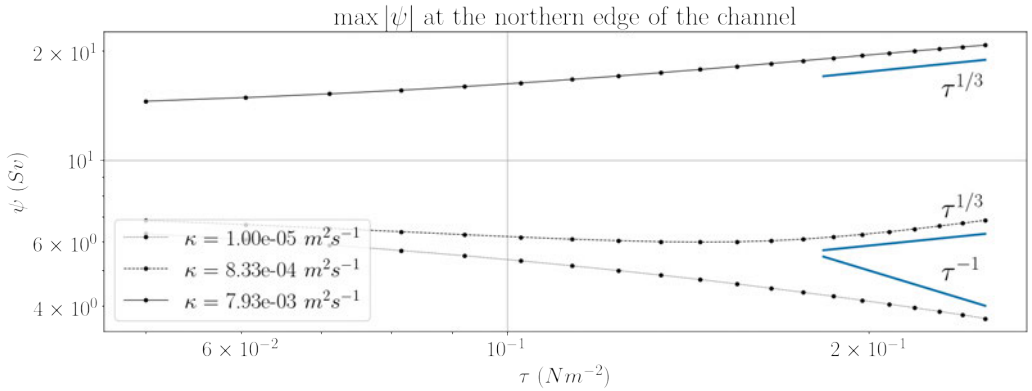

Figure 8: ψ_p as a function of τ for the case of bottom intensified diffusivity. Different lines represent different values of the bottom vertical diffusivity κ_b.

At the northern end of the channel, the overturning streamfunction satisfies

$$= -L\frac{(\kappa b_z)_z}{b_z} \approx -L\kappa\left(\frac{b_{zz}}{b_z} - \frac{1}{H}\right) \tag{84}$$

where we have approximated κ by $\kappa \approx \kappa_b e^{-(z+D)/H}$, valid when $\kappa_b \gg \kappa_t$. From the momentum equation we also know that $= -\tau/f + Ks$, giving the following balance

$$= -\frac{\tau}{f} + Ks \propto -L\kappa_b e^{-(d_p-D)/H}\frac{\delta}{H^2} \tag{85}$$

where $\delta/H^2 = b_{zz}/b_z - 1/H$ and d_p is the depth of the peak of the overturning circulation. In the diffusive limit, there is typically a leading order balance between b_{zz}/b_z and $1/H$ [8],

$$b_{zz} \approx \frac{1}{H}b_z. \tag{86}$$

This is a strong constraint on the vertical structure of the buoyancy in the basin. It says that both the stratification b_z and its gradient b_{zz} are exponentially decreasing towards the ocean bottom with an $e-$folding scale equivalent to that of the vertical diffusion. Since κ is small near the surface, this relationship is only valid at sufficient depths. The depths at which $b_{zz}/b_z = 1/H$ approximately holds is called the deep layer [8].

The existence of a deep layer implies that δ becomes small in the diffusive limit. The circulation is then proportional to δ, which is a measure of the the deviation of the vertical structure of the stratification from an exact exponential structure determined by a vertical decay scale of H.

So why is $\psi \propto \sqrt{\kappa}$ in the diffusive limit? In the case where diffusion is uniform, this is determined by the decrease in the vertical curvature of the buoyancy field ($b_{zz} \propto 1/\sqrt{\kappa}$) which leads to $\propto \kappa b_{zz}/b_z \propto \sqrt{\kappa}$. However, in the bottom intensified case, we see from figure 9 that both b_{zz} and b_z are insensitive to changes in κ for sufficiently large κ. Rather, we see that δ is now inversely proportional to $\sqrt{\kappa}$. That is, a larger vertical diffusivity makes the vertical structure of the stratification closer to an exponential with a vertical decay scale

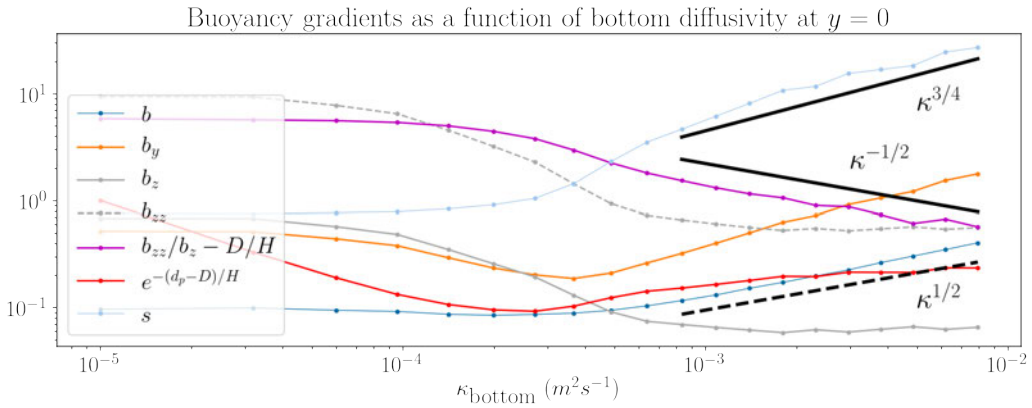

Figure 9: Buoyancy and its gradients as a function of vertical diffusivity for $\tau = 0.25 Nm^{-2}$ for the case of bottom-intensified vertical diffusion. The slope s is defined by $s = -b_y/b_z$.

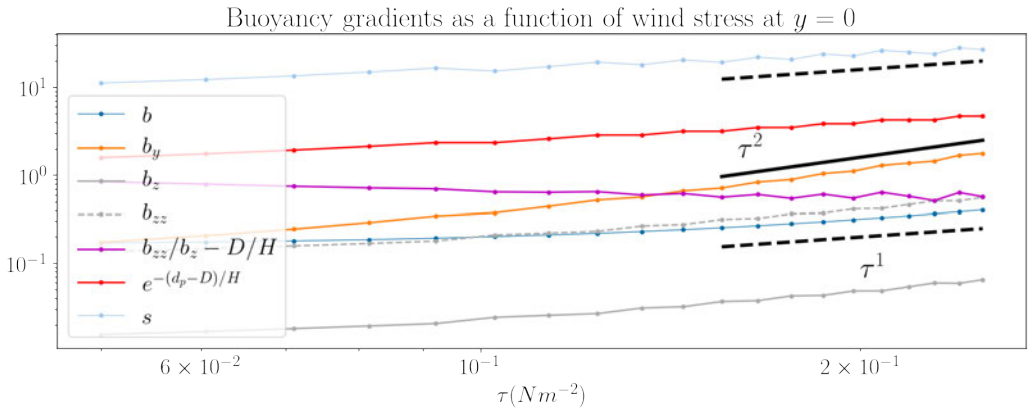

Figure 10: Buoyancy and its gradients as a function of wind stress τ for $\overline{\kappa} = 10^{-3} m^2 s^{-1}$ for the case of bottom-intensified vertical diffusion. The slope s is defined by $s = -b_y/b_z$.

of H. Along with the observation that the depth of the peak becomes insensitive to the strength of the diffusivity, we obtain the $\psi \propto \sqrt{\kappa}$ scaling.

In figure 10 we see that, unlike in the case of uniform diffusivity, the buoyancy and its gradients show a strong dependence on wind. In particular, b, b_z, and b_{zz} all scale linearly with τ whereas $b_y \propto \tau^2$. This is consistent with the balance at the northern edge of the basin. The balance may be rewritten as

$$-Kb_y \propto \left(\frac{\tau}{f} - L\kappa_b e^{-(D-d_p)/H}\frac{\delta}{H^2}\right) b_z. \tag{87}$$

Noting the b_z and the $e^{-(D-d_p)/H}$ are proportional to τ, we find that $b_y \propto \tau^2$.

In the diffusive limit, the large κ pins the vertical structure of the buoyancy at sufficient depths in the basin. In the deep layer (at $y = 0$), $b \approx b_0 e^{(z-D)/H} + b_1$ where b_0, b_1 are some constants, and so $b_z \approx \frac{1}{H} b_0 e^{(z-D)/H}$ and $b_{zz} \approx \frac{1}{H^2} b_0 e^{(z-D)/H}$. Thus, the fact that b, b_z, b_{zz} scale with τ implies that it is b_0 that scales with τ. We can interpret b_0/H as the stratification near the top of the deep layer (*i.e.* at the transition between the wind-driven adiabatic layer and the deep layer). Physically, increased wind forcing pushes more buoyancy (or, equivalently, stratification) downwards to the deep layer where then it decays with a decay scale of H towards the bottom. By pushing more buoyancy deeper into the ocean, a stronger overturning circulation is possible because of the large values of diffusion at depth (so that more water mass transformation takes place).

Note that $e^{-(D-d_p)/H}$ is proportional to τ and that δ is independent of wind. This implies that

$$\propto -L\kappa_b e^{-(D-d_p)/H}\frac{\delta}{H^2} \propto \tau \tag{88}$$

so that overturning should be linearly proportional to wind. However, from figure 8, we see that $\psi \propto \tau^{1/3}$. It turns out this inconsistency is due to the tapering scheme employed in the numerical implementation of Gent-McWilliams parametrization.

Figure 4 shows the dependence of the maximum of $|\psi|$ on the overturning circulation. We see that iso-ψ lines have positive slopes in (ψ, κ) space for low values of κ and negative slopes for large κ. This corresponds to the transition between ψ decreasing with wind stress in the adiabatic limit to ψ increasing with wind stress in the diffusive limit.

We can also look at how the results depend on the e-folding depth H of the diffusivity. The above results are for $H = 500m$. In figure 11 we show the dependence of ψ on both κ and τ in the case of $H = 250m$ and the case when $H = 750m$. When $H = 250$, essentially, diffusivity is weak everywhere in the water column except in a thin layer near the bottom boundary. Therefore, we see that, except for the largest values of wind and diffusivity, the overturning circulation weakens with stronger wind forcing. If H is too small, the bottom enhanced diffusion does not play a role in the dynamics of the overturning circulation and the overturning is essentially in the adiabatic limit.

Figure 11 also shows the case with $H = 750m$. Recall that, as $H \to \infty$, we recover a uniform κ and hence an overturning circulation that weakens with stronger wind forcing. We see that in the limit of weak diffusivity, ψ weakens with stronger winds, as expected in the adiabatic limit. As κ get larger, we observe that the dependence of ψ on wind forcing reverses and now ψ increases with increasing wind, as expected from the bottom-enhanced diffusive limit. At even larger values of κ, the overturning becomes relatively insensitive to

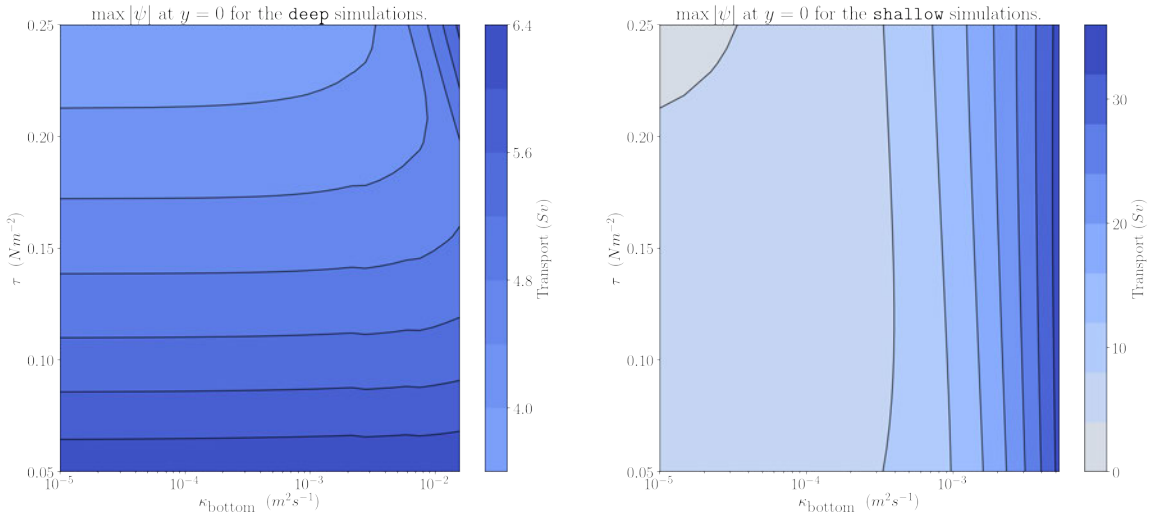

Figure 11: The maximum of $|\psi|$ as a function of κ and τ. The plot on the right is for an e-folding depth of $H = 250m$ and the plot on the left is for $H = 750m$.

κ, as expected from the $H \to \infty$ limit. From 11, we see that the overturning circulation displays a non-trivial dependence on wind forcing and that H needs to be known for even the sign of the sensitivity to be determined.

We now return to the issue of the tapering scheme [4] employed in the model. At the northern end of the channel, the boundary condition states that

$$= -L\frac{(\kappa b_z)_z}{b_z}. \tag{89}$$

In the numerical solver, however, the two sides of the equation are not equal due to the tapering scheme. Regions where $b_z \to 0$ are essentially interpolated through quadratically. In par-ticular, in the bottom boundary layer, the stratification becomes weak and the right hand side becomes large while the tapering scheme sends $\psi$to zero. Figure 12 shows both sides of the equation in the limit of weak, intermediate, and strong diffusivity for an intermediate value of wind stress. What is important to note in the figure is that in the case of large diffusivity, the strength of the overturning circulation is determined by the tapering scheme. The black line in the rightmost plot only has a minimum because the stratification in the bottom boundary layer is weak so the tapering scheme quadratically sends $\psi$to zero. This is unlike the leftmost plot in figure 12 where ψ(and $(\kappa b_z)_z/b_z$) possess minimum in the interior outside the tapered region.

When the bottom boundary layer becomes weakly stratified, the strength of the overturning circulation is therefore set by the tapering scheme instead of the dynamics of the model. This makes the results in the limit of large diffusion and large wind physically dubious. In the real ocean, weakly stratified regions are restratified through ageostrophic baroclinic instabilities (*e.g.* mixed-layer instabilities [2], [3] and symmetric instabilities [15], [16], [1]), so this suggests a link between the overturning circulation and the dynamics of the bottom boundary layer (that are not represented here).

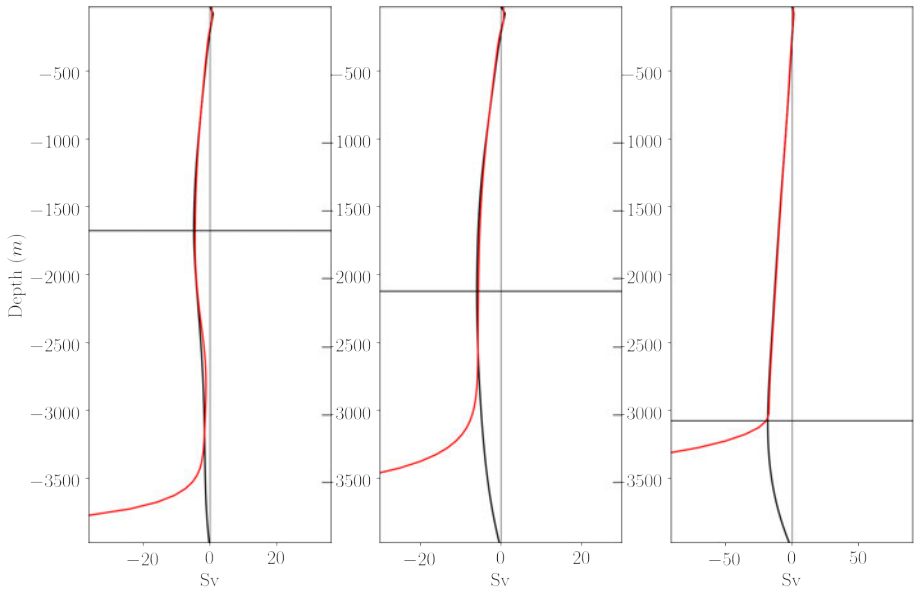

Figure 12: Examples of how the tapering scheme modifies the streamfunction. The red line is $(\kappa b_z)_z/b_z$ at $y = 0$. The black line represents the tapered streamfunction. The horizontal lines indicate the minimum of the tapered streamfunction. The wind strength is $\tau = 0.155Nm^{-2}$ while $\kappa_b = 2.0 \times 10^{-4}m^2s_{-1}, 8.3 \times 10^{-4}m^2s^{-1}$, and $7.9 \times 10^{-3}m^2s^{-1}$ for the left, middle, and right plots respectively.

In any case, the result that the overturning circulation intensifies with stronger wind forcing occurs for diffusivities and wind stresses that are small enough so that the tapering scheme is not creating an artificial minimum. Thus, the conclusion that the overturning circulation intensifies with increasing wind should be independent of the tapering scheme. However, the two possible scalings ($\psi \propto \tau^{1/3}$ and $(\kappa b_z)_z/b_z \propto \tau$) obtained are most likely dependent on the tapering scheme. In the first case, we are diagnosing $\psi = -\tau/f + \psi^\star$ where $\psi^\star \neq Ks$ but is rather some quadratic interpolation through a weakly stratified region. The position where ψ is diagnosed (at the minimum of ψ) *and* its actual value are determined by the tapering scheme. In the second case, the buoyancy fields are not tapered but the position where they are diagnosed is determined by the tapering scheme. This places more confidence in the second, linear, scaling. But as mentioned previously, the dependence on the tapering scheme suggests that in the real ocean, the relationship of the overturning circulation to wind stress and diffusion is sensitive to the dynamics of the bottom boundary layer. Therefore, even the second scaling may not be relevant for the real ocean.

7 Conclusion

In this report, we have derived the Nikurashin-Vallis model [12] of the overturning circulation beginning from the residual-mean theory presented in [14]. We then presented possible ways the overturning circulation and the buoyancy field may scale with wind stress and diffusion. In particular, for an ocean with vertically uniform diffusion, we found two dis-

tinct ways in which $\psi \propto \sqrt{\kappa}$. The first is the scaling theory presented in [12] that predicts that the stratification at the maximum of $|\psi|$ should decrease with increasing diffusivity as $b_z \propto 1/\sqrt{\kappa}$. Then, assuming b_y is constant, one obtains $\psi \propto -b_y/b_z \propto -\sqrt{\kappa}$. The alternative scaling presented here predicts that it is b_z that is constant at the maximum of $|\psi|$ and that $b_y \propto \sqrt{\kappa}$. This alternative scaling is found to agree with the numerical solutions.

We have also shown why the overturning circulation should be expected to depend on wind in the limit when vertical diffusion is exponentially enhanced towards the ocean bottom. In an ocean with uniform diffusion, the buoyancy field is determined to leading order by diffusive processes and the diapycnal velocity $\omega = (\kappa b_z)_z/b_z = \kappa b_{zz}/b_z$ is then determined by the vertical curvature of the leading order buoyancy field. This leads to an overturning circulation that is independent of wind. However, when mixing is bottom-intensified, the existence of a deep layer where $b_{zz} \approx b_z/H$ implies that the leading order buoyancy field does not contribute to water mass transformation. Instead, the diapycnal velocity ω is entirely determined by higher order corrections to the buoyancy field that depend on wind. Thus, in this model, the existence of a deep layer implies an overturning circulation that is sensitive to changes in wind forcing.

In addition, we have also determined the sign of the dependence of the overturning ψ on wind stress. If a deep layer exists, then stronger winds push more buoyancy into the deep layer where it then decays with the characteristic vertical scale of κ towards the ocean bottom. This causes the depth of the maximum of $|\psi|$ to increase and deepens the circulation to depths where diffusion is larger. The diapycnal velocity $\omega = (\kappa b_z)_z/b_z$ then increases because the effective κ experienced at the maximum of $|\psi|$ has increased. Therefore, the existence of a deep layer implies an overturning circulation that increases in magnitude as westerlies strengthen.

The characteristic vertical scale H of the diffusivity is a crucial parameter in determining the dependence of ψ on wind. If H is too small, then the overturning circulation does not 'feel' the bottom enhancement of diffusion and the overturning circulation is essentially in the adiabatic limit. If H is too large, then a deep layer cannot form and we recover a circulation that is independent of wind stress. We showed the results of a range of simulations in (τ, κ) space (Figure 11) for $H = 750m$ where the circulation weakens with wind for small κ, strengthens with wind for intermediate values of κ, and becomes independent of wind for large κ.

Finally, we found that the sensitivity of the overturning circulation to both wind stress and diffusion depends on the dynamics of the bottom boundary layer. This is seen in the model through the dependence of the circulation on the tapering scheme [4] used in the implementation of the Gent-McWilliams parameterization. For small values of vertical diffusion and wind, the diapycnal velocity ω exhibits a maximum in the ocean interior that is independent of the tapering. However, when wind stress or diffusion are large, then ω has no local maxima in the interior. Instead it grows monotonically towards the bottom because of the near vanishing stratification. Presumably, if processes in the bottom boundary layer are represented, the maximum would occur in the bottom boundary layer. In this model however, an artificial maximum is created as the tapering scheme quadratically interpolates through weakly stratified regions and sends ω to zero at the ocean bottom. Although the numerical results (such as how ψ scales with τ and κ) likely depend on the tapering scheme, it is found that the fact the sign of the sensitivity of ψ to both κ and τ in the

bottom-enhanced diffusive limit is independent of the tapering scheme.

8 Acknowledgments

I would like to thank Ali Mashayek and Geoffrey Stanley for advising this project.

References

[1] J. S. Allen and P. A. Newberger, *On symmetric instabilities in oceanic bottom boundary layers*, J. Phys. Oceanogr., (1998), pp. 1131–1151.

[2] G. Boccaletti, R. Ferrari, and B. Fox-Kemper, *Mixed layer instabilities and restratification*, J. Phys. Oceanogr., (2007), pp. 2228–2250.

[3] J. Callies, *Restratification of abyssal mixing layers by submesoscale baroclinic eddies*, J. Phys. Oceanogr., (2018), pp. 1995–2010.

[4] R. Ferrari, S. M. Griffies, A. J. Nurser, and G. K. Vallis, *A boundary-value problem for the parameterized mesoscale eddy transport*, Ocean Model., 32 (2010), pp. 143–156.

[5] P. R. Gent, J. Willebrand, T. J. McDougall, and J. C. McWilliams, *Parameterizing Eddy-Induced Tracer Transports in Ocean Circulation Models*, J. Phys. Oceanogr., (1995), pp. 463–474.

[6] I. M. Held and T. Schneider, *The surface branch of the zonally averaged mass transport circulation in the troposphere*, J. Atmos. Sci., (1999), pp. 1688–1697.

[7] J. Marshall and T. Radko, *Residual-mean solutions for the Antarctic Circumpolar Current and its associated overturning circulation*, J. Phys. Oceanogr., 33 (2003), pp. 2341–2354.

[8] A. Mashayek, R. Ferrari, M. Nikurashin, and W. R. Peltier, *Influence of enhanced abyssal diapycnal mixing on stratification and the ocean overturning circulation*, J. Phys. Oceanogr., 45 (2015), pp. 2580–2597.

[9] T. J. Mcdougall and P. C. Mcintosh, *The temporal-residual-mean velocity. Part I: Derivation and the scalar conservation equations*, J. Phys. Oceanogr., (1996), pp. 2653–2665.

[10] T. J. McDougall and P. C. McIntosh, *The temporal-residual-mean velocity. Part II: Isopycnal interpretation and the tracer and momentum equations*, J. Phys. Oceanogr., (2001), pp. 1222–1246.

[11] W. H. Munk, *Abyssal recipes*, Deep. Res. Oceanogr. Abstr., (1966).

[12] M. Nikurashin and G. Vallis, *A theory of deep stratification and overturning circulation in the ocean*, J. Phys. Oceanogr., 41 (2011), pp. 485–502.

[13] ——, *A theory of the interhemispheric meridional overturning circulation and associated stratification*, J. Phys. Oceanogr., 42 (2012), pp. 1652–1667.

[14] R. Plumb and R. Ferrari, *Transformed Eulerian-Mean Theory . Part I : Nonquasi-geostrophic Theory for Eddies on a Zonal-Mean Flow*, J. Phys. Oceanogr., 35 (2005), pp. 165–174.

[15] P. H. Stone, *On Non-Geostrophic Baroclinic Stability*, J. Atmos. Sci., (1966), pp. 390–400.

[16] ——, *On Non-Geostrophic Baroclinic Stability: Part II*, J. Atmos. Sci., (1970), pp. 721–726.

[17] W. R. Young, *An Exact Thickness-Weighted Average Formulation of the Boussinesq Equations*, J. Phys. Oceanogr., (2012), pp. 692–707.

Eddy Mixing of Biogeochemical Tracers

Channing J. Prend

August 19, 2019

1 Introduction

The ocean is characterized by motions at a range of scales. This has important consequences for oceanic biogeochemical processes, which are similarly multi-scale in nature. At the global and basin scales, the meridional overturning circulation (MOC) controls subsurface nutrient distributions, which in turn determine where photosynthesizing phytoplankton can grow on climatic time-scales [7, 15]. On shorter timescales, primary productivity has been observed to be closely linked to mesoscale and submesoscale processes [2, 3, 10]. This is evident from satellite images of ocean color, a proxy for phytoplankton biomass, which clearly show the expression of eddies and other small-scale structures in the flow (Figure 1).

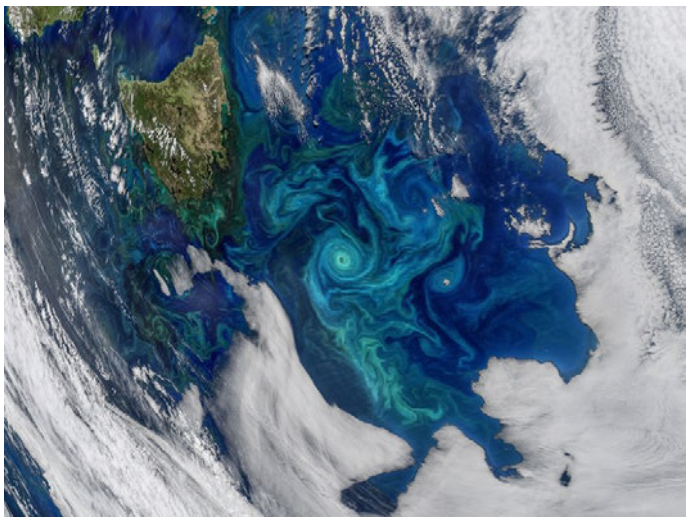

Figure 1: True color image of a phytoplankton bloom from the NASA MODIS satellite.

It has been suggested that accounting for (sub-)mesoscale productivity is necessary to close global budgets [8, 13]. This poses a problem for climate models, which rarely resolve processes smaller than the mesoscale. Therefore, the fluxes of tracers—such as nutrients and phytoplankton—associated with the unresolved dynamics must by parameterized. It is common to assume that the eddy fluxes of an arbitrary tracer, c, are proportional to the gradients in the mean field, the so-called gradient diffusion hypothesis [16]. In this

framework, the turbulent dispersion takes the form of an enhanced molecular diffusion:

$$\overline{u'c'} = -K_e \nabla \bar{c}, \tag{1}$$

where K_e is an effective diffusivity. However, it is not clear that this form of the eddy flux is appropriate for reactive tracers, which have some growth or decay in time that is independent of the flow and thus do not remain constant following a fluid parcel.

Here, we examine the turbulent transport of reactive biogeochemical tracers using an idealized nutrient-phytoplankton model. We consider only the generation of phytoplankton patchiness by the 2-D stirring of large-scale gradients [1], although it is noted that vertical nutrient transport associated with (sub-)mesoscale dynamics is also important in driving productivity at these scales [2, 6]. We show that the validity of the mixing-length approximation (1) for reactive tracers requires a separation between the timescales of the turbulent motions and the reaction. However, there are a number of cases in the atmosphere and ocean where we might expect the flow and reaction timescales to be of the same order, including phytoplankton growth in submesoscale eddies and carbon dioxide equilibration at small-scale air-sea interfaces. Therefore, these results have implications for the representation of sub-grid scale biogeochemical processes in global climate models.

2 Biological Model

Nutrient-phytoplankton-zooplankton (NPZ) models have been used in oceanographic research for decades. Given the inherently simplistic nature of NPZ models, some have questioned their efficacy. Still, NPZ models have been shown to capture fundamental aspects of plankton dynamics and are useful in making complex biological processes more tractable [5]. A general set of NPZ model equations can be written as:

$$\frac{DN}{Dt} = -f(I)g(N)P + (1-\gamma)h(P)Z + i(P)P + j(Z)Z \tag{2}$$

$$\frac{DP}{Dt} = f(I)g(N)P - h(P)Z - i(P)P \tag{3}$$

$$\frac{DZ}{Dt} = \gamma h(P)Z - j(Z)Z \tag{4}$$

where γ is zooplankton assimilation, and the 5 transfer functions are: phytoplankton response to light $f(I)$, phytoplankton nutrient uptake $g(N)$, zooplankton grazing $h(P)$, and phytoplankton $i(P)$ and zooplankton $j(Z)$ loss terms. Defining these transfer functions is nontrivial and *Franks* (2002) reviews many of the functional forms that have been used. Perhaps the simplest possible system one could consider has linear transfer functions and no zooplankton grazers. Since we are considering lateral stirring only, there is no depth dependence for any fields. Including explicit diffusion, Eq. (2)-(4) then become:

$$\frac{DN}{Dt} - \kappa\nabla^2 N = -\frac{\mu}{\tilde{N}_D} NP - \lambda N + \lambda N_D \tag{5}$$

$$\frac{DP}{Dt} - \kappa\nabla^2 P = \frac{\mu}{\tilde{N}_D} NP - \lambda P, \tag{6}$$

where μ [s^{-1}] is the uptake rate, and λ [s^{-1}] is the entrainment rate. These equations could describe the biological dynamics in the mixed-layer (ML; Figure 2), where nitrate is utilized for phytoplankton growth and resupplied by mixing of nutrient-rich waters from below, with $N = N_D$. There is also loss of N and P due to detrainment from this mixing across the ML base. $\tilde{N}_D$ is some characteristic N value (whereas N_D is spatially variable) that is included for dimensional reasons (so that the nonlinear growth term has the correct units). In principle, μ, λ, and N_D could all be spatially variable. The motivation for choosing this simplified system of equations is to understand the fundamental response to variations in parameters without introducing extraneous nonlinearity from the choice of transfer functions. Note that our goal is not to realistically model tracer concentration values or match observations directly.

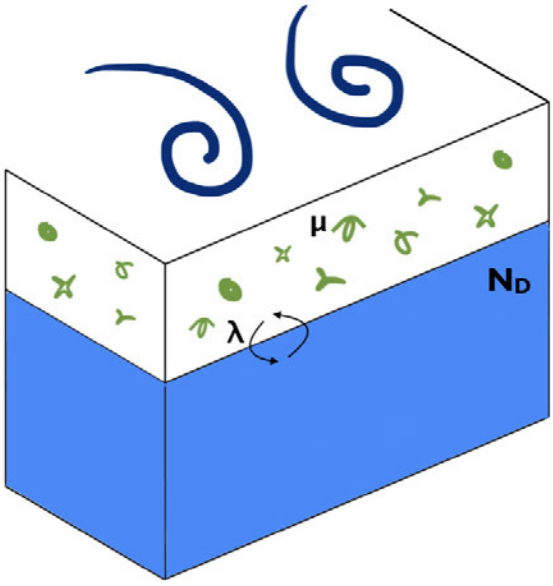

Figure 2: Schematic of mixed-layer plankton dynamics governed by Eq. (5) and (6).

To illustrate how the addition of reaction terms influences the effective diffusivity felt by a tracer, consider the equation for the total nitrogen in the system, $S = N + P$, obtained by adding together Eq. (5) and (6).

$$\frac{DS}{Dt} - \kappa \nabla^2 S = \lambda N_D - \lambda S \tag{7}$$

Note that the nonlinear growth term, which is an equal but opposite sign in the N and P equations, cancels. Therefore, there is a single reaction rate, λ, associated with the evolution of S. Here, the reaction terms represent a balance between resupply of nitrate to the ML from mixing with nutrient-rich deep waters (λN_D) and the detrainment of nutrients and phytoplankton ($-\lambda S$). Let's consider the case of a background gradient in N_D that is a function of y only, i.e., $N_D = \Gamma y$, with a periodic flow field of the form

$$\mathbf{u} = v_0(t) \sin(kx) \hat{\mathbf{y}} \tag{8}$$

Decomposing S into the background gradient and transient fluctuations driven by the flow field, $S = \Gamma y + S'(x,t)$, and plugging into Eq. (7) gives

$$\frac{\partial S'}{\partial t} + v\Gamma = -\lambda S' + \kappa \frac{\partial^2 S'}{\partial x^2}. \tag{9}$$

Assuming that S' is also separable and of the same form as the velocity field, i.e., $S' = S_0(t)\sin(kx)$, reduces Eq. (9) to an ordinary differential equation

$$\frac{dS_0}{dt} + v_0\Gamma = -\lambda S_0 - \kappa k^2 S_0. \tag{10}$$

Now taking v_0 to be wave-like, $v_0 = \tilde{v}\mathrm{e}^{-i\theta t}$, and solving Eq. (10) using the integrating factor $\mathrm{e}^{(\lambda+\kappa k^2)t}$ yields a solution for S_0 (and thus S'), which implies an eddy flux of

$$\overline{v'S'} = -\frac{\tilde{v}^2\Gamma(\lambda+\kappa k^2)}{\theta^2 + (\lambda+\kappa k^2)^2}. \tag{11}$$

$\bar{S}$ is Γy in this case, so mixing-length theory gives $\overline{v'S'} = -K_e\Gamma$. Thus, by Eq. (11) we find that the effective diffusivity is

$$K_e = \frac{\tilde{v}^2(\lambda+\kappa k^2)}{\theta^2 + (\lambda+\kappa k^2)^2} \tag{12}$$

We can see that the effective diffusivity depends directly on the entrainment rate, λ. To illustrate this, Eq. (12) is plotted in Figure 3 for varied λ with all other parameters held constant at values similar to those used in the simulations discussed in Section 4. To highlight the deviations from the passive tracer case, K_e is normalized by $K_e(\lambda{=}0)$, which is the effective diffusivity in the absence of reaction terms. For most values of λ, the effective diffusivity for a reactive tracer is smaller than for a passive tracer. In other words, as the entrainment rate increases, more nutrients and phytoplankton are mixed out of the ML, causing the S concentration to decrease and thus less tracer to be acted on by the effective diffusivity. However, note that for some small λ values, K_e is larger than $K_e(\lambda{=}0)$. This suggests a regime where the nutrient resupply (λN_D), also associated with the entrainment rate, is larger than the detrainment term ($-\lambda S$).

Figure 3 suggests that the inclusion of reaction terms can significantly modify the dispersion of a tracer—at least for certain reaction rates. Therefore, we expect the gradient-diffusion hypothesis will break down for reactive tracers under some parameter regimes. To gain insight into the relevant parameters that might control this for the nutrient-phytoplankton system, Eq. (5) and (6) can be nondimensionalized

$$\frac{\partial N^*}{\partial t^*} + \mathbf{u}^* \cdot \nabla_* N^* - Pe^{-1}\left(\nabla_*^2 N^*\right) = Da\left(-N^*P^* - \frac{\lambda}{\mu}(N^*) + \frac{\lambda}{\mu}N_D^*\right) \tag{13}$$

$$\frac{\partial P^*}{\partial t^*} + \mathbf{u}^* \cdot \nabla_* P^* - Pe^{-1}\left(\nabla_*^2 P^*\right) = Da\left(N^*P^* - \frac{\lambda}{\mu}(P^*)\right) \tag{14}$$

where the * denotes nondimensional variables. Biological reaction terms scale with the Damköhler number, $Da = \mu L/U$, which is the ratio of advective (L/U) and reactive ($1/\mu$) time scales; diffusive terms scale inversely with the Peclet number, $Pe = UL/\kappa$.

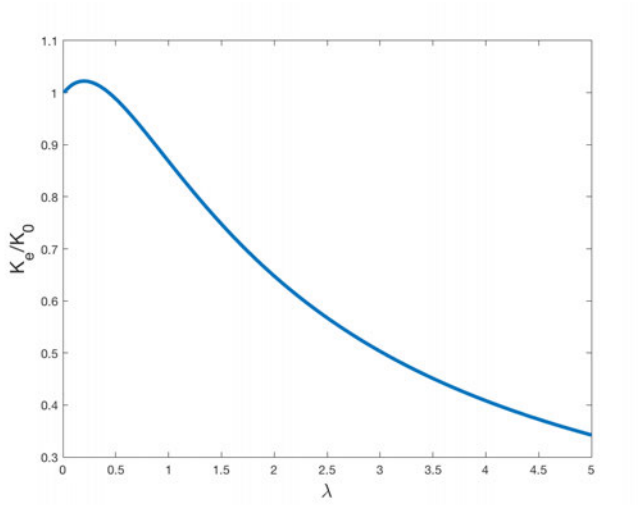

Figure 3: Effective diffusivity as a function of λ, normalized by the effective diffusivity for $\lambda = 0$ (i.e., passive tracer).

This system of equations is used to examine the validity of the mixing-length assumption for parameterizing eddy fluxes of nutrients and phytoplankton. First, the method of multiple scales is applied to the advection-diffusion equation for a passive tracer to show how $\overline{u'c'} = -K_e \nabla \overline{c}$ is derived, and then to the advection-diffusion-reaction equations given by (5) and (6) to show the effect of the biological reaction terms. Next, the dynamics of the system are explored in a 2-D stirring flow. Finally, we consider the relevance of these results to the parameterization of submesoscale productivity in global climate models.

3 Multiple Scale Analysis

3.1 Passive tracer case

Multiple scale analysis has been used to understand the evolution of a passive tracer [11]. We review this method to show how the gradient-diffusion hypothesis can be derived. In this case, we assume a scale separation between the turbulent eddies (ℓ) and the mean flow (L). Slow time and space variables are defined: $T = \epsilon t$ and $\mathbf{X} = \epsilon \mathbf{x}$, where $\epsilon \equiv \ell / L$. The evolution equation for a passive tracer with no sources or sinks is given by

$$\frac{\partial c}{\partial t} + \mathbf{u} \cdot \nabla c - \kappa \nabla^2 c = 0 \tag{15}$$

Plugging in the perturbation expansion $c = C_0(\mathbf{X}, T) + \epsilon C_1(\mathbf{x}, t; \mathbf{X}, T) + \mathcal{O}(\epsilon^2)$, and decomposing the velocity, where the mean flow is a function of the slow variables only, i.e., $\mathbf{u} = \mathbf{U}(\mathbf{X}, T) + \mathbf{u}'(\mathbf{x}, t; \mathbf{X}, T)$ yields

$$\mathcal{O}(1) : C_{0t} + (\mathbf{U} + \mathbf{u}') \cdot \nabla_x C_0 - \kappa \nabla_x^2 C_0 = 0 \tag{16}$$

Averaging over small and fast scales, all the terms on the left hand side go to 0 and we find that $C_0 = C_0(\mathbf{X}, T)$—as expected by construction. The first order solution is

$$\mathcal{O}(\epsilon) : C_{1t} + (\mathbf{U} + \mathbf{u}') \cdot \nabla_x C_1 - \kappa \nabla_x^2 C_1 = -C_{0T} - (\mathbf{U} + \mathbf{u}') \cdot \nabla_X C_0 \tag{17}$$

Averaging over small and fast scales, we find that

$$C_{0T} + \mathbf{U} \cdot \nabla_X C_0 = 0 \tag{18}$$

Subtracting this from (17) gives

$$C_{1t} + (\mathbf{U} + \mathbf{u}') \cdot \nabla_x C_1 - \kappa \nabla_x^2 C_1 = -\mathbf{u}' \cdot \nabla_X C_0, \tag{19}$$

which has solutions of the form

$$C_1 = -(\xi \cdot \nabla_{\mathbf{X}}) C_0, \tag{20}$$

where $\xi(\mathbf{x}, t)$ satisfies

$$\xi_t + (\mathbf{U} + \mathbf{u}') \cdot \nabla_{\mathbf{x}} \xi - \kappa \nabla_{\mathbf{x}}^2 \xi = \mathbf{u}' \tag{21}$$

Eq. (20) implies that $\overline{u_i' c'} = -D_{ij} \partial_{x_j} \bar{c}$, where $D_{ij} = \overline{u_i' \xi_j}$ is like an effective diffusivity. This is the mixing-length approximation. Now considering the second order solution

$$\mathcal{O}(\epsilon^2) : C_{2t} + (\mathbf{U}+\mathbf{u}') \cdot \nabla_x C_2 - \kappa \nabla_x^2 C_2 = -C_{1T} - (\mathbf{U}+\mathbf{u}') \cdot \nabla_X C_1 + 2\kappa \nabla_x \cdot \nabla_X C_1 + \kappa \nabla_X^2 C_0 \tag{22}$$

Averaging over small and fast scales, we find that

$$C_{1T} + \mathbf{U} \cdot \nabla_X C_1 = \kappa \nabla_X^2 C_0 + \overline{(\mathbf{u}' \cdot \nabla_X) \xi \cdot \nabla_X C_0} \tag{23}$$

It has been shown that summing the solvability conditions at $\mathcal{O}(\epsilon)$ and $\mathcal{O}(\epsilon^2)$ gives the evolution equation for the mean tracer concentration

$$\frac{\partial \bar{c}}{\partial t} + \mathbf{u} \cdot \nabla \bar{c} = \partial_{x_i} (D_{ij} \partial_{x_j} \bar{c}), \tag{24}$$

where D_{ij} is the effective diffusivity tensor. In other words, the evolution of the mean tracer concentration depends on the divergence of the eddy flux. The key point is that multiple scale analysis of the advection-diffusion equation for a passive tracer recovers the gradient-diffusion hypothesis. It should be noted that this analysis requires a scale separation between the turbulent eddies and the mean concentration structure. When these length scales are similar, nonlocal effects may dominate the eddy fluxes [9]. However, this is not the topic we consider here, instead we investigate the effects of adding biological reaction terms.

3.2 Reactive Tracer Case

Now we apply the same methods from Section 3.1 to the nutrient-phytoplankton system given by Eq. (5) and (6). Again we assume a scale separation between the turbulent eddies (ℓ) and the mean flow (L). Slow time and space variables are defined: $T = \epsilon t$ and $\mathbf{X} = \epsilon \mathbf{x}$, where $\epsilon \equiv \ell / L$. Plug in the perturbation expansions $P = P_0(\mathbf{X}, T) + \epsilon P_1(\mathbf{x}, t; \mathbf{X}, T) + \mathcal{O}(\epsilon^2)$, $N = N_0(\mathbf{X}, T) + \epsilon N_1(\mathbf{x}, t; \mathbf{X}, T) + \mathcal{O}(\epsilon^2)$ and decompose the velocity as before, i.e., $\mathbf{u} = \mathbf{U}(\mathbf{X}, T) + \mathbf{u}'(\mathbf{x}, t; \mathbf{X}, T)$. Note that we assume the mean flow and leading order biological behavior are a function of the slow variables only. The zeroth order solution is

$$\mathcal{O}(1) : P_{0t} + (\mathbf{U} + \mathbf{u}') \cdot \nabla_{\mathbf{x}} P_0 - \kappa \nabla_{\mathbf{x}}^2 P_0 = \mu P_0 N_0 - \lambda P_0, \tag{25}$$

$$\mathcal{O}(1) : N_{0t} + (\mathbf{U} + \mathbf{u}') \cdot \nabla_{\mathbf{x}} N_0 - \kappa \nabla_{\mathbf{x}}^2 N_0 = \mu P_0 N_0 - \lambda N_0 + \lambda N_D, \tag{26}$$

Averaging over small and fast scales gives $0 = \mu P_0 N_0 - \lambda P_0$ for Eq. (25), which implies that $N_0 = \lambda/\mu$ and thus $P_0 = N_D - \lambda/\mu$ by Eq. (26). The first order solution is

$$\mathcal{O}(\epsilon) : P_{1t} + (\mathbf{U} + \mathbf{u}') \cdot \nabla_{\mathbf{x}} P_1 - \kappa \nabla_{\mathbf{x}}^2 P_1 + P_{0T} + (\mathbf{U} + \mathbf{u}') \cdot \nabla_{\mathbf{X}} P_0 = \mu P_0 N_1 + \mu P_1 N_0 - \lambda P_1, \tag{27}$$

$$\mathcal{O}(\epsilon) : N_{1t} + (\mathbf{U} + \mathbf{u}') \cdot \nabla_{\mathbf{x}} N_1 - \kappa \nabla_{\mathbf{x}}^2 N_1 + N_{0T} + (\mathbf{U} + \mathbf{u}') \cdot \nabla_{\mathbf{X}} N_0 = -\mu P_0 N_1 - \mu P_1 N_0 - \lambda N_1, \tag{28}$$

If we now consider P_1 and N_1 that can be divided into a mean part (that is a function of slow time variables only) and a fluctuating part, i.e., $P_1 = \overline{P}_1(\mathbf{X}, T) + P_1'(\mathbf{x}, t, \mathbf{X}, T)$. Averaging over small and fast scales gives:

$$P_{0T} + \mathbf{U} \cdot \nabla_{\mathbf{X}} P_0 = \mu P_0 \overline{N}_1 + \mu \overline{P}_1 N_0 - \lambda \overline{P}_1 \tag{29}$$

Subtracting Eq. (29) from Eq. (27) gives an expression for fluctuating parts P_1' and N_1':

$$(\partial_t + (\mathbf{U} + \mathbf{u}') \cdot \nabla_{\mathbf{x}} - \kappa \nabla_{\mathbf{x}}^2) \begin{bmatrix} P_1' \\ N_1' \end{bmatrix} - \mathcal{B} \begin{bmatrix} P_1' \\ N_1' \end{bmatrix} = -\mathbf{u}' \cdot \nabla_{\mathbf{X}} \begin{bmatrix} P_0 \\ N_0 \end{bmatrix}, \tag{30}$$

where $\mathcal{B}$ is $\begin{bmatrix} \mu N_0 - \lambda & \mu P_0 \\ -\mu N_0 & -\mu P_0 - \lambda \end{bmatrix}$. Solutions to Eq. (30) can be written in the form

$$\begin{bmatrix} P_1' \\ N_1' \end{bmatrix} = -\int dt' \mathrm{e}^{-\mathcal{B}(t-t')} (\xi \cdot \nabla_{\mathbf{X}}) \begin{bmatrix} P_0 \\ N_0 \end{bmatrix}, \tag{31}$$

Note that Eq. (30) is in close analogy to Eq. (20) for the passive tracer, but with a different ξ—the forcing in Eq. (21) is $u'\delta(t - t')$. The key differences being the $\mathcal{B}$ term resulting from the reactions and the coupling between N and P. The second order solution is

$$\mathcal{O}(\epsilon^2) : P_{2t} + (\mathbf{U} + \mathbf{u}') \cdot \nabla_{\mathbf{x}} P_2 - \kappa \nabla_{\mathbf{x}}^2 P_2 + P_{1T} + (\mathbf{U} + \mathbf{u}') \cdot \nabla_{\mathbf{X}} P_1 - 2\kappa \nabla_x \cdot \nabla_X P_1 - \kappa \nabla_X^2 P_0 = \mu P_0 N_2 + \mu P_2 N_0 - \lambda P_2 + \mu P_1 N_1 \tag{32}$$

Averaging over small and fast scales gives the solvability condition:

$$\overline{P}_{1T} + (\mathbf{U} + \mathbf{u}') \cdot \nabla_{\mathbf{X}} \overline{P}_1 - \kappa \nabla_X^2 P_0 = \mu P_0 \overline{N}_2 + \mu \overline{P}_2 N_0 - \lambda \overline{P}_2 + \mu \overline{P_1 N_1} \tag{33}$$

Summing over our results at $\mathcal{O}(1)$, $\mathcal{O}(\epsilon)$, and $\mathcal{O}(\epsilon^2)$ gives:

$$\overline{P}_T + \mathbf{U} \cdot \nabla_{\mathbf{X}} \overline{P} - \kappa \cdot \nabla_{\mathbf{X}}^2 \overline{P} + \overline{\mathbf{u}' \cdot \nabla_{\mathbf{X}} P'} = \mu \overline{P} \overline{N} - \lambda \overline{P} + \overline{\mu P' N'} \tag{34}$$

We can see that the evolution of the mean tracer concentration depends on the divergence of the eddy flux. It should also be noted that Eq. (31) suggests that the eddy fluxes can be expressed in terms of the large-scale gradients. A general equation for the eddy flux of any set of reactive tracers, b_α, can be derived in terms of the Lagrangian covariance, as in [4]. For example, Eq. (31) can be expressed in terms of a Green's function

$$b_\alpha' = -\int d\mathbf{x}' dt' \ \mathrm{e}^{-\mathcal{B}_{\alpha\beta}(t-t')} G(\mathbf{x} - \mathbf{x}', t - t') u'(\mathbf{x}', t') \frac{\partial}{\partial x} \bar{b}_\beta(\mathbf{x}', t') \tag{35}$$

$$\overline{u'b'_\alpha} = -\int d\mathbf{x}' dt' \; \mathrm{e}^{-\mathcal{B}_{\alpha\beta}(t-t')} \overline{u'(\mathbf{x},t)G'(\mathbf{x}-\mathbf{x}',t-t')u'(\mathbf{x}',t')} \frac{\partial}{\partial x} \bar{b}_\beta(\mathbf{x}',t') \tag{36}$$

The $\mathbf{x}'$ integral will give the Lagrangian covariance, R_{ij},

$$R_{ij}(t-t') = \int d\mathbf{x}' \; \overline{u'(\mathbf{x},t)G'(\mathbf{x}-\mathbf{x}',t-t')u'(\mathbf{x}',t')} \tag{37}$$

Thus the eddy flux is

$$\overline{u'b'_\alpha} = -\int dt' \; \mathrm{e}^{-\mathcal{B}_{\alpha\beta}(t-t')} R_{ij}(t-t') \frac{\partial}{\partial x_j} \bar{b}_\beta \tag{38}$$

In the case of the nutrient-phytoplankton system, we can see from Eq. (31) that there is a coupling between N and P in the time-dependent components. Therefore, the mixing-length analogy would have the form

$$\overline{u'P'} = -K_{PP}\nabla_{\mathbf{X}}\overline{P} - K_{PN}\nabla_{\mathbf{X}}\overline{N} \tag{39}$$

$$\overline{u'N'} = -K_{NP}\nabla_{\mathbf{X}}\overline{P} - K_{NN}\nabla_{\mathbf{X}}\overline{N} \tag{40}$$

We can solve for these effective diffusivities by exploiting the eddy flux of S, which is simpler since Eq. (7) has no nonlinear reaction terms.

$$\overline{u'S'} = -K^\lambda \nabla \overline{S} \tag{41}$$

$$\overline{u'P'} + \overline{u'N'} = -K^\lambda(\nabla\overline{P} + \nabla\overline{N}) \tag{42}$$

Defining $A = P' + aS'$ and taking the evolution equation allows us to solve $a = -\mu\overline{P}/\mu\overline{P} - \lambda$. Then since $\overline{u'A'} = -K^{\mu\overline{P}}\nabla\overline{A} = \overline{u'P'} + a\overline{u'S'}$ we can plug in a and $\overline{u'S'}$ from above to solve for the effective diffusivities in Eq. (39) and (40). This gives

$$\overline{u'P'} = -\frac{\mu\overline{P}K^\lambda - \lambda K^{\mu\overline{P}}}{\mu\overline{P} - \lambda}\nabla\overline{P} - \frac{\mu\overline{P}(K^\lambda - K^{\mu\overline{P}})}{\mu\overline{P} - \lambda}\nabla\overline{N} \tag{43}$$

$$\overline{u'N'} = -\frac{\lambda(K^{\mu\overline{P}} - K^\lambda)}{\mu\overline{P} - \lambda}\nabla\overline{P} - \frac{\mu\overline{P}K^{\mu\overline{P}} - \lambda K^\lambda}{\mu\overline{P} - \lambda}\nabla\overline{N} \tag{44}$$

We can investigate when the cross term will become important by taking the ratio of K_{PP}/K_{PN} using the expressions for the effective diffusivities from Eq. (43).

$$\frac{K_{PP}}{K_{PN}} = \frac{K^\lambda - \frac{\lambda}{\mu\overline{P}}K^{\mu\overline{P}}}{K^\lambda - K^{\mu\overline{P}}} \tag{45}$$

From Eq. (45) we can see that K_{PP}/K_{PN} depends on the size of $\lambda/\mu\overline{P}$. Plugging in the leading order approximation $\overline{P} = N_D - \lambda/\mu$, we find that the importance of the cross term to the eddy flux depends on the ratio of reaction rates via a parameter that we'll call Rx

$$Rx = \frac{1}{\frac{\mu}{\lambda} - 1} \tag{46}$$

The results from this section demonstrate how the gradient-diffusion hypothesis results from the tracer evolution equations. However, the multiple scale analysis depends on there being a space and time scale separation between the turbulent eddies and the leading order biological behavior. Therefore, we might expect the relationship to break down when the timescales of the turbulent motions and reactions are similar. This is examined in the next section by investigating the dynamics of the nutrient-phytoplankton system in a 2-D stirring flow across a range of parameter values.

4 Numerical Simulations

4.1 Model setup

Here, we consider a 2-D stirring flow similar to the one in *Pierrehumbert* (2000). The velocity fields are generated by a streamfunction of the form

$$\Psi = \sum_{n=1}^{4} U_n \cos(k_{1n}x + k_{2n}y + \theta_n) \tag{47}$$

where the wavenumbers are selected so that the kinetic energy spectrum from the resultant velocity field has a $k^{-5/3}$ slope. The θ_n component is a randomized phase shift added at each time step to ensure that things are stirred up. Eq. (47) is essentially a simple way of generating a zero-mean, 2-D turbulent-like flow. The model domain is $4\pi \times 4\pi$ and doubly-periodic.

The physical model is coupled to the nutrient-phytoplankton system given by Eq. (5) and (6). N and P transport is represented by a first order upwind advection scheme. For example, the fluxes of a tracer, c, in the x and y direction, F_x and F_y, are given by

$$F_x = \frac{u}{\Delta x}(c^n_{i,j} - c^n_{i-1,j}),\ F_y = \frac{v}{\Delta y}(c^n_{i,j} - c^n_{i,j-1}) \tag{48}$$

A sinusoidal distribution is selected for μ, the uptake rate, which goes to 0 at the northern and southern boundary of the domain. Assuming that our model domain is an ocean basin, this north-south μ gradient is motivated by the fact that phytoplankton growth is light-dependent and there is a planetary-scale gradient of incoming solar radiation. A constant value is used for λ, the entrainment rate, although this could be spatially variable in principle. The initial N distribution is also selected to be sinusoidal, although with an east-west gradient to distinguish it from gradients in μ. The initial P distribution is determined from the leading order P solution in the multiple scale analysis ($P = N_D - \lambda/\mu$). Figure 4 gives an example of the N and P fields at discrete times for one of the simulations.

Our goal is to assess the validity of mixing-length theory, and the sensitivity of this result to different parameters. In order to do this, we can exploit the fact that the velocity field from Eq. (47) is zero-mean. Therefore, the tracer fluxes from the upwind advection scheme, i.e., Eq. (48), are equal to the eddy fluxes $\overline{u'P'}$ and $\overline{u'N'}$. It is also straightforward to calculate the gradients $\nabla\overline{P}$, and $\nabla\overline{N}$ from the mean tracer distributions. Using the time-averaged eddy fluxes and gradients in the mean fields (after the simulation reaches steady-state) we can then compute an effective diffusivity via a least squares fit assuming Eq. (1) holds. Comparing the actual diagnosed eddy flux with $K_e\nabla\overline{c}$ at each grid point

allows us to assess the validity of the mixing-length relationship. In the case where mixing-length theory holds perfectly, these points would all fall on the $1:1$ line. Figure 5 gives an example of what this looks like for the simulation depicted in Figure 4. Clearly the points do not depict the perfect linear relationship, and we can calculate the R^2 value to quantify the goodness of the fit. R^2 values near 1 suggest that the mixing length relationship holds, whereas smaller R^2 values indicate a break down of the theory. In the next section, we will show how varying different parameters impacts the validity of $\overline{u'c'} = K_e \nabla \overline{c}$.

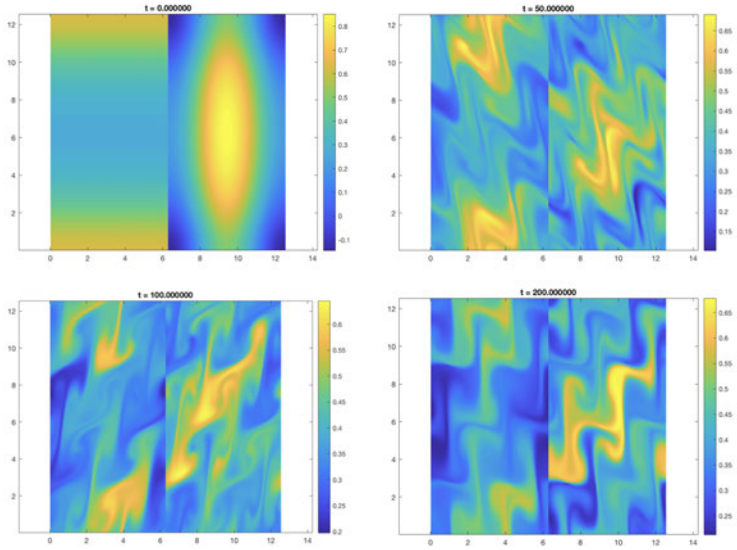

Figure 4: N (left) and P (right) for one of the simulations at (a) $t = 0$, (b) $t = 50$, (a) $t = 100$, (d) $t = 200$.

4.2 Perturbation experiments

We can gain some intuition into the parameters that control the efficacy of the mixing-length assumption by considering the nondimensionalized N-P model, Eq. (13) and (14). The biological reaction terms scale with Da, so in cases where $Da \ll 1$, the reaction terms are negligible at leading order and we can treat N and P as passive tracers. The other nondimensional parameters that may be important are Pe and the ratio of reaction rates, λ/μ. Several runs with varied molecular κ suggest that results are insensitive to changes in Pe. However, the system responds strongly to variations in Da and λ/μ. For example, the variance of the equilibrium P and N concentration is much higher when $Da \sim \mathcal{O}(1)$ due to the interaction between the stirring and biological growth (Figure 6). In the limit of slow or fast growth relative to the mixing, the system reaches an equilibrium that is much more homogeneous.

The validity of the mixing-length assumption, as measured by the R^2 value described in Section 4.1, also varies with Da. When $Da \ll 1$ the mixing-length theory holds—whether you consider $\overline{u'P'} = -K_e \nabla \overline{P}$ (Figure 7a) or $\overline{u'P'} = -K_{PP} \nabla \overline{P} - K_{PN} \nabla \overline{N}$ (Figure 7b). This result can be understood by remembering that when $Da \ll 1$, biological reaction terms are not important at leading order and thus N and P can be treated like passive tracers. When

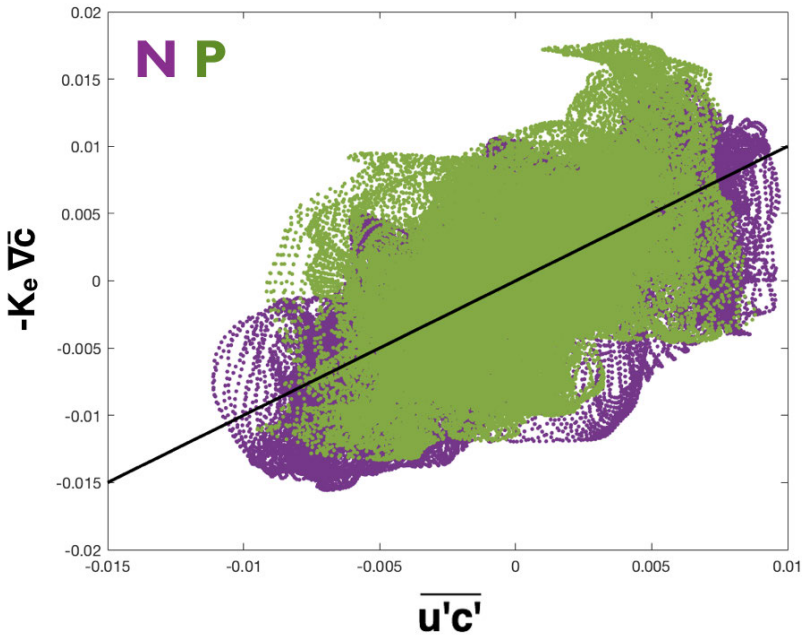

Figure 5: Calculated eddy flux of N (purple) and P (green) assuming that the mixing-length relationship holds vs the diagnosed eddy flux.

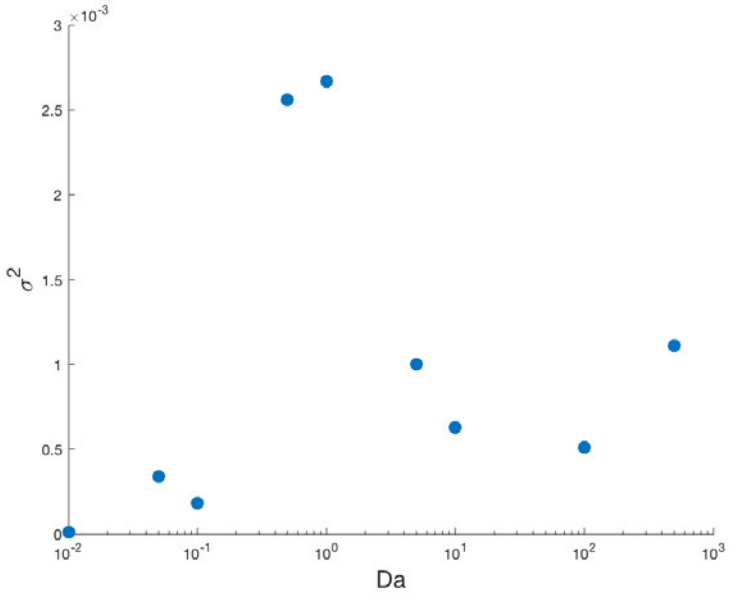

Figure 6: Variance of equilibrium P concentration versus Da.

$Da \sim \mathcal{O}(1)$, R^2 values are much lower (< 0.3), suggesting a break down of mixing-length theory. Recall that the derivation of the gradient-diffusion eddy flux relied on a space and time scale separation between the turbulent eddies and mean tracer concentration structure. This assumption will necessarily be violated when $Da \sim \mathcal{O}(1)$. When $Da \gg 1$, the R^2 values are larger than for $Da \sim \mathcal{O}(1)$, although there can be a significant difference between the R^2 if you assume $\overline{u'P'} = -K_e \nabla \overline{P}$ versus $\overline{u'P'} = -K_{PP} \nabla \overline{P} - K_{PN} \nabla \overline{N}$.

To understand the importance of the cross term, $K_{PN} \nabla \overline{N}$, recall the parameter Rx defined by Eq. (46), which is a measure of K_{PP}/K_{PN}. We can plot Rx as a function of μ/λ (Figure 8). Then we can calculate both of these ratios from our simulations and plot them colored by Da. Notice that for $Da \ll 1$, $K_{PP}/K_{PN} > 1$ regardless of μ/λ. Under this regime, the biological reaction terms are not important at leading order and so the eddy fluxes of N and P do not depend on the cross terms (i.e., N and P are effectively passive tracers). When $Da \sim \mathcal{O}(1)$, the points are scattered, perhaps because the mixing-length relationship itself breaks down under this regime. However, when $Da \gg 1$, the points fall closely on the predicted K_{PP}/K_{PN} curve. In other words, there are parameter regimes where the cross terms are important (and even dominant) in controlling the behavior of the eddy fluxes. For example, when $\mu/\lambda \gg 1$, $K_{PN} > K_{PP}$. Based on the nondimensionalized P equation (Eq. 14), this is when the entrainment term is negligible and thus the biological behavior is governed solely by the nonlinear growth term (which explicitly couples N and P). The fact that K_{PN} can actually be greater than K_{PP} has implications for climate models, which use more complex biological models and thus have even more cross terms that may be important in accurately representing the eddy fluxes.

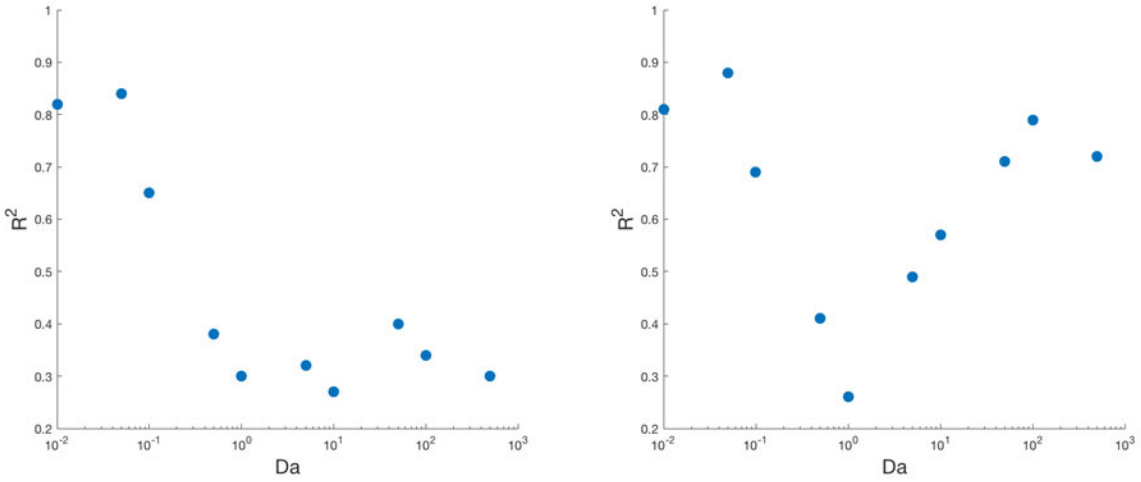

Figure 7: R^2 of the mixing-length eddy flux and "true" eddy flux versus Da assuming (a) $\overline{u'P'} = -K_e \nabla \overline{P}$ and (b) $\overline{u'P'} = -K_{PP} \nabla \overline{P} - K_{PN} \nabla \overline{N}$

5 Ocean Modeling Implications

We showed in Section 4 that there are certain parameter regimes where the gradient-diffusion hypothesis fails to represent the true eddy fluxes of N and P. But do these parameter

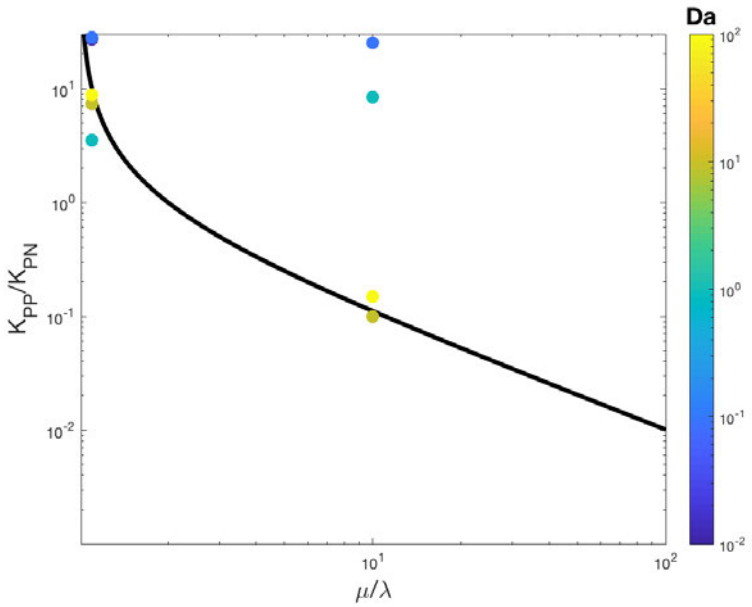

Figure 8: Theoretical prediction of K_{PP}/K_{PN} versus μ/λ (black line) and scatter points showing results from simulations (colored by Da).

regimes exist in the real ocean? And are these differences large enough to affect global biogeochemical budgets? The first question can be easily addressed. Damköhler numbers for various physical and biogeochemical processes in the ocean are given in Figure 9.

	Small scale $\tau_t \sim 10^2$s	Submesoscale $\tau_t \sim 10^5$s	Mesoscale $\tau_t \sim 10^7$s	Large scale $\tau_t \sim 10^8$s
Chemical Processes [2]				
Surface transfer of CO_2: $\tau \sim$1s	10^2	10^5	10^7	10^8
Hydration/hydroxylation: $\tau \sim$10s	10^1	10^4	10^6	10^7
Protolysis/hydrolysis: $\tau \sim 10^{-7}$s	10^9	10^{12}	10^{14}	10^{15}
Equilibration of CO_2: $\tau \sim 10^2$s	1	10^3	10^5	10^6
Biological Processes [52]				
Nutrient uptake: $\tau \sim 10^5$s	10^{-3}	1	10^2	10^3
Phytoplankton growth: $\tau \sim 10^5$s	10^{-3}	1	10^2	10^3
Phytoplankton loss: $\tau \sim 10^5$s	10^{-3}	1	10^2	10^3
Zooplankton growth: $\tau \sim 10^5$s	10^{-3}	1	10^2	10^3
Zooplankton loss: $\tau \sim 10^6$s	10^{-4}	0.1	10	10^2
Zooplankton reaction: $\tau \sim$10s	10^1	10^4	10^6	10^7

Figure 9: Da for various physical and biogeochemical processes in the ocean (Table from Kat Smith).

The approximate timescales associated with submesoscale processes and phytoplankton growth in the euphotic zone are comparable, $\mathcal{O}$(1 day). Therefore, we do expect that $Da \sim \mathcal{O}(1)$ regimes, where the mixing-length theory breaks down, apply to phytoplankton transport by submesoscale eddies. The implications of this are significant. Our results

suggest that parameterizations of sub-grid scale nutrient and phytoplankton eddy fluxes are invalid at submesoscales, but submesoscale productivity is known to be an important component in biogeochemical cycles [8, 13].

To investigate the error associated with applying the mixing-length theory in $Da \sim \mathcal{O}(1)$ regimes, we consider output from the Biogeochemical Southern Ocean State Estimate (B-SOSE). B-SOSE is an eddy-permitting, data assimilative model that uses ocean observations to constrain the MITgcm solution [17]. The configuration used in this analysis has $1/6^o$ horizontal resolution, 42 uneven vertical levels, and runs from January 1, 2013 to December 31, 2017. The motivation for using B-SOSE is twofold. First, productivity in the Southern Ocean has a dramatic seasonal cycle, so there are few zooplankton grazers at the time of spring bloom initiation. Thus, our simple nutrient-phytoplankton model may represent plankton dynamics better here than in other regions. Second, the Southern Ocean plays a major role in the global ocean circulation and carbon cycle through deep water formation and interbasin exchange. Therefore, understanding the magnitude of error in the mixing-length assumption in the Southern Ocean is key to determining the global implications.

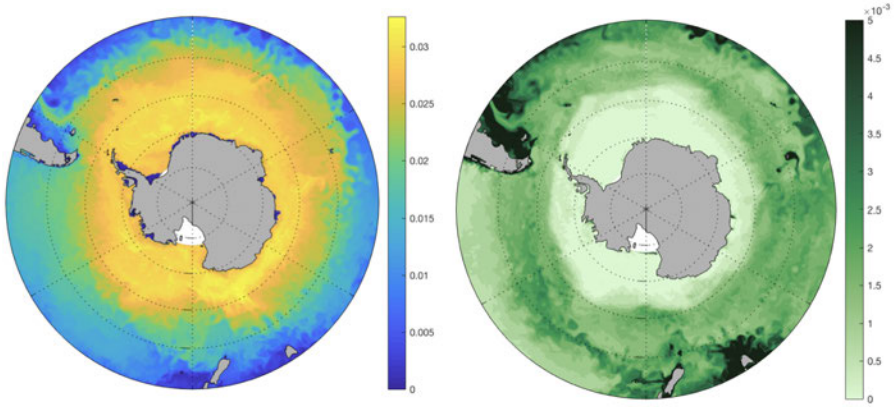

Figure 10: November 2013 mixed-layer averaged (a) nitrate [mol N/m^3] and (b) phytoplankton biomass [mol C/m^3] from B-SOSE.

Figure 10 shows maps of mixed-layer averaged nitrate and phytoplankton biomass for November 2013. This is early austral spring—roughly the time of bloom initiation in much of the Southern Ocean—and thus zooplankton terms may be negligible. Since the ultimate goal is to determine a feasible way of improving upon the accuracy of the eddy fluxes, we examine the inclusion of the cross term in Eq. (39) and (40). Figure 8 suggests that there are some regimes where the cross term actually dominates the eddy flux, and including a cross term in a climate model would be simple to do in practice. Gradients in N and P are calculated from the nitrate and phytoplankton biomass maps shown above. Note that phytoplankton biomass is converted from [mol C/m^3] to [mol N/m^3] using the Redfield ratio [14]. Using these gradients in N and P from B-SOSE, we calculate the eddy fluxes of P first assuming the standard gradient-diffusion hypothesis -$K_e\nabla\overline{P}$, and then including the cross term -$K_{PP}\nabla\overline{P}$-$K_{PN}\nabla\overline{N}$. Values for K_e, K_{PP}, and K_{PN} are chosen from the least-squares fitted effective diffusivities in one of the simulations from Section 4. The difference between these two eddy fluxes is shown in Figure 11. We can think of this map as showing the locations where the cross term significantly changes the magnitude of the eddy

flux. The basin-averaged discrepancy is minimal, but in some cases, such as around the Malvinas Current, these differences can be as large as 80% of the total eddy flux. This could have impacts on the distribution of upper trophic level organisms and spatial variability in biogenic carbon uptake. While the diffusivity values used here are not meaningful within B-SOSE, this calculation still suggests that accounting for the cross term could be important in regions with large gradients and low covariance between N and P. Furthermore, in more complex biological models—such as the eight component model used in B-SOSE—there are even more cross terms that might be relevant. Including cross terms could be a practical way to improve the accuracy of modeled eddy fluxes.

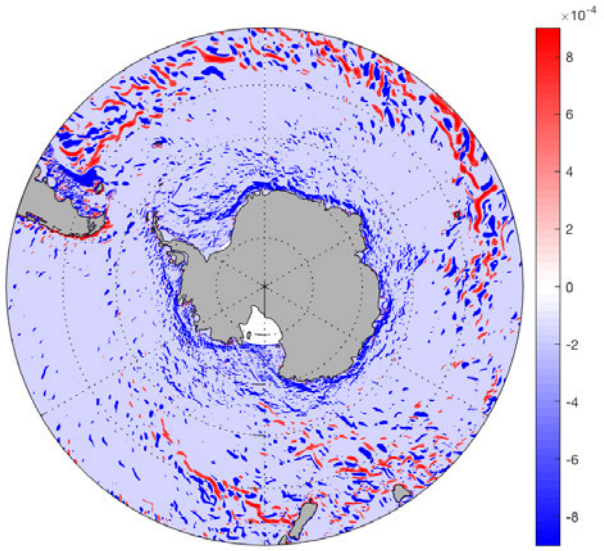

Figure 11: Map of $(-K_e\nabla\overline{P})-(-K_{PP}\nabla\overline{P}-K_{PN}\nabla\overline{N})$.

6 Conclusion

Phytoplankton biomass is quite patchy and spatially variable at the mesoscale and submesoscale, which has important implications for marine ecosystems and the global carbon cycle. Observational evidence suggests that turbulent eddies exert significant control over the distribution of phytoplankton at these scales. Understanding this coupling between physics and biology is necessary given the key role of (sub-)mesoscale productivity in global biogeochemical budgets. Since climate models do not resolve these scales, the transport of tracers associated with the unresolved dynamics must be parameterized. Here, we showed that the gradient-diffusion hypothesis, $-K_e\nabla\bar{c}$, is not necessarily a valid way of parameterizing eddy fluxes of reactive tracers. A multiple scale analysis suggests that this form of the mixing-length assumption is only valid when there is a time scale separation between the reaction and turbulent eddies, as well as a scale separation between the turbulent eddies and the mean tracer concentration structure. This is an important result for the climate modeling community since $Da \sim \mathcal{O}(1)$ for phytoplankton growth in submesoscale eddies, therefore the error associated with applying gradient-diffusion to represent eddy fluxes of

phytoplankton at the submesoscale could be significant.

For the idealized nutrient-phytoplankton system we considered, gradients in both N and P may be important to the eddy flux of either tracer. The significance of this cross term to the total eddy flux is determined by the ratio of the growth rate, μ, to the entrainment rate, λ. Adding this sort of cross term into a climate model could potentially provide a practical way of improving the representation of eddy fluxes of nutrients and phytoplankton. Perhaps a scheme that depends on the covariance between different model fields or incorporating an effective diffusivity that varies with reaction rates are possible avenues to pursue as well. Investigating these possibilities is necessary in order to improve the parameterization of submesoscale primary productivity, which in turn will help us to better predict the evolution of the oceanic carbon cycle on longer time scales.

7 Acknowledgments

Thanks to Glenn Flierl for his unwavering patience and vast knowledge of the topic. Thanks also to Kat Smith for helping make this project happen and offering essential advice at every step along the way. Alexis Kaminski, Charlie Doering, Amala Mahadevan, and Mara Freilich all provided useful feedback as well. Thanks to Julie Hildebrandt and Janet Fields, as well as the directors: Claudia Cenedese, Karl Helfrich, and Bruce Sutherland, who all worked hard to make sure the program ran smoothly. Finally, thanks to all the GFD staff and fellows for making the summer so enjoyable!

References

[1] Abraham, E. (1998). The generation of plankton patchiness by turbulent stirring. *Nature*, **391**, 577–580.

[2] Falkowski, P. G., D. Ziemann, Z. Kolber, and P. K. Bienfang (1991). Role of eddy pumping in enhancing primary production in the ocean. *Nature*, **352**, 55–58.

[3] Flierl, G., and D. J. McGillicuddy (2002). Mesoscale and submesoscale physical-biological interactions, in *Biological-Physical Interactions in the Sea*, A. R. Robinson, J. J. McCarthy, and B. J. Rothschild, Eds., *The Sea-Ideas and Observations on Progress in the Study of the Seas*, Vol. 12, John Wiley and Sons, 113–185.

[4] Flierl, G. Eddy fluxes of passive and reacting scalars.

[5] Franks, P. J. S. (2002). NPZ models of plankton dynamics: their construction, coupling to physics, and application. *Journal of Oceanography*, **58**, 379–387.

[6] Freilich, M. A., and A. Mahadevan (2019). Decomposition of vertical velocity for nutrient transport in the upper ocean. *Journal of Physical Oceanography*, **49**, 1561–1575.

[7] Ganachaud, A., and C. Wunsch (2002). Oceanic nutrient and oxygen transports and bounds on export production during the World Ocean Circulation Experiment. *Global Biogeochemical Cycles*, **16**, 1057.

[8] Levy, M., and A. P. Martin (2013). The influence of mesoscale and submesoscale heterogeneity on ocean biogeochemical reactions. *Global Biogeochemical Cycles*, **27**, 1139–1150.

[9] Lutz, T. Spooky Mixing at a Distance: Nonlocal Mixing from Stochastic Advection. Proceedings Volume of the 2018 Geophysical Fluid Dynamics Program.

[10] McGillicuddy, D. J. (2016). Mechanisms of physical-biological-biogeochemical interaction at the oceanic mesoscale. *Annual Review of Marine Science*, **8**, 125–159.

[11] Papanicolaou, G. and O. Pirroneau (1981). On the asymptotic behavior of motion in random flows, in *Stochastic Nonlinear Systems*, ed. L. Arnold and R. Lefever, Springer, 36–41.

[12] Pierrehumbert, R. T. (2000). Lattice models of advection-diffusion. *Interdisciplinary Journal of Nonlinear Science*, **10**, 61–74.

[13] Platt, T., and S. Sathyendranath (1988). Oceanic primary production: Estimation by remote sensing at local and regional scales. *Science*, **241**, 1613–1620.

[14] Redfield, A. C. (1934). On the proportions of organic derivatives in seawater and their relation to the composition of plankton. in *James Johnstone Memorial Volume*, 176–192 (Liverpool Univ. Press, Liverpool, 1934).

[15] Rintoul, S. R., and C. Wunsch (1991). Mass, heat, oxygen and nutrient fluxes and budgets in the North Atlantic Ocean. *Deep-Sea Research I*, **38**, 355–377.

[16] Taylor, G. I. (1921). Diffusion by continuous movements. *Proceedings of the Royal Society A*, **20**, 196–211.

[17] Verdy, A., and M. R. Mazloff (2017). A data assimilating model for estimating Southern Ocean biogeochemistry. *Journal of Geophysical Research: Oceans*, **122**, 6968–6988.

Reduced Models for Wave-balanced Flow Interactions

André Palóczy

August 19, 2019

1 Introduction and goals

Energy pathways in the ocean encompass the full range of scales from planetary, O(10^7 m) down to microscales, O(10^{-2} m). Energy is introduced in the ocean mostly at seasonal, planetary scales by the time-mean atmospheric forcing; at diurnal, planetary scales by the most energetic modes of the barotropic tide; and in the weather band (days to weeks) by the synoptic weather systems. This energy must either leave the ocean or be converted into internal energy at the Kolmogorov scale, O(1 cm) [3].

The routes mechanical energy takes from injection to dissipation in the ocean are currently an open problem. A group of candidates that has been gaining attention over the past decade includes processes involving the interaction of near-inertial waves (NIWs) with the mesoscale balanced flow, *e.g.*, [13, 12, 7]. Two broad classes of such processes can be identified: The first is generation of NIWs by mesoscale and submesoscale instabilities, oftentimes called *spontaneous* loss of balance. The second is the interaction of the balanced flow with existing NIWs by processes such as refraction, advection and dispersion, a mechanism that has been more studied in recent years and has been called *stimulated* loss of balance, *e.g.*, [7].

The goals of this project are to: **1)** Study the energy exchanges between NIWs and the balanced flow using idealized simulations and **2)** To derive a new asymptotic model to help develop an understanding of such interactions.

2 Non-asymptotic reduced models

2.1 The modified Thomas & Yamada (2019) model

The primary tool we employ in this work is a slightly modified form of the reduced model used by [10]. The starting point is the hydrostatic Boussinesq equations, with the assumption of constant buoyancy frequency N:

$$\boldsymbol{u}_t + \boldsymbol{u}\cdot\boldsymbol{\nabla}\boldsymbol{u} + w\boldsymbol{u}_z + \boldsymbol{f}\times\boldsymbol{u} + \boldsymbol{\nabla}p = 0, \tag{1}$$

$$p_z = b, \tag{2}$$

$$b_t + \boldsymbol{u}\cdot\boldsymbol{\nabla}b + wN^2 = 0, \tag{3}$$

$$\boldsymbol{\nabla}\cdot\boldsymbol{u} + w_z = 0, \tag{4}$$

where (u, v, w) are the velocity components of $\boldsymbol{u}$ in the $(\hat{\boldsymbol{x}}, \hat{\boldsymbol{y}}, \hat{\boldsymbol{z}})$ directions, respectively, p is pressure (normalized by a reference density ρ_0), $b \equiv -g\rho'/\rho_0$ is the buoyancy (where ρ' is the perturbation pressure), $\boldsymbol{\nabla} \equiv \hat{\boldsymbol{x}}\partial_x + \hat{\boldsymbol{y}}\partial_y$ is the horizontal gradient operator, $\boldsymbol{f} \equiv \hat{\boldsymbol{z}} f$ (where f is the inertial frequency) and N is the buoyancy frequency. We expand all variables in the following form:

$$\boldsymbol{u}(\boldsymbol{x}, z, t) = \boldsymbol{u_0}(\boldsymbol{x}, t) + \sum_{n=1}^{\infty} \boldsymbol{u}(\boldsymbol{x}, t)\phi_n'(z) \tag{5}$$

$$w(\boldsymbol{x}, z, t) = \sum_{n=1}^{\infty} w(\boldsymbol{x}, t)\phi_n(z) \tag{6}$$

$$p(\boldsymbol{x}, z, t) = p_0(\boldsymbol{x}, t) + \sum_{n=1}^{\infty} \lambda_n^{-2} p_n(\boldsymbol{x}, t)\phi_n'(z) \tag{7}$$

$$b(\boldsymbol{x}, z, t) = -\sum_{n=1}^{\infty} p_n(\boldsymbol{x}, t)N^2\phi_n(z) \tag{8}$$

where $\phi_{n=0}(z) = 1$, $\phi_{n>0} = \sin(n\pi z)$ is the solution of the Sturm-Liouville problem with constant stratification $N(z) = 1$ and rigid lid boundary conditions, *i.e.*,

$$\phi_n'' + \lambda_n^2 N^2 \phi_n = 0, \quad \text{with} \quad \phi_n(0) = \phi_n(1) = 0 \tag{9}$$

where the eigenvalues are $\lambda_{n=0} = 0$ and $\lambda_{n>0} = n\pi$.

Restricting 5-8 to the barotropic mode (subscript T) and the n-th baroclinic mode (subscript C) gives

$$\boldsymbol{u}(\boldsymbol{x}, t), p(\boldsymbol{x}, t) = [\boldsymbol{u_T}(\boldsymbol{x}, t), p_T(\boldsymbol{x}, t)] + [\boldsymbol{u_C}(\boldsymbol{x}, t), p_C(\boldsymbol{x}, t)] \times \sqrt{2}\cos\left(\frac{n\pi z}{H}\right) \tag{10}$$

$$w(\boldsymbol{x}, t), b(\boldsymbol{x}, t) = [w_C(\boldsymbol{x}, t), b_C(\boldsymbol{x}, t)] \times \sqrt{2}\sin\left(\frac{n\pi z}{H}\right), \tag{11}$$

Substituting 10-11 into 1-4 and using the orthogonality property of the modes results in equations similar to the linear shallow water equations for the n-th baroclinic mode ($n \geq 1$):

$$\partial_t \boldsymbol{u_T} + \boldsymbol{f} \times \boldsymbol{u_T} + \boldsymbol{\nabla} p_T + \mathrm{Ro}\big[\boldsymbol{u_T} \cdot \boldsymbol{\nabla}\boldsymbol{u_T} + \boldsymbol{u_C} \cdot \boldsymbol{\nabla}\boldsymbol{u_C} + \big(\boldsymbol{\nabla} \cdot \boldsymbol{u_C}\big)\boldsymbol{u_C}\big] = 0, \tag{12}$$

$$\boldsymbol{\nabla} \cdot \boldsymbol{u_T} = 0, \tag{13}$$

$$\partial_t \boldsymbol{u_C} + \boldsymbol{f} \times \boldsymbol{u_C} + \boldsymbol{\nabla} p_C + \mathrm{Ro}\big(\boldsymbol{u_T} \cdot \boldsymbol{\nabla}\boldsymbol{u_C} + \boldsymbol{u_C} \cdot \boldsymbol{\nabla}\boldsymbol{u_T}\big) = 0, \tag{14}$$

$$\partial_t p_C + \left(\frac{NH}{n\pi}\right)^2 \boldsymbol{\nabla} \cdot \boldsymbol{u_C} + \mathrm{Ro}\big(\boldsymbol{u_T} \cdot \boldsymbol{\nabla} p_C\big) = 0, \tag{15}$$

where the Rossby number is (with characteristic velocity and horizontal length scales U and L, respectively)

$$\mathrm{Ro} \equiv \frac{U}{fL}. \tag{16}$$

Taking curl of the T-mode's momentum equation 12 to eliminate p_T,

$$\partial_t \zeta_T + \mathrm{Ro}\boldsymbol{\nabla} \times \left[\boldsymbol{u_T} \cdot \boldsymbol{\nabla} \boldsymbol{u_T} + \boldsymbol{u_C} \cdot \boldsymbol{\nabla} \boldsymbol{u_C} + (\boldsymbol{\nabla} \cdot \boldsymbol{u_C})\boldsymbol{u_C}\right] = 0, \tag{17}$$

where $\zeta_T \equiv \partial_x v_T - \partial_y u_T$. Rescaling the baroclinic pressure as $p_C \to \mathrm{Bu}_n p_C$ gives the final set of equations:

$$\partial_t \zeta_T + \mathrm{Ro}\boldsymbol{\nabla} \times \left[\boldsymbol{u_T} \cdot \boldsymbol{\nabla} \boldsymbol{u_T} + \boldsymbol{u_C} \cdot \boldsymbol{\nabla} \boldsymbol{u_C} + (\boldsymbol{\nabla} \cdot \boldsymbol{u_C})\boldsymbol{u_C}\right] = 0, \tag{18}$$

$$\partial_t \boldsymbol{u_C} + \hat{\boldsymbol{z}} \times \boldsymbol{u_C} + \mathrm{Bu}_n \boldsymbol{\nabla} p_C + \mathrm{Ro}\big(\boldsymbol{u_T} \cdot \boldsymbol{\nabla} \boldsymbol{u_C} + \boldsymbol{u_C} \cdot \boldsymbol{\nabla} \boldsymbol{u_T}\big) = 0, \tag{19}$$

$$\partial_t p_C + \boldsymbol{\nabla} \cdot \boldsymbol{u_C} + \mathrm{Ro}\big(\boldsymbol{u_T} \cdot \boldsymbol{\nabla} p_C\big) = 0, \tag{20}$$

where the modal Burger number is (with a characteristic vertical length scale H)

$$\mathrm{Bu}_n \equiv \left(\frac{NH}{\lambda_n f L}\right)^2 \tag{21}$$

where the baroclinic mode is a high mode, rather than the first baroclinic mode considered by [10].

Two-dimensional models obtained from truncating three-dimensional equations to few modes have been used elsewhere in the literature, *e.g.*, [4, 2]. We call this the modified Thomas & Yamada (2019) model because [10] treated only the particular case where $\mathrm{Bu} = 1$, relevant to the first mode of the internal tide rather than near-inertial waves. This difference can be seen by considering the nondimensional dispersion relation for inertia-gravity waves:

$$\omega^2 = f^2(1 + \mathrm{Bu}_w), \tag{22}$$

where ω is the wave frequency, $\mathrm{Bu}_w \equiv [Nk_h/(fk_z)]^2$ is the wave Burger number, $k_h \equiv \sqrt{k_x^2 + k_y^2}$ is the magnitude of the horizontal wavenumber vector and k_z is the vertical component of the wavenumber vector. Since near-inertial waves have more energy content in high baroclinic modes, $\omega \approx f$, due to which $\mathrm{Bu}_w \ll 1$. This is the limit considered in this project. The dynamical components of the system described by 18-20 are represented schematically in Figure 1. The barotropic mode ($T-$mode) contains only geostrophically balanced energy, while the baroclinic mode contains both balanced energy ($G-$mode) and unbalanced inertia-gravity wave energy.

In order to further specialize the model to study the interactions between near-inertial waves and balanced flows, we supress the G-mode at every time step by inverting the linear baroclinic potential vorticity $q \equiv \zeta_C - p_C = \zeta_G - p_G$ and subtracting out the balanced velocity from the total baroclinic velocity vector $\boldsymbol{u_C}$. This is possible because only the balanced flow projects on q, since near-inertial waves have no linear potential vorticity.

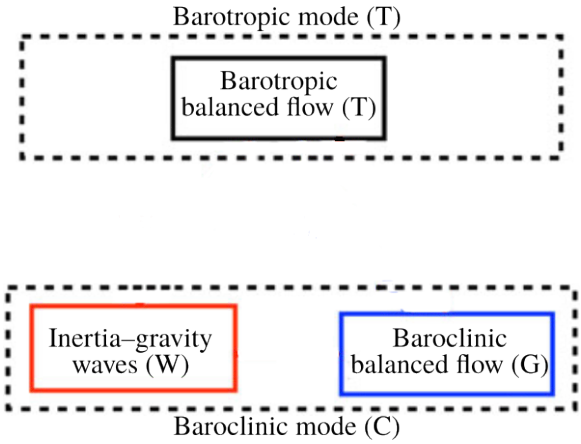

Figure 1: Schematic showing the three components of the modified Thomas & Yamada (2019) model: The barotropic mode (T-mode) consists only of purely geostrophically-balanced flow, while the baroclinic mode consists of geostrophically-balanced flow (G-mode) and unbalanced (near-inertial) wave motions (W-mode).

2.2 The coupled T-W model

A more elegant and less artificial approach to isolate interactions between near-inertial waves and a balanced barotropic flow is to seek a simpler, two-component model (Figure 2) where the prognostic variables are pure wave quantities. We start from the equations of motion (with the C subscript dropped):

$$\partial_t \boldsymbol{u_T} + \hat{\boldsymbol{z}} \times \boldsymbol{u_T} + \boldsymbol{\nabla} p_T = \boldsymbol{F_T^u}, \tag{23}$$
$$\partial_t \boldsymbol{u} + \hat{\boldsymbol{z}} \times \boldsymbol{u} + \mathrm{Bu} \boldsymbol{\nabla} p = \boldsymbol{F^u}, \tag{24}$$
$$\partial_t p + \boldsymbol{\nabla} \cdot \boldsymbol{u} = \boldsymbol{F^p}, \tag{25}$$

where $\boldsymbol{u}$ and $\boldsymbol{u_T}$ are, respectively, the baroclinic (wavy) and barotropic (geostrophically balanced) velocities and

$$\boldsymbol{F_T^u} \equiv -\mathrm{Ro}\big[\boldsymbol{u_T} \cdot \boldsymbol{\nabla} \boldsymbol{u_T} + \boldsymbol{u} \cdot \boldsymbol{\nabla} \boldsymbol{u} + (\boldsymbol{\nabla} \cdot \boldsymbol{u}) \boldsymbol{u}\big], \tag{26}$$
$$\boldsymbol{F^u} \equiv -\mathrm{Ro}\big(\boldsymbol{u_T} \cdot \boldsymbol{\nabla} \boldsymbol{u} + \boldsymbol{u} \cdot \boldsymbol{\nabla} \boldsymbol{u_T}\big), \tag{27}$$
$$\boldsymbol{F^p} \equiv -\mathrm{Ro}\big(\boldsymbol{u_T} \cdot \boldsymbol{\nabla} p\big) \tag{28}$$

we can define a velocity potential ϕ and a streamfunction χ such that

$$u = \phi_x - \chi_y, \tag{29}$$
$$v = \phi_y + \chi_x, \tag{30}$$
$$u + iv = \underbrace{(\partial_x + i\partial_y)}_{\equiv \partial_s} \underbrace{(\phi + i\chi)}_{\equiv A}. \tag{31}$$

Defining the Laplacian operator $\triangle \equiv \partial_x^2 + \partial_y^2$ and taking $\boldsymbol{\nabla}\cdot$24, $\boldsymbol{\nabla}\times$24 and $\triangle$25 yields, respectively,

$$\partial_t(\overbrace{\boldsymbol{\nabla}\cdot\boldsymbol{u}}^{\triangle\phi}) - \triangle\chi + \mathrm{Bu}\triangle p = \boldsymbol{\nabla}\cdot\boldsymbol{F^u}, \tag{32}$$

$$\partial_t(\underbrace{\boldsymbol{\nabla}\times\boldsymbol{u}}_{\triangle\chi}) + \triangle\phi = \boldsymbol{\nabla}\times\boldsymbol{F^u}, \tag{33}$$

$$\partial_t(\triangle p) + \triangle^2\phi = \triangle\boldsymbol{F^p}. \tag{34}$$

Taking 33 - 34,

$$\partial_t\triangle\big(\chi - p\big) + \triangle(1-\triangle)\phi = \boldsymbol{\nabla}\times\boldsymbol{F^u} - \triangle\boldsymbol{F^p}, \tag{35}$$

or

$$\boxed{\partial_t\big(\chi - p\big) + (1-\triangle)\phi = \triangle^{-1}\big(\boldsymbol{\nabla}\times\boldsymbol{F^u} - \triangle\boldsymbol{F^p}\big).} \tag{36}$$

From 32, we have

$$\partial_t(\triangle\phi) - \triangle(1-\mathrm{Bu}\triangle)\chi = \boldsymbol{\nabla}\cdot\boldsymbol{F^u}, \tag{37}$$

or

$$\boxed{\partial_t\phi - (1-\mathrm{Bu}\triangle)\chi = \triangle^{-1}(\boldsymbol{\nabla}\cdot\boldsymbol{F^u}).} \tag{38}$$

Adding 38 to $i\times$36 and defining the unbalanced streamfunction $\tilde{\chi} \equiv \chi - p$ gives

$$\partial_t\big(\phi + i\tilde{\chi}\big) - (1-\mathrm{Bu}\triangle)\tilde{\chi} + i\phi = \triangle^{-1}(\boldsymbol{\nabla}\cdot\boldsymbol{F^u}) + i\triangle^{-1}(1-\triangle)^{-1}(\boldsymbol{\nabla}\times\boldsymbol{F^u} - \triangle\boldsymbol{F^p}), \tag{39}$$

which can be rewritten in terms of $\tilde{A} \equiv \phi + i\tilde{\chi}$ (dropping the tilde):

$$\partial_t A + iA - \frac{i}{2}\mathrm{Bu}\triangle(A - \overline{A}) = \triangle^{-1}\big[\boldsymbol{\nabla}\cdot\boldsymbol{F^u} + i(1-\triangle)^{-1}(\boldsymbol{\nabla}\times\boldsymbol{F^u} - \triangle\boldsymbol{F^p})\big]. \tag{40}$$

Taking $\boldsymbol{\nabla}\times$23 gives the evolution equation for the barotropic streamfunction Ψ:

$$\partial_t\triangle\Psi = \boldsymbol{\nabla}\times\boldsymbol{F_T^u}. \tag{41}$$

Taking the spatial average (denoted by $\langle\bullet\rangle$) of the momentum equation 24:

$$\langle\boldsymbol{u}_t\rangle + \hat{\boldsymbol{z}}\times\langle\boldsymbol{u}\rangle + \langle\mathrm{Bu}\boldsymbol{\nabla}p\rangle = \langle\boldsymbol{F^u}\rangle \tag{42}$$

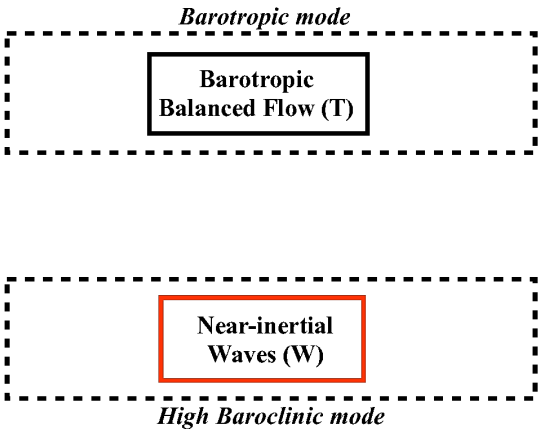

Figure 2: Schematic showing the two components of the $T-W$ model: The barotropic mode (T-mode) consists only of purely geostrophically-balanced flow, while the high baroclinic mode consists only of unbalanced (near-inertial) wave motions.

Defining $A_0 \equiv \langle u \rangle + i\langle v \rangle = u_0 + iv_0$ and manipulating the RHS:

$$\partial_t A_0 + iA_0 = -\frac{\mathrm{Ro}}{2}\langle \triangle(A + \overline{A})\mathcal{U}_T \rangle, \tag{43}$$

where $\mathcal{U}_T \equiv u_T + iv_T$. Equations 40, 41 and 43 form a set of evolution equations for the barotropic streamfunction Ψ (T-mode), the near-inertial wave amplitude A (W-mode) and the pure inertial oscillation amplitude A_0. The next step is to implement the T-W model numerically.

2.2.1 Energetics of the coupled T-W model

We may obtain equations for the kinetic energy of the divergent and rotational parts of the wave velocity by taking $\phi\times 37$ and $\chi\times 36$, respectively. The result is

$$\frac{\partial}{\partial t}\frac{1}{2}|\boldsymbol{\nabla}\phi|^2 - \boldsymbol{\nabla}\phi\cdot\boldsymbol{\nabla}\chi + \mathrm{Bu}\boldsymbol{\nabla}\phi\cdot\boldsymbol{\nabla}p = \boldsymbol{F^u}\cdot\boldsymbol{\nabla}\phi \tag{44}$$

and

$$\frac{\partial}{\partial t}\frac{1}{2}|\boldsymbol{\nabla}\chi|^2 + \boldsymbol{\nabla}\phi\cdot\boldsymbol{\nabla}\chi = -\chi(1-\triangle)^{-1}\big(\boldsymbol{\nabla}\times\boldsymbol{F^u} - \triangle\boldsymbol{F^p}\big). \tag{45}$$

We note that the second term on the left-hand sides of 44 and 45 appears with opposite signs in both equations and can therefore be interpreted as a conversion term that represents the kinetic energy transfers between the rotational and divergent parts of the wave field.
Using the fact that $p = \triangle\chi$, we can form a potential energy equation by taking $\triangle\chi\times 36$ to obtain

$$\frac{\partial}{\partial t}\frac{1}{2}(\triangle\chi)^2 + \triangle\chi\triangle\phi = \triangle\chi(1-\triangle)^{-1}\big(\boldsymbol{\nabla}\times\boldsymbol{F^u} - \triangle\boldsymbol{F^p}\big) \tag{46}$$

3 Parameter Sweep with the Linearized Modified Thomas & Yamada (2019) Model

Next, we explore the sensitivity of the energy changes to different barotropic flows in the linearized version of 18-20 (linearized about a steady barotropic balanced flow $\boldsymbol{U} = \hat{\boldsymbol{x}}U + \hat{\boldsymbol{y}}V$). We solve 18-20 using a standard pseudo-spectral code based on [9]. Figure 3 compares the evolution of wave kinetic, potential and total energies for simulations with barotropic balanced flows with randomized phase and increasing number of initial wavenumbers K_i.

The wave amplitude can be further approximately decomposed into clockwise and counter-clockwise motions as follows:

$$\mathcal{U} = A^- e^{-it} + A^+ e^{it} \tag{47}$$

So that the kinetic energy is

$$\frac{1}{2}\iint \overline{\mathcal{U}}\mathcal{U}\,dx\,dy = \frac{1}{2}\iint |A^-|^2 + |A^+|^2 + \overline{A^-}A^+ e^{+2it} + \overline{A^+}A^- e^{-2it}\,dx\,dy \tag{48}$$

and the potential energy is (using the fact that $p^+ = \overline{p^-}$)

$$\frac{1}{2}\iint \overline{p}p\,dx\,dy = \frac{1}{2}\iint 2|p^-|^2 + \overline{p^-}\,\overline{p^-}e^{+2it} + p^-p^-e^{-2it}\,dx\,dy \tag{49}$$

Figure 4 compares the evolution of the wave energy terms associated with positive (proportional to A^+) negative (proportional to A^-) and mixed (proportional to $\overline{A^+}A^-$ + c.c.) amplitudes. It can be seen that the cross component has magnitude comparable to the + and − components, indicating that this decomposition is non-orthogonal, contrary to the orthogonal decompositions used in *e.g.*, [5, 10].

4 Helmholtz Decomposition of Reduced Model Solutions

In this section we briefly compare the energy partitioning into rotational (balanced, non-divergent) and divergent (unbalanced, irrotational) motions in the linearized version of 18-20 with the partitioning in the simpler Young and Ben Jelloul (YBJ, [13]) model. The total velocity field can be decomposed into a velocity potential ϕ (irrotational) and a streamfunction (non-divergent) according to

$$= \triangle^{-1}\big(v_x - u_y\big), \tag{50}$$

$$\phi = \triangle^{-1}\big(u_x + v_y\big), \tag{51}$$

$$u + iv = (\partial_x + i\partial_y)(\phi + i\psi). \tag{52}$$

Figure 5 shows the spatial distribution of the wave kinetic energy density in a simulation of the linearized 18-20 system. Figure 6 shows the energy evolution in different reservoirs,

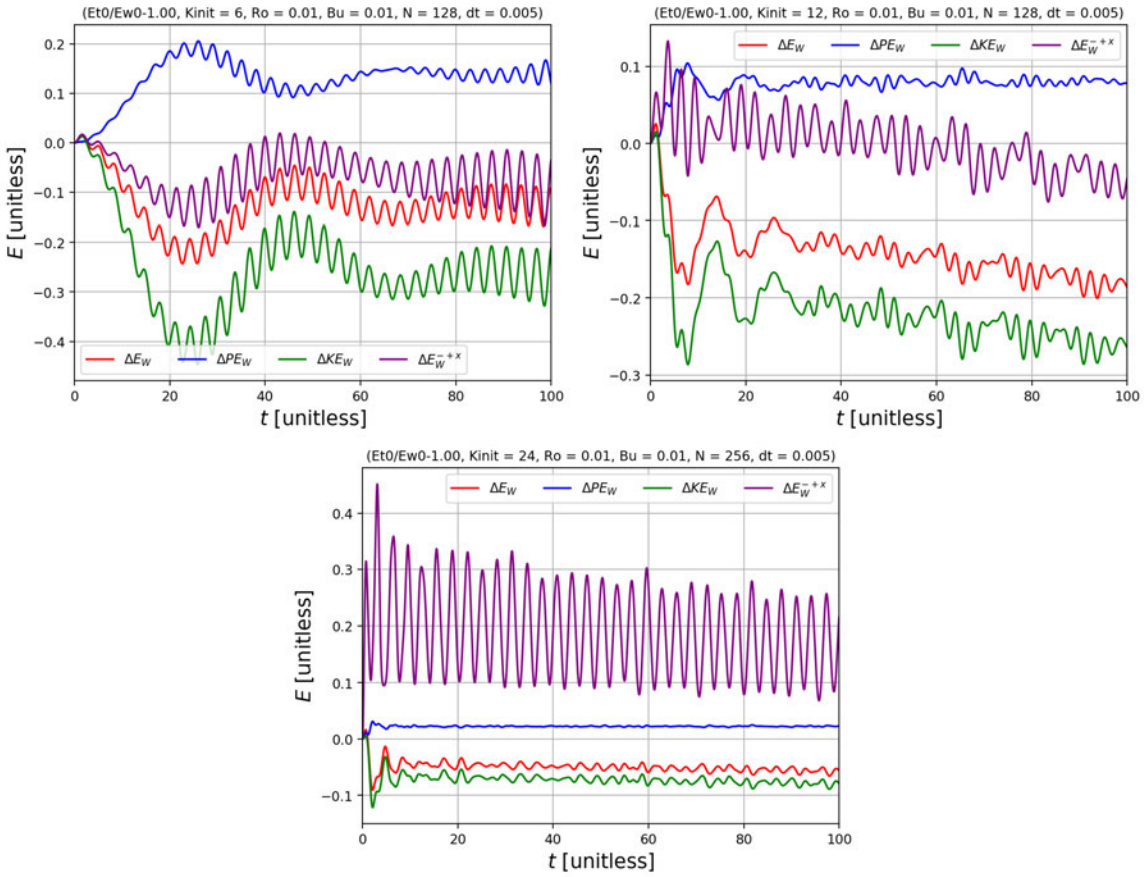

Figure 3: Wave energy changes for 6 (top left) 12 (top right) and 24 (bottom) initial wavenumbers in the system evolving according to Equations 18-20. Note that the wave potential energy gain is offset by the wave kinetic energy loss, causing the total wave energy to decrease.

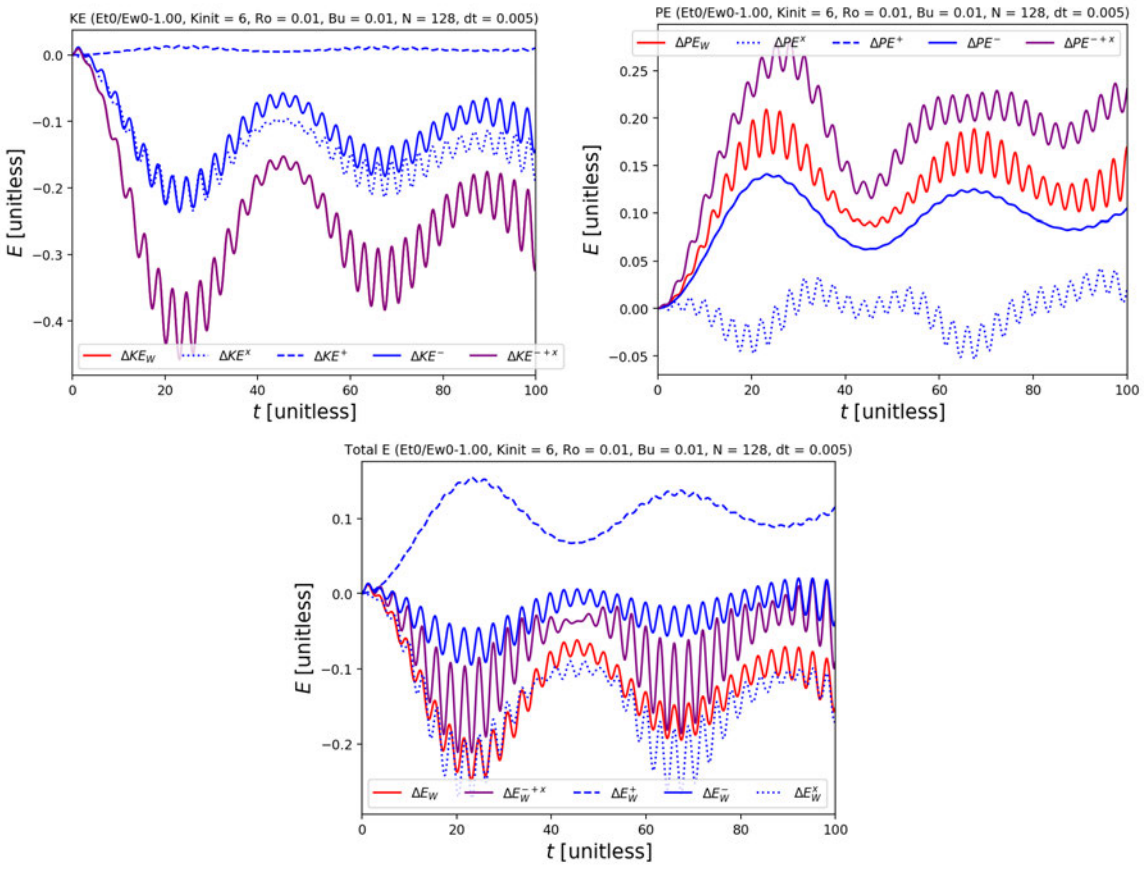

Figure 4: Kinetic (top left), potential (top right) and total (bottom) wave energy changes in the system evolving according to Equations 18-20 for the approximate decomposition in $+$, $-$ and x (cross) terms. Note that the cross terms are not negligible, indicating that this simplified decomposition is non-orthogonal.

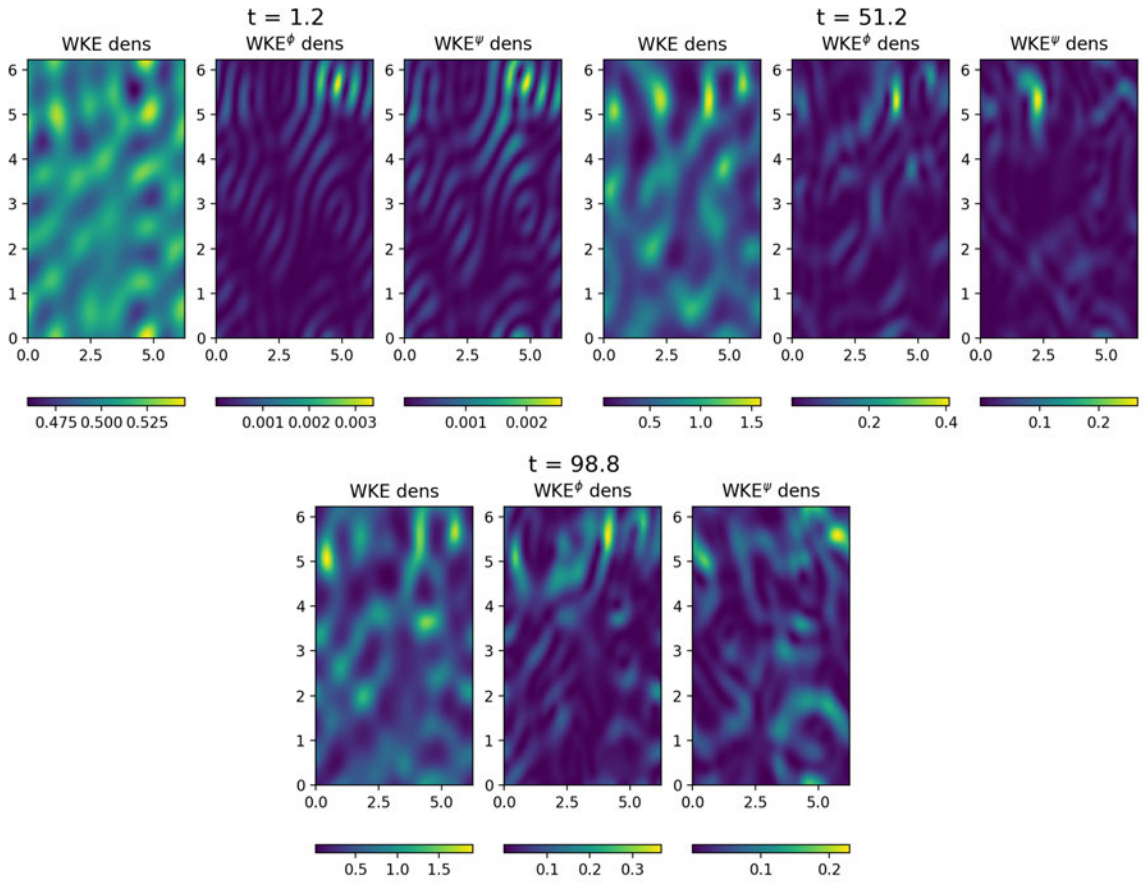

Figure 5: Kinetic energy density snapshots of a linearized 18-20 solution decomposed into rotational (ψ) and divergent (ϕ) parts.

which is similar in both systems: The purely inertial mode (inertial oscillations evolving according to 43, dashed black lines) loses kinetic energy while the near-inertial modes gain kinetic energy. This energy gain is approximately equipartitioned between rotational and divergent motions. It can also be seen that the wave kinetic energy decreases in the linearized 18-20 solution, while it stays constant in the YBJ solution, as predicted by one of its conservation laws [13]. The fact that the YBJ system conserves wave kinetic energy is one of its limitations.

5 Wave-balanced Flow Interaction: Case Studies

In this section we aim to gain some physical intuition on the wave-balanced flow interaction by analyzing a set of initial value problems with different barotropic flows as initial conditions. Specifically, we seek answers to the following questions:

1. How do different balanced flows couple with the near-inertial wave field?

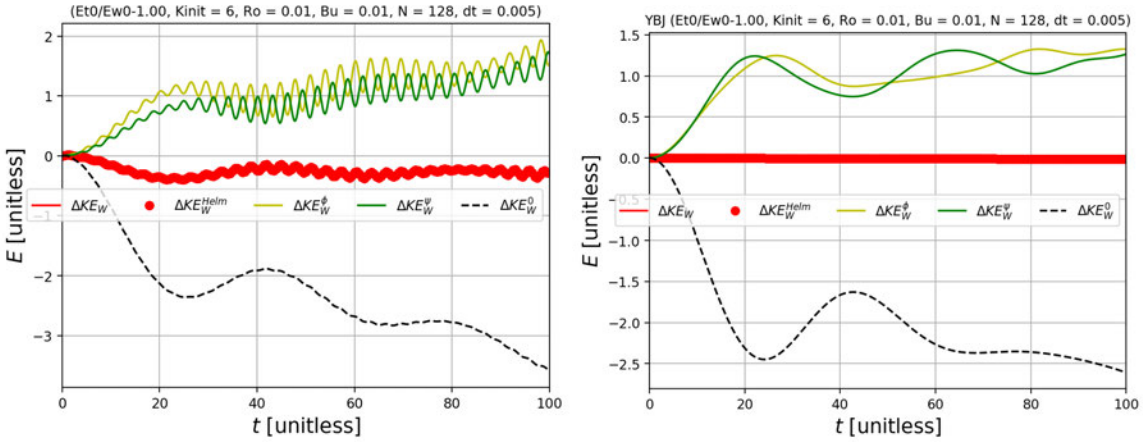

Figure 6: Energy changes for the linearized 18-20 system (left) and the YBJ system (right). The kinetic energy is decomposed into rotational (ψ, green) and divergent (ϕ, yellow) parts.

2. what is the direction of the energy transfers, *i.e.*, from balanced flow to waves or from waves to balanced flow?

The system simulated is 18-20, where the barotropic flow evolves according to Equation 18 and therefore has a two-way coupling with the near-inertial waves. The balanced part of the baroclinic mode is removed by inverting the potential vorticity. Although the two-component T-W model has not been numerically implemented yet, it is expected to give similar results.

We begin with an initial barotropic flow of a simple Gaussian anticyclone (Figure 7) in the presence of a spatially uniform inertial oscillation. As is well known in the literature (*e.g.*, [7]), wave kinetic energy density gets trapped inside anticyclonic vortices, as observed in this experiment (top-right panels in Figure 7). The total balanced energy increases at the expense of the total wave energy, and the skewness of the barotropic vorticity changes from negative to slightly positive by $t = 200$ (bottom panel of Figure 7), indicating a change in the predominance of anticyclones (negative vorticity) to cyclones (positive vorticity).

When the initial barotropic flow is a cyclone superimposed on a spatially uniform inertial oscillation, wave kinetic energy density is repelled from the core of the vortex (top-right panels of Figure 8), contrary to the anticyclonic case described in the previous paragraph. The skewness changes from positive to negative, also in contrast with the anticyclonic case. However, the energy changes of the cyclonic case are qualitatively similar to the anticyclonic case (bottom panel of Figure 8).

Does this energy pathway change direction as Ro $\to$ 1? Figure 9 shows results of a simulation identical to that in Figure 7, except for the Rossby number, which is set to 1. Numerical instability sets in very early on in the simulation, and total energy is no longer conserved after $t \approx 2.5$. However, if not an initial transient or a numerical artifact, the behavior seen at $t < 2.5$ could suggest that the energy exchange changes direction, with waves now extracting energy from the balanced flow. This would imply that it is possible to reproduce the behavior of fully three-dimensional, non-hydrostatic Boussinesq simulations at Ro ~ 1 (*e.g.*, [1]) with this simple two-dimensional model.

When the initial conditions have both anticyclones and cyclones randomly distributed across a few low wavenumbers, the behavior is qualitatively similar to when only one sign of vorticity is initially present, in the sense that anticyclones trap wave energy while cyclones repel it (upper-right panels of Figures 10 and 11). The energy changes are also similar, with the waves losing total energy while the balanced flow gains total energy. The wave energy is initially contained entirely in the purely inertial, spatially uniform mode ($k = 0$), but it decreases rapidly mirroring the increase in wave energy in the higher modes ($k \neq 0$). Importantly, the energy changes appear to be relatively insensitive to the relationship between Ro and Bu and the initial balanced/wave energy ratio, E_{t0}/E_{w0} (compare Figure 10, where $\mathrm{Bu} = \mathrm{Ro} = 0.01$ and $E_{t0}/E_{w0} = 1$, with Figure 11, where $\mathrm{Bu} = \mathrm{Ro}^2 = 0.01$ and $E_{t0}/E_{w0} = 0.01$). The vortices in the simulation where $E_{t0}/E_{w0} = 0.01$ are more deformed, with a less smooth vorticity distribution (compare upper-right panels of Figures 10 and 11), indicating that the balanced flow can be appreciably impacted by the near-inertial waves in this strong wave regime.

6 Asymptotic Model for NIWs-balanced Flow Interaction

In this section we derive a new asymptotic model that represents both clockwise and counterclockwise wave modes. We begin with the truncated equations derived by [9], linearized about a steady balanced barotropic flow, written in complex representation:

$$\mathcal{U}_t + i\mathcal{U} + 2\mathrm{Bu}p_{s^*} + \mathrm{Ro}F^u = 0, \tag{53}$$

$$p_t + \mathcal{U}_s + \overline{\mathcal{U}}_{s^*} + \mathrm{Ro}F^p = 0, \tag{54}$$

where

$$F_u \equiv \mathcal{U}_T + U\mathcal{U}_s + \overline{U}\mathcal{U}_{s^*} + \frac{i}{2}\big(\mathcal{U}\zeta + \overline{\mathcal{U}}\sigma\big), \tag{55}$$

$$F_p \equiv p_T + Up_s + \overline{U}p_{s^*}, \tag{56}$$

$$\zeta \equiv \triangle\Psi, \sigma \equiv \triangle^{\perp}\Psi \tag{57}$$

Following [9]'s Appendix B, the governing equations can be rewritten only in terms of velocity in complex representation as

$$\partial_t\big(\partial_{tt}^2 + 1 - 4\mathrm{Bu}\partial_{ss^*}^2\big)\mathcal{U} + \mathrm{Ro}R^u = 0 \tag{58}$$

$$\partial_t\big(\partial_{tt}^2 + 1 - 4\mathrm{Bu}\partial_{ss^*}^2\big)p + \mathrm{Ro}R^p = 0, \tag{59}$$

where

$$R^u \equiv iF_t^u - F_{tt}^u + i\mathrm{Bu}\big(F_{ss^*}^u - F_{ss}^u\big) + i\mathrm{Bu}\big(\overline{F_{ss^*}^u} - \overline{F_{s^*s^*}^u}\big) + 2\mathrm{Bu}\big(F_{s^*t}^p - iF_{s^*}^p\big) \tag{60}$$

$$R^p \equiv F_{st}^u + \overline{F_{s^*t}^u} + i\big(F_{s^*}^u - F_s^u\big) - F_{tt}^p - F^p. \tag{61}$$

We write the solutions as

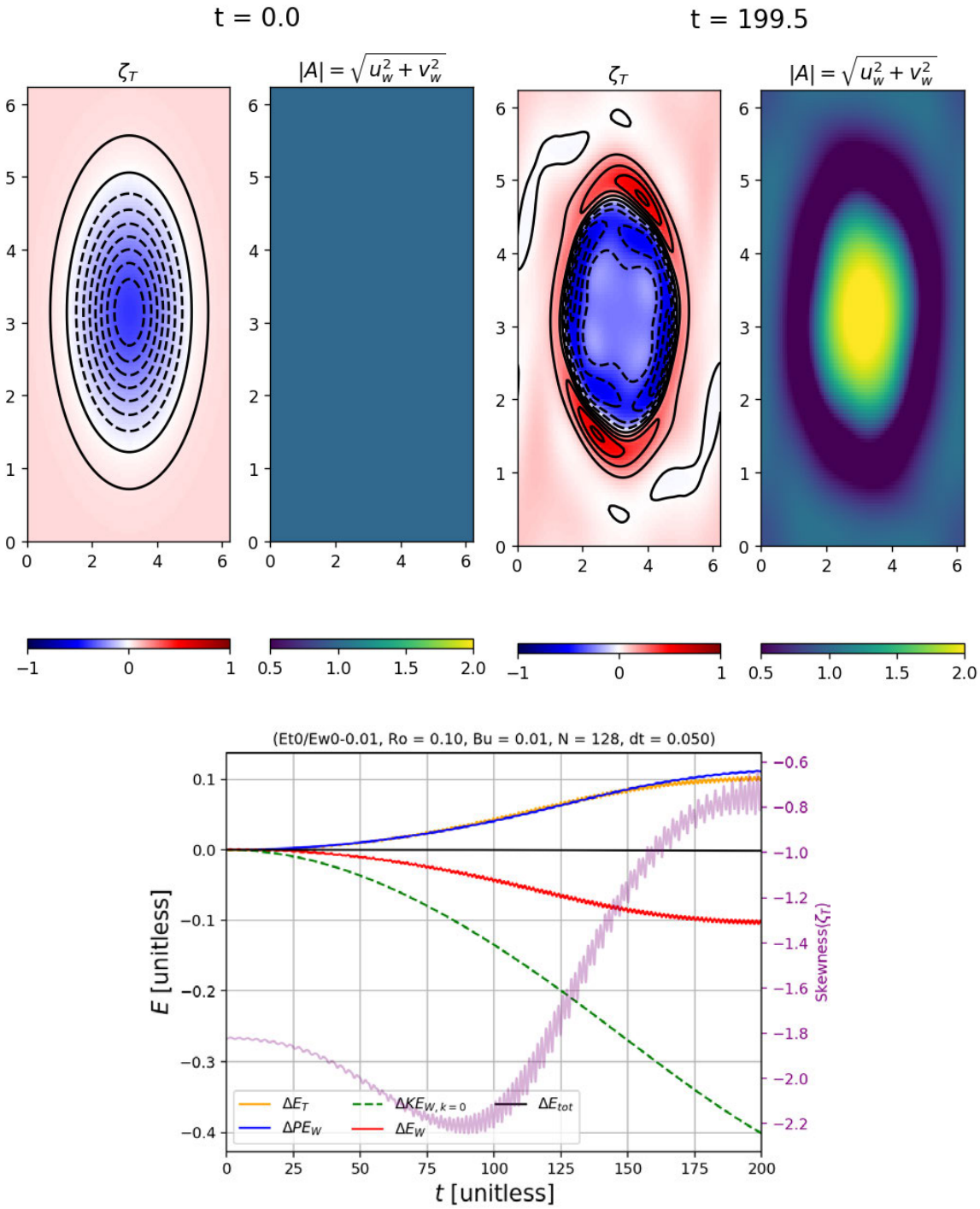

Figure 7: Coupled T-W wave energy changes (lower panel) and snapshots of the barotropic vorticity ζ_T and the wave amplitude $|A|$ (upper panels), initialized with a barotropic anticyclone. ΔE_T, ΔE_{tot}, ΔPE_W, $\Delta KE_{W,k=0}$ and ΔE_W are the balanced barotropic energy, the total (wave + balanced) energy, the wave potential energy, the wave kinetic energy in the purely inertial mode ($k = 0$) and the total wave energy, respectively. The purple line in the lower panel is the instantaneous skewness of the barotropic vorticity. E_{t0}/E_{w0} is the initial balanced-to-wave energy ratio, and N and dt are respectively the number of Fourier modes and the time step in the simulation.

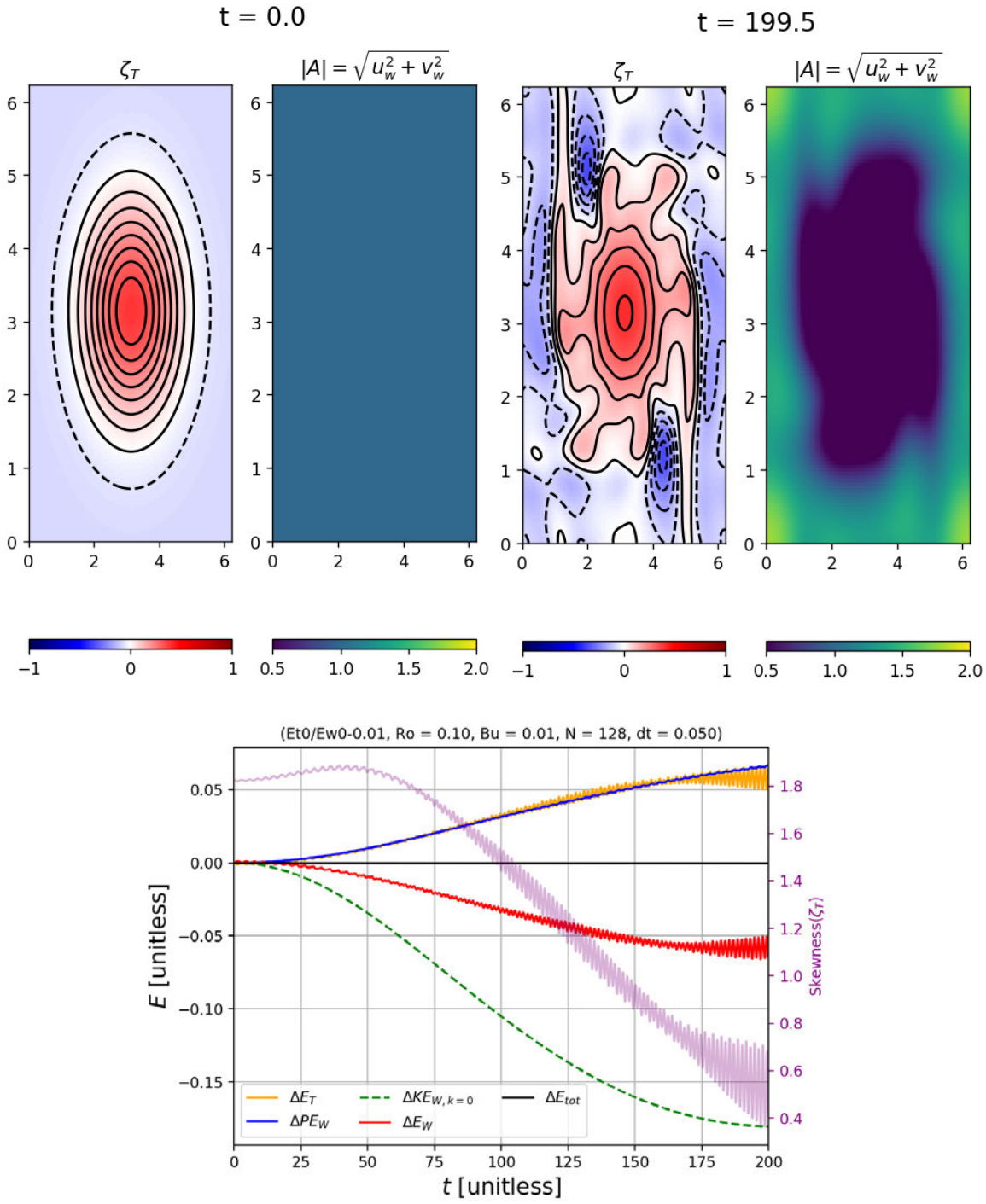

Figure 8: Same as Figure 7 but initialized with a barotropic cyclone.

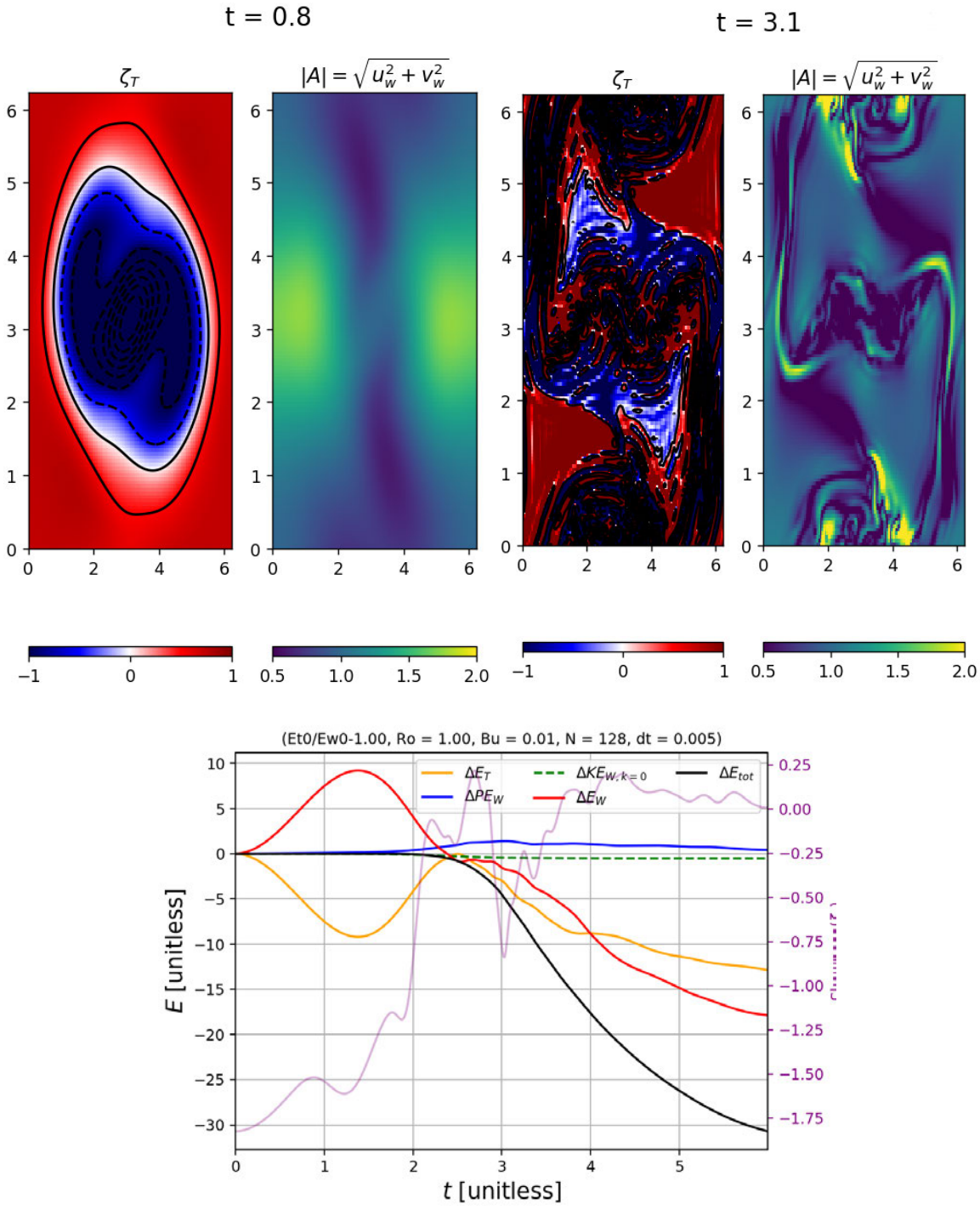

Figure 9: Same as Figure 7, but initialized with a barotropic anticyclone with Ro = 1.

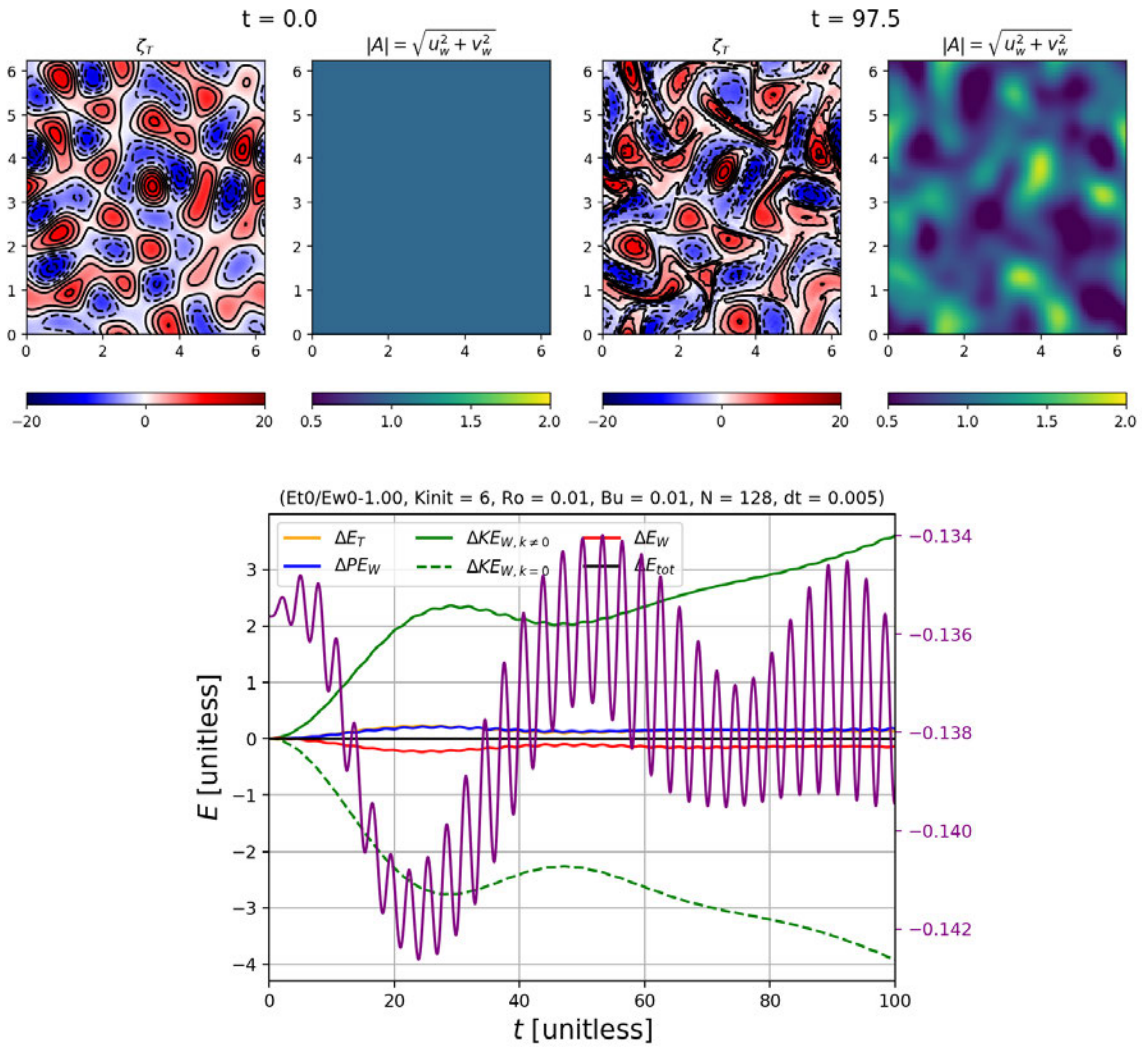

Figure 10: Same as Figure 7, but initialized with 6 wavenumbers with randomized phase and the same initial energy in the balanced and wave modes, *i.e.*, $E_{t0}/E_{w0} = 1$. Ro = Bu = 0.01.

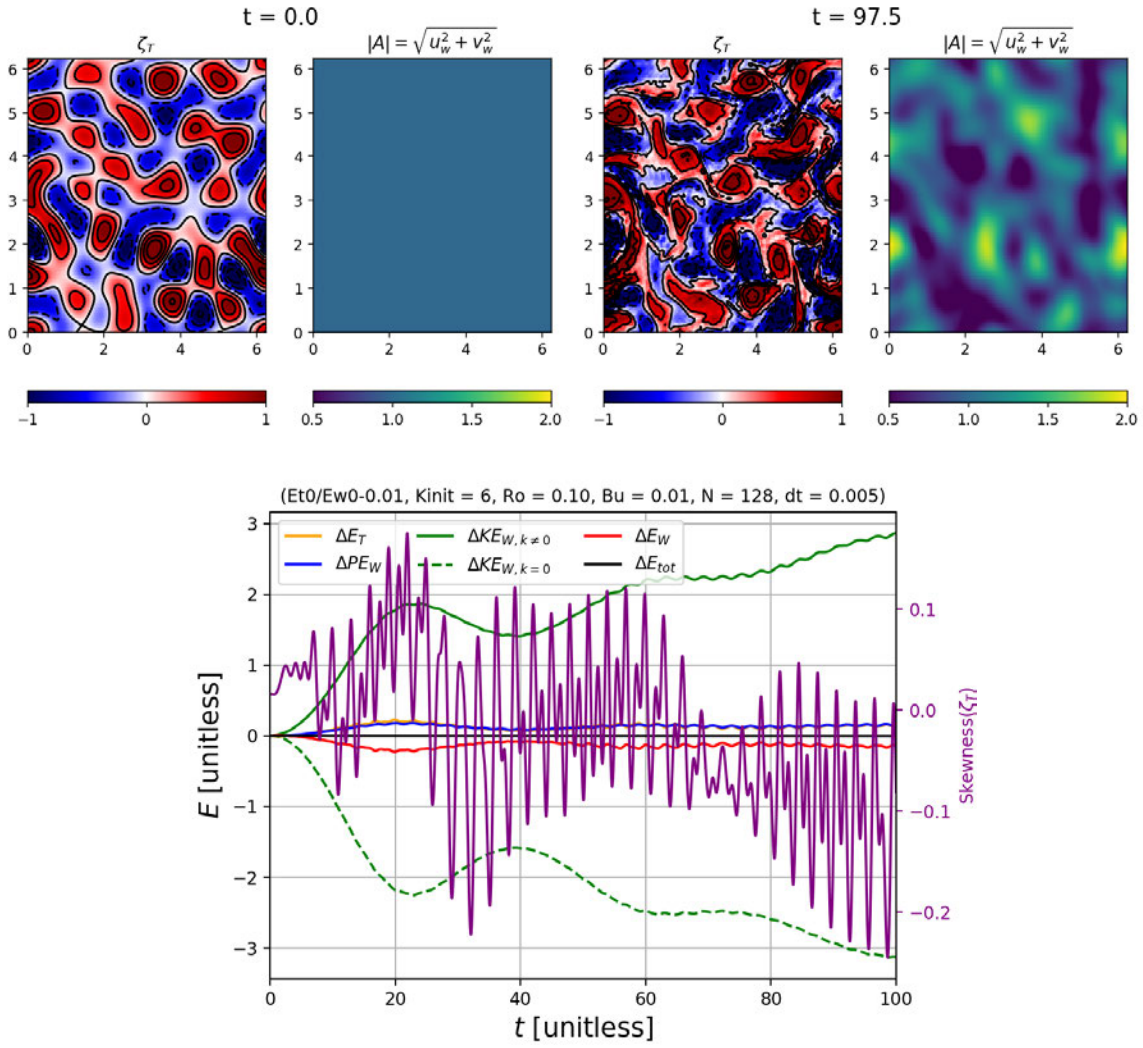

Figure 11: Same as Figure 7, but initialized with 6 wavenumbers with randomized phase, and a hundred times more initial energy in the wave modes, *i.e.*, $E_{t0}/E_{w0} = 0.01$. Ro = 0.1 and Bu = $\text{Ro}^2 = 0.01$).

$$\mathcal{U} = A^- e^{-i\omega t} + A^+ e^{+i\omega t}, \tag{62}$$

$$p = -\frac{i}{\omega}\big(A_s^- + \overline{A^+}_{s^*}\big)e^{-i\omega t} + \frac{i}{\omega}\big(A_s^+ + \overline{A^-}_{s^*}\big)e^{+i\omega t} \tag{63}$$

Expanding $\mathcal{U}$ and p in powers of Ro:

$$\mathcal{U} = \mathcal{U}^{(0)} + \mathrm{Ro}\mathcal{U}^{(1)} + \mathrm{Ro}^2\mathcal{U}^{(2)} + \cdots \tag{64}$$

and substituting in the momentum equation,

$$i\omega(\mp\omega^2 \pm 1 \mp 4\mathrm{Bu}\partial^2_{ss^*})A_0^\mp \qquad = 0 \tag{65}$$

$$\underbrace{i\omega(\mp\omega^2 \pm 1 \mp 4\mathrm{Bu}\partial^2_{ss^*})}_{\equiv\mathcal{M}^\mp} A_1^\mp \quad + R_0^\mp \quad = 0 \tag{66}$$

To obtain a single pair of equations for $A^\mp \equiv A_0^\mp + \mathrm{Ro}A_1^\mp$, we follow the reconstitution technique as used by *e.g.*, [6, 11, 8]. The first step is to add a small correction to the RHS of the $O(1)$ equations:

$$\mathcal{M}^\mp A_0^\mp \qquad\quad = \mathrm{Ro}\Phi^\mp \tag{67}$$

$$\mathcal{M}^\mp A_1^\mp \quad + R_0^\mp \quad = 0 \tag{68}$$

Take (67) + Ro × (68):

$$\mathrm{Ro}\Phi^\mp = -\mathrm{Ro}\big[\mathcal{M}^\mp A_1^\mp - R_0^\mp\big] \tag{69}$$

Substitute back in 67:

$$\mathcal{M}^\mp A^\mp + \mathrm{Ro}R_0^\mp = 0 \tag{70}$$

After some manipulations, the coupled equations for A^- and A^+ become:

$$\big[\mathcal{L}^\mp - 2\mathrm{Bu}(1+i)\partial^2_{ss^*}\big]A_T^\mp = 2\mathrm{Bu}(1+i)(\overline{A^\pm}_{Ts^*s^*} + \beta^\mp) - \mathcal{L}^\mp\alpha^\mp \cdots \tag{71}$$

$$\cdots \mp \frac{i\omega}{\mathrm{Ro}}\big(-\omega^2 + 1 - 4\mathrm{Bu}\partial^2_{ss^*}\big)A^\mp + DA^\mp, \tag{72}$$

where the hyperviscosity operator $D \equiv \nu\triangle^{2r}$ has been added and

$$\mathcal{L}^\mp \equiv \big\{\omega(\omega \pm 1) + i\mathrm{Bu}\big[\partial^2_{ss^*} - \partial^2_{ss} + \partial^2_{ss^*}(\bar{\bullet}) - \partial^2_{s^*s^*}(\bar{\bullet})\big]\big\}, \tag{73}$$

$$\alpha^\mp \equiv UA_s^\mp + \overline{U}A_{s^*}^\mp + \frac{i}{2}\big(A^\mp\zeta + \overline{A^\pm}\sigma\big), \tag{74}$$

$$\beta^\mp \equiv \big[U(A_{ss}^\mp + \overline{A^\pm}_{ss^*}) + \overline{U}(A_{ss^*}^\mp + \overline{A^\pm}_{s^*s^*})\big]_{s^*}. \tag{75}$$

in Cartesian coordinates, Equation 71 reads

$$\left[\mathcal{L}^{\mp} - \frac{1}{2}\mathrm{Bu}(1+i)\triangle\right]A_T^{\mp} = 2\mathrm{Bu}(1+i)\left(\frac{1}{4}\triangle^{\perp}\overline{A^{\pm}}_T + \beta^{\mp}\right) - \mathcal{L}^{\mp}\alpha^{\mp}\cdots \\ \cdots \mp \frac{i\omega}{\mathrm{Ro}}\big(-\omega^2 + 1 - \mathrm{Bu}\triangle\big)A^{\mp} + DA^{\mp}, \tag{76}$$

and

$$\mathcal{L}^{\mp} \equiv \omega(\omega \pm 1) + \frac{i}{2}\mathrm{Bu}\big(\partial_{yy}^2 + i\partial_{xy}^2\big) + \frac{i}{2}\mathrm{Bu}\big(\partial_{yy}^2 - i\partial_{xy}^2\big)(\overline{\bullet}). \tag{77}$$

If $\omega = 1$ and Bu, $A^+ \to 0$, the YBJ [13] amplitude equation is recovered for A^-:

$$\boxed{A_T^- + \boldsymbol{U}\cdot\boldsymbol{\nabla}A^- + \frac{i}{2}\left(A^-\zeta - \frac{\mathrm{Bu}}{\mathrm{Ro}}\triangle A^-\right) = 0.} \tag{78}$$

6.1 Numerical implementation

Our next goal is to solve 76 numerically. Equation 76 can be rewritten as

$$\left[(\omega \pm 1) - \frac{\mathrm{Bu}}{2}\tilde{\triangle}\right]A_T^{\mp} - \frac{\mathrm{Bu}}{2}(1+i)\triangle^{\perp}\overline{A_T^{\pm}} \pm i\omega(-\omega^2 + 1 - \mathrm{Bu}\triangle)A^{\mp} - DA^{\mp} = \cdots \\ \cdots - \mathcal{L}^{\mp}\alpha^{\mp} + 2\mathrm{Bu}(1+i)\beta^{\mp}, \tag{79}$$

and semi-discretized with a forward-in-time scheme as

$$\left[\omega(\omega \pm 1) - \frac{\mathrm{Bu}}{2}\tilde{\triangle}\right]\frac{A^{\mp(n+1)} - A^{\mp(n)}}{\mathrm{Ro}\delta t} - \frac{\mathrm{Bu}}{2}(1+i)\triangle^{\perp}\frac{\overline{A^{\pm(n+1)}} - \overline{A^{\pm(n)}}}{\mathrm{Ro}\delta t}\cdots \\ \cdots \pm i\omega(-\omega^2 + 1 - \mathrm{Bu}\triangle)A^{\mp(n+1)} - DA^{\mp(n+1)} = -\mathcal{L}^{\mp}\alpha^{\mp(n)} + 2\mathrm{Bu}(1+i)\beta^{\mp} \tag{80}$$

Multiplying through by $\mathrm{Ro}\delta t$ and rearranging yields:

$$\left[\omega(\omega \pm 1) - \frac{\mathrm{Bu}}{2}\tilde{\triangle} \pm i\omega\mathrm{Ro}\delta t(-\omega^2 + 1 - \mathrm{Bu}\triangle) - \mathrm{Ro}\delta t D\right]A^{\mp(n+1)} - \frac{\mathrm{Bu}}{2}(1+i)\triangle^{\perp}\overline{A^{\pm(n+1)}} = \cdots \\ \cdots \Bigg[\underbrace{\omega(\omega \pm 1) - \frac{\mathrm{Bu}}{2}\tilde{\triangle}}_{\equiv\tilde{\mathcal{L}^{\mp}}}\Bigg]A^{\mp(n)} - \frac{\mathrm{Bu}}{2}(1+i)\triangle^{\perp}\overline{A^{\pm(n)}} + \mathrm{Ro}\delta t\big(2\mathrm{Bu}(1+i)\beta^{\mp(n)} - \mathcal{L}^{\mp}\alpha^{\mp(n)}\big), \tag{81}$$

where

$$\tilde{\triangle} \equiv \partial_{xx}^2 + \partial_{yy}^2 + \partial_{xy}^2 + i\partial_{xx}^2 \tag{82}$$

and the (n) and $(n+1)$ superscripts indicate the time step at which the term is evaluated. Writing $A^{\mp}$ in terms of their real and imaginary parts, *i.e.*, $A^{\mp} = A_R^{\mp} + iA_I^{\mp}$, we have

$$\left[\tilde{\mathcal{L}^{\mp}} \pm i\omega \mathrm{Ro}\delta t(-\omega^2 + 1 - \mathrm{Bu}\triangle) - \mathrm{Ro}\delta t D\right]\left(A_R^{\mp} + iA_I^{\mp}\right)^{(n+1)} - \frac{\mathrm{Bu}}{2}(1+i)\triangle^{\perp}\left(A_R^{\pm} - iA_I^{\pm}\right)^{(n+1)} = \cdots$$
$$\cdots \tilde{\mathcal{L}^{\mp}}\left(A_R^{\mp} + iA_I^{\mp}\right)^{(n)} - \frac{\mathrm{Bu}}{2}(1+i)\triangle^{\perp}\left(A_R^{\pm} - iA_I^{\pm}\right)^{(n)} + \mathrm{Ro}\delta t\left(2\mathrm{Bu}(1+i)\beta^{\mp(n)} - \mathcal{L}^{\mp}\alpha^{\mp(n)}\right), \quad (83)$$

Equation 83 and its complex conjugate can be written respectively as

$$\mathcal{H}_1^{\mp} A_R^{\mp(n+1)} + i\mathcal{H}_1^{\mp} A_I^{\mp(n+1)} + \mathcal{H}_2 A_R^{\pm(n+1)} - i\mathcal{H}_2 A_I^{\pm(n+1)} = R^{\mp(n)} \quad (84)$$

and

$$\overline{\mathcal{H}_1^{\mp}} A_R^{\mp(n+1)} - i\overline{\mathcal{H}_1^{\mp}} A_I^{\mp(n+1)} + \overline{\mathcal{H}_2} A_R^{\pm(n+1)} + i\overline{\mathcal{H}_2} A_I^{\pm(n+1)} = \overline{R^{\mp(n)}}. \quad (85)$$

In matrix form,

$$\begin{bmatrix} \mathcal{H}_1^- & i\mathcal{H}_1^- & \mathcal{H}_2 & -i\mathcal{H}_2 \\ \overline{\mathcal{H}_2} & -i\overline{\mathcal{H}_2} & \overline{\mathcal{H}_1^+} & i\overline{\mathcal{H}_1^+} \\ \overline{\mathcal{H}_1^-} & -i\overline{\mathcal{H}_1^-} & \overline{\mathcal{H}_2} & i\overline{\mathcal{H}_2} \\ \overline{\mathcal{H}_2} & i\overline{\mathcal{H}_2} & \overline{\mathcal{H}_1^+} & -i\overline{\mathcal{H}_1^+} \end{bmatrix} \begin{bmatrix} A_R^{-(n+1)} \\ A_I^{-(n+1)} \\ A_R^{+(n+1)} \\ A_I^{+(n+1)} \end{bmatrix} = \begin{bmatrix} R^{-(n)} \\ R^{+(n)} \\ \overline{R^{-(n)}} \\ \overline{R^{+(n)}} \end{bmatrix} \quad (86)$$

The next step is to implement and time-step this system numerically.

7 Conclusions

The main results of this project are as follows:

- A new two-component 2D model seems to reproduce the energetics of more complex 3D models, *i.e.*, **energy transfer from NIWs to the balanced flow at low** Ro;
- This might be the simplest non-asymptotic two-component model that also captures **balanced energy dissipation at high** Ro;
- Idealized models such as the ones developed in this study can be used as **testbeds for parameterizations** for global 3D models in regions of high NIW energy (instead of artificially enhanced viscosity) and
- A **new asymptotic model** was derived for NIW-balanced flow interactions.

8 Next Steps

The next steps in this project are to

- Verify if the **direction of the energy exchange** (NIWs→balanced) changes as Ro = O(1) is approached (computationally demanding) and
- **Test the new asymptotic model** against the parent T-W model.

Acknowledgements

It is a pleasure to acknowledge the work of the directors, Claudia Cenedese, Bruce Sutherland and Karl Helfrich, in running a wonderful and inspiring GFD summer. Thanks to the other fellows and the GFD staff, visitors and seminar speakers for stimulating and insightful discussions. Many thanks to Jim Thomas for proposing and patiently supervising this project.

References

[1] R. Barkan, K. B. Winters, and J. C. McWilliams, *Stimulated Imbalance and the Enhancement of Eddy Kinetic Energy Dissipation by Internal Waves*, J. Phys. Oceanogr., 47 (2017), pp. 181–198.

[2] S. J. Benavides and A. Alexakis, *Critical transitions in thin layer turbulence*, J. Fluid Mech., 822 (2017), pp. 364–385.

[3] R. Ferrari and C. Wunsch, *The distribution of eddy kinetic and potential energies in the global ocean*, Tellus A, 62 (2010), pp. 92–108.

[4] D. M. Frierson, A. J. Majda, and O. M. Pauluis, *Large scale dynamics of precipitation fronts in the tropical atmosphere: A novel relaxation limit*, Commun. Math. Sci., 2 (2004), pp. 591–626.

[5] M. Remmel and L. Smith, *New intermediate models for rotating shallow water and an investigation of the preference for anticyclones*, J. Fluid. Mech., 635 (2009), pp. 321–359.

[6] A. Roberts, *An introduction to the technique of reconstitution*, SIAM journal on mathematical analysis, 16 (1985), pp. 1243–1257.

[7] C. B. Rocha, G. L. Wagner, and W. R. Young, *Stimulated generation: extraction of energy from balanced flow by near-inertial waves*, J. Fluid Mech., 847 (2018), pp. 417–451.

[8] J. Thomas, *New model for acoustic waves propagating through a vortical flow*, J. Fluid Mech., 823 (2017), pp. 658–674.

[9] J. Thomas, K. S. Smith, and O. Bühler, *Near-inertial wave dispersion by geostrophic flows*, J. Fluid. Mech., 817 (2017), p. 406–438.

[10] J. Thomas and R. Yamada, *Geophysical turbulence dominated by inertia–gravity waves*, J. Fluid Mech., 875 (2019), pp. 71–100.

[11] G. L. Wagner and W. R. Young, *A three-component model for the coupled evolution of near-inertial waves, quasi-geostrophic flow and the near-inertial second harmonic*, J. Fluid Mech., 802 (2016), pp. 806–837.

[12] J.-H. Xie and J. Vanneste, *A generalised-Lagrangian-mean model of the interactions between near-inertial waves and mean flow*, J. Fluid Mech., 774 (2015), pp. 143–169.

[13] W. R. Young and M. B. Jelloul, *Propagation of near-inertial oscillations through a geostrophic flow*, J. Mar. Res., 55 (1997), pp. 735–766.

Exploiting Sum-of-Squares Optimisation in Hamiltonian Chaos: Flip Times for the Double Pendulum

Jeremy P. Parker

August 19, 2019

1 Introduction

Sum-of-squares optimisation (SOS) is an analytic and computational method allowing one to find nonnegative polynomials satisfying prescribed constraints, through semi-definite programming (SDP) [15]. One important application of this method is to finding Lyapunov functions to prove stability of polynomial dynamical systems. In particular, when Galerkhin truncations are made of fluid dynamical systems, the resulting system is polynomial, and so this method can be applied [2].

Another application of SOS to dynamical systems proposed by Chernyshenko et al. [2] is the so-called 'auxiliary function method' to find bounds on infinite time averages of quantities. Thus far, applications have concentrated on dissipative systems [6, 7, 8], as otherwise infinite time averages over all possible initial conditions are not generally well defined.

A new application of sum-of-squares optimisation is to compute regions of attraction for sets. Introduced by Henrion and Korda [10], this method makes use of a function V which is required to decrease along trajectories of the system. A similar idea underlies the 'barrier function method' which is employed in our work. The barrier function method can give a guarantee that trajectories starting in one set do not enter another set within some finite or possibly infinite time.

The barrier function method has the advantage that it can be applied to non-dissipative systems, such as the Hamiltonian systems which underlie classical mechanics. One simple example of a Hamiltonian system which displays chaotic behaviour is the double pendulum, which is often used as an example in introductory courses and textbooks [18, 12]. Though the system has four dynamical variables – usually given as two angles and two angular velocities – it is more intuitive to understand than chaotic systems with three variables such as the Rössler and Lorenz systems (which are both dissipative).

Relatively little serious research has been focussed on the double pendulum, despite it being a favourite toy problem for introductory textbooks. Poincaré sections were studied by Stachowiak and Okada [16]. A fractal pattern in the time-to-flip plots which will be discussed in detail below was first discovered and discussed in an unpublished work Heyl [11] and has been studied by a number of student projects [5, 14], but is still not fully understood.

The fractal pattern means that, for arbitrarily long times, it is impossible to state whether for initial conditions within certain regions of phase space, the pendulum will flip [11]. We attempt to certify that sets of initial conditions do not flip within a certain time. The report proceeds as follows: in section 2, we present, in abstract terms, the barrier function method for certifying that trajectories starting in one semialgebraic set do not enter another in a given time. In section 3, we present the double pendulum model, and show how the barrier function method is formulated in this case. Section 4 compares the flip time from a direct solution of the governing equations with regions which we have certified do not flip, and section 5 briefly discusses and concludes the work. The appendices give some additional results which may help when applying the barrier function method to other systems.

2 Method

We consider a system with dynamical variables $\mathbf{x} = (x_1, \ldots, x_n) \in \mathbb{R}^n$, and dummy variables (such as Lagrange multipliers) $\mathbf{y} = (y_1, \ldots, y_m) \in \mathbb{R}^m$, which satisfy

$$\frac{dx_k}{dt} = f_k(\mathbf{x}, \mathbf{y}), \qquad k = 1, \ldots, n, \tag{1}$$

$$0 = g_k(\mathbf{x}, \mathbf{y}), \qquad k = 1, \ldots, m. \tag{2}$$

Here, the f_k and g_k are assumed to be polynomial. By introducing additional dummy variables, it is often possible to transform simple dynamical systems into this polynomial form (see appendix A).

Let X_0 be a semialgebraic set defined by

$$a_k^0(\mathbf{x}) = 0, \qquad k = 1, \ldots, N_0, \tag{3}$$

$$b_k^0(\mathbf{x}) \geq 0, \qquad k = 1, \ldots, M_0. \tag{4}$$

Again, we assume that the a_k and b_k are polynomial. In physically relevant situations, it will always be possible to approximate a set by a semialgebraic set, with accuracy increasing as the order or number of the polynomials is increased. Similarly, define X_1 by

$$a_k^1(\mathbf{x}) = 0, \qquad k = 1, \ldots, N_1, \tag{5}$$

$$b_k^1(\mathbf{x}) \geq 0, \qquad k = 1, \ldots, M_1. \tag{6}$$

Lemma 1. *Suppose there exist polynomials* $V(\mathbf{x},t), s_k(\mathbf{x},\mathbf{y},t), t_k(\mathbf{x},\mathbf{y},t)$ *such that*

$$\frac{\partial V}{\partial t} + \sum_{k=1}^{n} f_k \frac{\partial V}{\partial x_k} - s_0 t(T-t) - \sum_{k=1}^{m} s_k g_k \geq 0, \tag{7}$$

$$s_k \geq 0, \qquad k = 0, \ldots, m, \tag{8}$$

$$V - \sum_{k=1}^{M_0} r_k^0 a_k^0 - \sum_{k=1}^{N_0} s_k^0 b_k^0 \geq 0, \qquad t = 0, \tag{9}$$

$$s_k^0 \geq 0, \qquad k = 1, \ldots, N_0, \tag{10}$$

$$-1 - V - s_0^1 t(T-t) - \sum_{k=1}^{M_1} r_k^1 a_k^1 - \sum_{k=1}^{N_1} s_k^1 b_k^1 \geq 0, \tag{11}$$

$$s_k^1 \geq 0, \qquad k = 0, \ldots, N_1, \tag{12}$$

where the inequalities hold over all space and time unless otherwise stated. Then no trajectories starting inside X_0 *at* $t = 0$ *intersect* X_1 *when* $t \in (0,T)$.

Proof. Consider a trajectory starting at $\mathbf{x}^0 \equiv (x_1^0, .., x_n^0) \in X_0$ at $t = 0$. By equation (9), and the definition of X_0, we have

$$\begin{aligned} V(\mathbf{x}^0, 0) &\geq \sum_{k=1}^{M_0} r_k^0(\mathbf{x}^0) a_k^0(\mathbf{x}^0) + \sum_{k=1}^{N_0} s_k^0(\mathbf{x}^0) b_k^0(\mathbf{x}^0) \\ &= \sum_{k=1}^{M_0} r_k^0(\mathbf{x}^0) \cdot 0 + \sum_{k=1}^{N_0} s_k^0(\mathbf{x}^0) b_k^0(\mathbf{x}^0) \\ &= \sum_{k=1}^{N_0} s_k^0(\mathbf{x}^0) b_k^0(\mathbf{x}^0) \\ &\geq \sum_{k=1}^{N_0} s_k^0(\mathbf{x}^0) \cdot 0 \\ &= 0. \end{aligned}$$

Along a trajectory when $t \in (0,T)$,

$$\begin{aligned} \frac{DV}{Dt} &= \frac{\partial V}{\partial t} + \sum_{k=1}^{n} f_k \frac{\partial V}{\partial x_k} \\ &\geq 0, \end{aligned}$$

using (7) and the fact that $g_k(\mathbf{x},\mathbf{y}) = 0$ on the trajectory. Therefore, V is increasing in time, and in particular $V \geq 0$ for all $t \in (0,T)$. But, through similar reasoning to that above, (11) ensures that $V \leq -1$ for $\mathbf{x} \in X_1$ and $t \in (0,T)$, so this trajectory cannot intersect with X_1 in the time interval. □

The feasibility of the system (7-12), as well as a solution to it if one exists, can be found using sum-of-squares optimisation.

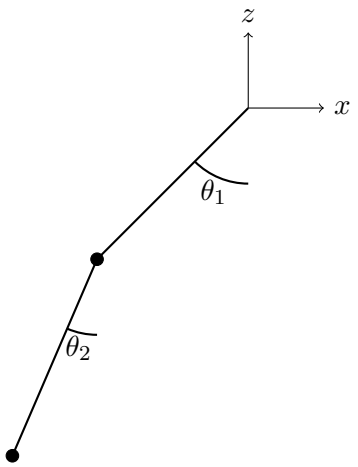

Figure 1: The conventions used for the double simple pendulum in this work.

3 The Double Pendulum

Two quantitatively different – though qualitatively very similar – double pendulum systems are commonly studied. The compound double pendulum uses two massive rods of equal length. Instead, we consider the double simple pendulum: two light, rigid rods of unit length connecting two point masses with unit mass. The angle the rods make with the vertical are θ_1 and θ_2, and they have corresponding angular velocities ω_1 and ω_2. Figure 1 shows a schematic of this setup. Let T_1 and T_2 be the tensions in each of the rods, and let $s_1 = \sin\theta_1$, $c_1 = \cos\theta_1$, $s_2 = \sin(\theta_2 - \theta_1)$ and $c_2 = \cos(\theta_2 - \theta_1)$. It is then possible to write down a Lagrangian, and derive in the usual way [17] the governing equations

$$\frac{d\omega_1}{dt} = s_2 T_2 - s_1, \tag{13}$$

$$\frac{d\omega_2}{dt} = -s_2 T_1, \tag{14}$$

$$\frac{dc_1}{dt} = -\omega_1 s_1, \tag{15}$$

$$\frac{ds_1}{dt} = \omega_1 c_1, \tag{16}$$

$$\frac{dc_2}{dt} = -(\omega_2 - \omega_1) s_2, \tag{17}$$

$$\frac{ds_2}{dt} = (\omega_2 - \omega_1) c_2, \tag{18}$$

and the constraints

$$c_1^2 + s_1^2 = 1, \tag{19}$$

$$c_2^2 + s_2^2 = 1, \tag{20}$$

$$T_1 - c_2 T_2 - \omega_1^2 - c_1 = 0, \tag{21}$$

$$2T_2 - c_2 T_1 - \omega_2^2 = 0. \tag{22}$$

We may interpret these physically: (13) and (14) represent Newton's second law for the angular velocities, with a balance between angular acceleration and the torques from tension and gravity. Equations (15-18) state that the rate of change of the angles are the angular velocities. Equations (19) and (20) are the normalisation constraints for the sines and cosines, and (21-22) ensure that tension balances centrifugal force and gravity in the direction parallel to each rod.

Note that by formulating using $\cos(\theta_2 - \theta_1)$ etc. instead of $\cos\theta_2$, the order of the polynomial system (13-22) is reduced by 1. The system is invariant under the reflection in the centreline

$$S : (\theta_1, \theta_2, \omega_1, \omega_2) \mapsto (-\theta_1, -\theta_2, -\omega_1, -\omega_2), \tag{23}$$

which is equivalent to

$$(T_1, T_2, \omega_1, \omega_2, c_1, s_1, c_2, s_2) \mapsto (T_1, T_2, -\omega_1, -\omega_2, c_1, -s_1, c_2, -s_2). \tag{24}$$

There is also a time-reversal symmetry which will not be relevant to us.

From the equations, it can be shown that the Hamiltonian

$$H = \omega_1^2 + \frac{1}{2}\omega_2^2 + c_2\omega_1\omega_2 - 2c_1 - (c_2c_1 - s_2s_1) + 3 \tag{25}$$

remains some constant value $H = E$ along trajectories.

3.1 Definition of the problem

There are numerous possible definitions of a 'flip' in the double pendulum system, each of which is quantitatively different but displays a similar fractal pattern. We define a flip as having occurred when the angle between the two rods, $\theta_2 - \theta_1$, becomes π, so that $c_2 = -1$. This does allow the possibility that the system approaches a flip but then moves back on itself, which intuitively one would not consider a flip. We wish to answer the following question: for which initial (stationary) conditions can we guarantee that a flip will not occur before time T?

The minimum energy required for a flip is clearly the energy at rest when $\theta_1 = 0$ and $\theta_2 = \pi$, giving $E = 2$. Therefore, any initial condition with energy less than 2, i.e.

$$2\cos\theta_1 + \cos\theta_2 \geq 1, \tag{26}$$

will never flip, and so the problem is trivial. On the other hand, if initially we have $\cos(\theta_2 - \theta_1) = -1$ then the time-to-flip is 0, and the problem is also trivial. A large region of the $\theta_1 - \theta_2$ plane remains, and here the time-to-flip displays a fractal-like pattern.

3.2 Rescaling

If we consider only those trajectories which start from rest ($\omega_1 = 0$, $\omega_2 = 0$), we must therefore have $E \leq 6$, and by construction, $E \geq 0$. Certainly then, ω_1 and ω_2 must lie within the region with boundary

$$\omega_1^2 + \frac{1}{2}\omega_2^2 + \omega_1\omega_2 = 6. \tag{27}$$

By extemising this expression, we find that $|\omega_1| \leq \Omega_1 \equiv 2\sqrt{3}$ and $|\omega_2| \leq \Omega_2 \equiv 2\sqrt{6}$. Solving (21) and (22),

$$T_1 = \left(2(\omega_1^2 + c_1) + c_2\omega_2^2\right) / \left(2 - c_2^2\right), \tag{28}$$

$$T_2 = \left(c_2(\omega_1^2 + c_1) + \omega_2^2\right) / \left(2 - c_2^2\right). \tag{29}$$

These give bounds

$$|T_1| \leq \tau_1 \equiv 2\Omega_1^2 + \Omega_2^2 + 2 = 50, \tag{30}$$

$$|T_2| \leq \tau_2 \equiv \Omega_1^2 + \Omega_2^2 + 1 = 37. \tag{31}$$

Suppose there is some particular region of time $t \in (0, T)$ in which we are interested. We may then define rescaled variables $\tilde{\omega_1} = \omega_1/\Omega_1$, $\tilde{T_1} = T_1/\tau_1$, $\tilde{t} = t/T$ etc. In this way, all variables are constained to lie between -1 and 1, which is of course automatically the case for s_1, c_1 etc. The equations now become (all tildes are immediately dropped for brevity)

$$\frac{d\omega_1}{dt} = f_{\omega_1} \equiv \frac{T}{\Omega_1}\left(s_2\tau_2 T_2 - s_1\right), \tag{32}$$

$$\frac{d\omega_2}{dt} = f_{\omega_2} \equiv -\frac{T}{\Omega_2} s_2\tau_1 T_1, \tag{33}$$

$$\frac{dc_1}{dt} = f_{c_1} \equiv -T\Omega_1\omega_1 s_1, \tag{34}$$

$$\frac{ds_1}{dt} = f_{s_1} \equiv T\Omega_1\omega_1 c_1, \tag{35}$$

$$\frac{dc_2}{dt} = f_{c_2} \equiv -T(\Omega_2\omega_2 - \Omega_1\omega_1)s_2, \tag{36}$$

$$\frac{ds_2}{dt} = f_{s_2} \equiv T(\Omega_2\omega_2 - \Omega_1\omega_1)c_2, \tag{37}$$

with constraints

$$0 = g_1 \equiv c_1^2 + s_1^2 - 1, \tag{38}$$

$$0 = g_2 \equiv c_2^2 + s_2^2 - 1, \tag{39}$$

$$0 = h_1 \equiv \tau_1 T_1 - c_2\tau_2 T_2 - \Omega_1^2\omega_1^2 - c_1, \tag{40}$$

$$0 = h_1 \equiv 2\tau_2 T_2 - c_2\tau_2 T_1 - \Omega_2^2\omega_2^2. \tag{41}$$

We may also constrain our system by considering only trajcetories whose energy is less than some maximum by

$$0 \leq b_E \equiv E_{max} - H. \tag{42}$$

Notice that all the f, g, h and b are polynomials.

3.3 Formulation of sum-of-squares problem

Let V be a polynomial in t, ω_1, ω_2, c_1, s_1, c_2 and s_2. If it holds that

$$\frac{\partial V}{\partial t} + \mathbf{f} \cdot \nabla V \geq 0, \tag{43}$$

the value of V increases along trajectories.

It is only necessary for this to be the case when our constraints g and h hold, so we require

$$\frac{\partial V}{\partial t} + \mathbf{f} \cdot \nabla V \geq g_1\sigma_1 + g_2\sigma_2 + h_1\sigma_3 + h_2\sigma_4 = 0, \tag{44}$$

where, for $i \in [1, 4]$, σ_i is any polynomial in t, ω_1, ω_2, c_1, s_1, c_2 and s_2, and also T_1 and T_2. We are only interested in trajectories which start stationary and are only interested in times up to T (rescaled to 1), so

$$\frac{\partial V}{\partial t} + \mathbf{f} \cdot \nabla V \geq g_1\sigma_1 + g_2\sigma_2 + h_1\sigma_3 + h_2\sigma_4 + t(1-t)\sigma_5 + b_E\sigma_6 \geq 0, \tag{45}$$

where again σ_5 and σ_6 are polynomials in t, ω_1, ω_2, c_1, s_1, c_2, s_2, T_1 and T_2, but are now also required to be nonnegative.

If we can find a solution with some C such that $V > C$ in the initial region, but $V \leq C$ in the 'flipped' region, then we guarantee no flip before T. To this end, we require

$$V|_{t=0} - C > b_0\sigma_7 + \omega_1^2\sigma_8 + \omega_2^2\sigma_9 \geq 0. \tag{46}$$

Here the σ are polynomials of ω_1, ω_2, c_1, s_1, c_2 and s_2 (no t or T_i dependence), and are non-negative. The initial region is defined by $b_0 \geq 0$ and $\omega_1 = \omega_2 = 0$. The last two terms ensure that we start with zero velocity. The strict inequality is implemented using some small fixed ϵ. We also need

$$C - V - g_1\sigma_{10} - g_2\sigma_{11} - t(1-t)\sigma_{12} - b_E\sigma_{13} - (c_2+1)\sigma_{14} \geq 0, \tag{47}$$

where now the σ depend on t, ω_1, ω_2, c_1, s_1, c_2 and s_2, but not T_i. Only σ_{12} and σ_{13} are required to be non-negative.

Therefore our full problem is to find coefficients for V and all σ_i, while requiring the following are sum-of-squares:

$$\frac{\partial V}{\partial t} + \mathbf{f} \cdot \nabla V - g_1\sigma_1 - g_2\sigma_2 - h_1\sigma_3 - h_2\sigma_4 - t(1-t)\sigma_5 - b_E\sigma_6, \tag{48}$$

$$\sigma_5, \tag{49}$$

$$\sigma_6, \tag{50}$$

$$V|_{t=0} - C - b_0\sigma_7 - \omega_1^2\sigma_8 - \omega_2^2\sigma_9 - \epsilon, \tag{51}$$

$$\sigma_7, \tag{52}$$

$$\sigma_8, \tag{53}$$

$$\sigma_9, \tag{54}$$

$$C - V - g_1\sigma_{10} - g_2\sigma_{11} - t(1-t)\sigma_{12} - b_E\sigma_{13} - (c_2+1)\sigma_{14}, \tag{55}$$

$$\sigma_{12}, \tag{56}$$

$$\sigma_{13}. \tag{57}$$

If V and the σ are all chosen to be invariant under S, then all of these expressions are invariant under S except (51), which may or may not be, depending on the choice of initial set $b_0 \geq 0$.

3.4 Systematic mapping of initial conditions

We restrict to the case that $\omega_1 = \omega = 2$ initially, and want to certify as non-flipping as much of the remaining $\theta_1 - \theta_2$ plane as possible. In order to exploit the problem's symmetry, we will consider sets of initial conditions defined by

$$b_0 = -\left\{R^2 - (c_1 - \cos\theta_1^0)^2 - (s_1 - \sin\theta_1^0)^2 - \left(c_2 - \cos(\theta_2^0 - \theta_1^0)\right)^2 - \left(s_2 - \sin(\theta_2^0 - \theta_1^0)\right)^2\right\}$$
$$\times\left\{R^2 - (c_1 - \cos\theta_1^0)^2 - (s_1 + \sin\theta_1^0)^2 - \left(c_2 - \cos(\theta_2^0 - \theta_1^0)\right)^2 - \left(s_2 + \sin(\theta_2^0 - \theta_1^0)\right)^2\right\},$$

so that $b_0 \geq 0$ gives a pair of hyperspheres in $s_1 - c_1 - s_2 - c_2$ space, parameterised by radius R and centre θ_1^0 and θ_2^0 and invariant under S. This transforms into a pair of oval shapes in $\theta_1 - \theta_2$ space.

Our method for mapping out which regions flip proceeds as follows:

1. Divide the $\theta_1 - \theta_2$ plane into a coarse grid of squares.
2. For each square (in parallel), solve a simple SOS problem to find the smallest set of the form $b_0 \geq 0$ which entirely contains the square, by minimising R and choosing θ_1 and θ_2 as the centre of the square.
3. For this region $b_0 \geq 0$, use another simple SOS problem to find the maximum energy, so that we may restrict ourselves to trajectories with less than this energy.
4. Attempt to find a solution to (48-57) for this region.
5. If a solution is found, all trajectories starting within $b_0 \geq 0$ are guaranteed not to flip. If not, we can subdivide the square into four smaller squares, and repeat the process.

4 Results

Figure 2a shows the time-to-flip, using the definition in section 3.1, as a function of the initial conditions, assuming $\omega_1 = \omega_2 = 0$ initially. This was calculated using the ode45 function in MATLAB, solving (13-22) directly. A complex fractal-like pattern is apparent. As the time goes to infinity, the vast majority of trajectories seem to flip, but there are certainly unstable periodic orbits which do not. It is believed that the 'wisps' which appear in figure 2a are those trajectories which start very close to simple periodic orbits, and so take a long time to flip.

Given such fine structures in the long time case, it is not obvious that after a short time, such as that presented in figure 2b, there are not small regions which flip very quickly. Since these figures are based on integrations starting at a grid of points, what appears to be a coherent region which does not flip is not guaranteed to be so. However, the method presented in section 2 allows us to certify that all trajectories starting within a simply connected set do not flip.

The system is parsed in YALMIP [13] and solved using Mosek [1]. YALMIP is able to automatically detect the symmetry in the system, and reduce the complexity of the resulting SDP accordingly. Despite this, the system is a very large one, and slow to solve.

The polynomials used in the system were chosen to be homogeneous to a certain degree N_d in the dynamical variables, and up to a certain degree N_t in time. So, for example, if $N_d = 2$ and $N_t = 3$, and supposing for brevity that V were to depend only on t, c_1 and s_1, it would be of the form

$$\begin{aligned} V = &\left(C_1 + C_2 c_1 + C_2 s_1 + C_3 c_1^2 + C_4 c_1 s_1 + C_5 s_1^2\right) \\ &+ \left(C_6 + C_7 c_1 + C_8 s_1 + C_9 c_1^2 + C_{10} c_1 s_1 + C_{11} s_1^2\right) t \\ &+ \left(C_{12} + C_{13} c_1 + C_{14} s_1 + C_{15} c_1^2 + C_{16} c_1 s_1 + C_{17} s_1^2\right) t^2 \\ &+ \left(C_{18} + C_{19} c_1 + C_{20} s_1 + C_{21} c_1^2 + C_{22} c_1 s_1 + C_{23} s_1^2\right) t^3; \end{aligned}$$

there are no $c_1^2 s_2^2$ terms.

Initially we chose $N_d = 4$ and $N_t = 4$, giving a total of 1050 unknown coefficients to be found, before symmetry reduction approximately halves this number. The results are shown in figure 3a. This degree is apparently insufficient to certify that regions near the boundaries found from direct calculation do not flip. It is possible, though unlikely, that there are trajectories not visible from the direct calculations which do flip in these regions. In order to test this, the tests near the boundaries were repeated with $N_d = 6$ and $N_t = 6$, at much greater computational cost (6468 total unknown coefficients), and in this case more regions were certified.

5 Conclusion

We have developed a new method to guarantee events in a dynamical system do not occur within a certain time period. The results confirmed what we believed to be true from direct computation of trajectories. Though we were able to do this only for modest time horizons, the method presented has several advantages.

Firstly, there is no discretisation in this computational method, in either space or time. This removes any possibility of trajectories which do flip existing within a set which appears not to. It also means we can be fairly confident of the accuracy of our results, so long as the SDP solver tells us the problem is well posed and well conditioned.

Secondly, the complexity of the problem does not necessarily scale with the size or dimensionality of the set of initial conditions we consider. So long as the trajectories within the initial region behave similarly, in some sense, then it is not more expensive to consider a larger region. Only when getting close to a flip/no flip boundary as seen in figure 2b is it necessary to include higher order polynomials. This means that we can certify large areas of initial conditions relatively cheaply, without the need for a large number of time integrations. In this proof-of-concept study, we have only considered initial conditions which start from stationary, $\omega_1 = \omega_2 = 0$. Though this intuitively makes sense, mathematically there is no reason one should consider only two dimensions. Our method is no more complex when considering a four-dimensional initial condition, whereas discretising a four-dimensional region of phase space is significantly more computationally demanding than a two-dimensional one.

Nevertheless, for this simple system, it is very cheap to perform accurate direct solutions of the equations, and we have only been able to attain modest time intervals using the barrier function method without using very large systems.

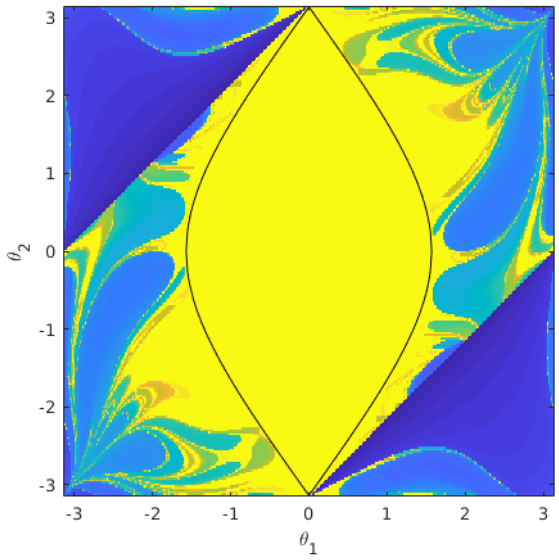

(a) Colour scale chosen so that $T = 0$ is blue, $T = 20$ or higher is yellow.

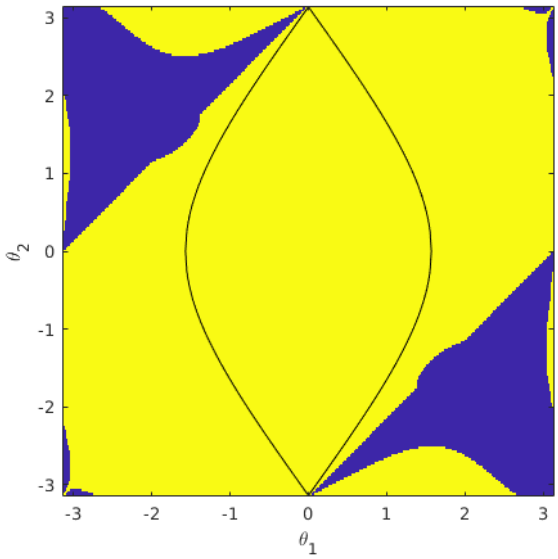

(b) Blue: $T < 4$, yellow: $T > 4$.

Figure 2: Time-to-flip T against initial conditions for the simple double pendulum, by direct solution of equations (13-22). The solid black line encloses the region for which flipping is energetically forbidden. The stable equilibrium is at the centre of the figures, and the three unstable equilibria are at the corners, the top and bottom centre and the left and right centre – recall that the plot is periodic in both directions. The two clear diagonal lines are the 'initially flipped' trajectories.

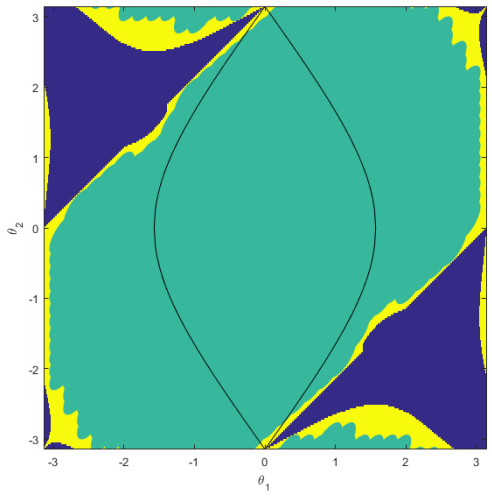

(a) Using degree 4 polnomials.

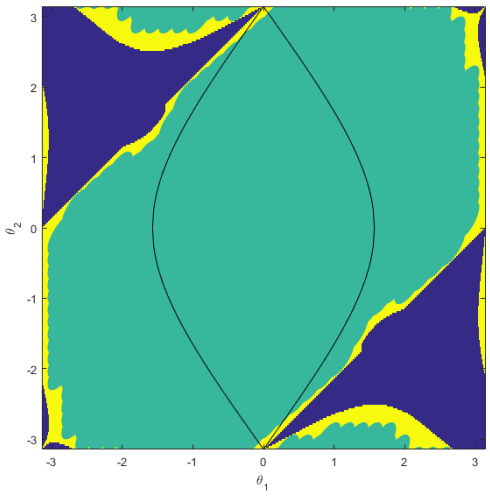

(b) Using degree 6 polynomials.

Figure 3: As per figure 2b but with regions guaranteed not to flip coloured in green. Notice the oval shapes from the sets of initial conditions defined by $b_0 \geq 0$.

6 Acknowledgements

The principal advisors on this project were David Goluskin and Charlie Doering, to whom the author owes much gratitude. Geoffrey Vasil and Phil Morrison provided many useful discussions, and Giovanni Fantuzzi gave helpful advice.

Appendices

A Some useful tricks for making systems polynomial

The barrier function method employed in this work, as well as the auxiliary function method of time averages, and the finding of Lyapunov functions using SOS, relies on dynamical systems being in the form

$$\frac{d\mathbf{x}}{dt} = \mathbf{f}(\mathbf{x}), \tag{58}$$

where, crucially, $\mathbf{f}$ must be a polynomial. In many simple and interesting dynamical systems, this is not the case.

A.1 Rational functions

Suppose we have a dynamical system

$$\frac{dx}{dt} = \frac{f(x)}{g(x)} \tag{59}$$

where $x \in \mathbb{R}^n$, and $f : \mathbb{R}^n \to \mathbb{R}^n$ and $g : \mathbb{R}^n \to \mathbb{R}$ are polynomials. Define a dummy variable

$$\lambda \equiv \frac{1}{g(x)}, \tag{60}$$

so that the system becomes polynomial:

$$\frac{dx}{dt} = \lambda f(x), \tag{61}$$

with the polynomial constraint

$$\lambda g(x) = 1. \tag{62}$$

For some polynomial $V(x) : \mathbb{R}^n \to \mathbb{R}$ to be increasing along trajectories is therefore equivalent to requiring

$$\lambda f(x) \cdot \nabla V(x) > (\lambda g(x) - 1)s(x, \lambda), \tag{63}$$

for all x and λ, for some polynomial s.

This method can be extended to matrix inverses, as well as to fractional powers.

A.2 Trigonometric functions

Suppose

$$\frac{dx}{dt} = f(x, \cos x, \sin x),$$

where $f : \mathbb{R}^3 \to \mathbb{R}$ is a polynomial. We may simply define $y = \cos x$, $z = \sin x$ and then the system becomes the simple polynomial system:

$$\begin{aligned}
\frac{dx}{dt} &= f(x, y, z), \\
\frac{dy}{dt} &= -zf(x, y, z), \\
\frac{dz}{dt} &= yf(x, y, z).
\end{aligned}$$

Note that the order of the system is one higher than that of the original polynomial, and there are three variables instead of one. Tricks like this can be combined, but may quickly lead to very large polynomial systems. Care is also required to ensure that the initial conditions for y and z are compatible with the definition.

In the special but common case

$$\frac{dx}{dt} = f(\cos x, \sin x),$$

the result is particularly simple:

$$\begin{aligned}
\frac{dy}{dt} &= -zf(y, z), \\
\frac{dz}{dt} &= yf(y, z).
\end{aligned}$$

Again, this system is only relevant to the original one when the initial conditions are chosen so that $y = \pm\sqrt{1 - z^2}$.

Similar tricks can be used for exponentials, other trigonometric functions, and compositions of these functions with polynomials.

B Discrete-time dynamical systems

All examples studied in this work have been continuous-time dynamical systems, in the form (58). However, many interesting dynamical systems, especially simple examples relevant to Hamiltonian systems [9, 3, 4] are discrete-time systems, or maps,

$$\mathbf{x}_{n+1} = \mathbf{f}(\mathbf{x}_n). \tag{64}$$

If $\mathbf{f}$ is a polynomial, we may formulate a barrier function method for this system, by finding polynomial $V(\mathbf{x}, n)$ such that

$$V(\mathbf{f}(\mathbf{x}), n+1) - V(\mathbf{x}, n) \geq 0 \tag{65}$$

over some number N of iterations. In practice, n should be rescaled to be between 0 and 1, by using N. Unfortunately, the composition of V with $\mathbf{f}$ gives a very high degree polynomial, which is slow and memory intensive to optimise over, so in practice only small N is possible.

References

[1] Erling D. Andersen and Knud D. Andersen. *The Mosek Interior Point Optimizer for Linear Programming: An Implementation of the Homogeneous Algorithm*, pages 197–232. Springer US, Boston, MA, 2000.

[2] S. I. Chernyshenko, P. Goulart, D. Huang, and A. Papachristodoulou. Polynomial sum of squares in fluid dynamics: a review with a look ahead. *Philosophical Transactions of the Royal Society A: Mathematical, Physical and Engineering Sciences*, 372(2020): 20130350, 2014.

[3] Boris Valerianovich Chirikov. Research concerning the theory of non-linear resonance and stochasticity. Technical report, CM-P00100691, 1971.

[4] Diego del Castillo-Negrete and P. J. Morrison. Chaotic transport by Rossby waves in shear flow. *Physics of Fluids A: Fluid Dynamics*, 5(4):948–965, 1993.

[5] Julius Elinson. Flip-over threshold for the double pendulum. 2013. URL `https://www.math.ust.hk/~machas/hmc-math164-nonlinear-dynamics.pdf`.

[6] G. Fantuzzi, D. Goluskin, D. Huang, and S. Chernyshenko. Bounds for deterministic and stochastic dynamical systems using sum-of-squares optimization. *SIAM Journal on Applied Dynamical Systems*, 15(4):1962–1988, 2016.

[7] David Goluskin. Bounding averages rigorously using semidefinite programming: Mean moments of the Lorenz system. *Journal of Nonlinear Science*, 28(2):621–651, Apr 2018. ISSN 1432-1467.

[8] David Goluskin and Giovanni Fantuzzi. Bounds on mean energy in the Kuramoto–Sivashinsky equation computed using semidefinite programming. *Nonlinearity*, 32(5):1705–1730, 2019.

[9] Michel Hénon. Numerical study of quadratic area-preserving mappings. *Quarterly of applied mathematics*, pages 291–312, 1969.

[10] Didier Henrion and Milan Korda. Convex computation of the region of attraction of polynomial control systems. *IEEE Transactions on Automatic Control*, 59(2):297–312, 2013.

[11] Jeremy S. Heyl. The double pendulum fractal. 2008.

[12] H.J. Korsch and H.J. Jodl. *Chaos: A Program Collection for the PC*. Springer Berlin Heidelberg, 2013. ISBN 9783662029916. URL `https://books.google.co.uk/books?id=3dLqCAAAQBAJ`.

[13] Johan Löfberg. Yalmip: A toolbox for modeling and optimization in matlab. In *Proceedings of the CACSD Conference*, volume 3. Taipei, Taiwan, 2004.

[14] May Palace and Jeffrey Emmert. Hidden fractals in the dynamics of the compound double pendulum. 2016. URL `http://www.csaapt.org/uploads/3/4/4/2/34425343/csaapt_maypalace_sp16.pdf`.

[15] Pablo A Parrilo. Semidefinite programming relaxations for semialgebraic problems. *Mathematical programming*, 96(2):293–320, 2003.

[16] Tomasz Stachowiak and Toshio Okada. A numerical analysis of chaos in the double pendulum. *Chaos, Solitons & Fractals*, 29(2):417–422, 2006.

[17] G. Vasil. Unpublished notes, 2019.

[18] Dare A Wells. *Schaum's outline of theory and problems of Lagrangian dynamics: with a treatment of Euler's equations of motion, Hamilton's equations and Hamilton's principle*. McGraw-Hill, 1967.

Symmetry Breaking of the Enceladus Ice Shell

Wanying Kang

August 20, 2019

1 Introduction

This study investigates why there is a hemispheric asymmetry of the ice thickness on Enceladus although the tidal forcing is perfectly symmetric between the two hemispheres. We consider a simple limit and treat the ice crust as a membrane covering the ocean which is modeled by a shallow water model. We propose that this asymmetry may arise from a symmetry breaking induced by a positive feedback, which can reinforce the tilting of the ice-ocean interface but only at large scales. With such a positive feedback, an infinitesimal initial asymmetry from random processes could end up in a finite interface tilting that may be balanced by the heat diffusion to the space. We will also show that this mechanism is efficient only for perturbations with wavenumber 1 meridionally (P_{10} modes), while the perturbations with smaller scales (wavenumber greater than 1) are not growing as fast. With this scale selectivity, we expect the interface topography to be dominated by wavenumber 1 or 3, consistent with the geysers gathering over the south pole of Enceladus.

In the following sections, we first investigate the mechanism using a 1 dimensional shallow water model covered by an ice membrane (section 2). We solve for modal growth rates of the interface perturbation through asymptotic expansion, compare the results with numerical simulations (section 2.2), and then we understand the positive feedback mechanism and the scale selective mechanism by keeping only the relevant terms (section 2.4). The tidal heating distribution generated with a "realistic" interface topography is estimated numerically in section 2.3, to be compared with the observed heat flux distribution. Next, we asymptotically solve the growth rate in 2 dimensional spherical coordinates and show that the results remain qualitatively similar to the 1 dimensional model (section 3.2). Finally, in section 4, we couple the tidal heating model with the evolution of the interface topography, and show that, starting from infinitesimal random noise, the interface topography can evolve to one that is tilted from one pole to the other. Discussions and conclusions are in section 5.

2 1D ice-covered shallow water

2.1 Model setup

We start from a minimum model for the Enceladus tides, a 1D shallow water model covered by an ice membrane representing a meridian on Enceladus. The governing equations for

the flow speed u, v and the surface deformation η are,

$$\partial_t v = -g\partial_y \eta - \frac{r_0}{H(y)/H_0} v - \partial_y R_{\rm ice} + f(y)u + F \quad (1)$$

$$\partial_t u = -\frac{r_0}{H(y)/H_0} u - f(y)v \quad (2)$$

$$\partial_t \eta = -\partial_y (H(y)v). \quad (3)$$

In the above equations, we assume all fields to be uniform in x direction (corresponding to the east-west direction on Enceladus), and thus all x derivative terms vanishes. The momentum equations are forced by Ekman damping, tidal forcing $F = -\partial_y U$ (U is the tidal potential), Coriolis force, and restoring force due to gravity $-g\partial_y \eta$ and due to ice deformation $-\partial_y R_{\rm ice}$. $H(y)$ is the depth of the ocean varying with y, and H_0 is the mean ocean depth. $g = 0.113$ m/s^2 is the gravitational acceleration rate on Enceladus and $\rho = 1000$ kg/m^3 is the water density. We parameterize $R_{\rm ice}$, the pressure that ice is exerting on the water, as a function of the deformation η. In order to get the proper formula, we write the momentum equation for a uniform ice membrane,

$$\overline{\sigma}\partial_{tt}\eta + \overline{\gamma}\partial_t \eta = \partial_y \overline{T}\partial_y \eta + \sigma R_{\rm ice}.$$

Here, $\overline{\sigma}$, $\overline{\gamma}$, $\overline{T}$ are the area mass density, damping coefficient, and surface tension of the ice membrane, and σ is the area mass density of the subsurface ocean. For the tidal mode, whose time variation can be written as $e^{-i\omega t}$, $R_{\rm ice}$ can be parameterized as

$$R_{\rm ice} = (-\partial_y \alpha \partial_y + \nu \partial_t)\eta, \quad (4)$$

where $\alpha = \overline{T}/\sigma$ is the ice spring constant, $\nu = \overline{\gamma}/\sigma$ is the ice damping rate. The first term comes from the surface tension; it has the form of a negative real number multiplying the deformation η and thus acts as an elastic restoring force. The two y derivatives are not combined together because, as will be mentioned later, we set α to be a function of ice thickness $\overline{H}$, which varies with y. The second term has the form of an imaginary number multiplying η, and thus represent the damping in the membrane. In the above formula, we keep the dominant real and imaginary terms, while dropping the inertial term $-(\omega^2\sigma/\rho)\eta$, because it is also in the form of a real number multiplying η, but, in the stiff membrane regime, is much smaller than the term due to surface tension. We adopt the ice modulus values from Beuthe (2018), who explicitly solves a thin ice model; the elastic restoring term associated with α induced by a 23 km thick ice shell is around $21.3g\overline{\sigma}/\sigma \sim 1.34$ times η if the deformation has degree-2 structure. On the other hand, the inertial term is only around $\overline{\sigma}\omega^2/\sigma \sim$ 1.6e-9 times η, which is clearly negligible. That is equivalent to say that the ice membrane can be thought of as weightless. In fact, the ice rheology is much more complex than what is considered here. We ignore the extra restoring force induced by the bending motions, and we do not consider the tangential rubbing motions which have been shown to be important for the heat generation. We explored some of these effects, which requires a lot of works, including some repetitive ones. To keep the physics picture clear, we decide not to include all the details and results, but to just present a simple case in detail and discuss the effects of the ignored factors in the conclusion (section 5).

Substituting Eq (4) into Eq (1) yields,

$$\partial_t v = -g\partial_y \eta - \frac{r_0}{H(y)/H_0} v - \partial_y \left(-\partial_y \alpha \partial_y + \nu \partial_t\right) \eta + f(y)u + F. \quad (5)$$

The ice membrane should be stiffer when it is thicker, so we let the ice spring constant vary with the ice thickness $\overline{H}$ following

$$\alpha(\overline{H}) = \alpha_0 (\overline{H}/\overline{H}_0)^{p_\alpha}. \quad (6)$$

The power p_α by default is set to 1. Choosing a different positive number does not affect the result qualitatively. We also allow the ice damping rate ν to vary with $\overline{H}$ to the same manner,

$$\nu(\overline{H}) = \nu_0 (\overline{H}/\overline{H}_0)^{p_\nu}. \quad (7)$$

But by default, it is turned off, i.e., $p_\nu = 0$. The ice depth $\overline{H}(y)$ and ocean depth $H(y)$ are decomposed into a mean value plus a variation.

$$\begin{aligned} H(y) &= H_0 + h(y) = H_0(1 + h'(y)) \\ \overline{H}(y) &= \overline{H}_0 + \overline{h}(y) = \overline{H}_0(1 + \overline{h}'(y)). \end{aligned}$$

Prime denotes the fluctuation relative to the mean. We link the ice depth variation with that of the ocean by assuming the column weight to be a constant. This is a reasonable choice as the bottom of the ocean cannot maintain a tangential stress to counterbalance the horizontal pressure gradient in a long term.

$$\begin{aligned} \overline{h}(y) &= -\frac{\rho}{\overline{\rho}} h(y) \\ \overline{h}'(y) &= -\frac{\rho H_0}{\overline{\rho}\,\overline{H}_0} h'(y) \equiv -\beta h'(y) \end{aligned} \quad (8)$$

We solve Eq (5), Eq (2), Eq (3) and Eq (6-8) in a domain corresponding to a meridian circle (domain size $L = 2\pi a$, where a is the radius of Enceladus), from south pole to north pole, and then back to south pole from the opposite side. This way we can use periodic boundary conditions and solve everything in Fourier space. The default parameter values are summarized in Table. 1.

2.2 Asymptotic solution

In this section, we assume that the interface topography is small ($h' << 1$), and solve for the projection of the leading order tidal heating profile onto this topography through asymptotic expansion. One difficulty facing us is that the Coriolis coefficient is varying with y, and thus if this term is to zeroth order, all modes will be excited by a single mode forcing. To make the problem analytically solvable, we can either set the Coriolis coefficient to be a constant, or assume the Coriolis terms are to the first order so that it will only appear in the first or higher order equation as a forcing. We choose the first. As demonstrated in Beuthe (2016) and as we will show later (section 2.4), the rotation effect is negligible with

Table 1: Parameter setups

Parameter Description	Symbol	Value	Units	Reference
Water density	ρ	1000	kg/m^3	–
Ice density	$\overline{\rho}$	900	kg/m^3	–
Surface gravity	g	0.113	m/s^2	–
Rotation rate (tidal frequency)	ω	5.308×10^{-5}	s^{-1}	–
Coriolis Coeff. at the poles	f_0	$2\omega = 1.062 \times 10^{-4}$	s^{-1}	–
Eccentricity	e	0.0047	–	–
Tidal potential Amp. in 1D	A	$1.5a^2\Omega^2 e = 1.26$	m^2/s^2	Tyler (2011)
Tidal forcing wavenumber in 1D	$\tilde{k}$	2	–	Tyler (2011)
Enceladus radius	a	252.1	km	–
Domain size	L	$2\pi a = 1584$	km	–
Mean ocean depth	H_0	37	km	Beuthe (2018)
Mean ice depth	$\overline{H}_0$	23	km	Beuthe (2018)
Ocean ice mass ratio	β	$\rho H_0/\overline{\rho}\overline{H}_0 = 1.79$	–	–
Ekman damping rate	r_0	0.05	day^{-1}	–
Ice spring constant	α_0	$21.3g/(4\pi/L)^2/\beta = 2.1 \times 10^{10}$	m^3/s^2	Beuthe (2018)
α's power dependence on $\overline{H}$	p_α	1	–	–
Ice damping rate	ν_0	$0.73g/\omega/\beta = 870$	m/s	Beuthe (2018)
ν's power dependence on $\overline{H}$	p_ν	0	–	–
Ice fusion energy	L_f	3.3×10^4	J/kg	–

a stiff ice shell (which is true). The tidal forcing and the interface topography are set to be sinusoidal (More complex structure can be decomposed into the sum of multiple sinusoidal modes, however, by doing so, we prevent different modes from interfering with each other),

$$U(y,t) = \Re\left[A\ \exp(iky - i\omega t)\right] \tag{9}$$

$$h'(y) = h_t\ \cos(k_t y) \equiv h_t h_1. \tag{10}$$

Tyler (2011) and Beuthe (2016) derive the eccentricity tide potential on Enceladus.

$$U_{\text{eccen}} = \Re\left[-\sqrt{\frac{4\pi}{5}}\frac{2}{3}Y_{2,0} + \sqrt{\frac{96\pi}{5}}\left(\frac{7}{8}Y_{2,2} - \frac{1}{8}Y_{2,-2}\right)\right]e^{-i\omega t} \tag{11}$$

The factor $\sqrt{4\pi/5}$ and $\sqrt{96\pi/5}$ come from the normalization factor of $Y_{2,0}$ and $Y_{2,2}$. We therefore choose $A = A_{2,0} = (3/2\sqrt{2})a^2\Omega^2 e, \tilde{k} \equiv L/(2\pi)k = 2$ to represent the $Y_{2,0}$ eccentricity tide. We divide an extra factor of $\sqrt{2}$ because we use a traveling wave form for the forcing, which contains one $\cos(ky)\cos(\omega t)$ mode plus one $\sin(ky)\sin(\omega t)$ mode. As such, the same amount of energy is put in the domain from north pole to south pole.

We use a traveling wave form for tidal potential to make sure everywhere in the domain is forced equally. Any inhomogeneity arises from the heating profile then can be attributed to the interaction between the tidal perturbation and the interface topography. Actually, a stationary forcing can be decomposed into two wave trains traveling in the opposite direction. Since this system has spatial inversion symmetry without the Coriolis effect (which will be shown to be a secondary effect), the projection of heating onto topography profile will not change when reversing the tidal forcing wave train. Because two dimensional dynamics is crucial for $Y_{2,2}$ tidal forcing, we leave the discussion to section 3, where we directly solve for the spherical coordinates. In the rest of this subsection, we will solve

for the projection of the tidal heating profile onto the interface topography for various topography wavenumbers, $\tilde{k}_t \equiv L/(2\pi)k_t = 1, 2, \ldots$.

We first expand v, u and η using small parameter h_t,

$$\begin{aligned} v &= v_0 + h_t v_1 + h_t v_2 + \ldots \\ u &= u_0 + h_t u_1 + h_t u_2 + \ldots \\ \eta &= \eta_0 + h_t \eta_1 + h_t \eta_2 + \ldots . \end{aligned}$$

The zeroth order equation set is,

$$\partial_t v_0 = -g\partial_y \eta_0 - r_0 v_0 - \partial_y \left(-\alpha_0 \partial_{yy} + \nu_0 \partial_t\right) \eta_0 + f_0 u + F \tag{12}$$

$$\partial_t u_0 = -r_0 u_0 - f_0 v \tag{13}$$

$$\partial_t \eta_0 = -H_0 \partial_y (v_0). \tag{14}$$

Substituting the plane wave solution

$$\begin{aligned} v_0(y,t) &= \Re[\tilde{v}_0 \exp(iky - i\omega t)] \\ u_0(y,t) &= \Re[\tilde{u}_0 \exp(iky - i\omega t)] \\ \eta_0(y,t) &= \Re[\tilde{\eta}_0 \exp(iky - i\omega t)] \end{aligned}$$

one can get the following specific solution,

$$\tilde{v}_0 = \frac{\omega k}{\delta_0} A \tag{15}$$

$$\tilde{u}_0 = \frac{-i f_0 \omega k}{(\omega + i r_0)\delta_0} A \tag{16}$$

$$\tilde{\eta}_0 = \frac{k^2 H_0}{\delta_0} A, \tag{17}$$

where

$$\delta_0 = -i\omega(-i\omega + r_0) + k^2 H_0 (g + \alpha_0 k^2 - i\omega\nu_0) + f_0^2/(1 + i r_0/\omega). \tag{18}$$

We then obtain the first order equation set by linearizing each term and keeping only the term proportional to h_t,

$$\begin{aligned} \partial_t v_1 &= -g\partial_y \eta_1 - r_0 v_1 - \partial_y \left(-\alpha_0 \partial_{yy} + \nu_0 \partial_t\right) \eta_1 + f_0 u_1 \\ &\quad + \beta \partial_y \left[-\alpha_0 p_\alpha \partial_y (h_1 \partial_y \eta_0) + \nu_0 p_\nu \partial_t \eta_0 h_1\right] + r_0 h_1 v_0 \end{aligned} \tag{19}$$

$$\partial_t u_1 = -r_0 u_1 - f_0 v_1 + r_0 h_1 u_0 \tag{20}$$

$$\partial_t \eta_1 = -H_1 \partial_y (v_1) + -H_0 \partial_y (h_1 v_0) \tag{21}$$

Interfering with $h_1 = \cos(k_t y) = (\exp(ik_t y) + \exp(-ik_t y))/2$ excites two modes in the first order equation, with wavenumber $k + k_t$ and $k - k_t$. Substituting the plane wave solution

$$\begin{aligned} v_1(y,t) &= \Re[\tilde{v}_1^+ \exp(i(k + k_t)y - i\omega t) + \tilde{v}_1^- \exp(i(k - k_t)y - i\omega t)], \\ u_1(y,t) &= \Re[\tilde{u}_1^+ \exp(i(k + k_t)y - i\omega t) + \tilde{u}_1^- \exp(i(k - k_t)y - i\omega t)], \\ \eta_0(y,t) &= \Re[\tilde{\eta}_1^+ \exp(i(k + k_t)y - i\omega t) + \tilde{\eta}_1^- \exp(i(k - k_t)y - i\omega t)], \end{aligned}$$

we get the amplitudes of the first order perturbation,

$$\begin{aligned}
\tilde{v}_1^{\pm} &= \frac{1}{2\delta_1^{\pm}} \{[\omega\beta(\alpha_0 p_\alpha k(k\pm k_t) - i\omega\nu_0 p_\nu)(k\pm k_t)]\,\tilde{\eta}_0 \\
&\quad - \left[i\omega r_0 + (g + \alpha_0(k\pm k_t)^2 - i\omega\nu_0)H_0(k\pm k_t)^2\right]\tilde{v}_0 \\
&\quad + [f_0 r_0/(1+ir_0/\omega)]\,\tilde{u}_0\} \qquad (22)\\
\tilde{u}_1^{\pm} &= \frac{1}{2\delta_1^{\pm}(-i\omega+r_0)} \{[-f_0\omega\beta(\alpha_0 p_\alpha k(k\pm k_t) - i\omega\nu_0 p_\nu)(k\pm k_t)]\,\tilde{\eta}_0 \\
&\quad \left[if_0\omega r_0 + f_0(g + \alpha_0(k\pm k_t)^2 - i\omega\nu_0)H_0(k\pm k_t)^2\right]\tilde{v}_0 \\
&\quad + \left[-i\omega r_0(-i\omega+r_0) + r_0(k\pm k_t)^2 H_0(g+\alpha_0(k\pm k_t)^2 - i\omega\nu_0)\right]\tilde{u}_0\big\} \qquad (23)\\
\tilde{\eta}_1^{\pm} &= \frac{H_0(k\pm k_t)}{2\delta_1^{\pm}\omega} \{[\omega\beta(\alpha_0 p_\alpha k(k\pm k_t) - i\omega\nu_0 p_\nu)(k\pm k_t)]\,\tilde{\eta}_0 \\
&\quad + \left[i\omega(-i\omega+2r_0) - f_0^2/(1+ir_0/\omega)\right]\tilde{v}_0 \\
&\quad + [f_0 r_0/(1+ir_0/\omega)]\,\tilde{u}_0\}\,. \qquad (24)
\end{aligned}$$

where

$$\delta_1^{\pm} = -i\omega(-i\omega+r_0) + (k\pm k_t)^2 H_0(g+\alpha_0(k\pm k_t)^2 - i\omega\nu_0) + f_0^2/(1+ir_0/\omega). \qquad (25)$$

Next, we derive the energy equation. We multiply $\rho v H(y)$ to Eq (5), multiply $\rho u H(y)$ to Eq (2), multiply $\rho(g - \partial_y\alpha(\overline{H})\partial_y)\eta$ to Eq (3), and add them together. After some integration by parts, we get

$$\begin{aligned}
&\partial_t\left[\tfrac{1}{2}\rho v^2 H + \tfrac{1}{2}\rho u^2 H + \tfrac{1}{2}\rho g\eta^2 + \tfrac{1}{2}\rho\alpha(\partial_y\eta)^2\right] \\
=\;& -\partial_y\left[\rho v H g\eta + \rho v H\partial_y(\alpha\partial_y\eta) - \rho\alpha(\partial_t\eta)(\partial_y\eta) + \rho\nu v H\partial_t\eta\right] \\
+\;& \rho v H F - \rho\nu(\partial_t\eta)^2 - \rho r_0 H_0(v^2+u^2). \qquad (26)
\end{aligned}$$

Clearly, the quadratic form on the left hand side is the energy of the system. The first term on the right hand side is the energy transport term; it vanishes after averaging over the domain. The first term on the second line is the energy source from the tidal forcing. The last two terms are the tidal heating generated in the ice and in the ocean, respectively.

Projecting the tidal heating onto the topography $h_1 = \cos(k_t y)$, keeping only the leading terms ($O(h_t)$ terms), and dividing everything by h_t (by doing so, the projected heating we get should not change with the topography amplitude as long as it is small enough), leads

to the projected heating rate associated with ice dissipation and Ekman friction,

$$
\begin{aligned}
P^{k_t}_{\text{ice}} &\equiv \frac{1}{Lh_t}\int_{-L}^{L}\rho\nu(\partial_t\eta)^2\cdot h_1\ dy \\
&= \frac{\rho\nu_0\omega^2}{Lh_t}\Re\int_{-L}^{L}(1-p_\nu\beta h_t\cos k_t y)\cos k_t y\cdot\ldots \\
&\quad \ldots\left[\tilde{\eta}_0 e^{iky}+h_t\tilde{\eta}_1^{+}e^{i(k+k_t)y}+h_t\tilde{\eta}_1^{-}e^{i(k-k_t)y}\right]^2 dy \\
&= \rho\nu_0\omega^2\Re\left[-\tfrac{1}{2}p_\nu\beta\tilde{\eta}_0\tilde{\eta}_0^{*}+\tilde{\eta}_1^{+}\tilde{\eta}_0^{*}+\tilde{\eta}_1^{-}\tilde{\eta}_0^{*}\right] \qquad (27)\\
P^{k_t}_{\text{ekman}} &\equiv \frac{1}{Lh_t}\int_{-L}^{L}\rho r_0 H_0(u^2+v^2)\cdot h_1\ dy \\
&= \frac{1}{Lh_t}\int_{-L}^{L}\rho r_0 H_0\left\{\Re\left[\tilde{v}_0 e^{iky}+h_t\tilde{v}_1^{+}e^{i(k+k_t)y}+h_t\tilde{v}_1^{-}e^{i(k-k_t)y}\right]^2\right. \\
&\quad \left.+\Re\left[\tilde{u}_0 e^{iky}+h_t\tilde{u}_1^{+}e^{i(k+k_t)y}+h_t\tilde{u}_1^{-}e^{i(k-k_t)y}\right]^2\right\}\cdot\cos(k_t y)\ dy \\
&= \rho r_0 H_0\Re\left[\tilde{u}_1^{+}\tilde{u}_0^{*}+\tilde{u}_1^{-}\tilde{u}_0^{*}+\tilde{v}_1^{+}\tilde{v}_0^{*}+\tilde{v}_1^{-}\tilde{v}_0^{*}\right] \qquad (28)\\
P^{k_t}_{\text{total}} &\equiv P^{k_t}_{\text{ice}}+P^{k_t}_{\text{ekman}}. \qquad (29)
\end{aligned}
$$

The question we intend to address in this study is whether the tidal heating can reenhance the interface topography and lead to symmetry breaking between the two hemisphere. The condition for this to happen is $P_{\text{total}} > 0$. In Fig. 1, we show the projected heating rate associated with ice dissipation and Ekman friction solved at $f_0 = 0$ (dashed curve) and $f_0 = 2\omega$ (solid curve). Here, we want to highlight three features without diving into the mechanisms, which will be discussed in section 2.4. 1) The ice dissipation is the dominant contributor, consistent with Beuthe (2016). 2) A constant Coriolis coefficient makes little difference because the ice restoring force dominates all other processes (see section 2.4), again consistent with Beuthe (2016). 3) Only large-scale interface topography (wavenumber 1 and 2) can be reenhanced by the tidal heating. As mentioned at the beginning, the scale selectivity (feature 3) is necessary to explain the fact that geysers cluster in one spot on Enceladus. The interface topography will be dominated by the fastest growing mode; if the small-scale interface perturbations grow equally fast or even faster, compared to the large-scale ones, the Enceladus would be "patchy", which means the geysers would have different scales and spread all over the globe. Mechanisms leading to the nonmonotonic dependence of $P^{k_t}_{\text{ice}}$, $P^{k_t}_{\text{ekman}}$ on k_t are proposed in section 2.4.

2.3 Numerical solution as a verification

To verify the asymptotic solution from the previous subsection, we numerically solve the same problem. With a numerical model, we can also lift the small perturbation assumption, and evaluate the heat flux distribution under a "realistic" interface topography.

We first decompose the solution into one component varying as $\cos\omega t$ and one as $\sin\omega t$.

$$
v(y,t) = v_c(y)\cos\omega t + v_s(y)\sin\omega t
$$

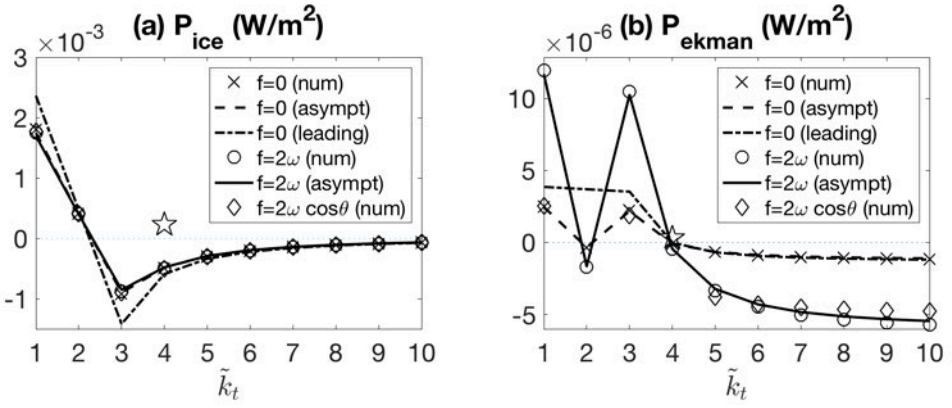

Figure 1: The projected tidal heating onto interface topography, associated with (a) ice dissipation and (b) Ekman friction. Lines are results from asymptotic solutions (Eq. 27-28), and markers are results from numerical solution. Coriolis effects are completely ignored when evaluating the cross markers, the dashed line and the dash dotted line, and a constant Coriolis effect are used when evaluating the results denoted by circles or the solid line. Diamond denotes numerical solution for a more realistic case where we adopt a spatial varying Coriolis coefficient $f(y) = f_0 \cos(y)$. The star denotes the $2k$ tide-tide interference mode (Eq. 50) induced by a stationary tidal forcing.

Other variables, such as $u,\ \eta,\ F$, are decomposed in the same manner. Substituting back to Eq (5), Eq (2) and Eq (3) yields,

$$\begin{aligned}
\omega v_s + \partial_y(g - \partial_y\alpha\partial_y)\eta_c + r'v_c + \partial_y\nu\omega\eta_s - fu_c &= F_c && (30)\\
-\omega v_c + \partial_y(g - \partial_y\alpha\partial_y)\eta_s + r'v_s - \partial_y\nu\omega\eta_c - fu_s &= F_s && (31)\\
\omega u_s + r'u_c + fv_c &= 0 && (32)\\
-\omega u_c + r'u_s + fv_s &= 0 && (33)\\
\omega\eta_s + \partial_y(Hv_c) &= 0 && (34)\\
-\omega\eta_c + \partial_y(Hv_s) &= 0. && (35)
\end{aligned}$$

Canceling $u_s,\ u_c$ from the first four equations above leads to

$$\begin{aligned}
\omega v_s + \partial_y(g - \partial_y\alpha\partial_y)\eta_c + r'v_c + \partial_y\nu\omega\eta_s - \frac{f^2}{\omega^2 + r'^2}\left(\omega u_s - r'v_c\right) &= F_c && (36)\\
-\omega v_c + \partial_y(g - \partial_y\alpha\partial_y)\eta_s + r'v_s - \partial_y\nu\omega\eta_c + \frac{f^2}{\omega^2 + r'^2}\left(\omega u_s + r'v_c\right) &= F_s. && (37)
\end{aligned}$$

where we have defined $r' = r_0 H_0/H$.

We then discretize Eq (34-(37)) into matrix form using second-order central difference, and solve for the tidal perturbation $v_c,\ v_s,\ u_c,\ u_s,\ \eta_c,\ \eta_s$ forced by a tide forcing,

$$F_c = -kA\sin(ky),\ F_s = kA\cos(ky).$$

Finally, we evaluate the total tidal heating profiles (without projecting onto the interface topography) using

$$\mathcal{H}_{\text{ice}} = \tfrac{1}{2}\rho\nu_0\omega^2\left(\eta_c^2+\eta_s^2\right) \tag{38}$$

$$\mathcal{H}_{\text{ekman}} = \tfrac{1}{2}\rho r_0 H_0\left(u_c^2+u_s^2+v_c^2+v_s^2\right) \tag{39}$$

$$\mathcal{H}_{\text{total}} = P_{\text{ice}}^{\text{num}}+P_{\text{ekman}}^{\text{num}}. \tag{40}$$

The factor of 1/2 comes from the mean value of sinusoidal profiles. To compare with the asymptotic solutions, we calculate the projected heating by inner multiplying the above $\mathcal{H}$ profiles and the topography h_1 (wavenumber k_t), and normalize it with $2/h_t$ (the factor of 2 is again from the mean value of sinusoidal profiles).

$$P_n^{\text{num},k_t} = \frac{2}{h_t}\overline{\mathcal{H}_n h_1}, \qquad n\in\{\text{ice},\text{ekman},\text{total}\} \tag{41}$$

We numerically solve the projected heating using a relatively small interface topography ($h_t = 0.1$) while keeping other parameters the same as in the asymptotic solution. The numerical results with $f_0 = 0$ and $f_0 = 2\omega$ are plotted in Fig. 1 as $\times$ and $\circ$ markers, to be compared with the asymptotic solution in the dashed line and solid line. The matching is almost perfect, even if the interface topography amplitude is almost 10% of the total ocean depth, indicating the asymptotic solutions can, at least, provide useful insight to explain the real world. We also investigate the effect of a spatial varying Coriolis coefficient ($\Diamond$ markers in Fig. 1). $P_{\text{ice}}^{k_t}$ and $P_{\text{ekman}}^{k_t}$ remains almost unaffected for most $\tilde{k}_t$, except $P_{\text{ekman}}^{k_t}$ increases by almost 10 times at $\tilde{k}_t = 2, 4$ (these two points are far off the domain we show). However, since $P_{\text{ekman}}^{k_t}$ is two orders of magnitude smaller than $P_{\text{ice}}^{k_t}$, none of these changes make a difference to $P_{\text{total}}^{k_t}$.

2.4 Mechanisms for symmetry breaking and scale selection

In this subsection, we will investigate the dominant balance of the 1D model, in order to understand the mechanisms for symmetry breaking and scale selection. We start by estimating the relative magnitude of the terms in δ_0. Unless we let Ekman friction damp out the ocean flow in a time scale comparable or shorter than 1 day (which is not likely), the r_0 associated terms are negligible. With an ocean deeper than $a^2\omega^2/g \sim 1.58$ km (which is possible, see Nimmo et al. (2011); Beuthe et al. (2016) and Tajeddine et al. (2017)), the inertial terms will, in turn, be dominated by the gravity term. The ice restoring force associated with α works as an extra gravity, and $4\alpha_0/a^2 = 1.35$ m/s^2 (for degree-2 deformation) is far beyond $g = 0.113$ m/s^2 and $\nu_0\omega = 0.046$ m/s^2. Therefore, the zeroth order solution can be well approximated by

$$\tilde{v}_0 \sim \frac{\omega}{\alpha_0 H_0 k^3}A \tag{42}$$

$$\tilde{u}_0 \sim 0 \tag{43}$$

$$\tilde{\eta}_0 \sim \frac{1}{\alpha_0 k^2}A, \tag{44}$$

$\tilde{u}_0 \sim 0$ because it is negligible compared to the v flow. Similarly, we can get an approximation for the first order solution,

$$\begin{aligned}
\tilde{v}_1^{\pm} &\sim \frac{1}{2\alpha_0 H_0 (k \pm k_t)^2} \left\{ [\omega\beta\alpha_0 p_\alpha k]\, \tilde{\eta}_0 - \left[\alpha_0 (k \pm k_t)^2 H_0\right] \tilde{v}_0 \right\} \\
&= -A \frac{\omega}{2\alpha_0 H_0 k^3} \left[\frac{-\beta p_\alpha k^2}{(k \pm k_t)^2} + 1 \right] \qquad (45) \\
\tilde{u}_1^{\pm} &\sim 0 \qquad (46) \\
\tilde{\eta}_1^{\pm} &\sim \frac{1}{2\alpha_0 (k \pm k_t)\omega} [\omega\beta\alpha_0 p_\alpha k]\, \tilde{\eta}_0 \\
&= A \frac{\beta p_\alpha}{2\alpha_0 k (k \pm k_t)} \qquad (47)
\end{aligned}$$

Substituting the approximate solution above into Eq (27) and Eq (39), we obtain the leading terms of projected heatings,

$$\begin{aligned}
P_{\text{ice}}^{\text{lead},k_t} &= A^2 \frac{\rho\nu_0\omega^2\beta}{\alpha_0^2 k^2} \left[-\frac{p_\nu}{k^2} + \frac{p_\alpha}{k^2 - k_t^2} \right] \qquad (48) \\
P_{\text{ekman}}^{\text{lead},k_t} &= A^2 \frac{\rho r_0 \omega^2 \beta}{\alpha_0^2 H_0 k^6} \left[\frac{p_\alpha k^2 (k^2 + k_t^2)}{(k^2 - k_t^2)^2} - \frac{1}{\beta} \right] \qquad (49)
\end{aligned}$$

The above leading order projected heatings are also plotted in Fig. 1 as a dash-dotted line. It explains most of the features in the full asymptotic solution (dashed line). Therefore, we take advantage of the simplicity of the leading order P to understand the physics.

1. Relative contribution from Ekman friction and ice dissipation. The relative importance of Ekman friction compared to the ice dissipation can be measured by $P_{\text{ekman}}^{\text{lead},k_t} / P_{\text{ice}}^{\text{lead},k_t} \sim r_0/(\nu_0 H_0 k^2)$. Substituting the default parameters yields a ratio of 0.0052, indicating the ice dissipation will dominate at least in the default setup. We note that we miss all of the baroclinic processes by using a shallow water formula, we do not consider the energy damped by eddy diffusion, and we set the ocean to be too deep for ocean tide resonance to occur (Tyler, 2011; Kamata et al., 2015). With these processes, the ocean tidal heating may play a much more important role (Tyler, 2011; Kamata et al., 2015; Wilson and Kerswell, 2018). Here, we mainly focus on the contribution from ice dissipation.

2. The mechanisms leading to the amplification of the interface topography. From Eq (48), we can clearly see which processes tend to amplify the interface topography. A positive dependence of ν on the ice thickness ($p_\nu > 0$) will smooth out the interface topography for all wavenumbers. Physically, a positive p_ν means the ice will damp the motion more efficiently and thus generate more heat when it is thicker, as a result, the interface inhomogeneity will be reduced. To the contrary, having α increase with ice thickness can possibly (when $k_t < k$) amplify the topography. This is because, in lack of the suppression from the ice shell, perturbations below a weaker (thin) ice are stronger, which will generate more heat and make the ice even thinner. We here assume $p_\alpha > p_\nu$, in order to take into account the fact that the thin ice region may be mushy, and hence more efficient in damping but less efficient in restoring perturbations.

3. The mechanisms for scale selectivity. We can understand the scale selectivity from Eq (48). The denominator of p_α term is $k^2 - k_t^2$. That means the tidal heating will amplify the interface topography with scale larger than that of the forcing. Mathematically, this $k^2 - k_t^2$ comes from the summation of η_1^+, which is proportional to $1/(k + k_t)$, and η_1^-, which is proportional to $1/(k - k_t)$. The latter dominates the former in magnitude, and its sign jumps from positive to negative as k_t gets larger than k, as a result, P_{ice} drops from positive to negative. That is to say, the existence of the $k - k_t$ mode is necessary for this jump. We will get back to this point when analyzing the tidal response in a 2D spherical geometry (section 3.2).

In terms of physics picture, when the forcing scale is smaller than the topography scale, the perturbations in the weak shell regions can not talk to those in the strong shell regions, instead, they respond to forcing independently. A weaker shell yields more flexibility for perturbation to develop, generating more heat, and vice versa. However, when the forcing scale is larger than the topography scale, the perturbation in the weak shell regions can now talk to those in the strong shell regions. Lacking flexibility, the strong shell regions tend to move as a whole following the tidal forcing, leaving gaps to be bridged by the weak shell regions. In this scenario, one can imagine that the perturbation amplitudes would peak in the strong shell regions because of the relatively large η amplitude.

In our model, the scale selectivity essentially comes from the different scale dependence of α and ν in our model. The ice damping rate ν has a fixed time scale, while the ice spring constant α increases with the perturbation wavenumber. This behavior naturally comes out of the ice membrane model we use. Setting a stronger ν for small-scale perturbations, the scale selectivity may disappear or reverse. In reality, the bending mode dominates large-scale perturbations, while the shear mode dominates small-scale ones. As shown in Beuthe (2018), the bending mode has a larger ν/α ratio than the shear mode. This will also preferentially let the large-scale topography grow.

4. The artificial resonance in the leading order solution. In Eq (48-39), both $P_{\text{ice}}^{\text{lead},k_t}$ and $P_{\text{ekman}}^{\text{lead},k_t}$ diverge at $k_t = k$, suggesting a resonance between the interface topography and the tidal forcing. However, in reality, the projected heating will not really go to infinity, because there are other terms that will not vanish at $k_t = k$ in the denominator δ_1 (Eq. 25). Thus, the leading order formula (Eq. 48 and Eq. 49) cannot be applied to the "near-resonant" state. Actually, the projected heatings do not even peak at $k_t = k = 2$. $k_t = 1$ topography is amplified even more efficiently.

5. The effects of a stationary tidal forcing. Since the tidal forcing we add here is a traveling wave, the tidal heating contributed purely by the zeroth order solution is uniform in the domain. However, for the real $Y_{2,0}$ tidal forcing, the tidal forcing is not a traveling wave meridionally, instead, it is closer to an oscillating $k = 2$ stationary pattern. The consequence of this is that the tidal heating from the zeroth order solution will naturally have a meridional variation with wavenumber 4.[1] For a pure stationary tidal forcing with

[1]In spherical coordinates, $Y_{4,0}$ is not the only mode gets excited by $Y_{2,0}$-$Y_{2,0}$ (interference between $Y_{2,2}$ and $Y_{2,-2}$ tides has a similar effect) tide interference; $Y_{2,0}$ is also excited. Here we focus on the $k = 4$ mode since we are in the context of Cartesian coordinates.

wavenumber k, half of the zeroth order tidal heating goes into wavenumber $2k$.

$$P_{\text{ice}}^{\text{stationary},2k} = \frac{1}{4}\rho\nu_0\omega^2\tilde{\eta}_0\tilde{\eta}_0^* = A^2\frac{\rho\nu_0\omega^2}{4\alpha_0^2k^4} \tag{50}$$

$$P_{\text{ekman}}^{\text{stationary},2k} = \frac{1}{4}\rho r_0 H_0 \Re\left[\tilde{u}_0\tilde{u}_0^* + \tilde{v}_0\tilde{v}_0^*\right] \tag{51}$$

This value is marked by a star in Fig. 1. Different from the tide-topography interference mode, which is our focus in this paper, the tide-tide interference mode does not rely on the topography. In absence of any topography suppression mechanism, it will cause the topography to grow linearly at a constant rate. To the contrary, the topography growth rate induced by the tide-topography interference mode increases with topography, and will lead to an exponential growth of topography. The topography structure can be dominated by either mode depending on its amplitude. As shown in Fig. 1, $P_{\text{ice}}^{\text{stationary},4}$ is roughly 1/10 of P_{ice}^{1}, indicating the wavenumber 1 topography induced by tide-topography interference is likely to dominant if the wavenumber 1 topography amplitude is greater than 37 km/10 = 3.7 km, which is approximately the amplitude of the hemispheric asymmetry component of the ice shell on Enceladus (Beuthe et al., 2016). This criterion will become lower as the topography-tide interference enhances at larger p_α (will be discussed in section 2.5).

In a long run, the topography structure is unlikely to grow to a state that the subsurface ocean exposes, instead, the topography amplitude is determined by the balance between the above topography enhancement mechanisms and the topography suppression mechanisms, such as the dependence of heat loss to space on ice thickness (Beuthe, 2019) or the down gradient ice sheet flow (Ashkenazy et al., 2018). With an efficient topography suppression mechanism, the topography is likely to be dominated by the tide-tide interference mode; with an inefficient topography suppression mechanism, the topography can grow larger, and its structure is likely to be dominated by the tide-topography interference mode instead.

6. Topography growth rate. We can get an estimation of the topography amplification time scale from asymptotic solution,

$$\begin{aligned} \frac{dh_t}{dt} &= \frac{P_{\text{total}}^{k_t}}{\overline{\rho}L_f}\frac{h_t}{H_0} \\ \tau^{k_t} &= \frac{\overline{\rho}L_f H_0}{P_{\text{total}}^{k_t}}. \end{aligned} \tag{52}$$

For the most unstable mode, $k_t = 1$, the $\tau^1 \sim 17$ Myr, which is pretty long. If this estimation is true, topography suppression mechanisms, such as the dependence of heat loss to space on ice thickness (Beuthe, 2019) or the down gradient ice sheet flow (Ashkenazy et al., 2018), may be able to stop the topography growth at a fairly low amplitude.

The above estimation is quite conservative. First, in above calculation, we assume the ice spring constant α_0 varies linearly with the ice thickness ($p_\alpha = 1$), however $\alpha_0 - \overline{H}_0$ relationship could be beyond linear relationship, if taking into account that the ice modulus is a decreasing function of temperature and that the fractures in the thin ice region can largely reduce the ice strength. Using $p_\alpha = 3$ will reduce the growing time scale to 1/3 of before, which is about 6 Myr. Second, we here only account for the $Y_{2,0}$ component of the

eccentricity tide, while ignoring the $Y_{2,2}$ and $Y_{2,-2}$ mode (basically because their dynamics cannot be well explained in 1D model). If assuming the other two modes contribute the same amount, that will reduce the growing time scale by 3/4, which gives 1.5 Myr. Last, in linear analysis, we assume a small topography amplitude and ignore the nonlinear interaction between different topography modes and tidal modes. The significance of the first and the last effect will be demonstrated by numerical calculations (section 2.5).

2.5 Numerical solution with a "realistic" interface topography

In this subsection, we numerically calculate the tidal heating profile under a realistic topography, adopted from Beuthe et al. (2016),

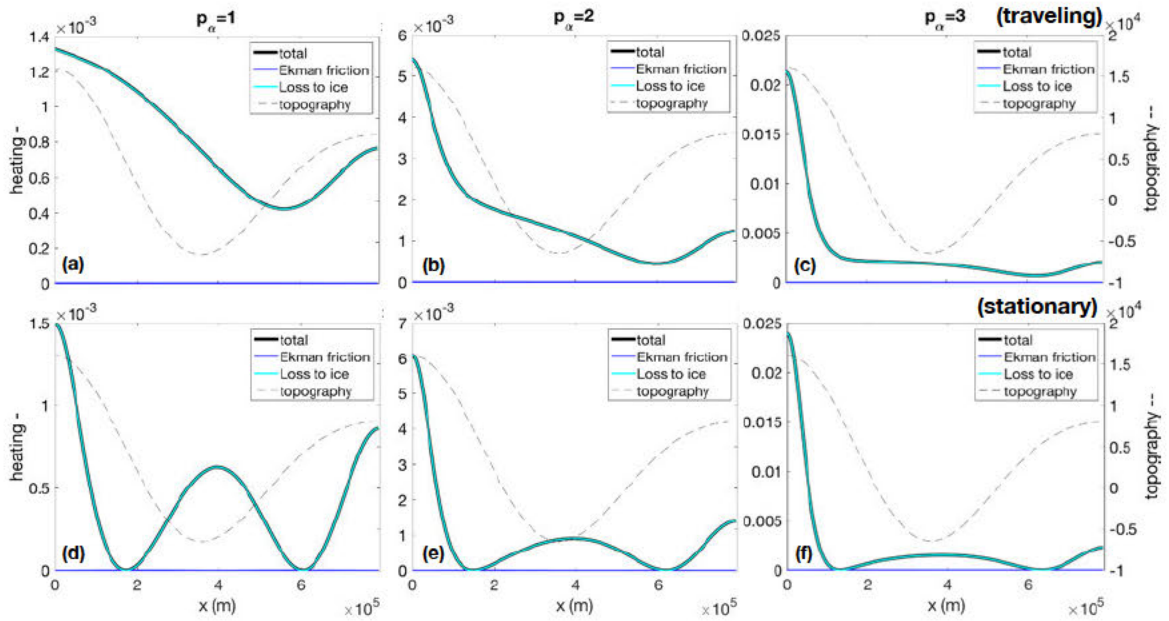

Figure 2: Full tidal heating profiles with realistic topography in Eq (53). Solid curves in blue, cyan and black denote the tidal heating contributed by Ekman friction, ice dissipation and the sum. Topography is shown in thin dashed curve for reference. The three panels in the top row are tidal heating forced by a traveling tidal forcing, with (a) $p_\alpha = 1$, (b) $p_\alpha = 2$ and (c) $p_\alpha = 3$. The bottom row is the same as the top row, except that the tidal forcing is stationary.

The full heating contributed by ice dissipation, Ekman friction and both are shown in Fig. 2(a-c) for $p_\alpha = 1, 2, 3$. Consistent with Eq (48), the dissipation in ice is roughly in phase with the topography and its projection onto topography increases with p_alpha. However, $P_{\rm ice}^{kt}$ does not increase with p_α linearly, instead the growth is much faster, due to the breakdown of the small topography assumption. It increases from 0.0005 to 0.0073

W/m^2 by over 14 times, as p_α triples. This unpredicted increase disappears when the topography amplitude is 1000 times smaller, suggesting that it should be attributed to the nonlinear interference with the finite amplitude topography.

Since the realistic topography has a finite amplitude and it is a mixture of multiple harmonic modes, even the projected heating at $p_\alpha = 1$, 0.0005 W/m^2, is higher than expected. The topography we use here is a mixture of wavenumber 1,2 and 3, whose amplitudes are $(A_1 = 1.5, A_2 = 9, A_3 = 2.5)$ km. If we assume that all three modes are independent of each other and their amplitudes are small enough, according to the asymptotic analysis, the projected heating should be $\sum_{i=1,2,3} A_i P^i_{\text{ice}} = 0.00031$ W/m^2. If we allow the interaction between the three modes but still assume the amplitude is small, the projected heating should be 0.00018 W/m^2 (we obtain this value by reducing the topography amplitude by 1000 times), which is only about 1/3 of the projected heating at high topography.

Again, because of the same reason, the structure of the ice dissipation profile changes as p_α increases (we do not expect the ice dissipation profile to exactly follow this realistic topography at the beginning because $P^{k_t}_{\text{ice}}$ varies with the topography wavenumber), becoming highly concentrated over the south pole, where the ice shell is thinnest, with a peak of over 20 mW/m^2. This highly concentrated tidal heating profile is consistent with the observation by Cassini (Howett et al., 2011), but the peak heat flux is a bit too low to explain a 4-20 GW of endogenic heat flux in the SPT region. Other processes are needed to generate enough heat. Possible candidates include the tidal heating generated in the core (Tobie et al., 2008; Behounkova et al., 2010; Beuthe, 2013), the tidal heating generated in the ice shell faults (Soucek et al., 2019), and the heating due to ocean tide resonance (Tyler, 2011; Kamata et al., 2015) and due to the ice shell liberation (Wilson and Kerswell, 2018).

Stationary pattern in the tidal forcing itself can also help form interface topography through tide-tide interference, but it may be dominated by the tide-topography interference when the topography is strong. We, therefore, also try a stationary $Y_{2,0}$ tidal forcing. The estimation in section 2.4 suggests a critical wavenumber 1 topography amplitude of 1/10 of the mean ocean depth, which gives 3.7 km. The wavenumber 1 component of the topography we use here is 1.5 km, about half of the critical amplitude. As expected, the heating profile for $p_\alpha = 1$ (Fig. 2d) has comparable amplitudes in the tide-topography interference mode (wavenumber 1) and the tide-tide interference mode (wavenumber 4). With a higher p_α, the critical amplitude should drop with $1/p_\alpha$. However, since a finite amplitude topography is unproportionally more efficient in term of reenhance itself, the tide-topography interference mode completely dominates the tide-tide interference mode when $p_\alpha = 2$ and 3.

3 2D ice-covered shallow water in spherical coordinates

3.1 Model setup

In this section, we solve the same problem in 2D spherical geometry. The purpose is to show the relevance of the 1D model in the previous section, and to highlight some new features coming out of the spherical geometry. The governing equation for a 2D shallow

water covered by an ice membrane can be written as

$$\partial_t \mathbf{v} = -g\nabla\eta - \frac{r_0 H_0}{H(\theta,\phi)}\mathbf{v} + \nabla\left(\nabla\cdot\alpha(\overline{H})\nabla - \nu(\overline{H})\partial_t\right)\eta + \nabla U \quad (54)$$

$$\partial_t \eta = -\nabla\cdot(H(\theta,\phi)\mathbf{v}). \quad (55)$$

The ocean depth H is decomposed into a mean value H_0 and a small amplitude topography $h(\theta,\phi)$. As before, we introduce a nondimensional number h_t for the topography amplitude so that $h(\theta,\phi)/H_0 = h_t h_1(\theta,\phi)$, where h_1 is set to a normalized spherical harmonic

$$h_1(\theta,\phi) = \frac{1}{\sqrt{2}}(Y_{l_t,m_t} + Y_{l_t,-m_t}) = \sqrt{2}P_{l_t,m_t}\cos(m_t\phi). \quad (56)$$

The factor $\sqrt{2}$ in the second equality drops when $m_t = 0$ (zonally symmetric topography).

The parameterization of α, ν are directly adopted from the 1D model. Coriolis effects are dropped here to allow analytical solution. As shown in the 1D model (section 2), the Coriolis effects are only secondary.

With spherical geometry, we directly use the full eccentricity tidal potential (Eq 9), which include a $Y_{2,0}$ mode, a $Y_{2,2}$ mode and a $Y_{2,-2}$ mode. Since the system has spatial reversion symmetry without rotation effect, the $Y_{2,2}$ mode has the same effect as the $Y_{2,-2}$ mode, we therefore combine them into one mode with a larger amplitude,

$$U_{\text{eccen}} = \Re\left[(A_{20}Y_{2,0} + A_{22}Y_{2,2})\, e^{-i\omega t}\right]. \quad (57)$$

where

$$A_{20} = -\sqrt{\frac{4\pi}{5}}\frac{2}{3},\ A_{22} = \sqrt{\frac{96\pi}{5}}\sqrt{\left(\frac{7}{8}\right)^2 + \left(\frac{1}{8}\right)^2}$$

3.2 Asymptotic solution

In this subsection, we solve the tidal heating induced by the $Y_{2,0}$ mode and by the $Y_{2,2}$ mode separately. By doing so, we intrinsically prevent different modes to interact with each other, and that is consistent with the way we calculate the combined $Y_{2,2}$ amplitude.

Asymptotically expanding the equation in the nondimensional topography h_t leads to a zeroth order equation that does not feel the inhomogeneity of H.

$$\partial_t \mathbf{v_0} = -(g - \alpha_0\nabla^2 + \nu_0\partial_t)\nabla\eta_0 - r_0\mathbf{v_0} + \nabla U \quad (58)$$

$$\partial_t \eta_0 = -H_0\nabla\cdot(\mathbf{v_0}). \quad (59)$$

To solve the zeroth order equation, we first do the Helmholtz decomposition to the flow field,

$$\mathbf{v} = \nabla\Phi - \nabla\times(\Psi\hat{\mathbf{r}}).$$

Taking divergence and time derivative of Eq (58) and canceling η using Eq (59) yields

$$\partial_{tt}\nabla^2\Phi_0 = H_0\nabla^2(g - \alpha_0\nabla^2 + \nu_0\partial_t)\nabla^2\Phi_0 - r_0\partial_t\nabla^2\Phi_0 + \partial_t\nabla^2 U. \quad (60)$$

Taking curl of Eq (58) and projecting onto $\hat{\mathbf{r}}$ yields

$$(\partial_t + r_0)\nabla^2\Psi_0 = 0. \tag{61}$$

The Ψ_0 equation is not forced without Coriolis effects. Even with a non-zero initial Ψ_0, it will damp out with time by Ekman friction.

$$\Psi_0 = 0 \tag{62}$$

The Φ_0 equation is forced by tidal forcing. Substituting the plane wave solution

$$\Phi_0 = \Re\left[\tilde{\Phi}_0^{lm} Y_{l,m} e^{-i\omega t}\right], \qquad l = 2,\ m = 0, 2$$

we get

$$\tilde{\Phi}_0^{lm} = \frac{-i\omega}{\delta_0^l} A_{lm}, \tag{63}$$

where

$$\delta_0^l = -i\omega(-i\omega + r_0) + \frac{l(l+1)}{a^2}\left(g + \alpha_0 \frac{l(l+1)}{a^2} - i\omega\nu_0\right) H_0.$$

Substitute the Φ_0^l solution to Eq (59), we get the solution for η_0^l,

$$\tilde{\eta}_0^{lm} = \frac{l(l+1)H_0}{a^2\delta_0^l} A_{lm}. \tag{64}$$

The first order equation is forced by the zeroth order solution,

$$(\partial_t + r_0)\mathbf{v_1} = (\alpha_0\nabla^2 - \nu_0\partial_t - g)\nabla\eta_1 - \beta\nabla(\alpha_0 p_\alpha \nabla\cdot(h_1\nabla) - \nu_0 p_\nu h_1 \partial_t)\eta_0 + r_0 h_1 \mathbf{v_0} \tag{65}$$

$$\partial_t \eta_1 = -H_0\nabla\cdot(\mathbf{v_1}) - H_0\nabla\cdot(\mathbf{v_0} h_1). \tag{66}$$

Similarly, we take divergence and time derivative of Eq (65) and substitute Eq (66) to cancel η_1.

$$\begin{aligned}\partial_{tt}\nabla^2\Phi_1 &= H_0\nabla^2(g - \alpha_0\nabla^2 + \nu_0\partial_t)\nabla^2\Phi_1 - r_0\partial_t\nabla^2\Phi_1 \\ &+ \partial_t r_0 \nabla\cdot(h_1\nabla\Phi_0) - \partial_t\alpha_0 p_\alpha\beta\nabla^2\nabla\cdot(h_1\nabla\Phi_0) + \partial_t\nu_0 p_\nu\beta\nabla^2(h_1\Phi_0) \\ &+ H_0(g - \alpha_0\nabla^2 + \nu_0\partial_t)\nabla^2\nabla\cdot(h_1\nabla\Phi_0).\end{aligned} \tag{67}$$

The solution should be in a plane wave form,

$$\Phi_1 = \frac{1}{\sqrt{2}} \sum_{|l-l_t|\le j\le l+l_t} \Re\left[\tilde{\Phi}_1^{jm+} Y_{j,m+m_t} e^{-i\omega t} + \tilde{\Phi}_1^{jm-} Y_{j,m-m_t} e^{-i\omega t}\right],$$

The factor $\frac{1}{\sqrt{2}}$ drops and the two modes merge into one when $m_t = 0$.

$$\Phi_1 = \sum_{|l-l_t|\le j\le l+l_t} \tilde{\Phi}_1^{jm} Y_{j,m} e^{-i\omega t}$$

In the following calculation, we do not explicitly consider the special case of $m_t = 0$. When it is true, $\tilde{\Phi}_1^{jm+}$ and $\tilde{\Phi}_1^{jm-}$ are identical to each other. Substitute the above solution form into Eq (67), we get

$$\begin{aligned}
\tilde{\Phi}_1^{jm\pm} &= \frac{1}{\delta_1^j}\Big\{ i\omega r_0 B(l,m,l_t,\pm m_t,j)\tilde{\Phi}_0^{lm} \\
&+ \left[i\omega\alpha_0\beta p_\alpha \frac{j(j+1)}{a^2} B(l,m,l_t,\pm m_t,j) - \omega^2\nu_0\beta p_\nu j(j+1) E(l,m,l_t,\pm m_t,j) \right] \tilde{\eta}_0^{lm} \\
&+ \left(g + \alpha_0 \frac{j(j+1)}{a^2} - i\omega\nu_0 \right) \frac{j(j+1)}{a^2} B(l,m,l_t,\pm m_t,j)\tilde{\Phi}_0^{lm} \Big\}, \qquad (68)
\end{aligned}$$

where

$$\begin{aligned}
\delta_0^j &\equiv j(j+1)(-i\omega)(-i\omega + r_0) + \frac{j^2(j+1)^2}{a^2}\left(g + \alpha_0 \frac{j(j+1)}{a^2} - i\omega\nu_0 \right) H_0 \\
B(l,m,l_t,\pm m_t,j) &\equiv \left[-l(l+1)E(l,m,l_t,\pm m_t,j) + C(l,m,l_t,\pm m_t,j) \right].
\end{aligned}$$

$C,\ E,\ B$ are spherical harmonics expansion coefficients such that

$$\begin{aligned}
Y_{l,m}Y_{l_t,m_t} &= \sum_{|l-l_t|\le j\le l+l_t} E(l,m,l_t,m_t,j) Y_{j,m+m_t} \\
\nabla Y_{l,m}\cdot\nabla Y_{l_t,m_t} &= \sum_{|l-l_t|\le j\le l+l_t} C(l,m,l_t,m_t,j) Y_{j,m+m_t} \\
\nabla\cdot(Y_{l_t,m_t}\nabla Y_{l,m}) &= \sum_{|l-l_t|\le j\le l+l_t} B(l,m,l_t,m_t,j) Y_{j,m+m_t}.
\end{aligned}$$

Their expressions are in Appendix. A.

η_1 can then be solved from Eq (66). Substitute the plane wave solution yields,

$$\tilde{\eta}_1^{jm\pm} = \frac{H_0}{i\omega a^2}\left[j(j+1)\tilde{\Phi}_1^{jm\pm} + B(l,m,l_t,m_t,j)\tilde{\Phi}_0^{jm\pm} \right]. \qquad (69)$$

Next, we solve for Ψ_1. Take curl of Eq (65) and projecting onto $\hat{\mathbf{r}}$, we get

$$(\partial_t + r_0)\nabla^2\Psi_1 = r_0(\nabla h_1 \times \nabla\Phi_0)\cdot\hat{\mathbf{r}}. \qquad (70)$$

Substituting the plane wave solution yields

$$\tilde{\Psi}_1^{jm\pm} = \frac{r_0 D(l,m,l_t,\pm m_t,j)}{j(j+1)(i\omega - r_0)}\tilde{\Phi}_0^{lm}, \qquad (71)$$

where D is also the spherical harmonics expansion coefficient (definition see Appendix. A), which satisfies

$$(\nabla Y_{l,m}\times\nabla Y_{l_t,m_t})\cdot\hat{\mathbf{r}} = \sum_{|l-l_t|\le j\le l+l_t} D(l,m,l_t,m_t,j) Y_{j,m+m_t}.$$

Finally, we derive the energy equation. Multiplying $\rho H\mathbf{v}$ to Eq (58), $(g+\nabla\alpha(\overline{H})\nabla)\eta$ to Eq (59), adding them together yields

$$\begin{aligned}\partial_t\left[\tfrac{1}{2}\rho|\mathbf{v}|^2H+\tfrac{1}{2}\rho g\eta^2+\tfrac{1}{2}\rho\alpha(\nabla\eta)^2\right] &= -\nabla\cdot\left[\rho H\mathbf{v}\left(g\eta+\nabla\cdot(\alpha\nabla\eta)\right)-\rho\alpha(\partial_t\eta)(\nabla\eta)+\rho\nu\mathbf{v}H\partial_t\eta\right]\\ &+ \rho H\mathbf{v}\cdot\nabla U-\rho\nu(\partial_t\eta)^2-\rho r_0H_0|\mathbf{v}|^2. \end{aligned}\tag{72}$$

Clearly, the last two terms in the second row are the tidal heating associated with ice dissipation and Ekman friction.

As in the 1D model (section 2), we project the tidal heating onto the topography and keep the leading order. In case of $m_t=0$,

$$\begin{aligned}P^{l_t}_{\text{ice}} &\equiv \frac{1}{h_t}\iint\rho\nu(\partial_t\eta)^2h_1\sin\theta d\theta d\phi\\ &= \frac{\rho\nu_0}{h_t}\iint(1-p_\nu\beta h_tY_{l_t,0})\omega^2\Re\left[\tilde\eta_0^{lm}Y_{l,m}+h_t\sum_{|j-l_t|\le l}\tilde\eta_1^{jm}Y_{j,m}\right]^2Y_{l_t,0}\sin\theta d\theta d\phi\\ &= \rho\nu_0\omega^2\Re\left[\tilde\eta_0^{lm*}\sum_{|j-l_t|\le l}E(l,-m,j,m,l_t)\tilde\eta_1^{jm}-\tfrac{1}{2}p_\nu\beta E(l,m,l,-m,0)\tilde\eta_0^{lm}\tilde\eta_0^{lm*}\right] \end{aligned}\tag{73}$$

$$\begin{aligned}P^{l_t}_{\text{ekman}} &\equiv \frac{\rho r_0H_0}{h_t}\iint|\mathbf{v}|^2h_1\sin\theta d\theta d\phi\\ &= \rho r_0H_0h_t\iint\left|\Re\left[\frac{\nabla\tilde\Phi_0^{lm}Y_{l,m}}{h_t}+\nabla\tilde\Phi_1^{jm}Y_{j,m}-\nabla\times(\hat{\mathbf{r}}\tilde\Psi_1^{jm}Y_{j,m})\right]\right|^2Y_{l_t,0}\sin\theta d\theta d\phi\\ &= \rho r_0H_0\tilde\Phi_0^{lm*}\sum_{|l-l_t|\le j\le l+l_t}\left[C(l,-m,j,m,l_t)\tilde\Phi_1^{jm}-D(l,-m,j,m,l_t)\tilde\Psi_1^{jm}\right] \end{aligned}\tag{74}$$

$$P^{l_t}_{\text{total}} \equiv P^{l_t}_{\text{ice}}+P^{l_t}_{\text{ekman}}.\tag{75}$$

Similarly, for $m_t\neq0$

$$P^{l_tm_t}_{\text{ice}} = \tfrac{1}{2}\rho\nu_0\omega^2\Re\left[\tilde\eta_0^{lm*}\tilde\eta_1^{jm\pm}\sum_{|j-l_t|\le l}\sum_{\pm}E(l,-m,j,m\pm m_t,l_t)-\tilde\eta_0^{lm*}\tilde\eta_0^{lm}p_\nu\beta E(l,m,l,-m,0)\right]\tag{76}$$

$$P^{l_tm_t}_{\text{ekman}} = \tfrac{1}{2}\rho r_0H_0\tilde\Phi_0^{lm*}\sum_{|j-l_t|\le l}\sum_{\pm}\left[C(l,-m,j,m\pm m_t,l_t)\tilde\Phi_1^{jm\pm}-D(l,-m,j,m\pm m_t,l_t)\tilde\Psi_1^{jm\pm}\right]\tag{77}$$

In this study, we focus on the zonally uniform topography, and thus we will use the formula for $m_t=0$.

In Fig. 3, we show the leading order $P^{l_t}_{\text{ice}}$ and $P^{l_t}_{\text{ekman}}$ solved under spherical geometry. Solid curve for the $Y_{2,0}$ tide and dashed curve for the $Y_{2,2}$ tide. In particular, the $Y_{2,0}$ solution is remarkably similar to the 1D model result (Fig. 1), indicating that the tidal response to this zonally symmetric $Y_{2,0}$ mode can mainly be explained by the 1D analysis

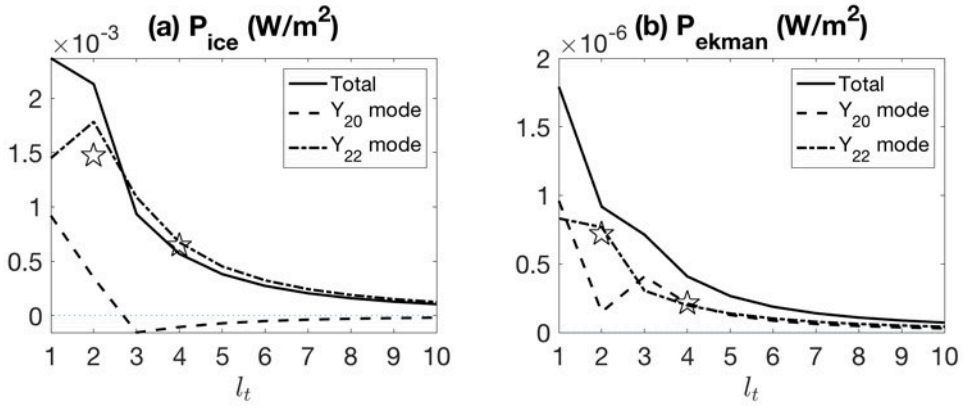

Figure 3: The projected tidal heating onto interface topography, associated with (a) ice dissipation and (b) Ekman friction. Shown are results from asymptotic solutions (Eq. 73-74).

in the previous section. As found in the 1D model, the ice dissipation is the dominant contributor to the projected tidal heating. Also consistently, only the large-scale interface topography with a total wavenumber of 1 or 2 can be reenhanced by the tidal heating, and $P^1_{\rm ice}$ is much larger than $P^2_{\rm ice}$. Again consistently, as the total wavenumber of topography l_t exceeds that of the tidal forcing $l = 2$, $P^{l_t}_{\rm ice}$ suddenly turns negative, and even higher l_t leads to a decrease of the magnitude of $P^{l_t}_{\rm ice}$. As demonstrated in section 2.4, the spatial scale of the topography relative to the forcing determines whether the ice shell deformation peaks at the thin (weak) ice regions or at the thick (strong) ice regions.

A new feature that does not exist in the 1D model is that the $P^{l_t}_{\rm ice}$ forced by $Y_{2,2}$ mode never turns negative. Mathematically speaking, this is because of the absence of the equivalent "$k - k_t$ mode", which causes the sign switch in 1D model (see discussion toward the end of section 2.4). Let us first consider a $Y_{2,0}$ tidal forcing interacting with a $Y_{3,0}$ topography, where sign switch occurs. Interference between $Y_{2,0}$ and $Y_{3,0}$ leads to $Y_{1,0}$, $Y_{3,0}$ and $Y_{5,0}$. The $Y_{1,0}$ mode is analogous to the $k - k_t$ mode in 1D model. We can see this from the dominant term of $\tilde{\eta}^j_1$, contribute by the $\overline{H}$ dependence of ice spring constant α,

$$\tilde{\eta}^{jm}_1 \sim \frac{\alpha_0 \beta p_\alpha H_0^2}{\delta^j_1 \delta^l_0 a^6} j^2 (j+1)^2 l(l+1) B(l, m, l_t, \pm m_t, j) A_{lm}. \tag{78}$$

The factor B controls the sign of $\tilde{\eta}^{jm}_1$. $\tilde{\eta}^{50}_1, \tilde{\eta}^{30}_1$ are positive, but $\tilde{\eta}^{10}_1$ is negative, just as in 1D model, $\tilde{\eta}^{+}_1$ is positive but $\tilde{\eta}^{+}_1$ is negative. The arising of the $Y_{1,0}$ mode through topography-forcing interference drags the $P_{\rm ice}$ from positive to negative.

The interference between a $Y_{2,2}$ forcing and a $Y_{3,0}$ topography is different from the above scenario. Only $Y_{3,2}$ mode and $Y_{5,2}$ mode form, while $Y_{1,2}$ is unphysical (l has to be greater than m in Y_{lm}) and thus absent. As a result, the sign of $P_{\rm ice}$ never flips when forced by a $Y_{2,2}$ tidal forcing. As k_t keeps increasing, the absolute value of the factor B decreases, leading to an overall reduction of the magnitude of $P^{l_t}_{\rm ice}$.

Physically speaking, a Y_{22} tidal forcing is roughly wavenumber 2 in the east-west direction and wavenumber 0 in the north-south direction (there is meridional magnitude

variation but the sign never changes). Such a forcing tends to distort the ice shell zonally, however, along a zonal circle, no topography exists. Therefore, the forcing always "thinks" the topography has a larger scale than itself. Following the arguments in section 2.4, $P_{\text{ice}}^{l_t}$ is therefore always positive.

Since the meridional structure of the tidal forcing is stationary, direct tide-tide interference can cause linear growth of some topography structure (see section 2.4 point 5 for discussions in the context of 1D Cartesian coordinates). For $Y_{2,0}$, $Y_{2,\pm 2}$ tide, $Y_{2,0}$ and $Y_{4,0}$ topography will be excited. We project the zeroth order heating profile onto $Y_{2,0}$ and $Y_{4,0}$ structures to get $P_{\text{ice/ekman}}^{\text{stationary},q}$ $(q = 2, 4)$,

$$P_{\text{ice}}^{\text{stationary},q} = \frac{1}{4}\rho\nu_0\omega^2\Re\left[\tilde{\eta}_0^{20*}\tilde{\eta}_0^{20}E(2,0,2,0,q) + \tilde{\eta}_0^{22*}\tilde{\eta}_0^{22}E(2,2,2,-2,q)\right] \tag{79}$$

$$P_{\text{ekman}}^{\text{stationary},q} = \frac{1}{4a^2}r_0H_0\Re\left[\tilde{\Phi}_0^{20*}\tilde{\Phi}_0^{20}C(2,0,2,0,q) + \tilde{\Phi}_0^{22*}\tilde{\Phi}_0^{22}C(2,2,2,-2,q)\right] \tag{80}$$

These values are scattered on Fig. 3 using stars. The ratio between $P_{\text{ice}}^{\text{stationary},q}$ and $P_{\text{ice}}^{l_t}$ provides an estimation of the relative amplitude of the tide-tide interference mode with total wavenumber q and the tide-topography interference mode with total wavenumber l_t (for the situation that the topography suppression mechanism did not depend on the topography scale). $P_{\text{ice}}^{\text{stationary},2}$, the dominant tide-tide interference mode, is just slightly lower than the most unstable topography-tide interference mode at $l_t = 1$, indicating that the tide-tide interference mode is likely to dominate unless the interface topography is greater than half of the mean depth of the ocean. However, as we noted in section 2.5, the actual topography amplitude threshold can actually be much lower because of the nonlinear effect induced by a finite amplitude topography. A larger p_α can further reduce the threshold and let the topography-tide interference mode dominant at lower topography amplitude by over 10 times.

4 Evolution of ice-ocean interface topography

4.1 Topography formation due to symmetry breaking in coupled 1D model

As shown in the linear instability type of analysis in the previous sections, a large-scale interface topography, if already exists, can be amplified by the tidal heating associated with ice dissipation. However, a linear theory prevents different modes from interacting with each other and does not tell us the relative phase of the different modes, whose effects are discussed in section 2.5. The next step is to demonstrate that the tide-topography interference can generate a large-scale interface topography from "nothing".

To do so, we start from a white noise initial interface topography (moving-averaged to prevent numerical instability) with amplitude 100 m, and let the topography evolve following

$$\frac{dh_t}{dt} = \frac{1}{\rho L_f}(\mathcal{H}_{\text{total}} - \langle\mathcal{H}_{\text{total}}\rangle), \tag{81}$$

where ρ and L_f are the density and fusion energy of water. h_t is the topography amplitude normalized by the mean ocean depth H_0, and $\langle\cdot\rangle$ denotes the domain average. One can

also replace h_t with the nonnormalized topography height, and equation does not change. $\mathcal{H}_{\text{total}}$ is the total tidal heating, calculated from the 1D numerical model in section 2.3 with the full Coriolis effect, $f = f_0 \cos(y/a)$.

The maintenance of the subsurface ocean is not our focus here, so we assume that some heating sources (e.g. the tidal heating generated in the core (Tobie et al., 2008; Behounkova et al., 2010; Beuthe, 2013), the tidal heating generated in the ice shell faults (Soucek et al., 2019), and the heating due to ocean tide resonance (Tyler, 2011; Kamata et al., 2015) and due to the ice shell liberation (Wilson and Kerswell, 2018)) plus the tidal heating we calculated here can exactly counterbalance the heat loss to the space. Practically, we subtract the domain average from the $\mathcal{H}_{\text{total}}$ before using it to update the topography, so that the mean ice thickness will not evolve.

We assume that the tidal heating, once generated, is directly used to melt the ice at the interface. This assumption will maximize the potential for tidal heating to change

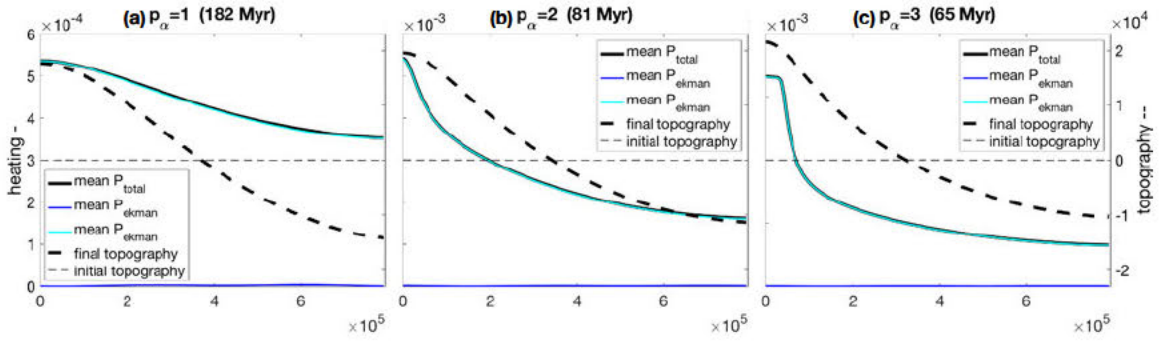

Figure 4: Evolution of ice-ocean interface topography. Initial and final state of the topography are shown in the thin and thick dashed curves. The time mean heating associated (without projection) with ice dissipation, ekman friction and total in units of W/m^2 are shown in cyan, blue and black curves. From left to right, shown are for $p_\alpha = 1, 2$ and 3.

We integrate the coupled system for about 180 Myr, and the initial and final state of the topography are shown in Fig. 4a. After 180 Myr, the tiny initial topography with random structure has evolved into a strong wavenumber 1 structure in the meridian circle (we only show half of the domain to represent a meridian from the north pole to the south pole). The amplitude of this topography reaches the depth of the ice, 23 km, meaning that the ice is completely melted at some locations. The sinusoidal varying Coriolis coefficient does not make a significant difference. Since our system has spatial translation invariance without the Coriolis term, the location of the melting point can be anywhere. But because the full domain represent a meridian circle on a sphere, the two half domains have to be symmetric to each other. The peak and trough of the wavenumber 1 topography have to locate at one

of the poles, although which pole is completely random.

In Fig. 4a, we also show the time-averaged full heating profiles associated with ice dissipation, ekman friction and the sum of both (thin solid lines), No projection to topography or mean subtraction has been done. The total tidal heating associated with ice dissipation dominates that associated with Ekman friction. As expected, the tidal heating peak collocates with the ice melting point.

As mentioned before, the dependence of the ice spring constant α_0 on the ice thickness may be beyond linear relationship. We test the sensitivity to p_α, and the same plot at $p_\alpha = 2$ and 3 are shown in Fig. 4b,c. As predicted by Eq. (48), the tidal heating projected onto topography increases linearly when the topography is small, and thus the time needed to form a significant topography reduces with $1/p_\alpha$, from ∼180 Myr to ∼80 Myr and to ∼60 Myr. With a finite topography, the projected heating increases with p_α faster than linearly (see section 2.5). But this effect does not affect the time scale of topography formation here because the system spends most time at very small topography, where linear asymptotic analysis applies.

5 Conclusions

Enceladus's ice shell thickness has a significant hemispheric asymmetric component, and the ice shell at the south pole is so thin that water vapor is ejected out of the ice shell (Iess et al., 2014). In this work, we propose a hypothesis to explain this unexpected strong hemispheric asymmetry: distribution of tidal heating on an icy moon with an inhomogeneous ice shell may be able to amplify the large-scale inhomogeneity in particular and break the symmetry between the two hemispheres. Starting from an infinitesimal hemispheric asymmetry, the mechanism can end up significantly thinning the ice shell at one of the poles. Unlike the two mechanisms proposed by Han and Showman (2010) and by Rozel, A et al. (2014), this new mechanism does not require the south pole to have any special property to begin with.

The key to examine the feasibility of the hypothesis is the tidal heat distribution on Enceladus whose ice shell thickness varies from place to place (we call this variation as topography). We used a membrane-covered shallow water model to represent the ice shell and ocean on Enceladus. The restoring force induced by the ice shell is parameterized to be proportional to the vertical displacement. All analyses were first done in 1D Cartesian coordinates and then in 2D spherical coordinates; results turned out to be consistent. The tidal heating we considered includes two components: the heating generated in the ocean due to Ekman friction at the top and bottom boundaries and the heating generated in the ice shell. At this stage, we assumed the work done by the ocean will be dissipated in the ice shell locally.

We first asymptotically solved the tidal heating in the weak topography limit and project the heating profile onto the topography imposed, to get the growth rate of a specific topography wavenumber. The heating generated in the ice shell (projected or not) is much stronger than that in the ocean, consistent with Beuthe (2016). The heating generated in the ice does amplify the topography, and the amplification is strongest for large scale topography anomalies, as how we expected a symmetry breaking mechanism would work. A numerical version of the model based on finite difference was used to verify the result, and the same analysis is done in 2D spherical coordinates to show the relevance of 1D model.

Dominant balances yielded a simpler solution form, helping clarify why the topography can be amplified and why large scale topography is particularly amplified. The ice shell is more easily perturbed by tidal forcing where it is thinner, and thus more heat and melt is concentrated to the regions with thinner ice. The restoring force induced by ice is stronger for perturbations at smaller scales, and thus the heat generation is prohibited for these scales.

We then used the numerical model to calculate the tidal heating for the observed topography in (Beuthe et al., 2016). The heating profile has a strong peak at the south pole as in observation (Howett et al., 2011). We finally coupled the ice-ocean interface topography and the tidal heating together, letting them evolve together. Starting from an infinitesimal random distributed topography, the topography can finally evolve to a state that one pole has particularly thin ice shell compare to anywhere else, suggesting the hypothesis may work.

However, toward the end of the summer program, we realized several caveats of the above hypothesis.

1. The tidal heating generated in the ice should not be proportional to the displacement of the ice, instead, it should be proportional to the horizontal derivative of the displacement: moving an ice plate up and down without deformation should not generate heat. To take this into account, we change the imaginary part of restoring force (the second term in the R_{ice} expression, Eq. (27)) to be proportional to the second derivative of η rather than η itself. As such, the ice dissipation will be proportional to the square of the vertical shear of the ice membrane $|\nabla\eta|^2$ instead of the vertical displacement $|\eta|^2$. It turns out that the ice-water interface topography can be amplified but large-scale topography is not selected any more[2]. When introducing the bending mode, the scale selectivity will be enhanced slightly, but still weak compared to the case we present in this report.

   We therefore need to find other sources for the scale selectivity. The suppression of topography by the ice flow is one potential source, because it smooths out small scale topographies more efficiently. We follow a similar path, solving for the heat generation in 1D and 2D geometry, through asympototic expansion and numerical simulation, and then we couple the heating with an ice flow model and let them both evolve the ice-ocean interface topography over time. Analytically, the new energy form provides some convenience in solving a leading order solution for finite amplitude topography (for derivations, please refer to Appendix section B). When this model is forced by the Y_{20} tidal component, the ice thickness also ends up to be particularly thin close to one of the poles, however, Y_{22} tidal component cannot lead to symmetry breaking because of the second caveat below.

2. The second caveat is that ice shell does not dissipate the energy input from the ocean locally. For an ice shell in the membrane limit, the restoring force acting on the ocean underneath is mainly due to the compression and extension of the ice shell, and the heat generation is mainly induced by the tangential shear motion (Beuthe,

[2]One can see this from the dominant balances. Multiplying Eq. (47) with the wavenumber $k \pm k_t$ before substituting into Eq. (27) will exactly cancel out the denominator under p_α in Eq. (48). There is a subtle preference to large-scale topographies in the full solution, but is too small to be a mechanism for symmetry breaking.

2019), which is completely ignored in our membrane-covered shallow water model. We didn't realize until much later that the tidal heating pattern over the globe without topography (homogeneous ice shell) controls which topography wavenumber can grow. Using our energy formula ($\mathcal{H}_{\rm ice} \propto |\nabla\eta|^2$ or $\mathcal{H}_{\rm ice} \propto |\eta|^2$, with and without bending mode), the total tidal heating induced by Y_{22} and Y_{20} (mostly Y_{22}) tidal components has a pattern that peaks at the equator rather than the poles, which is the pattern people obtained from a more sophisticated ice model (Beuthe, 2013, 2019). Starting from such an equator-amplified heating pattern mistakenly suppresses the growth of the hemispherically asymmetric modes, which is necessary for the symmetry breaking.

A Expressions of spherical harmonics expansion coefficients

$$
\begin{aligned}
C(l,m,l_t,\pm m_t,j) &\equiv -(-1)^{m\pm m_t}\frac{\sqrt{l(l+1)l_t(l_t+1)}}{2}\sqrt{\frac{(2l+1)(2l_t+1)(2j+1)}{4\pi}} \\
&\quad\times \begin{pmatrix} l, & l_t, & j \\ m, & \pm m_t, & -(m\pm m_t)\end{pmatrix}\left[\begin{pmatrix} l, & l_t, & j \\ 1, & -1, & 0\end{pmatrix}+\begin{pmatrix} l, & l_t, & j \\ -1, & 1, & 0\end{pmatrix}\right] \\
E(l,m,l_t,\pm m_t,j) &\equiv (-1)^{m\pm m_t}\sqrt{\frac{(2l+1)(2l_t+1)(2j+1)}{4\pi}} \\
&\quad\times \begin{pmatrix} l, & l_t, & j \\ m, & \pm m_t, & -(m\pm m_t)\end{pmatrix}\begin{pmatrix} l, & l_t, & j \\ 0, & 0, & 0\end{pmatrix} \\
D(l,m,l_t,\pm m_t,j) &\equiv i(-1)^{m\pm m_t}\frac{\sqrt{l(l+1)l_t(l_t+1)}}{2}\sqrt{\frac{(2l+1)(2l_t+1)(2j+1)}{4\pi}} \\
&\quad\times \begin{pmatrix} l, & l_t, & j \\ m, & \pm m_t, & -(m\pm m_t)\end{pmatrix}\left[\begin{pmatrix} l, & l_t, & j \\ 1, & -1, & 0\end{pmatrix}-\begin{pmatrix} l, & l_t, & j \\ -1, & 1, & 0\end{pmatrix}\right]
\end{aligned}
$$

The six-element matrices in above equations are the three j-symbol matrix.

B Tidal heating using the new energy form

In order to calculate the new ice dissipation

$$\mathcal{H}_{\rm ice} = \rho\nu_0\overline{|\partial_t\nabla\eta|^2} \tag{82}$$

the only field required is $\nabla\eta$.

This term can be solved from the dominant balance equation without small amplitude assumption, even in 2D spherical geometry. The dominant balance equations read

$$\nabla\left(\alpha_0\nabla\cdot(\overline{H}/\overline{H}_0)^{p_\alpha}\nabla\right)\eta = -\nabla U \tag{83}$$

$$\nabla\cdot(H(\theta,\phi)\mathbf{v}) = -\partial_t\eta. \tag{84}$$

Integrating both sides leads to

$$-\nabla\cdot\alpha(\overline{H})\nabla\eta = U = \Re\left[A_{lm}Y_{l,m}e^{-i\omega t}\right]. \tag{85}$$

We then decompose $\alpha(\overline{H})\nabla\eta$ into a divergence component Φ_η and a rotational component Ψ_η,

$$\alpha(\overline{H})\nabla\eta = \nabla\Phi_\eta + \nabla\times(\hat{\mathbf{r}}\Psi_\eta).$$

Only the divergence component Φ_η is forced by the tidal forcing on the right hand side. Φ_η can be solved.

$$\begin{aligned} -\nabla^2\Phi_\eta &= \Re\left[A_{lm}Y_{l,m}e^{-i\omega t}\right] \\ \Phi_\eta &= \frac{a^2}{l(l+1)}\Re\left[A_{lm}Y_{l,m}e^{-i\omega t}\right] \end{aligned} \tag{86}$$

The tidal heating generated by ice dissipation can be calculated by substituting the above equation into Eq. (82),

$$\begin{aligned} \mathcal{H}_{\rm ice} &= \rho\nu_0\overline{|\partial_t\nabla\eta|^2} \\ &= \frac{\rho\nu_0\omega^2}{\alpha(\overline{H})^2}\overline{\nabla\Phi_\eta\cdot\nabla\Phi_\eta} \\ &= \tfrac{1}{2}A_{lm}^2\frac{\rho\nu_0\omega^2}{\alpha(\overline{H})^2}\left(\frac{a^2}{l(l+1)}\right)^2\nabla Y_{l,m}\cdot\nabla Y_{l,m}^* \end{aligned}$$

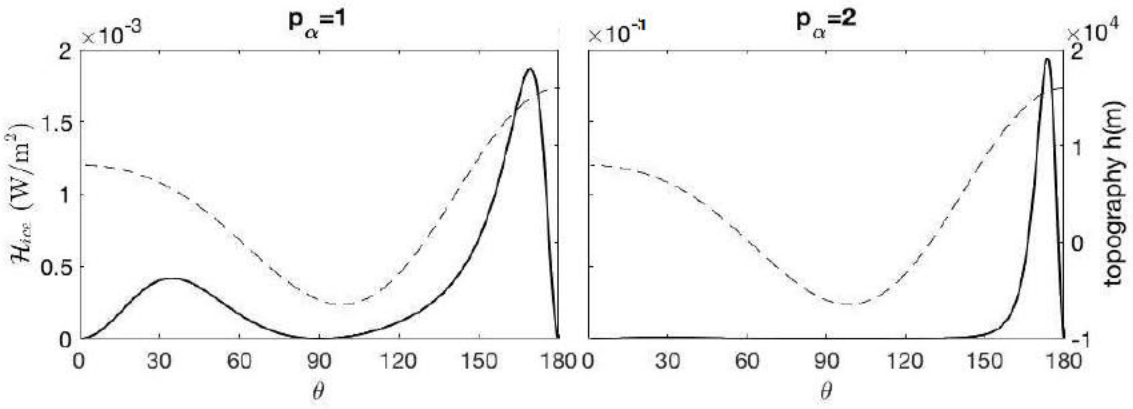

Figure 5: Full tidal heating profiles with realistic topography in Eq (53). Solid curves are tidal heating calculated from Eq. (87) with (a) $p_\alpha = 1$, (b) $p_\alpha = 2$, Topography is plotted in dashed curves for reference.

For any give topography $h' = h/H_0$, one can use the above formula to calculate the tide heat distribution. Without topography, the tidal heating distribution is determined by the structure of the tide, peaks at 45N/S (not shown). It does not peak at the poles or the equator, because the tide potential there is "flat". That will lead to a weak shear motion

there and hence a weak ice dissipation. With topography, the heating will be concentrated to the regions with a thinner, and thus weaker, ice shell, by the factor $(1 - \beta h')^{-2p_\alpha}$.

In Fig. 5, we show the tidal heating profile calculated with the "realistic" topography reconstructed by Beuthe et al. (2016, Eq. (53)). Panel (a) shows the result for $p_\alpha = 1$, and panel (b) shows for $p_\alpha = 2$. As expected, the tidal heating is concentrated to the south pole where the ice shell is thin, and a larger p_α makes the concentrating more efficient. In Fig. 5b, there is almost no heating to the north of 60S. Such a heating profile will, in turn, be able to amplify the interface topography, unless some topography suppression mechanisms stop it.

A larger p_α also lead to a much stronger heat flux in general. Note that the scale of panel (b) is 100 times larger than panel (a). The maximum tidal heating with $p_\alpha = 2$ reaches 200 $\mathrm{mW\,m^{-2}}$, which matches much better with the observed heat flux around 150 $\mathrm{mW\,m^{-2}}$ (Spencer et al., 2013; Howett et al., 2011) than the $p_\alpha = 1$ profile does.

Acknowledgements

This work was carried out during the 2019 Geophysical Fluid Dynamics Summer School at Woods Hole. The author thanks the GFD faculty for organizing the program and the Woods Hole Oceanographic Institution for hosting it, thanks Prof. Glenn Flierl for supervising this project and Prof. Geoff Vasil and Prof. Andrew Wells for inspiring discussions.

References

Ashkenazy, Y., Sayag, R., and Tziperman, E. (2018). Dynamics of the global meridional ice flow of Europa's icy shell. *Nature Astronomy*, 2(1):43–49.

Behounkova, M., Tobie, G., Choblet, G., and Cadek, O. (2010). Coupling mantle convection and tidal dissipation: Applications to Enceladus and Earth-like planets. *JGR*, 115(E9):189.

Beuthe, M. (2013). Spatial patterns of tidal heating. *Icarus*, 223(1):308–329.

Beuthe, M. (2016). Crustal control of dissipative ocean tides in Enceladus and other icy moons. *Icarus*, 280:278–299.

Beuthe, M. (2018). Enceladus's crust as a non-uniform thin shell: I tidal deformations. *Icarus*, 302:145–174.

Beuthe, M. (2019). Enceladus's crust as a non-uniform thin shell: Ii tidal dissipation. *Icarus*, 332:66 – 91.

Beuthe, M., Rivoldini, A., and Trinh, A. (2016). Enceladus's and Dione's floating ice shells supported by minimum stress isostasy. *Geophysical Research Letters*, 43(19):10,088–10,096.

Han, L. and Showman, A. P. (2010). Coupled convection and tidal dissipation in Europa's ice shell. *Icarus*, 207(2):834–844.

Howett, C. J. A., Spencer, J. R., Pearl, J., and Segura, M. (2011). High heat flow from Enceladus' south polar region measured using 10-600 cm-1 Cassini/CIRS data. *Journal of Geophysical Research-Atmospheres*, 116(E3):189.

Iess, L., Stevenson, D. J., Parisi, M., Hemingway, D., Jacobson, R. A., Lunine, J. I., Nimmo, F., Armstrong, J. W., Asmar, S. W., Ducci, M., and Tortora, P. (2014). The Gravity Field and Interior Structure of Enceladus. *Science*, 344(6179):78–80.

Kamata, S., Matsuyama, I., and Nimmo, F. (2015). Tidal resonance in icy satellites with subsurface oceans. *Journal of Geophysical Research*, 120.

Nimmo, F., Bills, B. G., and Thomas, P. C. (2011). Geophysical implications of the long-wavelength topography of the Saturnian satellites. *JGR*, 116(E11):897.

Rozel, A, Besserer, J, Golabek, G J, Kaplan, M, and Tackley, P J (2014). Self-consistent generation of single-plume state for Enceladus using non-Newtonian rheology. *Journal of Geophysical Research: Planets*, 119(3):416–439.

Soucek, O., Behounkova, M., Cadek, O., Hron, J., Tobie, G., and Choblet, G. (2019). Tidal dissipation in Enceladus' uneven, fractured ice shell. *Icarus*, 328:218–231.

Spencer, J. R., Howett, C. J. A., Verbiscer, A., Hurford, T. A., Segura, M., and Spencer, D. C. (2013). Enceladus Heat Flow from High Spatial Resolution Thermal Emission Observations. *European Planetary Science Congress*, 8:EPSC2013–840.

Tajeddine, R., Soderlund, K. M., Thomas, P. C., Helfenstein, P., Hedman, M. M., Burns, J. A., and Schenk, P. M. (2017). True polar wander of Enceladus from topographic data. *Icarus*, 295:46–60.

Tobie, G., Cadek, O., and Sotin, C. (2008). Solid tidal friction above a liquid water reservoir as the origin of the south pole hotspot on Enceladus. *Icarus*, 196(2):642–652.

Tobie, G., Choblet, G., and Sotin, C. (2003). Tidally heated convection: Constraints on Europa's ice shell thickness. *JOURNAL OF GEOPHYSICAL RESEARCH-ATMOSPHERES*, 108(E11):219.

Tyler, R. (2011). Tidal dynamical considerations constrain the state of an ocean on Enceladus. *Icarus*, 211(1):770–779.

Wilson, A. and Kerswell, R. (2018). Can libration maintain enceladus's ocean? *Earth and Planetary Science Letters*, 500:41–46.

The Evolution of Superharmonics Excited by Internal Tides in Non-Uniform Stratification

Lois Baker

August 20, 2019

1 Introduction

Energy input from winds and tides creates a diverse internal wave field in the Earth's stratified rotating oceans. Internal waves on a variety of scales transport energy and momentum throughout the global oceans, and are an important pathway by which energy is transferred from large scale forcing to small scales where mixing and dissipation can occur.

In 1966 Walter Munk proposed that in order to maintain the global overturning thermohaline circulation, a certain level of small scale isopycnal mixing is required [16]. The question of how much mixing takes place in the abyssal ocean to account for the required water mass transformation remains at the forefront of modern oceanographic research. In particular, global climate models (GCMs) are sensitive to the spatial distribution of mixing [7, 15], thus a proper understanding of the energy transfer from resolvable large scale features to unresolvable small scales is essential for GCM parametrizations.

Internal waves play a leading order role in this energy cascade and are the primary cause of diapycnal mixing e.g., [20], resulting in extensive research in recent decades into the generation, propagation and transition to turbulence of oceanic internal waves. In this work we investigate a mechanism for the extraction of energy from the large scale internal waves generated by tides, known as internal tides.

Tides with a semi-diurnal or diurnal frequency are ubiquitous in the ocean, forced by the gravitational pull of the moon or sun. This forcing directly creates a barotropic tide with uniform vertical structure and horizontal velocities of order 1 - 10 $\mathrm{cm\,s^{-1}}$. When the barotropic tide flows over bottom topography in the ocean, baroclinic internal tides are excited, possessing a rich vertical modal structure [5]. The important generation sites for these internal tides include mid-ocean ridges and island chains.

The linear theory for internal tide generation was first developed by Baines (1973) [2] and Bell (1975) [3]. The internal tide field near topography is primarily composed of beams with tidal frequency that radiate away from topography much like internal wave beams from an oscillating cylinder, as well as waves at a spectrum of superharmonic frequencies and quasi-steady trapped lee waves. Although the internal tide local to the generation site can have a complex vertical structure, the higher modes are more susceptible to vertical shear and are thus more likely to dissipate locally [10], leaving a far field composed primarily of low mode internal tides with tidal frequency. Even at generation sites with significant local dissipation, most internal wave energy propagates away to the far field as low modes [14].

These low modes can have wavelengths of order 100 - 200 km and are capable of propagating thousands of kilometres across ocean basins [17, 25].

It is estimated that the total energy content of the barotropic M2 (semi-diurnal lunar) tide is approximately 392 PJ [9] and the total energy content of the mode-1 M2 internal tide is 36 PJ [25], indicating an almost 10% conversion from the barotropic tide to mode-1 internal tides. However, the fate of this huge amount of mechanical energy contained in the low mode internal tides remains an open question [12]. Ultimately, this energy must be dissipated at small scales or used to irreversibly mix fluid across isopycnals.

An important mechanism for extracting energy from the low-mode internal tide is interaction with large and small amplitude topography and continental slopes, as reviewed in Sarkar and Scotti (2017) [19]. The predicted and observed ability for low mode internal tides to travel thousands of kilometres across entire ocean basins [17, 25] implies that ultimately internal tides will interact with topography, if they are not destroyed by other mechanisms during propagation. In particular, if the slope of large amplitude topography is critical or subcritical to the characteristic angle of internal tide beam propagation, energy density can be effectively focused by reflection at the slope, resulting in enhanced dissipation [11].

Parametric subharmonic instability (PSI) whereby the internal tide loses energy to smaller scale waves with approximately half the frequency has also been proposed as a possible mechanism for decay of the internal tide. This decay is predicted to be especially strong near the critical latitude 29°N where the subharmonics have frequency near the local inertial frequency [13]. Observations [1, 12] of a propagating internal tide beam north of the Hawaiian Ridge found enhanced dissipation consistent with particularly efficient PSI at this critical latitude, but found that it did not extract significant energy from the internal tide.

Other mechanisms proposed for the destruction of the internal tide include interaction with the mesoscale flow field [17] and nonlinear steepening at sufficiently large internal tide amplitudes [8, 6]. In practice, all of the above mechanisms and more are likely to contribute to internal tide dissipation, with relative importance varying geographically.

The focus of this work is a mechanism that could be responsible for energy transfer from the mode-1 internal tide to smaller scales but has received relatively little attention in the literature. It was realised by way of theory and simulations that internal waves in non-uniform stratification can generate superharmonics with half the wavelength of the original wave [4, 23]. Varma and Mathur (2017) [22] extended the theory to apply to more general nonlinear modal interactions between modes with different wavelengths. It was assumed in all of these studies that the superharmonic response had twice the frequency of the original wave, which we refer to as a 'steady state'.

Sutherland (2016) [21] ran fully nonlinear 2D Boussinesq simulations in an idealized domain with idealized stratification profiles and initialised with a mode-1 'parent' internal mode. It was found that superharmonics of the parent are generated, with highest amplitude near areas of strong stratification. These superharmonics were found to interact nonlinearly with the parent, and have the ability to introduce smaller vertical scales and distort the parent mode. It was noted that the superharmonic generated need not have twice the frequency of the parent, and that the superharmonic could undergo resonant growth to become significantly large even for a small amplitude parent.

This idea was examined further by Wunsch (2017) [24], who made the analogy of the

system to that of a harmonic oscillator. The superharmonic is forced by the nonlinear self-interaction of the parent at twice the parent frequency, which in certain parameter regimes is very close to the natural frequency of the superharmonic, allowing resonant growth of the superharmonic akin to that of a forced harmonic oscillator. This study assumed that after a period of initial growth, the transients would decay and the system would reach the steady state found in Diamessis et al. (2014)[4], and Varma and Mathur (2017) [22].

However, when run for longer times, simulations similar to those in Sutherland (2016) [21] are found to show a long timescale periodic evolution of the amplitude of the superharmonic, motivating the current study. Figure 1 shows the horizontal velocity field of the total flow and superharmonic component at several times, showing how the superharmonic grows from zero to some maximum amplitude before decaying back to zero. This behaviour repeats periodically with the same period. Here we investigate this phenomenon using a weakly nonlinear theory, and compare the results to simulations.

Section 2 will develop the theoretical framework of the problem, extending the established theory described in Diamessis et al. [4] to include time dependence of the superharmonic amplitude. In section 3, numerical simulations are introduced and compared to the theory derived in section 2. A weakly nonlinear theory for the feedback between the parent and the superharmonic is derived in section 4 and shown to improve on the theory from section 2 by taking account of the energy transfer from the parent. Section 5 compares the results of the weakly nonlinear theory to simulations. In section 6, the results from the previous sections are considered with realistic oceanic parameters and stratification to evaluate the possibility for these superharmonics to be important in the real ocean.

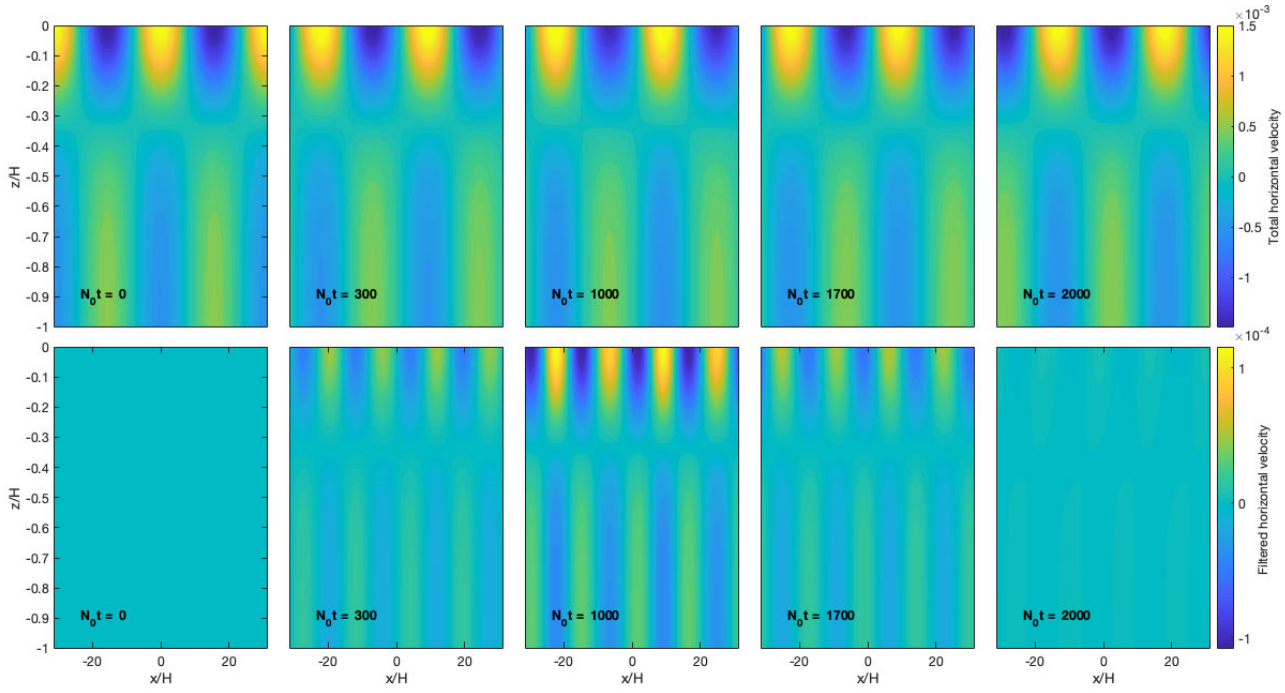

Figure 1: Snapshots of the 2D horizontal velocity field from nonlinear simulations described in section 3. Top: full horizontal velocity field at various times. Bottom: horizontal velocity field with parent wavenumber removed, showing generation, growth and decay of superharmonic over a period $N_0 t \simeq 2000$. Parent wavenumber $k = 0.2/H$, Coriolis parameter $f = 0.01 N_0$, stratification $N(z) = N_0 \exp(5z/H)$

2 Linear Theory

2.1 Governing equations

Consider a 2D inviscid Boussinesq fluid with stratification $N^2(z)$ and zero background velocity. The domain is periodic in the horizontal coordinate x and bounded in the vertical at $z = -H$ and $z = 0$. The flow satisfies the inviscid Boussinesq equations on an f-plane:

$$u_t + uu_x + wu_z - fv = -\frac{1}{\rho_0} p_x \,, \tag{1}$$

$$v_t + uv_x + wv_z + fu = 0 \,, \tag{2}$$

$$w_t + uw_x + ww_z = -\frac{1}{\rho_0} p_z + b \,, \tag{3}$$

$$b_t + ub_x + wb_z + wN^2 = 0 \,, \tag{4}$$

$$u_x + w_z = 0 \,, \tag{5}$$

where $\mathbf{u} = (u, v, w)$, p is the pressure, b is the buoyancy perturbation from the background stratification $N^2(z)$, f is the Coriolis parameter, ρ_0 is a reference density and $\frac{\partial}{\partial y} = 0$ since the domain is 2D.

Define the vorticity $\zeta = \hat{y} \cdot \nabla \times \mathbf{u} = u_z - w_x$ and the streamfunction ψ such that $u = -\psi_z$, $w = \psi_x$ satisfies (5), and $\zeta = -\nabla^2 \psi$. Taking the curl of the momentum equations (1) - (3) eliminates pressure to give the vorticity equation. The system is then represented by 3 equations:

$$\nabla^2 \psi_t + f v_z - b_x = \psi_z \nabla^2 \psi_x - \psi_x \nabla^2 \psi_z = \mathcal{N}_1 \,, \tag{6}$$

$$v_t - f\psi_z = \psi_z v_x - \psi_x v_z = \mathcal{N}_2 \,, \tag{7}$$

$$b_t + N^2 \psi_x = \psi_z b_x - \psi_x b_z = \mathcal{N}_3 \,, \tag{8}$$

where $\mathcal{N}_1$, $\mathcal{N}_2$, $\mathcal{N}_3$ denote the nonlinear terms. Combining (6) - (8) gives

$$\nabla^2 \psi_{tt} + f^2 \psi_{zz} + N^2 \psi_{xx} = \mathcal{N}_{1t} - f\mathcal{N}_{2z} + \mathcal{N}_{3x} \,, \tag{9}$$

where the LHS is linear in ψ, and the RHS contains nonlinear terms in ψ, v and b.

2.2 The parent mode

We seek horizontal periodic solutions of a single mode with the form

$$\psi(x, z, t) = \frac{1}{2} A_0 \hat{\psi}(z) e^{i(kx - \omega t)} + c.c. \,, \tag{10}$$

where k is the prescribed horizontal wavenumber of the parent mode, A_0 is a given small real amplitude, *c.c.* is the complex conjugate, and $\hat{\psi}(z)$ is normalised so that $\max |\hat{\psi}(z)| = 1$. To linear order in A_0, i.e., neglecting the RHS of (9), $\hat{\psi}$ satisfies the eigenvalue problem

$$\hat{\psi}'' + \frac{N^2(z) - \omega^2}{\omega^2 - f^2} k^2 \hat{\psi} = 0 \,, \tag{11}$$

with the free slip boundary conditions $\hat{\psi}(0) = \hat{\psi}(-H) = 0$. For prescribed k, the solution gives a set of eigenfunctions $\hat{\psi}$ with corresponding frequencies ω. If $N^2 = N_0^2$ is constant, the solutions are simply the harmonic modes

$$\hat{\psi} \propto \sin(mz)\,, \tag{12}$$

where for mode-1 waves $m = \frac{\pi}{H}$, and

$$\omega^2 = \frac{N_0^2 k^2 + f^2 m^2}{k^2 + m^2}\,. \tag{13}$$

Consider a mode-1 'parent' mode with given k and corresponding ω, and denote the vertical structure by $\hat{\psi}_1$. For convenience, let the phase $\phi = kx - \omega t$.

If N^2 is a function of z, (11) can be solved numerically for the mode $\hat{\psi}_1(z)$ and ω using Galerkin methods, described in section 3. We define a non-dimensional amplitude $\alpha \ll 1$ such that $A_0 = \frac{\omega d}{k}\alpha$, where d is a characteristic length scale of the stratification profile $N^2(z)$. The parent mode is thus given by

$$\psi^{(1)} = \frac{1}{2}\alpha\frac{\omega d}{k}\hat{\psi}_1(z)e^{i\phi} + c.c. \tag{14}$$

2.3 Response to parent mode self-interaction

Consider now the nonlinear terms in (9). The order α parent mode will self-interact in these terms to create an $O(\alpha^2)$ forcing for the next order correction to ψ. This forcing will have a part that is proportional to $e^{0i\phi}$, hence forcing a mean flow, and a part that is proportional to $e^{2i\phi}$, forcing a superharmonic with double the wavenumber of the parent. To calculate the nonlinear forcing terms, first use (7) - (8) to find the parent mode spanwise velocity $v^{(1)} = \frac{1}{2}A_0\hat{v}_1 e^{i\phi} + c.c.$ and buoyancy $b^{(1)} = \frac{1}{2}A_0\hat{b}_1 e^{i\phi} + c.c.$, giving the polarisation relations

$$\hat{v}_1 = \frac{if}{\omega}\hat{\psi}_1'\,, \qquad \hat{b}_1 = \frac{kN^2}{\omega}\hat{\psi}_1\,. \tag{15}$$

The forcing terms become (using (11) to replace second derivatives of $\hat{\psi}_1$):

$$\begin{aligned}
\mathcal{N}_1^{\{1,1\}} &= \psi_z^{(1)}\nabla^2\psi_x^{(1)} - \psi_x^{(1)}\nabla^2\psi_z^{(1)} \\
&= A_0^2\frac{ik^3(N^2)'}{4(\omega^2 - f^2)}\hat{\psi}_1^2 e^{2i\phi} + c.c.\,, \qquad (16)\\
\mathcal{N}_2^{\{1,1\}} &= \psi_z^{(1)}v_x^{(1)} - \psi_x^{(1)}v_z^{(1)} \\
&= -A_0^2\frac{fk}{4\omega}\left(\hat{\psi}_1'^2 + \frac{N^2(z) - \omega^2}{\omega^2 - f^2}k^2\hat{\psi}_1^2\right)e^{2i\phi} - A_0^2\frac{fk}{4\omega}\left(\hat{\psi}_1'^2 - \frac{N^2(z) - \omega^2}{\omega^2 - f^2}k^2\hat{\psi}_1^2\right) + c.c.\,, \qquad (17)\\
\mathcal{N}_3^{\{1,1\}} &= \psi_z^{(1)}b_x^{(1)} - \psi_x^{(1)}b_z^{(1)} \\
&= -A_0^2\frac{ik^2(N^2)'}{4\omega}\hat{\psi}_1^2 e^{2i\phi} + c.c.\,, \qquad (18)
\end{aligned}$$

where $\{1,1\}$ indicates the self-interaction of the parent mode. Substituting (16) - (18) into (9) gives

$$\nabla^2\psi_{tt} + f^2\psi_{zz} + N^2\psi_{xx} = \mathcal{G}_0(z) + \mathcal{G}_2(z)e^{2i\phi} + c.c.\,, \tag{19}$$

where

$$\mathcal{G}_0 = -\frac{\alpha^2 k\omega d^2 f^2}{4(\omega^2 - f^2)}\left(2(N^2-\omega^2)\frac{\partial}{\partial z}|\hat{\psi}_1|^2 + (N^2)'|\hat{\psi}_1|^2\right), \tag{20}$$

$$\mathcal{G}_2 = \frac{\alpha^2 k\omega d^2(4\omega^2 - f^2)(N^2)'}{4(\omega^2 - f^2)}\hat{\psi}_1^2\,. \tag{21}$$

Examination of (19) - (21) gives the result that in uniform stratification and for $f = 0$, monochromatic internal waves satisfy the fully nonlinear equations of motion. In a uniform stratification with rotation, the forcing forces a mean flow, but no superharmonics. Thus the generation of superharmonics is only possible in non-uniform stratification.

The total flow is now written as a sum of the parent $\psi^{(1)}$, the mean flow $\psi^{(0)}$ and the superharmonic $\psi^{(2)}$:

$$\psi = \psi^{(1)} + \psi^{(0)} + \psi^{(2)}\,. \tag{22}$$

In what follows, we separately consider the response to the forcing $\mathcal{G}_2$ on the superharmonic $\psi^{(2)}$ and the forcing $\mathcal{G}_0$ on the mean flow $\psi^{(0)}$.

2.3.1 Superharmonic generation

The superharmonic $\psi^{(2)}$ is given by

$$\nabla^2\psi^{(2)}_{tt} + f^2\psi^{(2)}_{zz} + N^2\psi^{(2)}_{xx} = \mathcal{G}_2(z)e^{2i\phi} + c.c.\,, \tag{23}$$

where we write

$$\psi^{(2)} = \frac{1}{2}\alpha^2\frac{\omega d}{k}\tilde{\psi}_2(z,T)e^{2i\phi} + c.c. \tag{24}$$

Crucially, the time dependence of the superharmonic $\psi^{(2)}$ is allowed to vary from the imposed forcing $e^{2i\phi}$ in the term $\tilde{\psi}_2(z,T)$, with some timescale T. We define the superharmonic field as disturbances with twice the wavenumber of the parent, thus with horizontal structure e^{2ikx}, but not necessarily with twice the frequency. This is motivated by simulations (see section 3) with the parent mode imposed as an initial condition that show growth of the superharmonic on a much longer timescale than the forcing ω^{-1}. We thus define a slow timescale $T = \epsilon t$ for the superharmonic evolution $\tilde{\psi}_2$, where $\epsilon \ll 1$ will later be defined explicitly. Note that this assumption need not be made a priori, and can be derived explicitly with a little more work.

We write the superharmonic structure $\tilde{\psi}_2$ as an expansion in vertical structure functions $\hat{\psi}_{2j}$:

$$\tilde{\psi}_2(z,T) = \sum_{j=1}^{\infty} a_j(T)\hat{\psi}_{2j}(z)\,. \tag{25}$$

The vertical structure functions $\hat{\psi}_{ij}$ have corresponding frequencies ω_{ij} and correspond to the ith horizontal mode and jth vertical mode. They are eigenfunctions of the generalization

of (11) to wavenumber ik, such that:

$$\hat{\psi}''_{ij} + i^2k^2\frac{N^2-\omega_{ij}}{\omega_{ij}^2-f^2}\hat{\psi}_{ij} = 0\,. \tag{26}$$

We can rearrange (26) into the Sturm-Liouville form

$$\mathcal{L}_i\hat{\psi}_{ij} = -w(z)\lambda_{ij}\hat{\psi}_{ij}\,, \tag{27}$$

where $\mathcal{L}_i = \frac{\partial^2}{\partial z^2} - i^2k^2$ is self-adjoint, $w(z) = (N^2-f^2)$, and $\lambda_{ij} = \frac{i^2k^2}{\omega_{ij}^2-f^2}$. Sturm-Liouville theory then states that for each i the eigenfunctions $\hat{\psi}_{ij}$ of (26) with frequency ω_{ij} are orthogonal with respect to the weight function $w(z)$, so that

$$\int_{-H}^{0}\hat{\psi}_{ij}(z)\hat{\psi}_{il}(z)w(z)dz = \delta_{jl}\int_{-H}^{0}(\hat{\psi}_{ij}(z))^2w(z)dz\,. \tag{28}$$

Substituting (24) and (25) into (23) gives

$$\sum_{j=1}^{\infty}\left(\epsilon^2\ddot{a}_j - 4i\omega\epsilon\dot{a}_j - 4\omega^2\left(\frac{4\omega^2-\omega_{2j}^2}{4\omega^2}\right)a_j\right)\frac{N^2-f^2}{\omega_{2j}^2-f^2}\hat{\psi}_{2j} = -\frac{d(4\omega^2-f^2)(N^2)'\hat{\psi}_1^2}{8(\omega^2-f^2)}\,, \tag{29}$$

where $\dot{a}$ denotes $\frac{\partial a}{\partial T}$. We now multiply through by another basis function $\hat{\psi}_{2l}$, integrate over $z\in[-H,0]$ and notice that the orthogonality condition (28) can be applied to give

$$\epsilon^2\ddot{a}_j - 4i\omega\epsilon\dot{a}_j - 4\omega^2\left(\frac{4\omega^2-\omega_{2j}^2}{4\omega^2}\right)a_j = -\frac{d(4\omega^2-f^2)(\omega_{2j}^2-f^2)}{8(\omega^2-f^2)}\frac{\int_{-H}^{0}(N^2)'\hat{\psi}_1^2\hat{\psi}_{2j}\,dz}{\int_{-H}^{0}(N^2-f^2)\hat{\psi}_{2j}^2\,dz}\,. \tag{30}$$

The first term of (30) is $O(\epsilon)$ smaller than the second term, and thus to leading order in ϵ it can be neglected. Let

$$\Delta_j = \frac{4\omega^2-\omega_{2j}^2}{4\omega^2}\,, \tag{31}$$

such that Δ_j is effectively the normalised difference between the superharmonic forcing frequency 2ω and natural frequency ω_{2j} of vertical mode j. The evolution of a_j at leading order in ϵ is thus given by

$$\dot{a}_j - \frac{i\omega\Delta_j}{\epsilon}a_j = -\frac{i\omega M_j}{2\epsilon}\,, \tag{32}$$

where M_j is the constant

$$M_j = \frac{4\omega^2-f^2}{4(\omega^2-f^2)}\cdot\frac{\omega_{2j}^2-f^2}{4\omega^2}\cdot\frac{d\int_{-H}^{0}(N^2)'\hat{\psi}_1^2\hat{\psi}_{2j}\,dz}{\int_{-H}^{0}(N^2-f^2)\hat{\psi}_{2j}^2\,dz}\,. \tag{33}$$

Note that steady solution of [4, 23, 22] can be found as a special case of (32) using the initial condition $a_j(0) = \frac{M_j}{2\Delta_j}$.

Here we impose the initial condition $a_j(0) = 0$ so that there is a pure parent mode at $t = 0$. The solution to (32) is then

$$a_j = \frac{M_j}{2\Delta_j}\left(1 - e^{\frac{i\omega\Delta_j}{\epsilon}T}\right)\,. \tag{34}$$

For two reasons the mode-1 coefficient is dominant, such that $a_1 \gg a_j$ when $j > 1$. Figure 2(a) shows M_j, Δ_j, and $\frac{M_j}{\Delta_j}$ against mode number j for an exponential stratification, showing that $M_1 \gg M_j$, $\Delta_1 \ll \Delta_j$ for $j > 1$, resulting in $\frac{M_1}{\Delta_1} \gg \frac{M_j}{\Delta_j}$. Figure 2(b) shows the corresponding stratification, parent mode structure $\hat{\psi}_1$, and the superharmonic mode-1 structure $\hat{\psi}_2$. Notice how similar $\hat{\psi}_1$ and $\hat{\psi}_{21}$ are, although no assumption on their similarity is made.

Firstly, recall from (33) that $M_j \propto \int_{-H}^{0} (N^2)' \hat{\psi}_1^2 \hat{\psi}_{2j}\, dz$. Since $\hat{\psi}_1$ is mode-1, $\hat{\psi}_1^2$ has a mode-1 structure with no internal zero crossings. Therefore, given certain conditions on N^2, such as $(N^2)'$ being single signed, $(N^2)'\hat{\psi}_1^2$ will map primarily onto $\hat{\psi}_{21}$, so that $M_1 \gg M_j$.

However, the most important reason for mode-1 dominance is the result

$$0 \lesssim \Delta_1 \ll \Delta_j, \qquad j > 1\,. \tag{35}$$

To see this, recall that Δ_j is effectively the difference between the superharmonic forcing frequency $2\omega(k)$ and the natural frequency $\omega_{2j}(k)$ of the superharmonic, which for mode-1 is by definition given by $\omega_{21}(k) = \omega(2k)$. Consider the dispersion relations shown in figure 3. The near linearity of the dispersion relation $\omega(k)$ means that $\omega(2k) \simeq 2\omega(k)$, so that $\Delta_1 \ll 1$. Notice also that this effect is more pronounced for $f = 0$. We therefore define the small parameter $\epsilon \equiv \Delta_1$. For stratification and wavenumber as in figure 2(a), $\epsilon = 0.11$ when $f = 0.01N_0$, and ϵ is an order of magnitude smaller at $\epsilon = 0.01$ when $f = 0$.

The result of this is that $a_1 \gg a_j$ for $j > 1$, and the superharmonic vertical structure is very near mode-1. This result is very robust to different stratifications. To illustrate this, table 1 shows the ratio between the maximum value of a_1 and a_2 (the next largest coefficient) for a range of realistic parameters and stratification profiles. The dominance of mode-1 is greater for lower f, lower wavenumber k, and larger e-folding depth d, but in all cases considered, the maximum value of a_1 is still greater than 15 times the maximum value of $|a_2|$. Changing the stratification profile, including adding in a mixed layer (and thereby allowing $(N^2)'$ to be multi-signed) is shown not to greatly affect the result.

The dominance of a_1 is now used to simplify the expression for the superharmonic at leading order. Writing $a \equiv a_1$, $\hat{\psi}_2 \equiv \hat{\psi}_{21}$, $\hat{\psi}_1 \equiv \hat{\psi}_{11}$, $\omega_{21} \equiv \omega_2$ and $M_1 \equiv M$:

$$\psi^{(2)} = \frac{1}{2}\alpha^2 \frac{\omega d}{k} a(T) \hat{\psi}_2 e^{2i\phi} + c.c.\,, \tag{36}$$

where from (34),

$$a(T) = \frac{M}{2\epsilon}\left(1 - e^{i\omega T}\right)\,. \tag{37}$$

The superharmonic therefore evolves on two timescales - it oscillates at the fast forcing frequency ω within an envelope that oscillates with slow frequency $\Omega = \epsilon\omega$. This periodicity is equivalent to an acoustic 'beat', whereby the constructive and destructive interference of two slightly different frequencies causes a longer timescale periodicity in volume at a frequency proportional to the difference between the two frequencies.

This behaviour is an extension of the 'near resonance' described in Wunsch (2017) [24]. As $\epsilon \to 0$, the forcing frequency approaches the natural frequency of the mode-1 superharmonic, and near resonance occurs. The amplitude of the superharmonic becomes

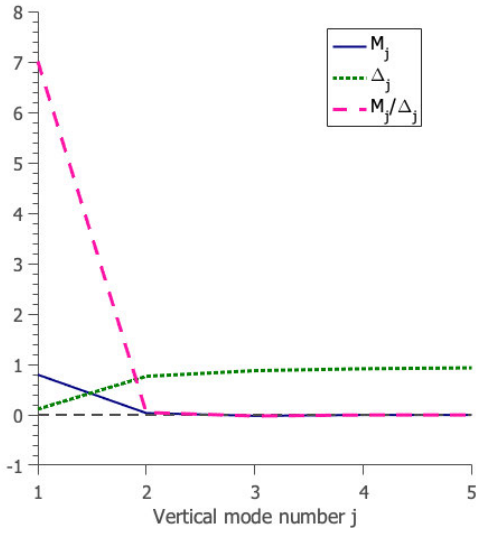

(a)

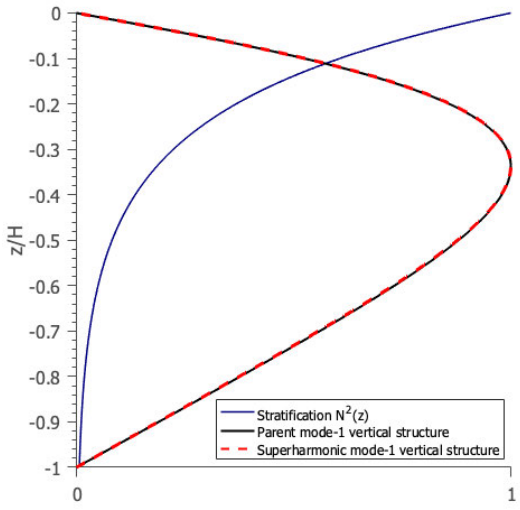

(b)

Figure 2: (a) M_j, Δ_j and M_j/Δ_j plotted against mode number j, in the case $k = 0.2/H$, $f = 0.01N_0$, $N^2 = N_0^2 e^{\frac{z}{d}}$, $d = 0.2$. (b) The stratification $N^2 = N_0^2 e^{\frac{z}{d}}$ for the same parameters, and the corresponding mode-1 parent vertical structure function $\hat{\psi}_1(z)$ and superharmonic vertical structure function $\hat{\psi}_{21}(z)$.

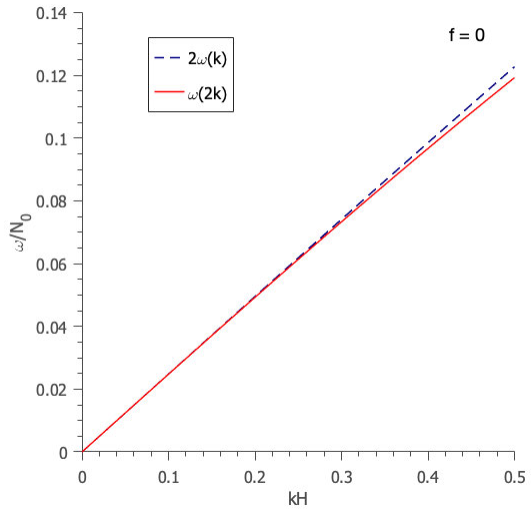

(a)

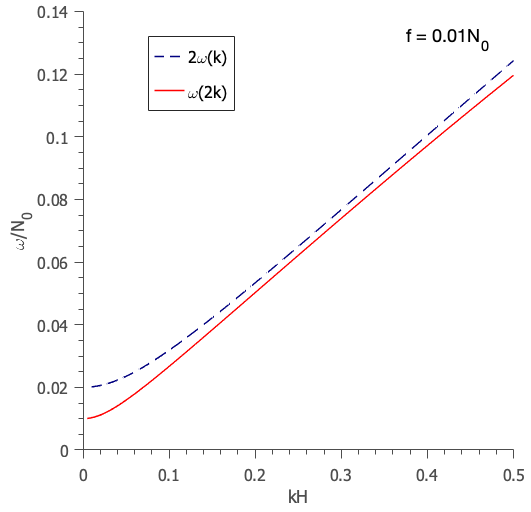

(b)

Figure 3: Twice the dispersion relation of the parent $2\omega(k)$ for the first vertical mode and the dispersion relation of the first vertical mode of the superharmonic $\omega(2k)$ for stratification $N^2 = N_0^2 e^{\frac{z}{d}}$, $d = 0.2$. (a) $f = 0$ (b) $f = 0.01N_0$

$\frac{f}{N_0}$	kH	Profile 1			Profile 2			Profile 3		
		d/H			z_{mix}/H			d/H		
		0.1	0.2	0.3	0.005	0.01	0.02	0.1	0.2	0.3
0	0.1	6972	7117	8908	7112	7079	6857	5082	6875	8506
	0.2	1745	1769	2208	1768	1760	1705	1296	1752	2167
	0.5	282	274	334	273	272	264	239	322	397
0.01	0.1	24	58	113	58	58	56	25	54	90
	0.2	48	150	308	150	149	145	49	134	240
	0.5	123	206	284	206	205	199	124	235	323
0.02	0.1	17	31	52	31	31	30	19	32	47
	0.2	23	56	107	56	55	54	26	54	89
	0.5	53	123	199	123	123	119	60	138	213

Table 1: Value of $\frac{\max|a_1|}{\max|a_2|}$ rounded to the nearest integer for various values of k, f, and stratification profiles N^2. Profile 1: Exponential stratification $N^2 = N_0^2 e^{\frac{z}{d}}$. Profile 2: Exponential stratification with a mixed layer of depth z_{mix}, given by $N^2(z) = \frac{1}{2}N_0^2 e^{\frac{z}{d}}\left(1 - \tanh\left(\frac{z+z_{mix}}{\sigma}\right)\right)$ with $\sigma = 0.001H$ and $d = 0.2H$. Profile 3: $N^2 = \frac{N_0^2 d^2}{(d-z)^2}$.

larger with a longer growth as $\epsilon \to 0$, until in the limit $\epsilon = 0$ the growth is linear and true resonance occurs.

Naturally, the superharmonic grows at the expense of the parent mode, so as the superharmonic grows relative to the parent, the parent must decay. The expression (37) predicts that the ratio of the maximum superharmonic amplitude to the parent amplitude is given by

$$\frac{\max \int_{-H}^{0} |\psi^{(2)}|^2 dz}{\int_{-H}^{0} |\psi^{(1)}|^2 dz} \sim \frac{\alpha^2}{\epsilon^2}\,. \tag{38}$$

This result assumes that the parent is forced to maintain its energy, and thus the superharmonic energy can exceed that of the parent mode for sufficiently small ϵ or large α. Therefore this theory is valid in the limit $\frac{\alpha}{\epsilon} \ll 1$, equivalent to assuming that the superharmonic does not grow large enough to extract energy from the parent. In section 4, we derive a weakly nonlinear (WNL) theory at next order in $\frac{\alpha}{\epsilon}$ to take account of the transfer of energy between the parent and the superharmonic.

2.3.2 Mean flow generation

The mean flow is given by

$$\nabla^2 \psi^{(0)}_{tt} + f^2 \psi^{(0)}_{zz} + N^2 \psi^{(0)}_{xx} = \mathcal{G}_0(z) + c.c. \tag{39}$$

We write

$$\psi^{(0)} = \frac{1}{2}\alpha^2 \frac{\omega d}{k} \tilde{\psi}_0(z,t) + c.c. \tag{40}$$

Similarly to the superharmonic case, we allow the mean flow to have time dependence, but here make no assumption on the timescale. We expand $\tilde{\psi}_0$ similarly to (25), although in

the absence of a suitable basis from (26) when $i = 0$, we impose the boundary conditions by using a sine expansion.

$$\tilde{\psi}_0(z,t) = \sum_{j=1}^{\infty} q_j(t)\sin(m_j z), \qquad m_j = \frac{j\pi}{H}\,. \tag{41}$$

Substituting (40) and (41) into (39) gives

$$\sum_{j=1}^{\infty} -m_j^2\sin(m_j z)(q_j'' + f^2 q_j) = \frac{2k\mathcal{G}_0(z)}{\alpha^2\omega d}\,. \tag{42}$$

Multiplying through by $\sin(m_l z)$, integrating over $z \in [-H, 0]$ and using the orthogonality property of the sine functions gives

$$q_j'' + f^2 q_j = f^2 P_j\,, \tag{43}$$

where

$$P_j = -\frac{4k\int_{-H}^{0}\mathcal{G}_0\sin(m_j z)\,dz}{m_j^2 f^2 H\alpha^2\omega d} \tag{44}$$

$$= \frac{k^2 d}{m_j^2 H(\omega^2 - f^2)}\int_{-H}^{0}\left(2(N^2-\omega^2)\frac{\partial}{\partial z}|\hat{\psi}_1|^2 + (N^2)'|\hat{\psi}_1|^2\right)\sin(m_j z)\,dz\,. \tag{45}$$

Suppose we impose $q_j(0) = q_j'(0) = 0$ for each j, then

$$q_j = P_j(1 - \cos ft)\,. \tag{46}$$

Thus the full mean flow is given by

$$\psi^{(0)} = \frac{1}{2}\alpha^2\frac{\omega d}{k}(1-\cos ft)\sum_{j=1}^{\infty}\sin(m_j z)P_j + c.c. \tag{47}$$

The mean flow therefore has a vertical structure such that the second derivative is proportional to the forcing, in contrast to the superharmonic vertical structure which is primarily mode-1. The time dependence takes the form of inertial oscillations, which is an interesting result in itself and requires further investigation.

A full treatment of the internal mode induced mean flow is not the focus of this study, and in what follows it will be neglected. However, it can be checked with a scaling argument on (47) that $\psi^{(0)} \sim O(\alpha^2)$, whereas the superharmonic $\psi^{(2)} \sim O(\frac{\alpha^2}{\epsilon})$, and thus the superharmonic dominates the mean flow. This is to be expected given the resonant behaviour derived in section 2.3.1. The mean flow is forced at $O(\alpha^2)$ by the parent, thus a flow of $O(\alpha^2)$ is induced. The superharmonic is forced at $O(\alpha^2)$, but the near resonance allows it to grow $O(\epsilon^{-1})$ larger.

3 Comparison of Linear Theory to Simulations

3.1 Simulations

This study was motivated by and is validated with fully nonlinear simulations, described in detail in Sutherland (2016) [21]. The 2D rotating Boussinesq equations (1) - (5) are solved in a rectangular domain with horizontally periodic boundary conditions and free slip at the top and bottom of the domain. The stationary stratification $N^2(z)$ is imposed, and is taken to be exponentially varying as $N^2 = N_0^2 e^{\frac{z}{d}}$, with an e-folding depth $d = 0.2$. Timescales are scaled by the maximum buoyancy frequency N_0 and lengthscales are scaled by the total domain depth H.

The simulations are initialised with the parent mode $\psi^{(1)}$, as defined in (10). Throughout, the wavenumber k of the parent is taken to be $k = 0.2/H$, representing long waves, with two wavelengths in the computational domain. The Coriolis parameter f is generally taken to be $f = 0.01N_0$ unless otherwise specified, which is typical throughout mid-latitudes. A range of amplitudes A_0 are considered.

For a given k, the mode-1 frequency ω and vertical structure $\hat{\psi}_1$ are first found from (11). This is solved numerically using a Galerkin method whereby $\hat{\psi}_1$ is written as a truncated sine series to satisfy the free slip boundary conditions, and the buoyancy frequency N^2 is written as a truncated cosine series. This transforms (11) to an algebraic matrix equation, where the eigenvectors give the coefficients of the sine expansion of $\hat{\psi}_1$ and the eigenvalues give the corresponding frequencies. The mode-1 solution is then used as the initial condition for the nonlinear simulations. Equivalently, the frequency ω could be set (by the tidal frequency, for example), and (11) solved for the wavenumber k. No noise is superimposed on the initial state, ensuring that PSI cannot grow.

The prescribed initial streamfunction $\psi^{(1)}(x, z, 0)$ is then used to determine the timestepped variables ζ, b, v. Vorticity ζ is found through $\zeta = -\nabla^2\psi$, and the corresponding initial spanwise velocity v and buoyancy b fields through the polarization relations (15). The fields are represented spectrally in the horizontal (with the added benefit of allowing easy analysis of different wavenumber components of the fields) and at evenly spaced grid points in the vertical. The timestepping uses a leapfrog scheme with an Euler backstep every 20 timesteps. The timestep for simulations presented here is 0.01 or 0.05, with increased time resolution found to improve small numerical errors but not change the fundamental results. The spatial vertical resolution is 257 or 1025 points, with the higher resolution again reducing small numerical errors.

For numerical stability, Laplacian diffusion is applied to the each of the vorticity, buoyancy and spanwise velocity equations for wavenumbers greater than $16k$ with Reynolds number 100,000 and Prandtl number 1. For the analyses considered here, the relevant wavenumbers are not subject to diffusion so it will not be considered further.

The primary metrics derived from the simulations for comparison with theory are the normalised superharmonic and parent amplitudes, defined for $i = 1, 2$ by

$$||\psi^{(i)}||^2(t) = \frac{\int_{-H}^{0} |\psi^{(i)}(x, z, t)|^2 \, dz}{\int_{-H}^{0} |\psi^{(1)}(x, z, 0)|^2 \, dz}, \tag{48}$$

where $\psi^{(1)}$ is the component of the full ψ field with wavenumber k (the 'parent') and $\psi^{(2)}$ is

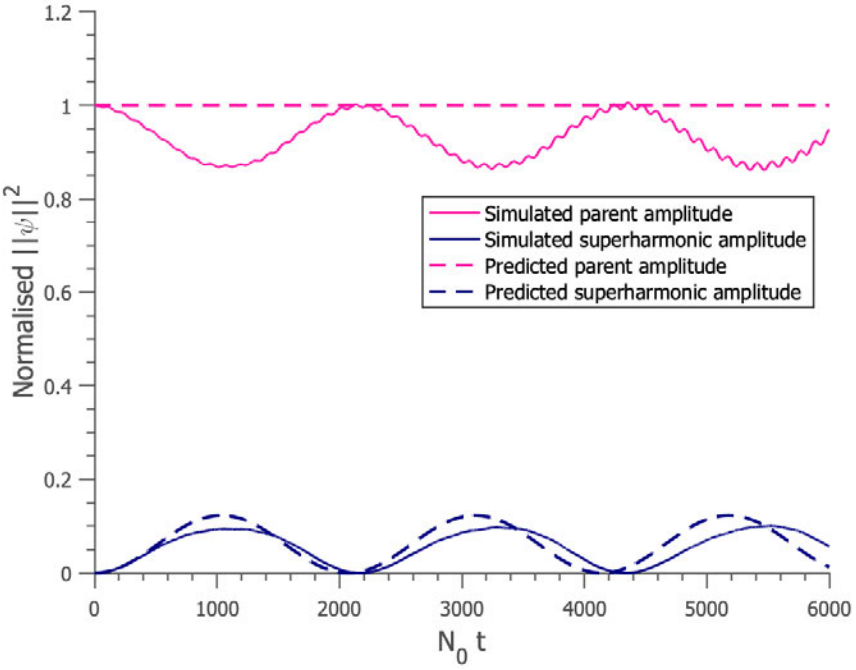

Figure 4: Simulations and predictions of the parent and superharmonic component of the normalised amplitude of ψ, as defined by (49), against time. $N^2 = N_0^2 e^{\frac{z}{d}}$, $d = 0.2H$, $k = 0.2/H$, $f = 0.01N_0$.

the component with wavenumber $2k$ (the superharmonic). Applied to the theoretical form (36) of the superharmonic, this gives:

$$||\psi^{(2)}||^2 = |a|^2 \frac{\int_{-H}^{0} \hat{\psi}_2^2 \, dz}{\int_{-H}^{0} \hat{\psi}_1^2 \, dz} \simeq |a|^2 \,. \tag{49}$$

When determining the amplitude or period of the superharmonic from the simulations (as in figures 5, 11, 12(a)), we take the amplitude as the first maximum in $||\psi^{(2)}||^2$, and the period as the time of the first minimum of $||\psi^{(2)}||^2$ after $t = 0$. For larger amplitude simulations in particular, the period and amplitude may not be constant with time. This is likely due to both nonlinear effects and numerical error. An investigation of these effects would require very long simulations, and is not considered here.

3.2 Results

Figure 4 shows the evolution in time of the superharmonic and parent from the simulations with a stratification $N^2 = N_0^2 e^{\frac{z}{d}}$, $d = 0.2H$, $f = 0.01N_0$, $\alpha = 0.01$ and $k = 0.2/H$ with predictions of the same quantity from section 2 superimposed. The small oscillations with frequency ω visible in the parent amplitude are purely numerical, and can be reduced with higher spatial resolution.

The prediction does indeed recreate the observed long timescale oscillation of the superharmonic, with period Ω correct to 5% accuracy. The predicted amplitude of the super-

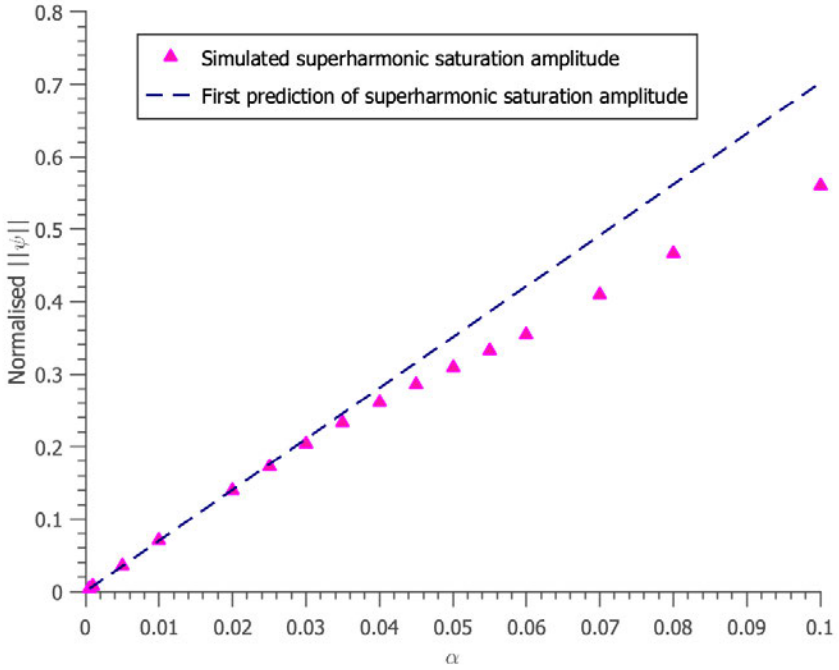

Figure 5: Simulated first maximum of superharmonic amplitude $||\psi||$ (pink triangles) and linear prediction of maximum superharmonic amplitude (blue dashed line).

harmonic is of the correct order of magnitude, but the prediction is a little high. This is because the prediction does not account for loss of energy from the parent into the superharmonic, which reduces the magnitude of the forcing on the superharmonic and thus the reduces the superharmonic amplitude. This issue is also clearly evident in the assumption that the parent stays constant, when it actually reduces comparably to the growth of the superharmonic over each oscillation.

In figure 5, the maximum amplitude of the superharmonic is plotted against the amplitude α of the parent. For small α the prediction is good, but as discussed, for large α it allows the superharmonic to grow to comparable size and eventually larger than the parent, which is both unphysical and inconsistent with the linear theory derived here. There must be a mechanism by which the growth of the superharmonic drains energy from the parent, reducing its amplitude. This then feeds back to the superharmonic by reducing the magnitude of the forcing from the parent self interaction. We now consider a weakly nonlinear theory to take account of these feedbacks.

4 Weakly Nonlinear Theory

We have in the preceding sections derived what is often referred to as a weakly nonlinear theory for the generation of superharmonics [4, 23, 24]. However, we view the theory thus far as linear, and reserve the term weakly nonlinear for what follows, in which we derive the feedback on the parent mode from the superharmonic.

We begin by deriving the next order correction to (36) - (37), taking the next order of the expansion (22). The nonlinear interaction of the superharmonic and the parent provides a forcing $\sim e^{i\phi}$, $e^{3i\phi}$ at order α^3, which can then modify the superharmonic through nonlinear interaction with the parent. Now we are working to next order, we extend our notation so that $\psi^{(n,s)}$ denotes a field with wavenumber nk at order α^s. Thus $\psi^{(1)} \equiv \psi^{(1,1)}$, $\psi^{(2)} \equiv \psi^{(2,2)}, \psi^{(0)} \equiv \psi^{(0,2)}$

Extending (22), let

$$\psi = \{\psi^{(1,1)} + \psi^{(0,2)} + \psi^{(2,2)}\} + \psi^{(1,3)} + \psi^{(3,3)}\,, \tag{50}$$

where the new terms $\psi^{(1,3)}$ and $\psi^{(3,3)}$ are the $O(\alpha^3)$ fields generated by the interaction of the parent and the superharmonic, with wavenumbers k and $3k$, respectively.

The order α^3 field $\psi^{(1,3)}$ will be referred to as the 'correction' to the parent mode, and the field $\psi^{(3,3)}$ will be referred to as the $3k$ superharmonic.

As shown in section 2.3.1, resonance between the forcing and the natural frequency of the superharmonic sets the structure of the superharmonic to be primarily mode-1. This result can be shown to carry through to all modes generated in this system, with the exception of the mean flow, as discussed in section 2.3.2. We thus assume that modes generated by nonlinear interactions take the vertical structure of the relevant mode-1 eigenfunction, such that

$$\psi^{(n,s)} = \frac{1}{2}\frac{\omega d}{k}\alpha^s g_{ns}(T)\hat{\psi}_n e^{in\phi} + c.c.\,, \tag{51}$$

where $\hat{\psi}_n \equiv \hat{\psi}_{n1}$ in (26), and $g_{ns}(T)$ introduces the slow time dependence as in section 2.3.1 where $g_{22}(T) \equiv a(T)$.

4.1 Parent - superharmonic generation of correction to parent

As in (51), we take the correction to the parent to be

$$\psi^{(1,3)} = \frac{1}{2}\frac{\omega d}{k}\alpha^3 c(T)\hat{\psi}_1 e^{i\phi} + c.c.\,, \tag{52}$$

where we have written $g_{13}(T) \equiv c(T)$.

The correction is forced by the parent - superharmonic interaction, thus from (9) the evolution equation is

$$\nabla^2\psi^{(1,3)}_{tt} + f^2\psi^{(1,3)}_{zz} + N^2\psi^{(1,3)}_{xx} = \mathcal{N}^{\{1,2\}}_{1t} - f\mathcal{N}^{\{1,2\}}_{2z} + \mathcal{N}^{\{1,2\}}_{3x}\,, \tag{53}$$

where $\{1,2\}$ indicates the part of the nonlinear interaction of the parent and the superharmonic that is proportional to $e^{i\phi}$. The calculation of the RHS forcing terms requires expressions for the superharmonic buoyancy $b^{(2,2)}$ and velocity $v^{(2,2)}$. From (7) - (8), they satisfy

$$v^{(2,2)}_t = f\psi^{(2,2)}_z + \mathcal{N}^{\{1,1\}}_2\,, \tag{54}$$

$$b^{(2,2)}_t = -N^2\psi^{(2,2)}_x + \mathcal{N}^{\{1,1\}}_3\,, \tag{55}$$

$$\tag{56}$$

where $\mathcal{N}_2^{\{1,1\}}$ and $\mathcal{N}_3^{\{1,1\}}$ are given by (17) and (18).

Recall from section 2.3.1 that $T = \epsilon t$, and $0 < \epsilon \ll 1$. In calculating the RHS of (53) we use the slowly varying approximation $\epsilon \dot{a} \ll \omega a$ to effectively treat $a(T)$ as constant in t, thus we are now working at leading order in ϵ.

The parent-superharmonic forcing in the RHS of (53) can now be calculated, giving:

$$\nabla^2 \psi_{tt}^{(1,3)} + f^2 \psi_{zz}^{(1,3)} + N^2 \psi_{xx}^{(1,3)} = \frac{1}{2}\alpha^3 \frac{\omega d}{k}(\mathcal{C}(z) + a(T)\mathcal{D}(z))e^{i\phi} + c.c.\,, \tag{57}$$

where $\mathcal{C}(z)$ and $\mathcal{D}(z)$ can be determined. Since $a(T) \sim O(\epsilon^{-1})$, we have $\mathcal{C} \ll a(T)\mathcal{D}$. The term $\mathcal{C}$ originates from the terms $\mathcal{N}_2^{\{1,1\}}$ and $\mathcal{N}_3^{\{1,1\}}$ in (53). These nonlinear terms are therefore negligible when $\epsilon \ll 1$, so that to leading order in ϵ the polarization relations (cf. (15)) hold for $v^{(2,2)}$, $b^{(2,2)}$. We thus neglect $\mathcal{C}$ at leading order. $\mathcal{D}(z)$ is given by

$$\begin{aligned}\mathcal{D}(z) = \frac{dk^2}{2}\Bigg[&\hat{\psi}_1\hat{\psi}_2(N^2)'\left(3 - \frac{4\omega^2 + 2f^2}{\omega_2^2 - f^2}\right) \\ &- 8f^2\hat{\psi}_1'\hat{\psi}_2\frac{N^2 - \omega_2^2}{\omega_2^2 - f^2} - 2f^2\hat{\psi}_1\hat{\psi}_2'\frac{N^2 - \omega^2}{\omega^2 - f^2} \\ &- 2f^2(\hat{\psi}_1'\hat{\psi}_2 + \hat{\psi}_1\hat{\psi}_2')\left(\frac{N^2 - \omega^2}{\omega^2 - f^2} + \frac{N^2 - \omega_2^2}{\omega_2^2 - f^2}\right) \\ &+ (2\hat{\psi}_1'\hat{\psi}_2 + \hat{\psi}_1\hat{\psi}_2')(N^2 - f^2)\left(\frac{\omega^2}{\omega^2 - f^2} - \frac{4\omega^2}{\omega_2^2 - f^2}\right)\Bigg]\,.\end{aligned} \tag{58}$$

Substituting (52) into (57) gives an ODE for $c(T)$ (cf. (30)):

$$-\frac{N^2 - f^2}{\omega^2 - f^2}\left(\epsilon^2\ddot{c}(T) - 2i\omega\epsilon\dot{c}(T)\right)\hat{\psi}_1 = a(T)\mathcal{D}(z)\,. \tag{59}$$

Again, we multiply through by $\hat{\psi}_1$ and integrate over $z \in [-H, 0]$ to give

$$\epsilon^2\ddot{c} - 2i\omega\epsilon\dot{c} = -a\frac{(\omega^2 - f^2)\int_{-H}^0 \mathcal{D}\hat{\psi}_1\,dz}{\int_{-H}^0 (N^2 - f^2)\hat{\psi}_1^2\,dz}\,. \tag{60}$$

Neglecting the first term on the LHS of $O(\epsilon^2)$, we obtain the simple ODE for c (cf. (34))

$$\dot{c} = -\frac{i\omega D}{2\epsilon}a\,, \tag{61}$$

where

$$D = \frac{(\omega^2 - f^2)\int_{-H}^0 \mathcal{D}\hat{\psi}_1\,dz}{\omega^2\int_{-H}^0 (N^2 - f^2)\hat{\psi}_1^2\,dz}\,. \tag{62}$$

Using the known form of $a(T)$ from (37) gives

$$\dot{c} = -\frac{i\omega DM}{4\epsilon^2}\left(1 - e^{i\omega T}\right)\,. \tag{63}$$

Integrating and using the initial condition $c(0) = 0$ (by definition of the correction to the parent) gives

$$c(T) = \frac{DM}{4\epsilon^2}\left(e^{i\omega T} - i\omega T - 1\right) . \tag{64}$$

It is immediately evident that there is a problem with the form (64) due to the term that is linear in T. In performing an asymptotic expansion, it is implicitly assumed that the higher order terms in α remain small compared to the terms at lower order in α. In this case, even when the superharmonic and correction are amplified by ϵ^{-1} due to resonance, it is still necessary to assume that $\frac{\alpha}{\epsilon} \ll 1$. The parent correction should be $O\left(\frac{\alpha^2}{\epsilon^2}\right)$ smaller than the parent, but we see here that the linear term in (64) is unbounded, and will ensure that at some time the parent correction is larger in amplitude than the parent itself.

Although clearly unphysical due to conservation of energy, this is once again a manifestation of resonance in the system. Previously, the superharmonic forcing was near resonant with its natural frequency, giving growth and decay on a long timescale. Here, the parent correction is forced at its true resonant frequency ω, causing pure resonance and linear growth. Clearly, there must be some nonlinear feedback mechanism between the parent and the superharmonic that acts to prevent this resonance, thereby conserving energy.

Figure 6 shows this new prediction of the parent, for comparison with figure 4. The superharmonic prediction remains the same as in the linear theory, but the addition of the resonant correction to the parent is certainly unphysical.

We conclude that the parent and superharmonic are so strongly coupled that it will be necessary to consider all orders of feedback. To do this, we consider a fully coupled parent - superharmonic system.

4.2 Fully coupled parent - superharmonic system

We now only consider the parent - superharmonic coupled system, neglecting the mean flow for reasons discussed previously, and also neglecting the third and higher order superharmonics. This removes the need for asymptotic expansion in amplitude α. The system is illustrated in the schematic in figure 7.

The neglect of the the $3k$ superharmonic $\psi^{(3,3)}$ can be justified by noting that, as in the generation of the correction above, it will be related to the superharmonic $\psi^{(2,2)}$ by

$$\|\psi^{(3,3)}\| \sim \frac{\alpha}{\epsilon}\|\psi^{(2,2)}\| , \tag{65}$$

where the ϵ in the denominator of (65) comes from the resonance between the forcing frequency 3ω and resonant mode-1 frequency ω_{31} of the $3k$ superharmonic, similarly to the original near resonant generation of the superharmonic from the parent. However, assuming $\alpha \ll \epsilon$, we neglect $\psi^{(3,3)}$. Despite appearing that they should be of the same order from (50), the key difference between the $3k$ superharmonic and the parent correction is the perfect resonance and coupling between the parent and the superharmonic, allowing the parent correction to grow as large as the superharmonic.

In order to derive the parent-superharmonic coupled system, we first redefine the streamfunction, making no assumption that the parent amplitude stays near its initial value:

$$\psi = \frac{1}{2}\frac{\omega d}{k}\left(\alpha p(T)\hat{\psi}_1 e^{i\phi} + \alpha^2 a(T)\hat{\psi}_2 e^{2i\phi}\right) + c.c. , \tag{66}$$

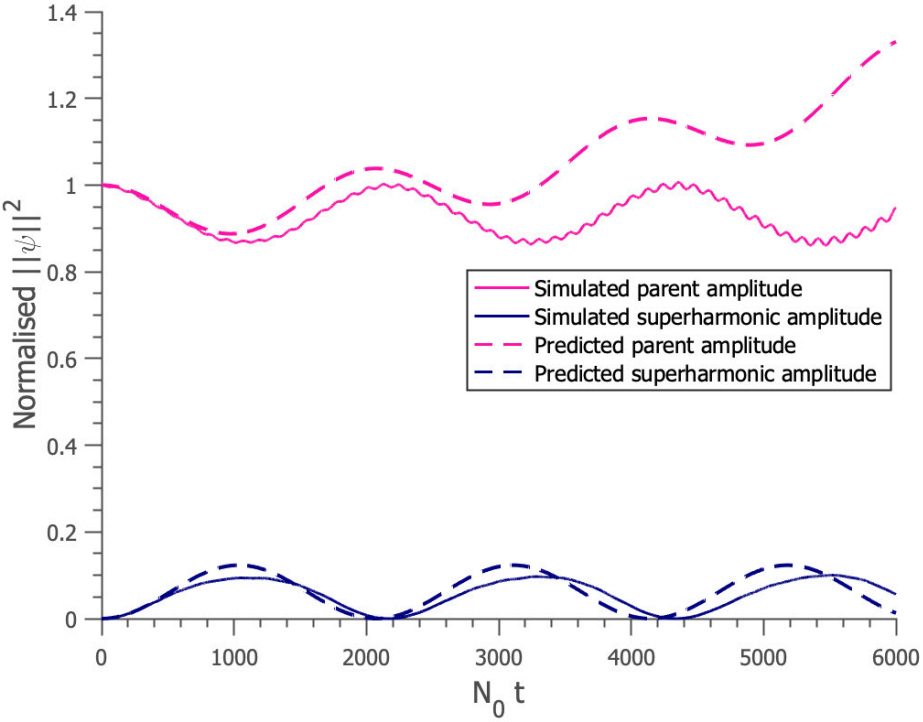

Figure 6: Simulations and first attempt at WNL predictions of the parent and superharmonic component of the normalised amplitude of ψ, as defined by (49), against time. $N^2 = N_0^2 e^{\frac{z}{d}}$, $d = 0.2H$, $k = 0.2/H$, $f = 0.01N_0$.

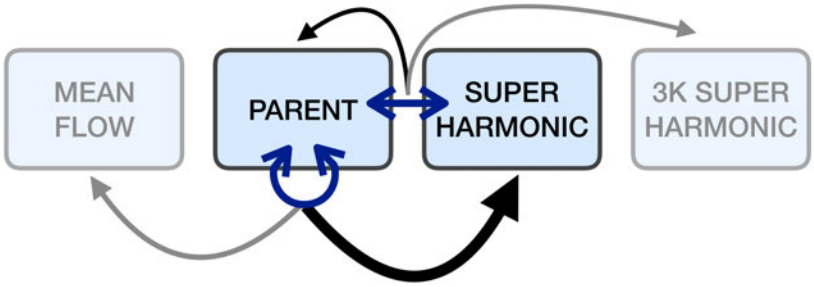

Figure 7: Diagram showing the pathways to be considered in the weakly nonlinear theory. The interactions are represented by blue arrows, and the forcing pathways by black. The parent-parent interaction forces the superharmonic, and the parent - superharmonic interaction feeds back to parent. The mean flow and $3k$ superharmonic are neglected.

where $p(T) = 1 + \alpha^2 c(T)$ is a slowly varying function to represent evolution in time of the parent field, $a(T)$ is the slowly varying superharmonic amplitude (no longer defined by (37)), and all other variables are as before.

It is very little work to extend the results of sections 2.3.1 and 4.1 to account for all orders of forcing. First, recall equation (37) for the first approximation of superharmonic amplitude a, with the assumption that the superharmonic is primarily mode-1 in the vertical:

$$\dot{a} - i\omega a = -\frac{i\omega M}{2\epsilon}\,. \tag{67}$$

We now simply add in all orders of forcing, accounting for the evolution in time of the parent forcing:

$$\dot{a} - i\omega a = -\frac{i\omega M}{2\epsilon}p^2\,, \tag{68}$$

where it is assumed that $\epsilon\dot{p} \ll \omega p$, so that time derivatives of p can be neglected at leading order in ϵ.

Next, recall the equation for the parent correction (61), and use the redefined form (66) to set $p = 1 + \alpha^2 c$, giving

$$\dot{p} = -\frac{i\alpha^2\omega D}{2\epsilon}a\,. \tag{69}$$

The RHS of (69) represents the parent-superharmonic forcing. The superharmonic evolution is already accounted for, thus we need only adjust to take account of the parent evolution:

$$\dot{p} = -\frac{i\alpha^2\omega D}{2\epsilon}ap^*\,, \tag{70}$$

where p^* is the complex conjugate, since the forcing is due to the product of the part of the superharmonic that is proportional to $e^{2i\phi}$ and the part of the parent that is proportional to $e^{-i\phi}$.

The equations (68) and (70) form a coupled nonlinear set of ODEs for $a(T)$ and $p(T)$.

4.3 Analysis of coupled system

The system (68) and (70) has several interesting properties that can be obtained analytically, and an asymptotic solution in the limit $\frac{\alpha}{\epsilon} \ll 1$.

4.3.1 Conservation law

A conservation law for $|a|$ and $|p|$ can be derived from (68) and (70) (see Appendix A for derivation):

$$|p|^2 + \frac{\alpha^2 D}{M}|a|^2 = 1\,. \tag{71}$$

This elegant result is evocative of conservation of energy - as energy drains from the parent, the superharmonic must gain a proportional amount of energy. Note that this result is somewhat surprising in this context, given that for the reduced system considered here, energy is not conserved because in reality energy transfers to the mean flow and higher horizontal and vertical modes.

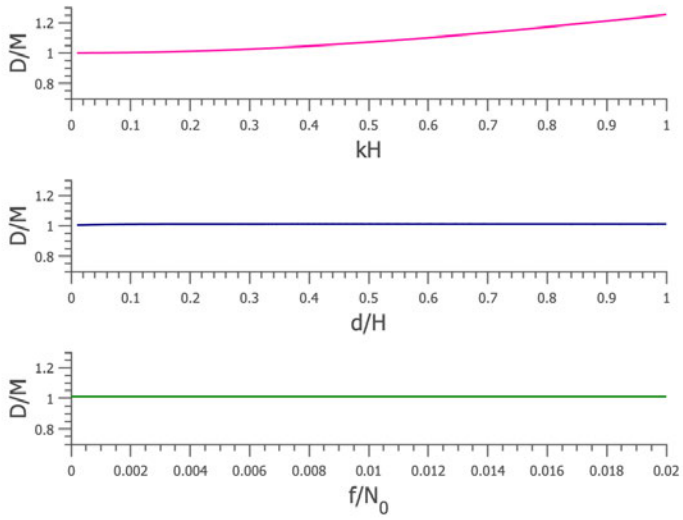

Figure 8: The value of $\frac{D}{M}$ against various parameters. Stratification is given by $N^2 = N_0^2 e^{\frac{z}{d}}$. Top: k varies, $f = 0.01N_0$, $d = 0.2H$ fixed. Middle: d varies, $f = 0.01N_0$, $kH = 0.2$ fixed. Bottom: f varies, $d = 0.2H$, $kH = 0.2$ fixed.

The factor $\frac{D}{M}$ gives a constant 'efficiency' which tells us how much the parent amplitude must decay as the superharmonic grows. The constants D and M can be simply calculated from (33) and (62) as a function of the wavelength k of the parent, the Coriolis parameter f and background stratification N^2. Figure 8 shows that for a range of parameters, the ratio $\frac{D}{M}$ is approximately 1. The interpretation of this is that the small differences in frequency and vertical structure of the parent and the superharmonic cause slightly different amplitudes for each for a given energy input.

Now that we have a simple relation between the absolute value of the amplitude of the parent and the superharmonic, we can further manipulate (68) and (70) to obtain one equation for $|p|$.

4.3.2 Dynamical system interpretation

The coupled nonlinear system (68) and (70) can be further manipulated (see Appendix B for derivation) to give

$$(1 - X)\ddot{X} + \dot{X}^2 + \omega^2 X = \frac{1}{2}\omega^2\delta^2(1 - X)^3\,, \tag{72}$$

where $X = 1 - |p|^2$, such that $X = \frac{\alpha^2 D}{M}|a|^2 \geq 0$ and $\delta^2 = \frac{MD\alpha^2}{\epsilon^2}$.

Remarkably, (72) can be written as a Hamiltonian system with generalised position X and generalised momentum P, such that:

$$H(X, P) = \frac{1}{2m(X)}P^2 + V(X)\,. \tag{73}$$

The generalised potential $V(X)$ and mass function $m(X)$ in this case are

$$V(X) = \frac{1}{2}\omega^2 \frac{2X-1}{(1-X)^2} - \frac{1}{2}\omega^2\delta^2 X\,, \tag{74}$$

$$m(X) = \frac{1}{(1-X)^2}\,, \tag{75}$$

and $\frac{dH}{dT} = 0$. The generalised position and momentum are given by the equations

$$\dot{X} = \frac{\partial H}{\partial P} \tag{76}$$

$$= (1-X)^2 P\,, \tag{77}$$

$$\dot{P} = -\frac{\partial H}{\partial X} \tag{78}$$

$$= (1-X)P^2 - \omega^2 \frac{X}{(1-X)^3} + \frac{1}{2}\omega^2\delta^2\,. \tag{79}$$

Combining (77) and (79) to eliminate P does indeed recover (72).

We use the property $\frac{dH}{dT} = 0$ to determine the constant H for this system. Notice from (70) that $a(0) = 0$ implies $\dot{p}(0) = 0$, so that $X(0) = \dot{X}(0) = 0$, and thus

$$H(X,P) = H(X(0),P(0)) = V(0)\,. \tag{80}$$

The solution is therefore a curve in (X,P) phase space given by

$$\frac{1}{2m(X)}P^2 + V(X) = V(0) \tag{81}$$

or, writing m and V explicitly using (74) and (75):

$$(1-X)^2P^2 + \omega^2\left(\frac{X^2}{(1-X)^2} - \delta^2 X\right) = 0\,. \tag{82}$$

Figure 9(a) shows the curve defined by (82), plotted in (X,P) phase space. Only the part of the curve that lies in the relevant domain $0 \le X \le 1$ is plotted. It is clear that there is a periodic orbit, which recovers the characteristically periodic behaviour that we expect from the superharmonic and parent as in the simulations in figure 4. There are stationary points at $(0,0)$ and $(X_{max},0)$ where the curve intersects $P = 0$. X_{max} is defined such that $V(X_{max}) = V(0)$.

Notice that $X = 0$ and $X = X_{max}$ are in fact solutions of (82), and therefore fixed points in the phase diagram. However, they are not solutions of (72), and not valid solutions to our system. In fact, $\dot{X} = 0$ is always a solution to $\frac{dH}{dT} = 0$. Explicitly, this solution is introduced when (72) is multiplied through by $\frac{\dot{X}}{(1-X)^3}$ before being integrated to form the Hamiltonian.

We wish to find the maximum amplitude of the superharmonic, at which $\dot{X} = 0$. This is given by the stationary point $X = X_{max}$ up to constants in the definition of X, and can be determined analytically by solving $V(X) = V(0)$. There are 3 solutions to the resulting

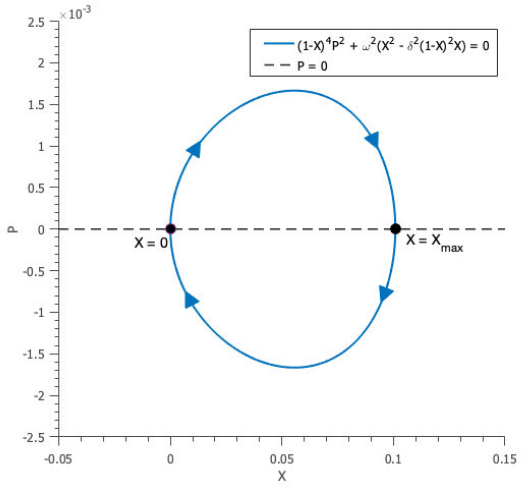

(a)

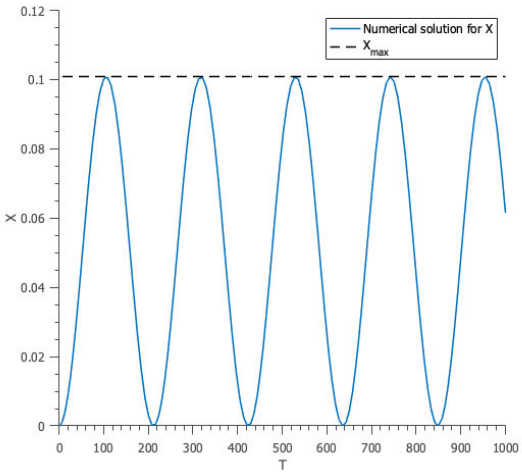

(b)

Figure 9: (a) A plot of the level set (82) on which the solution (X, P) lies. The points at which $P = 0$ are marked, corresponding to stationary points of X. (b) The numerical solution of (72), as represented in phase space in 9(a). The periodic orbit is evident, with maxima at $X = X_{max}$ and minima at $X = 0$. The solution is calculated using an ODE solver.

cubic equation; $X = 0$ represents the minima of the superharmonic amplitude, $X = X_{max}$ represents the maxima of the superharmonic amplitude, and some $X > 1$ is irrelevant as $X \leq 1$. Figure 9(b) shows the numerical solution for X, found using a numerical ODE solver. The solution appears to be near sinusoidal, and the oscillation between $X = 0$ and $X = X_{max}$ can be seen clearly. X_{max} is given by

$$X_{max} = 1 - \frac{1}{2\delta^2}\left((1+4\delta^2)^{\frac{1}{2}} - 1\right). \tag{83}$$

Recall that the weakly nonlinear theory for the coupled parent - superharmonic system is valid for $\frac{\alpha}{\epsilon} \ll 1$, or equivalently, $\delta \ll 1$. We therefore expand (83) for small δ, to obtain

$$X_{max} = \delta^2 - 2\delta^4 + O(\delta^6). \tag{84}$$

We are also interested in determining the frequency of the system, corresponding to the slow frequency of growth and decay of the superharmonic. Rewriting (82) in terms of X only gives

$$\dot{X}^2 + \omega^2(X^2 - \delta^2 X(1-X)^2) = 0. \tag{85}$$

Differentiating and dividing through by $\dot{X}$ removes the $\dot{X} = 0$ solution and recovers an equation reminiscent of simple harmonic motion:

$$\ddot{X} + \omega^2\left(X - \frac{1}{2}\delta^2(1-X)(1-3X)\right) = 0. \tag{86}$$

Finding the period or directly solving this equation requires solution of an elliptic integral. However, as before we can consider an asymptotic solution for $\delta \ll 1$. From (83), we know that $X \sim \delta^2$. At leading order in δ, (86) then becomes simple harmonic motion:

$$\ddot{X} + \omega^2 X = \frac{1}{2}\delta^2\omega^2. \tag{87}$$

This has the solution

$$X = \frac{1}{2}\delta^2(1 - \cos\omega T), \tag{88}$$

or, in terms of a and t:

$$|a|^2 = \frac{M^2}{2\epsilon^2}(1 - \cos\epsilon\omega t). \tag{89}$$

This fully recovers the initial prediction (37) of $|a|$.

At next order in δ, (86) becomes

$$\ddot{X} + \omega^2(1+2\delta^2)X = \frac{1}{2}\omega^2\delta^2. \tag{90}$$

Similarly to (87), this also has a simple harmonic form, with solution

$$X = \frac{\delta^2}{2(1+2\delta^2)}\left(1 - \cos\left(\omega\sqrt{1+2\delta^2}T\right)\right), \tag{91}$$

where the maximum value is consistent with (83) to $O(\delta^4)$. To the first two orders in δ, the solution is indeed sinusoidal. The exact solution will have small corrections at next order in δ.

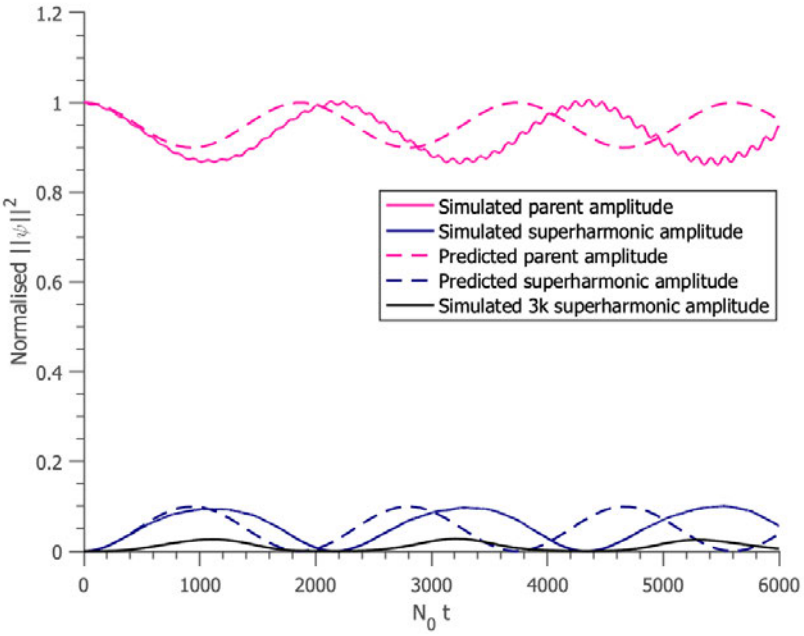

Figure 10: The simulated parent and superharmonic amplitudes for the set-up in figure 4 are plotted with the new WNL prediction, solved from (72) using a numerical ODE solver. The simulated $3k$ superharmonic is also plotted for reference.

5 Comparison of WNL Theory to Simulations

The weakly nonlinear theory is valid for $\frac{\alpha}{\epsilon} \ll 1$, and predicts that

1. The superharmonic and parent amplitude obey a conservation law $|p|^2 + \frac{\alpha^2 D}{M}|a|^2 = 1$.
2. The system is periodic, with frequency $\Omega = \epsilon\omega\sqrt{1 + \frac{2MD\alpha^2}{\epsilon^2}} + O(\frac{\alpha^3}{\epsilon^3})$.
3. The maximum amplitude of the superharmonic is given by

$$\max |a|^2 = \frac{M}{D\alpha^2}\left(1 - \frac{\epsilon^2}{2MD\alpha^2}\left(\sqrt{1 + \frac{4\alpha^2 MD}{\epsilon^2}} - 1\right)\right) \tag{92}$$

$$= \frac{M^2}{\epsilon^2}\left(1 - \frac{2M\alpha^2}{\epsilon^2}\right) + O\left(\frac{\alpha^4}{\epsilon^4}\right). \tag{93}$$

Figure 10 shows the simulation previously plotted in figure 4, with the prediction from section 2 replaced with the new weakly nonlinear theory. The parent is now shown to evolve with the same period as the superharmonic, greatly improving the constant prediction from the linear theory. The maximum superharmonic amplitude is also more accurate. This is illustrated for various parent amplitudes α in figure 11, which shows the amplitude of the first superharmonic maximum from simulations, from the linear prediction, and from the WNL prediction. The linear prediction is good for small α such that $\frac{\alpha}{\epsilon} \ll 1$ as previously

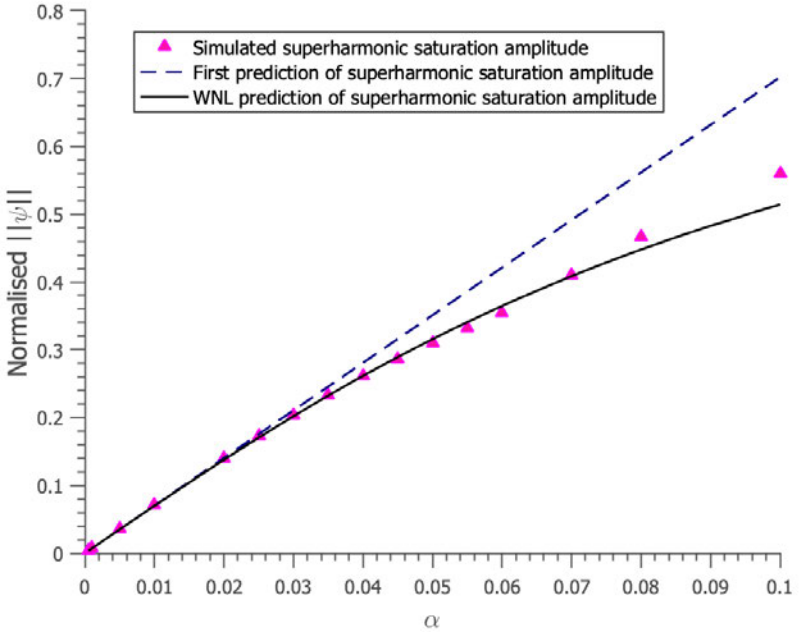

Figure 11: The results from figure 5 are replotted with the new WNL amplitude prediction, greatly improving the prediction of the superharmonic amplitude.

discussed, and consistent with the WNL solution (as is evident from the expansion (84)). However, for larger values of α, the WNL prediction greatly improves the linear prediction. At $\alpha = 0.05$ the WNL prediction is still good, despite a fairly large $\frac{\alpha}{\epsilon} = 0.44$.

From figure 10, it is clear that although the superharmonic amplitude prediction is good, the minimum parent amplitude is overestimated. This is likely due to the parent also losing energy to the mean flow and $3k$ superharmonic, which is not accounted for in the model. The $3k$ superharmonic from simulations is also plotted in figure 10. We expect the squared $3k$ superharmonic amplitude to be $O\left(\frac{\alpha^2}{\epsilon^2}\right)$ smaller than the superharmonic. Since $\frac{\alpha^2}{\epsilon^2} \simeq 0.2$ in this case, this is consistent with the size of the the simulated $3k$ superharmonic. Although not examined here, from simulations it is clear that the effect of the $3k$ superharmonic superimposing with the $2k$ superharmonic is to amplify and focus the peaks of the parent. The this could be an important mechanism in facilitating steepening of the parent when the $3k$ superharmonic is large enough.

The predicted period of the superharmonic and parent is shorter than that of the simulations. This effect appears amplified in figure 10 due to the cumulative error in the period, but the relative error in the period is approximately 15%. This error is consistent with the neglect of the next order in ϵ throughout the derivation of the model. When taking time derivatives, we often invoked $\epsilon \ll 1$ in order to neglect 2nd order terms. In this case, $\epsilon \simeq 0.1$, so a 10% error is expected.

The source of this error is investigated in figure 12(a). Simulations were run for different values of ϵ (by changing the value of f), whilst keeping $\frac{\alpha}{\epsilon}$ constant at 0.44. This was necessary because fixing α and allowing ϵ to become very large would cause $\frac{\alpha}{\epsilon}$ to become

large, invalidating the model. At first glance, both the linear prediction of the period $T = \frac{2\pi}{\epsilon\omega}$ and the WNL prediction of the period match well with the period from simulations. Figure 12(b) plots the relative error of the linear and WNL theories to the simulations. Interestingly, the linear theory appears to be better than the WNL theory at predicting the period. However, as predicted, the error in the WNL theory decreases for decreasing ϵ, suggesting that it is indeed due to the neglect of higher orders in ϵ.

6 Application to Realistic Oceanic Parameters

In this section we briefly consider the implications of the conclusions of sections 2 - 5 on the oceanic internal tide. We do not attempt to predict the generation of superharmonics, but rather to investigate whether there is potential for superharmonics to grow from the internal tide given realistic oceanic conditions.

We consider in particular the internal tide generated at the Hawaiian Ridge, where the far field propagation of the low mode internal tide has been the subject of multiple studies (e.g., [18, 1, 26]). We use the mooring data from mooring MP1 of Zhao et al. (2010) [26] to give estimates of the stratification profile and amplitude of the internal tide. The internal tide at this mooring is 218km NE of its generation site, and is dominated by the mode-1 signal from the M2 tide [26].

An idealized stratification profile is designed to roughly approximate the stratification profile in figure 2b of Zhao et al. (2010) [26]. Depth H is taken to be 5000m, and the stratification profile as exponential with a mixed layer:

$$N^2(z) = \frac{1}{2}N_0^2 e^{\frac{z}{d}}\left(1 - \tanh\left(\frac{z + z_{mix}}{\sigma}\right)\right), \tag{94}$$

where $N_0^2 = 1 \times 10^{-4}$, e-folding depth $d = 500$m, mixed layer depth $z_{mix} = 50$m and interface width $\sigma = 5$m.

The maximum along beam surface velocity of the mode-1 is taken to be $0.1\,\mathrm{m\,s^{-1}}$ from ADCP measurements at the mooring MP1. This corresponds to a non-dimensional parent amplitude of roughly $\alpha \simeq 0.02$.

The latitude at MP1 is $25.5°N$, giving $f = 6.3 \times 10^{-5}\,\mathrm{s^{-1}}$. The frequency ω is set by the frequency of the semidiurnal lunar (M2) tide, which has a period of 12.5 hours, giving $\omega = 1.4 \times 10^{-4}\,\mathrm{s^{-1}}$. Given the stratification profile, Coriolis parameter and frequency of the parent, the wavelength k of the parent is found by modifying the Galerkin method described in section 2, giving $k = 1.82 \times 10^{-5}\,\mathrm{m^{-1}}$, corresponding to a wavelength $\lambda = 182\,\mathrm{km}$. For comparison, a wavelength of 162km is used in Zhao et al. 2010 [26] to simulate the northward Hawaiian internal wave beam.

The ratio $\frac{\alpha}{\epsilon} = 0.13$, suggesting that in this case the superharmonic could grow to roughly 10% of the size of the parent.

If instead we consider the same stratification profile, amplitude and tidal frequency for a range of latitudes, we find that the maximum value of the superharmonic will be greatly amplified at lower latitudes. Figure 13(a) shows the maximum amplitude of the superharmonic relative to the parent calculated from both the linear theory (37) as $\max \alpha|a| = \frac{M\alpha}{\epsilon}$, and the WNL prediction (92). The linear theory predicts that the superharmonic will grow

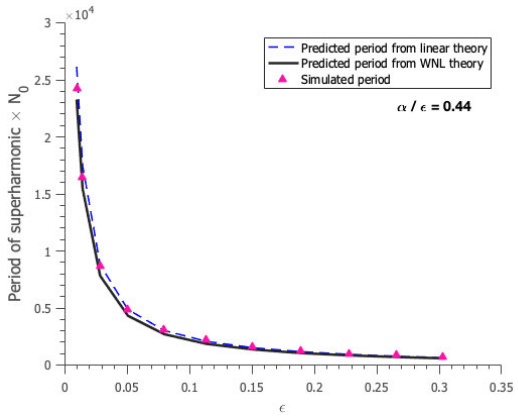

(a)

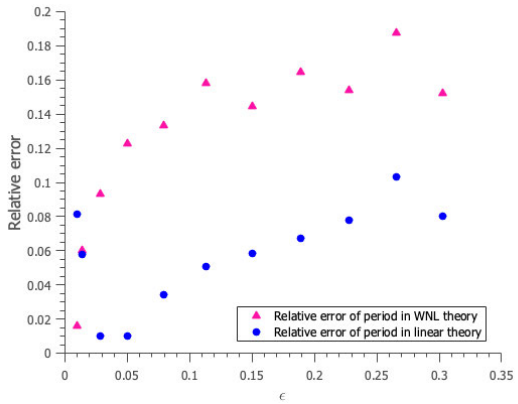

(b)

Figure 12: (a) The period of the long timescale superharmonic growth and decay against ϵ, for fixed $\frac{\alpha}{\epsilon} = 0.44$, as predicted by the linear theory $T = \frac{2\pi}{\epsilon\omega}$ (blue dashed) and by the asymptotic approximation to the weakly nonlinear theory from (91) (black solid). The period from simulations is marked with pink triangles. (b) The relative error between the period from linear theory and from simulations (blue circles) and between the period from WNL theory and from simulations (pink triangles).

to over twice the amplitude of the parent at the equator, which is unphysical. The WNL theory predicts that it will grow to 80% of the size of the superharmonic, which could be physical but is still outside of the realms where the WNL theory is valid. The WNL theory is formally valid for $\frac{\alpha}{\epsilon} \ll 1$, though is good for $\frac{\alpha}{\epsilon} \lesssim 0.5$, which is true at latitudes higher than $\sim 12°$N from figure 13(a).

At lower latitudes, the WNL theory breaks down because higher harmonics and further nonlinear effects are present. Therefore, despite the invalidity of our theory at low latitudes, we can predict that the superharmonics could become significantly amplified and grow large enough to excite further superharmonics, perhaps eventually facilitating the destruction of the internal tide via a cascade to smaller scales and eventual turbulence.

However, it is important to note that the time taken for the superharmonic to grow to its maximum value also increases with decreasing latitude. Figure 13(b) shows that the number of days for the superharmonic to reach its first maximum increases from 1.7 days at $25.5°N$ to 15 days at the equator according to the WNL prediction, or 40 according to the linear prediction. Both the linear and WNL theories are only formally valid for $\alpha \ll \epsilon$, so these estimates near the equator are likely to be inaccurate.

Rainville and Pinkel (2006) [17] estimate the propagation paths of certain known internal tide beams over a period of 21 days (see figure 1, Rainville and Pinkel (2006) [17]), calculated from a ray tracing approach using estimates of geographic distribution of the group velocity of internal tide beams. For example, an internal tide beam propagating NE of the Hawaiian Ridge is expected to reach the coast of Alaska in approximately 3 weeks, and a beam propagating SW from Hawaii could reach south of Fiji in 3 weeks, after crossing the equator. Therefore, it is possible that the internal tide could reside at low amplitudes for an insufficient time for superharmonics to attain their maximum amplitude. However, the superharmonic could certainly be significantly amplified in this time.

In order to determine how large the superharmonics could grow over the propagation of an internal tide beam, it would be necessary to modify our theory to account for slowly varying f, perhaps using a ray tracing approach similar to Rainville and Pinkel (2006) [17] to quantify the effect of changing ϵ on the growth of superharmonics. The change in amplitude of the internal tide as it loses energy during propagation should also be considered.

The conclusion of these rough analyses with realistic parameters is that superharmonic generation certainly could be important in the ocean, and for certain regions the WNL theory derived here will apply to their evolution.

7 Conclusion

A possible mechanism for the extraction of energy from the mode-1 internal tide in a rotating and non-uniformly stratified environment has been investigated theoretically and verified with fully nonlinear simulations.

In non-uniform stratification, an internal mode (the 'parent') has been shown theoretically to generate superharmonics with double the wavenumber through nonlinear self-interaction [4]. In this work, a theory was developed to extend the analysis of Diamessis et al. (2014) [4], Wunsch (2015) [23] and Sutherland (2016) [21] to allow for time evolution of the superharmonic in a general stratification $N^2(z)$.

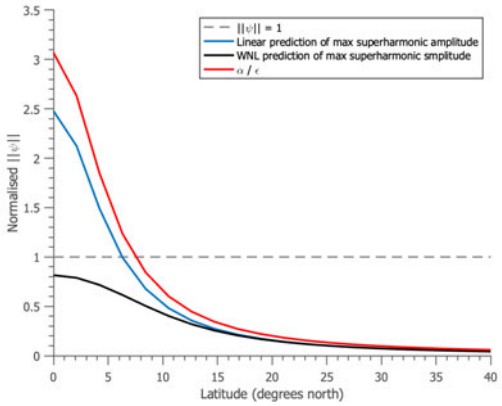

(a)

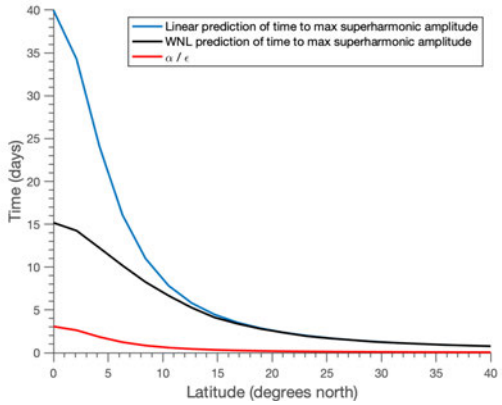

(b)

Figure 13: (a) The maximum amplitude of the superharmonic relative to the parent at different latitudes, calculated from the linear theory and WNL theory with stratification given by (94) for a parent internal tide with semidurnal frequency, and parameters given in the text. The value of $\frac{\alpha}{\epsilon}$, and the WNL theory is valid when $\frac{\alpha}{\epsilon} \ll 1$. $||\psi|| = 1$ is marked for reference, to show where the superharmonic is as large as the parent. (b) The number of days for the superharmonic to reach it's maximum amplitude, calculated as in figure 13(a).

A first order approach in which the parent amplitude is held constant was found to recreate a slow periodic growth and decay of superharmonic amplitude seen in simulations. This is due to near resonance between the forcing frequency $2\omega(k)$ of the parent-parent interaction and the natural frequency of the mode-1 component of the superharmonic $\omega(2k)$, and could also be compared to an acoustic 'beat'.

The resonance ensures that the mode-1 component of the superharmonic is much larger than higher mode components, even when the vertical structure of the forcing from the parent is not mode-1. A theory for the evolution of the superharmonic in the limit $\alpha \ll \epsilon \ll 1$ was developed, where α is the non-dimensional parent amplitude and ϵ is effectively the difference between the forcing frequency and the true frequency of the superharmonic. This 'linear' theory predicts low frequency periodicity with frequency $\Omega = \epsilon\omega$ and maximum superharmonic amplitude of $O\left(\frac{\alpha}{\epsilon}\right)$. The prediction is good in the limit $\frac{\alpha}{\epsilon} \ll 1$, that is when the maximum amplitude of the superharmonic is much smaller than the parent.

A weakly nonlinear theory was then developed to take account of the feedbacks between the parent and the superharmonic. A first attempt at asymptotic expansion in amplitude α was found to introduce an unphysical true resonance and linear growth into the system. It was concluded that the parent - superharmonic coupling is so strong as to necessitate consideration of all orders of feedback. A coupled parent - superharmonic system was then developed, neglecting the mean flow and higher harmonics of the parent. The resulting coupled set of nonlinear ODEs for the parent and superharmonic amplitude was shown to possess a conservation law linking the instantaneous amplitude of the parent to that of the superharmonic. Although this does not exactly represent energy conservation, this law ensures that the physical condition that the parent decays when the superharmonic grows (and vice versa) holds.

The nonlinear ODEs were manipulated to form an equation for the real magnitude of the superharmonic amplitude. Although this system does not have an analytic solution, it was shown to possess a Hamiltonian structure. This was exploited to find the maximum amplitude of the superharmonic analytically. An asymptotic solution for the superharmonic amplitude and period at next order in $\frac{\alpha}{\epsilon}$ was found, which is consistent at leading order in $\frac{\alpha}{\epsilon}$ with the initial linear prediction.

The solution to the coupled system was compared with the simulations and found to improve the prediction of the amplitude of the parent and superharmonic. Errors in the frequency Ω of the slow oscillation of the superharmonic were found to decrease with decreasing ϵ in the WNL theory, which is expected due to neglect throughout of higher orders in ϵ.

The weakly nonlinear theory is valid for $0 \ll \alpha \ll \epsilon \ll 1$. Typical oceanic parameters were shown to lie in this range, suggesting that this mechanism could take place in the real ocean. In particular, a primitive analysis of internal tide radiating from Hawaii showed that the superharmonics could be of significant size. In the case of internal tides approaching the equator, the superharmonics could grow large enough to excite further superharmonics, thus causing nonlinear steepening of the internal tide and potential for further cascade to smaller scales.

8 Further Work

Both the simulations and theoretical framework of this work are highly idealized. In reality, the other mechanisms mentioned previously for destruction of the internal tide (interaction with topography, PSI, interaction with mean flow) are likely to take place alongside the formation of superharmonics, perhaps modifying the generation mechanism.

The higher harmonics have been neglected in this analysis, but reference was made to the potential for higher harmonics to facilitate the eventual destruction of the internal tide given the right conditions. It was found in the simulations that the $3k$ superharmonic could superimpose with the $2k$ superharmonic to steepen the parent, perhaps creating conditions for nonlinear steepening described in Helfrich and Grimshaw (2008) [8]. This avenue could be explored numerically or by inclusion of the $3k$ superharmonic in the coupled system of section 4.

A natural extension of this work would be to consider the effect of varying f on the superharmonic amplification, as mentioned in section 6. This work could then be considered in an real oceanic context, and predictions made of the probable location and amplitude of superharmonics generated from known internal tide beams. Estimates of depth, stratification and internal tide amplitude could be used to map the global distribution of $\frac{\alpha}{\epsilon}$ to determine where this mechanism is likely to be important.

9 Appendices

Appendix A

We derive a conservation law for $|a|$ and $|p|$. Taking (70) and multiplying through by p^* gives

$$\dot{p}p^* = -\frac{i\alpha^2\omega D}{2\epsilon}a(p^*)^2\,. \tag{95}$$

Adding (95) to its complex conjugate:

$$\frac{\partial|p|^2}{\partial T} = -\frac{i\alpha^2\omega D}{2\epsilon}(a(p^*)^2 - a^*p^2)\,. \tag{96}$$

Using (68) do eliminate p from the RHS gives

$$\frac{\partial|p|^2}{\partial T} = -\frac{\alpha^2 D}{M}\frac{\partial|a|^2}{\partial T}\,. \tag{97}$$

Integrating and using initial conditions $a = 0$, $p = 1$ then gives the conservation law

$$|p|^2 + \frac{\alpha^2 D}{M}|a|^2 = 1\,. \tag{98}$$

Appendix B

An equation for $|p|$ alone is derived from equations (68) and (70). Begin by setting $a = Ae^{i\omega T}$, so that (68), (70) become

$$\dot{A} = -\frac{iM\omega}{2\epsilon} e^{-i\omega T} p^2 \,, \tag{99}$$

$$\dot{p} = -i\frac{\alpha^2 \omega D}{2\epsilon} e^{i\omega T} A p^* \,. \tag{100}$$

Rearranging (100) to find A then differentiating gives an expression for $\dot{A}$ in terms of p. Substituting into (99) gives an equation in p only:

$$\ddot{p}p^* - i\omega \dot{p}p^* - \dot{p}\dot{p}^* = -\frac{1}{4}\omega^2 \delta^2 |p|^4 \,, \tag{101}$$

where

$$\delta^2 = \frac{MD\alpha^2}{\epsilon^2} \,. \tag{102}$$

Adding the complex conjugate to (101) gives:

$$\frac{\partial^2}{\partial T^2}|p|^2 - 4|\dot{p}|^2 + i\omega(\dot{p}^* p - \dot{p}p^*) = -\frac{1}{2}\omega^2 \delta^2 |p|^4 \,. \tag{103}$$

Subtracting the complex conjugate from (101) gives:

$$\frac{\partial}{\partial T}(\dot{p}p^* - \dot{p}^* p) = i\omega \frac{\partial}{\partial T}|p|^2 \,. \tag{104}$$

Notice from (70) that since $a(0) = 0$, we have $\dot{p}(0) = 0$. Thus we can integrate (104) using $p(0) = 1$ to give

$$\dot{p}p^* - \dot{p}^* p = i\omega(|p|^2 - 1) \,. \tag{105}$$

Substituting (105) into (103) gives

$$\frac{\partial^2}{\partial T^2}|p|^2 - 4|\dot{p}|^2 + \omega^2(|p|^2 - 1) = -\frac{1}{2}\omega^2 \delta^2 |p|^4 \,. \tag{106}$$

We now use the identity

$$(\dot{p}p^* - \dot{p}^* p)^2 = ((\dot{|p|^2}))^2 - 4|\dot{p}|^2 |p|^2 \tag{107}$$

to find an expression for $|\dot{p}|$ in terms of $|p|$. Combining (105) and (107) gives

$$4|\dot{p}|^2 = \frac{((\dot{|p|^2}))^2 + \omega^2(|p|^2 - 1)^2}{|p|^2} \,. \tag{108}$$

Substituting (108) into (106) gives an equation in $|p|$ only:

$$|p|^2 \frac{\partial^2}{\partial T^2}|p|^2 - ((\dot{|p|^2}))^2 + \omega^2(|p|^2 - 1) = -\frac{1}{2}\omega^2 \delta^2 |p|^6 \,. \tag{109}$$

Writing $X = 1 - |p|^2$, (such that $X = \frac{\alpha^2 D}{M}|a|^2 \geq 0$), we have

$$(1 - X)\ddot{X} + (\dot{X})^2 + \omega^2 X = \frac{1}{2}\omega^2 \delta^2 (1 - X)^3 \,. \tag{110}$$

References

[1] M. H. Alford, J. A. MacKinnon, Z. Zhao, R. Pinkel, J. Klymak, and T. Peacock, *Internal waves across the Pacific*, Geophysical Research Letters, 34 (2007), pp. 0–5.

[2] P. G. Baines, *The generation of internal tides by flat-bump topography*, Deep-Sea Research and Oceanographic Abstracts, 20 (1973), pp. 179–205.

[3] T. H. Bell, *Lee waves in stratified flows with simple harmonic time dependence*, Journal of Fluid Mechanics, 67 (1975), pp. 705–722.

[4] P. Diamessis, S. Wunsch, I. Delwiche, and M. Richeter, *Nonlinear generation of harmonics through the interaction of an internal wave beam with a model oceanic pycnocline*, Dynamics of Atmospheres and Oceans, 66 (2014), pp. 110–137.

[5] C. Garrett and E. Kunze, *Internal Tide Generation in the Deep Ocean*, Annual Review of Fluid Mechanics, 39 (2007), pp. 57–87.

[6] R. H. Grimshaw, K. R. Helfrich, and E. R. Johnson, *Experimental study of the effect of rotation on nonlinear internal waves*, Physics of Fluids, 25 (2013).

[7] M. J. Harrison and R. W. Hallberg, *Pacific subtropical cell response to reduced equatorial dissipation*, Journal of Physical Oceanography, 38 (2008), pp. 1894–1912.

[8] K. R. Helfrich and R. H. J. Grimshaw, *Nonlinear Disintegration of the Internal Tide*, Journal of Physical Oceanography, 38 (2008), pp. 686–701.

[9] L. H. Kantha, *Tides—a modern perspective*, Marine Geodesy, 21 (1998), pp. 275–297.

[10] J. M. Klymak, S. Legg, M. H. Alford, M. Buijsman, and R. Pinkel, *The Direct Breaking of Internal Waves at Steep Topography*, 25 (2012), pp. 150–159.

[11] S. Legg, *Scattering of low-mode internal waves at finite isolated topography*, Journal of Physical Oceanography, 44 (2014), pp. 359–383.

[12] J. A. Mackinnon, M. H. Alford, O. Sun, R. Pinkel, Z. Zhao, and J. Klymak, *Parametric subharmonic instability of the internal tide at 29°N*, Journal of Physical Oceanography, 43 (2013), pp. 17–28.

[13] J. A. MacKinnon and K. B. Winters, *Subtropical catastrophe: Significant loss of low-mode tidal energy at 28.9*, Geophysical Research Letters, 32 (2005), pp. 1–5.

[14] J. A. MacKinnon, Z. Zhao, C. B. Whalen, S. M. Griffies, O. M. Sun, A. Barna, L. C. St. Laurent, M. C. Buijsman, A. V. Melet, B. K. Arbic, W. G. Large, M. Jochum, J. D. Nash, J. M. Klymak, R. Pinkel, R. Musgrave, J. K. Ansong, K. Polzin, E. P. Chassignet, A. Pickering, L. M. Merchant, H. L. Simmons, S. Diggs, B. Mater, S. R. Jayne, R. W. Hallberg, G. Danabasoglu, A. F. Waterhouse, D. S. Trossman, B. P. Briegleb, M. H. Alford, F. O. Bryan, E. Kunze, S. Legg, and N. J. Norton, *Climate*

Process Team on Internal Wave–Driven Ocean Mixing, Bulletin of the American Meteorological Society, 98 (2017), pp. 2429–2454.

[15] A. Melet, R. Hallberg, S. Legg, and K. Polzin, *Sensitivity of the ocean state to the vertical distribution of internal-tide-driven mixing*, Journal of Physical Oceanography, 43 (2013), pp. 602–615.

[16] W. H. Munk, *Abyssal recipes*, Deep-Sea Research and Oceanographic Abstracts, 13 (1966), pp. 707–730.

[17] L. Rainville and R. Pinkel, *Propagation of Low-Mode Internal Waves through the Ocean*, Journal of Physical Oceanography, 36 (2006), pp. 1220–1236.

[18] D. L. Rudnick, T. J. Boyd, R. E. Brainard, G. S. Carter, G. D. Egbert, M. C. Gregg, P. E. Holloway, J. M. Klymak, E. Kunze, C. M. Lee, M. D. Levine, D. S. Luther, J. P. Martin, M. A. Merrifield, J. N. Moum, J. D. Nash, R. Pinkel, L. Rainville, and T. B. Sanford, *From tides to mixing along the Hawaiian Ridge*, Science, 301 (2003), pp. 355–357.

[19] S. Sarkar and A. Scotti, *From Topographic Internal Gravity Waves to Turbulence*, Annual Review of Fluid Mechanics, 49 (2017), pp. 195–220.

[20] L. C. St. Laurent and C. Garrett, *The role of internal tides in mixing the deep ocean*, Journal of Physical Oceanography, 32 (2002), pp. 2882–2899.

[21] B. R. Sutherland, *Excitation of superharmonics by internal modes in non-uniformly stratified fluid*, Journal of Fluid Mechanics, 793 (2016), pp. 335–352.

[22] D. Varma and M. Mathur, *Internal wave resonant triads in finite-depth non-uniform stratifications*, Journal of Fluid Mechanics, 824 (2017), pp. 286–311.

[23] S. Wunsch, *Nonlinear harmonic generation by diurnal tides*, Dynamics of Atmospheres and Oceans, 71 (2015), pp. 91–97.

[24] ——, *Harmonic generation by nonlinear self-interaction of a single internal wave mode*, Journal of Fluid Mechanics, 828 (2017), pp. 630–647.

[25] Z. Zhao, M. H. Alford, J. B. Girton, L. Rainville, and H. L. Simmons, *Global observations of open-ocean mode-1 M2 internal tides*, Journal of Physical Oceanography, 46 (2016), pp. 1657–1684.

[26] Z. Zhao, M. H. Alford, J. A. Mackinnon, and R. Pinkel, *Long-range propagation of the semidiurnal internal tide from the Hawaiian Ridge*, Journal of Physical Oceanography, 40 (2010), pp. 713–736.

Free Convection With Large Viscosity Variation

Kelsey A. Everard

August 21, 2019

1 Introduction

Traditionally in geophysical fluid dynamics, an assumption of a constant viscosity is made at the outset of analysis. However, for many fluids, viscosity can be a strong function of temperature, potentially making this assumption as applied to some geophysical contexts invalid in the case of a flow in which temperature variation is present. For example, strong temperature dependent viscosity impacts the dynamics of mantle convection [14, 4, 16] and the ascent of diapirs [11, 7].

There exists a large body of research into the impact of a temperature dependent viscosity in cases of forced convection [9, 10, 13, 3]. However to our knowledge, there has yet to be a rigorous asymptotic treatment of the case of a temperature dependent viscosity in free convection. Furthermore, a majority of the previous investigations have considered a polynomial form of temperature dependence on viscosity [13], which is only acceptable in the case of very large temperature fluctuations relative to the background.

We extend current knowledge by considering the case of free convection under the condition of sufficiently small temperature fluctuations relative to the background isothermal state such that the temperature dependence of viscosity is exponential. We show that the exponential dependence of viscosity on temperature leads to an intriguing triple decked boundary layer structure which is not present in the case of polynomial dependence of viscosity on temperature. Consideration of the impact of large viscosity variations is particularly timely to accompany ongoing research into the shape dynamics of a dissolving solid which are being investigated using laboratory experiments of dissolving candy [8, 6, 15]. While the thermal analogue of dissolving candy is the case of a cooled wall, we begin investigations with the case of a heated wall, leaving the case of the cooled wall for future work.

We first define our problem and the assumptions that must be made for our results to be valid in Section 2. For completeness, we then consider the case of iso-viscous free convection in Section 5, the details of which can also be found in e.g., [1, 12]. We then address the case of free convection when the fluid viscosity is an exponential function of temperature in Section 6.

2 Model Formulation

Here, we consider the theoretical case of a vertical wall which is the $y-z$ plane centred at $x = 0$ where x is the horizontal wall-normal coordinate, y is the vertical wall-parallel coordinate, and z is the horizontal wall-parallel coordinate. We assume for simplicity that the dynamics are homogeneous in the z-direction, thus allowing for the simplification of the problem to 2D. Let $\mathcal{L}$ be the distance from the tip of the wall (the position of the wall that is either located at the most negative y location or at the most positive y location, depending on whether the wall is heated or cooled, respectively). The analysis herein will be applicable for $|y| > \mathcal{L}$, where $\mathcal{L}$ is defined such that $\mathcal{L} \gg \delta_{BL}$, where δ_{BL} is the thickness of the boundary layer separating the near-wall region where viscous effects are important. Since δ_{BL} is expected to continually increase in the $y-$direction, the requirement that $\mathcal{L} \gg \delta_{BL}$ can be understood as the requirement that $\frac{d\delta_{BL}}{dy} \ll 1$. Figure 1 gives a physical representation of the boundary layer structure.

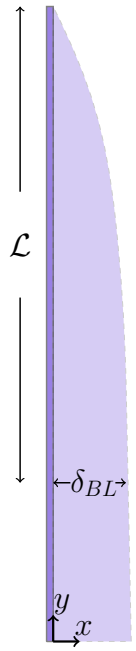

Figure 1: Diagram of boundary layer that forms when convection is forced by a cooled plate. The vertical (plate-parallel) direction is given by the y coordinate, and the horizontal (plate-normal) direction is given by the x coordinate. The case of a heated plate is the image of what is shown for the cooled plate about the x-axis. $\mathcal{L}$ is the vertical distance from the tip of the plate after which the boundary-layer approximation can be made. $\delta_{BL} = \delta_{BL}(y)$ is the boundary layer thickness.

With this assumption, we can apply the boundary-layer approximation to the governing equations. Upon the additional application of the Boussinesq approximation and an assumption of stationarity, we are left with the governing equations for the steady-state problem,

$$\frac{\partial u}{\partial x} + \frac{\partial v}{\partial y} = 0 \tag{1}$$

$$u\frac{\partial v}{\partial x} + v\frac{\partial v}{\partial y} = \alpha g \Delta T + \frac{\partial}{\partial x}\left(\nu \frac{\partial v}{\partial x}\right) \tag{2}$$

$$u\frac{\partial \Delta T}{\partial x} + v\frac{\partial \Delta T}{\partial y} = \kappa \frac{\partial^2 \Delta T}{\partial x^2} \tag{3}$$

$$u = 0,\ \ v = 0,\ \ \theta = 1 \text{ at } x = 0$$

$$u \to 0,\ \ v \to 0,\ \ \theta \to 0 \text{ as } x \to \infty$$

where u is the wall-normal (horizontal) velocity component, v is the wall-parallel (vertical) velocity component, $\Delta T = T(x, y) - T_0$ is the relative temperature difference, T_0 is the far-field (base-state) temperature, $\nu = \mu/\rho_0$ is the dynamic viscosity, ρ_0 is the density of the fluid at T_0, μ is the molecular viscosity, α is an expansion coefficient, g is the gravitational acceleration, and κ is the diffusivity of heat. It is worth noting that we have yet to make an assumption as to whether ν is a constant or not. In the following two sections we address the form of viscosity variation that we will consider, and we address the validity of the Boussinesq assumption under this specific form of viscosity variation.

These boundary conditions, particularly that for u at the wall, are the free-convection massless-transfer analogue of those used in the formative work of [2], who investigated the impact that the potential for mass transfer has on iso-viscous forced convection at a wall.

2.1 Validity of exponential form of temperature dependent viscosity

We will examine natural convection in a fluid whose viscosity is a function of temperature. We start with the Arrhenius equation for a temperature dependent viscosity,

$$\mu(T) = A\, e^{\frac{E_a}{R\,T}} \tag{4}$$

where $A = \text{Const.}$ is the exponential prefactor, E_a is an activation energy, R is an analogue to a gas constant, and T is the temperature in Kelvin. We are interested in the case of small deviations of the wall temperature, T_w, from the base-state, T_0, i.e., $|\Delta T| = |T_w - T_0| \ll T_0$. Let $T = T_0 + \Delta T$, and Taylor expand the argument of the exponential at T_0,

$$f(T) = T_0^{-1} - T_0^{-2}\Delta T + \mathcal{O}(|\Delta T|^2) \tag{5}$$

Substituting this expansion in to Equation (4),

$$\mu(T) = A\, e^{\frac{E_a}{R}\left(T_0^{-1} - T_0^{-2}\Delta T + \mathcal{O}(|\Delta T|^2)\right)} \tag{6}$$

$$\sim A\, e^{\frac{E_a}{R\,T_0}}\, e^{-\frac{E_a}{R\,T_0^2}\Delta T} \tag{7}$$

$$\mu(T) = \mu_0\, e^{-\beta \Delta T}. \tag{8}$$

Where $\mu_0 = A\, e^{\beta\, T_0}$ is the viscosity of the fluid at the far-field (base-state) temperature, T_0, and $\beta = \frac{E_a}{R T_0^2}$, E_a is the activation energy.

2.2 Validity of Boussinesq Approximation

Upon initial investigation, the Boussinesq approximation is in direct harmony with our formulation of the temperature dependent viscosity. This is evident since the Boussinesq approximation necessitates that $|\frac{\Delta\rho}{\Delta\rho_0}| \ll 1$ which under the assumption that $\frac{\Delta\rho}{\rho_0} = -\frac{\Delta T}{T_0}$ implies that $|\frac{\Delta T}{T_0}| \ll 1$, which is the condition that must be satisfied in order to use our formulation of the temperature dependent viscosity.

However, appropriate application of the Boussinesq approximation in the case of a temperature dependent viscosity is slightly more complicated. In the same way that density perturbations are important to gravitational acceleration, our problem set up implicitly states the importance of density perturbations on diffusion, which could have the potential to violate the requirements for the Boussinesq approximation. These density perturbations can be neglected, however, under the assumption that $\frac{d\rho}{dT} \ll \frac{d\mu}{dT}$. With this further assumption and the imposed uniform background temperature (density), we are free to define $\nu(T) = \rho_0^{-1}\mu(T)$ without further consideration.

2.3 Non-dimensionalisation and Similarity Scaling

For the problem at hand, we know that the temperature at the wall (T_w) is the driving term in the flow dynamics, thus making $\Delta T(x,y,t) = T(x,y,t) - T_0$ of leading order, at least near the wall. We accordingly non-dimensionalise ΔT as $\Delta T = \Theta\,\theta(\tau,\xi)$, where θ is the similarity form of temperature perturbation, $\Theta = T_w - T_0$, and τ and ξ are the similarity time and spatial variables to be found.

Upon the assumption that equations 1-3 fully capture the important dynamics, all terms must scale with one another for a balance to be possible. Thus, to satisfy continuity, we have,

$$\frac{u}{x} \sim \frac{v}{y}. \tag{9}$$

From equation (2), we have that,

$$\frac{u\,v}{x} \sim \frac{v^2}{y} \sim \alpha\, g\, \Theta \sim \nu_0\, \frac{v}{x^2} \tag{10}$$

which gives,

$$v \sim (\alpha\, g\, \Theta)^{\frac{1}{2}} y^{\frac{1}{2}}, \qquad u \sim (\nu_0^2\, \alpha\, g\, \Theta)^{\frac{1}{4}} y^{-\frac{1}{4}} \tag{11}$$

$$x \sim \left(\frac{\nu_0^2}{\alpha\, g\, \Theta}\right)^{\frac{1}{4}} y^{\frac{1}{4}} \tag{12}$$

with the independent similarity variable defined as,

$$\xi = \left(\frac{\alpha\, g\, \Theta}{\nu_0^2}\right)^{\frac{1}{4}} y^{-\frac{1}{4}} x. \tag{13}$$

We can implicitly satisfy continuity by considering the stream function, ψ, defined by $u = \frac{\partial \psi}{\partial y}$ and $v = -\frac{\partial \psi}{\partial x}$. It is readily observed from the scalings (11) that $\psi \sim (\nu_0^2 \, \alpha \, g \, \Theta)^{1/4} y^{3/4}$. We can define similarity versions of $u(x,y)$, $w(x,y)$, $\Delta T(x,y)$, and $\psi(x,y)$ as,

$$\psi(x,y) = (\nu_0^2 \, \alpha \, g \, \Theta)^{\frac{1}{4}} z^{\frac{3}{4}} \Psi(\tau, \xi) \tag{14}$$

$$\Delta T(x,y) = \alpha \, g \, \Theta \, \theta(\tau, \xi) \tag{15}$$

$$v(x,y) = -(\alpha \, g \, \Theta)^{\frac{1}{2}} y^{\frac{1}{2}} \Psi_\xi \tag{16}$$

$$u(x,y) = \frac{1}{4} (\nu_0^2 \, \alpha \, g \, \Theta)^{\frac{1}{4}} y^{-\frac{1}{4}} \left[3\Psi - \xi \, \Psi_\xi - 2\tau \Psi_\tau \right]. \tag{17}$$

Upon substitution of equations (14)-(17) into equations (1)-(3), we obtain the similarity form of the problem,

$$\frac{1}{2} \Psi_\xi^2 - \frac{3}{4} \Psi \, \Psi_{\xi\xi} = \theta - \left[\widehat{\nu} \Psi_{\xi\xi} \right]_\xi \tag{18}$$

$$Pr^{-1} \theta_{\xi\xi} - \frac{3}{4} \theta_\xi \Psi = 0 \tag{19}$$

$$\Psi = 0, \;\; \Psi_\xi = 0, \;\; \theta = 1 \text{ at } \xi = 0$$

$$\Psi_\xi \to 0, \;\; \theta \to 0 \text{ as } \xi \to \infty$$

where $Pr = \frac{\nu_0}{\kappa}$ is the Prandtl number.

3 Numerics

In addition to the matched asymptotic solutions, we solve the full problem numerically. However, in our numerical procedure, the boundary value problem (BVP) was reformulated as an initial value problem (IVP). This is done for two reasons, 1) to take advantage of Matlab's superior time integrating routines like `ode15s`, but more importantly, 2) because successfully implementing the problem at hand as a BVP in Matlab proved to be much more arduous than expected. Thus, numerically, we solved the following problem using a 'shooting method',

$$\frac{1}{2} \Psi_\xi^2 - \frac{3}{4} \Psi \, \Psi_{\xi\xi} = \theta - \left[\widehat{\nu} \Psi_{\xi\xi} \right]_\xi \tag{20}$$

$$\frac{\kappa}{\nu_0} \theta_{\xi\xi} - \frac{3}{4} \theta_\xi \Psi = 0 \tag{21}$$

$$\Psi = 0, \;\; \Psi_\xi = 0, \;\; \Psi_{\xi\xi} = \Psi_0'' \quad \text{at } \xi = 0$$

$$\theta = 1, \;\; \theta_\xi = \theta_0' \quad \text{at } \xi = 0$$

where Ψ_0'' and θ_0' are both unknown (shooting) parameters that are optimised such that the far-field solution sufficiently satisfies the far-field boundary conditions. While the shooting method is often a simple method for solving BVPs, this is not the case when the number of shooting parameters is greater than one. Despite this, shooting over the two parameters, Ψ_0'' and θ_0', proved to be simpler than solving the problem as a BVP.

The most difficult part was solving the case where $\varepsilon \equiv 0$ and $M = 0$ which we used as a baseboard for solving for non-zero ε and M. The initial difficulty laid in constraining the range of Ψ_0'' and θ_0' as much as possible. Luckily, Acrivos [2] briefly addressed an analogous case of free convection whereby a concentration gradient drives flow in the limit of a large Schmidt number. While Acrivos' focus was on the effects of a boundary that can move in the horizontal direction due to dissolution or solidification, the limiting case of this problem is that where the wall is stationary [2] which is analogous to our limiting case where viscosity is a constant. Acrivos [2] found that in the limit of a stationary wall and a very large Schmidt number, $\theta'(0) = 0.540$. Thus, we were able to constrain our search for θ_0'.

As a check on the use of the values given by Acrivos [2], the problem was solved for values of Ψ_0'' and θ_0' within a liberal buffer range. Fortunately, is was very clear when the values of Ψ_0'' and θ_0' were incorrect as the solution for θ would 'blow-up'. Thus, we were able to encode breaking conditions into the integration routine by defining `events`, of which ensuring that $1 + \text{tol} < \theta < -\text{tol}$ was the most important. When an `event` was triggered in the routine, integration was stopped and the time at which the `event` occurred was recorded. The values of Ψ_0'' and θ_0' that allowed for the longest time integration without an `event` being triggered were then used as the starting points for a bisective search for more precise values of Ψ_0'' and θ_0'. Figure 2 provides a visualisation of the length of time integration before an `event` was triggered and the resulting values of Ψ_0'' and θ_0' (red circle) that were used as the starting points for the bisective search.

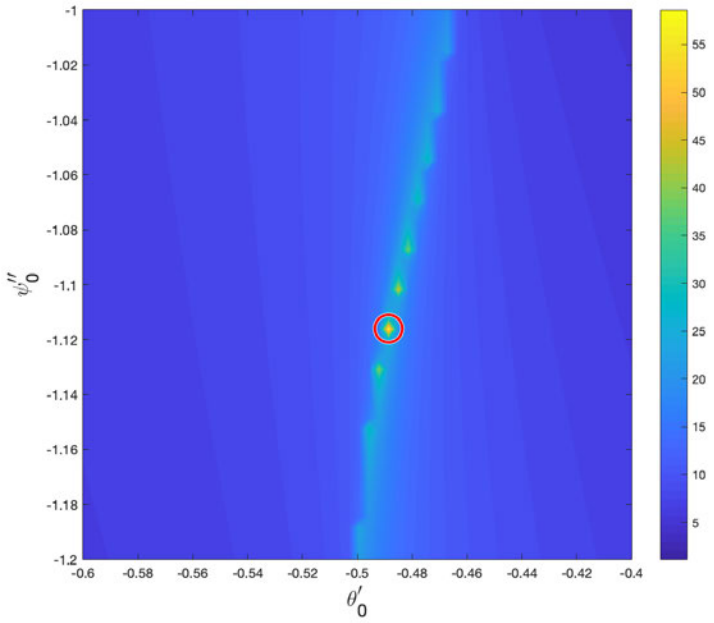

Figure 2: Contour plot of `event` trigger times during the time integration of Equations (20) and (21) for values of Ψ_0'' and θ_0'. A longer time before an event is triggered (more yellow) indicates that the Ψ_0'' and θ_0' pair is closer to the desired solution. The region circled in red was identified as the closest to the desired solution.

To identify the new values of Ψ_0'' and θ_0' for subsequent non-zero values of ε (see Section 4) and M (see Section 6), a bisective search was performed starting from the previous Ψ_0'' and θ_0' pair.

4 High Prandtl Number Limit, $Pr \gg 1$

As briefly discussed in the Introduction, all analysis herein applies in the limit as $Pr \to \infty$. Before delving in to the case of poly-viscous free convection in the large Pr limit, it is worthwhile to first consider how $Pr \to \infty$ affects the flow dynamics irrespective of the form of viscosity. Kuiken [5] was the first to our knowledge to fully solve the case of large Prandtl number free convection for the case of a constant fluid viscosity. Below, we present our own independent analysis of the problem, which was later discovered to be exactly what Kuiken [5] accomplished.

A Prandtl number greater than one ($Pr > 1$) means that the diffusivity of momentum is larger than that of heat ($\nu_0 > \kappa$). Thus, taking the limit $Pr \to \infty$ can be interpreted as considering the case where the diffusivity of momentum is so much larger than that of heat that diffusion of heat is comparably negligible (for the most part). For this reason, in the limit $Pr \to \infty$, the diffusion term in Eq. (19) is negligible compared to the advection term at least when $\xi \geq \mathcal{O}(1)$ and $\Psi \geq \mathcal{O}(1)$. We are then left with the problem,

$$\frac{1}{2}\Psi_\xi^2 - \frac{3}{4}\Psi\,\Psi_{\xi\xi} = \theta - \left[\widehat{\nu}\Psi_{\xi\xi}\right]_\xi \tag{22}$$

$$\frac{3}{4}\theta_\xi\Psi = 0 \tag{23}$$

$$\Psi = 0,\ \ \Psi_\xi = 0,\ \ \theta = 1 \text{ at } \xi = 0$$

$$\Psi_\xi \to 0,\ \ \theta \to 0 \text{ as } \xi \to \infty.$$

Equation (23) implies that either $\Psi = 0$ or $\theta_\xi = 0$, both of which satisfy the far-field boundary condition. $\Psi = 0$ obviously has issues since this would imply from Eq. (22) that $\theta = 0$ everywhere as well, which fails to satisfy the boundary condition at the wall. Additionally, $\theta_\xi = 0$ poses an issue since this implies that $\theta = \text{Const.}$, so either the boundary condition at the wall is satisfied or the far-field condition is satisfied, but not both. Regardless, it is apparent that there must be a boundary layer near $\xi = 0$ where the diffusion of heat is important since the problem dictates that the diffusion of heat is negligible only at least when $\xi \geq \mathcal{O}(1)$.

Given that there is a boundary layer near the wall, it is obvious that $\Psi = 0$ and $\theta = 0$ is incredibly problematic since any rescaling of the problem would only restate the original problem at hand in a new coordinate variable. Thus, it must be that in the 'outer' layer, $\theta_\xi = 0$, where the far-field condition on θ necessitates that $\theta_{outer} \equiv 0$. Since $\theta = 0$ in the

outer region, and the 'outer' problem is thus reduced to,

$$\begin{aligned}[\widehat{\nu}\Psi_{\xi\xi}]_\xi + \frac{1}{2}\Psi_\xi^2 - \frac{3}{4}\Psi\,\Psi_{\xi\xi} &= 0 \\ \Psi \to ?,\ \ \Psi_\xi \to ? \text{ as } \xi &\to 0 \\ \Psi \to 0 \text{ as } \xi &\to \infty.\end{aligned} \tag{24}$$

Where the boundary conditions on Ψ and Ψ_ξ at $\xi = 0$ have turned into matching conditions with the inner solution, $\Psi \to ?$ and $\Psi_\xi \to ?$, as $\xi \to 0$.

4.1 The 'Inner' Problem

We now turn to the 'inner' problem which should satisfy the boundary conditions at the wall and match with the outer solution. To begin, we consider a rescaling of the original problem with the knowledge that diffusion of heat must be leading order throughout the region and that since this region includes the boundary where the forcing $\theta = 1$ is applied, that the buoyancy term, θ in Equation (18) is of leading order as well.

Without loss of generality, let $\widehat{\nu} = 1$ (constant viscosity). Let $\varepsilon \equiv Pr^{-1} \ll 1$, $\xi = \varepsilon^a \zeta$, and $\Psi = \varepsilon^b \varphi$. Values of 'a' and 'b' must be found to obtain a leading order balance in,

$$\theta = \varepsilon^{2b-2a}\left[\frac{1}{2}\varphi_\zeta^2 - \frac{3}{4}\varphi\,\varphi_{\zeta\zeta}\right] + \varepsilon^{b-3a}\varphi_{\zeta\zeta\zeta} \tag{25}$$

$$0 = \varepsilon^{1-2a}\theta_{\zeta\zeta} - \frac{3}{4}\varepsilon^{b-a}\theta_\zeta\varphi. \tag{26}$$

From Equation (25), we find that either $b = 3a$, whereby viscous effects balance buoyancy effects, or $b = a$, whereby inertial effects balance buoyancy effects. Applying either $b = 3a$ or $b = a$ will allow for the diffusion of heat to be leading order in Eq. (26), but only the case where the diffusion of heat is balanced by advection (i.e., $b = 1 - a$) and $b = 3a$ allows for a leading order balance in both Eq. (26) and Eq. (25). Thus, $a = 1/4$ and $b = 3/4$ gives us a rescaled problem where the effects of inertia have importance in the higher-order balance, but no effect in the leading order. The 'inner' region to leading order thus satisfies,

$$\left(\widehat{\nu}\varphi''\right)' - \theta = 0 \tag{27}$$

$$\begin{aligned}\theta'' - \frac{3}{4}\,\varphi\,\theta' &= 0 \\ \theta = 1,\ \ \varphi = 0,\ \ \varphi' = 0 \text{ at } \zeta &= 0 \\ \theta \to 0,\ \ \varphi \to ? \text{ as } \zeta &\to \infty\end{aligned} \tag{28}$$

where the far-field boundary condition on the derivative of the stream function has turned into a matching condition with the outer-solution, $\varphi' \to ?$, as the inner variable, $\zeta \to \infty$. We obtain almost identical inner and outer problems as Kuiken [5], save a few differences in the signs of some terms (due to a different definition of the stream function), the leading numerical constants (due to a slight difference in definition of the similarity variables). These differences have no effect, however, on the dynamics, and will come out in the wash

when back transforming both our solutions and those presented in [5].

The purposes of the above exercise are to better understand the matching conditions between the inner thermal layer and the outer inertial layer and to lay the foundation for an in-depth consideration of the inner layer, which is the only region that should be affected by a temperature dependent viscosity. In the following section, we continue our solution to the problem of free convection in the limit $Pr \to \infty$, the purpose of which is to act as a testing ground for our numerics, and to elucidate the appropriate matching condition for the stream function, which is still at this point unknown (i.e., $\varphi \to ?$ as $\zeta \to \infty$).

5 Isoviscous Free Convection

For the iso-viscous case, we let $\widehat{\nu} \equiv 1$. It is worth recalling that isoviscous or not, the definition of the 'inner' and 'outer' regions discussed in Section 4 are unchanged. However, behaviour in the near-wall 'inner' region is affected by the form of viscosity, whereas the 'outer' region truly remains unchanged regardless of the form of viscosity. While taking $Pr \equiv \infty$ has no physical meaning, it does allow us to distill the interaction of the 'inner' and 'outer' regions and inform asymptotic matching between the two regions since the value of Pr will do little else but to shift the location of the transition from the 'inner' to the 'outer' regions.

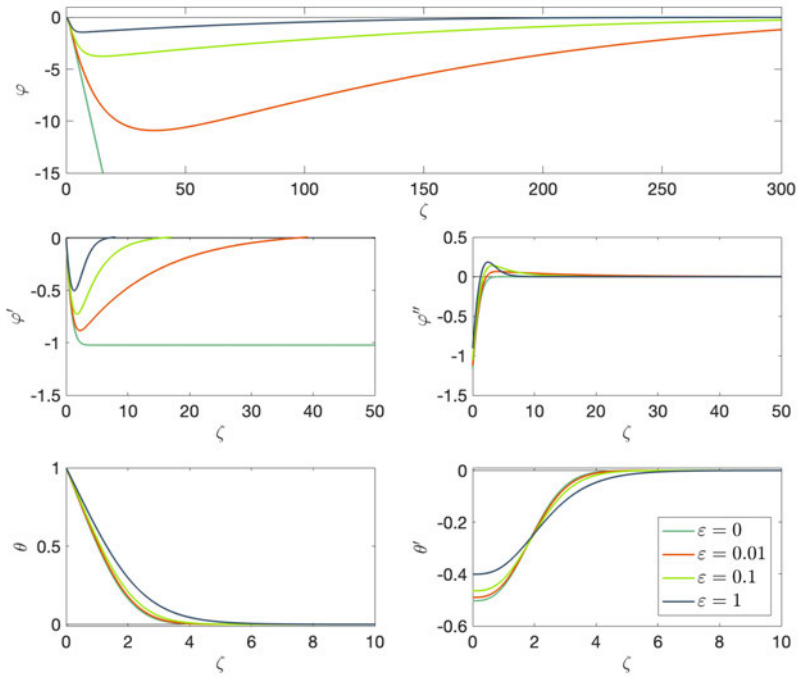

Figure 3: Numerical solution to the system of equations, (18) and (19) in terms of the 'inner' variables for (a) $\varepsilon = 0$, (b) $\varepsilon = 0.01$, (c) $\varepsilon = 0.1$, and (d) $\varepsilon = 1$, where $\varepsilon = Pr^{-1} = \kappa\,\nu_0^{-1}$.

For $\varepsilon = 0$ ($Pr \equiv \infty$), we see that the far-field boundary condition, $\varphi' \to 0$ is not satisfied (Figure 3). While at first glance, it may seem disastrous, this situation is to be expected for one main reason. Consider the Reynolds number, $Re = \frac{U\,L}{\nu}$ where U is a velocity scale and L is a length scale. The Reynolds number can be rewritten in terms of the Peclet number, Pe, which is the ratio of heat advection to heat diffusion, and the Prandtl number, Pr, as $Re = Pe\,Pr^{-1}$. In the case of natural convection, and as is the case in our problem, $Pe \sim \mathcal{O}(1)$, thus Re acts as an inverse Reynolds number. Given that $Pe \sim 1$, $Pr \equiv \infty$ implies that $Re \equiv 0$, thus an assumption that Pr is very large implies that $Re \ll 1$. However, this is only applicable in the region where there are thermal gradients to be advected and diffused. In the limit $Pr \to \infty$, momentum diffuses much slower than heat, thus the region where thermal gradients exist is much smaller than the region where momentum gradients exist, and ultimately, Pe increases outside of the thermal boundary layer, meaning that $Re \to \mathcal{O}(1)$. Thus, we see that to satisfy the condition that the far-field is stagnant, we must reintroduce inertial terms in the far-field as their absence leads to a Stokes-like paradox.

The overall consequence of this to the following analysis is that neglect of the inertial terms is only appropriate up to a certain distance from the wall, thus what we will refer to as a 'far-field' in the following sections is in reality not the 'furthest' far-field, but a far-field with respect to the region where inertia is negligible at the leading order. The order of this inertial-less region is computed in the next section, Section 5.1.

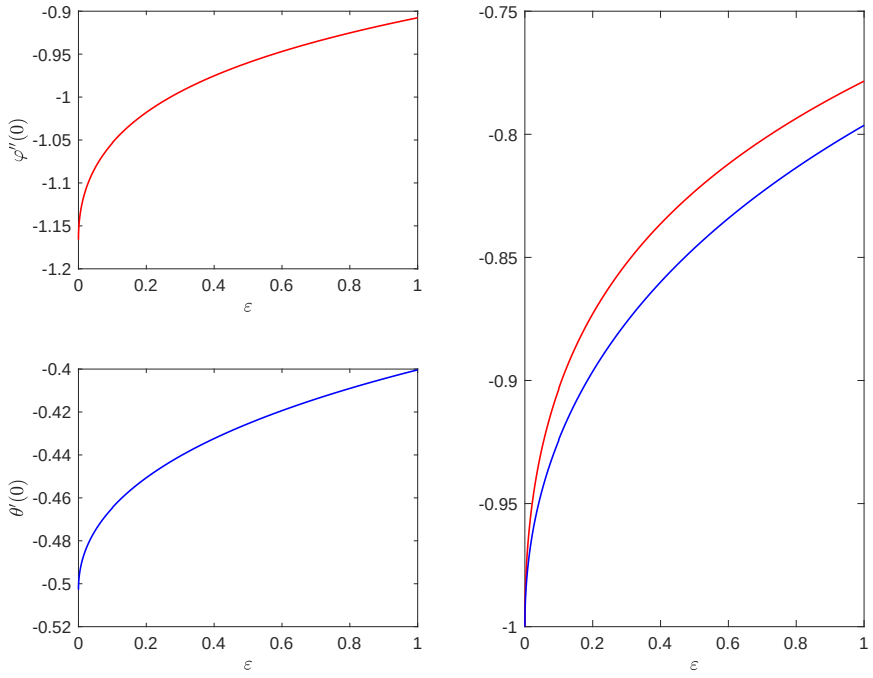

Figure 4: Change in wall stress ($\varphi''(0)$, red line) and wall heat flux ($\theta'(0)$, blue line) with increasing ε. Right-most figure portrays both $\varphi''(0)$ and $\theta'(0)$ rescaled by their respective values at $\varepsilon = 0$ to show that their change with ε is not identical.

5.1 Scale of the inertialess region

To compute the thickness of the inner, inertialess, region, we consider what happens when the buoyant forcing is no longer present. As evidenced by the numerical solution, in the 'furthest' far-field, there is no buoyancy forcing, thus, the viscous term must be balanced by inertia. We will refer to the region nearest to the wall as the inner region, and the 'furthest' far field as simply the far-field. In the far-field, we have the balance,

$$\varepsilon^{b-3a}\frac{d^3\varphi}{d\zeta^3} \sim \varepsilon^{1+2b-2a}\left[\varphi\frac{d^2\varphi}{d\zeta^2} + \left(\frac{d\varphi}{d\zeta}\right)^2\right]$$

which necessitates that $1 + a = -b$. From the numerical solution for $\varepsilon = 0$ (Figure 3), we know that $\frac{d\varphi}{d\zeta} \to$ Const. as $\zeta \to \infty$, thus in terms of the original similarity variables, ψ and ξ, we have that $\varepsilon^{a-b}\frac{d\psi}{d\xi} \sim v_\infty$, indicating that $a = b = \frac{1}{2}$. Thus, the thickness of the inner region is $\sim \mathcal{O}(Sc^{\frac{1}{2}})$, beyond which inertia becomes important to the flow dynamics.

6 Temperature-Dependent Viscosity

With a firm understanding of the behaviour of free convection in the limit of $Pr \to \infty$ regardless of the form of viscosity, we now consider what happens when viscosity is an exponential function of temperature. As stated in the introduction, herein, we will only address the case of a heated wall, saving the case of a cooled wall for future investigation.

In Sections 4 and 5, we have learned that in the inner inertialess layer, $\varphi'' \to 0$, i.e., the stream function in the inner layer should tend towards a linear function as the inner coordinate, $\zeta \to \infty$. This will allow for matching to the outer inertial layer and avoidance of a Stokes-like Paradox. Upon substitution of the exponential form of viscosity, Equation (8), into Equation (27), we obtain the inner problem that accounts for an exponential dependence of viscosity on temperature,

$$\left(e^{-M\theta}\varphi''\right)' - \theta = 0 \tag{29}$$

$$\theta'' - \frac{3}{4}\,\varphi\,\theta' = 0 \tag{30}$$

$$\theta = 1,\ \varphi = 0,\ \varphi' = 0 \text{ at } \zeta = 0$$

$$\theta \to 0,\ \varphi'' \to 0 \text{ as } \zeta \to \infty$$

where $M = \beta\,\Theta$ is the non-dimensional parameter that controls the sensitivity of viscosity to temperature perturbations. Since we consider the case of a heated wall, $M > 0$. While not relevant to the analysis provided herein, is worth noting that for the case of a cooled wall, $M < 0$ since $\Theta = T_w - T_0 < 0$.

Since M controls the sensitivity of the viscosity to temperature perturbations, for the case of a heated wall it is natural to consider the limit as $M \to \infty$. There are three ways in

which M can approach infinity, 1) the activation energy, $E_a \to \infty$, 2) the far-field temperature, $T_0 \to 0$, and 3) the wall temperature, $T_w \to \infty$. Since both 2) and 3) would imply a breakdown of the assumptions necessary for viscosity to be an exponential function of temperature, we will for the time being assume that $M \to \infty$ because $E_a \to \infty$, which is a property of the fluid, and set aside the case where $M \to \infty$ because $\Delta T \not\ll T_0$, which is not a property of the fluid, for future investigation.

The first point of business is to gain an understanding on how an exponential temperature dependence affects the dynamics of the thermal layer. For this, we numerically solve Equations (29) and (30) for increasing M from 0. We then use the numerical solutions to provide insight into how to approach the problem using matched asymptotic methods.

6.1 Case of a Heated Wall, $M > 0$

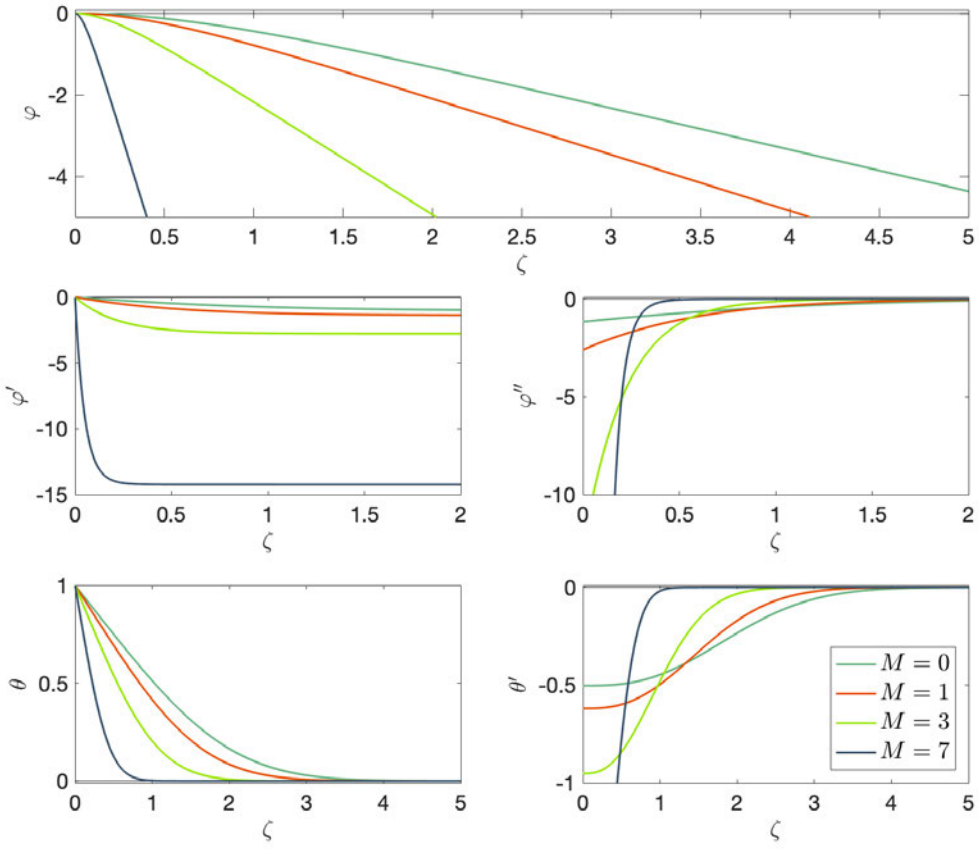

Figure 5: Numerical solution to the system of equations, (29) and (30) in terms of the 'inner' variables for $M = 0$, 1, 3, and 7. $\varepsilon \equiv \infty$.

Figure 5 provides the numerical solutions to Equations (29) and (30) for $M = 0$, 1, 3, and 7. It is apparent that with increasing sensitivity of viscosity to temperature perturbation for the case of a heated wall, the near-wall vertical velocity ($\sim -\varphi'$) increases dramatically, and

the region where the temperature decays to the far-field value decreases. Effectively, the wall-stress and the wall heat-flux increases dramatically. These results make some intuitive sense because as M increases away from zero, the viscosity of the fluid nearest to the wall decreases (see Figure 6), which means that there is less viscous drag on the fluid nearest the wall. Of course, complicating things is the fact that the fluid at the wall must be at rest, thus, as M increases, the stress at the wall increases because while the fluid must be at rest on the wall, the fluid is also compelled to motion in the region nearest the wall due to the reduced viscous resistance.

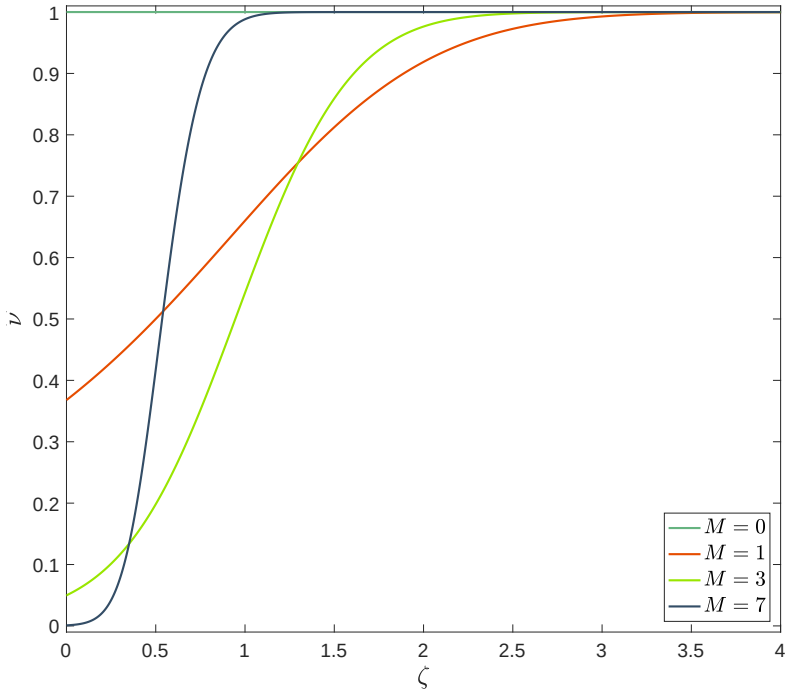

Figure 6: Viscosity, $\widehat{\nu} = \exp(-M\theta)$, with distance from the wall for $M = 0$, 1, 3, and 7.

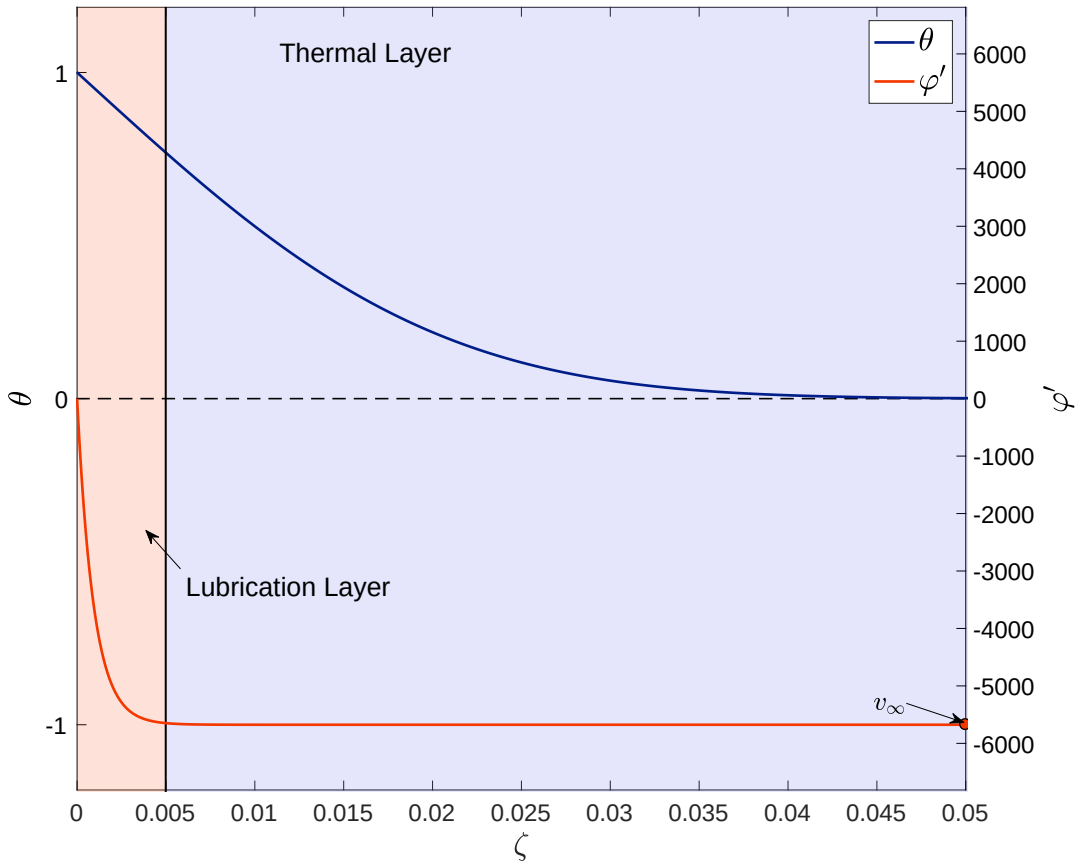

Figure 7: Derivative of the stream function, φ' (red line), and the temperature perturbation, θ (blue line), in the inner inertialess layer for $M = 20$. The lubrication layer is shaded light red and the thermal layer is shaded light blue. The x-axis is zoomed in sufficiently for the solutions within the lubrication layer to be visible.

The interplay of the zero-velocity boundary condition at the wall, and the reduced viscosity region nearest the wall leads to the development of the 'Lubrication Layer', where all of the vertical velocity shearing occurs. This reduced viscosity region exists because the temperature perturbation, $\theta \sim \mathcal{O}(1)$ (see Figure 7). Once θ decays sufficiently, the viscosity increases to the far-field value regardless of M in what we refer to as the general 'Thermal Layer' that exists for the isoviscous case.

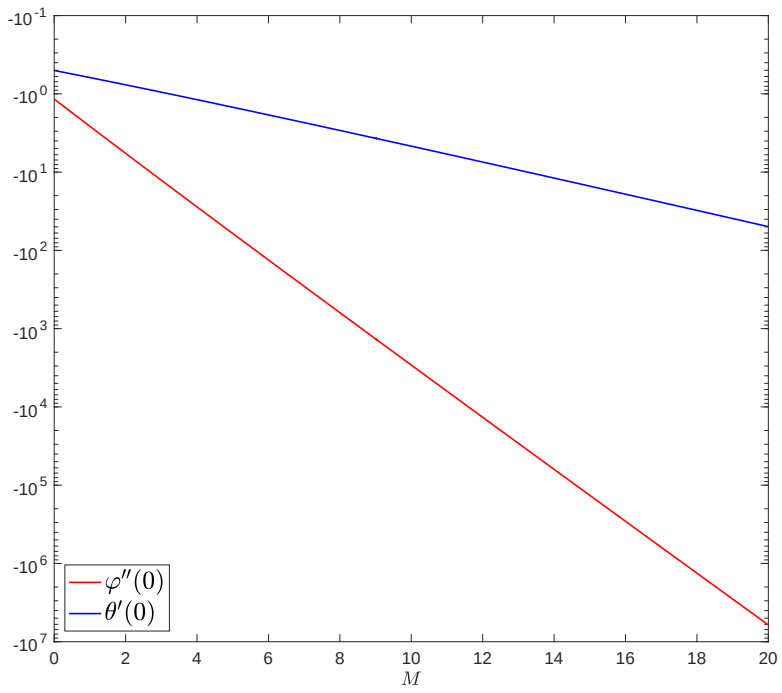

Figure 8: Dependence of the wall heat flux, $\theta'(0)$, and the wall stress, $\varphi''(0)$ on the strength of the temperature dependence of viscosity M. $y-$axis scale is logarithmic.

6.2 Asymptotic Anaylsis

Now that we have solved the problem numerically, we begin an analytical treatment to uncover the underlying scaling relationships dictating of the $M \to \infty$ limit. We begin by restating the problem,

$$\left(e^{-M\theta}\varphi''\right)' - \theta = 0 \tag{31}$$

$$\theta'' - \frac{3}{4}\,\varphi\,\theta' = 0 \tag{32}$$

$$\theta = 1,\ \varphi = 0,\ \varphi' = 0 \text{ at } \zeta = 0$$

$$\theta \to 0,\ \varphi'' \to 0 \text{ as } \zeta \to \infty$$

for which we now know there are two distinct regions, the Lubrication layer, and the Thermal layer.

6.2.1 Lubrication Layer

From the numerical solution, we know that the solution's behaviour is distinctly different between the near-wall region and the 'outer' boundary layer. We use this knowledge to our advantage, and first consider the dynamics near the wall, i.e., let $\zeta = \delta\,\chi$, $\varphi = \gamma\,\eta$, and

$\theta = 1 - \epsilon\,\phi$, where $\epsilon \ll 1$, and where δ is explicitly taken as the depth of the inner wall region.

$$\frac{e^{-M}\gamma}{\delta^3}\left(e^{M\,\epsilon\,\phi}\eta''\right)' - 1 = 0 \tag{33}$$

$$\phi'' - \frac{3}{4}\,\gamma\,\delta\,\eta\,\phi = 0 \tag{34}$$

Where we have recognised that $\epsilon\phi \ll 1$, and thus is certainly negligible to leading order in (33). Since $1 \neq 0$, we must impose that $\frac{e^{-M}\gamma}{\delta^3} \sim \mathcal{O}(1)$. Suppose also that $\gamma\,\delta \ll 1$. To leading order near the wall, we have that,

$$\left(e^{M\,\epsilon\,\phi}\eta''\right)' - 1 = 0 \tag{35}$$

$$\phi'' = 0 \tag{36}$$

$$\phi = 0,\ \eta = 0,\ \eta' = 0 \ \text{ at } \chi = 0 \tag{37}$$

$$\phi \sim 1,\ \eta'' \sim 0 \ \text{ for } \chi \gg 1 \tag{38}$$

Immediately, it is seen that $\phi = a\chi + b$, where $b = 0$ satisfies the boundary condition for $\chi = 0$, and $\phi' = a$ at the wall (in terms of the inner-inner variables). Upon substitution of this into (35), we obtain,

$$\left(e^{M\,\epsilon\,a\,\chi}\eta''\right)' - 1 = 0 \tag{39}$$

$$\int \eta'\,\mathrm{d}\eta = \int (C_0 + \chi)\,e^{-M\,a\,\epsilon\chi}\,\mathrm{d}\chi \tag{40}$$

$$\eta' = -(M\,a\,\epsilon)^{-2}\,(M\,a\,\epsilon\,C_0 + M\,a\,\epsilon\,\chi + 1)\,e^{-M\,a\,\epsilon\chi} + C_1 \tag{41}$$

Applying the boundary condition at the wall, $\eta' = 0$,

$$0 = -(M\,a\,\epsilon)^{-2}\,(M\,a\,\epsilon\,C_0 + 1) + C_1$$

$$C_1 = \frac{M\,a\,\epsilon\,C_0 + 1}{(M\,a\,\epsilon)^2}$$

Applying the far-field matching condition that $\frac{d\eta}{d\chi} \sim \frac{\epsilon}{\gamma}v_\infty$ as $\chi \to \infty$,

$$C_1 = \frac{\epsilon}{\gamma}v_\infty$$

Now, integrating Equation (41),

$$\eta = \frac{(M\,a\,\epsilon\,C_0 + M\,a\,\epsilon\,\chi + 2)\,e^{-M\,a\,\epsilon\chi}}{(M\,a\,\epsilon)^3} + C_1\chi + C_2 \tag{42}$$

Applying the boundary condition that $\eta = 0$ at $\chi = 0$,

$$0 = \frac{(M\,a\,\epsilon\,C_0 + 2)}{(M\,a\,\epsilon)^3} + C_2$$

$$C_2 = -\frac{(M\,a\,\epsilon\,C_0 + 2)}{(M\,a\,\epsilon)^3} = -\frac{C_1 + 1}{M\,a\,\epsilon}$$

Applying the far-field matching condition that $\eta \sim \frac{\epsilon}{\gamma} v_\infty \chi + \frac{\varphi_0}{\gamma}$ as $\chi \to \infty$,

$$\underbrace{\frac{\epsilon}{\gamma} v_\infty}_{C_1} \chi + \frac{\varphi_0}{\gamma} = C_1 \chi + C_2$$

$$C_2 = \frac{\varphi_0}{\gamma}$$

We then have the following equations from boundary and matching conditions,

$$C_1 = \frac{M\,a\,\epsilon\,C_0 + 1}{(M\,a\,\epsilon)^2} = \frac{\epsilon}{\gamma} v_\infty \tag{43}$$

$$C_2 = -\frac{(M\,a\,\epsilon\,C_0 + 2)}{(M\,a\,\epsilon)^3} = \frac{\varphi_0}{\gamma} \tag{44}$$

We can obtain an expression for C_0 from both Equations (43) and (44).

$$C_0 = \frac{\epsilon\, v_\infty\, M\, a\, \epsilon}{\gamma} - \frac{1}{M\,a\,\epsilon} \tag{45}$$

$$C_0 = -\frac{\varphi_0\,(M\,a\,\epsilon)^2}{\gamma} - \frac{2}{M\,a\,\epsilon} \tag{46}$$

Upon equating Equations (45) and (46), we obtain an expression for v_∞ in terms of the two unknowns, a and φ_0.

$$v_\infty = -\varphi_0\, M\, a - \frac{\gamma}{(M\,a)^2\,\epsilon^3} \tag{47}$$

6.2.2 Thermal Layer

From numerical solutions, we know that in the thermal layer, $\varphi' \sim \mathit{Constant}$. Since we want to consider the solution valid strictly in the thermal layer, we will let $\varphi' = \varphi_0$, from which it follows that $\varphi(\zeta) = v_\infty\,\zeta + \varphi_0$, and $\varphi'' = 0$, leaving us with the problem in the thermal layer,

$$\theta'' - \frac{3}{4}\,(v_\infty\,\zeta + \varphi_0)\,\theta' = 0 \tag{48}$$

$$\theta \to 0,\ \varphi'' \to 0 \text{ as } \zeta \to \infty$$

With the matching condition that $\theta \to 1 - \frac{\epsilon\, a}{\delta}\zeta$ as $\zeta \to 0$. Upon integrating once, we have,

$$\theta' = A_0 \exp\left(g\,\zeta - f\,\zeta^2\right) \tag{49}$$

where $f = -\frac{3}{8}\,v_\infty$ and $g = \frac{3}{4}\,\varphi_0$. Upon applying the matching condition that $\theta' \to -\frac{\epsilon, a}{\delta}$ as$\zeta \to 0$, we find that,

$$A = -\frac{\epsilon\, a}{\delta}$$

giving,

$$\theta' = -\frac{\epsilon\, a}{\delta} \exp\left(g\,\zeta - f\,\zeta^2\right) \tag{50}$$

Integrating once again,

$$\theta = -\frac{\epsilon\, a\sqrt{\pi}}{2\delta\sqrt{f}} \exp\left(\frac{g^2}{4f}\right) \operatorname{erf}\left(\frac{2f\zeta - g}{2\sqrt{f}}\right) + B \tag{51}$$

Applying the far-field condition that $\theta \to 0$ as $\zeta \to \infty$,

$$B = \frac{\epsilon\, a\sqrt{\pi}}{2\delta\sqrt{f}} \exp\left(\frac{g^2}{4f}\right)$$

Thus,

$$\theta = \frac{\epsilon\, a\sqrt{\pi}}{2\delta\sqrt{f}} \exp\left(\frac{g^2}{4f}\right)\left[1 - \operatorname{erf}\left(\frac{2f\zeta - g}{2\sqrt{f}}\right)\right] \tag{52}$$

Now, we want to ensure matching as $\zeta \to 0$. We expect that as $\zeta \to 0$, θ takes on the lubrication layer solution, thus we expect that as $\zeta \to 0$, $\theta \sim 1 - \frac{\epsilon\, a}{\delta}\zeta$. We can start by taking the limit of Equation (52) as $\zeta \to 0$.

$$\lim_{\zeta\to 0} \theta = 1 - \frac{\epsilon\, a}{\delta}\zeta = \lim_{\zeta\to 0} \frac{\epsilon\, a\sqrt{\pi}}{2\delta\sqrt{f}} \exp\left(\frac{g^2}{4f}\right)\left[1 - \operatorname{erf}\left(\frac{2f\zeta - g}{2\sqrt{f}}\right)\right]$$

In the limit as $\zeta \to 0$, we can Taylor expand the error function around $\zeta = 0$,

$$1 - \frac{\epsilon\, a}{\delta}\zeta = \frac{\epsilon\, a\sqrt{\pi}}{2\delta\sqrt{f}} \exp\left(\frac{g^2}{4f}\right)\left[1 - \left(-\operatorname{erf}\left(\frac{g}{2\sqrt{f}}\right) + \left(\frac{2\exp\left(-\frac{g^2}{4f}\right)}{\sqrt{\pi}}\right)\sqrt{f}\,\zeta\right)\right]$$

$$1 - \frac{\epsilon\, a}{\delta}\zeta = \frac{\epsilon\, a\sqrt{\pi}}{2\delta\sqrt{f}} \exp\left(\frac{g^2}{4f}\right)\left[1 + \operatorname{erf}\left(\frac{g}{2\sqrt{f}}\right)\right] - \frac{\epsilon\, a}{\delta}\zeta$$

As expected, since we've already matched the thermal gradients between the lubrication and thermal layers, we end up with a final matching condition on the integration constant, namely,

$$1 = \frac{\epsilon\, a\sqrt{\pi}}{2\delta\sqrt{f}} \exp\left(\frac{g^2}{4f}\right)\left[1 + \operatorname{erf}\left(\frac{g}{2\sqrt{f}}\right)\right]. \tag{53}$$

Thus, all of the information from which we can obtain the scaling laws is summarised as,

$$1 = \frac{\epsilon\, a\sqrt{8\pi}}{2\delta\sqrt{-3v_\infty}} \exp\left(-\frac{3\,\varphi_0^2}{8\,v_\infty}\right)\left[1 + \operatorname{erf}\left(\sqrt{-\frac{3\,\varphi_0^2}{8v_\infty}}\right)\right] \tag{54}$$

$$v_\infty = -\varphi_0\, M\, a - \frac{\gamma}{(M\, a)^2\, \epsilon^3} \tag{55}$$

With information from scaling arguments,

$$\frac{\gamma}{\delta^3 e^M} \sim 1 \tag{56}$$

and an educated guess,

$$\epsilon \sim M^{-1} \tag{57}$$

The issue remains that we are left with two equations and three unknowns. We are currently working on detangling this to get a rigorous asymptotic prediction of the scaling laws. For the time being, we estimate the scaling laws from our existing numerical solutions in the following section.

6.3 Estimation of Scaling Laws

While we currently are still working on deriving the scaling laws, it is possible to make predictions on the scaling laws using the numerical solutions that we have obtained and presented herein. Of particular interest is the relationship between the asymptotic parameter, M, and the Nusselt number, $Nu = hL/k$, which is the ratio of the convective to conductive heat transfer at a boundary, where h is a heat transfer coefficient (related to the heat flux at the boundary), L is a characteristic length scale, and k is the thermal conductivity. In the absence of motion, heat transfer is purely conductive and $Nu = 1$. Thus, the Nusselt number can be regarded as a measure of how much more efficient fluid motion (i.e., convection) makes the transfer of heat at a boundary. Since it should not only be expected that a temperature dependent viscosity would affect the fluid velocity, but has been shown that this is indeed the case (Figure 5), it is only natural that we ask further how a temperature dependent viscosity may affect the efficiency of heat transfer. Because thermal conductivity of a fluid is unaffected by the temperature of the fluid, and because L should also not be temperature dependent, only the heat transfer coefficient, h, is affected by M. Further, the changes to h are due to the changes in the heat flux at the wall. Thus, Nu should have the same scaling relationship with M as the heat flux at the surface, $\theta'(0)$.

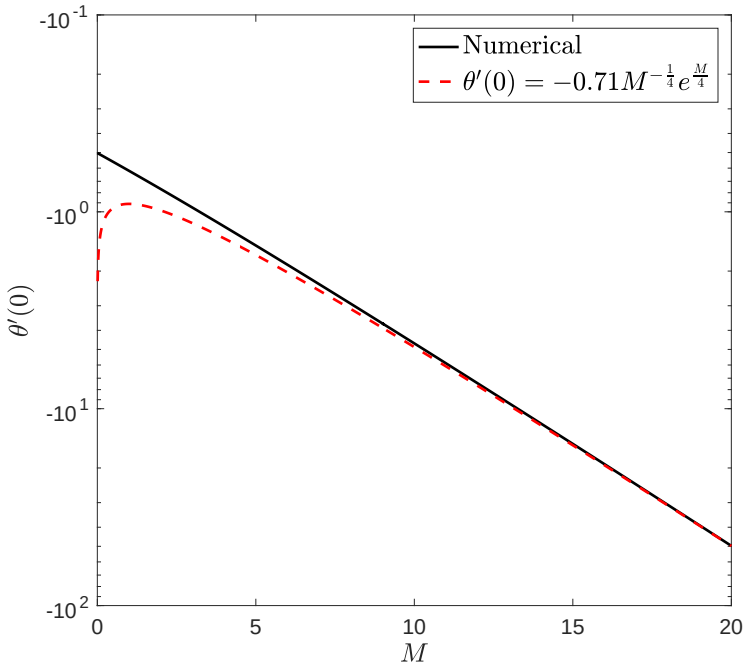

Figure 9: Wall heat flux, $\theta'(0)$, as a function of M. Numerical solution, as presented in Figure 8, is given as a solid black line. The estimated scaling relationship based upon the numerical solution is given as the dashed red line.

Via a more or less guess-and-check method, we have estimated that,

$$\theta'(0) \sim M^{-\frac{1}{4}}\, e^{\frac{M}{4}} \tag{58}$$

with an asymptotic pre-factor of -0.71. As should be expected, since we consider the limit as $M \to \infty$, the scaling relationship is slightly wonky around $M = 0$, but improves at larger values of M (Figure 9).

Another relationship of interest is that of the wall-stress, $\frac{\partial w}{\partial x}$, with M. In terms of our similarity system, $\frac{\partial w}{\partial x} \sim \varphi''$, thus the scaling relationship of the derivative of the stream function at the wall should be the same as the wall stress.

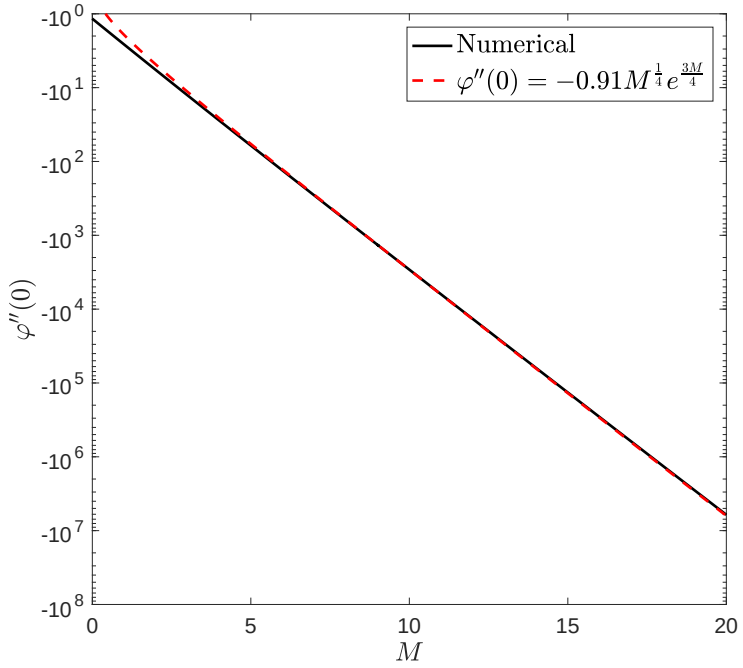

Figure 10: Wall stress, $\varphi''(0)$, as a function of M. Numerical solution, as presented in Figure 8, is given as a solid black line. The estimated scaling relationship based upon the numerical solution is given as the dashed red line.

Again, via a more or less guess-and-check method, we have estimated that the scaling relationship is,

$$\varphi''(0) \sim M^{\frac{1}{4}}\, e^{\frac{3\,M}{4}} \tag{59}$$

with an asymptotic pre-factor of -0.91. As was the case for the scaling relationship for the wall heat flux, we consider the limit as $M \to \infty$, thus the scaling relationship is expected to apply more accurately as M increases.

7 Conclusions

While an assumption of a constant viscosity may be appropriate in certain situations, in the cases where the fluid viscosity is a strong function of temperature, such an assumption can prove disastrous. Herein, we have presented the initial stages in our development of a full regime diagram for free convection with an exponential viscosity dependence on temperature. While we have yet to complete the asymptotic treatment of the problem, the scaling relationships that we have found using our numerical solutions are expected to be those that fall out in the final matching steps in our asymptotic analysis. Thus, we have found the universal scaling relationships that describe the dynamics of free convection with an exponentially temperature dependent viscosity for the case of a heated wall in the limit of high Prandtl number. This work lays the foundation for our future investigation into the case of a cooled wall, and eventual completion of the full $Pr - M$ regime diagram.

8 Acknowledgements

I am incredibly grateful to my amazing project supervisors, Sam Pegler and Megan Davies Wykes. An enormity of thanks is also owed to the program directors, Claudia Cenedese, Karl Helfrich, and Bruce Sutherland, and to Julie Hildebrandt and Janet Fields, all of whom worked tirelessly to ensure that the program was as wonderful as it was. Thanks to the principal lecturers who were far too generous with their patience, Colm-cille Caulfield and Stephanie Waterman. Finally, the summer would not have been the same were it not for the support of the GFD staff, the support and friendship of the fellows, and the unparalleled softball coaching of Charlie Doering.

References

[1] A. Acrivos, *A theoretical analysis of laminar natural convection heat transfer to non-newtonian fluids*, AIChE Journal, 6 (1960), pp. 584–590.

[2] ——, *The asymptotic form of the laminar boundary-layer mass-transfer rate for large interfacial velocities*, Journal of Fluid Mechanics, 12 (1962), pp. 337–357.

[3] M. E. Ali, *The effect of variable viscosity on mixed convection heat transfer along a vertical moving surface*, International Journal of Thermal Sciences, 45 (2006), pp. 60–69.

[4] A. Davaille and C. Jaupart, *Onset of thermal convection in fluids with temperature-dependent viscosity: Application to the oceanic mantle*, Journal of Geophysical Research: Solid Earth, 99 (1994), pp. 19853–19866.

[5] H. Kuiken, *An asymptotic solution for large prandtl number free convection*, Journal of Engineering Mathematics, 2 (1968), pp. 355–371.

[6] J. Mac Huang, M. N. J. Moore, and L. Ristroph, *Shape dynamics and scaling laws for a body dissolving in fluid flow*, Journal of Fluid Mechanics, 765 (2015).

[7] K. I. Mahon, T. M. Harrison, and D. A. Drew, *Ascent of a granitoid diapir in a temperature varying medium*, Journal of Geophysical Research: Solid Earth, 93 (1988), pp. 1174–1188.

[8] E. Nakouzi, R. E. Goldstein, and O. Steinbock, *Do dissolving objects converge to a universal shape?*, Langmuir, 31 (2014), pp. 4145–4150.

[9] H. Ockendon and J. Ockendon, *Variable-viscosity flows in heated and cooled channels*, Journal of Fluid Mechanics, 83 (1977), pp. 177–190.

[10] I. Pop, R. S. R. Gorla, and M. Rashidi, *The effect of variable viscosity on flow and heat transfer to a continuous moving flat plate*, International journal of engineering science, 30 (1992), pp. 1–6.

[11] N. M. Ribe, *Diapirism in the earth's mantle: Experiments on the motion of a hot sphere in a fluid with temperature-dependent viscosity*, Journal of Volcanology and Geothermal Research, 16 (1983), pp. 221–245.

[12] H. Schlichting and K. Gersten, *Boundary-layer theory*, Springer, 2016.

[13] V. Soundalgekar, H. S. Takhar, U. Das, R. K. Deka, and A. Sarmah, *Effect of variable viscosity on boundary layer flow along a continuously moving plate with variable surface temperature*, Heat and Mass transfer, 40 (2004), pp. 421–424.

[14] P. J. Tackley, *Effects of strongly temperature-dependent viscosity on time-dependent, three-dimensional models of mantle convection*, Geophysical Research Letters, 20 (1993), pp. 2187–2190.

[15] M. S. D. Wykes, J. Mac Huang, G. A. Hajjar, and L. Ristroph, *Self-sculpting of a dissolvable body due to gravitational convection*, Physical Review Fluids, 3 (2018), p. 043801.

[16] S. Zhong, M. T. Zuber, L. Moresi, and M. Gurnis, *Role of temperature-dependent viscosity and surface plates in spherical shell models of mantle convection*, Journal of Geophysical Research: Solid Earth, 105 (2000), pp. 11063–11082.

Maximal Heat Transport in Rayleigh–Bénard Convection: Reduced Models, Bifurcations, and Polynomial Optimization

Anuj Kumar

August 21, 2019

Abstract

A study on Rayleigh–Bénard convection by [12] has shown that at high Rayleigh number heat transfer due to steady convection rolls, maximized over horizontal wavenumber, is comparable to heat transfer in the turbulent flow. Although these convection rolls are unstable at high Rayleigh number, they continue to be the solution of the Boussinesq equations. Inspired by this study, we ask the quesiton, do steady states maximize heat transfer? Answering such questions is hard for the governing equations (PDEs), as obtaining exact bounds for PDEs is beyond current capabilities. However, for truncated models (ODEs) of the governing equations, using polynomial optimization, we can obtain sharp bounds on heat transfer. In this report, we study truncated models of two-dimensional Rayleigh–Bénard convection in a box with stress-free boundaries. Specifically, we study two models – an 8-mode model which is energy conserving in the dissipationless limit – also a 15-mode model which along with the energy conservation property satisfies a vorticity integral identity. In the 8-mode model, for the chosen values of parameters (Prandtl number, and the aspect ratio of the box), we show that steady states maximize the heat transfer except for a small range of Rayleigh number.

1 Introduction

Convection in a horizontal layer of fluid heated from below is known as the Rayleigh–Bénard convection. In this convection, viscosity and thermal diffusivity are the stabilizing elements, whereas the buoyancy is the destabilizing element. For small temperature difference across the layer, viscous forces dominate and the system remains in pure conduction state. When the temperature difference across the layer exceeds a threshold, the buoyancy force takes over, and the system becomes thermally unstable to convective rolls. Figure (1) shows a rough sketch of Rayleigh–Bénard convection after the first bifurcation. With further increase in temperature, in a sequence of bifurcations, the structure of the flow gradually becomes complex and eventually turbulent. Bénard was the first one to conduct quantitative experiments of this type of convection. Inspired by Bénard's experiments, Rayleigh studied ([9]) the stability of conduction state analytically to find out when thermal instability first occurs. He found out that the instability occurs when a non-dimensional quantity, now known as the Rayleigh number, exceeds a critical value. Physically speaking, the Rayleigh number represents the ratio of the destabilizing effect of buoyancy to the stabilizing effect

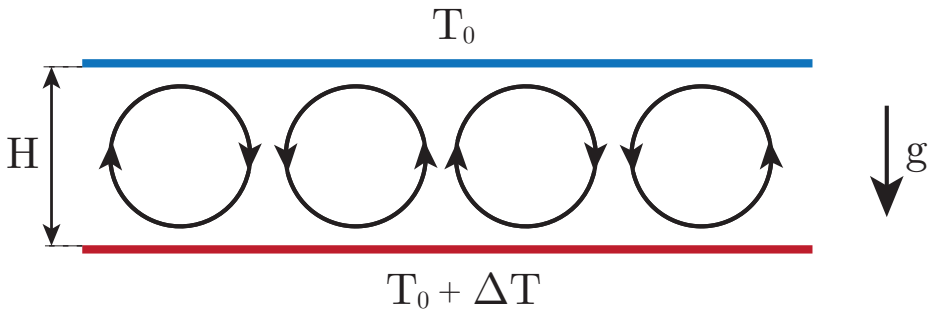

Figure 1: A typical flow structure in the Rayleigh–Bénard convection after the first bifurcation.

of viscous and thermal diffusion. Rayleigh number and Prandtl number (ratio of viscous and thermal diffusivities) are the two non-dimensional numbers that govern the convection.

In Rayleigh–Bénard convection, one important question that one wishes to understand is the variation of heat transfer as a function of Rayleigh and Prandtl number. Specifically, one assumes the power-law dependence of Nusselt number (non-dimensional heat transfer) on Rayleigh and Prandtl number, i.e. $Nu = CPr^{\alpha}Ra^{\beta}$ and interested in knowing the exponents (α, β). There are two popular theories of heat transfer which tries to answer this question. One of these theories is due to Priestly ([8]), Malkus ([6]), and Howard ([3]), which suggests a one-third dependence of the heat transfer on Rayleigh number ($Nu \sim Ra^{1/3}$), also known as the classical limit. Priestly's argument for this dependence goes as follows. Rayleigh number going to infinity can be thought of height of the fluid layer going to infinity. Based on which he argues that the effect of one boundary on the other boundary must vanish. The dimensional heat transfer, therefore, should become independent of the layer height, which then leads to the desired scaling. The other one is due to Spiegel([10]) and Kraichnan ([4]) which suggest a one-half dependence of the heat transfer on the Rayleigh number ($Nu \sim Ra^{1/2}$), also known as the ultimate limit. To justify this limit, one can think of Rayleigh number going to infinity as viscosity and thermal diffusivity going to zero. One can then argue that a blob of fluid can rise or fall freely without losing any heat, which then leads to one-half scaling.

There are several experimental studies to verify the above two theories for the convection between no-slip boundaries. Unfortunately, there is no consensus among these experimental studies at very high Rayleigh number. However, at moderately high Rayleigh number ($Ra \approx 10^9$), experiments are consistent with $Nu \sim Ra^{0.31}$. In a study on Rayleigh–Bénard convection between no-slip boundaries, [12] explored the fate of primary convection rolls at large Rayleigh number. It should be noted that the primary convection rolls become unstable beyond a critical Rayleigh number; however, these rolls continue to be the solution of the Boussinesq's equations. Figure (2) shows a typical structure of primary rolls at $Ra = 5{\times}10^6$. They found that heat transfer due to these primary rolls, when maximized over the aspect ratio, shows a similar type of scaling as the turbulent flow. This an interesting result since one can now ask whether studying the heat transfer due to primary rolls is sufficient to say something about the heat transfer in the turbulent flow. Our study is, in fact, inspired by this result. We ask the following question: Do steady states maximize heat

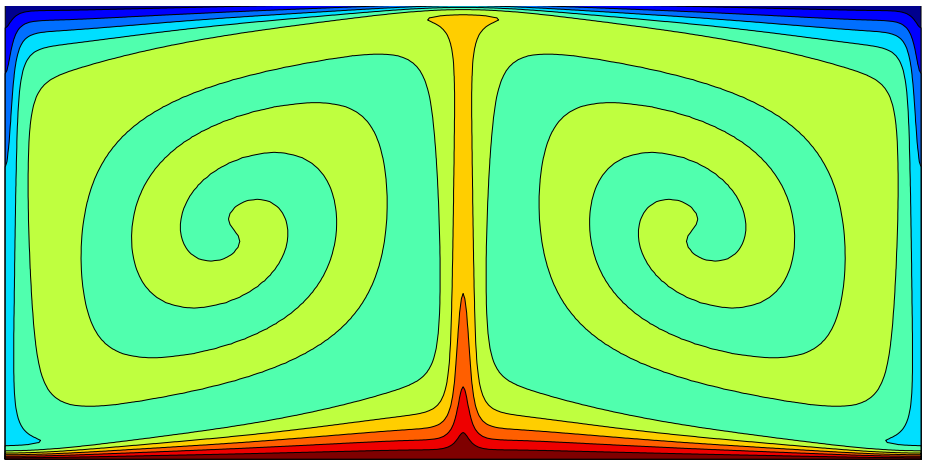

Figure 2: Temperature contours of primary solution at $Ra = 5 \times 10^6$ (Waleffe et al. 2015)

transfer in Rayleigh–Bénard convection?

Answering such questions is hard for PDEs because obtaining exact bounds on quantities for PDEs is beyond current capabilities. However, using polynomial optimization, we answer this question for the truncated models of the governing equations (ODEs). Specifically, we study the truncated models of Rayleigh–Bénard convection in a box with stress-free boundaries. Truncations using trigonometric functions for convection in a stress-free box are asymptotically accurate near the primary bifurcation. This is not the case for a no-slip box where truncations involve rather complicated functions. Our choice of convection in a stress-free box is therefore governed by the fact that trigonometric functions are more straightforward to handle.

While considering the truncations, it is good to retain some of the properties of original equations. Rayleigh–Bénard convection in a stress-free box has the energy-conserving property in the dissipationless limit. Also, the system satisfies a vorticity integral identity. In this report, we study two truncated models: 8-mode model and 15-mode model. The 8-mode model has only energy conserving property, while the 15-mode model satisfies the vorticity integral identity as well.

The rest of the report is arranged as follows. In section (2) we formulate the problem and discuss the linear stability analysis of the conduction state. In section (3) we discuss a general framework to find bounds on long-time average of a scalar quantity. In section (4), we illustrate method discussed in section (3) using a the example of Lorenz system. In section (5), we apply the method to find bounds on the Nusselt number for the 8-mode model. In section (6), we apply the method to find bounds on the Nusselt number for the 15-mode model. In section (7), we conclude and discuss the future work.

2 Problem Formulation

We consider the problem of two-dimensional vertical transport of heat in a horizontally placed box. We assume that the height of the box is H and the length of the box is L. The aspect ratio of the box (L/H) is Γ. The problem can be best described in the Cartesian

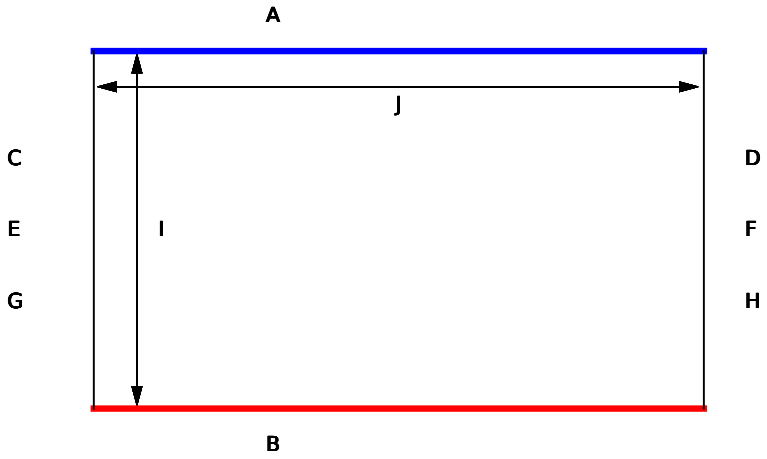

Figure 3: Problem schematic

coordinate system $\mathbf{x}' = (x', y')$. We place the origin of our coordinate system at the left-bottom corner of the box with x' is pointing to right and y' pointing upward. The governing equations of the fluid motion are the Boussinesq equations.

$$\begin{aligned}
&\nabla \cdot \mathbf{u}' = 0, \\
&\frac{\partial \mathbf{u}'}{\partial t'} + \mathbf{u}' \cdot \nabla \mathbf{u}' = -\frac{\nabla p'}{\rho} + \nu \nabla^2 \mathbf{u}' + g T' \mathbf{e}_{y'}, \\
&\frac{\partial T'}{\partial t'} + \mathbf{u}' \cdot \nabla T' = \kappa_T \nabla^2 T'.
\end{aligned} \tag{1}$$

The first equation is the continuity equation. The second equation is the momentum equation which includes the buoyancy forcing due to the variation in temperature. The last equation is the convection-diffusion equation of the temperature field. Here, $\mathbf{u}' = (u'_x, u'_y)$, p', and T' are the velocity field, pressure, and temperature, respectively. Whereas, ρ, ν, and κ_T are mean density, kinematic viscosity, and thermal diffusivity, respectively. g denotes the acceleration due to gravity and $\mathbf{e}_{y'}$ denotes the unit vector in the y'-direction. For simplicity, we consider the boundaries of the box to be stress-free with fixed temperature conditions on the top and the bottom walls and zero-flux condition on the sidewalls.

$$\begin{aligned}
&\frac{\partial u'_x}{\partial y'} = 0,\ u'_y = 0,\ T' = T_B \qquad \text{if} \quad y' = 0,\ 0 \le x' \le L, \\
&\frac{\partial u'_x}{\partial y'} = 0,\ u'_y = 0,\ T' = T_T \qquad \text{if} \quad y' = H,\ 0 \le x' \le L, \\
&\frac{\partial u'_y}{\partial x'} = 0,\ u'_x = 0,\ \frac{\partial T'}{\partial x'} = 0 \qquad \text{if} \quad x' = 0,\ 0 \le y' \le H, \\
&\frac{\partial u'_y}{\partial x'} = 0,\ u'_x = 0,\ \frac{\partial T'}{\partial x'} = 0 \qquad \text{if} \quad x' = L,\ 0 \le y' \le H.
\end{aligned} \tag{2}$$

Here, T_B and T_T are the temperature of the top and the bottom walls with $T_B > T_T$. At this point, we non-dimensionalize our system. We define non-dimensional variables as follows:

$$\mathbf{x} = \frac{\mathbf{x}'}{H/\pi},\ t = \frac{t'}{\kappa_T/(H/\pi)^2},\ \mathbf{u} = \frac{\mathbf{u}'}{\kappa_T/(H/\pi)},$$
$$p = \frac{p'}{\rho\left(\frac{\kappa_T \pi}{H}\right)^2} + \frac{g(T_B - T_T)H^3}{\kappa_T^2 \pi^3} y,\ T = \left(\frac{T' - T_B}{T_B - T_T}\right)\pi + \pi. \tag{3}$$

Notice, a factor of π is involved here as compare to the usual non-dimensionalization. This is done to make truncated models simple. The governing equations in the non-dimensional form are given by,

$$\begin{aligned}
&\nabla \cdot \mathbf{u} = 0,\\
&\frac{\partial \mathbf{u}}{\partial t} + \mathbf{u} \cdot \nabla \mathbf{u} = -\nabla p + Pr \nabla^2 \mathbf{u} + PrRaT\mathbf{e}_y,\\
&\frac{\partial T}{\partial t} + \mathbf{u} \cdot \nabla \mathbf{T} = \nabla^2 T,
\end{aligned} \tag{4}$$

where,

$$Ra = \frac{(T_B - T_T)H^3}{\kappa_T \nu \pi^4}, \quad Pr = \frac{\nu}{\kappa_T}. \tag{5}$$

Here, Ra is the Rayleigh number and Pr is the Prandtl number. Boundary conditions now reads as,

$$\begin{aligned}
&\frac{\partial u_x}{\partial y} = 0,\ u_y = 0,\ T = \pi \qquad \text{if} \quad y = 0,\ 0 \le x \le \Gamma\pi,\\
&\frac{\partial u_x}{\partial y} = 0,\ u_y = 0,\ T = 0 \qquad \text{if} \quad y = \pi,\ 0 \le x \le \Gamma\pi,\\
&\frac{\partial u_y}{\partial x} = 0,\ u_x = 0,\ \frac{\partial T}{\partial x} = 0 \qquad \text{if} \quad x = 0,\ 0 \le y \le \pi,\\
&\frac{\partial u_y}{\partial x} = 0,\ u_x = 0,\ \frac{\partial T}{\partial x} = 0 \qquad \text{if} \quad x = \Gamma\pi,\ 0 \le y \le \pi.
\end{aligned} \tag{6}$$

Figure (3) shows the problem schematic. In this report, we are interested in studying the long-time average of the heat transfer as a function of Rayleigh and Prandtl number. Non-dimensional heat flux which we call Nusselt number is given by,

$$Nu = \frac{1}{\Gamma\pi}\int_{x=0}^{\Gamma\pi} -\frac{\partial T}{\partial y}\bigg|_{y=0} dx. \tag{7}$$

Using the governing equations and with a bit of algebra, one can show that the long-time average of the Nusselt number can be expressed in four different ways.

$$\overline{Nu} = 1 + \overline{\langle u_y T \rangle} = 1 + \frac{1}{Ra}\overline{\langle |\nabla \mathbf{u}|^2 \rangle} = 1 + \overline{\langle |\nabla T|^2 \rangle} = \frac{1}{\Gamma\pi}\overline{\int_{x=0}^{\Gamma\pi} -\frac{\partial T}{\partial y}\bigg|_{y=0} dx}, \tag{8}$$

where overline deontes the long-time average.

$$\overline{[\ ]} = \lim_{T\to\infty} \int_{t=0}^{T} [\ ] dt. \tag{9}$$

To be more precise, one can think of the above limit as limit supremum. Also, the angle brackets denote the volume average.

$$\langle [\ ] \rangle = \frac{1}{\pi}\frac{1}{\Gamma\pi} \int_{y=0}^{\pi} \int_{x=0}^{\Gamma\pi} [\ ] dx dy. \tag{10}$$

The vorticity-perturbed-temperature formulation is well suited for our problem as it makes all the boundary conditions homogenous, and we have only two variables involved, vorticity and perturbed temperature. The governing equations in this formulation are given by,

$$\begin{aligned} &\frac{d\theta}{dt} + J\{\psi,\theta\} = \nabla^2\theta + \partial_y\psi, \\ &\frac{d\omega}{dt} + J\{\psi,\omega\} = Pr\nabla^2\omega + PrRa\partial_x\theta, \end{aligned} \tag{11}$$

along with the boundary conditions,

$$\begin{aligned} &\omega = 0, \theta = 0 \quad \text{on} \quad y = 0,\ 0 \le x \le \Gamma\pi, \\ &\omega = 0, \partial_x\theta = 0 \quad \text{on} \quad x = \Gamma\pi,\ 0 \le y \le \pi, \\ &\omega = 0, \theta = 0 \quad \text{on} \quad y = \pi,\ 0 \le x \le \Gamma\pi, \\ &\omega = 0, \partial_x\theta = 0 \quad \text{on} \quad x = 0,\ 0 \le y \le \pi. \end{aligned} \tag{12}$$

Here, ψ and ω denotes the stream function and the vorticity in spanwise direction. Relation between the stream function, the velocity field, and the vorticity is as follows:

$$\mathbf{u} = (\partial_y\psi, -\partial_x\psi), \qquad \omega = \partial_x u_y - \partial_y u_x = -\partial_x^2\psi - \partial_z^2\psi. \tag{13}$$

$\theta = T - (\pi - y)$ denotes the perturbed temperature which is a deviation in temperature from the linear conduction profile. $J\{\eta,\zeta\} = \eta_x\zeta_y - \eta_y\zeta_x$ is the Poisson bracket.

One can show that the total energy is conserved in the dissipationless limit, i.e., we have the following,

$$\begin{aligned} &\text{K.E.} = \frac{1}{2}\langle u_x^2 + u_y^2 \rangle, \qquad \text{P.E.} = -PrRa\langle Ty, \rangle \\ &\frac{d}{dt}\left(\text{K.E.} + \text{P.E.}\right) = 0. \end{aligned} \tag{14}$$

One other integral identity that the governing equations satisfy is,

$$\frac{d\langle\omega\rangle}{dt} - PrRa\langle\theta_x\rangle = 0. \tag{15}$$

While constructing the truncated model, we would like our truncation(ODEs) to satisfy certain integral identities inherited from the PDEs. Specifically, we look for truncation to satisfy the above two integral identities.

2.1 Linear stability analysis

In this section, we perform the linear stability analysis to find out when instability first occurs for the Rayleigh–Bénard convection in a stress-free box. To perform the linear stability analysis, we assume $|\psi| \ll 1$, and $|\theta| \ll 1$ for all $(x, y) \in (0, \pi) \times (0, \Gamma\pi)$ and we neglect the higher order terms (non-linear terms) in equations (11). Linearized equations are given by,

$$\begin{aligned} \frac{d\theta}{dt} &= \nabla^2\theta - \partial_x\psi, \\ \frac{d\omega}{dt} &= Pr\nabla^2\omega + PrRa\partial_x\theta, \end{aligned} \tag{16}$$

Since these equations are linear, one can consider the linear stability of the eigenmodes individually. Consider the following eigenmode decomposition.

$$\begin{aligned} \theta &= \hat{\theta}e^{\lambda t}\cos(n\alpha x)\sin(my), \\ \psi &= \hat{\psi}e^{\lambda t}\sin(n\alpha x)\sin(my), \end{aligned} \tag{17}$$

where $n, m \in \mathbb{Z}^+$, and $\hat{\theta}, \hat{\psi} \in \mathbb{C}$ are constants. Conduction state will be linearly unstable when $Re(\lambda) > 0$. Vorticity can be obtained in terms of stream function as follows.

$$\omega = -\nabla^2\psi = \hat{\psi}e^{\lambda t}(\alpha^2n^2 + m^2)\sin(n\alpha x)\sin(my). \tag{18}$$

Substituting these expressions into the linear equations, we obtain,

$$\begin{aligned} &\lambda\hat{\theta} = -\hat{\theta}(\alpha^2n^2 + m^2) - \hat{\psi}\alpha n, \\ &\implies \hat{\psi}\alpha n = -\hat{\theta}(\lambda + \alpha^2n^2 + m^2), \end{aligned} \tag{19}$$

and

$$\begin{aligned} &\lambda(\alpha^2n^2 + m^2)\hat{\psi} = -Pr(\alpha^2n^2 + m^2)^2\hat{\psi} - \alpha nPrRa\hat{\theta}, \\ &\implies (\alpha^2n^2 + m^2)(\lambda + Pr(\alpha^2n^2 + m^2))\hat{\psi} = -PrRa\alpha n\hat{\theta}. \end{aligned} \tag{20}$$

Consistency then requires,

$$\frac{\alpha n}{(\alpha^2n^2 + m^2)(\lambda + Pr(\alpha^2n^2 + m^2))} = \frac{(\lambda + \alpha^2n^2 + m^2)}{PrRa\ \alpha n}. \tag{21}$$

We obtain the following quadratic equation in λ.

$$\lambda^2 + \lambda(Pr + 1)(\alpha^2n^2 + m^2) + Pr(\alpha^2n^2 + m^2)^2 - \frac{PrRa\ \alpha^2n^2}{(\alpha^2n^2 + m^2)} = 0. \tag{22}$$

For instability to occur, we require,

$$\begin{aligned} &Pr(\alpha^2n^2 + m^2)^2 - \frac{PrRa\ \alpha^2n^2}{(\alpha^2n^2 + m^2)} < 0, \\ &\implies Ra > \frac{(\alpha^2n^2 + m^2)^3}{\alpha^2n^2}. \end{aligned} \tag{23}$$

Therefore, the critical Rayleigh number is,

$$Ra_l = \inf_{n,m\in\mathbb{Z}^+} \frac{(\alpha^2 n^2 + m^2)^3}{\alpha^2 n^2}. \tag{24}$$

In this report, we choose $\Gamma = \sqrt{2} \implies \alpha = 1/\sqrt{2}$. Therefore, the corresponding critical Rayleigh number is given by,

$$Ra_l = \inf_{n,m\in\mathbb{Z}^+} \frac{(n^2 + 2m^2)^3}{4n^2} = \frac{(1 + 2\times 1^2)}{4\times 1^2} = \frac{27}{4}. \tag{25}$$

2.2 Energy stability analysis

In this section, we perform the energy stability analysis of the conduction state. We multiply second equation in (11) by ω and first equation in (11) by θ to get the following equations.

$$\frac{1}{2}\frac{d\omega^2}{dt} + \frac{\nabla\cdot(\mathbf{u}\,\omega^2)}{2} = Pr(\nabla\cdot(\omega\nabla\omega) - |\nabla\omega|^2) + PrRa\;\omega\partial_x\theta. \tag{26}$$

$$\frac{1}{2}\frac{d\theta^2}{dt} + \frac{\nabla\cdot(\mathbf{u}\,\theta^2)}{2} = (\nabla\cdot(\theta\nabla\theta) - |\nabla\theta|^2) - \theta\partial_x\psi. \tag{27}$$

Perform (26) + $\gamma\times$(27), where $\gamma > 0$.

$$\begin{aligned}\frac{1}{2}\frac{d}{dt}\left(\omega^2 + \gamma\theta^2\right) + \frac{\nabla\cdot(\mathbf{u}\,(\omega^2+\gamma\theta^2))}{2} &= Pr(\nabla\cdot(\omega\nabla\omega)) + (\nabla\cdot(\theta\nabla\theta)) \\ &\quad -Pr|\nabla\omega|^2 - \gamma|\nabla\theta|^2 + PrRa\;\omega\partial_x\theta - \gamma\theta\partial_x\psi.\end{aligned} \tag{28}$$

Integration over whole volume ($\Omega = [0,\Gamma\pi]\times[0,\pi]$) gives,

$$\frac{1}{2}\frac{d}{dt}\int_\Omega\left(\omega^2+\gamma\theta^2\right) = \underbrace{-Pr\int_\Omega|\nabla\omega|^2 - \gamma\int_\Omega|\nabla\theta|^2 + PrRa\int_\Omega\omega\partial_x\theta - \gamma\int_\Omega\theta\partial_x\psi}_{\text{RHS}}. \tag{29}$$

At this point, we consider a fairly general form of ψ and θ in terms of trigonometric series.

$$\psi = \sum_{j=1}^{\infty}\sum_{i=1}^{\infty}\hat{\psi}_{i,j}\sin(i\alpha x)\sin(jy), \tag{30}$$

$$\theta = \sum_{j=1}^{\infty}\sum_{i=1}^{\infty}\hat{\theta}_{i,j}\cos(i\alpha x)\sin(jy). \tag{31}$$

Vorticity being the Laplacian of the stream function is then given by,

$$\implies \qquad \omega = -\nabla^2\psi = \sum_{j=1}^{\infty}\sum_{i=1}^{\infty}(i^2\alpha^2 + j^2)\hat{\psi}_{i,j}\sin(i\alpha x)\sin(jy). \tag{32}$$

Using these trigonometric series, we calculate the following integrals,

$$\int_\Omega |\nabla\omega|^2 = \frac{\pi^2}{4\alpha}\sum_{j=1}^{\infty}\sum_{i=1}^{\infty}(i^2\alpha^2+j^2)^3\hat{\psi}_{i,j}^2, \tag{33}$$

$$\int_\Omega |\nabla\theta|^2 = \frac{\pi^2}{4\alpha}\sum_{j=1}^{\infty}\sum_{i=1}^{\infty}(i^2\alpha^2+j^2)\hat{\theta}_{i,j}^2, \tag{34}$$

$$\int_\Omega \omega\partial_x\theta = \frac{\pi^2}{4\alpha}\sum_{j=1}^{\infty}\sum_{i=1}^{\infty}-i\alpha(i^2\alpha^2+j^2)\hat{\psi}_{i,j}\hat{\theta}_{i,j}, \tag{35}$$

$$\int_\Omega \omega\theta\partial_x\psi = \frac{\pi^2}{4\alpha}\sum_{j=1}^{\infty}\sum_{i=1}^{\infty}i\alpha\hat{\psi}_{i,j}\hat{\theta}_{i,j}. \tag{36}$$

Using this, we get the right hand side of equation (29) as follows:

$$\begin{aligned} RHS = &-Pr\frac{\pi^2}{4\alpha}\sum_{j=1}^{\infty}\sum_{i=1}^{\infty}(i^2\alpha^2+j^2)^3\hat{\psi}_{i,j}^2 - \gamma\frac{\pi^2}{4\alpha}\sum_{j=1}^{\infty}\sum_{i=1}^{\infty}(i^2\alpha^2+j^2)\hat{\theta}_{i,j}^2 \\ &-PrRa\frac{\pi^2}{4\alpha}\sum_{j=1}^{\infty}\sum_{i=1}^{\infty}-i\alpha(i^2\alpha^2+j^2)\hat{\psi}_{i,j}\hat{\theta}_{i,j} - \gamma\frac{\pi^2}{4\alpha}\sum_{j=1}^{\infty}\sum_{i=1}^{\infty}i\alpha\hat{\psi}_{i,j}\hat{\theta}_{i,j}. \end{aligned} \tag{37}$$

A factor of $\pi^2/4\alpha$ is removed for the convenience. Our aim is to find out smallest Ra_e such that for some $\hat{\psi}_{i,j}$'s and $\hat{\theta}_{i,j}$'s RHS first becomes positive. We note that for a given magnitude of $\hat{\theta}_{i,j}$ and $\hat{\psi}_{i,j}$ with negative correlation is more dangerous than the one with positive correlation. Infact, for given $\hat{\psi}_{i,j}$'s and Ra, $\hat{\theta}_{i,j}$'s with

$$\hat{\theta}_{i,j} = -\hat{\psi}_{i,j}\frac{\gamma i\alpha + RaPri\alpha(i^2\alpha^2+j^2)}{2\gamma(i^2\alpha^2+j^2)} \tag{38}$$

is the most dangerous combination. Substitute this expression in (37), we get,

$$RHS = -\sum_{j=1}^{\infty}\sum_{i=1}^{\infty}M_{i,j}\hat{\psi}_{i,j}^2, \tag{39}$$

where $M_{i,j}$ is given by,

$$M_{i,j} = \left(Pr(i^2\alpha^2+j^2)^3 - \frac{\left[\gamma i\alpha + RaPri\alpha(i^2\alpha^2+j^2)\right]^2}{4\gamma(i^2\alpha^2+j^2)}\right). \tag{40}$$

We are interested in studying energy stability analysis at $\alpha = 1/\sqrt{2}$. At this value of α,

$$M_{i,j} = Pr\frac{2(i^2+2j^2)^4\beta - i^2\left[Ra(i^2+2j^2)+2\beta\right]}{16\beta(i^2+2j^2)}, \tag{41}$$

where $\beta = \gamma/Pr$. We note that the choice of β totally depend on us. And we choose a $\beta > 0$ such that we can delay RHS from becoming not negative definite for as large Rayleigh

number as possible in order to obtain the best energy bound. We choose $\beta = 81/8$. For this value of β, we get,

$$M_{i,j} = Pr\frac{\frac{81}{4}(i^2+2j^2)^4 - i^2\left[Ra(i^2+2j^2)+\frac{81}{4}\right]}{162(i^2+2j^2)} \tag{42}$$

One can show that if $Ra < \frac{27}{4}$ then for each (i,j), $M_{i,j} > 0$ and therefore RHS< 0 for any $\hat{\psi}_{i,j}$. This implies that critical Rayleigh number for energy stability is

$$Ra_e \geq \frac{27}{4}. \tag{43}$$

However, the critical Rayleigh number for the energy stability has to be less that equal to the critical Rayleigh number for the linear stability, i.e.,

$$Ra_e \leq Ra_l = \frac{27}{4}. \tag{44}$$

This implies,

$$Ra_e = \frac{27}{4}. \tag{45}$$

Therefore, at $Ra = 27/4$ we have supercritical bifurcation.

3 Bounding Time Average for ODEs

In this report, we deal with truncated models, which are system of ODEs, and we are interested in finding upper bound on the Nusselt number, which is a scalar function. Therefore, before going to the specific problem, we setup a general framework of finding the upper bound on a long-time average of a scalar quantity where trajectories evolve in space according to a given dynamical system. Coniser an n-dimensional dynamical system such that every trajectory is bounded forward in time.

$$\dot{\mathbf{x}} = \mathbf{f}(\mathbf{x}), \quad \mathbf{x} \in \mathbb{R}^n,\ \mathbf{f} : \mathbb{R}^n \to \mathbb{R}^n. \tag{46}$$

We are interested in finding,

$$\max_{\mathbf{x_0}\in\mathbb{R}^n} \left[\underbrace{\lim_{T\to\infty} \frac{1}{T}\int_0^T \Phi(\mathbf{x}(t))dt}_{\overline{\Phi}} \right]. \tag{47}$$

Assume that we cannot calculate above integral analytically, which generally would be the case. The option then comes to one's mind is using numerical methods to calculate the maximum of the long-time average over all initial conditions. Calculating the long-time average for a given initial condition can be done with sufficient accuracy. However, the long-time average as a function of initial condition may not be a convex function; infact, it can be a discontinuous function. For example, starting with an unstable fixed-point or from

its neighboring point can give two completely different values of the long-time average. In that case, numerical methods such as steepest gradient method are not useful. Therefore, we need to come with another strategy to be able to compute the maximum of the long-time average of a scalar function. One such strategy is presented as follows.

Consider a scalar differentiable function V. Along any trajectory, we have,

$$\overline{\frac{dV(x(t))}{dt}} = \lim_{T\to\infty} \frac{1}{T}\int_0^T \frac{dV(x(t))}{dt}dt = \lim_{T\to\infty} \frac{V(x(T)) - V(x(0))}{T} = 0. \tag{48}$$

Above vanishes because every trajectory is bounded forward in time. Rate of change of a scalar function along a trajectory, using the chain rule can also be written as,

$$\frac{dV(x(t))}{dt} = \mathbf{f}\cdot\nabla V. \tag{49}$$

Combining (48) and (49), we get,

$$\overline{\mathbf{f}\cdot\nabla V} = 0. \tag{50}$$

This means that instead of looking at the long-time average of Φ, we can equivalently look at the long-time average of $\Phi + \mathbf{f}\cdot\nabla V$ for any scalar differentiable V. Next step is to carefully choose V such that we can bound $\Phi + \mathbf{f}\cdot\nabla V$ in space which would then prove a bound on the long-time average of $\Phi + \mathbf{f}\cdot\nabla V$ and therefore on the long-time average of Φ. Mathematically, it can be written as,

$$\max_{\mathbf{x}_0} \overline{\Phi} = \max_{\mathbf{x}_0} \overline{\Phi + \mathbf{f}\cdot\nabla V} \leq \sup_{\mathbf{x}} \Phi + \mathbf{f}\cdot\nabla V. \tag{51}$$

Since above is valid for all scalar differentiable function V, therefore we can obtain the best bound by trying all possible V's, i.e, we cand do the following.

$$\max_{\mathbf{x}_0} \overline{\Phi} \leq \inf_{V\in C^1(\mathbb{R}^n)} \sup_{\mathbf{x}} \Phi + \mathbf{f}\cdot\nabla V. \tag{52}$$

There is a theorem due to [11] which says that the above inequality is actually equatlity, i.e., there is a trajectory for which the long-time average of Φ becomes equal to R.H.S. in inequality (52).

$$\max_{\mathbf{x}_0} \overline{\Phi} = \inf_{V\in C^1(\mathbb{R}^n)} \sup_{\mathbf{x}} \Phi + \mathbf{f}\cdot\nabla V \tag{53}$$

Problem of integrating in time to calculate the long-time average has been converted into finindg a good scalar differentiable function V. At this point we notice that, for our truncated models, both $\mathbf{f}$ and Φ are polynomial. We restrict V to be a finite degree polynomial, and following ([1] and [2]), we use sum-of-squares method to prove bounds on the long-time average of Φ.

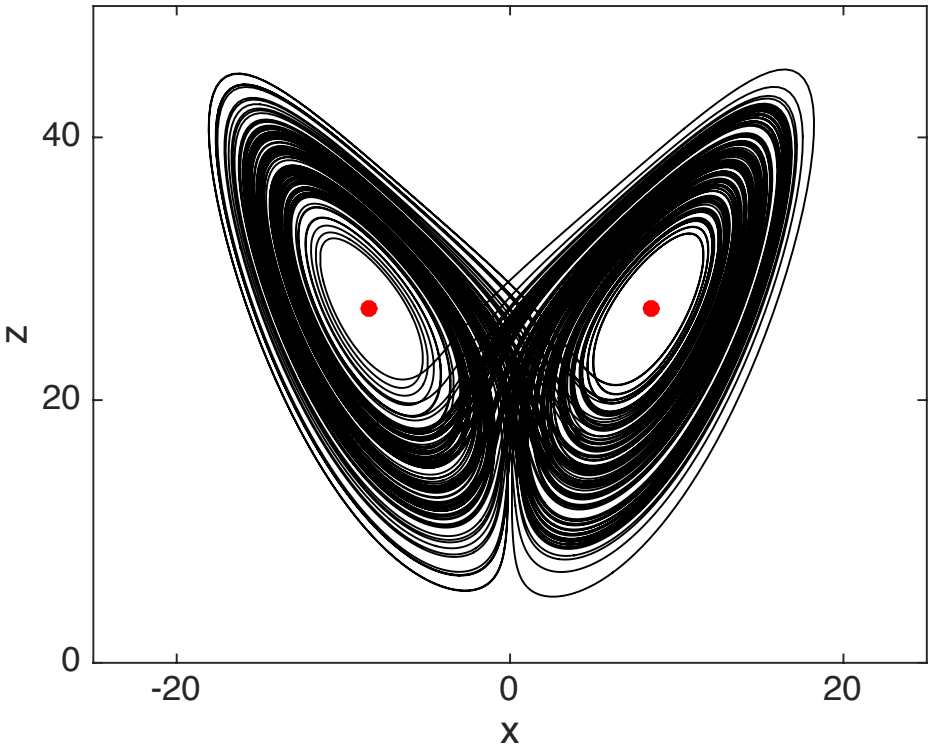

Figure 4: The Lorenz attractor and the steady states at parameter values ($\sigma = 10, \beta = 8/3, r = 28$).

4 Lorenz System: An Example

In 1960's Lorenz [5] derived a heavily truncated model of convection. Lorenz system is given by,

$$\mathbf{x} = (x, y, z), \quad \mathbf{f} = (-\sigma x + \sigma y, rx - y - xz, xy - \beta z). \tag{54}$$

Here, σ and r are Prandtl number and scaled Rayleigh number, whereas $\beta = 4(1 + a^2)^{-1}$ and a is the aspect ratio. The truncated Nusselt number of this system is given by,

$$Nu = 1 + \frac{2}{r} z. \tag{55}$$

Therefore, asking about the long-time average of the Nusselt number is equivalent to asking about the long-time average of z. Therefore, we first focus on the long-time average of z. Figure (4) shows the Lorenz attractor and the steady states for parameter values ($\sigma = 10, \beta = 8/3, r = 28$). From this figure it is not entirely obvious that the steady states maximize the heat transfer.

Analysis done next is similar to Malkus [7]. We use the general formulation from the last section. We choose V to be a second-degree polynomial.

$$V = \frac{C_1}{2\sigma} x^2 + \frac{C_2}{2}(y^2 + z^2) + C_3 z. \tag{56}$$

However, one can immediately notice that this is not the most general form of a second-degree polynomial in x, y, and z. We have use the fact that $\mathbf{f} \cdot \nabla V$ should not be a odd degree polynomial (in this case cubic). This is becuase an odd degree polynomial cannot be written as sum of squares of polynomials. Other fact which we have used is that V to have the reflection symmetries of the dynamical system. A theorem from ([2]) proves that bounds do not become any worse when restricting the polynomials to have the reflection symmetries of the dynamical system. Lorenz system has the following reflection symmetry.

$$(x, y, z) \mapsto (-x, -y, z). \tag{57}$$

One can notice that chosen form of V also has this reflection symmetry. After respecting the above mentioned facts, (56) is the most general expression of a second-degree polynomial. From the previous section, we know that the long-time average of z is equivalent to the long-time average of $z + \mathbf{f} \cdot \nabla V$, i.e.,

$$\begin{aligned} \overline{z} \quad &= \overline{z + \mathbf{f} \cdot \nabla V}, \\ &\overline{z + C_1(-x^2 + xy) + C_2(rxy - y^2) + C_2(-\beta z^2) + C_3(xy - \beta z)}. \end{aligned} \tag{58}$$

At this point, we choose, C_1, C_2 and C_3 carefully so that we can bound the quantity under the line in (58). The following choice will work,

$$C_1 = \frac{1}{\beta(r-1)},\ C_2 = \frac{1}{\beta(r-1)},\ C_3 = -\frac{1}{\beta}, \tag{59}$$

which results into,

$$\overline{z} = \overline{(r-1) - \frac{(x-y)^2}{\beta(r-1)} - \frac{(z-r+1)^2}{r-1}} \leq \overline{r-1} = r - 1. \tag{60}$$

Above is valid only if $r > 1$. Therefore, the bound on heat transfer for $r > 1$ is given by,

$$\overline{Nu} \leq 1 + \frac{2(r-1)}{r}. \tag{61}$$

Now we calculate the heat transfer due to steady states. Lornez system has the following non-trivial steady states for $r > 1$. Figure (5) shows the bifurcation diagram.

$$(x, y, z) = (\pm\sqrt{\beta(r-1)}, \pm\sqrt{\beta(r-1)}, r-1) \quad \text{if} \quad r > 1. \tag{62}$$

These steady states corresponds to steady rolls. Maximum heat transfer due to these steady states is given by,

$$\max_{SS} Nu = 1 + \frac{2(r-1)}{r} \tag{63}$$

This is equal to the bound on heat transfer for any trajectory (61). Therefore, we have found a bound on heat transfer for any trajectory and have shown that this bound is actually achieved by a steady state. For Lorenz system, we conclude that steady states maximize the heat transfer.

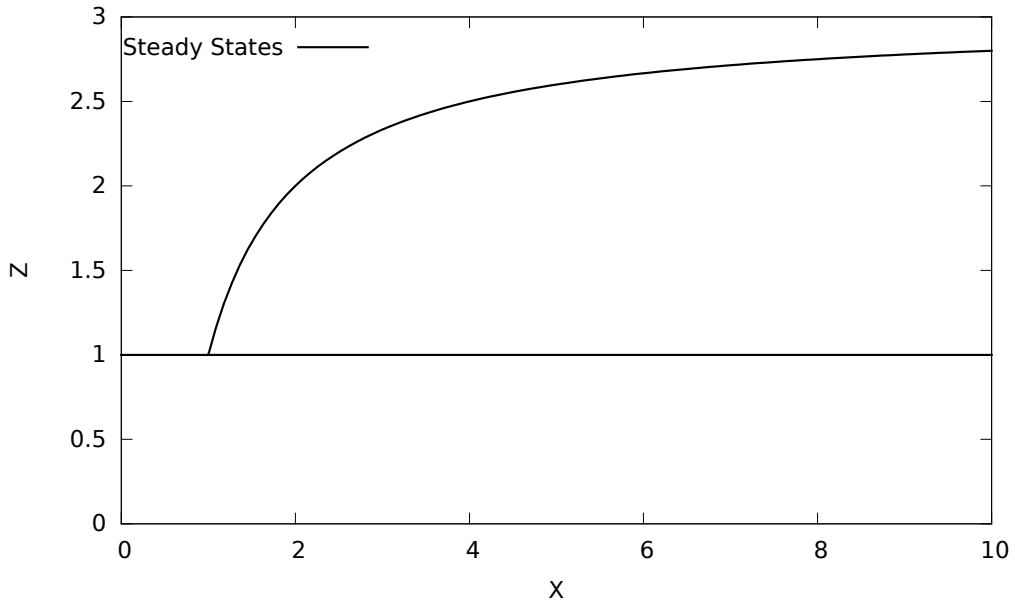

Figure 5: Steady states in the Lorenz system. Bifurcation occurs at $r = 1$.

5 The 8-mode Model

Consider the following truncation,

$$\omega(x,y,t) = \hat{\omega}_{1,1}(t)\sin(\alpha x)\sin(y) + \hat{\omega}_{1,2}(t)\sin(\alpha x)\sin(2y) + \hat{\omega}_{2,1}(t)\sin(2\alpha x)\sin(y), \quad (64)$$

$$\begin{aligned}\theta(x,y,t) \quad &= \hat{\theta}_{0,2}(t)\sin(2y) + \hat{\theta}_{0,4}(t)\sin(4y) \\ &+\hat{\theta}_{1,1}(t)\cos(\alpha x)\sin(y) + \hat{\theta}_{1,2}(t)\cos(\alpha x)\sin(2y) + \hat{\theta}_{2,1}(t)\cos(2\alpha x)\sin(y).\end{aligned} \quad (65)$$

The governing equations of individual modes can be obtained by substituting the above the truncation into the governing equations (11) and then projecting the resulting equations onto different eigenfunctions. The 8-mode model is given by,

$$\begin{aligned}\frac{d\hat{\omega}_{1,1}}{dt} + \frac{3}{4}\left(\frac{\alpha}{\alpha^2+4} - \frac{\alpha}{4\alpha^2+1}\right)\hat{\omega}_{1,2}\,\hat{\omega}_{2,1} = \\ -(\alpha^2+1)Pr\hat{\omega}_{1,1} - \alpha PrRa\hat{\theta}_{1,1},\end{aligned} \quad (66)$$

$$\frac{d\hat{\omega}_{1,2}}{dt} + \frac{3}{4}\left(\frac{\alpha}{4\alpha^2+1} - \frac{\alpha}{\alpha^2+1}\right)\hat{\omega}_{1,1}\,\hat{\omega}_{2,1} = -(\alpha^2+4)Pr\hat{\omega}_{1,2} - \alpha PrRa\hat{\theta}_{1,2}, \quad (67)$$

$$\frac{d\hat{\omega}_{2,1}}{dt} + \frac{3}{4}\left(\frac{\alpha}{\alpha^2+1} - \frac{\alpha}{\alpha^2+4}\right)\hat{\omega}_{1,1}\,\hat{\omega}_{1,2} = -(4\alpha^2+1)Pr\hat{\omega}_{2,1} - 2\alpha PrRa\hat{\theta}_{2,1}, \quad (68)$$

$$\frac{d\hat{\theta}_{0,2}}{dt} - \frac{\alpha}{2(1+\alpha^2)}\hat{\omega}_{1,1}\,\hat{\theta}_{1,1} - \frac{\alpha}{4\alpha^2+1}\hat{\omega}_{2,1}\,\hat{\theta}_{2,1} = -4\hat{\theta}_{0,2}, \tag{69}$$

$$\frac{d\hat{\theta}_{0,4}}{dt} - \frac{\alpha}{\alpha^2+4}\hat{\omega}_{1,2}\,\hat{\theta}_{1,2} = -16\hat{\theta}_{0,4}, \tag{70}$$

$$\frac{d\hat{\theta}_{1,1}}{dt} + \frac{3\alpha}{4(\alpha^2+4)}\hat{\omega}_{1,2}\,\hat{\theta}_{2,1} + \frac{3\alpha}{4(4\alpha^2+1)}\hat{\omega}_{2,1}\,\hat{\theta}_{1,2} + \frac{\alpha}{\alpha^2+1}\hat{\omega}_{1,1}\,\hat{\theta}_{0,2} = -(\alpha^2+1)\hat{\theta}_{1,1} - \frac{\alpha}{\alpha^2+1}\hat{\omega}_{1,1}, \tag{71}$$

$$\frac{d\hat{\theta}_{1,2}}{dt} - \frac{3\alpha}{4(\alpha^2+1)}\hat{\omega}_{1,1}\,\hat{\theta}_{2,1} - \frac{3\alpha}{4(4\alpha^2+1)}\hat{\omega}_{2,1}\,\hat{\theta}_{1,1} + \frac{2\alpha}{(\alpha^2+4)}\hat{\omega}_{1,2}\,\hat{\theta}_{0,4} = -(\alpha^2+4)\hat{\theta}_{1,2} - \frac{\alpha}{\alpha^2+4}\hat{\omega}_{1,2}, \tag{72}$$

$$\frac{d\hat{\theta}_{2,1}}{dt} + \frac{3\alpha}{4(\alpha^2+1)}\hat{\omega}_{1,1}\,\hat{\theta}_{1,2} - \frac{3\alpha}{4(\alpha^2+4)}\hat{\omega}_{1,2}\,\hat{\theta}_{1,1} + \frac{2\alpha}{4\alpha^2+1}\hat{\omega}_{2,1}\,\hat{\theta}_{0,2} = -(4\alpha^2+1)\hat{\theta}_{2,1} - \frac{2\alpha}{4\alpha^2+1}\hat{\omega}_{2,1}, \tag{73}$$

This model has the energy conservation property in the dissipationless limit. The total energy is given by,

$$E = KE + PE, \tag{74}$$

where,

$$KE = \frac{1}{2}\langle u^2 + v^2\rangle = \frac{1}{8}\left(\frac{\hat{\omega}_{1,1}^2}{\alpha^2+1} + \frac{\hat{\omega}_{1,2}^2}{\alpha^2+4} + \frac{\hat{\omega}_{2,1}^2}{4\alpha^2+1}\right), \tag{75}$$

$$PE = -PrRa\langle y(1-y+\theta)\rangle = PrRa\left(-\frac{\pi}{2} + \frac{\pi^2}{3} + \frac{\hat{\theta}_{0,2}}{2} + \frac{\hat{\theta}_{0,4}}{4}\right), \tag{76}$$

$$\frac{dE}{dt} = \frac{1}{4}\left(\frac{\hat{\omega}_{1,1}}{\alpha^2+1}\frac{d\hat{\omega}_{1,1}}{dt} + \frac{\hat{\omega}_{1,2}}{\alpha^2+4}\frac{d\hat{\omega}_{1,2}}{dt} + \frac{\hat{\omega}_{2,1}}{4\alpha^2+1}\frac{d\hat{\omega}_{2,1}}{dt}\right) + PrRa\left(\frac{1}{2}\frac{d\hat{\theta}_{0,2}}{dt} + \frac{1}{4}\frac{d\hat{\theta}_{0,4}}{dt}\right). \tag{77}$$

After substituting the expression of evolution of various quantities in time from (66-73), we obtain,

$$\frac{dE}{dt} = 0. \tag{78}$$

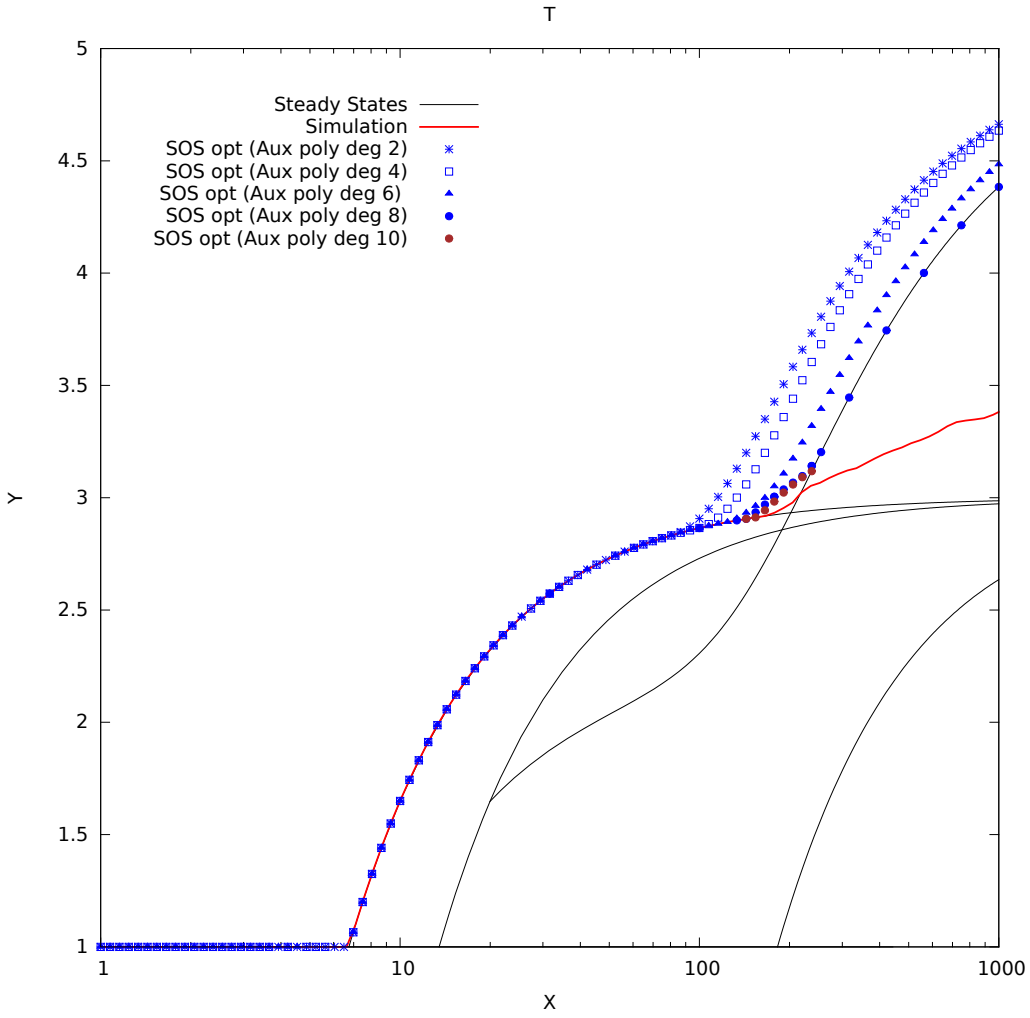

Figure 6: Black lines show the long-time average of the Nusselt number due to steady states. Red line shows result for $\overline{Nu}$ from a numerical simulation with random initial. The blue symbols denote the bound obtained using the sum-of-squares method.

5.1 The Nusselt number

The Nusselt number for the truncated model can be obtained by substituting (64) and (65) into the original expressions of the Nusselt number (8). We can obtain four different expressions for the truncated long-time average of the Nusselt, which may not necessarily be equal. However, for the 8-mode model, one can prove that equality holds among the four different expressions, i.e.,

$$\begin{aligned}
\overline{Nu} \quad &= 1 + \frac{1}{4}\left(\frac{\alpha\overline{\omega_{1,1}\theta_{1,1}}}{1+\alpha^2} + \frac{\alpha\overline{\omega_{1,2}\theta_{1,2}}}{4+\alpha^2} + \frac{2\alpha\overline{\omega_{2,1}\theta_{2,1}}}{4\alpha^2+1}\right) && \text{(79a)}\\
&= 1 + \frac{1}{Ra}\left(\overline{\omega_{1,1}^2} + \overline{\omega_{1,2}^2} + \overline{\omega_{2,1}^2}\right) && \text{(79b)}\\
&= 1 + \frac{1}{2}\left(4\overline{\theta_{0,2}^2} + 16\overline{\theta_{0,4}^2}\right) + \frac{1}{4}\left((\alpha^2+1)\overline{\theta_{1,1}^2} + (\alpha^2+4)\overline{\theta_{1,2}^2} + (4\alpha^2+1)\overline{\theta_{2,1}^2}\right) && \text{(79c)}\\
&= 1 - 2\overline{\theta_{0,2}} - 4\overline{\theta_{0,4}}. && \text{(79d)}
\end{aligned}$$

One can prove (79a) and (79d) are equal by talking the long-time average of equation

$$\frac{1}{2}\times(69) + \frac{1}{4}\times(70).$$

(79a) and (79b) can be shown to be equivalent by taking the long-time average of equation

$$\frac{1}{1+\alpha^2}\times(66) + \frac{1}{1+4\alpha^2}\times(67) + \frac{1}{4+\alpha^2}\times(68).$$

(79b) and (79c) can be shown to be equivalent by taking the long-time average of equation

$$\frac{-1}{PrRa}\left[\frac{\omega_{1,1}(66)}{1+\alpha^2} + \frac{\omega_{1,2}(67)}{4+\alpha^2} + \frac{\omega_{2,1}(68)}{1+4\alpha^2}\right] + \frac{\theta_{0,2}(69)}{2} + \frac{\theta_{0,4}(70)}{2} + \frac{\theta_{1,1}(71)}{4} + \frac{\theta_{1,2}(72)}{4} + \frac{\theta_{2,1}(73)}{4}.$$

5.2 The reflection symmetries

First rename the variables as follows:

$$(x_1, x_2, x_3, x_4, x_5, x_6, x_7, x_8) \equiv (\omega_{1,1}, \omega_{1,2}, \omega_{2,1}, \theta_{0,2}, \theta_{0,4}, \theta_{1,1}, \theta_{1,2}, \theta_{2,1}). \tag{80}$$

The 8-mode model has the following reflection symmetries.

$$\begin{aligned}
&(x_1, x_2, x_3, x_4, x_5, x_6, x_7, x_8) \mapsto (-x_1, -x_2, x_3, x_4, x_5, -x_6, -x_7, x_8),\\
&(x_1, x_2, x_3, x_4, x_5, x_6, x_7, x_8) \mapsto (-x_1, x_2, -x_3, x_4, x_5, -x_6, x_7, -x_8),\\
&(x_1, x_2, x_3, x_4, x_5, x_6, x_7, x_8) \mapsto (x_1, -x_2, -x_3, x_4, x_5, x_6, -x_7, -x_8).
\end{aligned}$$

That is to say that the 8-mode model is invariant under above transformations.

5.3 A uniform bound in the Rayleigh number, Prandtl number and aspect ratio

In this section, we prove a bound on the heat transfer for the 8-mode model which is uniformly valid in the Rayleigh number, Prandtl number, and aspect ratio and becomes asymptotically accurate in the limit of high Rayleigh number. We choose V to be a second degree polynomial, as follows.

$$V = c_1\theta_{02} + c_2\theta_{04} + c_3(2\theta_{02}^2 + 2\theta_{04}^2 + \theta_{11}^2 + \theta_{12}^2 + \theta_{21}^2). \tag{81}$$

This implies,

$$\begin{aligned} Nu + \mathbf{f}\cdot\nabla V = 1 - (2+4c_1)\theta_{02} - (4+16c_2)\theta_{04} - 16c_3\theta_{02}^2 - 64c_3\theta_{04}^2 - 2(\alpha^2+1)c_3\theta_{11}^2 \\ -2(\alpha^2+4)c_3\theta_{12}^2 - 2(4\alpha^2+1)c_3\theta_{21}^2 + \frac{\alpha(c_1-4c_3)}{2(1+\alpha^2)}\omega_{11}\theta_{11} + \frac{\alpha(c_2/2-2c_3)}{4+\alpha^2}\omega_{12}\theta_{12} \\ + \frac{\alpha(1-4c_3)}{1+4\alpha^2}\omega_{21}\theta_{21}. \end{aligned} \tag{82}$$

Choose, $c_1 = 4c_3$, and $c_2 = 2c_3$ which leads to,

$$\begin{aligned} Nu + \mathbf{f}\cdot\nabla V &= 1 - (2+4c_3)\theta_{02} - (4+32c_3)\theta_{04} - 16c_3\theta_{02}^2 - 64c_3\theta_{04}^2 - 2(\alpha^2+1)c_3\theta_{11}^2 \\ &\quad -2(\alpha^2+4)c_3\theta_{12}^2 - 2(4\alpha^2+1)c_3\theta_{21}^2 \\ &= 1 + \frac{(2+16c_3)^2}{64c_3} + \frac{(4+32c_3)^2}{256c_3} - \left(4\theta_{02}\sqrt{c_3} + \frac{2+16c_3}{8\sqrt{c_3}}\right)^2 - \left(8\theta_{04}\sqrt{c_3} + \frac{4+32c_3}{16\sqrt{c_3}}\right)^2 \\ &\quad -2(\alpha^2+1)c_3\theta_{11}^2 - 2(\alpha^2+4)c_3\theta_{12}^2 - 2(4\alpha^2+1)c_3\theta_{21}^2 \\ &\le 1 + \frac{(2+16c_3)^2}{64c_3} + \frac{(4+32c_3)^2}{256c_3}. \end{aligned} \tag{83}$$

The best bound is obtained when $c_3 = 1/8$.

$$Nu + \mathbf{f}\cdot\nabla V \le 1 + 2 + 2 = 5. \tag{84}$$

This gives us a bound on the long-time average of the heat transfer.

$$\implies \overline{Nu} = \overline{Nu + \mathbf{f}\cdot\nabla V} \le 5. \tag{85}$$

We note that this bound is indeed achieved in the limit of high Rayleigh number.

5.4 Bounds on the heat transfer

We are intersted in finding the maximum of the long-time average of the Nusselt number over all trjactories, i.e,

$$\max_{\mathbf{x}_0} \overline{Nu} = \max_{\mathbf{x}_0} 1 - 2\overline{\theta_{0,2}} - 4\overline{\theta_{0,4}}. \tag{86}$$

We use the method described in the section (3) followed by sum-of-squares method to find this bound. We choose V to polynomial of degree $2, 4, 6, 8$, and 10. Figure (6) shows the results. The bounds saturate to heat transfer due steady states for $Ra \lesssim 100$ using the second-degree polynomial and for $Ra \gtrsim 150$ using the eight-degree polynomial. For $100 \lesssim Ra \lesssim 150$, we suspect that a limit cycle maximize the heat transfer. Figure (7) shows the flow structure corresponding to four different branches of steady states in figure (6).

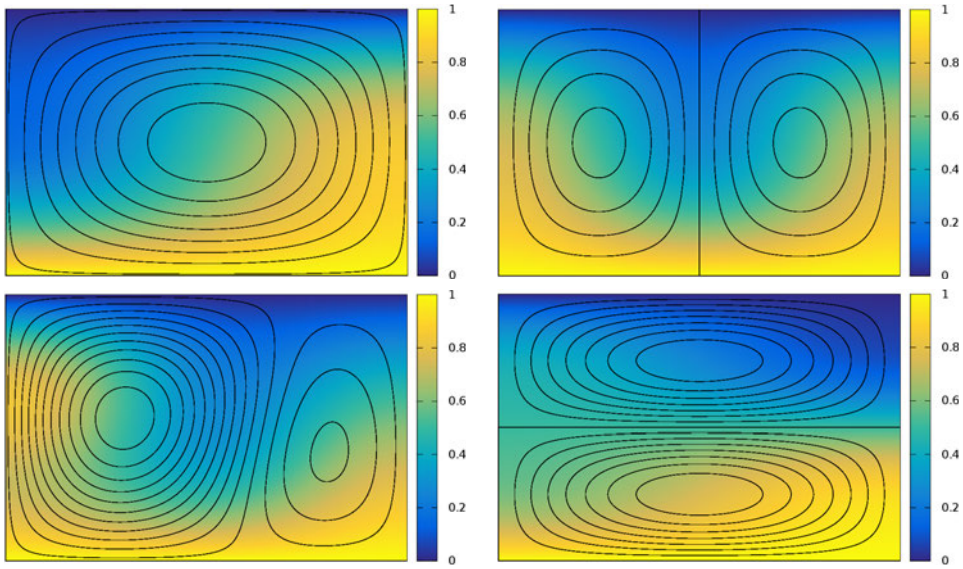

Figure 7: Steady states corresponding to four different branches of steady states in figure (6). Color contours shows the temperature variation scaled with π, i.e., T/π. The lines show the streamlines. One can easily guess the flow direction by looking at the temperature variation. The Rayleigh number corresponding to each of these figures is close to the Rayleigh number when these steady-states branches first appear.

6 The 15-mode Model

We consider the following truncation.

$$\begin{aligned}\omega(x,y,t) \quad &= \hat{\omega}_{1,1}(t)\sin(\alpha x)\sin(y) + \hat{\omega}_{1,2}(t)\sin(\alpha x)\sin(2y) + \hat{\omega}_{2,1}(t)\sin(2\alpha x)\sin(y) \\ &+\hat{\omega}_{1,3}\sin(\alpha x)\sin(3y) + \hat{\omega}_{3,1}\sin(3\alpha x)\sin(y) + \hat{\omega}_{3,3}\sin(3\alpha x)\sin(3y), \qquad (87)\end{aligned}$$

$$\begin{aligned}\theta(x,y,t) \quad &= \hat{\theta}_{0,2}(t)\sin(2y) + \hat{\theta}_{0,4}(t)\sin(4y) + \hat{\theta}_{0,6}\sin(6y) \\ &+\hat{\theta}_{1,1}(t)\cos(\alpha x)\sin(y) + \hat{\theta}_{1,2}(t)\cos(\alpha x)\sin(2y) + \hat{\theta}_{2,1}(t)\cos(2\alpha x)\sin(y) \\ &+\hat{\theta}_{1,3}\sin(\alpha x)\sin(3y) + \hat{\theta}_{3,1}\sin(3\alpha x)\sin(y) + \hat{\theta}_{3,3}\sin(3\alpha x)\sin(3y). \qquad (88)\end{aligned}$$

Rename the variables as follows:

$$\begin{aligned}&(x_1, x_2, x_3, x_4, x_5, x_6, x_7, x_8, x_9, x_{10}, x_{11}, x_{12}, x_{13}, x_{14}, x_{15}) \\ &\equiv (\hat{\omega}_{1,1}, \hat{\omega}_{1,2}, \hat{\omega}_{2,1}, \hat{\omega}_{1,3}, \hat{\omega}_{3,1}, \hat{\omega}_{3,3}, \hat{\theta}_{0,2}, \hat{\theta}_{0,4}, \hat{\theta}_{0,6}, \hat{\theta}_{1,1}, \hat{\theta}_{1,2}, \hat{\theta}_{2,1}, \hat{\theta}_{1,3}, \hat{\theta}_{3,1}, \hat{\theta}_{3,3}). \qquad (89)\end{aligned}$$

The governing equations of individual modes can be obtained by substituting the above truncation into the governing equation and then projecting the resulting equation onto different eigenfunctions. The 15-mode model is given by,

$$\dot{x}_1 \quad = -\frac{3}{4}\left(\frac{\alpha}{\alpha^2+4} - \frac{\alpha}{4\alpha^2+1}\right) x_2 x_3 - (\alpha^2+1)Prx_1 - \alpha PrRax_{10}, \qquad (90)$$

$$\dot{x}_2 = \frac{3}{4}\left(\frac{\alpha}{\alpha^2+1}-\frac{\alpha}{4\alpha^2+1}\right)x_1x_3+\frac{5}{4}\left(\frac{\alpha}{4\alpha^2+1}-\frac{\alpha}{\alpha^2+9}\right)x_3x_4$$
$$+\frac{5}{4}\left(\frac{\alpha}{4\alpha^2+1}-\frac{\alpha}{9\alpha^2+1}\right)x_3x_5-\frac{3}{4}\left(\frac{\alpha}{4\alpha^2+1}-\frac{\alpha}{9\alpha^2+9}\right)x_3x_6-(\alpha^2+4)Prx_2-\alpha PrRax_{11}, \tag{91}$$

$$\dot{x}_3 = -\frac{3}{4}\left(\frac{\alpha}{\alpha^2+1}-\frac{\alpha}{\alpha^2+4}\right)x_1x_2-\frac{5}{4}\left(\frac{\alpha}{\alpha^2+4}-\frac{\alpha}{\alpha^2+9}\right)x_2x_4$$
$$-\frac{5}{4}\left(\frac{\alpha}{\alpha^2+4}-\frac{\alpha}{9\alpha^2+1}\right)x_2x_5+\frac{3}{4}\left(\frac{\alpha}{\alpha^2+4}-\frac{\alpha}{9\alpha^2+9}\right)x_2x_6-(4\alpha^2+1)Prx_3-2\alpha PrRax_{12}, \tag{92}$$

$$\dot{x}_4 = \frac{5}{4}\left(\frac{\alpha}{\alpha^2+4}-\frac{\alpha}{4\alpha^2+1}\right)x_2x_3-(\alpha^2+9)Prx_4-\alpha PrRax_{13}, \tag{93}$$

$$\dot{x}_5 = \frac{5}{4}\left(\frac{\alpha}{\alpha^2+4}-\frac{\alpha}{4\alpha^2+1}\right)x_2x_3-(9\alpha^2+1)Prx_5-3\alpha PrRax_{14}, \tag{94}$$

$$\dot{x}_6 = -\frac{3}{4}\left(\frac{\alpha}{\alpha^2+4}-\frac{\alpha}{4\alpha^2+1}\right)x_2x_3-(9\alpha^2+9)Prx_6-3\alpha PrRax_{15}, \tag{95}$$

$$\dot{x}_7 = \frac{1}{2}\left(\frac{\alpha}{\alpha^2+1}\right)x_1x_{10}-\frac{1}{2}\left(\frac{\alpha}{\alpha^2+1}\right)x_1x_{13}+\left(\frac{\alpha}{4\alpha^2+1}\right)x_3x_{12}-\frac{1}{2}\left(\frac{\alpha}{\alpha^2+9}\right)x_4x_{10}$$
$$+\frac{3}{2}\left(\frac{\alpha}{9\alpha^2+1}\right)x_5x_{14}-\frac{3}{2}\left(\frac{\alpha}{9\alpha^2+1}\right)x_5x_{15}-\frac{3}{2}\left(\frac{\alpha}{9\alpha^2+9}\right)x_6x_{14}-4x_7, \tag{96}$$

$$\dot{x}_8 = \left(\frac{\alpha}{\alpha^2+1}\right)x_1x_{13}+\left(\frac{\alpha}{\alpha^2+4}\right)x_2x_{11}+\left(\frac{\alpha}{\alpha^2+9}\right)x_4x_{10}+3\left(\frac{\alpha}{9\alpha^2+1}\right)x_5x_{15}$$
$$+3\left(\frac{\alpha}{9\alpha^2+9}\right)x_6x_{14}-16x_8, \tag{97}$$

$$\dot{x}_9 = \frac{3}{2}\left(\frac{\alpha}{\alpha^2+9}\right)x_4x_{13}+\frac{9}{2}\left(\frac{\alpha}{9\alpha^2+9}\right)x_6x_{15}-36x_9, \tag{98}$$

$$\dot{x}_{10} = -\left(\frac{\alpha}{\alpha^2+1}\right)x_1x_7-\frac{3}{4}\left(\frac{\alpha}{\alpha^2+4}\right)x_2x_{12}-\frac{3}{4}\left(\frac{\alpha}{4\alpha^2+1}\right)x_3x_{11}$$
$$+\left(\frac{\alpha}{\alpha^2+9}\right)x_4x_7-2\left(\frac{\alpha}{\alpha^2+9}\right)x_4x_8-(\alpha^2+1)x_{10}-\frac{\alpha}{\alpha^2+1}x_1, \tag{99}$$

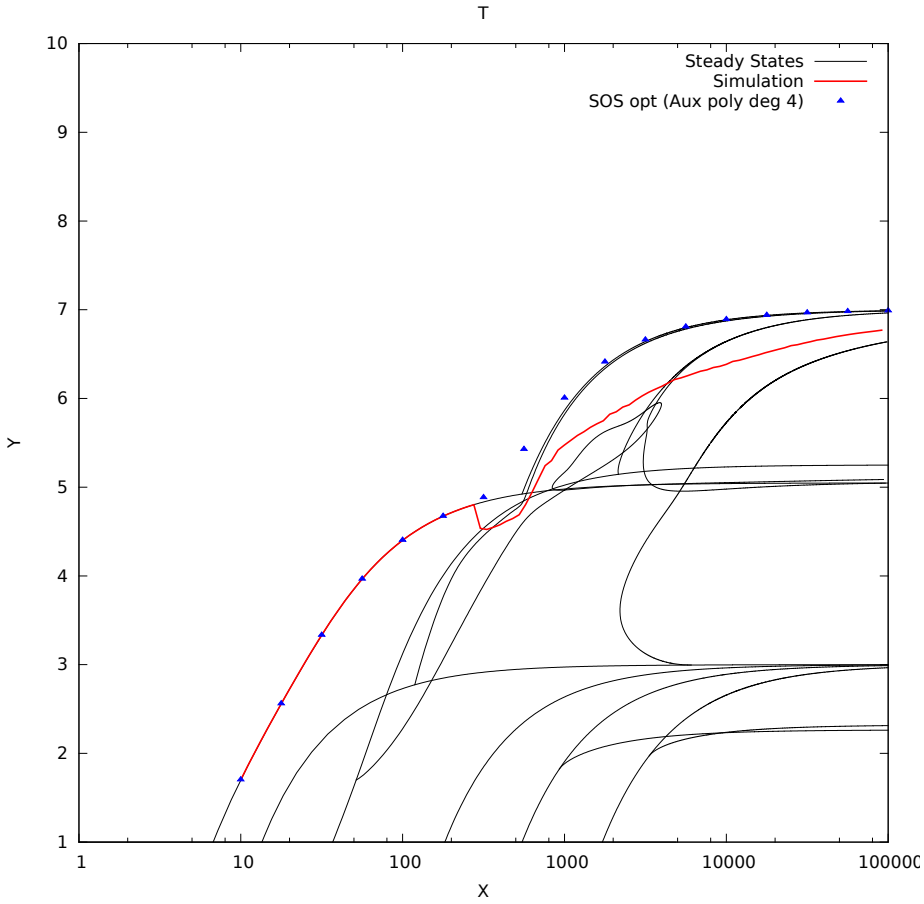

Figure 8: Black lines show the long-time average of the Nusselt number due to steady states. Red line shows result for $\overline{Nu}$ from a numerical simulation with random initial. The blue symbols denote the bound obtained using the sum-of-squares method.

$$\dot{x}_{11} = \frac{3}{4}\left(\frac{\alpha}{\alpha^2+1}\right)x_1x_{12} - 2\left(\frac{\alpha}{\alpha^2+4}\right)x_2x_8 + \frac{3}{4}\left(\frac{\alpha}{4\alpha^2+1}\right)x_3x_{10}$$
$$-\frac{5}{4}\left(\frac{\alpha}{4\alpha^2+1}\right)x_3x_{13} + \frac{5}{4}\left(\frac{\alpha}{4\alpha^2+1}\right)x_3x_{14} - \frac{3}{4}\left(\frac{\alpha}{4\alpha^2+1}\right)x_3x_{15} - \frac{5}{4}\left(\frac{\alpha}{\alpha^2+9}\right)x_4x_{12}$$
$$+\frac{5}{4}\left(\frac{\alpha}{9\alpha^2+1}\right)x_5x_{12} - \frac{3}{4}\left(\frac{\alpha}{9\alpha^2+9}\right)x_6x_{12} - (\alpha^2+4)x_{11} - \frac{\alpha}{\alpha^2+4}x_2, \quad (100)$$

$$\dot{x}_{12} = -\frac{3}{4}\left(\frac{\alpha}{\alpha^2+1}\right)x_1x_{11} + \frac{3}{4}\left(\frac{\alpha}{\alpha^2+4}\right)x_2x_{10} - \frac{5}{4}\left(\frac{\alpha}{\alpha^2+4}\right)x_2x_{13} - \frac{5}{4}\left(\frac{\alpha}{\alpha^2+4}\right)x_2x_{14}$$
$$+\frac{3}{4}\left(\frac{\alpha}{\alpha^2+4}\right)x_2x_{15} - 2\left(\frac{\alpha}{4\alpha^2+1}\right)x_3x_7 + \frac{5}{4}\left(\frac{\alpha}{\alpha^2+9}\right)x_4x_{11} - \frac{5}{4}\left(\frac{\alpha}{9\alpha^2+1}\right)x_5x_{11}$$
$$+\frac{3}{4}\left(\frac{\alpha}{9\alpha^2+9}\right)x_6x_{11} - (4\alpha^2+1)x_{12} - 2\frac{\alpha}{4\alpha^2+1}x_3, \quad (101)$$

$$\dot{x}_{13} = \left(\frac{\alpha}{\alpha^2+1}\right)x_1x_7 - 2\left(\frac{\alpha}{\alpha^2+1}\right)x_1x_8 + \frac{5}{4}\left(\frac{\alpha}{\alpha^2+4}\right)x_2x_{12} + \frac{5}{4}\left(\frac{\alpha}{4\alpha^2+1}\right)x_3x_{11}$$
$$-3\left(\frac{\alpha}{\alpha^2+9}\right)x_4x_9 - (\alpha^2+9)x_{13} - \frac{\alpha}{\alpha^2+9}x_4, \quad (102)$$

$$\dot{x}_{14} = \frac{5}{4}\left(\frac{\alpha}{\alpha^2+4}\right)x_2x_{12} - \frac{5}{4}\left(\frac{\alpha}{4\alpha^2+1}\right)x_3x_{11} - 3\left(\frac{\alpha}{9\alpha^2+1}\right)x_5x_7$$
$$+3\left(\frac{\alpha}{9\alpha^2+9}\right)x_6x_7 - 6\left(\frac{\alpha}{9\alpha^2+9}\right)x_6x_8 - (9\alpha^2+1)x_{14} - 3\frac{\alpha}{9\alpha^2+1}x_5, \quad (103)$$

$$\dot{x}_{15} = -\frac{3}{4}\left(\frac{\alpha}{\alpha^2+4}\right)x_2x_{12} + \frac{3}{4}\left(\frac{\alpha}{4\alpha^2+1}\right)x_3x_{11} + 3\left(\frac{\alpha}{9\alpha^2+1}\right)x_5x_7$$
$$-6\left(\frac{\alpha}{9\alpha^2+1}\right)x_5x_8 - 9\left(\frac{\alpha}{9\alpha^2+9}\right)x_6x_9 - (9\alpha^2+9)x_{15} - 3\frac{\alpha}{9\alpha^2+9}x_6. \quad (104)$$

This 15-mode model satisfies both the energy conservation property as well as the vorticity integral identity. There are four different truncated expressions of the Nusselt number (all equivalent) can be calculated for this model. The one we use for bounding purposes is given by,

$$\overline{Nu} = 1 - 2\overline{x_7} - 4\overline{x_8} - 6\overline{x_9}. \quad (105)$$

6.1 Bounds on heat transfer

The figure (8) shows the results for the 15-mode model. For this case, so far, we have calculated the bounds using a four-degree polynomial. In the future, we will obtain bounds using higher degree polynomial. Bounds from the four-degree polynomial saturate to heat transfer due to steady state before the emergence of the chaotic attractor. The figure (9) the flow structure corresponding to the braches which eventually tranfer the maximum heat in figure (8). These flow structures of steady states, however, are not entirely physical. Because the Rayleigh number at which these steady states branches first appear, the 15-mode truncation is not a good model of original governing equations (PDEs).

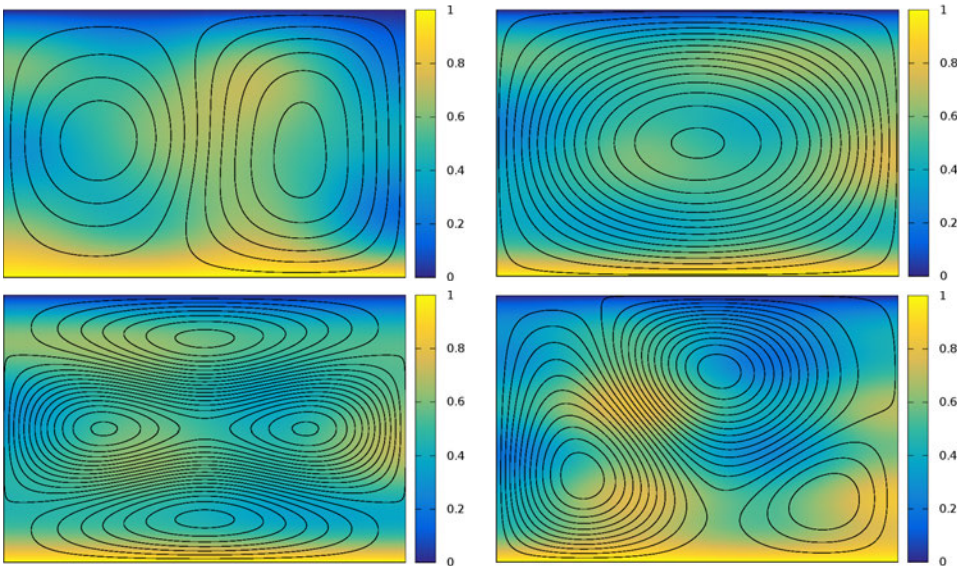

Figure 9: Steady states corresponding to four different branches which eventually maximize the heat transfer in figure (6). Color contours shows the temperature variation scaled with π, i.e., T/π. The lines show the streamlines. One can easily guess the flow direction by looking at the temperature variation. The Rayleigh number corresponding to each of these figures is close to the Rayleigh number when these steady-states branches first appear.

7 Conclusions and Future Work

We studied two truncated models of the Rayleigh–Bénard convection in a stress-free box. The 8-mode model satisfies the energy conservation property in the dissipationless limit. We obtain bounds on the heat transfer using the sum-of-squares method. Using a polynomial of two-degree bounds saturate to heat transfer due to steady states up to $Ra \lesssim 100$. For $Ra \gtrsim 150$ bounds saturate using an eight-degree polynomial. For the middle range, we suspect that there is a limit cycle which maximizes the heat transfer. Future work includes studying the effect of aspect ratio, similar to the study of Waleffe [12]. We want to check the hypothesis that if heat transfer due to steady states when optimized over wavenumber, gives the maximum possible heat transfer. Second, we want to study how variation in the Prandtl number changes the conclusions.

The 15-mode model satisfies both energy conservation property as well as the vorticity integral identity. For this case, so far, we have calculated the bounds using a four-degree polynomial. The bounds saturate to the steady-state before the emergence of the chaotic attractor. Future work for this model includes obtaining more strict bounds on heat transfer using higher degree polynomials.

Acknowledgement

I want to thank the program directors Bruce Sutherland, Claudia Cenedese and Karl Helfrich; principal lecturers Colm-cille Caulfield and Stephanie Waterman, and staff Janet

Fields and Julie Hildebrandt. I want to thank my advisors David Goluskin and Charles Doering for this beautiful problem and for their support. This program would not have been the same without softball; thanks to Charlie for coaching us. In the end, I would like to thanks all the fellows Houssam, Channing, André, Jeremy, Wanying, Lois, Kelsey, Alessia, Samuel, Jelle, and Wenjing for the wonderful summer.

References

[1] D. Goluskin, *Bounding averages rigorously using semidefinite programming: mean moments of the Lorenz system*, Journal of Nonlinear Science, 28 (2018), pp. 621–651.

[2] D. Goluskin and G. Fantuzzi, *Bounds on mean energy in the Kuramoto–Sivashinsky equation computed using semidefinite programming*, Nonlinearity, 32 (2019), p. 1705.

[3] L. N. Howard, *Convection at high Rayleigh number*, in Applied Mechanics, Springer, 1966, pp. 1109–1115.

[4] R. H. Kraichnan, *Turbulent thermal convection at arbitrary Prandtl number*, The Physics of Fluids, 5 (1962), pp. 1374–1389.

[5] E. N. Lorenz, *Deterministic nonperiodic flow*, Journal of the atmospheric sciences, 20 (1963), pp. 130–141.

[6] W. V. Malkus, *The heat transport and spectrum of thermal turbulence*, Proceedings of the Royal Society of London. Series A. Mathematical and Physical Sciences, 225 (1954), pp. 196–212.

[7] W. V. Malkus, *Non-periodic convection at high and low Prandtl number*, Mem. Societe Royale des Sciences de Liege, (1972), pp. 125–128.

[8] C. Priestley, *Convection from a large horizontal surface*, Australian Journal of Physics, 7 (1954), pp. 176–201.

[9] L. Rayleigh, *Lix. On convection currents in a horizontal layer of fluid, when the higher temperature is on the under side*, The London, Edinburgh, and Dublin Philosophical Magazine and Journal of Science, 32 (1916), pp. 529–546.

[10] E. A. Spiegel, *A generalization of the mixing-length theory of turbulent convection.*, The Astrophysical Journal, 138 (1963), p. 216.

[11] I. Tobasco, D. Goluskin, and C. R. Doering, *Optimal bounds and extremal trajectories for time averages in nonlinear dynamical systems*, Physics Letters A, 382 (2018), pp. 382–386.

[12] F. Waleffe, A. Boonkasame, and L. M. Smith, *Heat transport by coherent Rayleigh–Bénard convection*, Physics of Fluids, 27 (2015), p. 051702.

Exploiting Marginal Stability in Slow-Fast Quasilinear Dynamical Systems

Alessia Ferraro

August 21, 2019

Abstract

A new mathematical formalism that exploits the property of quasi-linear systems to self-tune towards marginally stable states is investigated. The inspiration for this study comes from the multi-scale analysis of strongly stratified flows, mathematically justified by the presence of scale separation, which yields to a simplified quasi-linear models. In this reduced description small-scale instabilities evolve linearly about a large-scale hydrostatic field (whose evolution is fully non-linear) and modify it via a feedback term. By analysing carefully constructed model problems, two different aspects of this reduced system are addressed. In the first case, a one-dimensional model is used to develop an algorithm capable of dealing with scenarios in which fluctuations exhibit positive growth rates on a fast time scale. In the second case an extension of the algorithm to a two-dimensional system is presented.

1 Introduction and Significance

Turbulence is ubiquitous in most of the geophysical flows relevant for the climate of the Earth, particularly in the oceans and the atmosphere. Turbulence involves the interaction of a vast range of spatiotemporal scales, as well as the coexistence of huge variety of physical phenomena. In the oceans, where energy is injected at global scales, $O(10^3 - 10^4)km$, and dissipation occurs at the Kolmogorov scale, $O(10)cm$ many different form of turbulence are manifest: while at the larger scales the combined effect of rotation and strong density stratification stirs the flow mainly on quasi-horizontal planes coincident with isopycnals, at the so-called microscale, $O(1 - 100)m$, turbulence is fully 3D and erodes the stable stratification. At this scale, the flow naturally develops an anisotropic layer structure, characterized by a vertical length scale h that is considerably smaller than the horizontal one (L) [8],[9]. The relative motion of these layers, gives rise to strong shear that can trigger small-scale instabilities, of Kelvin-Helmholtz and Holmboe type, introducing into the system an horizontal characteristic length scale comparable to layer thickness h. These small isotropic disturbances, although not resolved in numerical regional circulation and global climate models, play a fundamental role in the overall global circulation controlling the vertical mixing of denser water from the deep oceans.

Nevertheless several fundamental questions related to the strongly stratified turbulent regime are remain unanswered (e.g. the relative importance of spectrally local and non-local energy transfer and the importance of the initial stratification or the forcing mechanism on

mixing [13],[14],[10],[15]) making the parametrization of the small-scale processes a challenging task. The major obstacle in the investigation of the physical processes is the enormous range of scales that must be resolved in order to capture them. More precisely, the microscale spans from scales L that are small enough not to be affected by the Coriolis force to the Ozmidov scale $L_O = (\epsilon_h/N^3)^{1/2}$, the largest horizontal flow scale *not* to be influenced by stratification. Denoting by N the Brunt-Väisälä frequency, by $\epsilon_h \sim U^3/L$ the horizontal turbulent energy dissipation rate and by the horizontal Froude number $Fr_h = U/NL$ the inverse measure of the stratification strength, this scale range is then fixed by the last parameter, as the ratio $L/L_O = O(Fr_h^{-3/2})$. Thus, owing to the strong stratification ($Fr_h < 10^{-3}$) and the considerably high Reynolds number ($Re > 10^9$) required to achieve the strongly stratified turbulence regime, a full 3D direct simulation (DNS) would require a resolution of the order of 10^{18} grid points, far beyond current computational capabilities, as shown in figure 1 [16],[18],[17]. The development of new theoretical tools is therefore a prerequisite for further advancements in this subject. A better understanding of strongly stratified turbulence would not only provide a deeper insight on the role of the microscale in the global overturning circulation but it would also facilitate the development of new flow-control techniques.

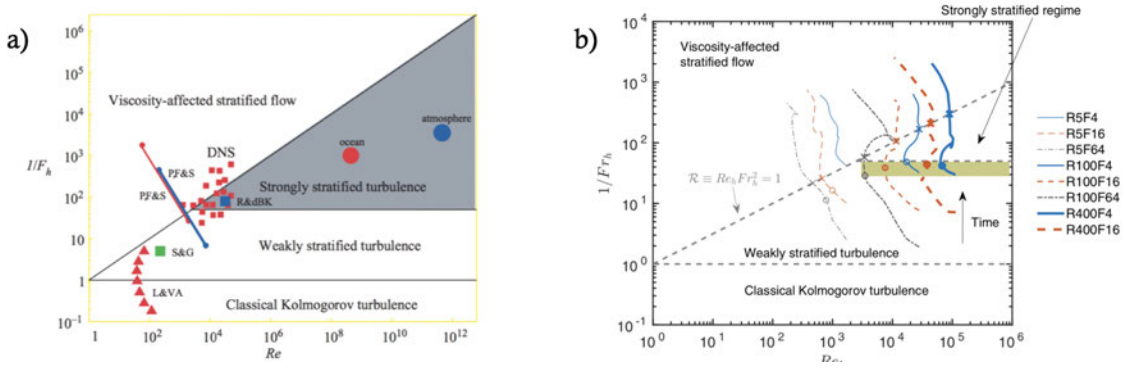

Figure 1: Stratified flow regime diagram as a function of the *Reynolds* number Re and the *Froude* number Fr a) from [16] and b) from [17]. Despite the huge increase of computational power over the past 12 years both diagrams show the gap in parameter space between the parameter regime numerically accessible and the one of interest for geophysical applications.

Scale separation in geophysical flows is very often related to the presence of a strong external constraint that is responsible for the coexistence of large-scale anisotropic and small-scale isotropic structures. This translates into the emergence of a dominant balance in the governing equations that can be mathematically exploited to derive simplified equations by means of multi-scale and asymptotic analysis. This approach has been successfully used by Julien and Knobloch to derive *reduced models* when rapid rotation or a strong magnetic field is applied to a flow system [2],[1] and by Rocha for flows subjected to strong stratification [4]. In the latter work, the multi-scale analysis of Boussinesq equations in the limit of small Fr_h number and large Re reveals two disparate spatiotemporal scales and yields to a set of coupled equations for the large anisotropic dynamics and the small-scale

disturbances. These two different spatiotemporal scales are indicated in equations (1.1)-(1.8) below by T, x for the slow dynamics and by $\tau = T/\epsilon$, $\chi = x/\epsilon$ for the fast dynamics where $\epsilon = \sqrt{Fr_h}$ is the small parameter in the multi-scale expansion. Denoting by $\mathbf{u}_\perp$, W, b, the horizontal velocity vector, the vertical velocity and the buoyancy deviation from a linear background profile, respectively, (1.1)-(1.4) show that in this specific limit the slowly varying fields (denoted by the overbar) obey the hydrostatic primitive equations and their dynamics is modified by the cumulative effect of the small-scale fluctuations (denoted by the prime) via the eddy momentum and the buoyancy fluxes highlighted in red. The evolution of the fast dynamical modes ((1.5)-(1.8)) instead, is described by a linear and homogeneous system coupled to the slow dynamics via the mean-field coefficients highlighted in blue. An interesting feature of this reduced system is the two-ways coupling between the slow and the fast dynamics: the feedback produced by the fluctuations on the mean variable is not sign-definite meaning that its effect may be stabilizing or destabilizing in nature.

$$\partial_T \overline{\mathbf{u}}_\perp + \overline{\mathbf{u}}_\perp \cdot \nabla_{x_\perp} \overline{\mathbf{u}}_\perp + \overline{W} \partial_z \overline{\mathbf{u}}_\perp = -\nabla_{x_\perp} \overline{p} - \partial_z (\overline{W' \mathbf{u}'_\perp}) + \frac{1}{Re_b} \partial_z^2 \overline{\mathbf{u}}_\perp + \overline{\mathbf{f}}_\perp \tag{1.1}$$

$$0 = -\partial_z \overline{p} + \overline{b} \tag{1.2}$$

$$\partial_T \overline{\mathbf{u}}_\perp + \overline{\mathbf{u}}_\perp \cdot \nabla_{x_\perp} \overline{\mathbf{u}}_\perp + \overline{W} \partial_z \overline{b} = -\overline{W} - \partial_z (\overline{W' b'_\perp}) + \frac{1}{PrRe_b} \partial_z^2 \overline{b} \tag{1.3}$$

$$\overline{\nabla} \cdot \overline{\mathbf{u}}_\perp + \partial_z \overline{W} = 0 \tag{1.4}$$

$$\partial_\tau \mathbf{u}'_\perp + \overline{\mathbf{u}}_\perp \cdot \nabla_{\chi_\perp} \mathbf{u}'_\perp + W' \partial_z \overline{\mathbf{u}}_\perp = -\nabla_{\chi_\perp} p' + \frac{Fr_h}{Re_b} (\nabla^2_{\chi_\perp} + \partial_z^2) \mathbf{u}'_\perp \tag{1.5}$$

$$\partial_\tau W' + \overline{\mathbf{u}}_\perp \cdot \nabla_{\chi_\perp} W' = -\partial_z p' + b' + \frac{Fr_h}{Re_b} (\nabla^2_{\chi_\perp} + \partial_z^2) W' \tag{1.6}$$

$$\partial_\tau \mathbf{u}'_\perp + \overline{\mathbf{u}}_\perp \cdot \nabla_{\chi_\perp} \mathbf{b}' + W' \partial_z \overline{b} = -W' + \frac{Fr_h}{PrRe_b} \left(\nabla^2_{\chi_\perp} + \partial_z^2 \right) b' \tag{1.7}$$

$$\nabla^2_{\chi_\perp} \cdot u'_\perp + \partial_z W' = 0 \tag{1.8}$$

The resulting system may be viewed as a generalized quasi-linear model (GQL), in that the evolution of the fast variables is linearized around slowly varying mean fields and the fluctuation-fluctuation interactions are retained only when they feed back onto the mean flow. Although the quasi-linear (QL) approximation has been used in the past to enable the investigation of simplified flow systems [19], here it should be emphasized that the quasi-linearity is an intrinsic feature of the asymptotic behaviour of the strongly-stratified dynamical system and not the result of an *ad hoc* approximation. Owing to the linearized evolution of the fluctuations, the first issue concerning slow-fast QL systems is related to the

choice of a suitable integration method. Although co-evolution of the mean and fluctuation dynamics on the same fast temporal scale (i.e. the single-time QL algorithm) may ensure accuracy, it does not take computational advantage of the multi-scale nature of the system. On the other hand, the application of the heterogeneous multi-scale algorithm, although more efficient, introduces many arbitrary choices for the inizialization and the duration of the fast-time integrations.

Based on the observation that many slow-fast QL systems have the tendency of self-organize around marginally stable states, Michel & Chini [3] have recently proposed a new integration strategy that exploits a marginal stability constraint. Building upon their work, the present study aims to further develop this methodology, with the final goal of tailoring a numerical algorithm for simulations of the reduced Boussinesq equations in the strongly-stratified regime relevant to the ocean. This goal will be pursued by making use of two different model problems, each designed to serve a distinct purpose: in section 2 the twofold nature of the feedback terms will be addressed on a 1D model problem, while in section 3 an extension of the algorithm to a 2D QL model will be presented.

2 1D Model Problem

In the following section, we will first illustrate the methodology, retracing the fundamental steps in the development by Michel & Chini [3], and then investigate the stabilizing nature of the fluctuation-induced feedback on the slow dynamics.

In this first example the slow field $U(z,t)$ and the fast fluctuations $\eta(z,t)$ evolve according to

$$\frac{\partial U}{\partial t} = F - \nu U - \eta^2 e^{-U^2} \tag{2.1}$$

$$\epsilon \frac{\partial \eta}{\partial t} = U\eta e^{-U^2} + \frac{\partial^2 \eta}{\partial z^2} - \epsilon \eta^3 \tag{2.2}$$

where $F(z,t)$ is a space and time dependent forcing and νU is a linear damping. As in the stratified flow problem the slow variable feels the effect of the fluctuations via a quadratic feedback, here multiplied by the exponential term in (2.1), $\eta^2 e^{-U^2}$; and the fluctuations in turn are "advected" by the mean flow via the term $U\eta e^{-U^2}$. The scale separation is set by the small parameter ϵ in (2.2) (analogous of the Fr number in the reduced Boussinesq equations).

Explicitly taking into account the temporal scale separation by introducing two time scales $t \to (T, \tau)$, with $T = t$ and $\tau = T/\epsilon$ and positing the following asymptotic expansions for U and η

$$U = U_0 + \epsilon U_1 + \epsilon^2 U_2 + O(\epsilon^3) \tag{2.3}$$

$$\eta = \eta_0 + \epsilon \eta_1 + \epsilon^2 \eta_2 + O(\epsilon^3) \tag{2.4}$$

a two-scale reduced system governing the leading-order dynamics ($O(1)$ for the mean variable and $O(1/\epsilon)$ for the fluctuations) can be obtained [3]:

$$\frac{\partial U_0}{\partial T} = F - \nu U_0 - \overline{\eta_0^2} e^{-U_0^2} \tag{2.5}$$

$$\frac{\partial \eta_0}{\partial \tau} = U_0 e^{-U_0^2} \eta_0 + \frac{\partial^2}{\partial z^2} \eta_0 \tag{2.6}$$

where the overbar $\overline{(\cdot)}$ indicates an average over the fast time τ and $U_0 = U_0(z, T)$, only. Because the evolution equation for the fluctuations is linear and homogeneous in the fluctuation field and autonomous in the fast time τ, it is not restrictive to assume solutions of the form $\eta_0 = A(T)\hat{\eta}_0(z, T)e^{\sigma(T)\tau}$ where $A(T)$ is a slowly varying amplitude; $\hat{\eta}_0(z, T)$ is a vertical structure function; and $\sigma(T)$ is a growth rate. Substituting this ansatz into (2.5)-(2.6), it is immediately clear that for the feedback term to be physically meaningful the fast-time average (2.7) has to converge, excluding then the possibility for positive growth rates if $A(T) \neq 0$. If $\sigma < 0$ there is an exponential decay ($\sigma < 0$) of the fluctuations on the fast time scale and, hence, a zero feedback on the slow dynamics; consistently $A(T)$ is set to zero in this case. If $\sigma > 0$, however, the fluctuation field could grow without bound while the mean field U_0 remains "frozen", invalidating the asymptotic scaling (unless $A(T)$ =0). This observation suggests that the system naturally selects a zero growth rate by self-adjusting to a marginally stable state. Correspondingly the asymptotic analysis must attempt to enforce the condition $\sigma \leq 0$.

$$\overline{\eta_0^2} = |A|^2 |\hat{\eta}_0|^2 \lim_{\tau_f \to \infty} \frac{1}{\tau_f} \int_0^{\tau_f} e^{\sigma\tau} d\tau \tag{2.7}$$

Therefore, the simplified equations for the leading-order dynamics can be reduced to an initial-value problem for the evolution of U_0 and to an eigenvalue problem for the fluctuations $\hat{\eta}_0$ being the vertical eigenfunction associated with the zero eigenvalue σ_0:

$$\frac{\partial U_0}{\partial T} = F - \nu U_0 - |A|^2 |\hat{\eta}_0|^2 e^{-U_0^2}, \tag{2.8}$$

$$\sigma \hat{\eta}_0 = \left(U_0 e^{-U_0^2} + \frac{\partial^2}{\partial z^2} \right) \hat{\eta}_0, \tag{2.9}$$

where the linear operator

$$\mathcal{L} = U_0 e^{-U_0^2} + \frac{\partial^2}{\partial z^2} \ . \tag{2.10}$$

Notice that the operator $\mathcal{L}$ is self-adjoint and singular with a 1D nullspace.

The fast and slow dynamics are now coupled by the presence of an unknown amplitude for which an evolution equation has to be derived. As shown in Michel & Chini [3], the standard procedure of imposing a solvability condition on the higher-order terms in the expansion of η does not yield in this case to a closed set of equations, and an alternative constraint has to be found. The key idea of this new approach is to exploit the natural

tendency of the slow dynamics to evolve near to a state of marginal stability, as noted above, in order to prescribe the fluctuation amplitude required to maintain that state. Consequently the slow time derivative of the growth rate has to be zero whenever the growth rate $\sigma = \sigma_0 \equiv 0$. To derive the necessary condition, we take the slow time derivative of the leading-order eigenvalue problem (2.9):

$$\mathcal{L}\frac{\partial \hat{\eta_0}}{\partial T} = -\left(\frac{\partial \mathcal{L}}{\partial T}\right)\hat{\eta_0} + \frac{d\sigma}{dT}\hat{\eta_0} + \sigma\frac{\partial \hat{\eta_0}}{\partial T} \tag{2.11}$$

$$\mathcal{L}\frac{\partial \hat{\eta_0}}{\partial T} = (1-2U_0^2)\frac{\partial U_0}{\partial T}e^{-U_0^2} + \frac{d\sigma}{dT} \tag{2.12}$$

upon setting $\sigma = \sigma_0 = 0$. For (2.12) to be solvable the Freedholm alternative (solvability condition) requires the right-hand side of (2.12) to be perpendicular to the nullspace of the adjoint operator $\mathcal{L}^\dagger$, which in this case is $\mathcal{L}$ itself. Thus, taking the inner product of (2.12) with $\hat{\eta_0}$ and using the normalization $\int_0^{L_z} |\hat{\eta_0}|^2 dz = 1$, an evolution equation for the growth rate on the slow time scale can be obtained

$$(\mathcal{L}\partial_T\hat{\eta_0}, \hat{\eta_0}^\dagger) = (\partial_T\hat{\eta_0}, \mathcal{L}^\dagger\eta_0^\dagger) = 0 \tag{2.13}$$

$$(\mathcal{L}\partial_T\hat{\eta_0}, \hat{\eta_0}^*) = \int_0^{L_z}\left((1-2U_0^2)\frac{\partial U_0}{\partial T}e^{-U_0^2} + \frac{d\sigma}{dT}\right)|\hat{\eta_0}|^2 dz \tag{2.14}$$

$$\frac{d\sigma}{dT} = \int_0^{L_z}(1-2U_0^2)(F-\nu U_0)e^{-U_0^2}|\hat{\eta_0}|^2 dz - |A|^2\int_0^{L_z}(1-2U_0^2)e^{-2U_0^2}|\hat{\eta_0}|^4 dz \tag{2.15}$$

Renaming the two integrals in (2.15) as

$$\alpha = \int_0^{L_z}(1-2U_0^2)(F-\nu U_0)e^{-U_0^2}|\hat{\eta_0}|^2 dz, \qquad \beta = \int_0^{L_z}(1-2U_0^2)e^{-2U_0^2}|\hat{\eta_0}|^4 dz \tag{2.16}$$

yields

$$\frac{d\sigma}{dT} = \alpha - |A|^2\beta. \tag{2.17}$$

Imposing the marginal stability condition $d_T\sigma = 0$ when $\sigma(T) = 0$, yields an expression for the amplitude that ensures the slow dynamics remains tangent to the marginally stable manifold:

$$A = \sqrt{\alpha/\beta} \tag{2.18}$$

It is straightforward to notice that the amplitude expression (2.18) is only defined for positive ratios of α and β. In this example, as in the stratified flow problem, however either α nor β is sign-definite. While negative values of α increase the stability of the system, eventually leading to a zero amplitude for the fluctuations (as is clear from (2.17)), negative

values of β necessarily drive the system away from the marginally stable condition. In the latter scenario, the marginally stable manifold ceases to exist and the fluctuations quickly attain an asymptotically large magnitude due to the linear instability mechanism. This inevitably causes the slow variable U_0 to respond on the fast time scale, resulting in a bursting dynamics, that eliminates the scale separation initially present in the system. In order to accommodate turbulent events associated to positive growth rates the two fields must be co-evolved on the fast time scale until the marginal-stability manifold is restored, i.e. until $\sigma = 0$ again. As pointed out in [3], the integration of the initial finite-ϵ set of equations (2.1)-(2.2) is not the only co-evolution strategy that is appropriate for this fast dynamical regime. Instead, by positing the modified asymptotic expansions

$$\begin{aligned} U &= U_0 + \epsilon U_1 + \epsilon^2 U_2 + O(\epsilon^3), \\ \eta &= \frac{1}{\sqrt{\epsilon}}\eta_0 + \sqrt{\epsilon}\eta_1 + \epsilon\sqrt{\epsilon}\eta_2 + O(\epsilon^2\sqrt{\epsilon}), \end{aligned} \tag{2.19}$$

which incorporate the asymptotic amplification of η, the following modified reduced system is obtained:

$$\frac{\partial U_0}{\partial \tau} = -\eta_0^2 e^{-U_0^2} \tag{2.20}$$

$$\frac{\partial \eta_0}{\partial \tau} = U_0 \eta_0 e^{-U_0^2} + \frac{\partial^2 \eta_0}{\partial z^2} - \eta_0^3 \tag{2.21}$$

Equation (2.21) retains the cubic non-linearity present in the original set of equations, mechanism responsible for the saturation of the exponentially growing instabilities, and thus (2.20)-(2.21) is not of QL form. Nevertheless, the system (2.20)-(2.21) has the great computational advantage of not including the small parameter ϵ, allowing for larger numerical time-steps.

A further option to integrate the reduced system (2.8)-(2.9) when bursting events occur and no fluctuation amplitude can be determined, is inspired by gradient descent techniques. Because of the fast and abrupt growth of the fluctuations in this regime it is reasonable to assume they dominate the evolution equation of the mean variable U_0, making the forcing F and the damping νU negligible (as also confirmed by the asymptotic analysis above). Then, although $A(T)$ is unknown, the mean variable U_0 can be updated in the direction that minimizes $d_T\sigma$ making use of the eigenfunction $\hat{\eta}_0$ resulting from the linear eigenvalue problem (2.9):

$$\frac{\partial U_0}{\partial T} = C|\hat{\eta}_0|^2 e^{-U_0^2} \tag{2.22}$$

where C is an arbitrary constant.

2.1 Numerical Implementation and Results

The accuracy of the reduced QL algorithm presented above has been assessed via comparison with the results obtained from direct numerical simulations of the full system. A Python code was written in-house and implemented within the open-source framework Dedalus [5], for this purpose. All of the simulations are performed with a second-order Runge Kutta time-stepping algorithm ($dt = 10^{-2}$ for the QL model and $dt = 5 \times 10^{-3}$ for the DNS) a damping coefficient $\nu = 1$ and a forcing term $F = 1+0.5cos(z)$. The original set of equations (2.1)-(2.2) and the corresponding reduced model (2.8)-(2.9) are solved in a periodic domain with $L_z = 2\pi$ using a Fourier and Chebyshev discretization scheme respectively, with 64 grid points in each case. The use of a Chebyshev spectral method, although not optimal for problems having periodic boundary conditions, is dictated by the necessity of solving the eigenvalue problem with non-constant coefficients (2.9) within the Dedalus framework, which is presently only possible using Chebyshev polynomials.
The small parameter ϵ in the full system, responsible for the scale separation, is fixed to 0.02 and the initial condition for the fluctuations, only needed in the finite-ϵ DNS, to $\eta_0(z,t) = cos(z)$.

In the first test case the initial condition for the mean variable is $U_0(z,0) = -1$, corresponding to a stable state of the slow dynamics. Since the initial growth is negative, the amplitude of the fluctuations is initially set to zero. Accordingly, the mean field U_0 is updated on the slow time scale in absence of the feedback, only subject to the action of forcing and damping, until the marginal-stability is reached.
Once the real part of σ, whose value together with the eigenfunction $\hat{\eta}_0$ are obtained by solving the linear eigenvalue problem, approaches zero the amplitude $A(T)$ is computed using (2.18).
The results obtained from the QL model are compared to those obtained from the DNS in figures 2 and 3, where space-time diagrams of the slow variable $U_0(z,t)$ and of the fluctuations η_0 respectively, are presented. As is clearly evident, the reduced model not only to qualitatively captures the long term dynamics of the full system but also the detailed quantitative features of the structures underlying it, from the wavelength to the amplitude and the phase. This agreement between the QL model (a) and the DNS (b) is even more remarkable given the finite value of ϵ chosen to set the scale separation in the full system.

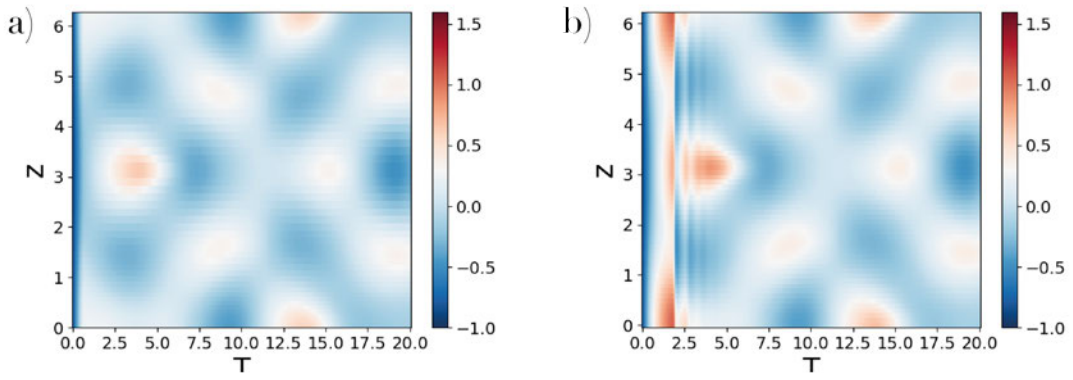

Figure 2: Space-time evolution of the slow variable U_0 resulting from a) the QL model simulation and b) the DNS at $\epsilon = 0.02$.

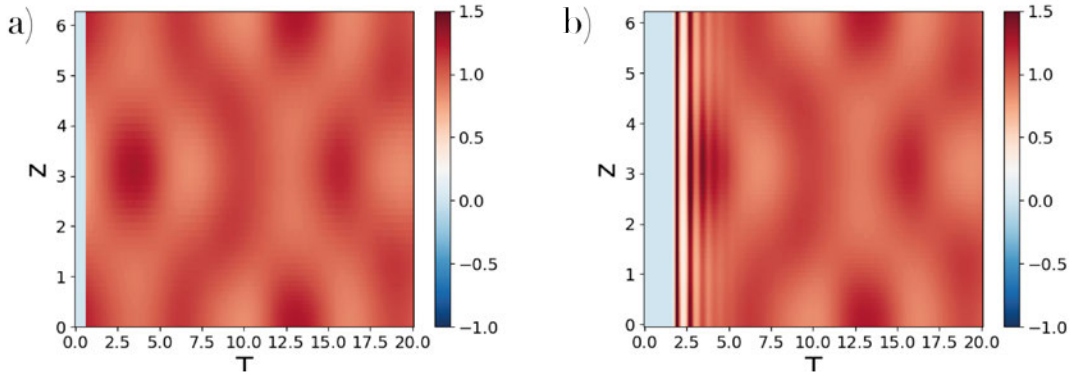

Figure 3: Space-time evolution of the (fast) fluctuation field η_0 obtained from a) the QL model and b) the DNS at $\epsilon = 0.02$.

The only significant observable difference in the two dynamics relates to the initial transient. As evident in figure 4, where the energy of the mean field (in black) and the fluctuation (in red) both for the QL simulation (dashed line) and the DNS are shown, the full system exhibits fast bursting events before relaxing onto the marginally stable manifold while it occurs instantaneously in the reduced system because of the slaving of the amplitude. From figure 5(a), which shows the evolution of the real part of the growth rate on the slow time scale, this test case does not exhibit fast bursting events: once the marginal stability condition is reached, it is maintained for the entire duration of the simulation.

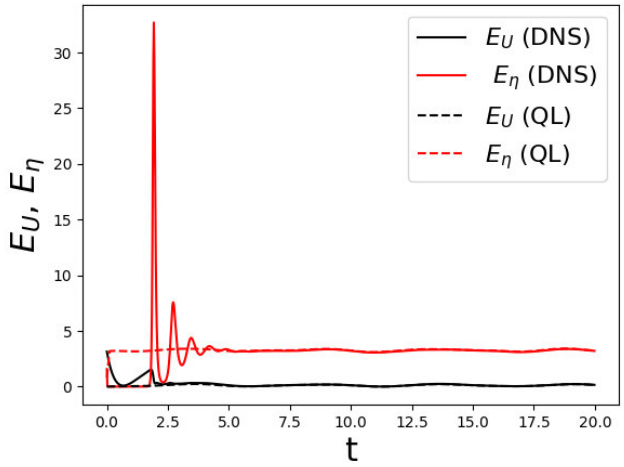

Figure 4: Time series of the fluctuation energy (in red) and the mean field energy (in black) from the QL model simulations (dashed lines) and the DNS at $\epsilon = 0.02$ (solid lines)

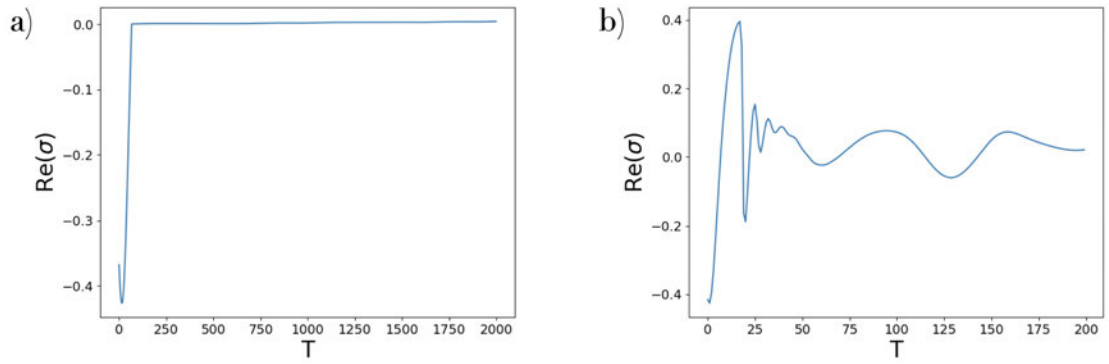

Figure 5: Temporal evolution of the growth rate σ associated to the linear eigenvalue problem a) on the slow time for the QL model and b) on the fast time for the DNS when starting from a stable initial condition $U_0(z, 0) = -1$

To assess the efficacy of the three strategies presented in section 2, for coping with fluctuation events associated either with an initial positive growth rate or with subsequent occurrences of positive feedback (i.e. $\beta < 0$) for $\sigma = 0$, the second test case has been initialized with a positive initial condition $U_0(z, 0) = 1$, corresponding to an unstable state. That is, co-evolution of the two fields is necessary if either the initial state is already characterized by $\sigma > 0$ or whenever $\beta < 0$, meaning that the fluctuation-induced feedback has a destabilizing effect on the mean field. In the specific case presented here, both of these conditions happen to be satisfied at the initial time.

Figure 6 shows the evolution of the growth rate during the same co-evolution event

simulated using the three different techniques: finite-ϵ DNS (eq. (2.1)-(2.2)), ϵ-free DNS (eq. (2.20)-(2.21)) and gradient descent (eq.(2.22)). The initial conditions for the fluctuations necessary to initialize the DNS in the first two cases are generated using the eigenfunction $\hat{\eta}_0$ resulting from the linear eigenvalue problem and the amplitude computed in the previous iteration or a randomly generated one when no amplitude is available (as in this case where co-evolution happens at $t = 0$) or is zero. The higher efficiency, in terms of number of time steps required to return to a (marginally) stable condition, of the last two methods is attributable to the absence of the small parameter ϵ, allowing for a time step about two orders of magnitude larger than the one used for the full DNS.

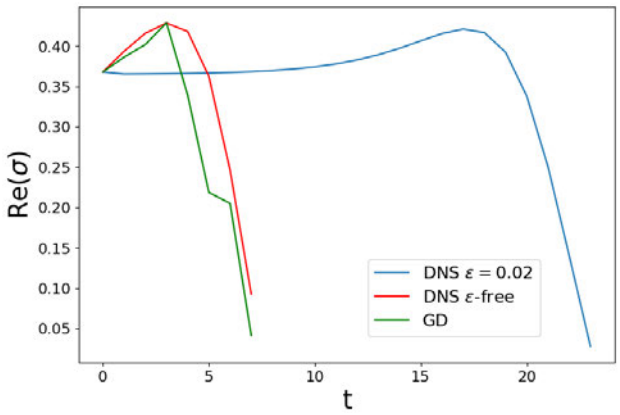

Figure 6: Comparison between the temporal evolution of the real part of the growth rate σ during a co-evolution event simulated using three different techniques: finite-ϵ DNS (blue), ϵ-free DNS (red), gradient descend (green).

Figure 7 shows a flowchart of the algorithm developed for this 1D model problem, highlighting with different colors the three possible satbility scenarios and summarizing the logical steps implemented in each of those.

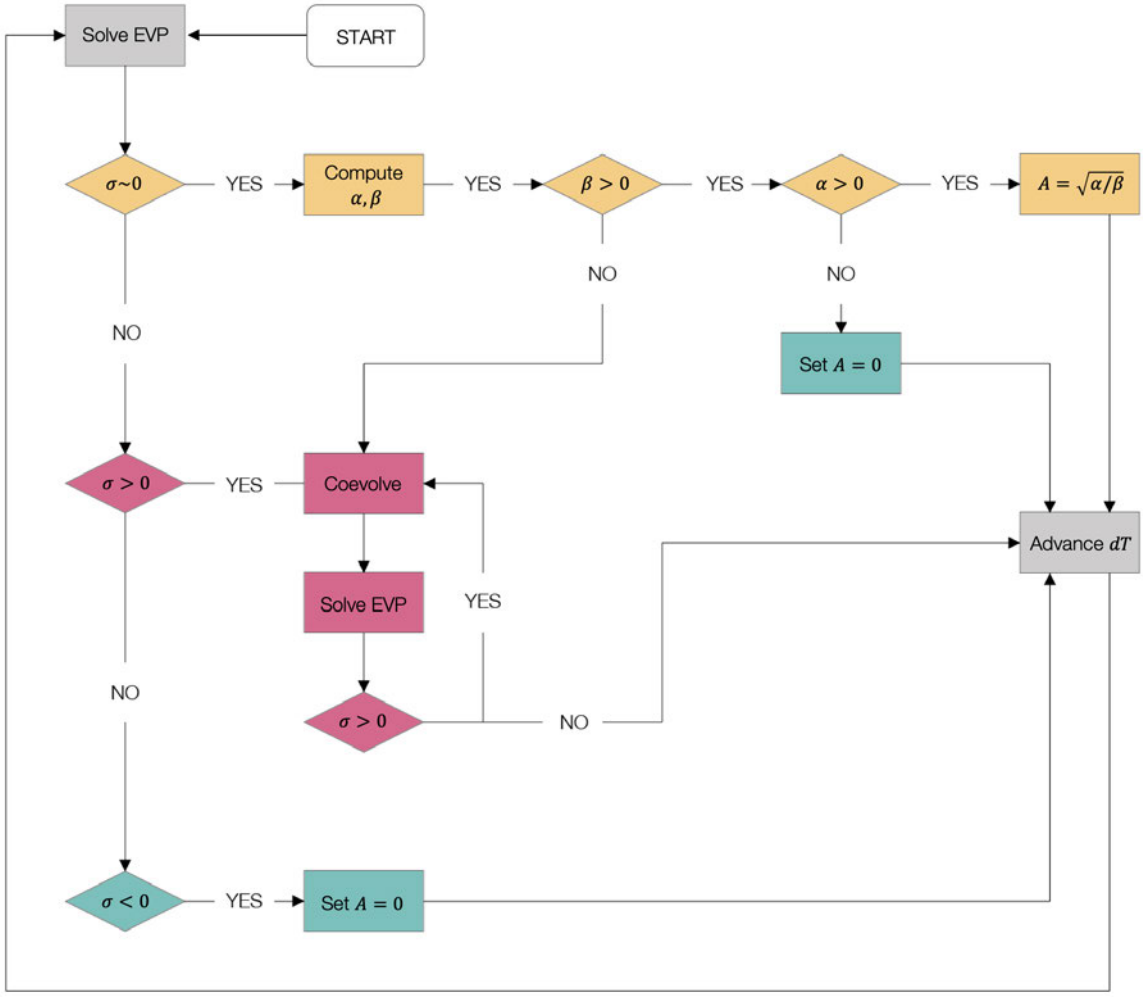

Figure 7: Flowchart of the 1D QL algorithm. The loop is started by solving the linear eigenvalue problem for the maximum growth rate σ and the corresponding eigenfunction $\hat{\eta}_0$. When negative growth rates characterize the state of the system, the green blocks are executed: the slowly-varying amplitude of the fluctuation is set to zero and the mean field is updated on the slow time scale without any feedback term. Once marginal stability (zero growth rate) is realized the slaving of the amplitude activates (blocks in yellow) and the mean field is updated on the slow time with the amplitude prescribed to ensure its marginal stability. The red circuit is entered whenever an unstable ($\sigma > 0$) or potentially unstable ($\beta < 0$) situation is realized. The mean field and the fluctuations are time-stepped together on the fast time scale until the growth rate resulting from the linear eigenvalue problem again becomes non-positive.

3 2D Model Problem

Inspired by the stratified flow system, where the layers exhibit an horizontal structure and the mean flow, we have designed a model problem to capture this features and extend the algorithm presented in the previous section to the 2D case.

The slow-evolving variable $U(x,z,t)$ and the fluctuations $\eta(x,z,t)$ now satisfy the following set of equations

$$\frac{\partial U}{\partial t} + U\frac{\partial U}{\partial x} = F(x,z,t) - \nu U - \epsilon^2 \left(\frac{\partial \eta}{\partial x}\right)^2 + D\left(\frac{\partial^2}{\partial x^2} + \frac{\partial^2}{\partial z^2}\right) U \tag{3.1}$$

$$\epsilon\frac{\partial \eta}{\partial t} = -\eta - \epsilon^2 U\frac{\partial^2 \eta}{\partial x^2} - \epsilon^4\frac{\partial^4 \eta}{\partial x^4} + \frac{\partial^2 \eta}{\partial z^2} - \epsilon\eta^3 \tag{3.2}$$

In addition to the previous case, where the dynamics of the mean field was controlled by an external forcing , a linear damping and the cumulative effect of the fast modes, here we introduce a diffusive and an inertial term, like in the Boussinesq equation (1.1). The fluctuation feedback in 3.1, also has been replaced by a flux-type term, suggestive of the eddy flux and buoyancy flux in real system. As regards the fluctuations the evolution equation is a modified version of the Swift-Hohenberg operator $\partial_t\psi = r\psi - (1+\nabla^2)^2\psi + \mathcal{N}(\psi)$ where the bifurcation parameter r is here the mean field $U(x,t)$ and it multiplies the second term on the right-hand side instead of the first one. The reason behind this choice is to provide a playground as near to reality as possible but relatively more controllable and comparable to known cases.

As done in §2, owing the scale separation due to the small parameter ϵ, we apply multi-scale analysis, this time introducing a slow-fast time scale and a large-small spatial scale.

$$\begin{aligned} t &\to (T,\tau) \qquad & T &= t \text{ and } \tau = T/\epsilon \\ x &\to (X,\chi) \qquad & X &= x \text{ and } \chi = X/\epsilon \end{aligned}$$

$$\begin{aligned} U &= U_0 + \epsilon U_1 + \epsilon^2 U_2 + O(\epsilon^3) \\ \eta &= \eta_0 + \epsilon\eta_1 + \epsilon^2\eta_2 + O(\epsilon^3) \\ F &= F_0 + \epsilon F_1 + \epsilon^2 F_2 + O(\epsilon^3) \end{aligned}$$

Solving the first equation (3.1) order by order in ϵ, the independency of U of the fast time τ is obtained at order $O(\epsilon^{-1})$ (being $\partial_\tau U_0 = 0$) and the reduced dynamics at $O(1)$

$$\frac{\partial U_0}{\partial T} + \frac{\partial U_1}{\partial \tau} + U_0\frac{\partial U_0}{\partial x} + U_0\frac{\partial U_1}{\partial \chi} + U_1\frac{\partial U_0}{\partial \chi} = F - \nu U_0 + D\frac{\partial^2 U_0}{\partial z^2} - \left(\frac{\partial \eta_0}{\partial \chi}\right)^2 \tag{3.3}$$

Introducing then the average over fast time τ and space χ defined for a generic function ψ as

$$\overline{\psi}(x,z,t,\epsilon) = \lim_{\tau_f, L_{\chi_f}\to\infty} \int_0^{\tau_f}\int_0^{L_{\chi_f}} \psi(\chi,x,z,\tau,t,\epsilon)d\tau d\chi \tag{3.4}$$

the final evolution equation for the mean variable $U_0(\chi,x,z,t,\epsilon)$ reads

$$\frac{\partial U_0}{\partial T} + U_0\frac{\partial U_0}{\partial x} = F - \nu U_0 + D\frac{\partial^2 U_0}{\partial z^2} - \overline{\left(\frac{\partial \eta_0}{\partial \chi}\right)^2} \tag{3.5}$$

As for the fluctuation field the dynamics at the leading order $O(\epsilon^{-1})$ results

$$\frac{\partial \eta_0}{\partial \tau} = -\eta_0 - U_0\frac{\partial^2 \eta_0}{\partial \chi^2} - \frac{\partial^4 \eta_0}{\partial \chi^4} + \frac{\partial^2 \eta}{\partial z^2} \tag{3.6}$$

Not surprisingly the evolution equation for the fast modes is again linear and homogeneous and modal solutions are allowed

$$\eta_0 = A(T)\hat{\eta}_0(x,T)e^{\sigma(T)\tau}e^{ik(T)\chi} + c.c. \tag{3.7}$$

where $A(T)$ a real amplitude, the real part of σ is the growth rate and k the horizontal wave number. Substituting the ansatz (3.7) into (3.5)-(3.6) the Generalized Quasi Linear (GQL) model is obtained

$$\frac{\partial U_0}{\partial T} + U_0\frac{\partial U_0}{\partial x} = F - \nu U_0 + D\frac{\partial^2 U_0}{\partial z^2} - 2|A|^2k^2|\hat{\eta}_0|^2 \tag{3.8}$$

$$\sigma\hat{\eta}_0 = \left(-1 + k^2U_0 - k^4 + \frac{\partial^2}{\partial z^2}\right)\hat{\eta}_0 \tag{3.9}$$

We point out that the marginal stability requirement, necessary for the feedback term in (3.5) not to blow up (see §2), has been already taken in to account substituting a zero growth rate while fast averaging over τ and χ.
The backbone of the model, consisting of an initial value problem for the slow variable and an eigenvalue problem for the fast one, reoccurs in this 2D example with the major differences being the k-structure of the fluctuations and the dependence of the mean field on slow x. The latter feature, introduced by the convective term in (3.1), allows for the interaction between low Fourier modes, turning the strict mean U_0 in a slow varying mean (hence the categorization under Generalized Quasi Linear model)

Although of fundamental importance in the real stratified flow system, for purposes of simplifications the dependence of U_0 on the slow coordinate x (and thus the presence of convective term) will be from now on neglected, postponing the investigation to future work.

3.1 Algorithm for Strict QL Models

The elimination of the slow spatial coordinate x from (3.1)-(3.2) leads to the following strict QL system:

$$\frac{\partial U_0}{\partial T} = F(z,T) - \nu U_0 - 2k^2|A|^2|\hat{\eta}_0|^2 + D\frac{\partial^2 U_0}{\partial z^2} \tag{3.10}$$

$$\sigma\hat{\eta}_0 = \left(-1 + k^2 U_0 - k^4 + \frac{\partial^2}{\partial z^2}\right)\hat{\eta}_0 \equiv \mathcal{L}\hat{\eta}_0 \tag{3.11}$$

where the average over the fast spatial coordinate χ in 3.4 is now interpreted as a strict streamwise average.

By inspection of (3.11) that the linear operator $\mathcal{L}$ is again singular and self-adjoint as in the 1D case but now also depends on the wavenumber k. This dependency introduces the need for an additional constraint on the growth rate in order to ensure the marginal stability condition in time: not only the total time derivative of the growth rate but also its partial derivative with respect to k must vanish when marginal stability is satisfied. More simply, the tangency condition to the marginal-stability manifold in time has to be satisfied by the fastest growing mode. Pragmatically the eigenvalue problem (3.11) must be solved multiple times, i.e. for varying k to find the mode that first undergoes an instability. Moreover the number of marginally stable modes and the wavenumbers associated with each of them can change in time, requiring for the last step to be repeated, in principle, at each time iteration. Being the eigenvalue problem at the core of the slow-fast QL systems presented in this work, as well as the computational bottleneck, in the remainder of this section we derive an algorithmic structure for slaving the amplitude to the mean field and for predicting the wavenumber k in the condition of marginal stability, limiting for the moment the complexity to one marginally stable mode.

To enforce the first constraint $d_T\sigma = 0$ (holding z fixed) when $\sigma = 0$, we take the slow-time derivative of the eigenvalue problem (3.11).

$$\mathcal{L}\frac{\partial\hat{\eta}_0}{\partial T} = -\left(\frac{\partial\mathcal{L}}{\partial T}\right)\hat{\eta}_0 + \frac{d\sigma}{dT}\hat{\eta}_0 + \sigma\frac{\partial\hat{\eta}_0}{\partial T}, \tag{3.12}$$

yielding

$$\begin{aligned}\mathcal{L}\frac{\partial\hat{\eta}_0}{\partial T} &= \left(-k^2\frac{\partial U_0}{\partial T} + (2k^2 - U_0)\frac{\partial k^2}{\partial T}\right)\hat{\eta}_0 + \frac{d\sigma}{dT}\hat{\eta}_0 \\ &= -k^2\left(F - \nu U_0 + D\frac{\partial^2 U_0}{\partial z^2} - 2|A|^2k^2|\hat{\eta}_0|^2\right)\hat{\eta}_0 + (2k^2 - U_0)\frac{\partial k^2}{\partial T}\hat{\eta}_0 + \frac{d\sigma}{dT}\hat{\eta}_0\end{aligned} \tag{3.13}$$

A solvability condition for (3.13) can be obtained by taking the inner product of (3.13) with $\hat{\eta}_0^\dagger$ (equivalent to requiring the solutions to be orthogonal to the nullspace of $\mathcal{L}^\dagger$, that in this case equals the nullspace of $\mathcal{L}$, i.e. $\mathcal{L}$ is self-adjoint):

$$(\mathcal{L}\partial_T\hat{\eta}_0, \hat{\eta}_0^\dagger) = (\partial_T\hat{\eta}_0, \mathcal{L}^\dagger\hat{\eta}_0^\dagger) = 0. \tag{3.14}$$

Consequently,

$$(\mathcal{L}\partial_T\hat{\eta}_0, \hat{\eta}_0^\dagger) = -k^2\int_0^{L_z}\frac{\partial U_0}{\partial T}|\hat{\eta}_0|^2dz - \frac{\partial k^2}{\partial T}\int_0^{L_z}U_0|\hat{\eta}_0|^2dz + 2k^2\frac{\partial k^2}{\partial T} + \frac{d\sigma}{dT} = 0, \tag{3.15}$$

yielding an evolution equation for the wave number k associated with the fastest-growing mode:

$$\frac{\partial k^2}{\partial T} = \frac{k^2\int_0^{L_z}\left(F - \nu U_0 + D\dfrac{\partial^2 U_0}{\partial z^2}\right)|\hat{\eta}_0|^2dz - 2k^4|A|^2\int_0^{L_z}|\hat{\eta}_0|^4dz - \dfrac{d\sigma}{dT}}{2k^2 - \int_0^{L_z}U_0|\hat{\eta}_0|^2dz}, \tag{3.16}$$

provided the amplitude can be determined.

Substituting the solvability condition (3.16) into (3.13), which is tantamount to subtracting the projection of the right-hand side that lies in the nullspace of $\mathcal{L}$, we obtain

$$\begin{aligned}\mathcal{L}\frac{\partial\hat{\eta}_0}{\partial T} = &-k^2(F - \nu U_0 + \partial_z^2 U_0)\hat{\eta}_0 + 2|A|^2k^4|\hat{\eta}_0|^2\hat{\eta}_0 + \frac{d\sigma}{dT}\hat{\eta}_0 \\ &+ (2k^2 - U_0)\frac{k^2\int_0^{L_z}(F - \nu U_0 + \partial_z^2 U_0)|\hat{\eta}_0|^2dz - 2k^4|A|^2\int_0^{L_z}|\hat{\eta}_0|^4dz - \dfrac{d\sigma}{dT}}{2k^2 - \int_0^{L_z}U_0|\hat{\eta}_0|^2dz}\hat{\eta}_0\end{aligned} \tag{3.17}$$

With the aim of isolating the unknown amplitude $A(T)$, the problem (3.17) can then be split into two subproblems that can be independently solved (recalling that $d_T\sigma = 0$ when $\sigma = 0$):

$$\frac{\partial\hat{\eta}_0}{\partial T} = k^2\hat{\eta}_\alpha + 2|A|^2k^4\hat{\eta}_\beta + \frac{d\sigma}{dT}\hat{\eta}_\sigma, \tag{3.18}$$

where

$$\mathcal{L}\hat{\eta}_\alpha = -\left(F - \nu U_0 + D\frac{\partial^2 U_0}{\partial z^2}\right)\hat{\eta}_0 + (2k^2 - U_0)\frac{\int_0^{L_z}(F - \nu U_0 + \partial_z^2 U_0)|\hat{\eta}_0|^2dz}{2k^2 - \int_0^{L_z}U_0|\hat{\eta}_0|^2dz}\hat{\eta}_0, \tag{3.19}$$

$$\mathcal{L}\hat{\eta}_\beta = |\hat{\eta}_0|^2\hat{\eta}_0 - (2k^2 - U_0)\frac{\int_0^{L_z}|\hat{\eta}_0|^4dz}{2k^2 - \int_0^{L_z}U_0|\hat{\eta}_0|^2dz}\hat{\eta}_0. \tag{3.20}$$

$$\mathcal{L}\hat{\eta}_\sigma = \frac{d\sigma}{dT}\left[1 - \frac{(2k^2 - U_0)}{2k^2 - \int_0^{L_z}U_0|\hat{\eta}_0|^2dz}\right]\hat{\eta}_0 \tag{3.21}$$

Although the solvability of the two problems (3.19)-(3.20) is guaranteed by the Freedholm alternative, the orthogonality of the respective right-hand sides (RHS) to the kernel of $\mathcal{L}$

can not be perfectly achieved numerically. This issue can be overcome making use of a generalized inverse resulting from a singular-value decomposition (SVD) of the operator $\mathcal{L}$. The great advantage of the SVD (consisting in a generalized eigenvalue decomposition) is that it actually solves the least squares problem minimizing the quantity $||\mathcal{L}\partial_T\hat{\eta}_0 - RHS||^2$, and therefore already satisfies the solvability condition (removing the part of RHS lying in the range of $\mathcal{L}$) [6], [7].

We now proceed to enforce the second constraint $\partial_{k^2}\sigma = 0$ (holding z, T, and A fixed) when $\sigma = 0$, taking this time the k-derivative of (3.11)

$$\mathcal{L}\frac{\partial\hat{\eta}_0}{\partial k^2} = -\left(\frac{\partial\mathcal{L}}{\partial k^2}\right)\hat{\eta}_0 + \frac{\partial\sigma}{\partial k^2}\hat{\eta}_0 + \sigma\frac{\partial\hat{\eta}_0}{\partial k^2} \tag{3.22}$$

$$\mathcal{L}\frac{\partial\hat{\eta}_0}{\partial k^2} = -\left(k^2V + U_0 - 2k^2\right)\hat{\eta}_0 \tag{3.23}$$

where we have defined the sensitivity of the slow field U_0 with respect to the wavenumber as $V = \partial_{k^2}U_0$ [1]. The evolution equation for V (that will be used subsequently) can be obtained by differentiating w.r.t. k^2 the evolution equation (3.10) for U_0:

$$\frac{\partial V}{\partial T} = -\nu V + D\frac{\partial^2 V}{\partial z^2} - 2|A|^2k^2\left(\hat{\eta}_0^\dagger\frac{\partial\hat{\eta}_0}{\partial k^2} + c.c.\right) - 2|A|^2|\hat{\eta}_0|^2 \tag{3.24}$$

We now take the inner product of (3.23) with $\hat{\eta}_0^\dagger$ to obtain a solvability condition

$$(\mathcal{L}\partial_{k^2}\hat{\eta}_0, \hat{\eta}_0^\dagger) = (\partial_{k^2}\hat{\eta}_0, \mathcal{L}^\dagger\hat{\eta}_0^\dagger) = 0 \tag{3.25}$$

$$2k^2 = k^2\int_0^{L_z} V|\hat{\eta}_0|^2dz + \int_0^{L_z} U_0|\hat{\eta}_0|^2dz \tag{3.26}$$

Substituting (3.26) into (3.23) yields an equation for the sensitivity of the eigenfunction $\hat{\eta}_0$ with respect to changes in the wavenumber:

$$\mathcal{L}\frac{\partial\hat{\eta}_0}{\partial k^2} = -\left(k^2V + U_0\right)\hat{\eta}_0 + \left(k^2\int_0^{L_z} V|\hat{\eta}_0|^2dz + \int_0^{L_z} U_0|\hat{\eta}_0|^2dz\right)\hat{\eta}_0 \tag{3.27}$$

that can be solved, as done for (3.19) and (3.20) making use of the SVD.

By next taking the slow time derivative of the solvability condition (3.26),

$$\begin{aligned}\frac{\partial k^2}{\partial T} = {} & k^2\frac{\int_0^{L_z}\partial_T V|\hat{\eta}_0|^2dz + \int_0^{L_z} V(\hat{\eta}_0^\dagger\partial_T\hat{\eta}_0 + c.c.)dz}{2 - \int_0^{L_z} V|\hat{\eta}_0|^2dz} + \\ & + \frac{\int_0^{L_z}\partial_T U_0|\hat{\eta}_0|^2dz + \int_0^{L_z} U_0(\hat{\eta}_0^\dagger\partial_T\hat{\eta}_0 + c.c.)dz}{2 - \int_0^{L_z} V|\hat{\eta}_0|^2dz},\end{aligned} \tag{3.28}$$

[1] Given the dependency of the eigenfunction $\hat{\eta}_0$ on the wavenumber k, we are inclined to assume the same intrinsic dependency for the mean field U_0 on k when marginal stability is realized. Whether this dependency is realized (at fixed T) remains a subject of ongoing investigation.

and substituting (3.16) into the left-hand side and (3.10), and (3.24), (3.18) into the right-hand side of (3.28) we eventually obtain an equation to determine the amplitude analogous to that for the 1D model problem:

$$\frac{d\sigma}{dT} = \alpha - 2|A|^2 k^2 \beta, \qquad A = \sqrt{\frac{\alpha}{2k^2\beta}}, \tag{3.29}$$

After renaming the integrals as follows,

$$\begin{aligned}
I_{u1} &= \int_0^{L_z} (F - \nu U_0 + D\partial_z^2 U_0)|\hat{\eta}_0|^2 dz & I_{v1} &= \int_0^{L_z} (-\nu V + D\partial_z^2 V)|\hat{\eta}_0|^2 dz \\
I_{u2} &= \int_0^{L_z} U_0 |\hat{\eta}_0|^2 dz & I_{v2} &= \int_0^{L_z} V|\hat{\eta}_0|^2 dz \\
I_{u3} &= \int_0^{L_z} U_0(\hat{\eta}_0^\dagger \hat{\eta}_\alpha + c.c.)dz & I_{v3} &= \int_0^{L_z} V(\hat{\eta}_0^\dagger \hat{\eta}_\alpha + c.c.)dz \\
I_{u4} &= \int_0^{L_z} U_0(\hat{\eta}_0^\dagger \hat{\eta}_\beta + c.c.)dz & I_{v4} &= \int_0^{L_z} V(\hat{\eta}_0^\dagger \hat{\eta}_\beta + c.c.)dz \\
I_{u5} &= \int_0^{L_z} L_z U_0(\hat{\eta}_0^\dagger \hat{\eta}_\sigma + c.c.)dz & I_{v5} &= \int_0^{L_z} L_z V(\hat{\eta}_0^\dagger \hat{\eta}_\sigma + c.c.)dz \\
I_g &= \int_0^{L_z} (\hat{\eta}_0^\dagger \partial_{k^2} \hat{\eta}_0 + c.c.)|\hat{\eta}_0|^2 dz & I_\eta &= \int_0^{L_z} |\hat{\eta}_0|^4 dz,
\end{aligned} \tag{3.30}$$

the expressions for α and β now, read

$$\alpha = -\frac{I_{u1}I_{u2} + k^2(2k^2 - I_{u2})(I_{u3} + I_{v1} + k^2 I_{v3})}{2 + (2k^2 - I_{u2})(I_{u5} + k^2 I_{v5})} \tag{3.31}$$

$$\beta = \frac{k^4(2k^2 - I_{u2})I_{v4} - I_\eta(1 - I_{u2})}{2 + (2k^2 - I_{u2})(I_{u5} + k^2 I_{v5})}. \tag{3.32}$$

With A known, k can be predicted using (3.16), with $d_T\sigma = 0$.

As in the 1D case, β is not sign-definite, meaning that the fluctuation can drive the dynamics away from the local marginal stability manifold. Whenever marginal stability is compromised, the adoption of a co-evolution technique is a crucial step for the efficacy of QL models.

As in §2 we show below that, with a different choice for the rescaling of equations (3.1)-(3.2), an ϵ-free reduced model describing the bursting regime can be obtained. Specifically, we posit the revised expansions

$$\begin{aligned}
U &= U_0 + \epsilon U_1 + \epsilon^2 U_2 + O(\epsilon^3), \\
\eta &= \frac{1}{\sqrt{\epsilon}}\eta_0 + \sqrt{\epsilon}\eta_1 + \epsilon\sqrt{\epsilon}\eta_2 + O(\epsilon^2\sqrt{\epsilon})
\end{aligned}$$

and obtain the following set of leading-order equations for the bursting regime:

$$\frac{\partial U_0}{\partial \tau} + U_0 \frac{\partial U_0}{\partial \chi} = -\left(\frac{\partial \eta_0}{\partial \chi}\right)^2 \tag{3.33}$$

$$\frac{\partial \eta_0}{\partial \tau} = -\eta_0 - U_0 \frac{\partial^2 \eta_0}{\partial \chi^2} - \frac{\partial^4 \eta_0}{\partial \chi^4} + \frac{\partial^2 \eta_0}{\partial z^2} - \eta_0^3 \tag{3.34}$$

Once more, the leading-order dynamics for the mean field U_0 is dominated by the effect of the fluctuation-iduced feedback and the cubic non-linearity is recovered in the evolution equation for the fluctuation field, crucial for the saturation of the instabilities. However, in this specific case where the mean field does not explicitly depend on the horizontal spatial coordinate, the QL model is essentially 1D, making the gradient descent technique preferable over DNS as the co-evolution method.

Figure 8 shows the updated flowchart for the 2D extension of the QL algorithm, summarizing all of the logical steps that constitute the procedure and the conditions under which they are executed.

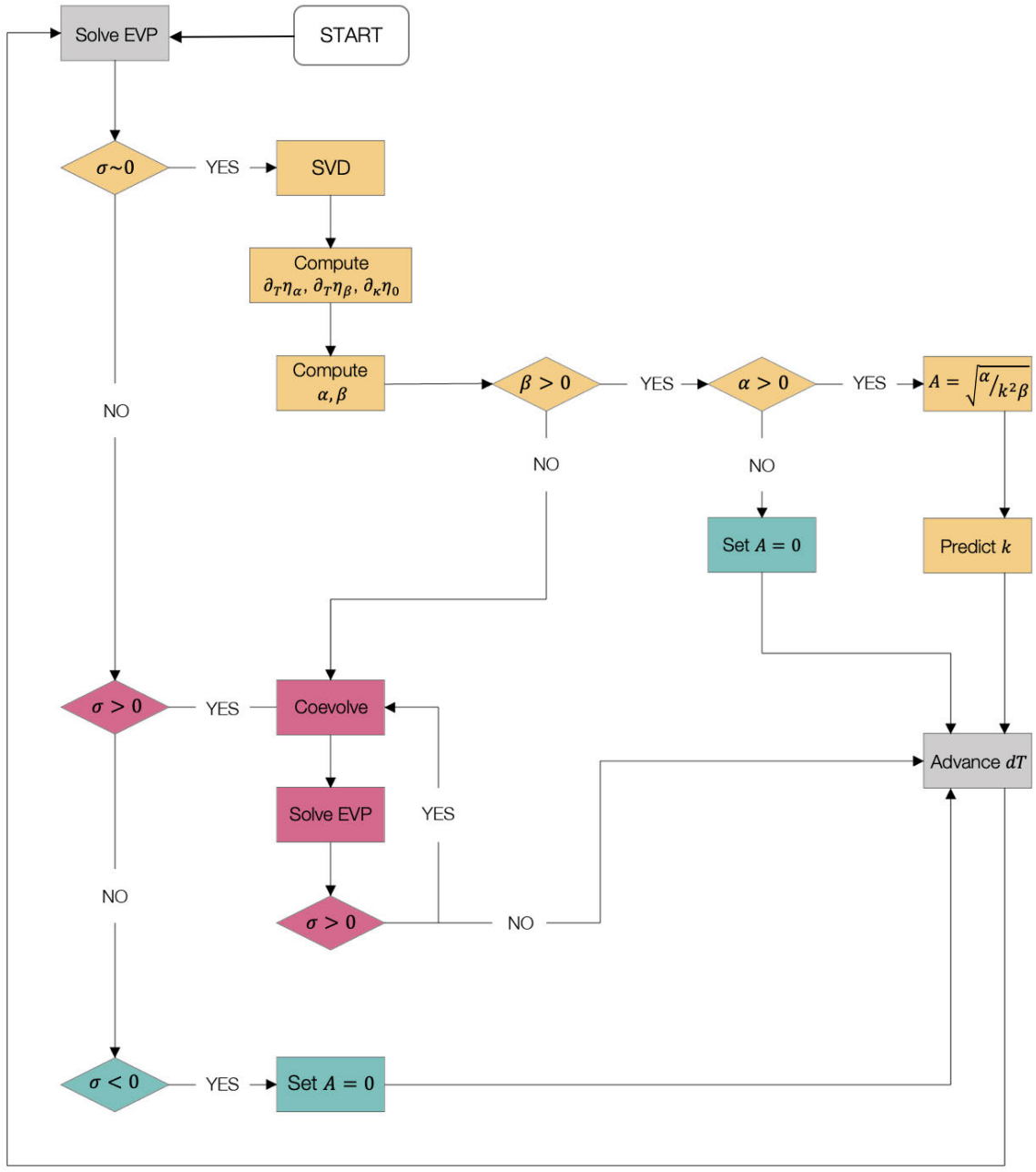

Figure 8: Flowchart of the 2D QL algorithm. The loop is started by solving the linear eigenvalue problem for the maximum growth rate σ and the corresponding eigenfunction $\hat{\eta}_0$. When negative growth rates characterize the state of the system, the green blocks are executed: the slowly-varying amplitude of the fluctuation is set to zero and the mean field is updated on the slow time scale without any feedback term. Once marginal stability (zero growth rate) is realized the slaving of the amplitude activates (blocks in yellow) and the mean field is updated on the slow time with the amplitude prescribed to ensure its marginal stability. The red circuit is entered whenever an unstable ($\sigma > 0$) or potentially unstable ($\beta < 0$) situation is realized. The mean field and the fluctuations are time-stepped together on the fast time scale until the growth rate resulting from the linear eigenvalue problem again becomes non-positive.

4 Conclusions and Future Work

In the limit of small Froude and large Reynolds numbers, stratified shear flows exhibit a strongly constrained form of turbulent dynamics. Multi-scale analysis of this phenomenon leads to a set of reduced, quasi-linear stystem of equations where fields evolving on different spatiotemporal scales are coupled. The dynamics of the fast variables, or fluctuations, is linear around the slow-evolving mean flow, with the fluctuations being advected by the mean flow and producing a feedback on it. Because the evolution of the fluctuations is linear the only possible long-term dynamics requires the system to self-adjust around a marginal-stability manifold. Michel and Chini [3] recently have shown for a 1D model problem that this scenario can be realized in slow-fast QL systems by appropriately slaving the fluctuations dynamics to the mean field so that zero growth rates are ensured.
The interaction between the slow and fast fields in stratified flows, however, is not sign-definite, potentially allowing for the fluctuations to intermittently prevent marginal stability from being attained. Accordingly, in the second section of this study, we investigated a simplified 1D dynamical system and its corresponding asymptotic QL reduction, specifically addressing the two-way nature of the fluctuation feedback. Inspired by the approach of Michel and Chini [3] we have developed a numerical procedure that can properly accomodate bursting events associated with positive fluctuation growth rates. The algorithm simulates the QL system, exploiting the multi-scale nature of the problem, when stability or marginal stability is satisfied and simulates/emulates the full non-linear system otherwise. In the first case, the fluctuation amplitude is set so that zero growth rates can be reached and then maintained, while in the second one, the co-evolution of the two fields is performed. In this regard three different methods were tested: finite-ϵ DNS (the full non-linear system), ϵ-free DNS (the rescaled system for the bursting regime) and a gradient descent technique. The first two methods explicitly reintroduce the fluctuation non-linearities in the dynamics, which generally are not negligible when fluctuation amplitudes are large and which may be crucial for the saturation of instabilities. The third method exploits information from the eigenvalue problem by shooting in the direction provided by its linear eigenfunctions. The computational expense of the last two approaches, ϵ-free DNS and the gradient descent technique, is shown to be one order of magnitude smaller than that of the full DNS, owing the absence of the small parameter ϵ, which enables larger numerical time-steps. However the gradient descent technique, although crude, has the advantage in many cases (as remarked in the third section) of not requiring further information or arbitrary choices, like the domain size and initial conditions for the fast field, other then the ones already present in the QL approximation.

Considering the structure of the stratified flow system of interest, the next crucial step is the 2D extension of slow-fast QL formalism. In the third section we develop an algorithm for a 2D model problem in which a strict QL approximation is made (i.e. unlike in the real system slow spatial modulation is suppressed). Because of the explicit spatial structure of the fluctuation fields two constraints are needed to slave the fluctuation dynamics and ensure the marginally stable dynamics: the zero fluctuation growth rate condition must persist in time and this condition has to be realized for the fastest growing mode. Limiting here the analysis to a single marginally stable mode, the derivation yields a relatively simple

expression to slave the amplitude of the fluctuations to the slow field and to an evolution equation for the wavenumber of the fastest-growing mode once the fluctuation amplitude is determined.

The objectives of future work will be to implement this 2D algorithm numerically and then to reincorporate slow spatial modulation of the mean and fluctuation fields. The long-term aim is to enable simulations of strongly stratified turbulence in geophysically-relevant parameter regimes, although we expect the slow-fast QL formalism will find wide applicability in turbulence sub-grid modeling.

5 Acknowledgement

I would like to express my thanks in the first place to Greg Chini (University of New Hampshire) and Colm Caulfield (University of Cambridge) for proposing and advising this project. Their scientific guidance and suggestions during the summer were of great importance for the success of the project. Dwight Barkley (University of Warwick), Laurette Tuckerman (ESPCI) and Geoff Vasil (The University of Sydney) are also acknowledged for the many inspiring conversations throughout the course of the project. I finally thank the directors of the GFD program 2019, Claudia Cenedese, Karl Helfrich, and Bruce Sutherland, and the entire staff for making this great experience possible.

References

[1] Julien, K., Knobloch, E., 2007. Reduced models for fluid flows with strong constraints. *J. Math. Phys.*, 48, 065405.

[2] Sprague, M., Julien, K., Knobloch, E., Werne, J., 2006. Numerical simulation of an asymptotically reduced system for rotationally constrained convection. *Journal of Fluid Mechanics*, 551, 141-174.

[3] Michel, G., Chini, G.P., 2019. Multiple scale analysis of slow-fast quasi-linear systems. *Proc. R. Soc. A*, 475, 20180630.

[4] Rocha, C.B., 2015. Coupled reduced equations for strongly stratified flows. *GFD report.*

[5] Burns, K. J., Vasil, G. M., Oishi, J. S., Lecoanet, D., Brown, B. P., 2019. Dedalus: A Flexible Framework for Numerical Simulations with Spectral Methods. *arXiv preprint arXiv*, 1905.10388.

[6] Businger, P. A., Golub, G. H., 1969. Algorithm 358: singular value decomposition of a complex matrix [F1, 4, 5]. *Communications of the ACM*, 12, 564-565

[7] Newell, A.C., Passot, T., Souli, M., 1990. The phase diffusion and mean drift equations for convection at finite Rayleigh numbers in large containers. *J. Fluid Mech.*, 220, 187-252

[8] Billant, P., Chomaz, J. M., 2001. Self-similarity of strongly stratified inviscid flows. *Physics of Fluids, American Institute of Physics*, 13 (6), 1645-1651.

[9] Riley, J., Lindborg, E., 2010. Recent progress in stratified turbulence. In Davidson, P., Kaneda, Y., Sreenivasan, K. (Eds.), *Ten Chapters in Turbulence*, 7, 269-317, Cambridge University Press.

[10] Tang, W., Caulfield, C., Kerswell, R., 2019. A prediction for the optimal stratification for turbulent mixing. *Journal of Fluid Mechanics*, 634, 487-497.

[11] Maffioli, A., Brethouwer, G., Lindborg, E., 2016. Mixing efficiency in stratified turbulence. *Journal of Fluid Mechanics*, 794, R3.

[12] Garanaik, A., Venayagamoorthy, S., 2019. On the inference of the state of turbulence and mixing efficiency in stably stratified flows. *Journal of Fluid Mechanics*, 867, 323-333.

[13] Oglethorpe, R., Caulfield, C., Woods, A., 2013. Spontaneous layering in stratified turbulent Taylor–Couette flow.*Journal of Fluid Mechanics*, 721, R3.

[14] Venaille, A., Gostiaux, L., Sommeria, J., 2017. A statistical mechanics approach to mixing in stratified fluids.*Journal of Fluid Mechanics*, 810, 554-583.

[15] Portwood, G., De Bruyn Kops, S., Taylor, J., Salehipour, H., Caulfield, C.,2016. Robust identification of dynamically distinct regions in stratified turbulence. *Journal of Fluid Mechanics*, 807, R2.

[16] Brethouwer, G., Billant, P., Lindborg, E., Chomaz, J., 2007. Scaling analysis and simulation of strongly stratified turbulent flows. *Journal of Fluid Mechanics* 585, 343-368.

[17] Zhou, Q., Diamessis, P. J. 2019. Large-scale characteristics of stratified wake turbulence at varying Reynolds number. *Physical Review Fluids* 4(8), 084802.

[18] Bartello, P., Tobias, S., 2013. Sensitivity of stratified turbulence to the buoyancy Reynolds number. *Journal of Fluid Mechanics*, 725, 1-22.

[19] Tobias, S., Marston, J., 2017. Three-dimensional rotating Couette flow via the generalised quasilinear approximation. *Journal of Fluid Mechanics* 810, 412-428.

A Mushy Source for the Geysers of Enceladus

Samuel Boury

August 21, 2019

1 Introduction

The outer solar system may harbor life, and a promising location is Enceladus, a tiny moon of Saturn [3] (figure 1), due to its observed cryovolcanism and inferred liquid ocean. This rock-cored icy satellite has a liquid ocean covered by a thin outer ice shell [14]. Tidal heating [8, 14] due to Enceladus' orbital eccentricity around Saturn likely maintains the liquid ocean. At the South Pole, where hot activity has been recorded at the surface [10, 15], fractures penetrate into the ice shell and emit geysers of salty ice crystals ($\sim 1\%$ salt), i.e., cryovolcanoes [12].

Figure 1: Left: Saturn and Enceladus. Right: Light illuminating geysers of water and salts on the South pole of Enceladus. The diameter of Enceladus is about 500 km and the geysers can reach heights of hundreds of km. From the *Cassini mission*, NASA.

It has been proposed that shear heating along the fractures (figure 2) explains surface temperature anomalies on the ice shell adjacent to the fractures around the South Pole [6, 8], and may explain the plume genesis if the shear heating is large enough to cause melting. Prevailing models have treated pure fresh ice, but the ice shell is likely a binary mixture of salts and water. Partial melting of the salt and ice mixture can result in the formation of a mushy layer, which is a reactive porous layer of fresh ice crystals and saline

liquid brine, and allows for convection of the interstitial fluid with a corresponding heat transport [16].

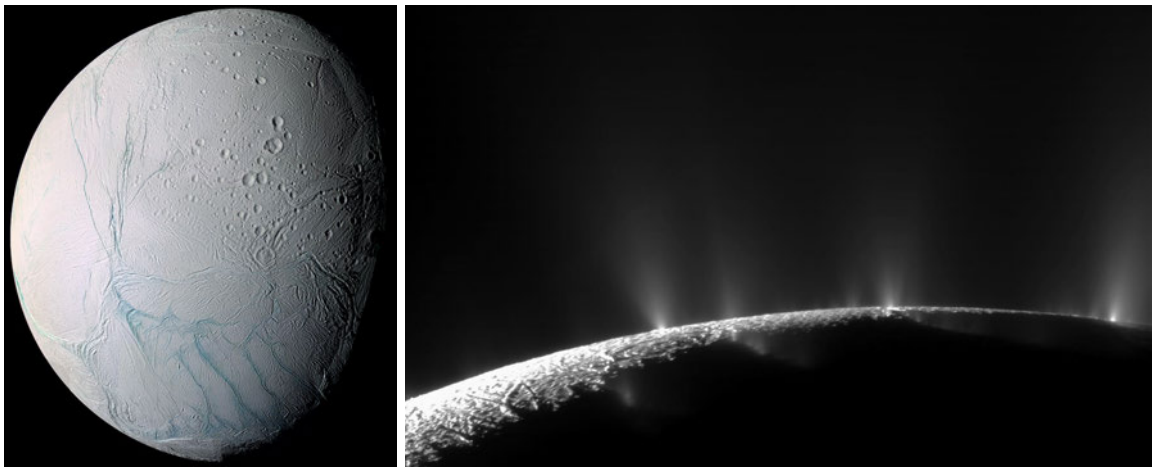

Figure 2: Left: Enceladus, in false colours, with the cracks at the South Pole (light blue stripes). Right: Geysers blowing from the cracks. From the *Cassini mission*, NASA.

Nimmo et al. [8] proposed a model of partial depth cracks in fresh ice to supply water to the geysers of Enceladus. This model, however, does not provide a source for the observed liquid saline water that seems to have experienced serpentisation reactions consistent with contact of a liquid ocean with the solid core [12]. An alternative approach, widely used, considers cracks through the full depth of the ice shell, down to an inner liquid ocean located under the 20 km thick ice shell (see figure 3(a)) [11, 13, 20]. Nonetheless, such cracks are difficult to maintain through the full depth of the ice shell. In this study, we adapt the first of these two models, and investigate a potential source for salts. We consider a new model where a crack stops at a finite depth within the the ice shell. Through frictional heating along the crack, a mushy region with salty water flowing through an icy matrix is formed, and provides water and salt for geysers (see figure 3(b)).

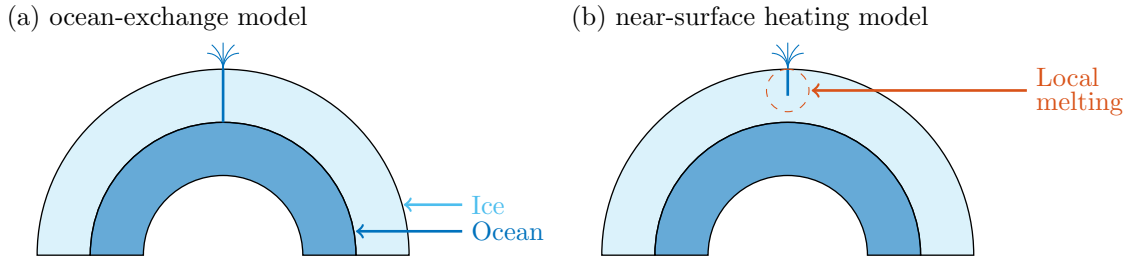

Figure 3: Two different models for the cracks: (a) full depth crack, going from the surface to the underneath ocean; and (b) partial depth crack with localised ice melting through frictional heating, creating a "mush". For further details, see [8] and [14].

We model the crack by a partial depth crack, in a 2D ice region (figure 4(a)). Due to tidal forcing, the two sides of the crack rub against each other, acting as a heat source. To

build insight we here consider an illustrative problem where the frictional heating along the crack generates a constant heat flux and is modelled by a sharply peaked Gaussian along x (horizontal direction) with no z variation (vertical direction). The reason for this is to approximate a delta function which describes heating localised along the crack. We expect this to result in partial melting of the eutectic ice shell (figure 4(b)). Due to heating at the crack, the ice shell starts to melt and forms a mushy region in which salty water is flowing through an ice matrix, and convective motion is expected to be sustained by the heat source and the resulting relatively fresh meltwater released by melting [7]. The ice-mush boundary can evolve freely and either expand or contract with changes in solid fraction and porosity. In order to have a better understanding of the flow close to the crack, we here focus on a second simplified model with a full depth crack in a mushy region (figure 4(c)). We below show that using the near-eutectic approximation, which means that the solute composition S of the system is close to the eutectic composition S_E, and assuming that the permeability does not depend strongly on porosity, the problem simplifies to porous media convection with a constant Gaussian heat flux located at the crack. Whilst this model neglects some physical processes relevant to the dynamics in an Enceladus-like setting, the goal is to yield an analytically tractable problem capturing the key elements of the convective boundary layer flow near to a heated crack in order to build initial insight.

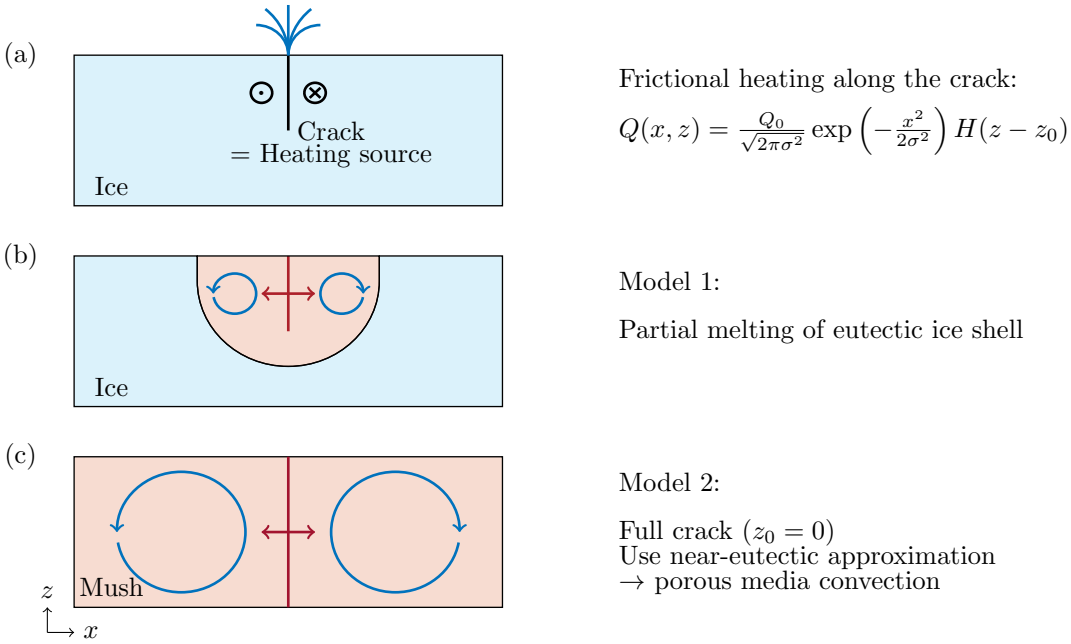

Figure 4: Crack modelling: (a) partial depth crack in an ice layer, with frictional heating (constant Gaussian heat flux multiplied by a Heaviside function); (b) partial depth crack with frictional heating producing partial melting of the eutectic ice shell; and (c) full depth crack in a mushy region with constant heat flux and porous convection. In (c) we assume a constant temperature $T = T_E$ and no vertical velocity for the flow at the top and bottom boundaries.

In this report, we explain how the frictional heating and the mushy region along the

crack could be a plausible source of geysers on Enceladus. In section 2, we illustrate the key features of the flow using solutions from Direct Numerical Simulations (DNS). In section 3, we derive the theoretical framework suitable for our study and we show that different behaviours may exist close to the crack. This gives us an overall picture of the problem. We quantitatively check the relevant scalings by comparison with the DNS in section 4. Conclusions and discussions are drawn in section 5.

2 Direct Numerical Simulation and Comments

We consider a porous ice shell in the configuration of figure 4(c) (model 2). The model is assumed to be 2D and we define H as the vertical extension of the domain, which corresponds to the depth of the crack. In this configuration, the relevent variables are the temperature, the liquid salinity, and the velocity, and localised melting produces a *mushy region* close to the crack, with a given permeability and porosity. We here assume that the permeability is constant, and that the porosity depends slowly on the solid fraction. We will justify, in section 3, that the problem reduces to porous media convection.

We run Direct Numerical Simulations using Dedalus [1] in this idealised framework. We use a constant Gaussian heating along the crack,

$$Q(x,z) = \frac{Q_0}{\sqrt{2\pi\sigma^2}} \exp\left(-\frac{x^2}{2\sigma^2}\right), \tag{1}$$

where Q_0 is the heating coefficient and σ the width of the Gaussian, and solve the dimensionless set of equations for porous media convection (see next section). Preliminary results are presented in figure 5 to provide context for the subsequent discussion.

The left panel in figure 5 shows contours of the stream function in the steady state, in a DNS with $H = 7$ (size of the crack, in length units) and $Q_0 = 100$ (dimensionless heating source). Two convective cells are created, one flowing clockwise (in red) and one flowing anti-clockwise (in blue). They are symmetric right-left but the up-down symmetry is broken. From the thin layer close to the crack, we can infer the existence of a vertical boundary layer in which the flow is accelerated vertically to the top. The right panel in figure 5 shows the instability triggered when the heating is increased further, to $Q_0 = 180$. The study of this instability, however, is beyond the scope of this work.

We focus primarily on the boundary layer flow near the crack supplied by a reservoir of far field mush, which could supply the geysers. These dynamics are common to both model 1 and model 2 (figure 4)(b) and (c)). The far-field return flow will be more strongly influenced by the specific far-field boundary conditions and the geometry of the mushy inclusion. Hence, whilst the generic feature of a return flow is common to both model 1 and model 2, the specific scalings of the far-field dynamics in figure 5) may differ somewhat from that in the more detailed model 1. Hence we focus less on the far field and, in the next sections, we show that there are different behaviours close to the crack and we quantitavely explain them.

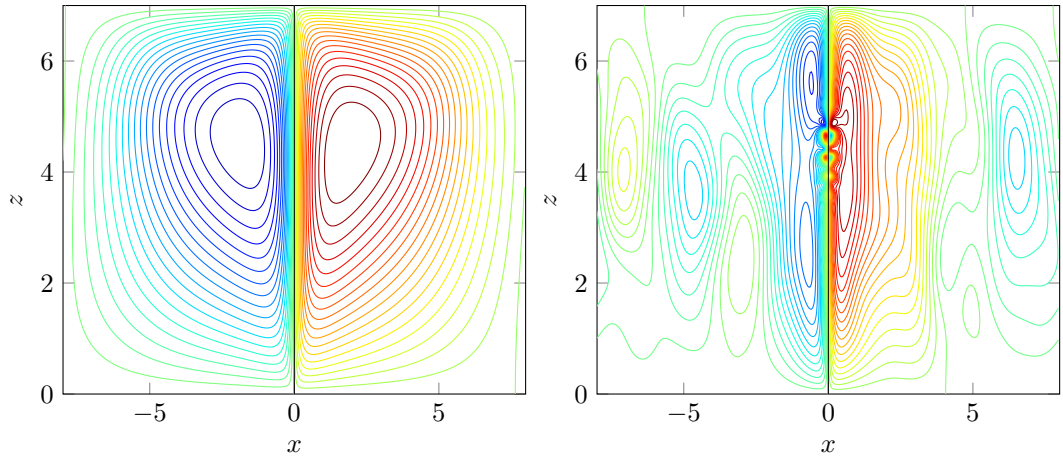

Figure 5: Contours of stream function in a DNS using Dedalus [1], imposing a constant Gaussian heat flux on a full crack located at $x = 0$, and zero buoyancy and vertical velocity at the top and at the bottom of the domain. Red is clockwise and blue is anti-clockwise. Left: Steady state reached at relatively low heating $Q_0 = 100$. Right: Instability triggered while increasing heating, at $Q_0 = 180$.

3 Theory of Mushy Regions

A *mushy region*, or a *mush*, is a region in which the solid-liquid interface has become so convoluted that the solid forms a matrix of crystals bathed in the remaining fluid [18]. Porous sea ice is an example of such a mushy layer [16]. Relevant parameters in such a system are the temperature T, the salinity (solute) S of the liquid, the solid fraction ϕ (i.e. $\phi = 1$ means everything is solid, $\phi = 0$ means everything is liquid), and the velocity of the flow running through the porous media $\mathbf{u} = (u, 0, w)$. In this section, we first state the general equations of the physics of mushy regions. Then, we derive the theoretical framework appropriate for our study by neglecting terms proportional to small parameters, using assumptions corresponding to a so-called near-eutectic approximation.

3.1 General equations

3.1.1 Heat equation

The temperature in the mush is governed by the advection-diffusion equation

$$\frac{\partial T}{\partial t} + (\mathbf{u} \cdot \nabla) T = \kappa \nabla^2 T + \underbrace{\frac{L}{C_p} \frac{\partial \phi}{\partial t}}_{\text{phase change}} , \tag{2}$$

with L the latent heat, C_p the heat capacity, and κ the thermal diffusivity assumed to be constant. Compared to the classical advection-diffusion equation, an additional term is included to take into account the contribution of latent heat transfer from the phase changes.

3.1.2 Solute equation

The salinity, or solutal composition, of the liquid part in the mush is governed by an advection-diffusion equation. Due to the low diffusivity of salt, we neglect the diffusive term compared to the thermal diffusivity. The temporal variation of the salinity only accounts for the liquid phase, which means in the $(1-\phi)$ liquid fraction. We therefore consider

$$(1-\phi)\frac{\partial S}{\partial t} + (\mathbf{u}\cdot\nabla)S = \underbrace{S\frac{\partial \phi}{\partial t}}_{\text{melting}}, \tag{3}$$

where an additional term for the melting contribution to account for brine rejection during freezing, or freshening during melt. In this model, we assume that no salt is frozen into the ice crystals (pure ice).

3.1.3 Local themodynamic equilibrium

In the mush, the liquid and solid phases are in equilibrium. Transition from a fully solid system to a fully liquid system occurs by increasing the temperature T, at constant salinity S, through system of solid and liquid (figure 6). While in this region, the liquid phase and the solid phase are at the same temperature but have different salinities: the solid phase has $S = 0$, and the salinity of the liquid phase aligns on the *liquidus*. The liquidus is the border line $T_L(S)$ between the liquid region and the region with liquid and solid. At first order, we assume that this relation is linear and write

$$T = T_L(S) = T_f - m(S - S_0), \tag{4}$$

with S_0 a given solute concentration, T_f the freezing temperature at $S = S_0$, and m a constant parameter.

3.1.4 Momentum equation: Darcy's Law

The flow in the mush is governed by Darcy's law, which is a reduction of the Navier-Stokes equations for flow in a porous media with no inertia

$$\frac{\mu}{\Pi}\mathbf{u} = -\nabla P + \rho\mathbf{g}, \tag{5}$$

with μ the viscosity, Π the permeability, ρ the density, and $\mathbf{g}$ the gravity field. In this equation, $\mathbf{u} = (u, 0, w)$ and P stand for the velocity and the pressure fields.

3.1.5 Mass (continuity) equation

Considering an incompressible flow, assuming that solid and liquid densities are equal, we also have the continuity equation

$$\nabla\cdot\mathbf{u} = 0. \tag{6}$$

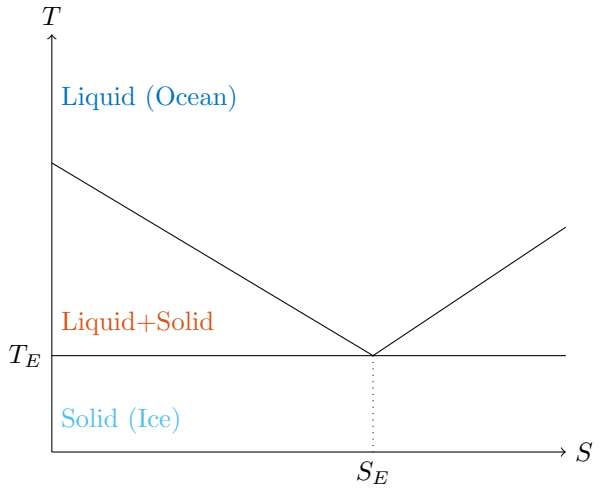

Figure 6: Idealised phase diagram for a binary alloy of water and salt. T_E and S_E are the eutectic temperature and salinity. The line between the liquid phase and the liquid + solid phase is called the liquidus and is assumed to be linear at first order [17, 18]. Geysers on Enceladus are mostly composed of water and salt (NaCl), with volatile gases (CO_2, N_2, CO, CH_4) in the gas phase [12].

3.1.6 Complete set of equations

Therefore, the complete set of equations is

$$\frac{\partial T}{\partial t} + (\mathbf{u}\cdot\nabla)T = \kappa\nabla^2 T + \frac{L}{C_p}\frac{\partial \phi}{\partial t}, \tag{7}$$

$$(1-\phi)\frac{\partial S}{\partial t} + (\mathbf{u}\cdot\nabla)S = S\frac{\partial \phi}{\partial t}, \tag{8}$$

$$T = T_L(S) = T_f - m(S - S_0), \tag{9}$$

$$\frac{\mu}{\Pi}\mathbf{u} = -\nabla P + \rho\mathbf{g}, \tag{10}$$

$$\nabla\cdot\mathbf{u} = 0. \tag{11}$$

3.2 Buoyancy

In Darcy's law (5), the density of the fluid ρ is a function of the temperature and of the salinity, which we approximate as

$$\rho(T,S) = \rho_0\left(1 - \alpha_T(T - T_0) + \alpha_S(S - S_0)\right), \tag{12}$$

where ρ_0 is a reference density, α_T and α_S are constant parameters, and T_0 and S_0 are reference temperature and salinity. From the liquidus equation (4), however, temperature and salinity are linearly related through a constant coefficient m, and the density ρ can be written as a function that depends only on temperature. We have

$$\rho(T) = \rho_0\left(1 - \alpha(T - T_0)\right), \tag{13}$$

with $\alpha = \alpha_T + \alpha_S/m$. The coefficient α_S/m can often dominate, in which case the buoyancy is controlled by the meltwater released by phase changes as the system rapidly relaxes to local thermal equilbrium.

We define the buoyancy b as a linear function of temperature

$$b = \alpha g \rho_0 (T - T_0), \tag{14}$$

so that

$$\rho g = \rho_0 g - b. \tag{15}$$

We will write both the advection-diffusion equation for heat (2) and the advection-diffusion equation for salinity (3) in terms of b. In Darcy's law, the constant term $\rho_0 \mathbf{g}$ can be included in a redefined pressure field.

The buoyancy can be fully determined using a boundary condition that closes the system. Considering the Gaussian heating model, when the width of the heat flux source σ goes to zero, it behaves like an imposed flux condition at $x = 0$ as

$$F = -\lambda \frac{\partial T}{\partial x} = -\frac{\lambda}{\alpha g \rho_0} \frac{\partial b}{\partial x}, \tag{16}$$

where F is a constant heat flux, parametrising the problem, and λ the thermal conductivity of water, assumed to be the same in the liquid and the ice.

3.3 Dimensionless equations

We consider a characteristic length scale H, corresponding to the vertical size of the crack, and a characteristic time scale H^2/κ, where κ is the thermal diffusivity. We therefore construct a characteristic velocity scale κ/H. This leads us to the definition of dimensionless lengths, time, and velocities:

$$x, z \;\rightarrow\; \tilde{x} = \frac{x}{H}, \tilde{z} = \frac{z}{H}, \qquad t \;\rightarrow\; \tilde{t} = \frac{\kappa t}{H^2}, \tag{17}$$

and

$$u, w \;\rightarrow\; \tilde{u} = \frac{Hu}{\kappa}, \tilde{w} = \frac{Hw}{\kappa}. \tag{18}$$

A similar scaling can also be found for the buoyancy and the pressure

$$b \;\rightarrow\; \tilde{b} = \frac{H \Pi_0 b}{\kappa \mu}, \qquad \text{and} \qquad p \;\rightarrow\; \tilde{p} = \frac{\Pi_0 p}{\kappa \mu} - \frac{g H \Pi_0 \rho_0}{\kappa \mu} z. \tag{19}$$

For the sake of clarity, the dimensionless variables will be noted without tildes. Hence, the dimensionless equations are

$$\frac{\partial b}{\partial t} + (\mathbf{u} \cdot \nabla) b = \nabla^2 b + \mathscr{S} Ra \frac{\partial \phi}{\partial t}, \tag{20}$$

$$(1 - \phi) \frac{\partial b}{\partial t} + (\mathbf{u} \cdot \nabla) b = (b + \mathscr{C} Ra) \frac{\partial \phi}{\partial t}, \tag{21}$$

$$\mathbf{u} = -\nabla p + b, \tag{22}$$

$$\nabla \cdot \mathbf{u} = 0. \tag{23}$$

where $\mathscr{S}$ is the Stefan number defined as

$$\mathscr{S} = \frac{\lambda L}{C_p F H}, \tag{24}$$

and $\mathscr{C}$ the compositional ratio

$$\mathscr{C} = \frac{\lambda (T_L(S_s) - T_0)}{FH}. \tag{25}$$

The dimensionless form of the heat flux sideways boundary condition can also be written in terms of the buoyancy b

$$F = -\lambda \frac{\partial T}{\partial x} \;\rightarrow\; \frac{\alpha g \rho_0 \Pi_0 H^2}{\kappa^2 \mu C_p} F = -\frac{\partial \tilde{b}}{\partial \tilde{x}}, \tag{26}$$

and introduces a porous medium Rayleigh number Ra as

$$Ra = \frac{\alpha g \rho_0 \Pi_0 F H^2}{\kappa^2 \mu C_p}, \tag{27}$$

that represents the ratio of buoyant to dissipative mechanisms (thermal and viscous). This Rayleigh number allows us to write the boundary condition in a simpler way

$$Ra = -\frac{\partial b}{\partial x}, \tag{28}$$

with dimensionless variables. In the DNS, we therefore identify the dimensionless heat flux F to the Rayleigh number Ra. It can also be used to define a natural length scale h
written as

$$h = \sqrt{\frac{H^2}{Ra}} = \left(\frac{\kappa^2 \mu C_p}{\alpha g \rho_0 \Pi_0 F} \right)^{1/2}. \tag{29}$$

3.4 Near-eutectic approximation

Using the compositional ratio $\mathscr{C}$ defined as

$$\mathscr{C} = \frac{\lambda (T_L(S_s) - T_0)}{FH}, \tag{30}$$

the two advection-diffusion equations for heat and salinity write in dimensionless form

$$\frac{\partial b}{\partial t} + (\mathbf{u} \cdot \nabla) b = \nabla^2 b + \mathscr{S} Ra \frac{\partial \phi}{\partial t}, \tag{31}$$

$$\frac{\partial}{\partial t} \left[\mathscr{C} Ra \phi + b(1 - \phi) \right] + (\mathbf{u} \cdot \nabla) b = 0. \tag{32}$$

We now consider the near-eutectic approximation as described by Fowler [4] and in the 2007 GFD lectures [19]. Under this assumption, the composition of the system is close to the eutectic composition S_E (see figure 6). We consider a limit where b is order 1 and $\mathscr{C}$ large, with the solid fraction $\phi = \mathcal{O}(1/\mathscr{C}) \ll 1$. Approximating $(1 - \phi) b \simeq b$ at leading

order in (32) yields to an equation for $\partial_t \phi$ in terms of $\partial_t b$. Then, eliminating $\partial_t \phi$ from (31) results in (33), an advection-diffusion equation for the buoyancy that does not involve the solid fraction ϕ

$$\Omega \left[\frac{\partial b}{\partial t} + (\mathbf{u} \cdot \nabla) b \right] = \nabla^2 b, \tag{33}$$

where $\Omega = 1 + \mathscr{S}/\mathscr{C}$ represents a modified dimensionless heat capacity, which accounts for the impact of phase changes and latent heat transfer that occurs during warming or cooling of the solid matrix.

3.5 Collapsed equation

From now, we focus on 2D dynamics in the plane (x, z) containing the crack. We will show that the remaining equations (10), (11), and (33), can all collapse into a single equation of a single function. This equation will help us to understand the physics involved in the problem.

From the continuity equation (6), we define a streamfunction ψ so that the horizontal and vertical velocities u and w write

$$u = -\frac{\partial \psi}{\partial z} \qquad \text{and} \qquad w = \frac{\partial \psi}{\partial x}. \tag{34}$$

Then, from the horizontal projection of Darcy's law, which involves cross-derivatives of the pressure field and of the streamfunction, we define a potential φ so that p and ψ can be written as

$$p = \frac{\partial \varphi}{\partial z} \qquad \text{and} \qquad \psi = \frac{\partial \varphi}{\partial x}. \tag{35}$$

Using this potential, the vertical projection of Darcy's law becomes an equation for φ and the buoyancy b,

$$\nabla^2 \varphi = b. \tag{36}$$

As a result, all relevant functions of the problem can be expressed using derivatives of the potential φ, as

$$\begin{aligned} p &= \partial_z \varphi, & (37)\\ &= \partial_x \varphi, & (38)\\ u &= -\partial_x \partial_z \varphi, & (39)\\ w &= \partial_x^2 \varphi, & (40)\\ b &= \nabla^2 \varphi = \partial_x^2 \varphi + \partial_z^2 \varphi. & (41) \end{aligned}$$

From these results and using the advection-diffusion equation for b (33), we obtain a collapsed equation for φ that is

$$\Omega \left[\partial_t \nabla^2 \varphi - \partial_x \partial_z \varphi \; \partial_x \nabla^2 \varphi + \partial_x^2 \varphi \; \partial_z \nabla^2 \varphi \right] = \nabla^4 \varphi. \tag{42}$$

As Ω is a parameter of order 1, by renormalising the potential φ and the time variable t as

$$\varphi \; \rightarrow \; \frac{1}{\Omega} \varphi \qquad \text{and} \qquad t \; \rightarrow \; \Omega t, \tag{43}$$

the equation for φ writes without explicit dependence in Ω. Hence, we have the following equation with three different contributions

$$\underbrace{\partial_t \nabla^2 \varphi}_{\text{temporal}} - \underbrace{\partial_x \partial_z \varphi \partial_x \nabla^2 \varphi + \partial_x^2 \varphi \partial_z \nabla^2 \varphi}_{\text{non-linear advection}} = \underbrace{\nabla^4 \varphi}_{\text{diffusion}} . \tag{44}$$

In our study, we will consider steady states for buoyancy and velocity, so the temporal contribution will always be neglected, and relevant balances will involve the non-linear advection term and the diffusive term. We focus on steady solutions after the initial transient adjustment after warming begins (e.g. figure 5, left), but note that at sufficiently large Rayleigh number the transient dynamics can potentially trigger an instability, as shown in figure 5(right). Interestingly, the two non-linear contributions have the same scaling in terms of numbers of x and z derivatives, due to continuity.

Note that the heat flux boundary condition can also be expressed in terms of φ as

$$F = -\partial_x b = -\partial_x \nabla^2 \varphi \text{ at } x = 0. \tag{45}$$

3.6

Different regimes

The buoyancy is given by the Laplacian of φ and, as such, it involves x and z derivatives. These derivatives may or may not have the same scalings, which leads to three different idealised cases:

1. If $\partial_x \sim \partial_z$, both derivatives contribute to the buoyancy and the region is **isotropic**.
2. If $\partial_x \gg \partial_z$, the horizontal variations are more important than the vertical variations, which is characteristic of a **vertical boundary layer**.
3. If $\partial_x \ll \partial_z$, the horizontal variations are less important than the vertical variations, which is characteristic of a **horizontal boundary layer**.

3.6.1 Isotropic scaling

We define the following scalings for x, z, and φ

$$x, z \;\rightarrow\; L \qquad \text{and} \qquad \varphi \;\rightarrow\; A, \tag{46}$$

where x and z have the same scaling due to isotropy.

The scaling of the heat flux boundary condition gives

$$F = -\partial_x b \simeq -\underbrace{\partial_x \nabla^2 \varphi}_{\frac{A}{L^3}}, \tag{47}$$

leading to

$$A \sim F L^3 \sim L^3. \tag{48}$$

We assume that the system is in a steady state, so that temporal derivatives have no contribution and the scaling of the potential equation writes

$$\partial_t \nabla^2 \varphi - \underbrace{\partial_x \partial_z \varphi \partial_x \nabla^2 \varphi + \partial_x^2 \varphi \partial_z \nabla^2 \varphi}_{\frac{A^2}{L^5}} = \underbrace{\nabla^4 \varphi}_{\frac{A}{L^4}} \tag{49}$$

and, reinjecting the flux scaling into the potential equation, we obtain that

$$\partial_x\partial_z\varphi\partial_x\nabla^2\varphi + \partial_x^2\varphi\partial_z\nabla^2\varphi \sim \frac{A^2}{L^5} \sim L, \tag{50}$$

$$\nabla^4\varphi \sim \frac{A}{L^4} \sim \frac{1}{L}, \tag{51}$$

meaning that the non-linear terms and the diffusive term have different scalings, in L and in $1/L$ respectively. Two asymptotic behaviours can therefore be described:

1. $L \ll 1$: The diffusive term dominates the equation and is at least one order of magnitude in L higher than the non-linear terms. The regime is diffusive, which means that $\mathbf{u}\cdot\nabla b \approx 0$, and the buoyancy satisfies a Poisson equation. From the scaling of φ, we have $b \sim L$ and $w \sim L$; and
2. $L \gg 1$: The non-linear terms dominate the equation.

3.6.2 Vertical boundary layer

We define the following scalings for x, z, and φ

$$x \to L_x, \qquad z \to L_z \sim z, \qquad \text{and} \qquad \varphi \to A, \tag{52}$$

where $L_z \sim z$. In this case, the variations along z are small compared to the variations along x and the scaling length L_x is expected to be a function of z [2, 5].

We assume that the system is in a steady state, so that temporal derivatives have no contribution. Given that $\partial_x \gg \partial_z$, we neglect the z derivatives compared to x derivatives and the scaling of the potential equation writes

$$\partial_t\nabla^2\varphi - \underbrace{\partial_x\partial_z\varphi\partial_x(\partial_x^2\varphi+\partial_z^2\varphi) + \partial_x^2\varphi\partial_z(\partial_x^2\varphi+\partial_z^2\varphi)}_{\frac{A^2}{L_z L_x^4}} = \underbrace{\partial_x^4\varphi}_{\frac{A}{L_x^4}} + \partial_z^4\varphi, \tag{53}$$

leading to

$$A \sim L_z \sim z. \tag{54}$$

The same method gives a scaling of the sideways-diffusive heat flux boundary condition

$$F = -\partial_x b \simeq -\underbrace{\partial_x(\partial_x^2\varphi}_{\frac{A}{L_x^3}} + \partial_z^2\varphi), \tag{55}$$

then

$$L_x \sim (A/F)^{1/3} \propto z^{1/3}. \tag{56}$$

From these scalings, we define L_x as

$$L_x = h^{2/3}z^{1/3} \tag{57}$$

where h is the characteristic length defined from the Rayleigh number and the size of the crack H in equation (29), and a self-similar variable η by

$$\eta = \frac{x}{L_x} = \frac{x}{h^{2/3}z^{1/3}}. \tag{58}$$

Therefore, the potential φ can be written in terms of a function f as

$$\varphi = z f(\eta). \tag{59}$$

As we are neglecting the z derivatives, we have

$$w = b = \partial_x^2 \varphi \qquad \text{and} \qquad p = \partial_z \varphi, \tag{60}$$

and we obtain the following scalings for w and b

$$w \sim z^{1/3} \qquad \text{and} \qquad b \sim z^{1/3}. \tag{61}$$

Replacing φ by $zf(\eta)$ in the collapsed advection-diffusion equation, we derive a self-similar ordinary differential equation for f,

$$(f'')^2 - 2f'f''' - 3f'''' = 0, \tag{62}$$

with the boundary conditions

$$\underbrace{f'''(0) = -1}_{\text{flux at } x=0}, \qquad \underbrace{f'(0) = 0}_{u=0 \text{ at the crack}} \qquad \text{and} \qquad \underbrace{f''(\eta^*) = 0 \quad \text{with} \quad \eta^* \quad \text{“large”}}_{\text{constant } b \text{ in the far field}}. \tag{63}$$

Note that the final condition of constant buoyancy in the far field (for η^* “large”) is equivalent to zero vertical velocity in the far field.

3.6.3 Horizontal boundary layer

We define the following scalings for x, z, and φ

$$x \;\to\; L_x \sim x, \qquad z \;\to\; L_z, \qquad \text{and} \qquad \varphi \;\to\; A, \tag{64}$$

where $L_x \sim x$ as the variations along x are small compared to the variations along z. The scaling length L_z is expected to be a function of x.

We assume that the system is in a steady state, so that temporal derivatives have no contribution. Given that $\partial_x \ll \partial_z$, we neglect the x derivatives and the scaling of the potential equation writes

$$\partial_t \nabla^2 \varphi - \underbrace{\partial_x \partial_z \varphi \partial_x (\partial_x^2 \varphi + \partial_z^2 \varphi) + \partial_x^2 \varphi \partial_z (\partial_x^2 \varphi + \partial_z^2 \varphi)}_{\frac{A^2}{L_z^3 L_x^2}} = \partial_x^4 \varphi + \underbrace{\partial_z^4 \varphi}_{\frac{A}{L_z^4}}, \tag{65}$$

leading to

$$A \sim L_x^2 / L_z \sim x^2 / L_z, \tag{66}$$

where $L_z(x)$ has to be determined.

As for the vertical boundary layer, we introduce a similarity variable ζ

$$\zeta = \frac{z}{L_z(x)}, \tag{67}$$

and the potential φ therefore writes in terms of a function g as

$$\varphi = \frac{x^2}{L_z(x)} g(\zeta). \tag{68}$$

We determine $L_z(x)$ by specifying that the buoyant heat flux coming from below is transported sideways (see figure 7). A full solution of the problem will require asymptotic matching of the incoming fluxes. However, to determine the scalings this only needs to be true in an order-of-magnitude sense; the whole buoyant heat flux, corresponding to the heat flux at the entire crack (i.e. sum of the flux $1/h^2$ emitted over the crack of length H), is going sideways through this top region, meaning

$$\int ub\mathrm{d}z \sim \frac{H}{h^2} \qquad \text{as} \qquad h \to 0. \tag{69}$$

Computing the left-hand side

$$\int ub\mathrm{d}z = \frac{x^3}{L_z(x)^4} \int \left[g''(\zeta) \left(2g'(\zeta) - \frac{xL_z'(x)}{L_z(x)} \left(\zeta g''(\zeta) + 2g'(\zeta) \right) \right) \right] \mathrm{d}z. \tag{70}$$

Then, the balance of the heat fluxes gives

$$L_z(x) = \frac{h^{1/2} x^{3/4}}{H^{1/4}}. \tag{71}$$

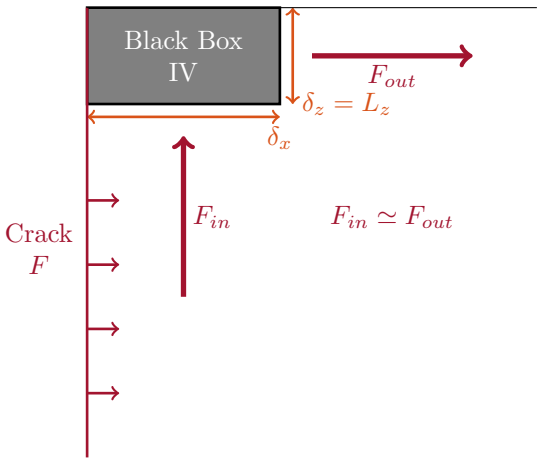

Figure 7: Balance of heat fluxes.

Hence, the potential φ writes

$$\varphi = \frac{H^{1/4} x^{5/4}}{h^{1/2}} g(\zeta). \tag{72}$$

As we are neglecting the x derivatives, we have

$$w = \partial_x^2 \varphi \qquad \text{and} \qquad b \simeq \partial_z p = \partial_z^2 \varphi, \tag{73}$$

which implies that the hydrostatic balance holds at leading order in this boundary layer, and the pressure gradient writes

$$\partial_z p = \partial_z^2 \varphi = \frac{H^{3/4}}{h^{3/2} x^{1/4}} g''(\zeta). \tag{74}$$

4 Four Different Regions

4.1 DNS

Using the above scaling arguments, we can define four different domains for the DNS results presented in figure 5(left). They are shown in figure 8, labeled I, II, III, and IV, starting from the bottom of the crack, and correspond to the different scalings derived in section 3. These domains yield contrasting behaviour of the along-crack profiles of w, b, and $\partial_z p$ (see figure 9). The interest in these three quantities is motivated by the relation $b = \nabla^2 \varphi = w + \partial_z p$, showing that the buoyancy, the vertical velocity, and the vertical pressure gradient, are linearly related.

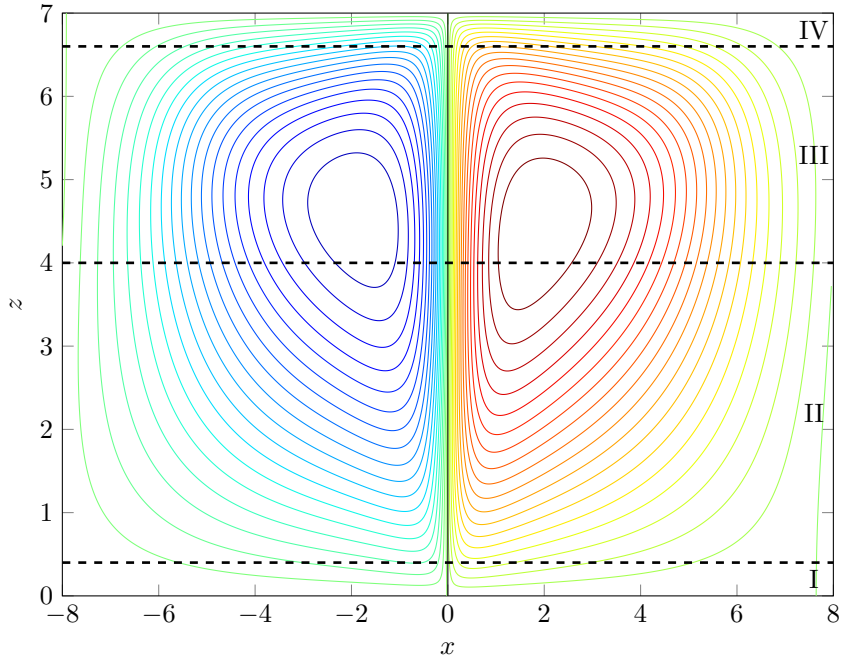

Figure 8: Contours of stream function in a DNS, imposing a heat flux on a full crack located at $x = 0$. We identify four different regions, labeled I, II, III, and IV, from the bottom to the top of the domain.

These four regions have different scalings, that can be explained as follow:

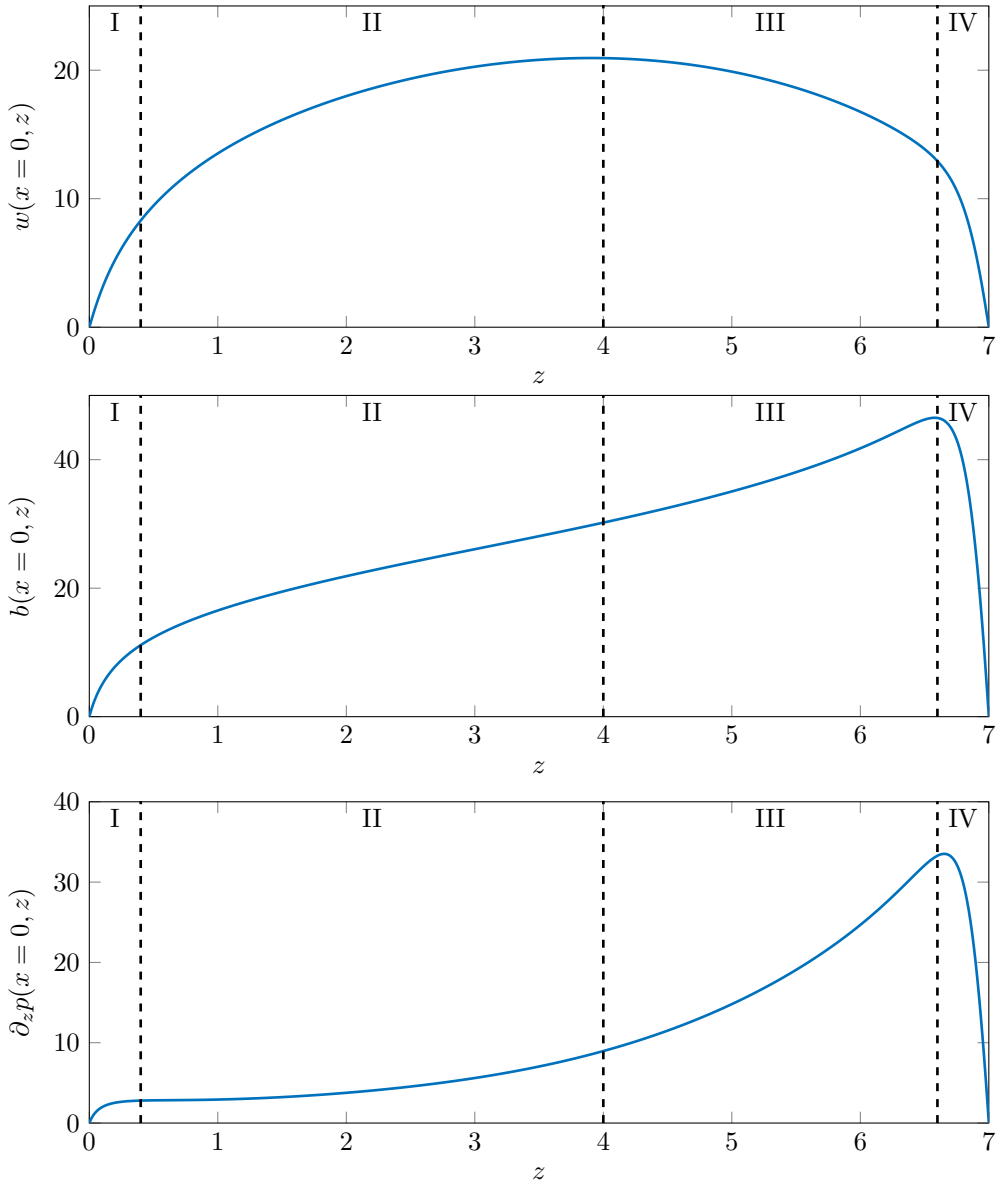

Figure 9: Profiles along the crack. Top: Vertical velocity w. Middle: Buoyancy b. Bottom: Vertical pressure gradient $\partial_z p$.

1. **Region I**: Tip behaviour, in a small regularisation region. All quantities are small and the region is isotropic. Diffusive terms dominate and the buoyancy satsifies a Poisson equation. Because this region is isotropic, we expect the variation along the length of the crack to satisfy $w \sim z$ and $b \sim z$ as discussed in section 3.6.1;

2. **Region II**: Rising plume region, described by a vertical boundary layer in which horizontal spatial derivatives dominate. The buoyancy is mostly given by the vertical velocity $b \simeq w$. Due to the vertical boundary layer, $z^{1/3}$ scalings are expected as discussed in section 3.6.2;

3. **Region III**: Connection region, between II and IV, where b, w, and $\partial_z p$ are of the same order of magnitude. The region is isotropic and the non-linear terms dominate the collapsed equation. The incoming plume flow from below carries most of the buoyancy flux, which is advected through this region and the additional heating at the wall does not change the buoyancy flux substantially, remaining of the same order of magnitude throughout this region; and

4. **Region IV**: Top corner region, with the scaling of a top boundary layer, bringing the heat flux sideways. The buoyancy is nearly in hydrostatic balance with the vertical pressure gradient, so $b \simeq \partial_z p$. Again, this region is diffusive and we expect the linear scalings derived in section 3.6.1. The fluxes, however, point towards a region that grows with x with a horizontal boundary layer as in section 3.6.3 and its scalings for the pressure gradient.

Figure 10 presents log-log plots of the vertical velocity and of the buoyancy in which the different scalings predicted analytically in the theory section 3 are tested. Figures 10(a) and (b) show log-log plots of the vertical velocity along the crack, starting from the bottom and starting from the top, respectively. We first observe a linear scaling $w \propto z$ in region I, two $1/3$ scalings $w \propto z^{1/3}$ and $w \propto (H-z)^{1/3}$ in region II and III, and a linear scaling $w \propto (H-z)$ in region IV. Figures 10(c) and (d) show log-log plots of the buoyancy along the crack, starting from the bottom and starting from the top, respectively. Similarly to the vertical velocity, we first observe a linear scaling $w \propto z$ in region I, a $1/3$ scalings $w \propto z^{1/3}$ in region II and a minus $1/3$ scaling $w \propto (H-z)^{-1/3}$ in region III, and a linear scaling $w \propto (H-z)$ in region IV. As discussed below, scalings for regions I, II, and IV, are consistent with the theoretical expectations. Region III, however, shows interesting scalings that are still to be explained.

We now look for more quantitative arguments of the different scalings.

4.2 Region I

Close to the tip, at the bottom of the crack, the vertical velocity, the buoyancy, and the pressure gradient are small. All terms contribute to the equations as the region is isotropic. The scalings of the potential equation

$$\partial_t \nabla^2 \varphi - \partial_x \partial_z \varphi \partial_x \nabla^2 \varphi + \partial_x^2 \varphi \partial_z \nabla^2 \varphi = \nabla^4 \varphi, \tag{75}$$

and the flux

$$F = -\partial_x b \simeq -\partial_x \nabla^2 \varphi, \tag{76}$$

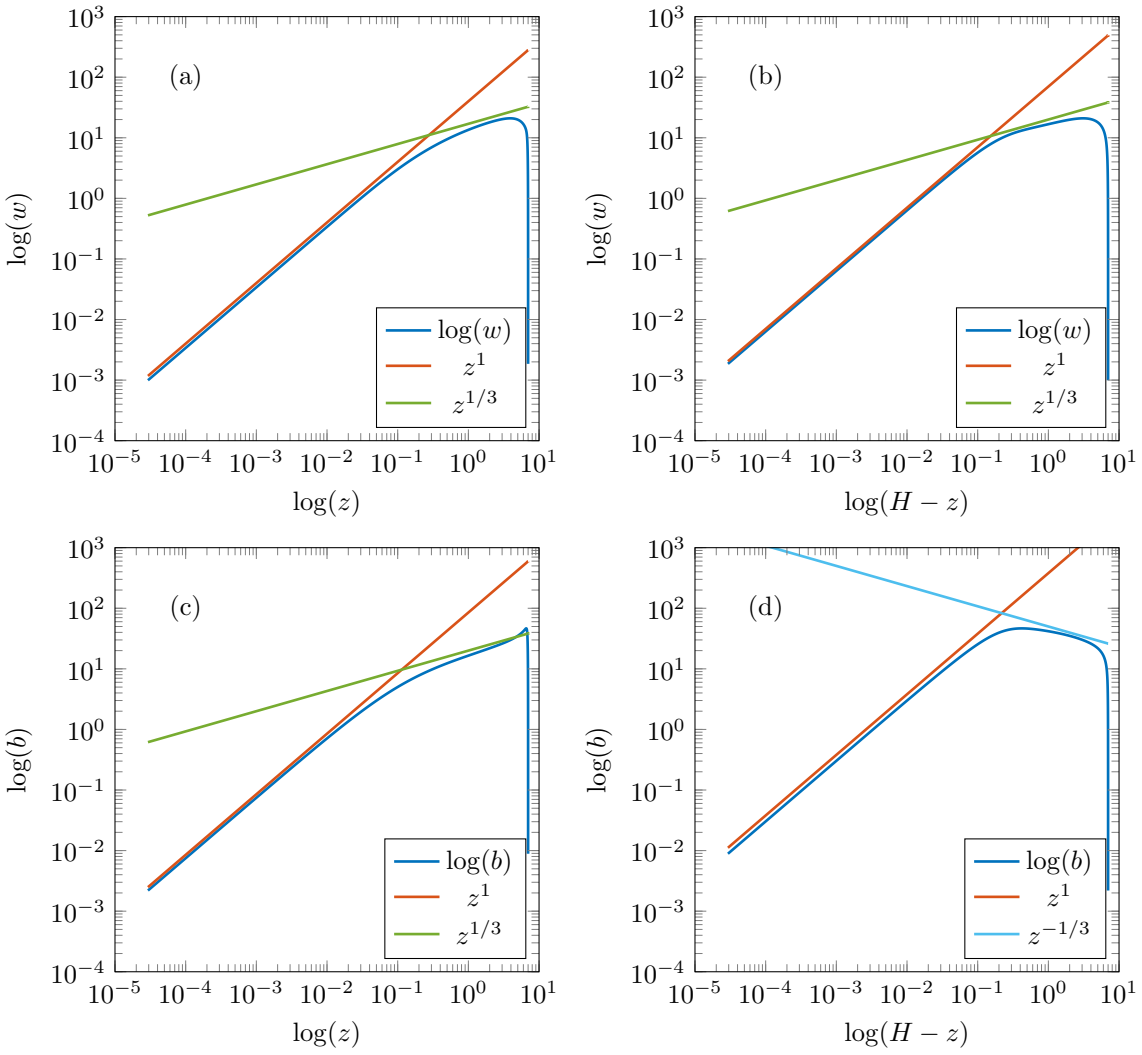

Figure 10: Scalings inferred from the profiles along the crack. (a): Vertical velocity from the bottom; (b): Vertical velocity from the top; (c): Buoyancy from the bottom; and (d): Buoyancy from the top.

gives

$$\partial_x\partial_z\varphi\partial_x\nabla^2\varphi + \partial_x^2\varphi\partial_z\nabla^2\varphi \sim \frac{A^2}{L^5} \sim L, \tag{77}$$

$$\nabla^4\varphi \sim \frac{A}{L^4} \sim \frac{1}{L}. \tag{78}$$

As shown before (section 3.6.1), because the length scale is small, this region is diffusive and has a linear scaling for b and w with z, that is observed in figure 10(a) and (c).

4.3 Region II

In region II, the flow acts like a rising buoyant plume described by the vertical boundary layer from section 3.6.2. The lateral extent of this region at the bottom, connecting to region I, is of order h, and increases with z. From equation (61), our theory predicts a scaling in $z^{1/3}$ for w and b which is observed in the log-log plot in figures 10(a) and (c). In figure 11, we present horizontal slices of the vertical velocity (left) and of the buoyancy (right) at different depths in region II (plain lines), rescaled in the horizontal variable by $z^{1/3}$ as well as in amplitude. There is a good collapse at $x = 0$, close to the crack. The superimposed dashed line is the self-similarity solution of equation (62) and (63), which are recalled here

$$(f'')^2 - 2f'f''' - 3f'''' = 0, \tag{79}$$

and

$$\underbrace{f'''(0) = -1}_{\text{flux at } x=0}, \qquad \underbrace{f'(0) = 0}_{u=0 \text{ at the crack}} \qquad \text{and} \qquad \underbrace{f''(\eta^*) = 0 \quad \text{with} \quad \eta^* \quad \text{“large”}}_{\text{constant } b \text{ in the far field}}. \tag{80}$$

This is computed using Dedalus over 256 Chebyshev nodes, enough to ensure that the far field boundary condition is satisfied. Numerical convergence of the solution is obtained after a few iterations. The computed solutions show a good agreement with the data. The profiles diverge from the similarity solution in the far field, due to the influence of the return flow that is not included in the boundary layer model.

4.4 Region III

Region III is an isotropic region connecting regions II and IV. Figure 12 shows how this connection region behaves. We recall that

$$b = w + \partial_z p, \tag{81}$$

from the definition of the potential φ. In region II, as seen before, the vertical boundary layer model leads to $w \simeq b$ and $\partial_z p$ is negligible, whereas in region IV, $b \simeq \partial_z p$ and w has a small contribution. The only way this configuration can occur is to have an isotropic transition region in between, in which w and $\partial_z p$ have the same order of magnitude, with w decreasing while $\partial_z p$ increases. This behaviour is observed in domain III in figure 12.

From the log-log plots in figures 10 (b) and (d), we infer two empirical scalings: a $(z-H)^{1/3}$ scaling for w, and a $(z-H)^{-1/3}$ scaling for b. Figure 13 presents horizontal slices of vertical velocity (left) and buoyancy (right) rescaled by $1/3$ and $-1/3$ power laws, showing

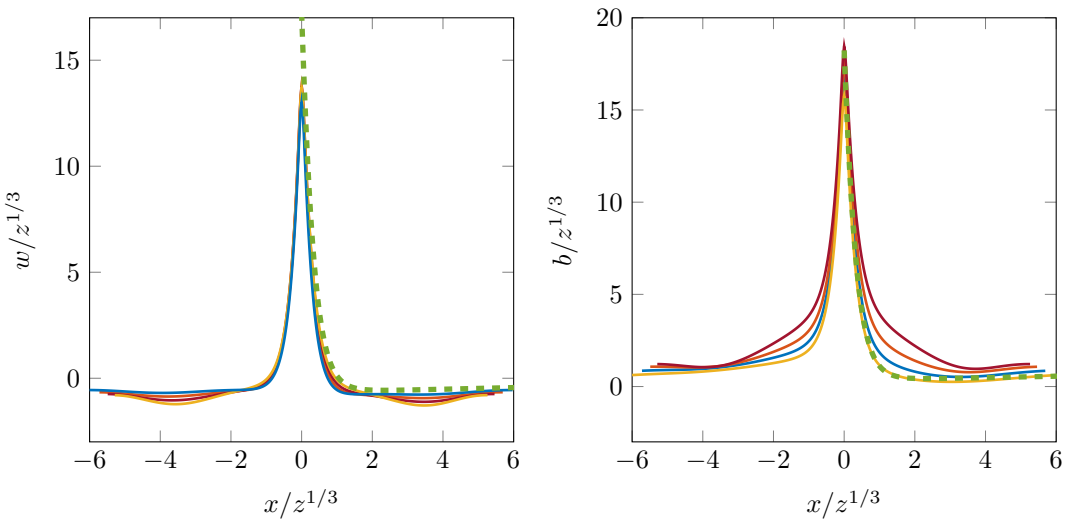

Figure 11: Left: Horizontal slices of vertical velocity at different depths in region II (plain lines) and self-similarity solution (dashed line). Right: Horizontal slices of buoyancy at different depths in region II (plain lines) and self-similar solution to (62)-(63) (dashed line). The colours correspond to different depths randomly chosen.

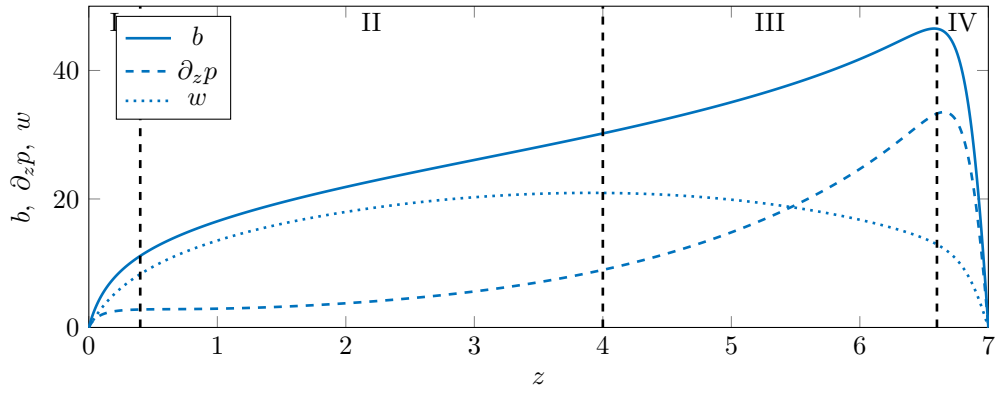

Figure 12: Buoyancy (plain line), vertical pressure gradient (dashed line), and vertical velocity (dotted line) taken along the crack.

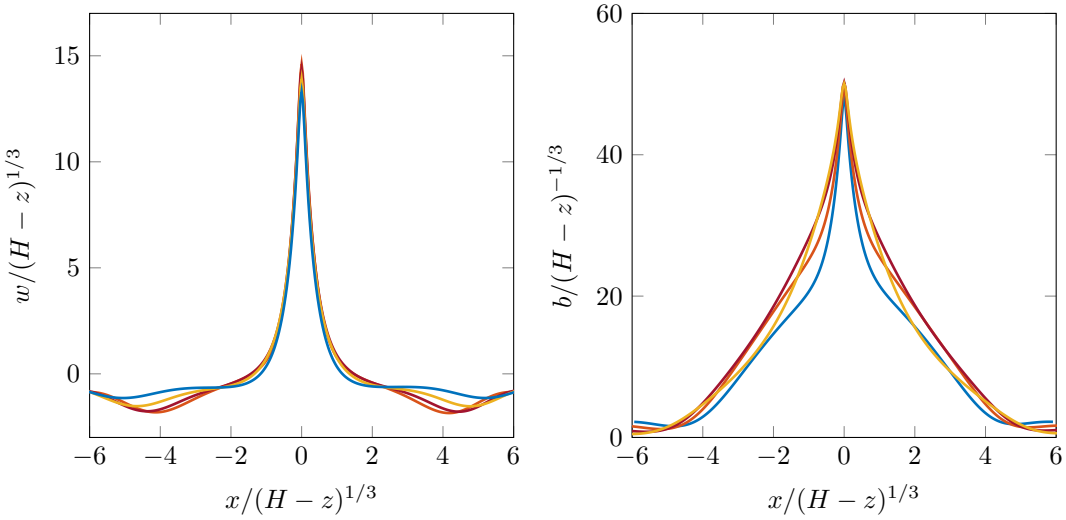

Figure 13: Left: Horizontal slices of vertical velocity at different depths in region III. Right: Horizontal slices of buoyancy at different depths in region III.

a good collapse close to the crack. The collapse is better for w than for b, pointing towards a transition between a vertical boundary layer in which w is set and a fully isotropic region dominated by fluxes. This collapse, however, is curious as it does not correspond to the boundary layer described in the previous sections, and still awaits a theoretical explanation.

4.5 Region IV

Region IV is the top region and has the scalings of the horizontal boundary layer in which the flow spreads horizontally. In this region, the pressure gradient reaches a maximum and has the largest contribution to the buoyancy. According to equation (74), the peak in the vertical profile of the pressure gradient should increase and move upwards as we increase the Rayleigh number. Figure 14 shows results from DNS at various Rayleigh numbers, with this increasing peak. For each of these profiles, we measure the amplitude of the peak $\max(\partial_z p)$ and its location z_m from the top of the crack. Figure 15 presents these data in log-log plots. For the amplitude of the peak (figure 15(left)) we have a $Ra^{3/4}$ scaling (or $h^{-3/2}$) consistent with the theory. For the location z_m (figure 15(right)), we have a $Ra^{-1/2}$ scaling (or h) also consistent with the theory.

The linear behaviour in the top corner can be described using a stagnation point solution. A series expansion of the stream function in this region gives

$$\psi = Ax + Bz + Cx^2 + Dxz + Ez^2, \tag{82}$$

and the corresponding velocities are

$$u = -\partial_z \psi = -B - Dx - 2Ez, \tag{83}$$

$$w = \partial_x \psi = A + 2Cx + Dz. \tag{84}$$

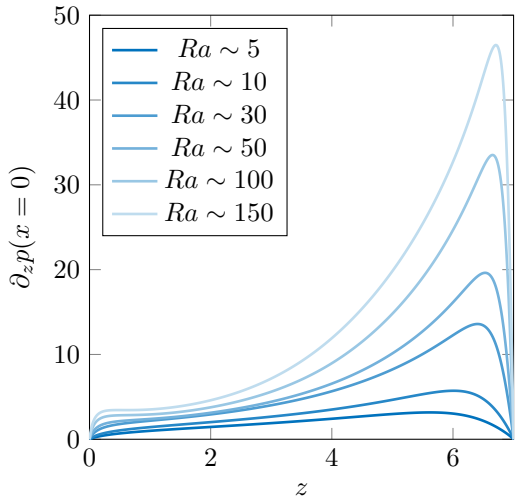

Figure 14: Along crack profiles of the vertical pressure gradient for different Rayleigh numbers (corresponding to different heating prefactors Q_0).

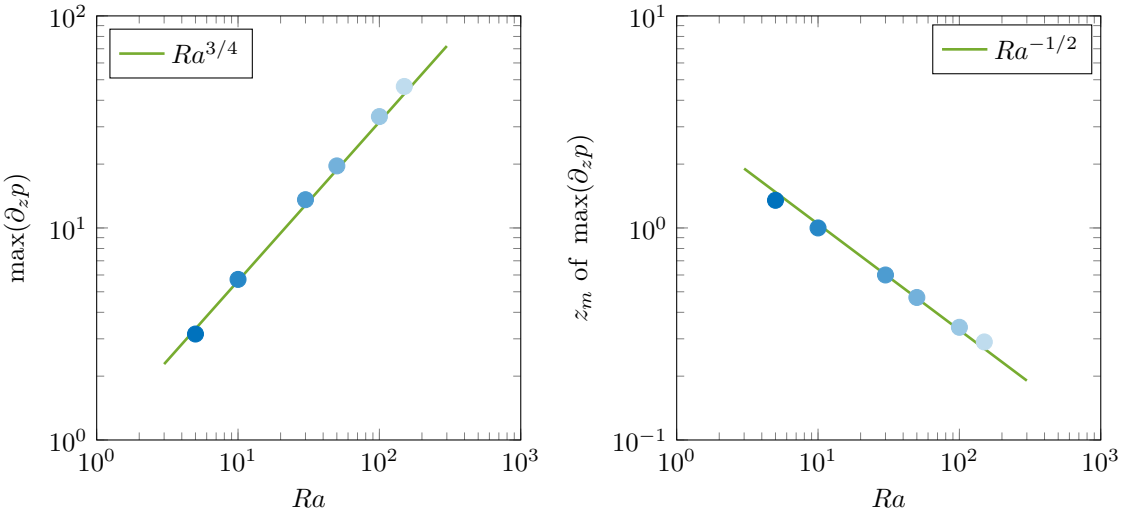

Figure 15: Scaling laws with Rayleigh number in log-log plots. Left: Amplitude of the peak of pressure gradient, with a $Ra^{3/4}$ law. Right: Location of the peak, starting from the top, with a $Ra^{-1/2}$ law.

The different coefficients can be determined as follow. Firstly, there is no horizontal velocity at $x = 0$ so $B = E = 0$. Secondly, there is no vertical velocity at $z = 0$ so $A = C = 0$. Finally, the stream function is

$$= Dxz, \tag{85}$$

with D a coefficient to be determined. It ensures a linear scaling in z for w. The coefficient D depends on matching to the flow from the incoming isotropic region; this calculation is challenging and not pursued here.

5 Conclusions and Discussion

5.1 Different regimes

We derived a simple model of frictional heating along a crack in a porous media, that mimics the mushy region created around a crack in the ice shell of Enceladus. Through Direct Numerical Simulations and construction of approximate asymptotic solutions, we checked that our theoretical model provides a good description of the phenomenon. Four different regions were identified along the crack, starting from the bottom to the top: a diffusive region, a rising plume (vertical boundary layer), an isotropic connection region, and a top layer. These regions and their scalings are summarised in figure 16.

5.2 Melting rate

The advection-diffusion equation for b and the solute and heat equations give an equation for the solid phase evolution, or melting rate, depending on the potential φ. In a dimensionless form this yields

$$\frac{\partial \phi}{\partial t} = -\frac{1}{Ra\mathscr{C}\Omega}\nabla^4\varphi. \tag{86}$$

In this model, we assume that the system reaches a steady state for the flow and for the buoyancy (and temperature). Although we do not consider porosity variation here (Π is a constant and is equal to Π_0), the expected change to porosity can be estimated as the solid fraction is allowed to vary over a slow timescale, and $\partial_t\phi$ is non-zero.

The melting rate ($\partial_t\phi \sim -\nabla^4\varphi$) in the DNS is presented in figure 17, in which areas with decreasing solid fraction are shown in red. Positive value for $-\partial_t\phi$ means that the solid fraction is decreasing, corresponding to ice melting. A strong and localised region of melting is identified at the top of the crack, corresponding to region IV, with a vertical extent of order h. This confirms the importance of the top region in the melting problem, which is therefore likely to be the source of geysers. The solutions are likely relevant if a pre-existing porous region is suddenly heated. In this DNS, as the initial condition is of pure eutectic, the solution for the melting rate becomes unphysical, which is why small regions of freezing appear close to the crack and the results cannot be applied directly to the crack problem. This freezing is a slower process than the melting, as $-\partial_t\phi$ varies over more than an order of magnitude between the freezing and the melting region at the crack, and even more if we look at the top region. It is likely that this behaviour would be suppressed with a feedback of the porosity on the flow, as a solid fraction equal to 1 would prevent the

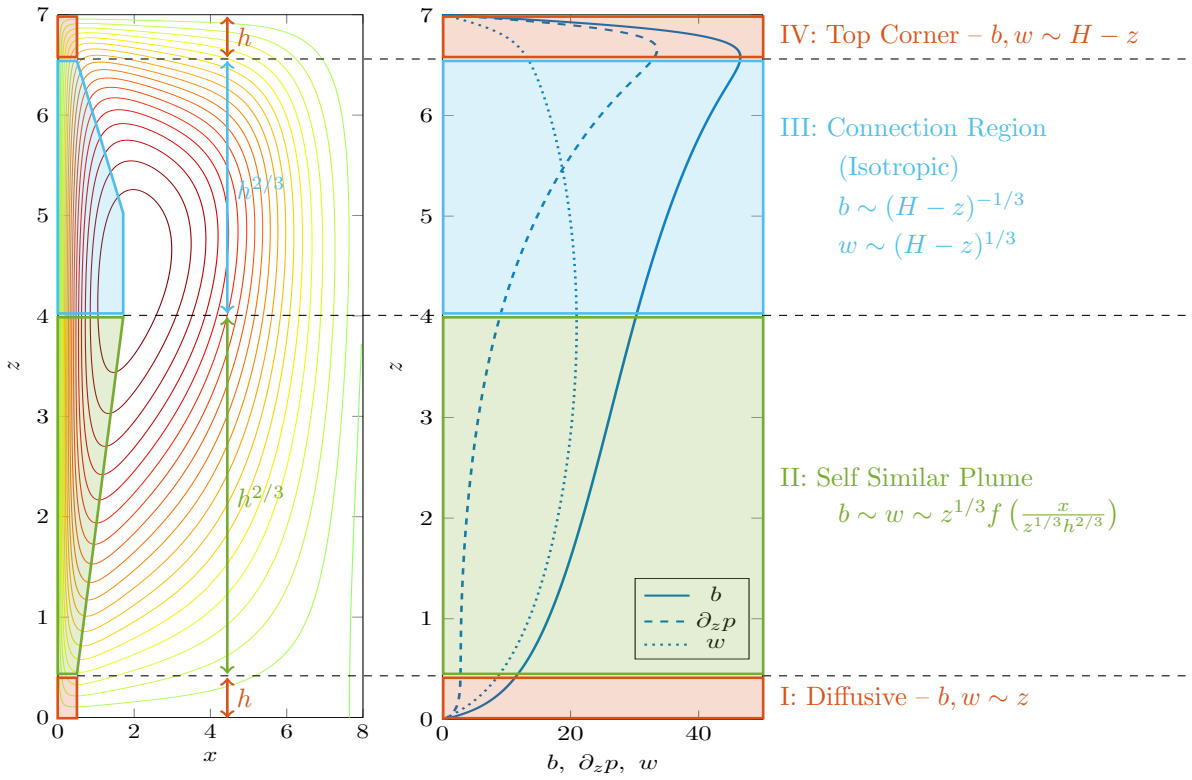

Figure 16: Left: Contours of stream function in the steady state. Right: along crack profiles of vertical velocity, pressure gradient, and buoyancy. Four different regions, labeled from I to IV, are identified with different scaling laws.

liquid from flowing. The relevent scalings, however, are still a good approximation of what is happening.

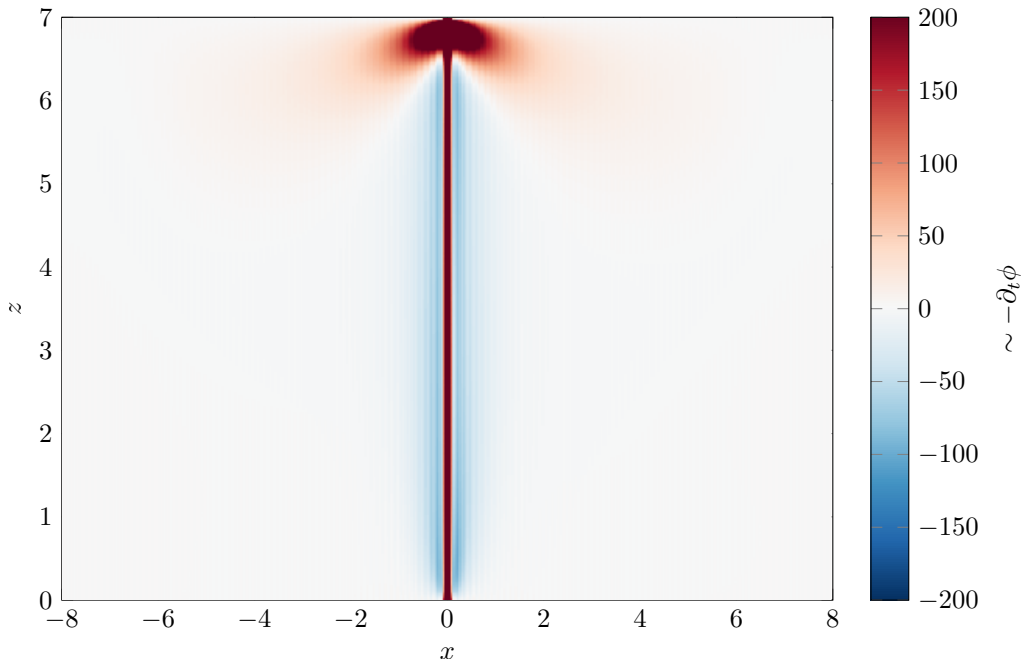

Figure 17: Melting rate, or solid fraction change, from the DNS (red shows melting).

5.3 Importance of the top region

The vertical extension of the top region can be estimated through the Rayleigh number, as $Ra = (H/h)^2$. From the previous derivation, the Rayleigh number can be expressed into a classical Rayleigh number, often used in convection problems, with a fixed multiplicative factor

$$Ra = \frac{g\alpha \Pi_0 C_p F H^2}{\kappa^2 \nu} = \left(\frac{g\alpha \Delta T H^3}{\nu\kappa}\right) \frac{\Pi_0 C_p F}{\kappa \Delta T H} \equiv \left(\frac{g\alpha \Delta T H^3}{\nu\kappa}\right) \frac{\Pi_0}{H^2}. \tag{87}$$

All parameters in this formula can be estimated, at least in order of magnitude [9, 14], assuming that the material properties are similar to terrestrial sea ice

$$\begin{aligned} g &= 10^{-1}\ \mathrm{m}\cdot\mathrm{s}^{-2}, \\ \alpha &= 10^{-2}\ \mathrm{K}^{-1}, \\ \Delta T &= 10\ \mathrm{K}, \\ \kappa &= 10^{-5}\ \mathrm{m}^2\cdot\mathrm{s}^{-1}, \\ \nu &= 10^{-6}\ \mathrm{m}^2\cdot\mathrm{s}^{-1}, \\ H &= 10\ \mathrm{km}, \\ \Pi_0 &= 10^{-10}\ \mathrm{m}^2, \end{aligned}$$

where we assume that the media has high solid fraction and low porosity, so the thermal diffusivity κ is well approximated by that of the solid. Hence

$$Ra \sim 100 \qquad \text{and} \qquad h \sim 1 \text{ km}, \tag{88}$$

meaning that the top region is localised over a short depth near the surface.

5.4 Discussion

In this study, we developped a simple model of buoyant plume generated through shear-heating of a crack. We adapted Nimmo et al.'s model of a finite depth crack [8] to consider mushy dynamics of an impure partially melted ice and salt mixture, and assumed that a constant heat flux is applied along the crack due to tidal heating. We identified four different regions created along the crack through the heating process, and we show that the relevent part of the crack that dominates the melting is located near the surface over a short depth. The proposed mechanism is robust and the different scalings observed in Direct Numerical Simulations agree well with the theory.

Contrary to the partial crack model of Nimmo et al. [8], the melting process we describe can supply salts to the geyser plumes. Also, it does not involve a full depth crack and does not rely on the assumption that the cracks at the surface are connected to an inner liquid ocean [11, 13, 20]. All the melting process, water and salts supply, happen close to the crack in a finite depth region and are enhanced in the very top region, over a depth estimated to be of order 1 km. We are only investigating the possible source mechanism for geysers, and the steady state regime we describe is only valid at short times, as it breaks as soon as the solid fraction goes to zero. We have also modelled a closed system, and hence the model cannot directly explain the ejection of water by geysers.

Different assumptions, however, are still to be tested. For example, the top boundary condition for temperature would be radiative and should match with observational data [14]. Moreover, different scalings still remain with no explanation: region III, in particular, shows two different scalings for the buoyancy and the vertical velocity, but they do not match with our theoretical developments. In this region, it is very likely that the vertical velocity matches with region II, whereas the buoyancy and the pressure fields match with region IV, and that the total heat flux is conserved, but we have no supporting mathematical evidence of that. No analytical result for region I, at the bottom of the crack, has been properly derived. Attempts to obtain the buoyancy and the vertical velocity from Green's functions have been made assuming a delta function heating. However, the results show a slightly different scaling than the DNS. The explanation for that is presumably due to the finite width of the Gaussian in the DNS, versus the delta function spike of heating in the analytical approximation. The top region IV could be better understood by defining regions IV and V: one being the top corner, the other one being the horizontal boundary layer that extends near the surface in the x direction. Different scalings can then be tested in region V accordingly to the horizontal boundary layer theory from section 3.6.3.

A more accurate description of the problem could be derived, relaxing the constant porosity assumption. The flow would then feel a feedback from the melting of the mush and the phase change itself, as the porosity would be a function of the solid fraction. The influence of the boundaries needs to be more specifically parametrised too, as there should

be a boundary between the mushy region and the pure ice region, that can evolve through time as the mush is growing. The existence of a physical instability triggered at sufficiently high Rayleigh number could be explored in some more details. Starting from the linear steady state, such an instability is likely to occur with an intense and short-lived forcing, which might be enough to create strong intermittent eruptive geysers.

References

[1] K. J. Burns, G. M. Vasil, J. S. Oishi, D. Lecoanet, and B. P. Brown, *Dedalus: A flexible framework for numerical simulations with spectral methods*, (2019).

[2] P. Cheng and W. J. Minkowycz, *Free convection about a vertical flat plate embedded in a porous medium with application to heat transfer from a dike*, Journal of Geophysical Research, 82 (1977), p. 7B0014.

[3] M. K. Dougherty, L. W. Esposito, and S. M. Krimigis, *Saturn from Cassini-Huygens*, Springer, 2009.

[4] A. C. Fowler, *The formation of freckles in binary alloys*, Journal of Applied Mathematics, 35 (1985), pp. 159 – 174.

[5] P. Guba and M. G. Worster, *Free convection in laterally solidifying mushy regions*, Journal of Fluid Mechanics, 558 (2006), pp. 69 – 78.

[6] T. A. Hurford, P. Helfenstein, G. V. Hoppa, R. Greenberg, and B. G. Bills, *Eruptions arising from tidally controlled periodic openings of rifts on enceladus*, Nature, 447 (2007), pp. 292 – 294.

[7] D. B. Ingham and S. N. Brown, *Flow past a suddenly heated vertical plate in a porous medium*, Proceedings of the Royal Society of London. Series A, 403 (1986), pp. 51 – 80.

[8] F. Nimmo, J. R. Spencer, R. T. Pappalardo, and M. E. Mullen, *Shear heating as the origin of the plumes and heat flux on enceladus*, Nature, 447 (2007), pp. 289 – 291.

[9] C. Polashenski, K. M. Golden, D. K. Perovich, E. Skyllingstad, A. Arnsten, C. Stwertka, and N. Wright, *Percolation blockage: A process that enables melt pond formation on first year arctic sea ice*, Journal of Geophysical Research: Oceans, 122 (2017), pp. 1 – 28.

[10] C. C. Porco, P. Helfenstein, A. C. Thomas, A. P. Ingersoll, J. Wisdom, R. West, G. Neukum, T. Denk, R. Wagner, R. Roatsch, S. Kieffer, E. Turtle, A. McEwen, T. V. Johnson, J. Rathbun, J. Veverka, D. Wilson, J. Perry, J. ans Spitale, A. Brahic, J. A. Burns, D. A. D., L. Dones, C. D. Murray, and S. Squyres, *Cassini observes the active south pole of enceladus*, Science, 311 (2006), pp. 1393 – 1401.

[11] F. Postberg, S. Kempf, J. Schmidt, N. Brillantov, A. Beinsen, B. Abel, U. Buck, and R. Srama, *Sodium salts in e-ring ice grains from an ocean below the surface of enceladus*, Nature, 459 (2009), pp. 1098 – 1101.

[12] F. Postberg, J. Schmidt, J. Hillier, S. Kempf, and R. S. Srama, *A salt-water reservoir as the source of a compositionally stratified plume on enceladus*, Nature, 474 (2011), pp. 620 – 622.

[13] N. M. Schneider, M. H. Burger, E. L. Schaller, M. E. Brown, R. E. Johnson, J. S. Kargel, M. K. Dougherty, and N. A. Achilleos, *No sodium in the vapour plumes of enceladus*, Nature, 459 (2009), pp. 1102 – 1104.

[14] J. R. Spencer and F. Nimmo, *Enceladus: An active ice world in the saturn system*, Annual Review of Earth and Planetary Sciences, 41 (2013), pp. 693 – 717.

[15] J. R. Spencer, J. C. Pearl, M. Segura, F. M. Flasar, A. Mamoutkine, P. Romani, B. J. Buratti, A. R. Hendrix, L. J. Spilker, and R. M. C. Lopes, *Special research articles cassini encounters enceladus: Background and the discovery of a south polar hot spot*, Science, 311 (2006), pp. 1401 – 1405.

[16] A. J. Wells, J. R. Hitchen, and J. R. G. Parkinson, *Mushy-layer growth and convection, with application to sea ice*, Philosophical Transactions A, 377 (2019), p. 20180165.

[17] M. G. Worster, *Solidification of an alloy from a cooled boundary*, Journal of Fluid Mechanics, 167 (1986), pp. 481 – 501.

[18] ——, *Solidification of fluids*, in Perspectives in Fluid Dynamics, G. K. Batchelor, H. K. Moffatt, and M. G. Worster, eds., Cambridge University Press, 2000, ch. 8, pp. 393–444.

[19] ——, *GFD program lectures notes*, GFD Program, 2007.

[20] M. Y. Zolotov, *An oceanic composition on early and today's enceladus*, Geophysical Research Letters, 34 (2007), p. L23203.

Optimal Mixing of a Passive Scalar Field in Kolmogorov Flow

Jelle B. Will

August 22, 2019

1 Introduction

Mixing is a topic that, rightfully, garners a lot attention in the fluid dynamics community. This is due to its wide applicability to a wide range of problems both from natural phenomena to industrial applications. An understanding of mixing is crucial to being able to predict and comprehend ocean circulations as well as spreading of pollutants in both the ocean and atmosphere. Additionally, there is much interest from industry due to mixing playing a major role in getting chemical agents to react, an everyday example being combustion in a car engine. The underlying physical mechanisms are, from a pure physics perspective, also very interesting and complex. The interplay between convective mixing and molecular diffusion makes even the most basic problems quite challenging and oftentimes counter intuitive.

In this work we will be focusing on a mixing type of problem. In a practical sense, this means that we have a fluid phase with all the related governing equations and a dispersed phase, droplets, bubbles and/or particles which are affected by the fluid. In our case we are dealing with a passive field, which means the dispersed phase will not affect the primary phase, the interaction is one-way coupled. In this system the dispersed phase will be advected and diffused, thus altering its distribution over time. This needs to be quantified in some way but we will get back to that later. The process of redistribution of the dispersed phase is called mixing.

The more conventional approach to study mixing is to perform simulations or experiments and study the resulting flow and scalar fields a posteriori to quantify the amount of mixing that occurred. In this work our aim is to investigate mixing from a different perspective, assuming that we can prescribe the initial flow field or perturbations; what initial state will give us the most extreme outcome? Or a specific result we desire? This approach can provide valuable insight into the parameters and structures that enhance or reduce mixing in a specific type of flow.

One especially interesting case is that of inertial particles (particles with a different density than that of the fluid phase), which was the original motivation for this project. In this case one can, for instance, ask: "How can we achieve the highest local concentration?" This problem is highly relevant in both natural as well as industrial flows. Consider for instance the growth of droplets or snowflakes in a cloud, or clustering of sediments in a river, ocean, or waste treatment plant. What all these scenarios have in common is that the fluid phase is turbulent. Kinetic energy is injected at some scale that drives the flow, this energy is

then cascaded down to smaller scales until it dissipates at the viscous length scale. Particles that are not density matched will interact with this spectrum in interesting ways: due to centrifugal pressure, light particles will preferentially concentrate in the cores of eddies, heavy particles on the other hand will be ejected and cluster on the outside of vortices. As a result, for inertial particles we obtain structures as seen in the work by Calzavarini et al. [2]. This type of problem is also common in industrial applications, such as the extraction of minerals from a slurry by means of bubble injection and stirring. Here the bubbles (light particles) have to collide and gather the minerals (heavy particles) so they can float to the top and be skimmed off. However, a lot of ore is being thrown out because of poor mixing of these two dispersed phases. Therefore, understanding the interaction between inertial particles is a very relevant field of investigation with a lot of implications and applications.

As a first step towards the more complicated particulate problem, we will be content to look at mixing of a passive scalar field in a model two-dimensional shear flow. The question we aim to answer is: "what initial perturbation of the background flow will give us the best mixed state after a set amount of time has passed?" The answer to this question is not trivial, as was addressed by Danckwerts (1952) [3], who showed that owing to the interplay between advection and diffusion the creation of complex flow patterns is desired. Even for relatively simple systems this sometimes results in surprising solutions, as shown in the work by Thiffeault et al. (2004) [10].

2 The Numerical Experiment

2.1 The base code

For the simulations we made use of a pseudo-spectral DNS code developed by Stephan Stellmach. The code, colloquially called PADDI (**PA**rallel **D**ouble **DI**ffusion), was developed for the main purpose of solving double diffusive convection problems. This makes it very suitable as a basis of the current project since all the routines for solving the equations for both the fluid phase and the scalar field are already present. We use Adam-Bashforth third order backwards differencing for the time integration of our velocity and scalar fields. Furthermore, we are only running the code in its two-dimensional mode.

2.2 Experimental setup

We will be dealing with a single numerical setup throughout this work. The case we are considering is that of a two-dimensional shear flow in a doubly periodic domain. The horizontal extent of the domain is 0 to 4π and the vertical is 0 to 2π as is shown in Fig. 1. A numerical resolution of 256 and 128 Fourier modes in the horizontal and vertical directions is used. The flow is incompressible and is forced in the horizontal direction by a sinusoidal body forcing. This system is known as a Kolmogorov flow. The profile of the background, or base, flow is given by:

$$\begin{aligned} \bar{u}_x(z) &= \sin(z) \\ \bar{u}_z &= 0. \end{aligned} \tag{1}$$

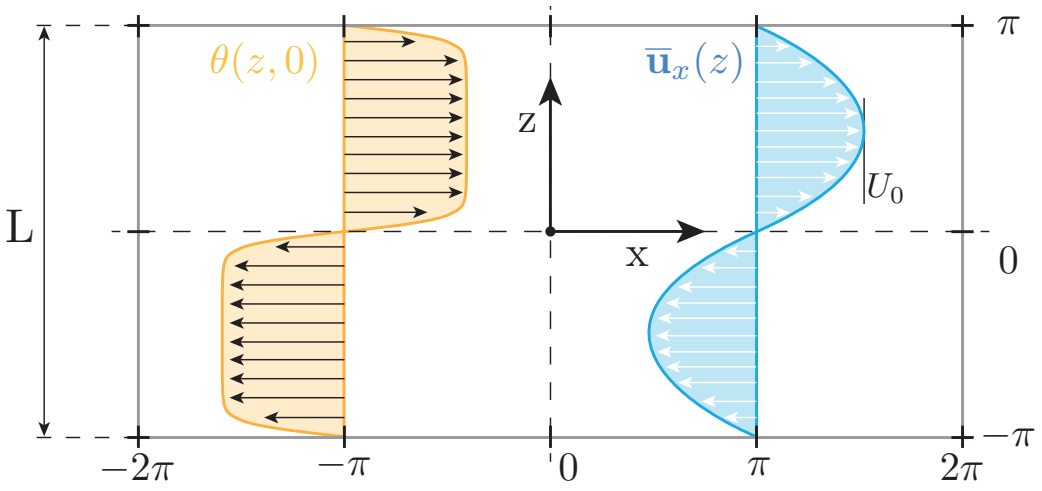

Figure 1: Schematic overview of the numerical experiment. The domain size, velocity field and passive scalar distributions at $t = 0$ are shown.

Here, the amplitude of the corresponding dimensional background flow will define our our unit velocity U_0 and the wave length of this forcing defines the unit length scale L. The resulting flow profile is shown in Fig. 1. We then use the standard decomposition of the total velocity as follows:

$$\boldsymbol{U}(\boldsymbol{x}, t) = \bar{\boldsymbol{u}}(z) + \boldsymbol{u}(\boldsymbol{x}, t), \tag{2}$$

where $\bar{\boldsymbol{u}}$ is the aforementioned base flow which only depends on the vertical coordinate and $\boldsymbol{u}$ is the perturbation velocity field superimposed on this base flow. There are no assumptions made regarding the relative magnitude of the two velocities.
Additionally, at time $t = 0$ we assume the existence of a passive scalar field, denoted by θ, in its unmixed state. In all results discussed here the same initial profile for the scalar field is used, given by:

$$\theta(z, 0) = \tanh\left(\frac{10\sin(z)}{\tanh(z)}\right). \tag{3}$$

This profile is also shown in Fig. 1. Note that the mean of the scalar field over the entire domain is equal to zero and that the inflection points of both the velocity and the scalar field profiles are at the same vertical positions. This profile is chosen for simplicity but can be motivated from potential applications in geophysical flows. In oceanic flows, for instance, the density (salinity, temperature) profiles often form horizontal layers, in the form of thermohaline staircases. [8]. These span large horizontal extents but are quite narrow in the vertical direction. Also these respective layers can have opposite velocities at the interface, making them susceptible to shear instabilities. The current configuration can be seen as a much simplified model for mixing in those types of systems.
It is, however, important to realize that the profile chosen here is somewhat arbitrary and that it will affect the resulting optimization. The steepness of the profile and exact align-ment might affect the outcome significantly.

The equations governing this system are the two-dimensional continuity, Navier-Stokes, and advection-diffusion equations. These are further characterized by the kinematic viscosity ν, i.e. diffusivity of momentum in the flow, and the molecular diffusivity of the scalar field κ. Thus, we obtain two dimensionless quantities, namely the Reynolds and Péclet numbers defined as:

$$Re = \frac{U_0 L}{\nu}, \tag{4}$$

$$Pe = \frac{U_0 L}{\kappa}. \tag{5}$$

These two dimensionless quantities are coupled through the Prandtl number:

$$Pr = \frac{Pe}{Re} = \frac{\nu}{\kappa}. \tag{6}$$

Using these definitions and assumptions we can write down the governing equations in dimensionless form as follows:

$$\partial_t \boldsymbol{u} + \boldsymbol{U} \cdot \boldsymbol{\nabla} \boldsymbol{u} + \boldsymbol{u} \cdot \boldsymbol{\nabla} \bar{\boldsymbol{u}} + \boldsymbol{\nabla} p - Re^{-1} \boldsymbol{\nabla}^2 \boldsymbol{u} = 0 \tag{7}$$

$$\boldsymbol{\nabla} \cdot \boldsymbol{u} = 0 \tag{8}$$

$$\partial_t \theta + \boldsymbol{U} \cdot \boldsymbol{\nabla} \theta - Pe^{-1} \boldsymbol{\nabla}^2 \theta = 0. \tag{9}$$

We will refer to these equations as the direct or forward equations from now on. We impose the background flow and initial condition for the scalar field as given in equations 1 and 3. The initial condition for the perturbation velocity field is a variable of our problem and will be optimized for. The initial perturbation velocity field for the first iteration of the optimization will in all cases be random noise, the amplitude of which is constraint by how much we want to perturb the initial system. This is achieved by normalizing the random velocity field by dividing by its standard deviation and then applying a scaling factor.
Here, two types of results will be presented. The first simulations are run at a constant Reynolds number, $Re = 50$ as defined by Eq. 4. The second case is at constant Péclet number, $Pe = 50$.

2.3 The mixing norm

In order to optimize our mixing we need a quantity that accurately reflects the "mixedness" of our passive scalar field. A measure for how well a field is "mixed" needs to reflect how uniform the distribution is throughout the field. A basic approach consists of using the variance or its L^2-norm of the scalar field, defined as:

$$\text{Var } \theta = \frac{1}{V_\Omega} ||\theta||^2 = \frac{1}{V_\Omega} \int_\Omega \theta(\boldsymbol{x}, T)^2 d\Omega \tag{10}$$

This parameter possesses all the properties we are looking for, since it quantifies deviations from the mean value. If the field is completely mixed it has a value of zero, and if it is completely binary it has a maximum value. This norm will be called the cost functional, or

measure to optimize. In this work we want to obtain the minimum value of this measure at a specific final (or terminal) time, called T hereafter. Note that the variance cannot decrease as a result of stirring i.e. without diffusion. Therefore in the limit of $Pe \to \infty$, the variance will not be reduced and thus no mixing is taking place according to this measure. Alternate norms are discussed in references [5] and [9].

3 Optimization Using the DAL Method

In this section we give an overview of the algorithm that is used to find the initial perturbation of the background flow that optimizes mixing at a fixed terminal time. This method is closely related to the work of Foures et al.(2014) [5] and the work by Kerswell et al. (2014) [6]. First we describe the basic idea of the approach and then provide additional detail on the exact implementation of this method for our system.

The goal of the algorithm is to obtain the minimum value of our cost functional at time T, which is $\mathrm{Var}(\theta)$ as given in equation 10. We want to find the initial perturbation velocity field $\boldsymbol{u}(\boldsymbol{x}, 0)$ that accomplishes this. For the current problem, the optimal solution would be one where the velocity perturbations go to infinity in amplitude because they have not been constrained yet. To this end we constrain the solutions by stating that:

$$\int_\Omega |\boldsymbol{u}_0|^2 \, \mathrm{d}\Omega = \int_\Omega |\boldsymbol{u}(\boldsymbol{x}, 0)|^2 \, \mathrm{d}\Omega = 2E_0, \tag{11}$$

where E_0 is a finite number. For all cases considered here this is $\sqrt{2}$ percent of the energy in the background flow.

We approach this problem by formulating and then iteratively minimize the constrained Lagrangian:

$$\mathscr{L} = \mathscr{L}(\boldsymbol{u}, \theta, p, \boldsymbol{u}^\dagger, \theta^\dagger, p^\dagger). \tag{12}$$

$$\begin{aligned}
\mathscr{L} = & \underbrace{\int_\Omega \theta(\boldsymbol{x}, T)^2 \, d\Omega}_{\text{cost functional}} - \int_0^T \int_\Omega p^\dagger \underbrace{\boldsymbol{\nabla} \cdot \boldsymbol{u}}_{\text{continuity}} \, \mathrm{d}\Omega \mathrm{d}t \\
& - \int_0^T \int_\Omega \underbrace{\left(\partial_t \boldsymbol{u} + \boldsymbol{U} \cdot \boldsymbol{\nabla} \boldsymbol{u} + \boldsymbol{u} \cdot \boldsymbol{\nabla} \bar{\boldsymbol{u}} + \boldsymbol{\nabla} p - Re^{-1} \boldsymbol{\nabla}^2 \boldsymbol{u}\right)}_{\text{Navier-Stokes}} \cdot \boldsymbol{u}^\dagger \, \mathrm{d}\Omega \mathrm{d}t \\
& - \int_0^T \int_\Omega \theta^\dagger \underbrace{\left(\partial_t \theta + \boldsymbol{U} \cdot \boldsymbol{\nabla} \theta - Pe^{-1} \boldsymbol{\nabla} \theta\right)}_{\text{advection-diffusion}} \, \mathrm{d}\Omega \mathrm{d}t.
\end{aligned} \tag{13}$$

Here the variables denoted by † are Lagrange multipliers that ensure that the system satisfies the constraints imposed by the continuity, Navier-Stokes and advection-diffusion equations. In the following sections these will be referred to as the adjoint variables. It is important to realize that the boundary conditions do not impose any constraints since the domain is periodic. For an optimal solution the derivative of $\mathscr{L}$ with respect to any variable

should be equal to zero. Variations with respect to the adjoint variables merely recover the constraints. However, the variation with respect to the variables $\boldsymbol{u}$, p, and θ, give us an additional set of equations to be satisfied and are computed in appendix A. They result in a system of evolution equations for the adjoint variables:

$$\partial_t \boldsymbol{u}^\dagger + \boldsymbol{U} \cdot \boldsymbol{\nabla} \boldsymbol{u}^\dagger - \boldsymbol{u}^\dagger \cdot \boldsymbol{\nabla} \boldsymbol{U}^T + \nabla p^\dagger + Re^{-1} \boldsymbol{\nabla}^2 \boldsymbol{u}^\dagger = \theta^\dagger \boldsymbol{\nabla} \theta \tag{14}$$

$$\boldsymbol{\nabla} \cdot \boldsymbol{u}^\dagger = 0 \tag{15}$$

$$\partial_t \theta^\dagger + \boldsymbol{U} \cdot \boldsymbol{\nabla} \theta^\dagger + Pe^{-1} \boldsymbol{\nabla}^2 \theta^\dagger = 0. \tag{16}$$

These equations are reminiscent of the direct equations governing the system (equations 7, 8 and 9). There are, however, some important differences. Firstly, note that the forward velocity and scalar fields are present in these equations. As a result, knowledge of the direct fields at every timestep will be required to integrate the adjoint equations in time numerically. This complicates matters since storing this data is quite memory intensive. Secondly, note how the sign of the diffusion terms in the momentum and scalar equations has switched. When integrated forward in time, these equations will thus be anti-diffusive. However, we will be evolving the adjoint variables $\boldsymbol{u}^\dagger$,$\theta^\dagger$, and $p^\dagger$ backwards in time so that will not be an issue. Finally, the adjoint Navier-Stokes equation is forced by a term containing the scalar field from the advection-diffusion equation. This implies that the scalar field will affect the updated initial velocity fields, as required.
In addition to these evolution equations, we obtain a number of important relationships between the direct and adjoint variables at the target time T, which are used to initialize the adjoint variables at the start of the backward loop. These relations are:

$$\boldsymbol{u}^\dagger(\boldsymbol{x}, T) = \boldsymbol{0}, \qquad \theta^\dagger(\boldsymbol{x}, T) = 2\theta(\boldsymbol{x}, T). \tag{17}$$

An optimal solution is found when $\delta \mathscr{L} / \delta \boldsymbol{u}(\boldsymbol{x},\, 0) = 0$. When this is not the case, the gradient of the Lagrangian can then be used to update the initial condition for the velocity perturbations. Since for an arbitrary perturbation velocity field this will not be the case, then:

$$\frac{\delta \mathscr{L}}{\delta \boldsymbol{u}(\boldsymbol{x}, 0)} = \boldsymbol{u}(\boldsymbol{x}, 0)^\dagger. \tag{18}$$

We can use $\boldsymbol{u}(\boldsymbol{x}, 0)^\dagger$, obtained from the backward loop, into a gradient descent-type algorithm to update $\boldsymbol{u}(\boldsymbol{x}, 0)$, and restart the loop based on this new, improved, guess.

Now we will give a step-by-step approach of the DAL algorithm as implemented in this work. A schematic overview is also given in Fig. 2.

Step 0. Create a random initial velocity field $\boldsymbol{u}_{(0)}(\boldsymbol{x}, 0)$ such that the energy of the field is constrained by the equation 11.

The subscripts here indicate the index of the iteration in the DAL algorithm. In order to determine the new initial condition we loop through the following steps over and over until the convergence criteria have been met.

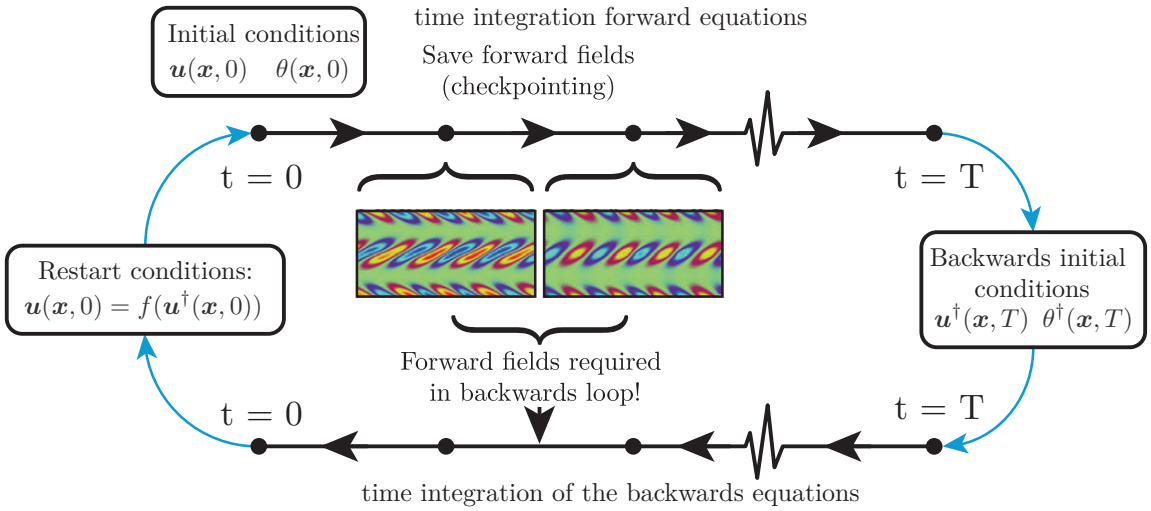

Figure 2: Schematic showing the procedure followed by the adjoint looping algorithm.

Step 1. Using the initial condition for $\boldsymbol{u}_{(n)}(\boldsymbol{x},0)$ and the fixed initial condition for $\theta_{(n)}(\boldsymbol{x},0)$ as given in Eq. 3, we integrate the full system of equations forward in time from $t=0$ until the terminal time T is reached. Here we obtain our final state $\boldsymbol{u}_{(n)}(\boldsymbol{x},T)$ and $\theta_{(n)}(\boldsymbol{x},T)$.

Step 2. Using equations 17 we determine the initial conditions for the adjoint equations which are $\boldsymbol{u}^\dagger_{(n)}(\boldsymbol{x},T)$ and $\theta^\dagger_{(n)}(\boldsymbol{x},T)$.

Step 3. Starting from these initial conditions we integrate the adjoint equations given by 14, 15 and 16 backwards in time from $t=T$ to $t=0$. Thus, we obtain the $\boldsymbol{u}^\dagger_{(n)}(\boldsymbol{x},0)$ and $\theta^\dagger_{(n)}(\boldsymbol{x},0)$.

Step 4. The final state of the backwards velocity field can be used to determine $\delta\mathscr{L}/\delta\boldsymbol{u}(\boldsymbol{x},0)$ as shown in equation 18. This is the gradient of the augmented Lagrangian function with respect to the initial velocity perturbation. By moving along this gradient, updating the new initial velocity field, we can iteratively move towards an optimum. To do this we simply employ a steepest decent approach to reach this minimum value of our Lagrangian.

$$\boldsymbol{u}_{(n+1)}(\boldsymbol{x},0) = \boldsymbol{u}_{(n)}(\boldsymbol{x},0) + \varepsilon \left(\frac{\delta\mathscr{L}}{\delta\boldsymbol{u}}\right)_{(n)} \tag{19}$$

$$= \boldsymbol{u}_{(n)}(\boldsymbol{x},0) + \varepsilon \boldsymbol{u}^\dagger_{(n)}(\boldsymbol{x},0) \tag{20}$$

The parameter ε is a parameter that can be varied for each iteration in order to improve convergence of the final solution.

Step 5. Finally, we apply the energy constraint since our solution is not beholden to this at this moment. To do so we rescale the amplitude of $\boldsymbol{u}_{(n)}(\boldsymbol{x},0)$ to conform the constraint on the initial energy. Schematically this is shown in Fig. 3.

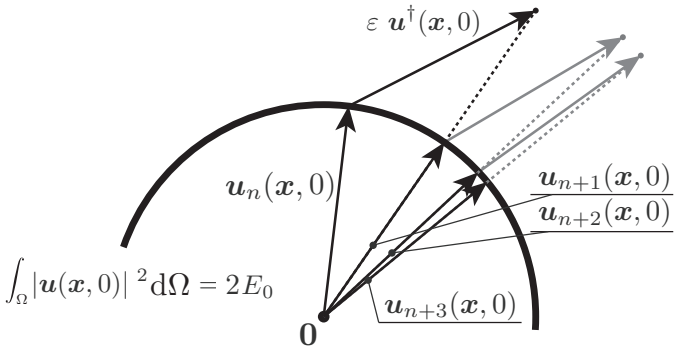

Figure 3: A mathematical representation of the state space of the initial perturbation field $\boldsymbol{u}(\boldsymbol{x}, 0)$. The thick black line represents the energy constraint; all initial fields are constraint to lie on this surface. Starting from an initial system state designated by the subscript n we obtain the gradient of $\delta\mathscr{L}\,/\delta\boldsymbol{u}(\boldsymbol{x}, 0) = \boldsymbol{u}(\boldsymbol{x}, 0)$, using steepest descent we add this to state vector obtaining a new guess for the optimal perturbation. As is shown in the graphic the energy of this state does not satisfy the energy constraint, therefore it is rescaled and a perturbation velocity field for step $n + 1$ is obtained. This process is iterated until the desired convergence is reached.

3.1 Dealing with the required direct fields

As was noted before, the backwards time integration of the adjoint equations requires knowledge about the forward fields at each timestep. It is it practically impossible to save both the scalar field and the velocity field at every time step, therefore the following method, shown schematically in Fig. 4, was employed. During the forward time-integration of the direct equations both fields were saved in an external file at regular time intervals of length Δt_s, as shown in the top half of the image. The value of Δt_s was kept smaller than 100 time steps for all cases. During the backwards time-integration of the adjoint equations the forward fields were loaded back into memory but only for two times. Consider a time t = t*, shown in Fig. 4. To reconstruct the forward fields at $t*$, for this time the fields of the forward loop at times $n\Delta t_s$ and $(n + 1)\Delta t_s$ are loaded into memory. Using these, a simple linear interpolation is performed to determine the approximate fields at time $t = t^*$:

$$\begin{aligned}\boldsymbol{u}(\boldsymbol{x}, t^*) &= \boldsymbol{u}(\boldsymbol{x}, n\Delta t_s) + (\boldsymbol{u}(\boldsymbol{x}, (n+1)\Delta t_s) - \boldsymbol{u}(\boldsymbol{x}, n\Delta t_s))\frac{t^* - n\Delta t_s}{\Delta t_s}\\ \theta(\boldsymbol{x}, t^*) &= \theta(\boldsymbol{x}, n\Delta t_s) + (\theta(\boldsymbol{x}, (n+1)\Delta t_s) - \theta(\boldsymbol{x}, n\Delta t_s))\frac{t^* - n\Delta t_s}{\Delta t_s}\end{aligned} \tag{21}$$

This method worked remarkably well and no significant issues were observed.

3.2 Obtaining convergence

The convergence of the steepest descent method can be accelerated by a suitable choice of the parameter ε that is adapted dynamically during each successive loop. For this we use the method laid out by Pringle et al. (2012) [7] which was also employed and adapted by

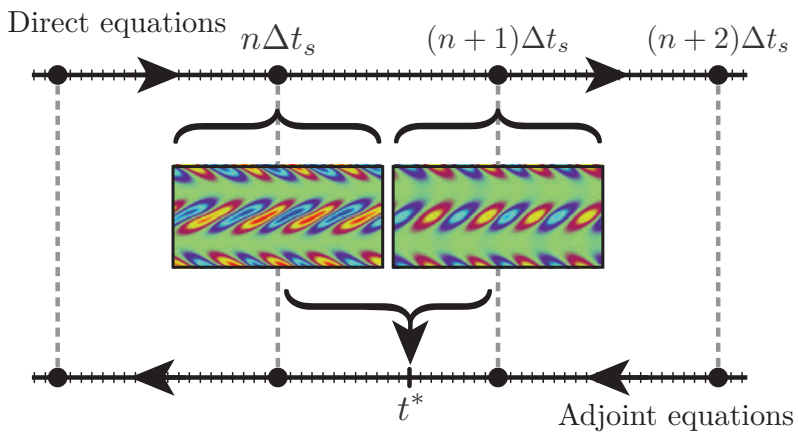

Figure 4: Schematic representation of the method used to store, retrieve

Eaves (2016)[4]. We initially start out with $\varepsilon = 1$, and then adapt its value (reducing it or increasing it) following 3 criteria. The first is:

$$\int_\Omega |\theta_n(\boldsymbol{x}, T)|^2 \, \mathrm{d}\Omega < \int_\Omega |\theta_{n-1}(\boldsymbol{x}, T)|^2 \, \mathrm{d}\Omega \tag{22}$$

which simply states that the cost functional must decrease at each iteration. If this is not the case, this could indicate that we overshot our minimum and need to be more refined in looking for the optimal perturbation. We then reduce the value of ε by a factor of 5. If Eq. 22 is satisfied on the other hand, the value is unchanged and the next criteria are checked, which brings us to the second criterion:

$$\int_\Omega |\boldsymbol{u}_n^\dagger(\boldsymbol{x}, 0)|^2 \, \mathrm{d}\Omega < 4 \int_\Omega |\boldsymbol{u}_{n-1}^\dagger(\boldsymbol{x}, 0)|^2 \, \mathrm{d}\Omega \tag{23}$$

which prohibits any rapid increase in the amplitude of the initial condition (prior to rescaling). This could cause a large overshoot which is not desirable. If equation 23 is not satisfied, then ε is again reduced by a factor of five.
The final criterion considers the angle between two respective update vectors, called d: :

$$d = \frac{\int_\Omega \boldsymbol{u}_{(n-1)}^\dagger(\boldsymbol{x}, 0) \cdot \boldsymbol{u}_{(n)}^\dagger(\boldsymbol{x}, 0) \, \mathrm{d}\Omega}{\sqrt{\int_\Omega (\boldsymbol{u}_{(n-1)}^\dagger(\boldsymbol{x}, 0))^2 \, \mathrm{d}\Omega \int_\Omega (\boldsymbol{u}_{(n)}^\dagger(\boldsymbol{x}, 0))^2 \, \mathrm{d}\Omega}}. \tag{24}$$

Three distinctive cases can be distinguished based on the alignment of the two successive vectors. Firstly, if the value of d is positive, this corresponds to a change in the "angle" in state space of less than 90°. Note that if d is equal to 1, they are they are exactly parallel and the vectors are in the same direction. Secondly, when the value is zero the angle is exactly 90°. Finally, if the value of d is negative, this implies that the angle is greater than 90°, the state vector is essentially "turning around". In our case, a negative value is not possible due to the fact that increasing the energy of the system is always a valid solution for enhancing the mixing, thus the state vector will always point outwards from the energy

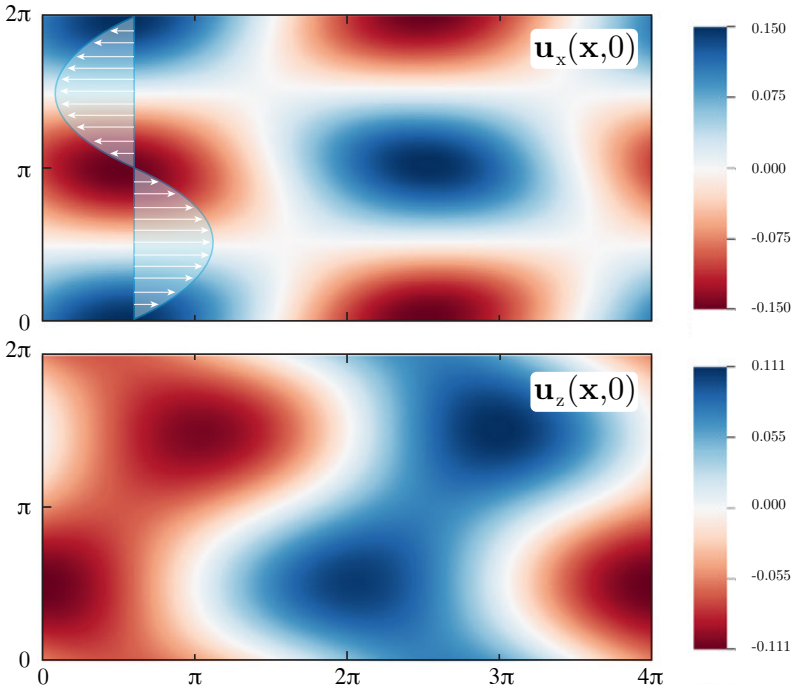

Figure 5: The initial perturbation velocity field corresponding to that of the fastest growing mode corresponding to the mode 1 instability of wavenumber 0.5. The top image shows the u_x-field and the background forcing profile. The bottom part of the figure shows the u_z-field.

constraint hyper sphere as shown in Fig. 3. We still use this quantity when $d > 0.95$, i.e. we are heading in right direction, then the value of ε is increased by a factor of two, otherwise it is left unchanged.

Finally, we say that the system has converged when $d \geq 0.99$ and $\mathrm{Var}(\theta_{(n)}(\boldsymbol{x}, T)) - \mathrm{Var}(\theta_{(n-1)}(\boldsymbol{x}, T)) < 0.001$.

4 Results

In this section we present the results of the various optimizations performed. The cases we ran can be split into two categories as mentioned previously, constant Reynolds and constant Péclet number runs. The exact values for each of these optimizations can be found here:

Constant Reynolds number cases:

For the constant Reynolds case, four values of the Péclet number were chosen, corresponding to Prandtl numbers of 0.1, 1, 3.333, and 10. For each of these Prandtl numbers simulations were performed at 9 target times T, thus resulting in 38 simulations in total. The

nondimensional target times are given by:

Target times (T): 1.25 2.5 5 10 12.5 15 20 25 50

Constant Péclet number cases:

Additionally, we were interested in the effect of changing the Reynolds number. The Péclet number was kept constant at 50 while the Reynolds number was varied over the following values: 5, 15, 50, 166.66, and 500, resulting in Prandtl numbers of 10, 3.333, 1, 0.3, and 0.1, respectively. Here only 6 target times were attempted.

Target times (T): 1.25 2.5 5 10 15 25

4.1 Non-optimized mixing strategies

A useful metric against which to compare the performance of our optimization algorithm can be obtained by considering three distinctive mixing strategies that can be defined a priori. These methods are not obtained from the adjoint looping approach, but instead consist of an initial perturbation velocity field that is naturally evolved forward in time. The three mixing strategies we will compare to are the following:

- **Pure diffusion**: The first approach consists of not mixing the fluid at all. This corresponds to the case of pure diffusion of the scalar field throughout the domain from its initial condition. Numerically this is accomplished by evolving the system forward in time for a null initial condition for the velocity field, and without any body forcing. For this case we monition the time-evolution of the variance of theta for each of the 4 molecular diffusivities we examine in this work, i.e., corresponding to Péclet number of 5, 50, 166, and 500.

- **Random perturbations**: An alternative mixing strategy is to initiate the velocity perturbations with random noise. In this case we solve the forward equations (including body forcing), for the given values of both the Reynolds and Péclet numbers. Contrary to the case of pure diffusion, advection will play a role here and the scalar field mixing will be enhanced by advection.The resulting time evolution of the variance of the scalar field is shown in Fig. 8.

- **Fastest growing mode**: While both of the previous cases provide interesting points of comparison for the optimal solutions, they are not expected to be particularly "competitive" in terms of mixing. A better mixing strategy would be to choose an initial condition that will increase the kinetic energy in the system as fast as possible, namely, the fastest growing linearly-unstable mode of the system. For a 2D Kolmogorov flow in a domain with an 2:1 aspect ratio, this mode takes the form of a single roll-like structure. Here we will call this state a mode 1 structure since in the horizontal extent of the domain, there is exactly a single period present. In other words, the horizontal wavenumber is equal to 0.5 in a domain of length 4π. This perturbation field is shown in Fig. 5. The field as shown in this figure is rescaled to satisfy our energy constraint given by 11 and is used to initialize these simulations.

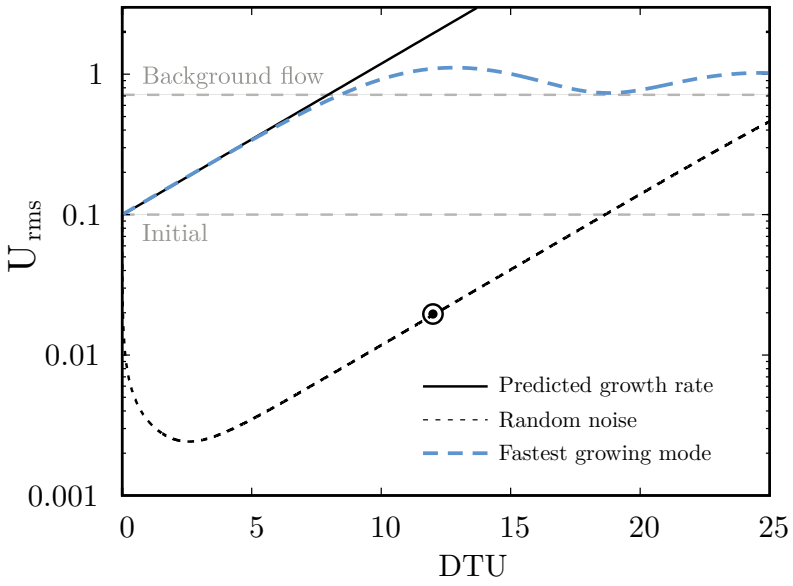

Figure 6: Evolution of the rms value of the velocity field with time for the cases of random forcing and for the case initialized with the fastest growing mode. Overplotted is the analytically obtained growth rate. Also shown are the energy in the background flow and the energy level of the initial perturbation, which in all cases are identical.

The flow field for the fastest-growing mode was obtained from the cases forced by random noise. In Fig. 6 the time evolution of the root-mean-squared velocity for this case is shown as the black dashed line. We see that the kinetic energy first decays, then at around $t = 3$ starts increasing again. By time $t = 12$, most of the energy in the system is contained in a single mode (mode 1, described above and pictured in Fig. 5), and is growing exponentially. We then extract the velocity field at that time ($t = 12$), and rescale its amplitude to satisfy the energy constraint (Eq. 11). Finally, we use that initial condition in the forward problem, and integrate the forward equations in time. An example is shown in Fig. 6 as the blue dashed line. We can see that in this case there is no initial phase during which root-mean-squares velocity decays, and that instead, it immediately triggers the exponential growth phase. We also see that the energy level saturates close to the value of the background flow.

A semi-analytical growth rate for Kolmogorov flow was determined in appendix B. We plot this fastest growth rate of the instability in Fig. 6, as indicated by the solid black line. It is identical to that observed in the numerical simulations.

4.2 Constant Reynolds number

First, we investigate how the optimal perturbations depend on the Prandtl number (or equivalently, Péclet number) and terminal time, while holding the Reynolds number constant. In Fig. 7 we are showing variance of the scalar field as a function of the terminal

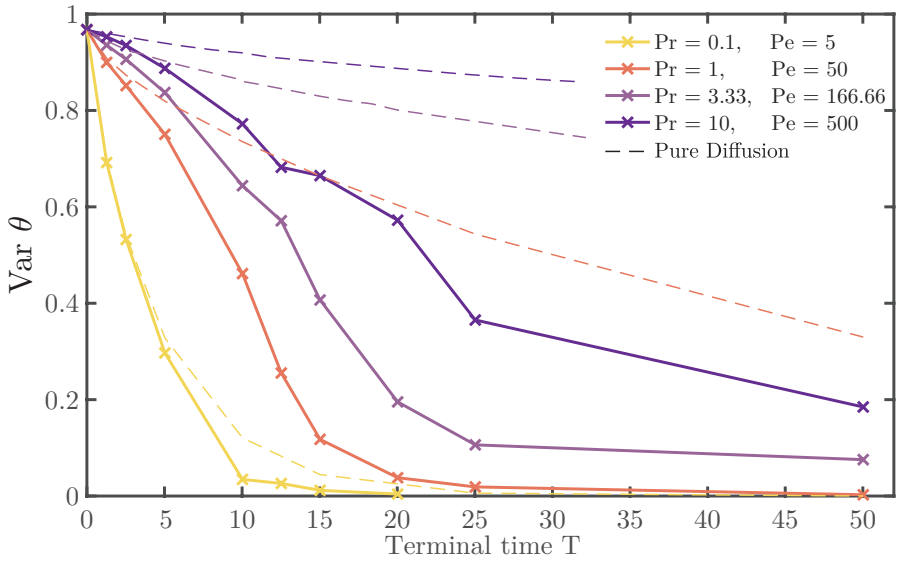

Figure 7: The variance of the scalar field at each of the terminal times for all four of the Prandtl numbers for a constant Reynolds number of 50.

time T, for various Prandtl numbers. Each data point is the result of converged iterations of the DAL algorithm described in Sec. 3. The marker and line color indicates from light to dark increasing Prandtl number over the range $Pr = 0.1$ (for which $Pe = 5$, which is strongly diffusive) to $Pr = 10$ (corresponding to $Pe = 500$, weakly diffusive). Additionally, the purely diffusive results obtained as described in Sec. 4.1 are shown as dashed lines for each of the four molecular diffusivities considered. Note that for the highest molecular diffusivity we only obtained converged results up to terminal times of 20, after which no solutions could be found that would (significantly) optimize the final mixed state.
In this figure, we first note that the scalar field is mixed much more efficiently at lower Prandtl number due to the higher molecular diffusion, as is expected. For the $Pr = 0.1$ case we even see that there is little difference between the stirred and unstirred (purely diffusive) case for short terminal times. Only for the cases of terminal times between ap-proximately 5 and 20 do we see significant improvement. For all other Prandtl numbers the optimally mixed case does a lot better compared to pure diffusion, as is expected.
We can also compare the results from our simulations to the two other reference cases discussed in Sec. 4.1; the system initialized with respectively random noise and the fastest growing mode. Fig. 8 shows four different plots for the different Prandtl number cases. Here the actual time-evolution of each of the optimized cases is shown. The terminal time is indicated by a circular marker. These are compared with the diffusive solution (dashed line) and the case initialized with the fastest-growing mode (solid black line), respectively. We confirm that for all cases the optimal solution outperforms both of these other mixing strategies.

Furthermore, one way to check the internal consistency of our optimized results is by checking if the results we obtain are unique. For each of the terminal times the variance of the scalar field at that time must be the lower than for any other initial condition. Any

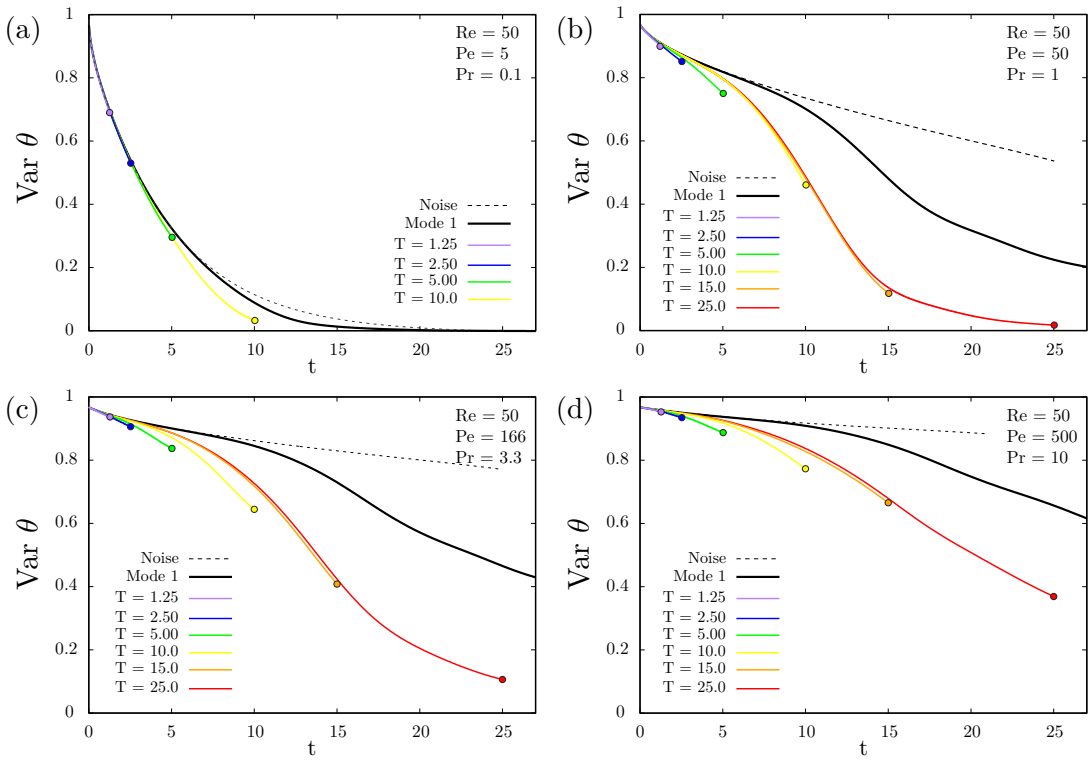

Figure 8: Time-evolution of the variance of the scalar field at $Re = 50$, for various values of Pr (from top left to bottom right, $Pr = 0.1$, 1, 3.3 and 10), and various terminal times T. Also shown are the forward cases initialized with random noise (dotted line) and with the fastest growing mode (i.e. mode 1 structure) (solid black line).

perturbation in the velocity field should result in a worse outcome. In Fig. 8 this means that all the markers indicating solutions at the terminal time need to have a scalar variance that is below any of the other case at that time. This is confirmed for all the solutions we have obtained in this work.

Additionally, we note a strong dependence on Prandtl number: for low Prandtl number the impact of optimal mixing is marginal but becomes more important for higher values. In fact, for these cases the optimal perturbation outperforms even the fastest growing mode by a very significant margin. This is shown more clearly in Fig. 9(a). which shows the ratio:

$$\Theta = \frac{\mathrm{Var}(\theta(\boldsymbol{x},0)) - \mathrm{Var}(\theta(\boldsymbol{x},T))_{op}}{\mathrm{Var}(\theta(\boldsymbol{x},0)) - \mathrm{Var}(\theta(\boldsymbol{x},T))_{fgm}} \tag{25}$$

for each of the terminal times and Prandtl numbers. The ratio Θ compares the reduction of the variance between $t = 0$ and $t = T$ for the fastest growing mode (fgm) and that for the optimal perturbation case (op).

It is interesting to see that the maximum improvement appears to happen at a specific terminal time, around t = 15. In this figure we can distinguish 3 different regions, whereby the mixing efficiency of the optimal perturbations (compared with mode 1) first increases

with T for short times, then reaches a maximum, then decays again for large T.

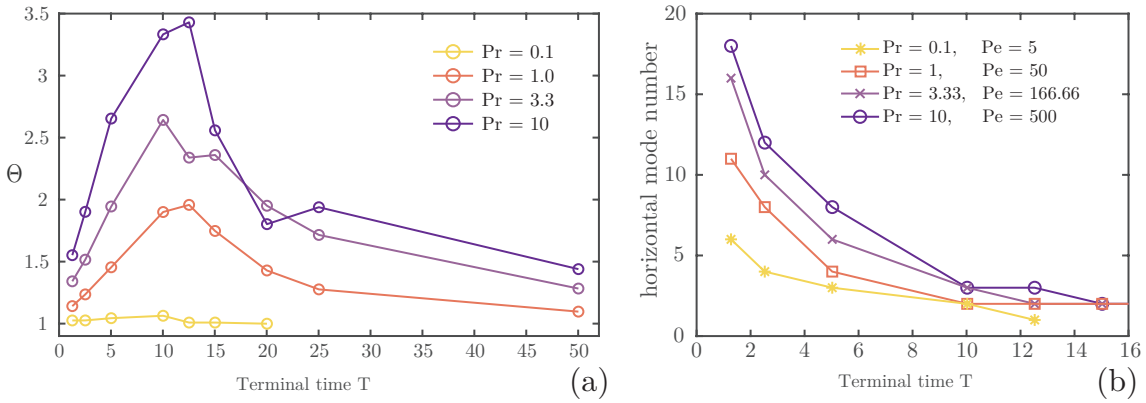

Figure 9: (a) The ratio of improvement of the optimal solution when compared to perturbing the system by its fastest growing mode. An optimum can be observed, independent of Prandtl number around 10-15 dimensionless time units. (b) The horizontal wavenumber (here wavenumber 1 corresponds to a wavelength of 4π), i.e., the number of structures we observed at $t = 0$ in the $\boldsymbol{u}_z$ velocity field (see Fig.10).

4.3 Structures in the optimal perturbation field

A good way to understand how the optimal perturbations are able to promote efficient mixing is by analyzing the initial perturbations and the resulting flow up until the terminal time. The dependence on the Prandtl number and the terminal time is of primary importance. In Fig. 10 we show a collection of snapshots of both the velocity fields and the passive scalar field for the $Pr = 1$ case. Using these, we will explain the behavior that we observe in Fig. 9.

Firstly, for short terminal times (left column Fig. 10) the optimal perturbations are concentrated around the region where the gradient in the scalar field is largest. The optimal solution consists of a sawtooth-like interface in the scalar field, creating as large a surface for diffusion as possible. As can be seen from the final state of the scalar field over this short time horizon, the perturbations only managed to cause mixing very close to this interface. We can also observe that at $t = 0$ all structures are inclined against the shear flow, while by $t = T$ they have turned with the shear. This is known as the *Orr-mechanism*, as also observed in reference [1] figure 5. This mechanism enables the vortices to extract energy from the shear flow and thus, hypothetically, perform additional mixing.

In the analysis, one parameter that we consider is the number of vortices we observe in the x-direction of the domain. We will characterize this in terms of a so called "mode number" n. For example, the fastest growing mode is a mode 1 structure since exactly one period fits in the domain. For short terminal time we observe a very high mode number, corresponding to large number of small scale structures in the velocity field as can be seen in the first column of Fig. 10. For increasing terminal times this mode number is reduced as is

depicted in Fig. 9(b), for short terminal times the mixed scalar field gets this characteristic sawtooth-like structure. Additionally,we observe a positive correlation of the mode number with the Prandtl number (i.e., the mode number increases when Pr increases, everything else being kept equal). Both these effects make sense from a physical perspective. The size of the velocity perturbation structures should depend on the distance over which molecular diffusion can work within the time constraint set by the terminal time. If molecular diffusivity is higher or the terminal time is larger, then the structures will be larger, thus the mode number lower and vice versa.

For intermediate terminal times, shown in the middle column of Fig. 10, it can be seen that the initial velocity field in both x- and z-direction contains two horizontal wavelengths. In Fig. 9(b) it can be observed that for terminal times greater than 15 this holds for all Prandtl numbers (except $Pr = 0.1$). The initial the sawtooth structures become space filling and evolve into two elegant spirals in the scalar field as shown at the bottom of the middle column. This pattern is very regular and provides very efficient mixing for these intermediate times. In fact, this pattern provides the greatest improvement over the case initialized with the fastest-growing mode (see Fig. 9(a)), despite being linearly stable! Indeed, going back to the stability analysis from appendix B, we note that the system is actually linearly stable to a structure of mode 2 (there called $k = 1$ since the width of the domain is 4π). However, with targeted initial velocity perturbations we can trigger this mode (temporarily), and it clearly improves mixing of the passive scalar field when compared to the fastest growing mode, mode one.
For $Pr = 0.1$ on the other hand the mode 2 perturbations are nor preferred. This is due to the high molecular diffusivity, which causes the entire θ-field to be successfully mixed due to pure diffusion by $T \sim 15$ (see Fig. 8(a)). In this case it no longer matters how the flow is perturbed, the end state is always very well mixed.

Finally, for terminal times greater than 15 we observe that the optimal solutions still perform better than the fastest growing mode (Fig. 9(a)). But the difference becomes smaller and smaller as the terminal time increases. This is, of course, obvious since the variance of the scalar field can not be reduced below 0, and for $t \to \infty$ the scalar field will be fully homogenized regardless of the initial condition. In the right column of Fig. 10 we can see that even for terminal times as large as 50, the initial flow field at $t = 0$ shows the wavenumber 2 structure. However, this mode only persists until approximately $t = 30$ into the run, after which it transitions into a mode 1 structure.This can be seen in the velocity field at time $t = 50$, shown in the third column third row in Fig. 10. For higher Prandtl numbers the results are similar, indicating that for long term gains it is still better to start with the mode 2 structure and not the fastest growing mode.

Previously, we made the observation that there is a maximum in the value of Θ at approximately $T \approx 12$ regardless of Pr (except for $Pr = 0.1$), as can be observed in Fig. 9(a). A possible explanation is that this terminal time coincides with the saturation in energy in the fastest growing mode as shown by the blue dashed line in Fig. 6. This moment corresponds with the time at which the wavenumber one structure starts mixing more efficiently as is shown by enhanced reduction in $\mathrm{Var}(\theta)$ as seen in Fig. 8(b,c and d). Note that the

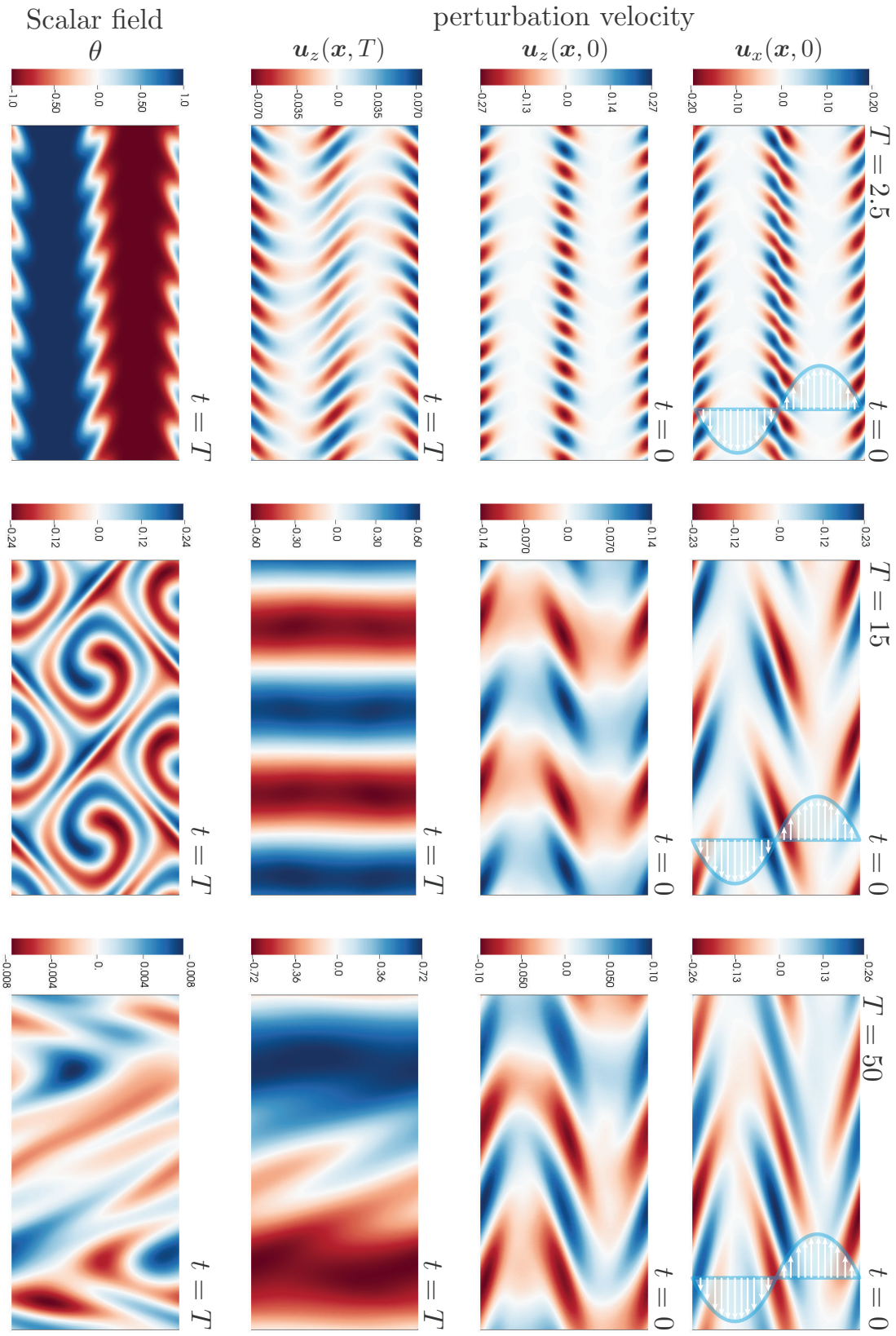

Figure 10: All results here are for the case of$Re = Pe = 50$, i.e. $Pr = 1$. Each column is for a different terminal time as is shown at the top, respectively, from left to right $T = 2.5$, 15, and 50.The bottom row of the figure shows the final, optimal mixed state of the scalar field. The top two rows show the initial velocity perturbation field that resulted in this final state, these fields are shown at $t = 0$. The third row shows the perturbation velocity fields in the vertical direction at the terminal time $t = T$.

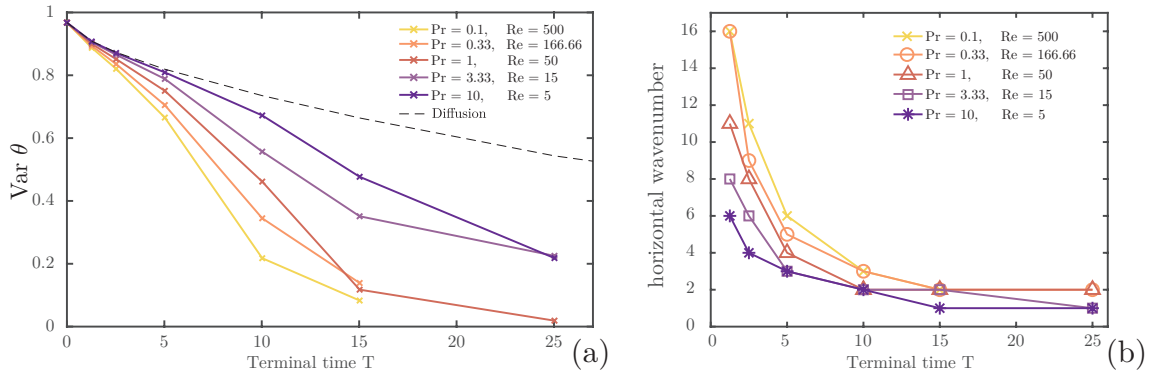

Figure 11: (a) For a constant Péclet number of 50 the optimized final variance of the scalar field is shown for a series of terminal times. The Reynolds number is varied here from 0.1 to 10 in five steps indicated by the line color. (b) The number of horizontal modes observed for all aforementioned cases.

time at which the mode 1 instability becomes dominant is just dependent on the Reynolds number of the flow, which is constant in all these simulations. This is in agreement with our results.

4.4 Constant Péclet number

In this second investigation, we are interested in studying the effect of the Reynolds number on the optimal perturbations. To do so, we kept the Péclet number constant at 50 while varying the Reynolds number over two decades from 5 to 500, thus obtaining a Prandtl number range of 10 to 0.1, respectively. The results for the variance at terminal time T are depicted in Fig. 11(a). The trend with Reynolds number is as expected. For fixed terminal time, the scalar variance decreases with increasing Reynolds number, or equivalently, increased effect of stirring.

In order to check these results we can again look for internal consistency in the data. We expect that for identical terminal times with increasing Reynolds numbers the scalar variance at the terminal time should be lower in all cases. However, in Fig. 11(a) we see that at least two data points, for $Pr = 1$ and 0.33 at $T = 15$ and for $Pr = 3.33$ and 10 at $T = 25$, where this appears not to be the case. These results require further investigation to understand what is happening for these cases.

Additionally, for this set of experiments we investigated the number of horizontal structures we observed in the initial velocity perturbation field. These results are shown in term of the horizontal mode number in Fig. 11(b). The first thing to note here is the similar trend of a decrease in the mode number with increasing terminal times, regardless of Reynolds number. As in Sec. 4.3 we also see that (for sufficiently large Re, greater than 15) mode 2 becomes favored around $T = 15$. This result deserves some more detailed investigation. Perhaps the terminal time at which the mode number goes down to 1 is dependent on Reynolds number.

We observe that the mode number increases with Reynolds number for short terminal

time ($T < 15$). This result is also expected since the Reynolds number affects the momentum diffusivity, therefore at lower Reynolds numbers, with the systems fixed amount of initial energy, less stirring can be accomplished within a fixed time-horizon. Thus making it more optimal to go for a reduced number of larger structures compared to a large number of low energy ones.

5 Conclusion

We have successfully implemented the Direct Adjoint Looping algorithm and integrated it in the existing PADDI code. Our code computes the optimal initial velocity perturbations to the base Kolmogorov flow that result in the most mixed state, defined as the state that minimizes the variance of the scalar field, at a given target time. Two scenarios were examined, one for constant Reynolds, and one for constant Péclet number while varying the Prandtl number over the range from 0.1 to 10 in both cases.

The most significant finding is that the optimal perturbation to the background Kolmogorov flow that achieves maximum mixing in a finite time is almost never the fastest growing mode of the base system. This result is quite counter-intuitive, and shows that having the fastest growing kinetic energy, these perturbations are not particularly efficient at mixing. Instead, we find that other kinds of perturbations can improve the mixing efficiency significantly even though these modes might even be linearly stable.
We found three main regimes for the optimal perturbations depending on the terminal time and Prandtl number. For short terminal times, the optimal perturbations take the form of small scale vortices concentrated at the gradients in the scalar field. This effect gets enhanced at higher Reynolds and Péclet numbers. For longer terminal times and higher molecular diffusivity the structures have a smaller horizontal wavenumber. For intermediate terminal times we find that perturbations with mode 2 are the optimal choice. For even larger terminal times we find that the system initially still prefers the mode 2 mode for optimal mixing. However, after a while it reverts back to the mode 1 structure corresponding to the fastest growing mode.
When varying the Reynolds number and keeping the Péclet number constant the results are in line with our expectations. The higher the Reynolds number the more mixing can be achieved at any target time T. Over the examined Reynolds number range from 5 to 500, the size of the perturbation structures decreases for increasing Reynolds number. For increasing terminal times the mode number becomes lower, for $Re \geq 50$ it appears to converge to the wavenumber 2 structure. For lower Reynolds number the structures appear to tend towards the fastest growing mode for larger terminal times.

Using the code we developed in this work we managed to obtain interesting results regarding the fundamental nature of optimal mixing in two-dimensional shear flows. It was found that, surprisingly, the fastest growing mode will not always provide the best mixing. This result appears to not depend on the terminal time for sufficiently high Reynolds and Péclet numbers, but appears to be quite robust and universal. This result can have further implications for how mixing is approached in industrial applications and in the understanding of mixing in environmental flows.

6 Acknowledgments

I would like to thank Pascale Garaud and Colm-cille Caulfield for their supervision of this project. My gratitude also goes out to Tom Eaves for discussing this project with me and his helpful comments and suggestions, as well as Stephan Stellmach for providing the original PADDI code. Additionally, I am very thankful to the organizers, staff, fellow fellows and all the visitors who made the GFD program an unforgettable and enjoyable experience.

References

[1] K. M. Butler and B. F. Farrell, *Three-dimensional optimal perturbations in viscous shear flow*, Physics of Fluids A: Fluid Dynamics, 4 (1992), pp. 1637–1650.

[2] E. Calzavarini, M. Kerscher, D. Lohse, and F. Toschi, *Dimensionality and morphology of particle and bubble clusters in turbulent flow*, Journal of Fluid Mechanics, 607 (2008), pp. 13–24.

[3] P. Danckwerts, *The definition and measurement of some characteristics of mixtures*, Applied Scientific Research, Section A, 3 (1952), pp. 279–296.

[4] T. S. Eaves, *Generalised nonlinear stability of stratified shear flows: adjoint-based optimisation, Koopman modes, and reduced models*, PhD thesis, Department of Applied Mathematics and Theoretical Physics, University of Cambridge, 2016.

[5] D. P. G. Foures, C. P. Caulfield, and P. J. Schmid, *Optimal mixing in two-dimensional plane poiseuille flow at finite Péclet number*, Journal of Fluid Mechanics, 748 (2014), pp. 241–277.

[6] R. R. Kerswell, C. C. T. Pringle, and A. P. Willis, *An optimization approach for analysing nonlinear stability with transition to turbulence in fluids as an exemplar*, Reports on Progress in Physics, 77 (2014).

[7] C. C. Pringle, A. P. Willis, and R. R. Kerswell, *Minimal seeds for shear flow turbulence: using nonlinear transient growth to touch the edge of chaos*, Journal of Fluid Mechanics, 702 (2012), pp. 415–443.

[8] R. Tait and M. Howe, *Thermohaline staircase*, Nature, 231 (1971), p. 178.

[9] J.-L. Thiffeault, *Using multiscale norms to quantify mixing and transport*, Nonlinearity, 25 (2012), p. R1.

[10] J.-L. Thiffeault, C. R. Doering, and J. D. Gibbon, *A bound on mixing efficiency for the advection–diffusion equation*, Journal of Fluid Mechanics, 521 (2004), pp. 105–114.

Appendix A: Complete Derivation of the Adjoint Equations

In this appendix we will show how the adjoint equations as presented in Eqs. 14, 15 and 16 are obtained. We start from the constrained Lagrangian consisting of the cost functional that we try to optimize and the equations imposing the constraints on the system, i.e. the continuity, Navier-Stokes and advection-diffusion equations:

$$\begin{aligned}\mathscr{L} = &\underbrace{\int_\Omega \theta(\boldsymbol{x},T)^2 \, d\Omega}_{\text{cost functional}} - \int_0^T \int_\Omega p^\dagger \underbrace{\boldsymbol{\nabla}\cdot\boldsymbol{u}}_{\text{continuity}} \, \mathrm{d}\Omega\mathrm{d}t \\ &- \int_0^T \int_\Omega \underbrace{\left(\partial_t \boldsymbol{u} + \boldsymbol{U}\cdot\boldsymbol{\nabla}\boldsymbol{u} + \boldsymbol{u}\cdot\boldsymbol{\nabla}\boldsymbol{U} + \boldsymbol{\nabla}p - \mathrm{Re}^{-1}\boldsymbol{\nabla}^2\boldsymbol{u}\right)}_{\text{Navier-Stokes}}\cdot\boldsymbol{u}^\dagger \, \mathrm{d}\Omega\mathrm{d}t \\ &- \int_0^T \int_\Omega \theta^\dagger \underbrace{\left(\partial_t\theta + \boldsymbol{U}\cdot\boldsymbol{\nabla}\theta - \mathrm{Pe}^{-1}\boldsymbol{\nabla}\theta\right)}_{\text{advection-diffusion}} \, \mathrm{d}\Omega\mathrm{d}t. \end{aligned} \tag{26}$$

Each of the constraint equations is multiplied by a Lagrange multiplier, denoted by a superscript †, called the adjoint variables.
We are looking for an optimal solution that gives us the minimum value of the cost functional. If a solution is optimal, then any perturbation at any point in time or at any position in space will increase the cost functional. Therefore, we are are looking for a system state where the first variation with respect to the forward variables p, $\boldsymbol{u}$, and θ, has to be equal to zero. Mathematically:

$$\frac{\partial\mathscr{L}}{\partial p(\boldsymbol{x},t)} \approx \frac{\mathscr{L}(\boldsymbol{u},\theta,p+\delta p,\boldsymbol{u}^\dagger,\theta^\dagger,p^\dagger) - \mathscr{L}(\boldsymbol{u},\theta,p,\boldsymbol{u}^\dagger,\theta^\dagger,p^\dagger)}{\delta p} = 0 \tag{27}$$

$$\frac{\partial\mathscr{L}}{\partial \boldsymbol{u}(\boldsymbol{x},t)} \approx \frac{\mathscr{L}(\boldsymbol{u}+\delta\boldsymbol{u}^\dagger,\theta,p,\boldsymbol{u}^\dagger,\theta^\dagger,p^\dagger) - \mathscr{L}(\boldsymbol{u},\theta,p,\boldsymbol{u}^\dagger,\theta^\dagger,p^\dagger)}{\delta \boldsymbol{u}} = \boldsymbol{0} \tag{28}$$

$$\frac{\partial\mathscr{L}}{\partial \theta(\boldsymbol{x},t)} \approx \frac{\mathscr{L}(\boldsymbol{u},\theta+\delta\theta,p,\boldsymbol{u}^\dagger,\theta^\dagger,p^\dagger) - \mathscr{L}(\boldsymbol{u},\theta,p,\boldsymbol{u}^\dagger,\theta^\dagger,p^\dagger)}{\delta \theta} = 0 \tag{29}$$

We will go over each of these variations in the following sections.

1. Pressure

We will start with the first variation with respect to the pressure term, Eq. 27. The pressure p only shows up in the Lagrangian (26), in the Navier-Stokes part of the constraints. Thus, taking the first variation of equation with respect to the pressure we obtain:

$$\frac{\partial\mathscr{L}}{\partial p(\boldsymbol{x},t)}\delta p(\boldsymbol{x},t) \approx \int_0^T \int_\Omega \boldsymbol{u}^\dagger\cdot\boldsymbol{\nabla}\delta p \, \mathrm{d}\Omega\mathrm{d}t = 0 \tag{30}$$

We want to use the fact that this should hold for any arbitrarily small perturbation δp. Using integration by parts we obtain:

$$\int_0^T \int_\Omega \underline{\boldsymbol{\nabla}\cdot(\boldsymbol{u}^\dagger\delta p)} - \delta p \, \boldsymbol{\nabla}\cdot\boldsymbol{u}^\dagger \mathrm{d}\Omega\mathrm{d}t = 0. \tag{31}$$

Using the fact that our domain is periodic we know the that the integral of the underlined term $\nabla \cdot (\boldsymbol{u}^\dagger \delta p)$, is equal to zero, leaving us with second term. Since this should hold for any arbitrary δp this means that for this to be true we need to satisfy:

$$\boldsymbol{\nabla} \cdot \boldsymbol{u}^\dagger = 0. \tag{32}$$

This is identical to the continuity equation, for the adjoint velocity field.

2. Velocity

Next, we will consider the variation of the Lagrangian as given in Eq. 26 with respect to the forward velocity $\boldsymbol{u}$. We consider only the terms that contain the velocity:

$$\mathscr{L}_u = -\int_0^T \int_\Omega \underbrace{p^\dagger \boldsymbol{\nabla} \cdot \boldsymbol{u}}_{\text{I}} + (\underbrace{\partial_t \boldsymbol{u}}_{\text{II}} + \underbrace{\boldsymbol{U} \cdot \boldsymbol{\nabla} \boldsymbol{u} + \boldsymbol{u} \cdot \boldsymbol{\nabla} \boldsymbol{U}}_{\text{III}} - \underbrace{Re^{-1} \boldsymbol{\nabla}^2 \boldsymbol{u}}_{\text{IV}}) \cdot \boldsymbol{u}^\dagger + \underbrace{\theta^\dagger \boldsymbol{U} \cdot \boldsymbol{\nabla} \theta}_{\text{V}} \, \mathrm{d}\Omega \mathrm{d}t. \tag{33}$$

We will start with the first term. Using integration by parts we obtain:

$$(I): \ \frac{\partial \mathscr{L}_u^I}{\partial \boldsymbol{u}(\boldsymbol{x},t)} \delta \boldsymbol{u}(\boldsymbol{x},t) \approx -\int_0^T \int_\Omega \underline{\boldsymbol{\nabla} \cdot (\delta \boldsymbol{u} p^\dagger)} + \underbrace{\delta \boldsymbol{u} \cdot \boldsymbol{\nabla} p^\dagger}_{\text{a}} \mathrm{d}\Omega \mathrm{d}t. \tag{34}$$

The underlined term is equal to zero because of divergence in a periodic domain. The term designated by a remains and will be a part of the adjoint system of equations. Additionally, no further algebra is required here since $\delta \boldsymbol{u}$ is already outside of any derivatives.
Moving on to term II in Eq. 33, this term is interesting since it contains the time-derivative. Using integration by parts we now obtain the following two terms:

$$(II): \ \frac{\partial \mathscr{L}_u^{II}}{\partial \boldsymbol{u}(\boldsymbol{x},t)} \delta \boldsymbol{u}(\boldsymbol{x},t) \approx -\int_\Omega [\delta \boldsymbol{u} \cdot \boldsymbol{u}^\dagger]_0^T \, \mathrm{d}\Omega + \int_0^T \int_\Omega \underbrace{\delta \boldsymbol{u} \cdot \partial_t \boldsymbol{u}^\dagger}_{\text{b}} \, \mathrm{d}\Omega \mathrm{d}t. \tag{35}$$

Note that the first term is evaluated at the initial and final times only. None of the other terms will give us contributions containing $\boldsymbol{u}^\dagger$ evaluated at $t = 0$ or $t = T$. Therefore, we directly obtain the following two relations:

$$\boldsymbol{u}^\dagger(\boldsymbol{x}, 0) = 0 \tag{36}$$

$$\boldsymbol{u}^\dagger(\boldsymbol{x}, T) = 0. \tag{37}$$

The relation in Eq. 36 is the convergence criterion, which is used to update the guess for the new initial perturbation velocity field. The second relationship, Eq. 37, gives us the initial state for adjoint velocity field used in the backwards time integration. The term in Eq. 35 labeled as b is ready for use and added to the final adjoint equation.
The terms designated by (III) in Eq. 33 are just the extended version of $\boldsymbol{U} \cdot \boldsymbol{\nabla} \boldsymbol{U}$. We treat both these terms together:

$$\begin{aligned}(III): \ \frac{\partial \mathscr{L}_u^{III}}{\partial \boldsymbol{u}(\boldsymbol{x},t)} \delta \boldsymbol{u}(\boldsymbol{x},t) &\approx -\int_0^T \int_\Omega ((\boldsymbol{u} + \delta \boldsymbol{u} + \bar{\boldsymbol{u}}) \cdot \boldsymbol{\nabla} (\boldsymbol{u} + \delta \boldsymbol{u} + \bar{\boldsymbol{u}}) \ ... \\ &\qquad - (\boldsymbol{u} + \bar{\boldsymbol{u}}) \cdot \boldsymbol{\nabla} (\boldsymbol{u} + \bar{\boldsymbol{u}})) \cdot \boldsymbol{u}^\dagger \, \mathrm{d}\Omega \mathrm{d}t \qquad (38) \\ &\approx -\int_0^T \int_\Omega (\underbrace{\delta \boldsymbol{u} \cdot \boldsymbol{\nabla} \boldsymbol{U}}_{1} + \underbrace{\boldsymbol{U} \cdot \boldsymbol{\nabla} \delta \boldsymbol{u}}_{2}) \cdot \boldsymbol{u}^\dagger \, \mathrm{d}\Omega \mathrm{d}t. \qquad (39)\end{aligned}$$

Now we first we deal with term 1:

$$-\int_0^T \int_\Omega (\delta \boldsymbol{u} \cdot \boldsymbol{\nabla} \boldsymbol{U}) \cdot \boldsymbol{u}^\dagger \, \mathrm{d}\Omega \mathrm{d}t. = -\int_0^T \int_\Omega \underbrace{(\boldsymbol{u}^\dagger \cdot \boldsymbol{\nabla} \boldsymbol{U}^T) \cdot \delta \boldsymbol{u}}_{\mathrm{c}} \, \mathrm{d}\Omega. \tag{40}$$

Note, that we had to transpose the matrix $\boldsymbol{\nabla U}$ because we had to move $\delta \boldsymbol{u}$ to the back so all dot products with this vector are on the same side. Term c is ready and will be used in the final expression of the adjoint equation.
The second term from Eq. 39 becomes:

$$-\int_0^T \int_\Omega (\boldsymbol{U} \cdot \boldsymbol{\nabla} \delta \boldsymbol{u}) \cdot \boldsymbol{u}^\dagger \, \mathrm{d}\Omega \mathrm{d}t = -\int_0^T \int_\Omega \boldsymbol{U} \cdot \boldsymbol{\nabla} (\delta \boldsymbol{u} \cdot \boldsymbol{u}^\dagger) - \underbrace{(\boldsymbol{U} \cdot \boldsymbol{\nabla} \boldsymbol{u}^\dagger) \cdot \delta \boldsymbol{u}}_{\mathrm{d}} \, \mathrm{d}\Omega. \tag{41}$$

For which the first term can be expended as:

$$-\boldsymbol{U} \cdot \boldsymbol{\nabla} (\delta \boldsymbol{u} \cdot \boldsymbol{u}^\dagger) = -\underline{\boldsymbol{\nabla} \cdot (\boldsymbol{U} (\delta \boldsymbol{u} \cdot \boldsymbol{u}^\dagger))} + (\delta \boldsymbol{u} \cdot \boldsymbol{u}^\dagger) \underline{\nabla \cdot \boldsymbol{U}}, \tag{42}$$

both of these underlined divergence terms are equal to zero and just drop out due to the doubly periodic domain. Thus the only remaining contribution, the term designated as d in Eq. 41, is added to the adjoint equation.
Now we will deal with the second to last term, term IV in equation 33:

$$(IV): \ \frac{\partial \mathscr{L}_u^{IV}}{\partial \boldsymbol{u}(\boldsymbol{x}, t)} \delta \boldsymbol{u}(\boldsymbol{x}, t) \approx -\int_0^T \int_\Omega Re^{-1} \boldsymbol{\nabla}^2 \delta \boldsymbol{u} \cdot \boldsymbol{u}^\dagger \, \mathrm{d}\Omega \mathrm{d}t. \tag{43}$$

We isolate the term $\boldsymbol{\nabla}^2 \delta \boldsymbol{u}$ and focus on rewriting it. First:

$$-\boldsymbol{\nabla}^2 \delta \boldsymbol{u} \cdot \boldsymbol{u}^\dagger = -(\boldsymbol{\nabla} (\underline{\boldsymbol{\nabla} \cdot \delta \boldsymbol{u}}) - \boldsymbol{\nabla} \times (\boldsymbol{\nabla} \times \delta \boldsymbol{u})) \cdot \boldsymbol{u}^\dagger. \tag{44}$$

The underlined term is equal to zero due to divergence and a periodic domain. We impose the identity $\delta \omega = \boldsymbol{\nabla} \times \delta \boldsymbol{u}$. Continuing expanding the term on the right we obtain:

$$(\boldsymbol{\nabla} \times \delta \omega) \cdot \boldsymbol{u}^\dagger = \underline{\boldsymbol{\nabla} \cdot (\delta \omega \times \boldsymbol{u}^\dagger)} - \delta \omega \cdot (\boldsymbol{\nabla} \times \boldsymbol{u}^\dagger). \tag{45}$$

The underlined term is again equal to zero. Substituting in the identity $\omega^\dagger = \boldsymbol{\nabla} \times \boldsymbol{u}^\dagger$ and expanding further:

$$-(\boldsymbol{\nabla} \times \delta \boldsymbol{u}) \cdot \omega^\dagger = -\underline{\boldsymbol{\nabla} \cdot (\delta \boldsymbol{u} \times \omega^\dagger)} + \delta \boldsymbol{u} \cdot (\boldsymbol{\nabla} \times \omega^\dagger). \tag{46}$$

The underlined term drops out, and the final term can be rewriten as follows:

$$\delta \boldsymbol{u} \cdot (\boldsymbol{\nabla} \times \omega^\dagger) = \boldsymbol{\nabla} \times (\boldsymbol{\nabla} \times \boldsymbol{u}^\dagger) \cdot \delta \boldsymbol{u} = \boldsymbol{\nabla}^2 \boldsymbol{u}^\dagger \cdot \delta \boldsymbol{u} \tag{47}$$

Thus giving us the following final expression for term IV that will be added to the adjoint equations:

$$\frac{\partial \mathscr{L}_u^{IV}}{\partial \boldsymbol{u}(\boldsymbol{x}, t)} \delta \boldsymbol{u}(\boldsymbol{x}, t) \approx -\int_0^T \int_\Omega \underbrace{Re^{-1} \boldsymbol{\nabla}^2 \boldsymbol{u}^\dagger \cdot \delta \boldsymbol{u}}_{\mathrm{e}} \, \mathrm{d}\Omega \mathrm{d}t. \tag{48}$$

The final term V in Eq. 33 comes from the advection-diffusion equation and gives us the following contribution:

$$(V): \ \frac{\partial \mathscr{L}_u^V}{\partial \boldsymbol{u}(\boldsymbol{x},t)}\delta\boldsymbol{u}(\boldsymbol{x},t) \approx -\int_0^T \int_\Omega \underbrace{\theta^\dagger \boldsymbol{\nabla}\theta\delta\boldsymbol{u}}_{\text{f}} \ \mathrm{d}\Omega\mathrm{d}t \tag{49}$$

Now compiling all the terms, a through f, obtained in Eqs. 34, 35, 40, 41, 48, and 49 we obtain the complete form of the first variation with respect to the velocity $\boldsymbol{u}$:

$$\int_0^T \int_\Omega \Big(\partial_t \boldsymbol{u}^\dagger + \boldsymbol{U}\cdot\boldsymbol{\nabla}\boldsymbol{u}^\dagger - \boldsymbol{u}^\dagger\cdot\boldsymbol{\nabla}\boldsymbol{U}^T + \nabla p^\dagger + Re^{-1}\boldsymbol{\nabla}^2\boldsymbol{u}^\dagger - \theta^\dagger\boldsymbol{\nabla}\theta\Big)\cdot\delta\boldsymbol{u} \ \mathrm{d}\Omega\mathrm{d}t = \boldsymbol{0}. \tag{50}$$

This should hold for any arbitrary $\delta\boldsymbol{u}$, thus we obtain the adjoint equation for $\boldsymbol{u}^\dagger$:

$$\partial_t \boldsymbol{u}^\dagger + \boldsymbol{U}\cdot\boldsymbol{\nabla}\boldsymbol{u}^\dagger - \boldsymbol{u}^\dagger\cdot\boldsymbol{\nabla}\boldsymbol{U}^T + \nabla p^\dagger + Re^{-1}\boldsymbol{\nabla}^2\boldsymbol{u}^\dagger = \theta^\dagger\boldsymbol{\nabla}\theta. \tag{51}$$

3. Scalar Field

Finally, we take the first variation of Eq. 26 with respect to the scalar field θ. Note that this is the only term that appears in the first term of $\mathscr{L}$. Our Lagrangian with terms containing θ looks as follows:

$$\mathscr{L}_\theta = \int_\Omega \underbrace{\theta(\boldsymbol{x},T)^2}_{\text{I}} \ \mathrm{d}\Omega - \int_0^T\int_\Omega \theta^\dagger(\underbrace{\partial_t\theta}_{\text{II}} + \underbrace{\boldsymbol{U}\cdot\boldsymbol{\nabla}\theta}_{\text{III}} - \underbrace{Pe^{-1}\boldsymbol{\nabla}^2\theta}_{\text{IV}}) \ \mathrm{d}\Omega\mathrm{d}t. \tag{52}$$

Starting from term I:

$$(I): \ \frac{\partial \mathscr{L}_\theta^I}{\partial\theta(\boldsymbol{x},t)}\delta\theta(\boldsymbol{x},t) \approx \int_\Omega (\theta(\boldsymbol{x},T)+\delta\theta(\boldsymbol{x},T))^2 - \theta(\boldsymbol{x},T)^2 \ \mathrm{d}\Omega \tag{53}$$

$$\approx \int_\Omega \underbrace{2\theta(\boldsymbol{x},T)\delta\theta(\boldsymbol{x},T)}_{\text{a}} + h.o.t. \ \mathrm{d}\Omega. \tag{54}$$

Note that similar to Eq. 37 this term is evaluated at the terminal time. However in this case this is not the only contribution that is evaluated at time $t = T$. The second term from Eq. 52 will also give a contribution:

$$(II): \ \frac{\partial \mathscr{L}_\theta^{II}}{\partial\theta(\boldsymbol{x},t)}\delta\theta(\boldsymbol{x},t) \approx -\int_0^T\int_\Omega \theta^\dagger\partial_t\theta \ \mathrm{d}\Omega\mathrm{d}t. \tag{55}$$

Using integration by parts we obtain:

$$-\int_0^T\int_\Omega \theta^\dagger\partial_t\theta \ \mathrm{d}\Omega\mathrm{d}t = \int_\Omega [\delta\theta \ \theta^\dagger]_0^T \ \mathrm{d}\Omega + \int_0^T\int_\Omega \underbrace{\delta\theta \ \partial_t\theta^\dagger}_{\text{b}} \ \mathrm{d}\Omega\mathrm{d}t. \tag{56}$$

The second term designated as b is a term that we use in the adjoint equation for the scalar field. The first term on the right hand side is evaluated at time $t = 0$ and $t = T$ and gives us the following relationship:

$$-\int_\Omega [\delta\theta \ \theta^\dagger]_0^T \ \mathrm{d}\Omega = \int_\Omega \underbrace{-\delta\theta(\boldsymbol{x},T)\theta^\dagger(\boldsymbol{x},T)}_{\text{c}} + \underbrace{\delta\theta(\boldsymbol{x},0)\theta^\dagger(\boldsymbol{x},0)}_{\text{d}} \ \mathrm{d}\Omega \tag{57}$$

The condition for θ at time zero, designated by d in Eq. 57 is not relevant in our case, the backwards $\theta^\dagger$ value at this time is not used to update the initial conditions for the forward fields. On the other hand the term c is very important. Combined with term b from Eq. 56 this gives us the following condition:

$$\theta^\dagger(\boldsymbol{x}, T) = 2\theta(\boldsymbol{x}, T) \tag{58}$$

This relation provides the initial condition for $\theta^\dagger$ for the backwards loop based on the final field of θ from the forward time integration.
Moving on to term (III) from Eq. 52, this results in the following contribution:

$$(III): \ \frac{\partial \mathscr{L}_\theta^{III}}{\partial \theta(\boldsymbol{x}, t)} \delta\theta(\boldsymbol{x}, t) \approx -\int_0^T \int_\Omega \theta^\dagger \boldsymbol{U} \cdot \boldsymbol{\nabla} \delta\theta \ \mathrm{d}\Omega \mathrm{d}t. \tag{59}$$

Using integration by parts we obtain:

$$-\int_0^T \int_\Omega \theta^\dagger \boldsymbol{U} \cdot \boldsymbol{\nabla} \delta\theta \ \mathrm{d}\Omega \mathrm{d}t = \int_0^T \int_\Omega \underline{-\boldsymbol{\nabla} \cdot (\theta^\dagger \boldsymbol{U} \delta\theta)} + \underbrace{\delta\theta \boldsymbol{\nabla} \cdot (\boldsymbol{U}\theta^\dagger)}_{\mathrm{e}} \ \mathrm{d}\Omega \mathrm{d}t. \tag{60}$$

The underlined term is equal to zero due to divergence in a periodic domain. Term e can be rewritten as

$$\int_0^T \int_\Omega \delta\theta \boldsymbol{\nabla} \cdot (\boldsymbol{U}\theta^\dagger) \ \mathrm{d}\Omega \mathrm{d}t = \int_0^T \int_\Omega \underbrace{\boldsymbol{U} \cdot (\boldsymbol{\nabla}\theta^\dagger)\delta\theta}_{\mathrm{f}} + \theta^\dagger \underline{\boldsymbol{\nabla} \cdot \boldsymbol{U}} \delta\theta \ \mathrm{d}\Omega \mathrm{d}t. \tag{61}$$

The underlined term drops out, leaving only the term f which will contribute to the adjoint equation. The final contribution comes from the term IV in Eq. 52:

$$(IV): \ \frac{\partial \mathscr{L}_\theta^{IV}}{\partial \theta(\boldsymbol{x}, t)} \delta\theta(\boldsymbol{x}, t) \approx -Pe^{-1} \int_0^T \int_\Omega \theta^\dagger \boldsymbol{\nabla} \cdot (\boldsymbol{\nabla} \delta\theta) \ \mathrm{d}\Omega \mathrm{d}t \tag{62}$$

$$\approx -Pe^{-1} \int_0^T \int_\Omega \underline{\boldsymbol{\nabla} \cdot (\theta^\dagger \boldsymbol{\nabla} \delta\theta)} - \boldsymbol{\nabla} \delta\theta \cdot \boldsymbol{\nabla} \theta^\dagger \ \mathrm{d}\Omega \mathrm{d}t \tag{63}$$

$$\approx Pe^{-1} \int_0^T \int_\Omega \underline{-\boldsymbol{\nabla} \cdot (\delta\theta \boldsymbol{\nabla} \theta^\dagger)} + \underbrace{\delta\theta \boldsymbol{\nabla}^2 \theta^\dagger}_{\mathrm{g}} \ \mathrm{d}\Omega \mathrm{d}t. \tag{64}$$

The underlined terms again drop out and only the term labeled by f will contribute. Now we combine all the terms labeled by a, b, f, and g from Eqs. 54, 56, 61, and 64 to obtain the following expression:

$$\int_0^T \int_\Omega \delta\theta (\partial_t \theta^\dagger + \boldsymbol{U} \cdot \boldsymbol{\nabla} \theta^\dagger + Pe^{-1} \boldsymbol{\nabla}^2 \theta^\dagger) \ \mathrm{d}\Omega \mathrm{d}t = 0, \tag{65}$$

which needs to hold for any arbitrary perturbation of $\delta\theta$. Thus we obtain our adjoint equation for θ. This is very similar to the regular advection diffusion equation except for the sign in front of the diffusive term:

$$\partial_t \theta^\dagger + \boldsymbol{U} \cdot \boldsymbol{\nabla} \theta^\dagger + Pe^{-1} \boldsymbol{\nabla}^2 \theta^\dagger = 0 \tag{66}$$

Appendix B: Determining the fastest growing mode in the system

We start with the periodic forcing velocity corresponding to the 2D Kolmogorov flow defined as:

$$\bar{\boldsymbol{u}} = \sin(z)\hat{e}_x \tag{67}$$

The linearized versions of the Eq. 7 in 2D thus become:

$$\frac{\partial u_i}{\partial t} + \bar{u}_j\partial_j u_i + u_j\partial_j\bar{u}_i = -\partial_i p + \mathrm{Re}^{-1}\partial_{jj}u_i. \tag{68}$$

Substituting in the forcing as defined in Eq. 67 we obtain:

$$\begin{aligned}\partial_t u_x + \sin(z)\partial_x u_x + u_z\partial_z\sin(z) &= -\partial_x p + Re^{-1}\partial_{jj}u_x\\ \partial_t u_z + \sin(z)\partial_x u_z &= -\partial_z p + \mathrm{Re}^{-1}\partial_{jj}u_z.\end{aligned}$$

Assuming an ansatz of the form $\propto e^{ik_x x+\lambda t}$ for all dependent variables, we get

$$\begin{aligned}\lambda u_x + ik_x\sin(z)u_x + u_z\cos(z) &= -ik_x p + \mathrm{Re}^{-1}\left(\partial_{zz} - k_x^2\right)u_x\\ \lambda u_z + ik_X\sin(z)u_z &= -\partial_z p + Re^{-1}\left(\partial_{zz} - k_x^2\right)u_z\end{aligned}$$

Eliminating p between these two equations yields

$$\begin{aligned}\lambda\left(\partial_z u_x - ik_x u_z\right) + ik_x\left(\cos(z)u_x + \sin(z)\partial_z u_x\right) + \cos(z)\partial_z u_z - \sin(z)u_z&\\ -(ik_x)^2\sin(z)u_z = \mathrm{Re}^{-1}\left(\partial_{zz} - k_x^2\right)\left(\partial_z u_x - ik_x u_z\right)&\end{aligned}$$

Using the continuity equation we have $u_x = -(ik_x)^{-1}\partial_z u_z$. Thus we obtain the following expression:

$$\begin{aligned}\lambda\left(-(ik_x)^{-1}\partial_{zz}u_z - ik_x u_z\right) - \sin(z)\partial_{zz}u_z - u_z\sin(z) + k_x^2\sin(z)u_z =&\\ \mathrm{Re}^{-1}\left(\partial_{zz} - k_x^2\right)\left(-(ik_x)^{-1}\partial_{zz}u_z - ik_x u_z\right).&\end{aligned} \tag{69}$$

Now let:

$$u_z = \sum_{n=-N}^{N} w_n e^{inz}. \tag{70}$$

Substituting this expression into Eq. 69:

$$\begin{aligned}\lambda\left(-(ik_x)^{-1}\sum_n w_n(-n^2)e^{inz} - ik_x\sum_n w_n e^{inz}\right) - \sin(z)\left(\sum_n w_n(-n^2)e^{inz}\right)&\\ -\sum_n w_n(1-k_x^2)\sin(z)e^{inz} = \mathrm{Re}^{-1}\sum_n(n^2+k_x^2)\left(-(ik_x)^{-1}n^2 w_n e^{inz} + ik_x w_n e^{inz}\right)&\end{aligned} \tag{71}$$

Using Euler's identity we rewrite $\sin(z) = (e^{iz} - e^{iz})/2i$, so

$$\begin{aligned}\lambda\sum_n\left(\frac{n^2 w_n}{ik_x} - ik_x w_n\right)e^{inz} + \sum_n n^2 w_n\frac{e^{i(n+1)z} - e^{i(n-1)z}}{2i}&\\ -\sum_n w_n(1-k_x^2)\frac{e^{i(n+1)z} - e^{i(n-1)z}}{2i} = \mathrm{Re}^{-1}\sum_n(n^2+k_x^2)\left(ik_x - \frac{n^2}{ik_x}\right)w_n e^{inz}&\end{aligned}$$

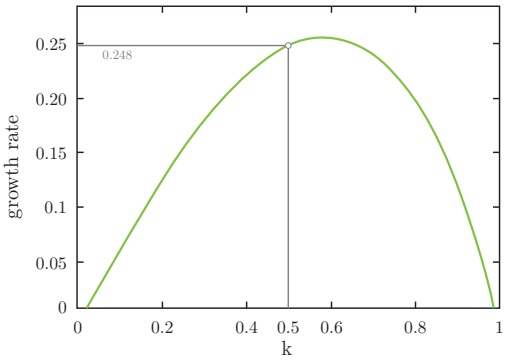

Figure 12: In this figure we show the analytical results for the growth rate as a function of wavenumber. $k = 0.5$ corresponds to a wave length of 4π, which exactly fits into our computational domain once, i.e. the mode one structure. The wavenumber $k = 1$ corresponds to the mode 2 structures, and does not have a positive growth rate.

Multiplying everything with ik_x we get

$$\lambda \sum_n \left(n^2 w_n + k_x^2 w_n\right) e^{inz} + \sum_n n^2 k_x w_n \frac{e^{i(n+1)z} - e^{i(n-1)z}}{2} - \sum_n w_n k_x (1 - k_x^2) \frac{e^{i(n+1)z} - e^{i(n-1)z}}{2}. \\ = -\mathrm{Re}^{-1} \sum_n (n^2 + k_x^2)(k_x^2 + n^2) w_n e^{inz}$$

Projecting this equation onto each Fourier mode, we get

$$\lambda w_n (n^2 + k_x^2) + \frac{(n-1)^2 k_x w_{n-1}}{2} - \frac{(n+1)^2 k_x w_{n+1}}{2} - \frac{k_x (1 - k_x^2) w_{n-1}}{2} \\ + \frac{k_x (1 - k_x^2) w_{n+1}}{2} = -\mathrm{Re}^{-1} (n^2 + k_x^2)^2 w_n \qquad (72)$$

rewriting:

$$\lambda w_n = -\mathrm{Re}^{-1} (n^2 + k_x^2) w_n \\ + \frac{k_x}{2} \left[\left((n+1)^2 - (1 - k_x^2)\right) \frac{w_{n+1}}{n^2 + k_x^2} + \left((1 - k_x^2) - (n-1)^2\right) \frac{w_{n-1}}{n^2 + k_x^2} \right]. \qquad (73)$$

In order to reconstruct an initial velocity field based on the wave-number with the maximum growth rate, we pick $k = 1/2$ which corresponds closely to the fastest growing mode and fits periodically in our domain. Because the horizontal extent of our domain is 4π a wavenumber of $k = 0.5$ fits exactly once in this domain. Thus:

$$u_x(x, z) = \mathrm{Re}\left(-\frac{n w_n}{k_x} (\cos(nz + k_x x) + i \sin(nz + k_x x)) \right) \qquad (74)$$

$$u_z(x, z) = \mathrm{Re}\left((\cos(nz + k_x x) + i \sin(nz + k_x x)) \right) \qquad (75)$$

Structure and Stability of Flow Around Noncircular Islands

Wenjing Dong

August 22, 2019

1 Introduction

1.1 Motivation

Closed flows around an island can form in the ocean in several situations: first, when an island posseses a sufficiently steep bottom slope, potential vorticity contours can be closed due to the topographic effect; second, island-trapped inertial or subinertial waves induced by tidal or planetary waves may cause currents around islands; finally, wind with lateral shear blowing over an island can also lead to closed flows. In these situations, the flow around islands can be be unstable to perturbations. In [6], it is shown that vortex dipoles can be shed from circular islands when the steady state is unstable. Since coastal waters near islands are rich in chemical and biological material, vortex dipoles shed from an island can transport the biogeochemical material. Thus, the stability of flow around islands is important to biogeochemical tracer transport.

Previous studies on stability of flow around islands can be two-dimensional or three-dimensional. In [6], the stability of two vorticity rings attached to a circular island with zero net vorticity is studied in a two-dimensional setting. Depending on the ratio of the outer radius of the two layer vorticity, the flow can be unstable. In [12], the stability of two-dimensional quasi-geostrophic circular flow around a circular island with bottom slope is investigated. They find that sufficiently steep bottom slope can stabilize the flow because the absolute vorticity dominates the relative vorticity. However, islands are never circular in the real world. One natural question is how the shape of islands affect the steady state and stability of the flow. This will also provide insight on whether a circular island is a good approximation to a noncircular island. To answer these questions, we start studying the steady flow and its stability around a noncircular island in a two-dimensional domain.

In 2D, a single elliptic vortex patch (called Kirchhoff vortex) rotates at a constant angular velocity. The vortex patch is stable to small perturbations when $a/b < 3$ (see [8]), where a and b are, respectively, the long and short axes of the ellipse. This result suggests that for an elliptic island the aspect ratio is an important factor to the stability of the steady states around islands. Thus, we restrict our attention to elliptic islands. The method used is very general and applicable to islands of any shape.

The report is organized as follows: in §2 we compute the steady state around a slightly perturbed circular island using asymptotic analysis; in §3 we compute the evolution of a small azimuthal mode n perturbation added to the steady circular flow around circular islands. The results are used to verify the contour dynamics code and the simulated annealing

method for computing steady states. The contour dynamics code is described in §4 and the simulated annealing method is described in §5. In §6, we show the steady states around elliptic islands with different aspect ratios. Finally, in §7 we study the linear stability of the steady states in §6 of small perturbations.

1.2 Problem set-up

Hereafter, we consider the 2D Euler equation. A vortex patch denoted by A is attached to the island Ω (see figure 1). The vorticity $q = v_x - u_y$ is zero outside A. By non-dimensionalization, it suffices to assume $q = 1$ in A.

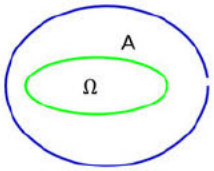

Figure 1: Illustration of the domain. Ω represents an island. $q = q_0$ in A and $q = 0$ in $\mathbb{R}^2 \setminus (A \cup \Omega)$.

2 Steady State around a Slightly Perturbed Circular Island

In this section, we study the steady flow around an island perturbed by azimuthal mode n, i.e., the boundary of the island is $(1 + \xi\cos(n\theta), \theta)$ in polar coordinate where $\xi \ll 1$. Let the outer boundary of the vortex patch be $(b + \eta(\theta, t), \theta)$. We compute the steady solution up to $O(\xi^2)$.

To this end, we expand the streamfunction ψ and η as

$$\psi = \psi_0 + \psi_1 + \psi_2, \tag{1}$$

$$\eta_1 = \eta_1 + \eta_2 + O(\xi^3), \tag{2}$$

where $\eta_1 = \hat{\eta}_1\cos(n\theta)$, $\eta_2 = e + f\cos(2n\theta)$. The vorticity field is expanded as

$$q = H(b+\eta-r) = H(b-r) + \delta(b-r)\eta_1 + \delta(b-r)\eta_2 - \frac{1}{2}\eta_1^2\frac{d}{dr}\delta(b-r). \tag{3}$$

Expanding equation $\Delta\psi = q$, we have

$$\Delta\psi_0 = H(b-r), \tag{4}$$

$$\Delta\psi_1 = \delta(b-r)\eta_1, \tag{5}$$

$$\Delta\psi_2 = \delta(b-r)\eta_2 - \frac{1}{2}\eta_1^2\frac{d}{dr}\delta(b-r). \tag{6}$$

Next, we expand boundary conditions for ψ. The boundary condition at $r = 1$ is $\psi(r + \xi\cos(n\theta), \theta) = const.$ After expansion, it becomes

$$\psi_0(1,\theta) = const, \tag{7}$$

$$\psi_1(1,\theta) + \frac{d}{dr}\psi_0(1,\theta)\xi\cos(n\theta) = const, \tag{8}$$

$$\psi_2(1,\theta) + \frac{d}{dr}\psi_1(1,\theta)\xi\cos(n\theta) + \frac{1}{2}\frac{d^2}{dr^2}\psi_0\xi^2\cos^2(n\theta) = const. \tag{9}$$

The boundary condition at $r = b + \eta$ is

$$\partial_t\eta + \frac{v(b+\eta,\theta)}{b+\eta}\frac{\partial\eta}{\partial\theta} = -\frac{1}{b+\eta}\frac{\partial\psi}{\partial\theta}. \tag{10}$$

For steady state, the boundary conditions become

$$v_0(b)\frac{d\eta_1}{d\theta} + \frac{\partial\psi_1}{\partial\theta}(r,\theta) = 0, \quad r = b \tag{11}$$

$$v_0(b)\frac{d\eta_2}{d\theta} + \frac{\partial\psi_2}{\partial\theta}(r,\theta) = -[v_0'(r)\eta_1 + v_1(r,\theta)]\frac{d\eta_1}{d\theta} - \partial_r\partial_\theta\psi_1(r,\theta)\eta_1, \quad r = b. \tag{12}$$

Solving ψ_0, we find

$$\psi_0(r,\theta) = \begin{cases} \frac{r^2}{4} - \frac{b^2}{4} + a_0\ln(r/b), & r < b \\ (a_0 + b^2/2)\ln(r/b), & r > b, \end{cases} \tag{13}$$

where a_0 is determined by the circulation on the island (determined later).

According to equation (5), we write ψ_1 as

$$\psi_1(r,\theta) = \cos(n\theta)\begin{cases} b_0(r/b)^n + b_1(r/b)^{-n}, & r < b \\ b_2(r/b)^{-n}, & r > b, \end{cases} \tag{14}$$

After applying boundary conditions to ψ_1, we have

$$b_0 = -\frac{b}{2n}\hat{\eta}_1, b_1 = -\left(\frac{a_0}{b} + \frac{b}{2}\right)\hat{\eta}_1 + \frac{b}{2n}\hat{\eta}_1, b_2 = -\left(\frac{a_0}{b} + \frac{b}{2}\right)\hat{\eta}_1, \tag{15}$$

and

$$\hat{\eta}_1 = \frac{(1+2a_0)n}{(2a_0b^{n-1} + b^{n+1})n - b^{n+1} + b^{1-n}}\xi. \tag{16}$$

By boundary condition (12), ψ_2 consists of azimuthal modes 0 and $2n$. Thus, we write $\psi_2 = \phi_0(r) + \phi_2(r)\cos(2n\theta)$. Substituting this into equation (6), we have

$$\frac{1}{r}(r\phi_0')' = e\delta(b-r) - \frac{1}{4}\frac{d}{dr}\delta(r-b)\hat{\eta}_1^2, \tag{17}$$

$$\frac{1}{r}(r\phi_2')' - \frac{4n^2}{r^2}\phi_2 = f\delta(b-r) - \frac{1}{4}\frac{d}{dr}\delta(r-b)\hat{\eta}_1^2. \tag{18}$$

Solving these two equations in regions $r < b$ and $r < b$, we have

$$\phi_0(r) = \begin{cases} c_1 + c_2\ln r, & r < b \\ c_3\ln r, & r > b, \end{cases} \tag{19}$$

$$\phi_2(r) = \begin{cases} d_1(r/b)^{2n} + d_2(r/b)^{-2n}, & r < b \\ d_3(r/b)^{-2n}, & r > b. \end{cases} \tag{20}$$

Next, we determine the matching conditions for ϕ_0 and ϕ_2. For any smooth function $h(r)$ with compact support, we introduce the notation $< f, h >= \int_{r>1} h(r)g(r)$. Then

$$\left\langle \frac{1}{r}(r\phi_0')', h \right\rangle = \left\langle \phi_0, \left(r \left(\frac{h}{r} \right)' \right)' \right\rangle. \tag{21}$$

By splitting the integral domain into $(1, b)$ and (b, ∞), we find

$$\begin{aligned} \left\langle \phi_0, \left(r \left(\frac{h}{r} \right)' \right)' \right\rangle &= h'(b)[\phi_0(b^-) - \phi_0(b^+)] \\ &\quad + h(b) \left[\frac{\phi_0(b^+) - \phi_0(b^-)}{b} + \phi_0'(b^+) - \phi_0'(b^-) \right]. \end{aligned} \tag{22}$$

Using equation (17), we also have

$$\left\langle \frac{1}{r}(r\phi_0')', h \right\rangle = eh(b) + \frac{1}{4}h'(b)\hat{\eta}_1^2. \tag{23}$$

Therefore, by the two equations above, we have

$$\frac{1}{4}\hat{\eta}_1^2 = \phi_0(b^-) - \phi_0(b^+), \quad e = \phi_0'(b^+) - \phi_0'(b^-) - \frac{\hat{\eta}_1^2}{4b}. \tag{24}$$

Repeating the process for ϕ_2, we have

$$\frac{1}{4}\hat{\eta}_1^2 = \phi_2(b^-) - \phi_2(b^+), \quad f = \phi_2'(b^+) - \phi_2'(b^-) - \frac{\hat{\eta}_1^2}{4b}. \tag{25}$$

Applying matching conditions to ϕ_0 and ϕ_2, we have

$$c_1 = \frac{1}{4}\hat{\eta}_1^2, \quad c_3 = c_2 + \frac{\hat{\eta}_1^2}{4} + eb, \tag{26}$$

$$d_1 + d_2 - d_3 = \frac{1}{4}\hat{\eta}_1^2, \quad -d_1 + d_2 - d_3 - \frac{fb}{2n} = \frac{1}{8n}\hat{\eta}_1^2. \tag{27}$$

Applying boundary condition for ψ_2 at $r = 1$, i.e., equation (9), we have

$$\frac{d_1}{b^{2n}} + d_2 b^{2n} = -\frac{1}{2}\left[\left(\frac{1}{4} - \frac{a_0}{2} \right) \xi^2 + \left(\frac{nb_0}{b^n} - nb_1 b^n \right) \xi \right]. \tag{28}$$

Next, we apply boundary condition for ψ_2 at $r = b$, i.e., equation (12). The RHS of equation (12) is

$$RHS = \frac{n}{2}\hat{\eta}_1 \sin(2n\theta) \begin{cases} \left(\frac{1}{2} - \frac{a_0}{b^2} \right) \hat{\eta}_1 + 2\frac{n}{b}(b_0 - b_1), & r = b^- \\ \left(-\frac{a_0}{b^2} - \frac{1}{2} \right) \hat{\eta}_1 - 2n\frac{b_2}{b}, & r = b^+. \end{cases} \tag{29}$$

Using the formulae for b_0, b_1, b_2, $RHS(b^+) - RHS(b^-) = \frac{n}{2}\hat{\eta}_1^2 \sin(2n\theta)$. The LHS of equation (12) is

$$LHS = -2n \sin(2n\theta) \left[\left(\frac{a_0}{b} + \frac{b}{2} \right) f + \phi_2(b) \right], \tag{30}$$

and we have the same jump as the RHS does by using equation (27). Thus it suffices to match RHS and LHS at b^+, i.e.,

$$\left(\frac{a_0}{b}+\frac{b}{2}\right)f+d_3=-\frac{\hat{\eta}_1}{4}\left[\left(-\frac{a_0}{b^2}-\frac{1}{2}\right)\hat{\eta}_1-2n\frac{b_2}{b}\right]. \tag{31}$$

Hence equations (27), (28), (31) are 4r equations about 4 unknows d_1, d_2, d_3, f.

To determine c_1, c_2, c_3, e, we need to apply the circulation constraint on the island. Define b as the radius of the circle that has the same area enclosed by the contour. By Kelvin's theorem, the circulation on the contour is conserved. That is, the total area enclosed by the contour is conserved by Stokes theorem. Thus,

$$\int_0^{2\pi}\int_b^{b+\eta_1+\eta_2} r dr d\theta = O(\xi^3). \tag{32}$$

This equation leads to

$$e=-\frac{1}{4b}\hat{\eta}_1^2, \quad \text{and} \quad c_2=c_3. \tag{33}$$

Finally, we consider the circulation around the island. The circulation $\int_{\partial\Omega}\boldsymbol{u}\cdot d\boldsymbol{x}$ in the polar coordinate is

$$\begin{aligned}
\Gamma_0 &= \int_{\partial\Omega}\left(\frac{\partial\psi}{\partial r}\hat{\theta}-\frac{1}{r}\frac{\partial\psi}{\partial\theta}\hat{r}\right)\cdot(dr\hat{r}+rd\theta\hat{\theta}) \\
&= \int_{r=1+\xi\cos(n\theta)} r\frac{\partial\psi}{\partial r}-\frac{1}{r}\frac{\partial\psi}{\partial\theta}\frac{dr}{d\theta}d\theta \\
&= \int_0^{2\pi}[1+\xi\cos(n\theta)](\partial_r\psi_0+\partial_r\psi_1+\partial_r\psi_2)-\frac{-\xi n\sin(n\theta)}{1+\xi\cos(n\theta)}(\partial_\theta\psi_1+\partial_\theta\psi_2)d\theta \\
&= \int_{r=1}\partial_r\psi_0+\partial_r\psi_1+\xi\cos(n\theta)\partial_r\psi_0+ \\
&+ \int_{r=1}\partial_r\psi_2+\xi\cos(n\theta)\partial_r\psi_1+n\xi\sin(n\theta)\partial_\theta\psi_1+O(\xi^3) \\
&= \Gamma_0+\int_{r=1}\partial_r\psi_2+\xi\cos(n\theta)\partial_r\psi_1+n\xi\sin(n\theta)\partial_\theta\psi_1+O(\xi^3),
\end{aligned} \tag{34}$$

where $O(\xi)$ terms vanish and $\int_{r=1}\partial_r\psi_0=\Gamma_0$. This leads to

$$2\pi c_2=-\frac{n}{2}\xi\left[\left(\frac{b_0}{b^n}-b_1b^n\right)-n\left(\frac{b_0}{b^n}+b_1b^n\right)\right]. \tag{35}$$

Hence, all the coefficients have been determined provided the linear system about d_1, d_2, d_3, f has a unique solution.

2.1 Interpretation of the results

We analyze the amplitude of the first order solution $\hat{\eta}_1$,

$$\hat{\eta}_1=\frac{(1+2a_0)n}{(2a_0b^{n-1}+b^{n+1})n-b^{n+1}+b^{1-n}}\xi.,$$

where $\Gamma_0=\pi(2a_0+1)$. The solution has the following properties:

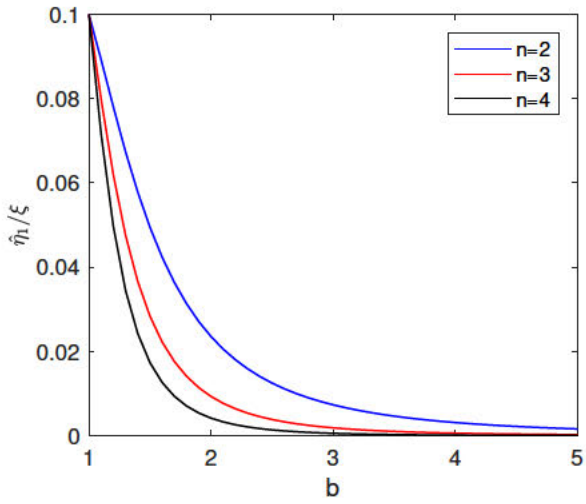

Figure 2: The variation of $\hat{\eta}_1/\xi$ with respect to b for $\Gamma_1 = \pi$.

- When $n \neq 1$ and $\Gamma_0 = 0$, $\hat{\eta}_1 = 0$ for any mode number n. Thus, the flow does not feel the perturbation of the island in this case. Of course, the next order solution is nonzero.
- When $n = 1$, $\hat{\eta}_1 = \xi$.
- $\hat{\eta}_1 \xi$ can be negative. For example, when $\xi > 0$, $\hat{\eta}_1 < 0$, $n = 2$, the island is stretched in x direction, but the steady state is squeezed in x direction relative to the circle $r = b$.
- Figure 2 shows that the ratio of $\hat{\eta}_1/\xi$ for $\Gamma_0 = \pi$. When b increases, the ratio decreases very quickly. Even when the contour is not far from the boundary, the effect of the perturbation of the island on the steady state is negligible. We will find similar phenomena in §6 for elliptic islands. Comparing mode 2, 3, and 4, we find $\hat{\eta}_1$ is smaller for larger mode number.

3 An Initial Value Problem for a Circular Island

In this section, we study the evolution of a small perturbation added to the circular flow around a circular island. The results will be used to verify the contour dynamics code.

Consider the initial vorticity $q(r, \theta, 0) = H(\eta_0 \cos(n\theta) + b - r)$, where $\eta_0 \ll 1$. By the previous section, the streamfunction for the circular flow is

$$\psi_0(r, \theta) = \begin{cases} \frac{r^2}{4} - \frac{b^2}{4} + b_0 \ln(r/b), & r < b \\ (b_0 + b^2/2) \ln(r/b), & r > b, \end{cases} \tag{36}$$

where $b_0 + 1/2 = \Gamma_0/(2\pi)$.

As in the previous section, the streamfunction ψ_1 caused by the perturbation is subject to

$$\Delta\psi_1(r, \theta) = \delta(b - r)\eta(\theta, t), \quad \psi_1(1, \theta) = const, si \tag{37}$$

Without loss of generality, we take the constant$\psi_1(1,\theta)$ to be zero so that the solutionψ_1 is unique.

The calculation differs from the previous section result in the boundary condition at $r=b$. In particular,at $r=b+\eta(\theta,t)$ is

$$\frac{D\eta}{Dt}=u_r, \quad \text{at} \quad r=b+\eta(\theta,t), \tag{38}$$

where u_r is the radial velocity. To the leading order, the above equation is

$$\partial_t\eta+u_\theta(b)\frac{1}{b}\partial_\theta\eta=-\frac{1}{b}\partial_\theta\psi_1, \tag{39}$$

where $u_\theta(b)$ is the tangential velocity induced by ψ_0. The circulation conservation on the boundary of the island implies

$$\int_{x\in\partial\Omega}\frac{\partial\psi_1}{\partial n}dS(x)=0. \tag{40}$$

Since the equations and boundary conditions for ψ_1 and η are linear and $\eta(\theta,0)=\eta_0\cos(n\theta)$, we write $\psi_1(r,\theta,t)=g(r)\eta(\theta,t)+c$ and $\eta(\theta,t)=F_0(t)\cos(n\theta)+F_1(t)\sin(n\theta)$. Solving ψ_1 and applying boundary condition at $r=1$, we have

$$g(r)=\begin{cases} c_0(r/b)^n+d_0(r/b)^{-n}, & r<b \\ d_1(r/b)^{-n}, & r>b. \end{cases} \tag{41}$$

$$c_0=-\frac{b}{2n}, \quad d_0=\frac{1}{2nb^{2n-1}}, \quad d_1=-\frac{b}{2n}+\frac{1}{2nb^{2n-1}}. \tag{42}$$

By substituting ψ_1 and η into equation (39) and applying initial conditions to η, we have

$$F_0(t)=\eta_0\cos\left(\frac{n}{b}[g(b)+u_\theta(b)]t\right), \quad F_1(t)=\eta_0\sin\left(\frac{n}{b}[g(b)+u_\theta(b)]t\right) \tag{43}$$

Thus,

$$\eta(\theta,t)=\eta_0\cos\left(\frac{n}{b}[g(b)+u_\theta(b)]t-n\theta\right). \tag{44}$$

In particular, η is a periodic function and the period is $T=2\pi b/|u_\theta(b)+g(b)|$. Substituting the value of $u_\theta(b)$ into this formulae, we get

$$T=\frac{4\pi b^2}{(n-1)b^2+b^{2-2n}+n(\Gamma_0/\pi-1)}. \tag{45}$$

When the denominator is zero, $\eta(\theta,t)=\eta_0\cos(n\theta)$ is a steady solution.

Remarks:

- For $n=1$, $T=\frac{4\pi^2b^2}{\Gamma_0}$. In particular, when $\Gamma_0=0$, $\eta(\theta,t)=\eta_0\cos(n\theta)$ is a steady solution.
- For each n, there is a unique circulation such that η is in a steady solution.

4 Contour Dynamics with an Island by Integral Methods

In this section, we describe our contour dynamics code with an island of arbitrary shape. The streamfunctionψ is subject to the following conditions:

$$\Delta\psi = q \quad \text{in} \quad \mathbb{R}^2 \setminus \overline{\Omega}, \tag{46}$$

$$\psi = const \quad \text{on} \quad \partial\Omega, \tag{47}$$

$$\sim \frac{\Gamma_0 + \int q(x)dx}{2\pi} \ln|x| + O(1), \quad \text{when} \quad |x| \to \infty \tag{48}$$

where $\Gamma_0 + \int q(x)dx$ is the total circulation, and the last condition is necessary because of the infinite domain. The solution ψ is unique once the constant value of ψ on $\partial\Omega$ has been chosen (see [2]).

Green function is often used to calculate the streamfunction for domains with obstacles of special shapes, e.g., circular or planar obstacles, because an analytical expression exists. However, in a complex domain with an obstacle of arbitrary shape, calculating Green function becomes complicated. Thus, we use a different approach to find the streamfunction. We make use of the free space Green function $G(x,y) = \frac{1}{2\pi}\ln|x-y|$ in $\mathbb{R}^2$. Denote $\mathbb{R}^2 \setminus \overline{\Omega}$ by Ω^c. Define

$$\phi(x) = \int_{\Omega^c} G(x,y)q(y)dy, \tag{49}$$

Then $\Delta\phi = q$ and $\phi \sim \int q(y)dy/(2\pi)\ln|x|$ when $|x| \to \infty$.

Let $f = \psi - \phi$, then f is the solution to

$$\Delta f = 0 \quad \text{in} \quad \Omega^c, \tag{50}$$

$$f = c - \phi \quad \text{on} \quad \partial\Omega, \tag{51}$$

$$\sim \frac{\Gamma_0}{2\pi}\ln|x| + O(1), \quad \text{when} \quad |x| \to \infty. \tag{52}$$

f can be solved by both single-layer and double-layer potential methods. Since single-layer potential method takes less numerical computation and works better with contour dynamics method, we use single-layer potential method.

We seek a single-layer potential solution $f(x) = \int_{y\in\partial\Omega} G(x,y)h(y)dS(y)$, where $h(y)$ is a smooth function defined on $\partial\Omega$. We assume $\partial\Omega$ is smooth. Then it is clear $f(x)$ is harmonic in $\mathbb{R}^2 \setminus \partial\Omega$. When $|x| \to \infty$, $f(x) \sim \frac{\int_{y\in\partial\Omega} h(y)dS(y)}{2\pi}\ln|x|$. Thus the boundary conditions on f become

$$\int_{y\in\partial\Omega} G(x,y)h(y)dS(y) = c - \phi(x) \quad \text{on} \quad \partial\Omega, \tag{53}$$

$$\int_{y\in\partial\Omega} h(y)dS(y) = \Gamma_0. \tag{54}$$

It is shown in [5] that given Γ_0, there exists a unique solution $h(y)$ and c satisfying the equations (53) and (54). Since computing $\phi(x)$ requires integrating normal velocity along

the boundary $\partial\Omega$, we take the tangential derivative of equation (53). In [11], it is shown that we can move the tangential derivative inside the integral sign, thus we have

$$\int_{y\in\partial\Omega} \partial s_x G(x,y)h(y)dS(y) = -\partial s_x \phi(x) \quad \text{on} \quad \partial\Omega, \tag{55}$$

where ∂s_x denotes the tangential derivative. Equation (55) always has a solution and the homogeneous equation has only one linearly independent solution (see Hsiao and Maccamy 1973). Let the homogeneous solution be $h_0(y)$ and a particular solution be $h_1(y)$. Then we can write $h(y) = c_0 h_0(y) + h_1(y)$. Equation (54) implies

$$c_0 = \frac{\Gamma_0 - \int_{y\in\partial\Omega} h_1(y)dS(y)}{\int_{y\in\partial\Omega} h_0(y)}. \tag{56}$$

Remark. That equations (53) and (54) alway have a solution implies the denominator in equation (56) is non-zero.

Velocity (u, v) on the contour ∂A is

$$(u,v) = \left(-\partial_{x_2}\phi(x) - \int_{\partial\Omega} \partial_{x_2} G(x,y)h(y)dS(y), \partial_{x_1}\phi(x) + \int_{\partial\Omega} \partial_{x_1} G(x,y)h(y)dS(y)\right), \tag{57}$$

where

$$(-\partial_{x_2}\phi(x), \partial_{x_1}\phi(x)) = \left(-\int_{\partial A} G(x,y)dy_1, -\int_{\partial A} G(x,y)dy_2\right), \tag{58}$$

by integration by parts. Therefore, velocity can be written as integral along contours and a 2D grid is not needed. Moreover, the velocity consists of two parts: the first part is induced by the vorticity field; the second part is induced by point vortices of strength $h(y)$ on the boundary of the island. The point vortices are added to make the total normal velocity vanish on the boundary of the island by equation (55).

4.1 Validation

We validate the contour dynamics code using the solution η in §3. In particular, we consider a circular island. The initial boundary of the vortex is $r = 2 + 0.1\cos(n\theta)$, where $n = 1, 2$ and the circulation around the island $\Gamma_0 = 0, 10$. Figure 3 shows the results for the four cases. For $\Gamma_0 = 0$, $n = 1$, the figure shows that the initial state is approximately a solution consistent with the result in §3. For the other three cases, the figure shows that $\eta(\theta, t)$ is a periodic function of t for any θ in time and the predicted phase speed ω/n where $\omega = 2\pi/T$ (T is determined by (45)) is consistent with the plots of η. The right panel of the figure shows the spectrum of $\eta(0, t)$ peaks at the predicted frequency. Thus, we conclude the contour dynamics code is reliable.

5 Hamiltonian Simulated Annealing Method

In this section, we describe the Hamiltonian simulated annealing method used to find steady states of the 2D Euler equation.

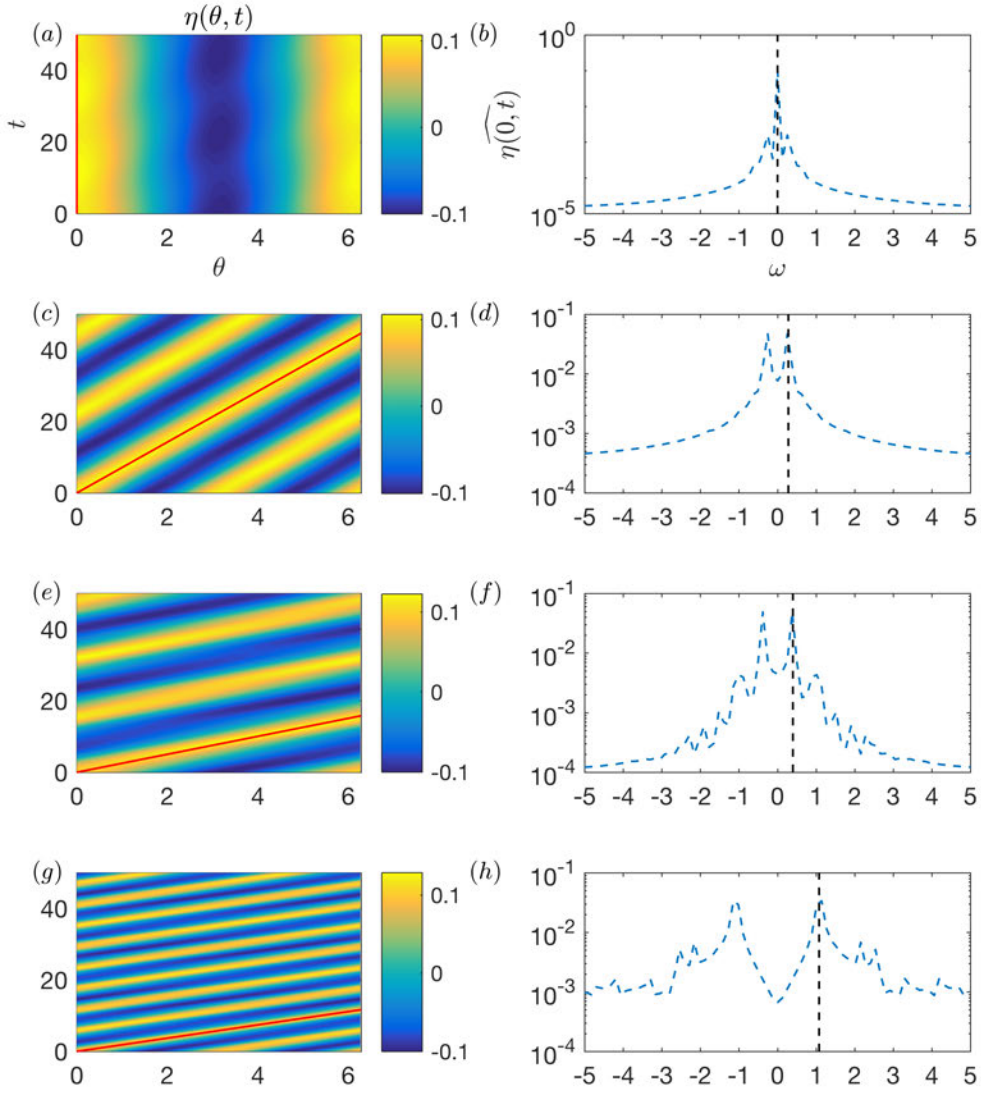

Figure 3: Left panel: $\eta(\theta, t)$ plotted in $\theta - t$ coordinate. Right panel: the Fourier transform $\widehat{\eta(0,t)}$. From top to bottom: $\Gamma_0 = 0, n = 1$; $\Gamma_0 = 0, n = 2$; $\Gamma_0 = 10, n = 1$; $\Gamma_0 = 10, n = 2$. The red line is $\theta = \omega/nt$ where $\omega = 2\pi/T$ is the frequency predicted in section §3. The dashed black line denotes the predicted frequency.

5.1 Hamiltonian structure

2D Euler equation can be formulated in terms of a Hamiltonian system using the following Poisson bracket (see [9] and [10])

$$\{F, G\} = \int q \left[\frac{\delta F}{\delta q}, \frac{\delta G}{\delta q} \right], \tag{59}$$

where $[,]$ is the usual Jacobian. The Poisson bracket defined above in an infinite domain is anti-symmetric, bilinear, and satisfies the Jacobi identity. The Hamiltonian (also the finite part of the kinetic energy) can be defined as

$$H[q] = -\frac{1}{2} \int dx q(x)\psi(x) = -\frac{1}{2} \int \int dx' q(x) G(x, x') q(x'). \tag{60}$$

By the symmetry property of the Green function G and evolution equation of vorticity, $q_t = \{q, H\}$.

Since integration by parts is used in many derivations and it is no longer possible to write $\psi(x) = \int q(y)G(x, y)dy$, we need modify the Hamiltonian. Following the above approach, we make use of the Green function for Ω^c. By [7], there exists a Green function $g(x, y)$ such that

$$\Delta_x g(x, x') = \delta(x - x'), \forall x, x' \in \Omega^c, \tag{61}$$

$$g(x, x') = const \quad \forall x \in \partial\Omega, \tag{62}$$

$$\int_{\partial\Omega} \frac{\partial g(x, x')}{\partial n} dS(x) = 0, \tag{63}$$

where $\frac{\partial g(x,x')}{\partial n}$ is the outer limit of normal derivative of $g(x, x')$ with respect to x,

$$g(x, x') \sim \frac{1}{2\pi} \ln |x - x'| + O(\frac{1}{|x - x'|}), \quad \text{when} \quad x \to \infty \tag{64}$$

$$\frac{g(x, x')}{\partial n} \sim \frac{1}{2\pi} \frac{1}{|x - x'|} + O(\frac{1}{|x - x'|^2}), \quad \text{when} \quad x \to \infty, \tag{65}$$

where $\frac{g(x,x')}{\partial n}$ is the outer normal derivative on a large circle $|x - x'| = c$ with respect to x. Importantly, $g(x, x')$ is symmetric, i.e.,

$$g(x, x') = g(x', x). \tag{66}$$

Physically, $g(x, x')$ is the streamfunction induced by a point vortex at x' outside of an island which has zero circulation.

Let ψ_0 be the streamfunction induced by the circulation around the island alone. Then ψ_0 is subject to

$$\Delta\psi_0 = 0, \quad \in \partial\Omega^c, \tag{67}$$

$$\int_{\partial\Omega} \frac{\partial \psi_0}{\partial n} = \Gamma_0, \tag{68}$$

$$= const, \quad \text{on} \quad \partial\Omega. \tag{69}$$

By the previous section, we know ψ_0 exists and is unique up to a constant. Indeed, we can take

$$\psi_0 = \frac{\Gamma_0}{\int_{\partial\Omega} h_0(y)dS(y)} \int_{\partial\Omega} G(x,y)h_0(y)dS(y), \tag{70}$$

where $h_0(y)$ is an eigenfunction to the equation (53). The streamfunction induced by the vortex patch outside of the island can be written as

$$\psi(x) - \psi_0(x) = \int_{\Omega^c} g(x,x')q(y)dy. \tag{71}$$

To use the symmetry property of the green function, we define

$$H[q] \;=\; -\int_{\Omega^c} q(x)\psi_0(x) - \frac{1}{2}\int_{\Omega^c} q(x)(\psi(x) - \psi_0(x)) \tag{72}$$

Then $\frac{\delta H}{\delta q} = -\psi$ by symmetry of $g(x,x')$, and

$$\{q,H\} = \int_{\Omega^c} q(x') \left[\frac{\delta q(x)}{\delta q(x')}, \frac{\delta H}{\delta q(x')}\right] = -\left[q, \frac{\delta H}{\delta q}\right] = [q,\psi], \tag{73}$$

where integration by parts is used and justified because $\delta q/\delta x$ is a Dirac mass. Thus, the the evolution equation of the vorticity q can be written as

$$q_t = \{q,H\}. \tag{74}$$

For any functional F which has a functional derivative $\delta F/\delta q$, we have

$$\begin{aligned}
F_t &= \lim_{\Delta t\to 0} \frac{F[q(t+\Delta t)] - F[q(t)]}{\Delta t} \\
&= \lim_{\Delta t\to 0} \frac{F[q(t) + \Delta t q_t(t) + o(\Delta t)] - F[q(t)]}{\Delta t} \\
&= \int \frac{\delta F}{\delta q} q_t(t) \\
&= \int \frac{\delta F}{\delta q}[q,\psi] \\
&= \int \partial_1(q\delta F/\delta q)\partial_2\psi - \partial_2(q\delta F/\delta q)\partial_1\psi - q[\delta F/\delta q, \psi] \\
&= -\int_{\partial\Omega} \delta F/\delta q[\partial_2\psi n_1 - \partial_1\psi n_2] + \{F,H\} = \{F,H\},
\end{aligned} \tag{75}$$

where integration by parts and $\quad = const$ on $\partial\Omega$ are used in the last equality sign. In particular, we have $H_t = 0$ by antisymmetry of the bracket. Although H is not the usual kinetic energy, it is equivalent to kinetic energy because the first term $\int q(x)\psi_0(x)dx$ can be shown to be conserved.

5.2 Simulated annealing

Following [3], a symmetric bracket $(F,G)_{SA}$ with smoothing can be defined as

$$(F,G)_{SA} = \int_{\Omega^c}\int_{\Omega^c} dx'dx''\{F,q(x')\}g(x',x'')\{q(x''),G\}, \tag{76}$$

where $g(x',\ x'')$ is the green function for our domain. This is clearly symmetric by the antisymmetry of the Poisson bracket. This symmetric bracket differs from that in [3] in that $g(x',\ x'')$ is used instead of the free space Green function to ensure boundary terms vanish when computing $(H,H)_{SA}$. Indeed,

$$\begin{aligned}(H,H)_{SA} &= -\int_{\Omega^c}\int_{\Omega^c} dx'dx''[q(x'),\psi(x')]g(x',x'')[q(x''),\psi(x'')] &(77)\\ &= -\int_{\Omega^c} dx'\Phi(x')\Delta\Phi(x'), &(78)\end{aligned}$$

where $\Phi(x') = \int_{\Omega^c} dx''g(x'd,x'')[q(x''),\psi(x'')]$ is the streamfunction outside the island induced by vorticity field $[q(x''),\psi(x'')]$ with zero circulation on the island. By the asymptotic behavior of $g(x,x')$ at $|x|\to\infty$ (see equation 64 and 65), we have

$$\Phi(x) \to \frac{\int_{\Omega^c}[q,\psi]}{2\pi}\ln|x| + O(\frac{1}{|x|}) \quad \text{when} \quad x\to\infty, \tag{79}$$

and

$$\partial_r\Phi \to \frac{\int_{\Omega^c}[q,\psi]}{2\pi}\frac{1}{|x|} + O(\frac{1}{|x|^2}) \quad \text{when} \quad x\to\infty. \tag{80}$$

Futhermore, $\int_{\Omega^c}[q,\psi] = 0$ because we assume q has compact support and $\quad = const$ on $\partial\Omega$. Thus, the asymptotic behavior of $\Phi(x)$ becomes

$$\Phi(x) \sim O(\frac{1}{|x|}), \quad \partial_r\Phi \sim O(\frac{1}{|x|^2}) \quad \text{when} \quad x\to\infty. \tag{81}$$

Using the asymptotic behavior of $\Phi(x)$, we get

$$\begin{aligned}(H,H)_{SA} &= -\lim_{R\to\infty}\int_{|x|=R}\Phi(x)\frac{\partial\Phi(x)}{\partial n}dS(x) + \int_{\partial\Omega}\Phi\frac{\partial\Phi(x)}{\partial n}dS(x) + \int_{\Omega^c}|\nabla\Phi(x)|^2 &(82)\\ &= \int_{\Omega^c}|\nabla\Phi(x)|^2. &(83)\end{aligned}$$

where the second term vanishes because Φ is constant on $\partial\Omega$ and has no circulation around the island. Thus, the dynamics generated by

$$\frac{dF}{dt} = \beta\{F,H\} + \alpha(F,H)_{SA}, \tag{84}$$

ensures the Hamiltonian H changes monotonically.

5.3 The contour dynamics version of the simulated annealing method

For piecewise vorticity distribution with only one contour, the bracket of $\{F, H\}$ becomes

$$\begin{aligned}\{F,H\} &= q_0 \int_{A\setminus\overline{\Omega}} \left[\frac{\delta F}{\delta q}, \frac{\delta H}{\delta q}\right] = -q_0 \int_{A\setminus\overline{\Omega}} \partial_1 \frac{\delta F}{\delta q}\partial_2\psi - \partial_2\frac{\delta F}{\delta q}\partial_1\psi \qquad (85)\\ &= -q_0\left\{\int_{\partial A} - \int_{\partial\Omega}\right\}\frac{\delta F}{\delta q}\frac{\partial\psi(y)}{\partial\tau}dS(y) \qquad (86)\\ &= q_0\int d\sigma \frac{\delta F}{\delta q}\partial_\sigma\frac{\delta H}{\delta q}, \qquad (87)\end{aligned}$$

where the integral on $\partial\Omega$ vanishes by integral by parts and $\psi = const$ on $\partial\Omega$, and $(X(\sigma), Y(\sigma))$ is a parametrization of the outer boundary of the vortex patch ∂A. In [4], a symmetric bracket is defined as

$$(F,G)_{SA} = \int d\sigma\{F, X^i(\sigma)\}\{X^i(\sigma), G\}, \qquad (88)$$

where $(X^1, X^2) = (X, Y)$. We note that smoothing is not used in this definition of the symmetric bracket. Using the definition of $\{,\}_{SA}$, we have

$$(H,H)_{SA} = -\int d\sigma\{X,H\}^2 + \{Y,H\}^2 \le 0. \qquad (89)$$

The dynamics generated by $F_t = \alpha(F, H)_{SA}$ evolves the Hamiltonian monotonically depending on the sign of α. By evolving the contour by velocity $((X, H)_{SA}, (Y, H)_{SA})$, we evolve the dynamics under the symmetric bracket.

Let $\{X, H\} = \tilde{u}$, $\{Y, H\} = \tilde{v}$. By the definition of the bracket, we have

$$\tilde{u} = \frac{Y_\sigma}{X_\sigma^2 + Y_\sigma^2}\frac{\partial\psi}{\partial\sigma} = \frac{Y_\sigma}{\sqrt{X_\sigma^2 + Y_\sigma^2}}u_n, \qquad (90)$$

$$\tilde{v} = -\frac{X_\sigma}{X_\sigma^2 + Y_\sigma^2}\frac{\partial\psi}{\partial\sigma} = -\frac{X_\sigma}{\sqrt{X_\sigma^2 + Y_\sigma^2}}u_n, \qquad (91)$$

where u_n is the normal velocity. Let $||X_\sigma|| = \sqrt{X_\sigma^2 + Y_\sigma^2}$. We evolve the boundary of the vortex patch by $\alpha(u_{SA}, v_{SA})$:

$$u_{SA} = (X,H)_{SA} = q_0^2\frac{Y_\sigma}{||X_\sigma||^2}\partial_\sigma\left(\frac{Y_\sigma}{||X_\sigma||^2}\tilde{u} - \frac{X_\sigma}{||X_\sigma||^2}\tilde{v}\right) = q_0^2\frac{Y_\sigma}{||X_\sigma||^2}\partial_\sigma\left(\frac{u_n}{||X_\sigma||}\right), \qquad (92)$$

$$v_{SA} = (Y,H)_{SA} = -q_0^2\frac{X_\sigma}{||X_\sigma||^2}\partial_\sigma\left(\frac{Y_\sigma}{||X_\sigma||^2}\tilde{u} - \frac{X_\sigma}{||X_\sigma||^2}\tilde{v}\right) = -q_0^2\frac{Y_\sigma}{||X_\sigma||^2}\partial_\sigma\left(\frac{u_n}{||X_\sigma||}\right). \qquad (93)$$

Equations (89), (90), and (91) implies

$$(H,H)_{SA} = 0 \quad \text{if and only if} \quad \int d\sigma u_n^2\sqrt{X_\sigma^2 + Y_\sigma^2} = 0. \qquad (94)$$

Thus, a solution corresponding to $(H,\ H)_{SA} = 0$ is a steady solution to vorticity field. Moreover, $(H,\ H)_{SA} = 0$ if and only if $(u_{SA},\ v_{SA}) = 0$. Indeed, equations (92) and

(93) show that $(u_{SA}, v_{SA}) = 0$ when $(H, H)_{SA} = 0$. On the other hand, $(u_{SA}, v_{SA}) = 0$ implies $u_n = c||X_\sigma||$ by equation (92) and (93). By conservation of the circulation, $\int d\sigma u_n ||X_\sigma|| = c \int d\sigma ||X_\sigma||^2 = 0$. Thus, $c = 0$ and $u_n = 0$. We note that although the Hamiltonian changes monotonically, it is not guaranteed that the steady state is a local maximum or minimum point of H under isovortical sheet (see [1])

5.4 Validation

We check the simulated annealing method against the steady circular flow around a circular island and the steady state for a slightly perturbed island computed in §2. The constant α should be chosen as negative so that the Hamiltonian increases, otherwise the Hamiltonian continues to decrease and does not evolve to the desired steady state (see [3] for further discussion). For all the calculations, we choose $\alpha = -1$. The resolution of the contour is $\Delta\theta = 5\pi/180$ and the resolution of the island is $\Delta\theta = \pi/180$. Time step is chosen as $\Delta t = 1/128$.

5.4.1 The steady state around a circular island

We let the radius of the island $r = 1$ and initialize the contour by $b = 2 + 0.5\cos(n\theta)$, where $n = 1, 2$. The circulation around the island $\Gamma_0 = 0, 10$. For each initial condition, the corresponding steady contour is $r = \sqrt{4.125}$.

Figure 4 shows the evolution of the contour under the symmetric bracket. The boundary of the contour seems to be unchanged from $t = 0$ to $t = 100$. Later, the contour differs from the circular steady state significantly. At $t = 540$, the contour almost intersects the boundary of the island. After $t = 540$, the contour becomes irregular and not differentiable and the results are shown here. Figure 5 shows that initially H_t decreases, implying that the contour may evolve toward the circular steady state. However, H_t experiences a long period of increasing, consistent with the horizontal shift of the contour. The rapid increase of H_t after $t = 540$ is caused by the incorrect intersection of the contour with the island. For finer spatial and time resolution, the contour still does not converge to its steady state. There are two possible reasons for the failure of the method: the first one is other constraints need be added to make the contour converge to its steady state; the contour dynamics code is accurate enough.

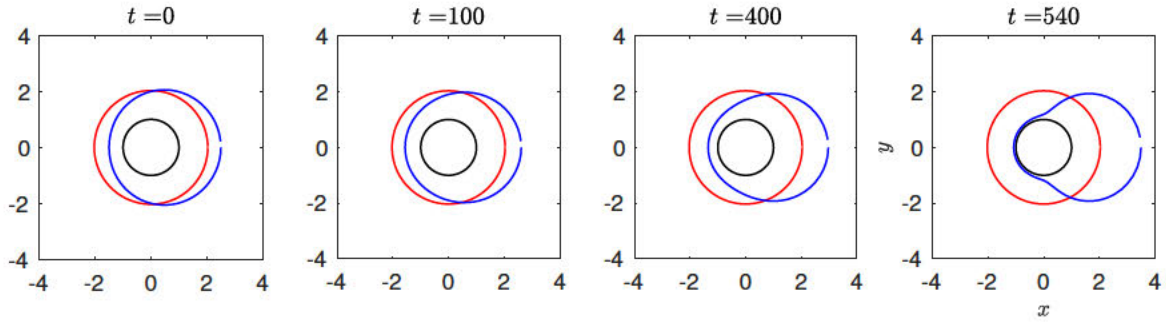

Figure 4: The evolution of the contour (blue line) initialized by $r = 2 + 0.5\cos(\theta)$ for $\Gamma_0 = 0$ under the symmetric bracket dynamics. The red line is the steady state circle $r = \sqrt{4.125}$.

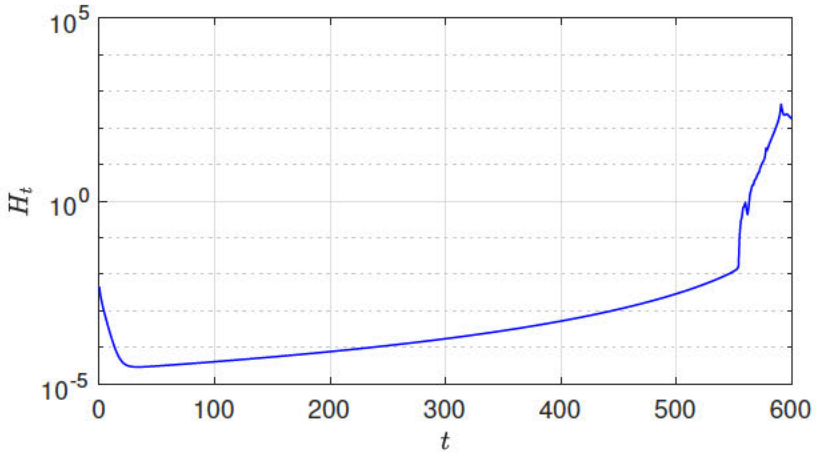

Figure 5: The evolution of H_t for initial contour $r = 2 + 0.5\cos(\theta)$, $\Gamma_0 = 0$ under the symmetric bracket dynamics.

Figure 6 shows that the contour with mode 2 perturbation already converges to the steady state at $t = 100$. Thus, the simulated annealing method can find the the steady state for contours perturbed by mode 2. Also note that the amplitude of mode 2 is finite.

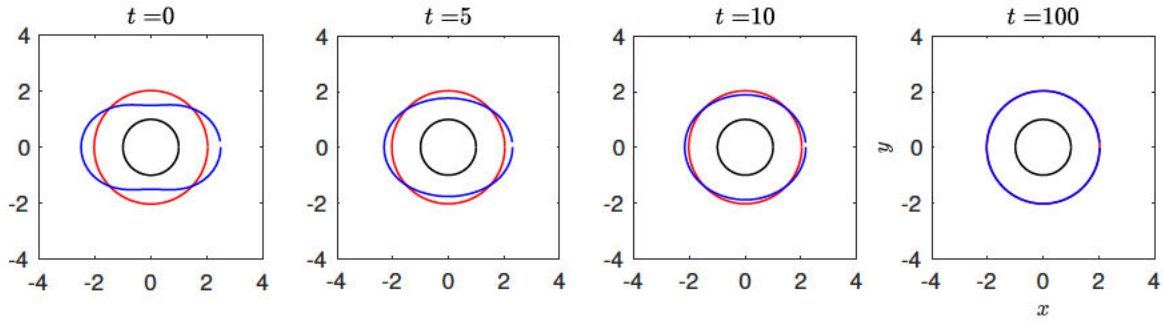

Figure 6: The evolution of the contour (blue line) initialized by $r = 2+0.5\cos(2\theta)$ for $\Gamma_0 = 0$ under the symmetric bracket dynamics. The red line is the steady state circle $r = \sqrt{4.125}$.

Figure 7 shows that for $\Gamma_0 = 10$, the contour initialized by mode 1 perturbation can converge to the steady state. Figure 8 shows that for $\Gamma_0 = 10$, the contour perturbed by mode 2 perturbation can converge to the steady state. Moreover, compared to the results for $\Gamma_0 = 10$, the convergence occurs much faster. At $t = 10$, steady state has been reached. In conclusion, the simulated annealing method can find the correct steady for most initial conditions except for the mode 1 perturbation with zero circulation around the island.

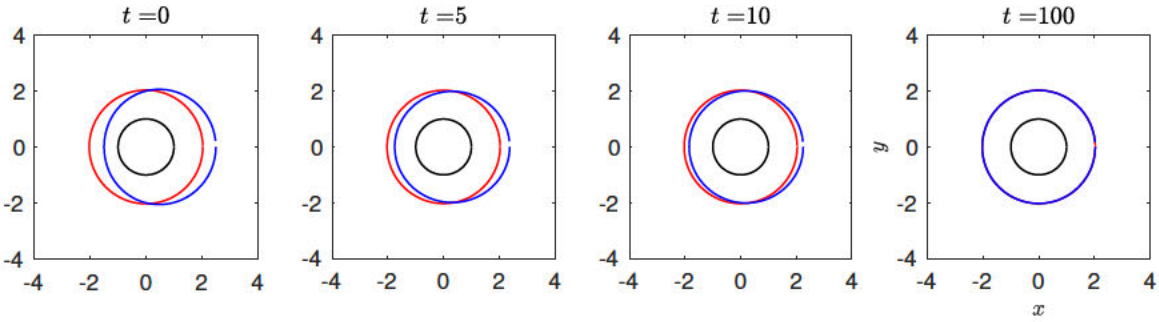

Figure 7: The evolution of the contour (blue line) initialized by $r = 2+0.5\cos(\theta)$ for $\Gamma_0 = 0$ under the symmetric bracket dynamics. The red line is the steady state circle $r = \sqrt{4.125}$.

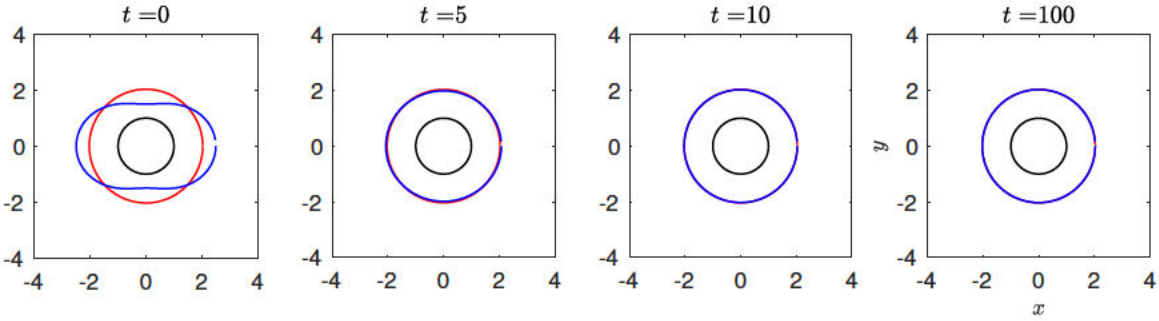

Figure 8: The evolution of the contour (blue line) initialized by $r = 2+0.5\cos(\theta)$ for $\Gamma_0 = 0$ under the symmetric bracket dynamics. The red line is the steady state circle $r = \sqrt{4.125}$.

5.5 The steady state around a slightly perturbed island

Let the boundary of the perturbed island be $r = 1 + 0.1\cos(2\theta)$. The initial contour is $r = 2$. We check the steady state computed by simulated annealing method with the leading order solution in §2 for $n = 2$ and $\Gamma_0 = \pi$. By (16), $\eta_1 = 0.235\cos(2\theta)$. Figure 9 shows that the numerical η_1 computed by the simulated annealing method is also mode 2; indeed, $\eta_1 = 0.234\ \cos(2\theta)$. Thus the steady state computed by the simulated annealing method agrees with the linear theory. Note the nonzero mode 4 can be explained by next order solution.

6 Steady Flows around an Elliptic Island

We compute steady flows around an elliptic island using the simulated annealing method. Denote the boundary of the island by $x^2/a^2 + y^2/b^2 = 1$. We use $\sqrt{Area/\pi}$, where $Area$ is the area of the island, as the characteristic length scale and vorticity q_0 as a time scale to non-dimensionalize all the variables. Therefore, we can assume the area of the island is fixed as 0.5π and $q_0 = 1$.

The aspect ratio $\lambda = b/a$ of the vortex patch, the vortex patch area Γ_1, and the circulation around the island Γ_0 are the three parameters determining the steady states. We

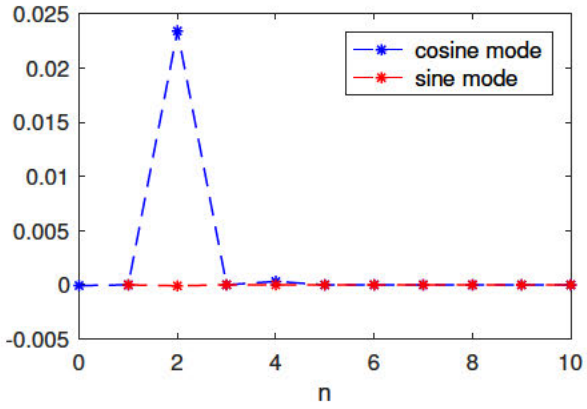

Figure 9: Mode decomposition of $\eta(\theta)$ of the steady solution computed by simulated annealing method for $n = 2$, $\Gamma_0 = \pi$.

set circulation around the island to be zero, and vary the other two parameters. Figure 10 shows the parameters used for this study.

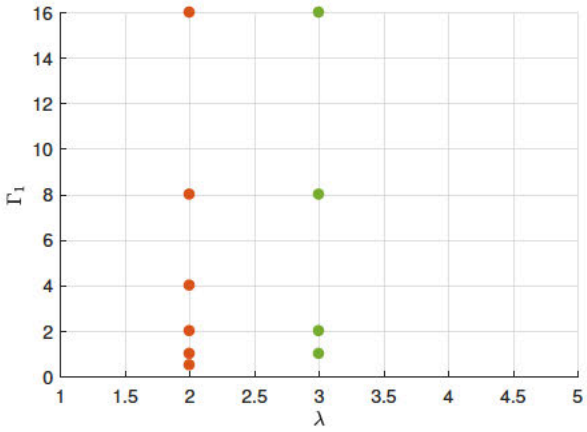

Figure 10: Filled circle points are parameters used for calculating steady states.

6.1 The effect of vortex area

Figure 11 shows the evolution of H_t under the symmetric bracket for $\lambda = 2$ and $\Gamma_1 = \pi$. H_t continuously decreases until reaching a very small value and then stays to that value. Due to numerical error, H_t can never reach exact zero. Figure 12 shows the evolution of the contour. The steady state contour is more similar to a circle than an ellipse, although the aspect ratio of the island is not close to 1.

Figure 13 shows that when the area of the vortex patch increases, the effect of the island on the steady state becomes smaller. For $\Gamma_1 \geq 2\pi$, the contour is already indistinguishable from a circle.

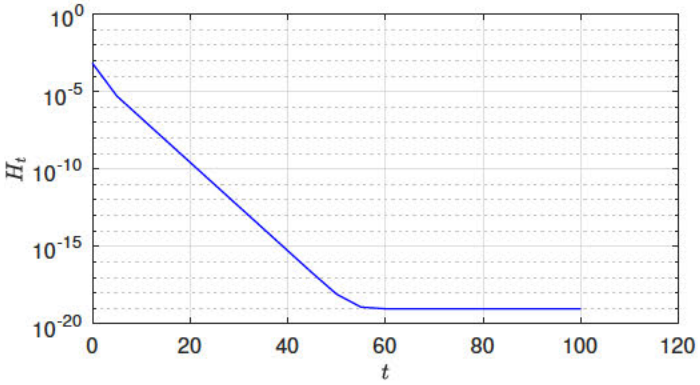

Figure 11: The time evolution of H_t for $\Gamma_1 = \pi$.

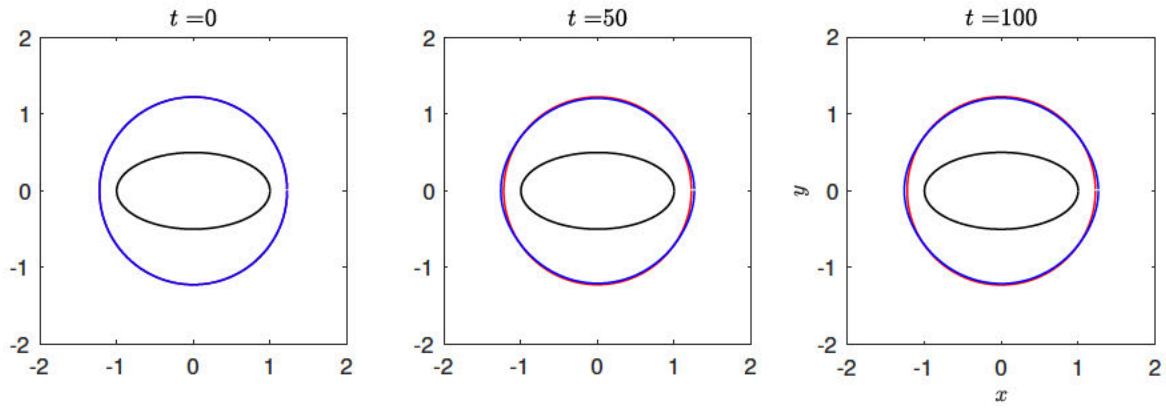

Figure 12: The evolution of the contour (blue) around an elliptic island (black) for $\Gamma_0 = 0, \Gamma_1 = \pi$, $b = 0.5$. The red line is a circle with the same area centered at the origin.

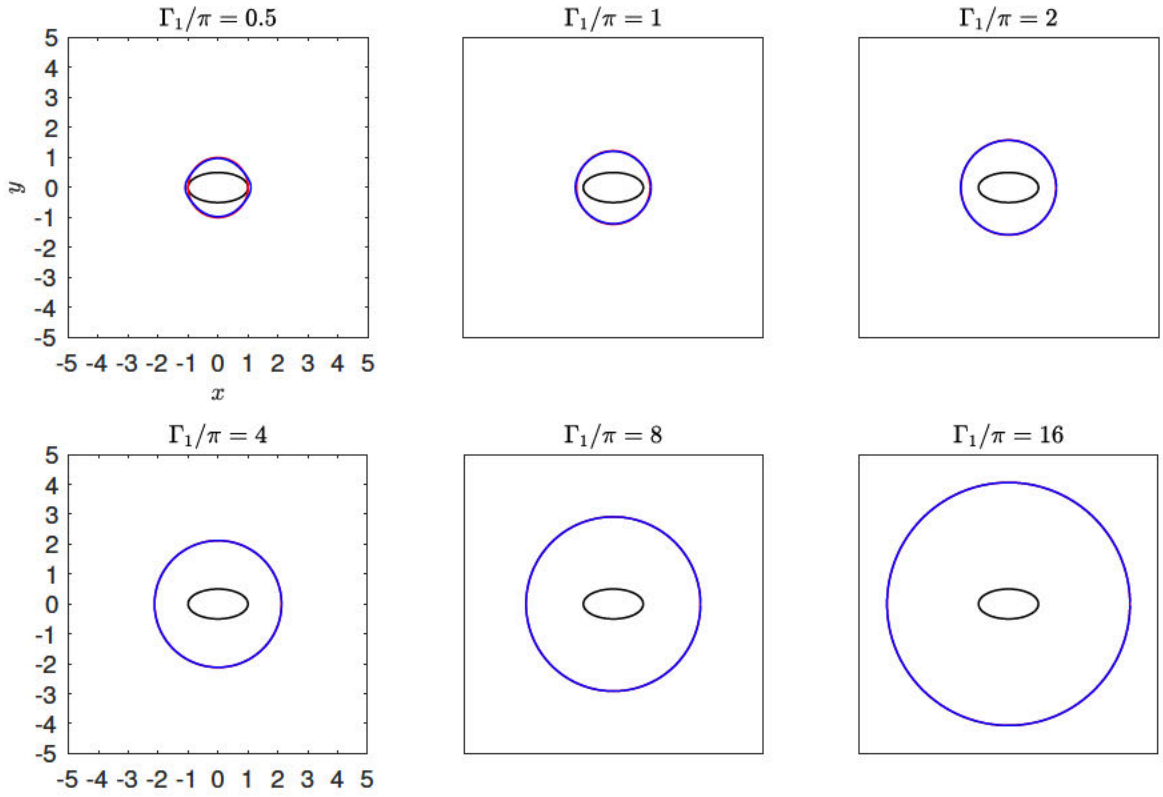

Figure 13: Steady states for aspect ratio $\lambda = 2$. The blue line is the steady state contour, and the red lines are circles with the area of the vortex patch.

6.2 The effect of aspect ratio

In the previous subsection, we have shown that the steady state is similar to an ellipse for a small vortex area. Figure 14 shows that the effect of an island is more significant for a larger aspect ratio for a fixed vortex area. This is consistent with our physical intuition. Similar to the results of $\lambda = 2$, when the vortex area is sufficiently large, the steady state is indistinguishable from a circle.

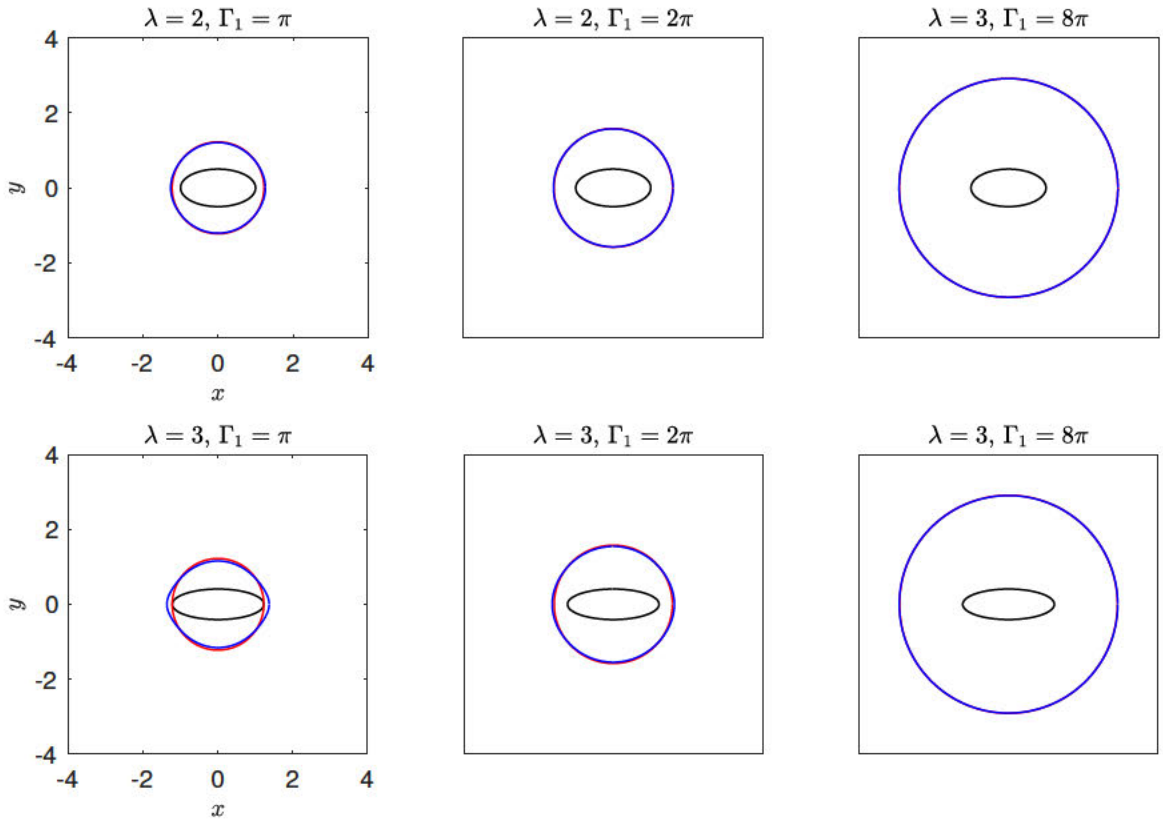

Figure 14: Steady states for aspect ratio $\lambda = 2, 3$ and $\Gamma_1 = \pi, 2\pi, 8\pi$.

7 Linear Stability Analysis

7.1 Methods

We introduce coordinate system (ξ, θ) where $\xi = (x^2 + y^2)/2$ and $\theta = \arctan(y/x)$. The definition of η is different from that of previous sections. For this coordinate $\frac{\partial(\xi,\theta)}{\partial(x,y)} = 1$. Let the contour of the steady state be $\xi = \xi_0(\theta)$. Suppose the perturbed contour is $\xi = \xi_0(\theta) + \eta(\theta)$. We demand the perturbation conserves the area, i.e., $\int_0^{2\pi} \eta(\theta) d\theta = 0$, thus η can be written as a Fourier series with zero mean.

Since $\xi = \xi_0(\theta) + \eta(\theta, t)$ is a material line, we have

$$\frac{\partial}{\partial t}\eta(\theta,t) + \frac{\partial(\psi, \xi_0(\theta) + \eta(\theta,t) - \xi)}{\partial(x,y)} = 0. \tag{95}$$

Using $\frac{\partial(\xi,\theta)}{\partial(x,y)} = 1$, the equation above in the transformed coordinate becomes,

$$\frac{\partial}{\partial t}\eta(\theta,t) + \frac{\partial(\psi, \xi_0(\theta) + \eta(\theta,t) - \xi)}{\partial(\xi,\theta)} = 0. \quad \text{at} \quad \xi = \xi_0(\theta) + \eta(\theta,t). \tag{96}$$

Define $U = -\partial_\theta \psi$, and $V = \partial_\xi \psi$. Then the linearized equation of 96 becomes

$$\partial_t \eta + V(\xi_0(\theta),\theta)\partial_\theta \eta + \partial_\xi^2 \psi(\xi_0,\theta)\eta \frac{d\xi_0}{d\theta} + \partial_\xi \partial_\theta \psi(\xi_0,\theta)\eta = 0. \tag{97}$$

Denote this equation by $\partial_t \eta = L\eta$.

Let $U_1 = U(\xi_0 + \eta, \theta)$, $V_1 = V(\xi_0 + \eta, \theta)$,$U_0 = U(\xi_0, \theta)$, $V_1 = V(\xi_0, \theta)$, then

$$U_1 - U_0 = -\partial_\xi \partial_\theta \psi(\xi_0,\theta)\eta + O(\eta^2), \quad V_1 - V_0 = \partial_\xi^2 \psi(\xi_0,\theta)\eta. \tag{98}$$

Therefore, we can approximate the linear operator L as

$$L\eta = -V_0 \partial_\theta \eta - (V_1 - V_0)\frac{d\xi_0}{d\theta} + (U_1 - U_0) + O(\eta^2). \tag{99}$$

Substituting $\eta(\theta,t) = \sum_{n\geq 1} a_n \cos(n\theta) + \sum_{n\geq 1} b_n \sin(n\theta)$ into the linear dynamics, we have

$$\sum_{n\geq 1} \frac{da_n}{dt}\cos(n\theta) + \sum_{n\geq 1}\frac{db_n}{dt}\sin(n\theta) = \sum_{n\geq 1} a_n L(\cos(n\theta)) + \sum_{n\geq 1} b_n L(\sin(n\theta)). \tag{100}$$

Projecting on each mode leads to

$$\frac{da_m}{dt} = \sum_{n\geq 1} a_n \frac{1}{\pi}\int d\theta \cos(m\theta) L(\cos(n\theta)) + \sum_{n\geq 1} b_n \frac{1}{\pi}\int d\theta \cos(m\theta) L(\sin(n\theta)). \tag{101}$$

We define four $N \times N$ matrices $M^{1,1}, M^{1,2}, M^{2,1}, M^{2,2}$ and two vectors (a_n) and (b_n) such that

$$(a_n) = M^{1,1}(a_n) + M^{1,2}(b_n), \quad (b_n) = M^{2,1}(a_n) + M^{2,2}(b_n). \tag{102}$$

The element $M^{1,1}_{m,n}$ is the projection of $L(\cos(n\theta))$ on $\cos(m\theta)$, $M^{1,2}_{m,n}$ is the projection of $L(\sin(n\theta))$ on $\cos(m\theta)$. We use the right hand side of equation 99 to approximate $L(\cos(n\theta))$ and $L(\sin(n\theta))$; indeed, we perturb the steady state contour by $\varepsilon\eta$ and compute the right hand side of equation 99 to approximate $L(\cos(n\theta))$ and divide the result by ε.

In general, we can write the evolution equation of (a_n) and (b_n) into one equation, i.e. $A_t = \pm MA$, where $A_m = a_m$ for $1 \leq i \leq N$ and $A_m = b_{i-m}$ for $N+1 \leq i \leq 2N$, and

$$M = \begin{bmatrix} M^{1,1} & M^{1,2} \\ M^{2,1} & M^{2,2} \end{bmatrix}. \tag{103}$$

The system is stable when the eigenvalue is negative or complex with nonpositive real part.

For elliptic islands, by symmetry, $M^{1,1} = 0$ and $M^{2,2} = 0$. Hence, we have

$$\frac{d^2a}{dt^2} = M^{1,2}M^{2,1}a, \quad \frac{d^2b}{dt^2} = M^{2,1}M^{2,1}b. \tag{104}$$

If both $M^{1,2}$ and $M^{2,1}$ are invertible, $M^{1,2}M^{2,1}$ and $M^{2,1}M^{2,1}$ share eigenvalues and eigenvectors of the two matrices are related. In that case, it suffices to calculate the eigenvalue of $M^{1,2}M^{2,1}$ or $M^{2,1}M^{2,1}$ to examine the stability of the steady states.

7.2 Results

For all the steady states computed, $M^{1,2}$ and $M^{2,1}$ are invertible. Moreover, there is only positive eigenvalue for $M^{1,2}M^{2,1}$ or $M^{2,1}M^{2,1}$. Figure 15 (a) shows the eigenvector of $M^{1,2}M^{2,1}$ (consine modes) for $\Gamma_1 = 0.5\pi$ and $\lambda = 2$. The eigenvector only projects on odd modes, which is likely to be related to the steady state and island project only on even modes. Moreover, the eigenvector is dominant by mode 1. Thus, the instability mechanism is likely to be a triad instability. The exploration of the mechanism is the subject of future studies.

Figure 15 (b) shows that for a fixed aspect ratio of the island, the growth rate (the positive eigenvalue) of the eigenmode decreases with the vortex area Γ_1. This is consistent with physical intuition since when the vortex patch becomes larger, the shape of the island becomes less important. However, the growth rate seems to have a long tail of decaying, suggesting that growth rate is never zero. Exploring this phenomena and finding the stability boundary are subjects for future studies. For a fixed vortex area, the growth rate for $\lambda = 3$ is larger than that for $\lambda = 2$. This is consistent with the Kirchhoff vortex being unstable for large aspect ratio.

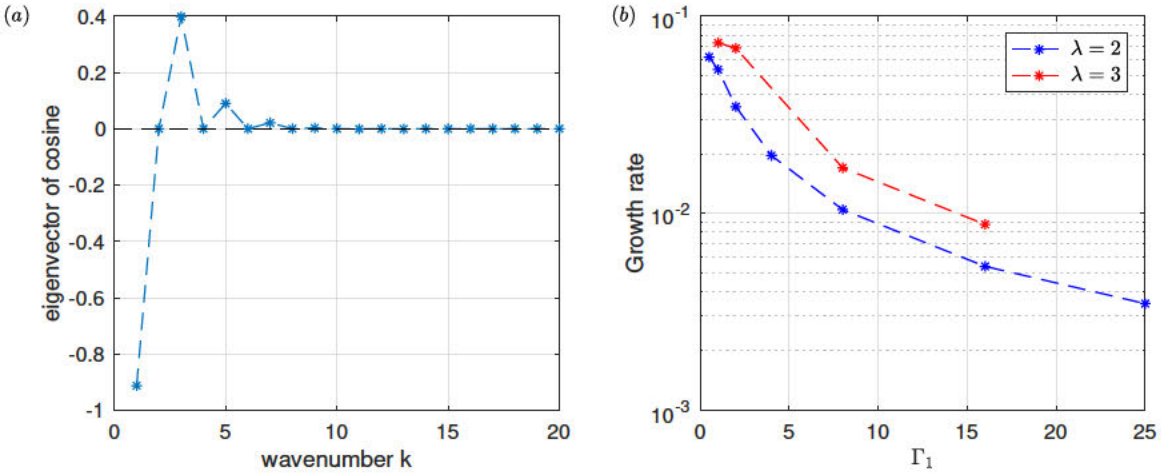

Figure 15: (a) Eigenvector of $M^{1,2}M^{2,1}$ for $\Gamma_1 = 0.5\pi$, $\lambda = 2$. (b)The growth rate of the eigenmode perturbation. 10.

We verify the linear stability analysis results by perturbing the steady states by mode 1 perturbation with amplitude being 5e-4, and evolving the contour using the nonlinear contour dynamics code. Figure 16 (a) shows odd modes other than mode 1 are excited

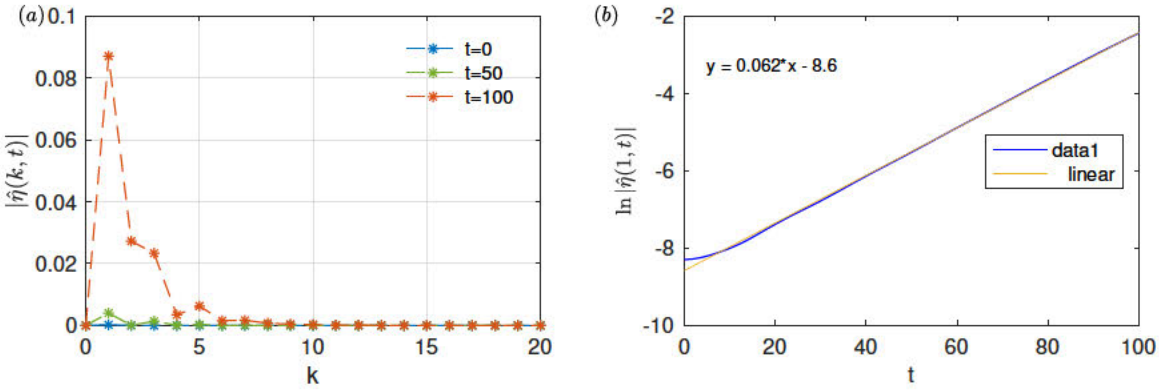

Figure 16: $(a)|\hat{\eta}(k,t)|$ at $t = 0, 50, 100$. (b) The evolution of mode 1 $ln|\hat{\eta}(1,t)|$ (blue line) and a linear fitting (yellow line).

and mode 1 dominates the spectrum, which is consistent with the linear stability results. Mode 4 is also slightly excited probably due to nonlinear effects. Figure 16 (b) shows the evolution of mode 1. Mode 1 starts to grow approximately exponentially after a short time. The fitted growth rate 0.062 is the same as the growth rate predicted by the linear stability analysis. Although the flow should be nonlinear at the end of the simulation, the mode 1 is still growing approximately exponentially. Figure 17 shows that vortex patch shifts to the upper right region of the island when it becomes unstable. This is consistent with mode 1 perturbation being dominant.

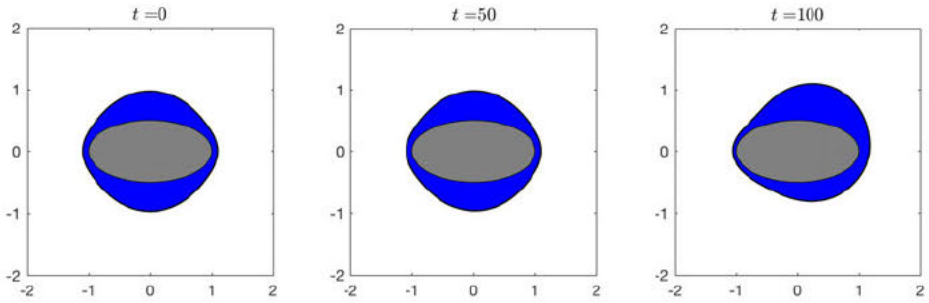

Figure 17: The evolution of the contour perturbed by mode 1 for $\Gamma_1 = 0.5\pi$, $\lambda = 2$. The gray shaded region is the island. The blue shaded region is the vortex patch.

Figure 18 (a) shows that η only consists of even modes when the steady state is perturbed by mode 2. This can be explained as following: since the evolution equation of η is nonlinear with quadratic terms and the steady state $\xi_0(\theta)$ consists of even modes only, odd modes are not generated by quadratic interaction. At $t = 100$, the amplitude of mode 2 is almost the same as its initial amplitude. Panel (b) shows mode 2 mainly oscillates and does not grow exponentially. The oscillation is related to the nonlinear interaction between modes. Therefore, we conclude instability cannot grow from mode 2 initial perturbation.

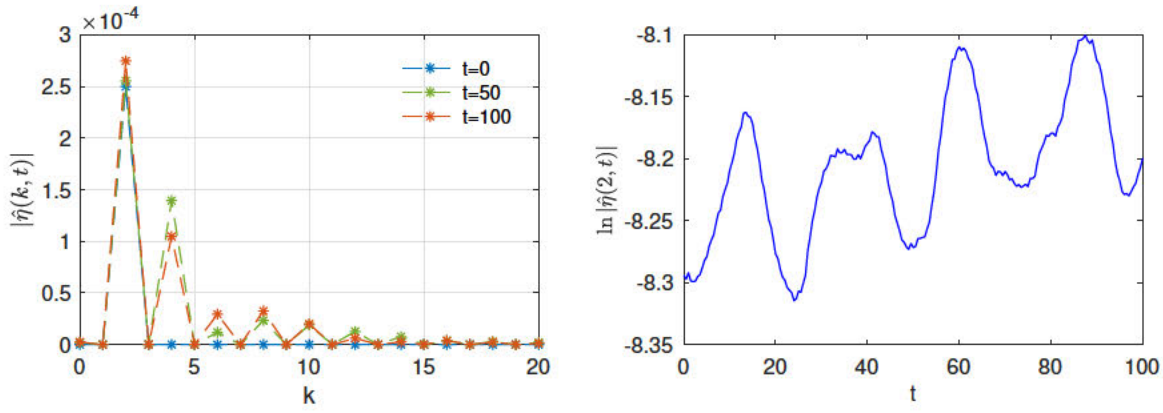

Figure 18: $(a)|\hat{\eta}(k,t)|$ at $t = 0, 50, 100$. (b) The evolution of mode 1 $ln|\hat{\eta}(2,t)|$ (blue line) and a linear fitting (yellow line).

Finally, we compare the fitted growth rate with the growth rate predicted by linear stability analysis for $\lambda = 2$. Since the initial growth period of mode is not exponential, we only fit $|\hat{\eta}(1,t)|$ after the adjusting period. For $\Gamma_1 > 8\pi$, the fitted growth rate becomes sensitive on the choice of the period of time for linear fitting, thus the evolution of mode 1 is only fitted for $\Gamma_1 \leq 8\pi$. Figure 19 shows that the fitted growth rate collapses on the predicted growth rate by linear stability analysis.

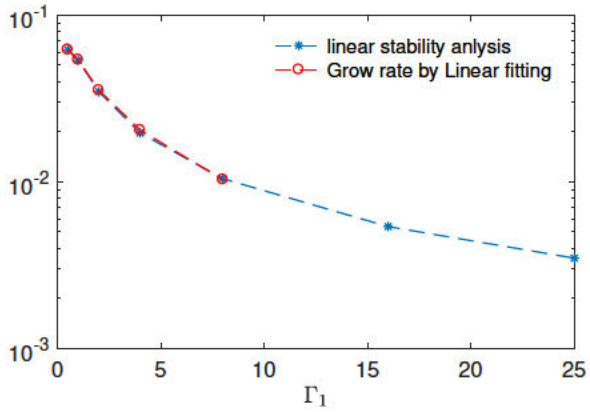

Figure 19: The predicted growth rate and the linear fitted growth rate for $\lambda = 2$.

8 Conclusions

Steady states around elliptic islands have been computed by contour dynamics simulated annealing method as a first step towards computing steady states around islands of any shape. The steady states around elliptic islands are similar to those around circular islands. Only when the aspect ratio of the islands is large or the area of the vortex is very small, the effect of the shape of the islands on the steady states becomes noticeable. Fourier analysis shows that the steady state containes nonzero azimuthal mode two.

The linear stability of steady states is analyzed and compared with fully nonlinear simulations by the contour dynamics code. When rotation symmetry of the island is broken, steady flow around a noncircular island can be unstable even with a single-signed radial vorticity gradient. Moreoever, the steady state is more unstable for a larger aspect ratio of elliptic islands and smaller vortex area, which is consistent with physical intuition.

9 Future Work

Since the contour dynamics simulated annealing method cannot find the steady state around a circular island when the initial contour is perturbed by mode one, it is likely that the contour dynamics code is not sufficiently accurate. In fact, the contour dynamics code involves some singularity related to the free space Green function and the layer potential method. Future work includes improving the accuracy of the contour dynamics code by integration by parts. An alternative approach is using an Eulerian approach and comparing the results by Eulerian approach with those obtained by the contour dynamics method.

All the steady states around elliptic islands in the report are shown to be unstable. However, the steady states should be stable when the vortex is sufficiently large. Thus, another future work is to find the stability boundary of steady states around elliptic islands in terms of the aspect ratio, vortex area, and circulation around the island. Futhermore, it would also be interesting to examine the steady states and stability around islands of other shapes.

Acknowledgements

I would like to thank my two advisors Glenn Flierl and Phil Morrison for their mentorship during the summer. Phil is a great teacher and gave me a clear and fascinating lecture on Hamiltonian system. Glenn's physical insights always turn out to be true, which makes me realize the importance of physical intuition. I would also like to thank the three directors Claudia Cenedese, Karl Helfrich, and Bruce Sutherland for organizing this year's summer school. Finally I would like to thank my advisor Oliver Bühler for recommending the summer school.

References

[1] V. I. Arnold, *A variational principle for three-dimensional steady flows of an ideal fluid*, in Vladimir I. Arnold-Collected Works, Springer, 1965, pp. 1–7.

[2] D. Colton, *Partial differential equations: an introduction*, Courier Corporation, 2004.

[3] G. Flierl and P. J. Morrison, *Hamiltonian–dirac simulated annealing: application to the calculation of vortex states*, Physica D: Nonlinear Phenomena, 240 (2011), pp. 212–232.

[4] G. R. Flierl, P. J. Morrison, and R. Vilasur Swaminathan, *Jovian vortices and jets*, Fluids, 4 (2019), p. 104.

[5] G. Hsiao and R. C. MacCamy, *Solution of boundary value problems by integral equations of the first kind*, SIAM Review, 15 (1973), pp. 687–705.

[6] Z. Kizner, V. Makarov, L. Kamp, and G. Van Heijst, *Instabilities of the flow around a cylinder and emission of vortex dipoles*, Journal of Fluid Mechanics, 730 (2013), pp. 419–441.

[7] C. Lin, *On the motion of vortices in two dimensions: I. existence of the kirchhoff-routh function*, Proceedings of the National Academy of Sciences of the United States of America, 27 (1941), p. 570.

[8] A. Love, *On the stability of certain vortex motions*, Proceedings of the London Mathematical Society, 1 (1893), pp. 18–43.

[9] P. J. Morrison, *Hamiltonian field description of two-dimensional vortex fluids and guiding center plasmas*, tech. rep., Princeton Univ., NJ (USA). Plasma Physics Lab., 1981.

[10] ——, *Poisson brackets for fluids and plasmas*, in AIP Conference proceedings, vol. 88, AIP, 1982, pp. 13–46.

[11] N. Muskhelishvili and J. Radok, *Singular integral equations: boundary problems of function theory and their application to mathematical physics.*, Courier Corporation, 2008.

[12] M. Rabinovich, Z. Kizner, and G. Flierl, *Bottom-topography effect on the instability of flows around a circular island*, Journal of Fluid Mechanics, 856 (2018), pp. 202–227.

REPORT DOCUMENTATION PAGE	1. Report No. WHOI-2025-12	2.	3. Recipient's Accession No.
4. Title and Subtitle 2019 Program of Study: Stratified Turbulence and Ocean Mixing Processes			5. Report Date December 2025 6.
7. Author(s) Claudia Cenedese, Bruce Sutherland, and Karl Helfrich			8. Performing Organization Rept. No. 10. Project/Task/Work Unit No.
9. Performing Organization Name and Address Woods Hole Oceanographic Institution			11. Contract(C) or Grant(G) No. (C) (G) OCE-1829864
12. Sponsoring Organization Name and Address National Science Foundation Program Manager Dr. Baris M. Uz 15 Eisenhower Avenue Alexandria, VA 22314			13. Type of Report & Period Covered Technical Report 14.

15. Supplementary Notes

This report should be cited as: Woods Hole Oceanographic Institution Technical Report, WHOI-2025-12 https://doi.org/

16. Abstract (Limit: 200 words)

The 2019 Geophysical Fluid Dynamics Summer Study Program theme was Stratified Turbulence and Ocean Mixing Processes. Two principal lecturers, Stephanie Waterman (University of Victoria) and Colm-cille Caulfield (University of Cambridge), were our expert guides for the first two weeks. Colm covered the theoretical aspects of stratified turbulence, from simple scaling laws to sophisticated, modern numerical results. Stephanie kept the enthusiastic audience grounded with her lectures on ocean mixing processes, observations, and their many technical challenges.

17. Document Analysis

a. Descriptors

Geophysical fluid dynamics,
Stratified Flows,
Ocean Mixing Processes

b. Identifiers/ Open-Ended Terms

c. COSATI Field/ Group

18. Availability Statement	19. Security Class (This Report)	21. No. of Pages
Approved for public release, distribution unlimited	20. Security Class (This Page)	22. Price